

MICROBEAM ANALYSIS

1981

Roy H. Geiss, *Editor*

Proceedings of the 16th Annual Conference
of the
Microbeam Analysis Society
Vail, Colorado, 13-17 July 1981



San Francisco Press, Inc.

547 Howard Street, San Francisco, California 94105

PUBLISHER'S NOTICE

Proceedings of the Annual Conference of the Microbeam Analysis Society are published in hard covers starting with the 14th (1979). Back copies are available from San Francisco Press at \$25 each. Spiral-bound copies of the 1974, 1975, 1976, and 1978 *Proceedings* are also available from San Francisco Press, at \$20. The 1977 issue is out of print, but selected papers from that meeting (held in conjunction with the 8th International Conference on X-ray Optics and Microanalysis) have been published in full length, in hard covers, and are available as a separate publication at \$90.

San Francisco Press is also the publisher of the *Proceedings of the 1981 Workshop on Analytical Electron Microscopy* (\$25) and of L. L. Marton's classic *EARLY HISTORY OF THE ELECTRON MICROSCOPE* (\$3.50) in hard covers.

Printed in the U.S.A.

ISSN 0146-6725

Table of Contents*

Officers of the Microbeam Analysis Society (1981).	vi
Sustaining members' information.	vii
1. SCANNING ELECTRON MICROSCOPY.	1
†Newbury: Characteristics of backscattered electron detectors for SEM	1
†Morris: Type-2 magnetic contrast: Applications to observing domains in magnetic materials	9
†Davidson: Backscattered electrons in the SEM: Techniques and uses in metallurgy.	17
†Beall: The application of electron beam induced current.	24
2. COMPUTER APPLICATIONS	30
†McCarthy, Fritz, Lee: Acquisition, storage, and display of video and x-ray images.	30
†Smith, McGuire: Signal processing techniques in Auger electron spectroscopy.	35
Chambers: Digitally controlled x-ray mapping	43
Hamilton, Navapbour, Goetze: Automation system for qualitative and semiquantitative electron microprobe analysis	45
Couch, Gantz, Lusk, Lechene: Automation of electron-probe microanalysis with the use of microprocessor control.	49
Stott, Chatfield, Mérange: SEM-based automated fiber counting	53
Fritz, McCarthy, Lee: Interactive software for automated particulate analysis.	57
Blaha, Myklebust, Etz: Automation of NBS laser-Raman microprobe.	61
3. SPECIAL TECHNIQUES.	65
†Park: What's new about the secondary electron yield?	65
†Adar: Developments in Raman microanalysis.	67
Etz: Empirical quantitation in Raman microprobe analysis	73
†Doyle, Wing, Peercy: Nuclear microprobe analysis	79
Reed: Secondary-ion spectra of rare earths	87
Ramsey, Hausdorff: Applications of small-area infrared analysis to semiconductor processing problems.	91
Demoney: Surface analysis by ELS microprobe.	96
†Rosenkwaig: Thermal-wave electron microscopy	105
4. SEM APPLICATIONS.	109
Wilson, Beall, Echols: SEM voltage contrast techniques for the analysis of memory circuits	109
Piety, Miller, Evans, Silva: Investigation of gate shorts in CMOS devices by electron beam induced current and internal SEM probes.	113
Geiss, Sedgwick, Hanchett, Depp: Backscattered electron channeling contrast applied to laser-annealed polysilicon	119
Hembree, Jensen, Marchiando: Monte Carlo simulation of submicrometer linewidth measurements in the scanning electron microscope.	123
Wells: Calculation of Type-1 magnetic contrast in the scanning electron microscope	127
†Othmer, Hopkins: Use of a modulated SEM beam for solar cell diagnostics.	131
5. GEOLOGICAL APPLICATIONS	139
Ridley: A microprobe study of crystallization trends of feldspars in silicate liquids.	139
Quick, Chodos, Albee: Detection of small, systematic compositional variations in peridotite by electron microprobe point counting analysis (PCA) with an energy dispersive detector	143
Friel, Mitchell: Organic oxygen and sulfur analysis of various coal macerals	148
Nabelek, Langmuir, Bence: The polybaric history of Famous Basalt 527-1-1: Evidence from trace elements in olivine	151
Speer, Solberg: Petrography of the U-bearing minerals in granitic rocks.	155
Solberg, Abrecht, Hewitt: Graphical procedures for the refinement of electron microprobe analysis of fine-grained particles	160
Solberg, Craig: Chemical variations in gold from the Central Appalachians of Virginia.	163

*An Author Index appears on p. 378.

†Invited paper.

Mitchell, Ludi: SEM and chemical evaluation of coal ash and related erosion and corrosion from some Western coals	167
Berry, Annamalai, Analysis of ion exchange resin used in uranium solution mining: An SEM and EDS study.	171
6. QUANTITATIVE ANALYSIS—BULK	174
Brown, Packwood, Milliken: Quantitative electron probe microanalysis with Gaussian expression for $\phi(\rho z)$ curves	174
Newbury, Myklebust: Monte Carlo electron trajectory calculations of x-ray generation in tilted, solid specimens.	175
Miller: Determination of composition and thickness of zinc sulfide films doped with Cu and Mn, by means of electron probe data and Monte Carlo calculations	178
Konopka, Rez: Accuracy of peak-to-background method for quantitative analysis.	183
Russ, Hare: Characterization of heterogeneous polycrystalline materials.	186
Parker: Dependence of ZAF corrections on tilt and azimuth.	190
De Groot: Method of ZAF analysis in the SEM in cases in which the take-off angle is unknown.	195
Parker: Empirically determined dependence of effective take-off angle on tilt and azimuth	199
7. BIOMEDICAL APPLICATIONS	203
Coleman, Young, Wade: Role of intracellular membranes in transcellular calcium transport.	203
McConville: Ultrastructural examination of urinary and biliary calculi with proton-induced x-ray emission and x-ray microanalysis	206
Myers, Van, Warner: Ultrastructural distribution of sulfur in human hair	210
Bonventre, Rabito: Electron microprobe analysis of cultured (LLC-PK ₁) renal epithelial cells.	213
Ingram, Ingram, Nichols: An electron-probe adaptation for biology.	215
Ingram, Ingram: Simple microforge for picoliter pipet constrictions.	219
Perrins, Alben, Shpirt: SEM/EDX analysis of granular activated carbon from a water treatment facility	222
Waitzkin, Abraham: Effect of sterol structure on intracellular sodium and potassium in mycoplasma capricolum.	226
Gay, Rosenstiel, Van Duin: Investigation of fly ash particles with respect to the morphology and surface enrichment of matrix and trace elements.	229
Davidson, Gause: ZPS analysis of flyash changes due to guinea pig alveolar macrophage exposure.	237
8. MATERIALS APPLICATIONS.	241
+Garratt-Reed, Vander Sande, Imeson: Analytical electron microscopy at MIT.	241
Romig: Quantitative x-ray microanalysis of U-Nb alloys with the STEM	249
Gumz, Walsh: Cathodoluminescence image analysis technique for oxide inclusion classification of nickel-base superalloys	258
Lyman: Analytical electron microscopy of catalyst materials.	261
Landau, Riga, Justi, Goo: Rapid technique to determine extent of Pt-Si reaction in very thin films.	265
Kirkendall, Hannsen: Electron probe study of electrochemical corrosion of Ti/Pd/Ag contacts on Si.	269
DeNatale, Howitt: Investigation of in situ radiation damage to glass in electron microscope	273
McElfresh, Howitt: Electron microscopy of leached glasses.	276
Watari: Some analytical use of STEM for study of oxidation on metals	279
Votava: ASEM analysis of unfired ceramic compacts.	283
9. SURFACE STUDIES	287
+Katz: Applied surface analysis	287
Krohn: An alternative approach to the surface-excitation model in SIMS	296
+Rucklidge, Kilius, Gorton: Ultrasensitive SIMS with nuclear accelerator.	299
Lindfors, Black: Investigation of lithium gas reactions by AES and XPS	303

10. QUANTITATIVE ANALYSIS—THIN FILMS.	309
Glitz, Notis, Williams Goldstein: Considerations of x-ray absorption for STEM x-ray analysis of Ni Al foils.	309
Schreiber, Wims: Quantitative x-ray microanalysis thin film method with K-, L-, and M-lines.	313
Schreiber, Wims: Relative intensity factors for K-, L-, and M-shell x-ray lines. . . .	317
Fiori, Swyt, Gorlen: Application of the top-hat digital filter to a nonlinear spectral unraveling procedure in energy-dispersive x-ray microanalysis.	320
Zaluzec: On the geometry of the absorption correction for AEM.	325
Zaluzec: Propagation of errors in quantitative AEM microanalysis by XEDS and EELS. . .	329
Kerr, Titchmarsh, Boyes: Simple calculations of x-ray spatial distributions applied to high resolution microanalysis.	333
11. INSTRUMENTATION.	336
Furman, Evans: Direct-imaging laser mass analyzer.	336
Wittry: Prospects for room-temperature solid-state x-ray detectors in electron probe microanalysis	339
Recent developments in secondary ion mass spectrometry: A bibliography of SIMS, 1976-1980	342
Author index	378

Officers of the Microbeam Analysis Society (1981)

MAS Executive Council

President: James R. Coleman, University of Rochester
Past President: Oliver C. Wells, IBM Yorktown Heights, N.Y.
President Elect: Robert L. Myklebust, National Bureau of Standards
Treasurer: Mary C. Finn, Lincoln Laboratory
Secretary: Charles E. Fiori, Bldg. 13, Rm. 3W13, NIH, Bethesda, MD 20205
(301) 496-2599

Members at Large

Dale E. Newbury, National Bureau of Standards
Peter Statham, Link Systems Ltd., High Wycombe, England
David C. Joy, Bell Laboratories, Murray Hill, N.J.
Phillip B. DeNee, Inhalation Toxicology Research Institute
Constance K. Barsky, Owens-Corning, Granville, O.
Fred Schamber, Tracor Northern Inc., Middleton, Wis.

Honorary Members

L. S. Birks, Naval Research Laboratory
Raymond Castaign, University of Paris (Orsay)
I. B. Borovskii, Academy of Sciences, Moscow
Peter Duncumb, Tube Investments Research Laboratories, England
Gunji Shinoda, Osaka University
V. E. Cosslett, University of Cambridge

Sustaining Members' Information

AMRAY INC.

160 Middlesex Turnpike
Bedford, MA 01730

Contact: James Furlog, (617) 275-1400

Product Line: Manufacturer and distributor of scanning electron microscopes and a complete line of accessories.

Sales Offices:

George Russell, Gerald Cameron Jr., and Ken Benoit, Merchantsville, N.J., (609) 662-3922
Warren Johnson, Cleveland, Ohio, (216) 579-0035
Tom Levesque, Dallas, Tex., (214) 247-3542
Henry Levesque, Bedford, Mass., (617) 275-1400
Don Pollock, Lico, Inc., Bedford, Mass., (617) 275-8310
Dr. Bart Yatchmenoff, San Francisco, Calif., (415) 964-5900
Dr. Bart Yatchmenoff, Los Angeles, Calif., (714) 830-1332

BABCOCK AND WILCOX RESEARCH CENTER

Alliance Research Center
Box 835
Alliance, OH 44601

Contact: Alex S. Miller, (216) 821-9110, Ext. 360

Bausch & Lomb/ARL

Box 129
Sunland, CA 91040

Contact: Michael McCool, (213) 352-6011

Product Line: Nanolab scanning electron microscopes, SEMQ electron microprobe/SEM, image analyzers. Sequential and multichannel x-ray fluorescence systems, x-ray diffraction, sequential and multichannel inductively coupled plasma spectrometers, atomic emission spectrometers, instrument automation and data-handling systems.

Sales Offices:

Box 129, Sunland, CA 91040, (213) 352-6011
En Vallaire, CH-1024 Ecublens, Switzerland, 021/34 97 01
Richard C. Bailey, 5901 Christie Ave., Emeryville, CA 94608, (415) 654-5601
Robert A. Nesman, Box 1005, Woburn, MA 01801
Parker H. Brinkman, 905 West Hillgrove Ave., La Grange, IL 60524

CALIBER INC.

11735 Bowman Green Drive
Reston, VA 22090

Contact: Arthur Smith, (703) 471-1905

Product Line: Sales and service of energy dispersive x-ray microanalysis systems manufactured by Link Systems Ltd.

CAMBRIDGE INSTRUMENTS INC.

40 Robert Pitt Drive
Monsey, NY 10952

Product Line: Research scanning electron microscopes and accessories, research production beam microfabrication systems, image analysis equipment.

Contact: Peter W. Boutell, (914) 356-3331

Sales Offices:

Dick Harniman, Monsey, N.Y., (914) 356-3331
Don Nelson, Pittsburgh, (412) 561-0313
Mike Webber, Atlanta, (404) 926-9636
John Pong, California, (714) 893-1609
Jack Oltheten, Montreal, (514) 337-4343

CAMECA INSTRUMENTS, INC.

37 Brownhouse Road
Stamford, CT 06902

Contact: Barbara Alton, (203) 348-5252

Product Line: Electron probe analyzers, scanning electron microscopes, combination SEM/EMP instruments and ion mass analyzers. The IMS-3F, a new SIMS instrument, has the features of improved performance at a lower price. The new IMS is the only direct imaging instrument available. The CAMECA MBX is a flexible combination SEM/EMP with an extensive array of accessories.

Sales Offices:

Robert D. Boies, Box 262, Reedley, CA 93654, (209) 266-6372
Thomas Fisher, 37 Brownhouse Road, Stamford, CT 06902, (203) 348-5252

EDAX INTERNATIONAL, INC.

Box 135
Prairie View, IL 60069

Contact: Peter Blakeslee, (312) 634-0600

Product Line: Manufactures energy-dispersive x-ray analysis systems for x-ray microanalysis in SEMs, TEMs, and electron probes, as well as energy-dispersive x-ray fluorescence spectrometers. System configurations from basic qualitative to fully automated quantitative (with computer control and data processing) are available, including an automated WD/ED system with stage and spectrometer controls.

Sales Offices:

V. Balmer, 637 Sunnyside Rd., Vermilion, OH 44089, (216) 967-4148
E. Martin, Box 547, New Rochelle, NY 10802, (914) 576-3117
J. Moore, Box 2253, Boulder, CO 80306, (303) 443-3610

EG & G ORTEC

100 Midland Road
Oak Ridge, TN 37830

Contact: Michael J. Kirchoff or Tim Bates, (615) 482-4411, Ext. 500 or 501

Product Line: Energy-dispersive systems for electron optical microscopes of all types. Wavelength-dispersive system electronics. Backscattered electron detection systems.

Sales Offices:

Dick Tischler, 21360 Center Ridge Rd., Rm. 304, Cleveland, OH (216) 333-1244
Bob Bardorf, Box 3355, Oak Ridge, TN 37830, (615) 482-4411
Dave Butterfield, 29 Lumni Key, Bellevue, WA 98006, (800) 251-9732
Gene Embry, Box 631, Cary, NC 27511, (800) 251-9732
Dick Neiman, 21718 Rotherham Dr., Spring, TX 77379, (713) 353-0079
Joe Redmond, Box 6041, Boston, MA 02209, (800) 251-9732
Charles Thomas, 22971 Triton Way, Suite C, Laguna Hills, CA 92653 (714) 770-6434
Val Johnson, Box 1678, Boulder, CO 80306, (800) 251-9732
Peeter Kark, 500 West University Pkwy, #3H, Baltimore, MD (301) 948-6858
Earl Klugman, 310 Melvin Dr., Northbrook, IL 60062, (312) 498-5858

CHARLES EVANS & ASSOCIATES

1670 S. Amphlett Boulevard, Suite 120
San Mateo, CA 94402

Contact: Charles Evans or Richard Blattner, (415) 572-1601

GATAN, INC.

780 Commonwealth Drive
Warrendale, PA 15086

Contact: Terry Donovan, (412) 776-5260

Product Line: Designs and manufactures equipment for electron microscopy and surface analysis. The EM product range includes electron energy loss spectrometer (EELS); ion beam milling equipment; and specialized (S) TEM stages. For surface analysis and depth profiling a scanning ion microprobe (SIPS/SIMS) is available plus scanning ion beam systems for selective-area thinning and imaging.

GERHARD WITZSTOCK PUBLISHING HOUSE INC.

381 Park Avenue South, Suite 1123
New York, NY 10016

Contact: Monika Magid, (212) 686-7280

Product Line: Publishes *Scanning: International Journal of Scanning Electron Microscopy and Related Methods*. *Scanning* provides an international and interdisciplinary medium for the rapid exchange of information among all scientists interested in scanning electron microscopy. It publishes original scholarly papers of a practical nature, report-in new analytical, methodological, and specimen-preparation aspects of SEM.

HITACHI SCIENTIFIC INSTRUMENTS

460 E. Middlefield Road
Mountain View, CA 94043

Contact: Rod Norville

Product Line: Transmission and scanning electron microscopes and related accessories.

Sales Offices:

Ronald Lunn, Box 366, Princeton, MA 01541, (617) 756-5331
Morton Harloe, 1701 Golf Rd., Rolling Meadows, IL 60008, (312) 981-8750
Michael E. Mullen, 2909 Oregon Court, Unit B-3, Torrance, CA 90502, (213) 320-4738
Ronald E. McDuffie, K. Davis, and A. Sandler, 1383 Piccard Dr., Rockville, MD 20850, (301) 840-1650

INTERNATIONAL SCIENTIFIC INSTRUMENTS, INC.

3255-6C Scott Boulevard
Santa Clara, CA 95051

Contact: Robert Ruscica, (408) 727-9840

Product Line: Scanning electron microscopes with a full complement of accessories including WDX spectrometers. The ISI SEM line includes: Alpha-9, Super IIIA, ISI-40, ISI S-100B, and ISI DS-130. Also in the product line is our new light/transmission electron microscope, the ISI LEM-2000. A complete line of scanning electron microscopes suited for any application and budget.

Sales Offices:

Bill Maguire, Avon Park South, 20 Tower Lane, Bldg. 2, Avon, CT 06001, (202) 677-0016
Bud Bowen, 415 W. Golf Rd., Suite 37, Arlington Heights, IL 60005, (312) 437-7790
Lewis Rumppler, Santa Clara, Calif.
Mike Ivey, Los Angeles, Calif.
Richard Lois, 6655 Hillcroft, Suite 100, Houston, TX 77081, (713) 777-0321

JEOL U.S.A., INC.

11 Dearborn Road
Peabody, MA 01960

Contact: Drew Brown, (617) 535-5900

Product Line: Manufacturers and dealers of scanning electron microscopes, transmission electron microscopes, scanning transmission electron microscopes, electron probe micro-analyzers, scanning Auger microprobes, and energy loss analyzers.

Sales Offices:

John Bonnici, New Jersey, (201) 254-5600
Thayer Brickman, San Francisco, (415) 697-9220
Paul Enos, Texas, (817) 267-6011
Jack Francis, Ohio, (513) 232-7350
Thomas Gildea, Massachusetts, (617) 535-5900
Ray Gundersdorff, Maryland, (301) 953-2959
Jean-Pierre Slakmon, Canada, (514) 482-6427 (Soquelec, Ltd.)
Robert Steiner, Illinois, (312) 825-7164

KEVEX CORPORATION

1101 Chess Drive
Foster City, CA 94404

Contact: Henry S. Culver, (415) 573-5866

Product Line: Analytical systems for x-ray energy spectrometry, wavelength-dispersive x-ray spectrometry, Auger and electron energy spectrometry. Detector/cryostats and analytical spectrometer systems are compatible with all electron microprobe, scanning electron microscopes and transmission electron microscopes in current production. Systems are available for both qualitative and quantitative analysis.

Sales Offices:

Robert Johnson, 1101 Chess Dr., Foster City, CA 94404, (415) 573-5866
Dana Kelley, 46 Knollwood, West Hartford, CT 06110, (617) 256-4961
Blaise Fleischmann, 3974 Bonnington Ct. N.E., Atlanta, GA 30341, (404) 455-1694
Steven Miller, 602 S. Fairview, Park Ridge, IL 60068, (312) 398-1333
Frank Mannino, 769 Shadow Lake Dr., Thousand Oaks, CA 91360, (805) 495-1632
Aptec Engineering, 4251 Steeles Avenue West, Downsview, Ont., Canada M3N 1V7,
(416) 661-9722

KRISEL CONTROL, INC.

16 Farsta Court
Rockville, MD 20850

Contact: Christos Hadidiacos, (301) 762-1790

Product Line: Automation equipment for electron microprobe/microscope, featuring on-line data acquisition and reduction using Alpha and ZAF correction schemes. Single-crystal automation system for on line data collection, centering, calculation of orientation matrix, and refinement of cell parameters for an x-ray diffractometer.

WALTER C. McCrone Associates, INC.

2820 South Michigan Avenue
Chicago, IL 60616

Contact: Ian M. Stewart, (312) 842-7100

Product Line: Analytical services in disciplines such as pharmaceuticals, forensic sciences, contamination control, metallography, air and water pollution, painting and document authentication, and corrosion. Analytical tools available: electron and ion microprobes, TEM, SEM, EMMA, ESCA, XRD, XRF, GC-MS, IR-UV, FTIR, optical microscopy,

and MOLE, laser Raman microprobe. Instruments Division, McCrone Accessories and Components, range of instruments and accessories for light and electron microscopy.

MICRON INC.

Box 3536
Wilmington, DE 19807

Contact: James F. Ficca Jr., (302) 998-1184

Product Line: Scanning electron microscopy, electron spectroscopy, electron probe x-ray analysis, transmission electron microscopy, quantitative image analysis, x-ray diffraction, x-ray fluorescence, optical microscopy and metallography, micro hardness, optical emission spectroscopy, differential scanning calorimetry, ultra microtomy, sample preparation.

MICROSPEC CORPORATION

265-G Sobrante Way
Sunnyvale, CA 94086

Contact: Richard C. Wolf, 883 Lilac Lane, Los Altos, CA 94022, (415) 941-3057

Product Line: WDX-2A wavelength-dispersive x-ray spectrometer systems. X-ray microanalysis systems for use as accessories on scanning electron microscopes and other electron beam instruments. Capable of x-ray analysis of all elements down to beryllium, atomic number 4. Unique design permits attachment to most SEM electron columns.

PHILIPS ELECTRONIC INSTRUMENTS, INC.

85 McKee Drive
Mahwah, NJ 07430

Contact: Don Rodgers, (201) 529-3800

Product Line: The latest and most advanced scanning electron microscopes and transmission electron microscopes available.

Sales Offices:

Bruce Roberts, 1104 U.S. Highway 130, Suite A, Cinnaminson, NJ 08077, (609) 829-4454
Dennis Ahr, Clark Bldg., Suite 503, 5565 Sterrett Ave., Columbia, MD 21044, (301) 930-2100
Larry Williams, 7094 Peachtree Indust. Blvd., Suite 220, Norcross, GA 30071, (404) 449-7206
Ron Powley, 7525 Long Avenue, Skokie, IL 60077, (312) 676-1714
Harold Oemke or Harry Ittner, 3000 Scott Blvd.(S.113), Santa Clara, CA 95050, (408) 727-5333

PHYSICAL ELECTRONICS DIVISION OF PERKIN-ELMER CORP.

6509 Flying Cloud Drive
Eden Prairie, MN 55344

Contact: Robert C. Cargill, (612) 941-5540

Product Line: ESCA/Auger electron spectrometers, scanning Auger microprobes, thin-film analyzers, secondary ion mass spectrometers, specialized combination systems, and a broad range of components including electron energy analyzers, sputter-etching systems, specimen manipulators, x-ray generators, UV sources, and sample introduction stages. Also operates an analytical service laboratory for custom surface analysis.

Sales Offices:

Boston, New York, Washington, Pittsburgh, Chicago, Dallas, Minneapolis, Seattle, San Jose, and Los Angeles.

Contact Minnesota for local contact.

PRINCETON GAMMA-TECH

1200 State Road
Princeton, N.J. 08540

Contact: Stan Zeichner, (609) 924-8980

Product Line: X-ray energy dispersive microanalysis systems. An application laboratory and extensive program library.

Sales Offices:

Joe Piersante, Route 2, Box 50-A16, Gainesville, GA 30501, (404) 887-9100
Don Dunkin, 1200 State Road, Princeton, NJ 08540, (609) 924-7310
Denny Cannon, Box 36157, Denver, CO 80236, (303) 978-0786
Dick Stancher, 17756 Kings Park Lane, Houston, Tex.

QBI INTERNATIONAL

2034 Golden Gate Avenue
San Francisco, CA 94115

Contact: Quentin A. Brown, (415) 929-1622

Product Line: Signal processors for the scanning electron microscope and STEM. Video systems for the electron microprobe. X-ray systems for the electron microprobe. Crystals and detectors. Stage and goniometer drive systems. Computer control of the SEM or electron microprobe. Computerized data acquisition systems.

Sales Office:

Box 6A, Russell Road, Bloomington, IN 47401, (812) 336-6244

C. M. TAYLOR CORPORATION

Box 7087
Stanford, CA 94305

Contact: Dr. Charles M. Taylor, (408) 245-4229

Product Line: Various types of multi-element standards for microbeam analysis by SEM, microprobe, and ion probe using energy, wavelength, and mass spectrometers. The standards available exceed 135 different metals, alloys, or compounds. Bence-Albee standards are available. Also supply sample holders for ARL-EMX and ARL-EMX-SM stages and many types of sample holders and polishing jigs for sample preparation. Offer analytical services to customers desiring electron beam microprobe analysis, MAC-5 instrument.

M. E. TAYLOR ENGINEERING INC.

11506 Highview Avenue
Wheaton, MD 20902

Contact: M. E. (Gene) Taylor, (301) 942-3418

Product Line: Scintillators for SEMs and microprobes, backscatter and secondary electron detectors of the quartz light pipe/scintillator design. Other products include Brimrose image intensifiers, ISI filaments and apertures, specimen mounts and adhesive tabs.

Sales Offices:

Agar Aids, 66A Cambridge Rd., Stansted, Essex, England OM24 8DA
Science Services, Badstr. 13, D-8000 München 70, Federal Republic of Germany

TECHNICS EMS INC.

7950 Cluny Court
Springfield, VA 22153

Contact: Diane Hurd or Robert Barr, (703) 569-7200

Product Line: Secondary ion mass spectrometers and electron energy loss spectrometers.
Preparation and peripheral equipment for the electron microscope.

Sales Offices:

1754 Junction Avenue, San Jose, CA 95112
Milhertshotener-Str. 8, 8000 Munich 40, Federal Republic of Germany

TRACOR NORTHERN

2551 West Beltline Highway
Middleton, WI 53562

Contact: Tyler North, (608) 831-6511

Product Line: Wide range of data processing instrumentation for qualitative and quantitative x-ray analysis. Products include data acquisition, reduction, and automation for electron microprobe, SEM, TEM, and STEM. Featuring simultaneous EDS/WDS acquisition/reduction, digital beam control allowing for digital mapping, line scans, and other digital image processing. And now particle location, sizing, and elemental characterization. Flexible packaging allows instrument to be also used for ELS, Auger, ESCA, SIMS, etc. Other products are used in nuclear, optical, signal-averaging, and medical applications.

Sales Offices:

Suite 260, 2425 Bisso Lane, Concord, CA 94520, (415) 825-8190
Technical Instrument Co., Suite 106, 4215 Beltwood Parkway, Dallas, TX 75234,
(214) 387-0606
Scientific Systems Sales Corp., 6901 Jericho Turnpike, Syosset, NY 11791, (516) 921-3737
Contemporary Science, Inc., Box 205, 500 E. Northwest Highway, Mt. Prospect, IL 60056,
(312) 255-3793
Pulcir, Inc., Box 357, Oak Ridge, TN 37830, (615) 483-6358
Tremby Associates, 119 Quincy NE, Albuquerque, NM 87108, (505) 266-8616
EMCAR Marketing, Inc., 8041 W. I-70 N. Service Rd., Arvada, CO 80002, (303) 424-0108
Allan Crawford Associates, Ltd., 6503 Northam Dr., Mississauga, Ont., Canada L4V 1J2,
(416) 678-1500
Alva Nuclear, SA, Apartado Postal 12-626, Mexico 12, D.F., Mexico 5167454
Tracor Europa, B. V., Schiphol Airport Amsterdam, Bldg. 106, P. O. Box 7553, Amsterdam,
The Netherlands, (020) 41-1865
Also representatives in: Great Britain, West Germany, France, Japan, India, Malaysia,
Taiwan, Singapore, Thailand, Australia, Argentina, and Brazil.

TRACOR X-RAY INC.

Box 1389
1400 D Stierlin Road
Mountain View, CA 94042

Contact: William D. Stewart, (415) 969-9400

Product Line: Automated x-ray analysis systems, including x-ray tube excited and source excited; Si(Li) x-ray detection systems for use on scanning electron microscopes, transmission electron microscopes, and electron microprobes; Si(Li) x-ray detectors for basic research; and portable x-ray spectrometers.

Sales Offices:

The Buhrke Company, 2180 Sand Hill Road, Menlo Park, Calif., (415) 854-5629
International Instrument Corp., 64 E. Main St., Marlton, N.J., (609) 983-6550
Instruments and Technology, 220 E. 14th St., Naperville, Ill., (312) 355-7748
North Eastern Analytical Corp., 17 Sherman Rd., Millis, Mass., (617) 376-4132
Technical Instrument Co., 4215 Beltwood Pkwy., Suite 106, Dallas, TX 75234
Pulcir, Inc., Box 357, Oak Ridge, TN 37830, (615) 483-6358

Scanning Electron Microscopy

CHARACTERISTICS OF BACKSCATTERED ELECTRON DETECTORS FOR SCANNING ELECTRON MICROSCOPY

D. E. Newbury

The imaging signal used most frequently in scanning electron microscopy in past years has been derived from secondary electrons, augmented with a small but significant backscattered electron component, and detected with an Everhart-Thornley scintillator-photomultiplier detector. With this detector, useful images of rough objects can be readily obtained with the composite secondary and backscattered electron signal. The images can be easily interpreted as to the sense of the topography of the specimen in most cases, because of the existence of a close analogy between the apparent illumination in the SEM image and the top illumination which exists in ordinary visible-light illumination of large objects.¹ Over recent years, the pure backscattered electron signal has been recognized as a rich source of information that reveals many interesting characteristics of the specimen and forms a valuable complement to the normal secondary-electron image. Contrast effects due to compositional differences, crystallographic effects, magnetic structure, and topography can be obtained in the backscattered-electron signal.² The utilization of the backscattered-electron signal has been encouraged by the development of a variety of high-performance backscattered-electron detectors. In fact, there is now such a variety of detectors that the microscopist may be bewildered at the choice. In this survey, the major types of backscattered electron detectors are described and compared.

Properties of Backscattered Electrons

The characteristics of an appropriate detector for backscattered electrons are determined by the particular properties of the signal we want to measure. The backscattered-electron signal is modified in the following ways by the properties of the sample to produce contrast in an image.

1. *Number Effects.* The total number of electrons backscattered from the sample varies as a function of atomic number (Fig. 1), sample tilt (Fig. 2), and internal magnetic fields.³

2. *Energy Effects.* Because of energy loss due to inelastic scattering within the specimen, backscattered electrons emerge from the sample with an energy range from 0 to E_0 , the incident beam energy (Fig. 3). The loss in energy which a beam electron suffers prior to escaping the specimen is a direct measure of the distance traveled within the sample. The energy spectrum varies with the atomic number of the specimen, with the tilt, and with the take-off angle above the surface at which the spectrum is measured.⁴

3. *Trajectory Effects.* Backscattered electrons emerge from the specimen with a distinct angular distribution. For normal beam incidence (0° tilt), the angular distribution is in the form of a cosine function relative to the surface normal; for highly tilted specimens, the angular distribution is sharply peaked in the forward scattering direction (Fig. 4).

Contrast information may be present in any or all of these three properties of the backscattered electrons. All available detectors are sensitive to number effects. Angular and energy distribution effects can be measured with certain detectors, but generally with less specificity. For detecting angular effects, the critical parameters are the take-off angle of the detector, the solid angle of collection, and the detector location relative to the specimen and beam.

Types of Backscattered Electron Detectors

Backscattered electron detectors commonly in use fall into four categories: (1) scintillators, (2) secondary-electron conversion with detection by a biased scintillator, (3) solid-state diodes, and (4) specimen current. The major properties discussed below are summarized in Table 1.

The author is with the Center for Analytical Chemistry, National Bureau of Standards, Washington, DC 20234.

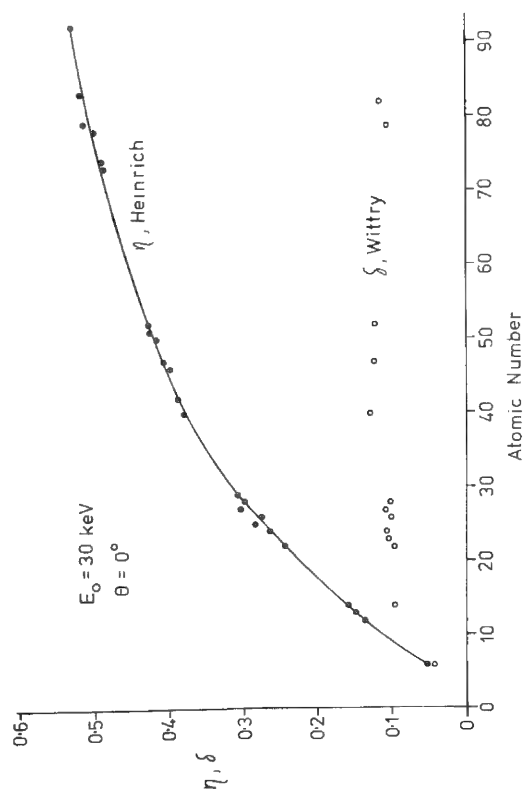


FIG. 1.--Backscattered-electron coefficient η vs atomic number, at beam energy of 30 keV and 0° tilt.¹

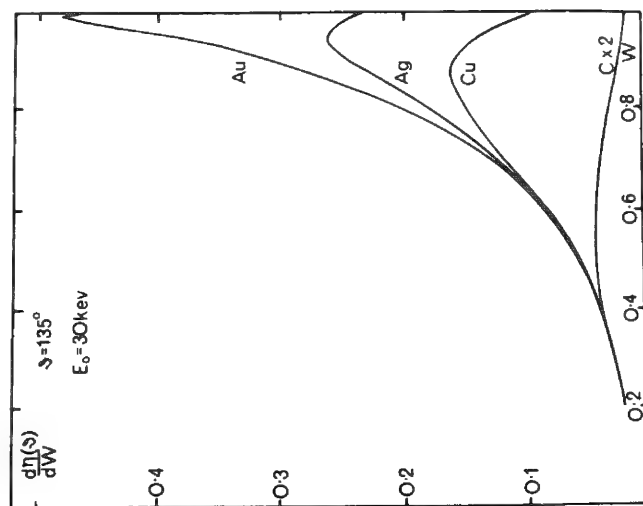


FIG. 3.--Energy distribution of backscattered electrons at emergence angle of 45° ; beam energy, 30 keV; 0° tilt.⁴

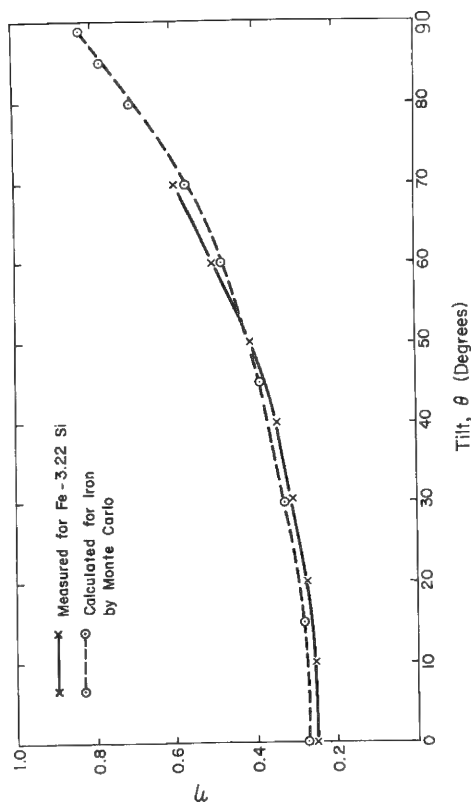


FIG. 2.--Backscattered electron coefficient η vs specimen tilt at beam energy of 30 keV; sample iron-3.22 silicon.¹

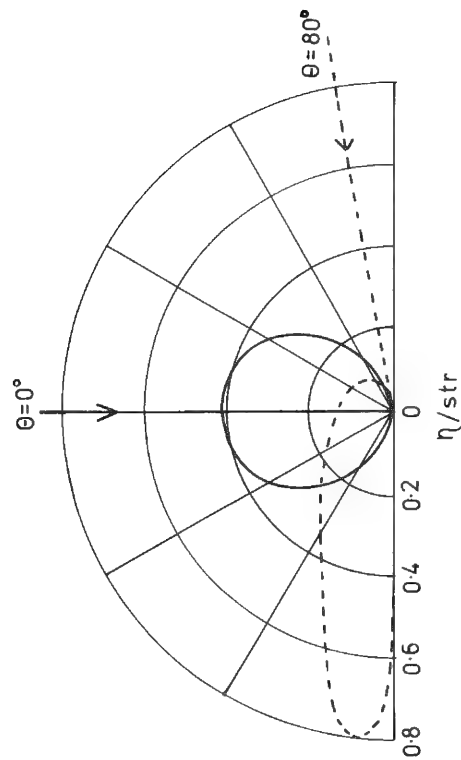


FIG. 4.--Angular distribution of backscattered electrons at 0° and 80° tilt.¹

TABLE 1.--Characteristics of backscattered electron detectors.

Type	Solid Angle steradians	Trajectory Contrast	Energy Response	Maximum Scan Speed
Scintillator (Everhart - Thornley)	0.05	Yes	Positive	TV
Scintillator (modified large face Everhart - Thornley)	0.5-1	Yes	Positive	TV
Scintillator (Robinson)	$\pi - 2\pi$	No	Positive	TV
Scintillator (Wells low loss)	0.05	Yes	Energy selecting	1 f/s
Scintillator Array	π	Selectable	Positive	TV
Conversion	π	No	Negative	TV
Solid state (solar cell)	0.5	Yes	Positive	1 f/s
Solid state (annular)	π	No	Positive	1 f/s (TV)
Solid state (array)	π	Selectable	Positive	1 f/s
Specimen Current	2π (equivalent)	No	None	1 f/s

Scintillator Detectors

Everhart-Thornley Detector. The Everhart-Thornley detector commonly available in the SEM (Fig. 5) detects backscattered electrons under all bias conditions.⁵ If the Faraday cage bias is negative or the accelerating potential is reduced to zero, the detector is completely insensitive to secondary electrons. Energetic backscattered electrons can still excite the scintillator. Electrons scattered into the solid angle of the detector contribute to the signal, with only a minor component of backscattered electrons collected after re-scattering from the walls of the specimen chamber. Because of the small solid angle of collection and the low take-off angle relative to an untilted specimen, the detector is highly directional and has poor collection efficiency. The solid angle is of the order of 0.05 sr. The scintillator has a positively sloped energy response and produces an increasing signal with increasing electron energy.

With the Everhart-Thornley detector operating in its usual mode for secondary electrons, i.e., a positive bias on the Faraday cage (e.g., +300 V) and an accelerating bias on the scintillator (+10 kV), additional backscattered electrons are detected indirectly through collection of secondary electrons which are generated when electrons backscattered from the specimen strike the walls of the sample chamber. This process increases the ef-

fective solid angle of collection, although an exact calculation is difficult and depends on the collection bias and chamber configuration and materials. Of course, the signal also contains a large component of secondary electrons produced directly at the specimen, which makes interpretation of the backscattered electron component of the signal difficult. All scintillator-photomultiplier systems have the advantage of a wide frequency response, which allows scanning at television rates.

Large-angle Scintillator. The simplest modifications to the Everhart-Thornley detector to improve its performance for backscattered electron imaging are to increase the physical size of the scintillator and to remove the Faraday cage to provide a larger solid angle of collection (Fig. 6).^{6,7} Depending on the size and the specimen-to-detector distance, an improvement of an order of magnitude in solid angle is possible. The detector is still asymmetrically placed relative to the beam, but its larger size reduces the sensitivity to trajectory effects somewhat. Secondary electrons can still be collected by application of a +10kV bias to the scintillator to serve both as a collection and accelerating potential. However, the presence of an unshielded high-voltage field in the sample chamber can cause astigmatism in the electron beam, which may limit the approach of the detector to the specimen. Proper selection of the scintillator is necessary to obtain adequate gain and resistance to degradation under bombardment by energetic electrons.⁸ Calcium fluoride doped with europium provides good efficiency, rapid decay of excitation, and high resistance to degradation, and is readily available in large diameters.

Symmetric Large-angle Scintillator. A further gain in collection angle can be realized if the scintillator is placed directly over the specimen (Fig. 7).⁹ Depending on the dimensions, the solid angle may approach 2π sr. The detector is now symmetric relative to the beam and is much less subject to trajectory contrast effects at normal beam incidence, such as those which dominate topographic contrast. At normal incidence, this detector is best suited to detecting number effects, such as atomic number contrast and the number component of topographic contrast. Because of the location of the detector above the sample, the sample should not be tilted, unless one wants to gain sensitivity to trajectory contrast effects by creating an effective asymmetry.

Low-loss Detector. Wells has described a special detector for "low-loss" backscattered electrons which is useful for imaging at extremely high spatial resolution, of the order of 5 nm, and with great surface specificity, of the order of 3 nm in depth.¹⁰ Backscattered electrons that exit from the sample with an energy within 1% of that of the incident beam are necessarily restricted to very short path lengths in the sample because the rate of energy loss due to inelastic scattering is high. These low-loss backscattered electrons thus carry information that is restricted both to the immediate lateral area of the beam impact and to a shallow surface layer. Wells has demonstrated both high lateral resolution from bulk specimens as well as true surface microscopy.¹¹ The low-loss electron detector consists of a conventional scintillator-photomultiplier system with a negatively biased grid placed between the detector and specimen to provide energy selection (Fig. 8). By adjusting the grid bias, one can vary the energy fraction of electrons accepted. The low-loss image is especially sensitive to trajectory effects; as a result, topographic contrast is extremely strong.

Conversion Detector

A second method to increase the solid angle of collection of the conventional Everhart-Thornley detector for backscattered electrons is to make use of the secondary electrons generated by the backscattered electrons which miss the detector but strike the chamber walls (backscatter-to-secondary conversion).^{12,13} To eliminate the secondaries generated at the specimen itself from the imaging signal, a grid is placed above the sample and biased negatively. The backscattered electrons pass through the grid openings unaffected, strike the chamber walls and final lens polepiece, and generate secondaries (Fig. 9). These secondaries are collected by the positive bias on the Faraday cage of the Everhart-Thornley detector. To improve the signal further, a material with a high secondary electron coefficient, such as MgO, can be placed on the final lens polepiece in close proximity to the specimen. The normal secondary-plus-backscattered electron image can be obtained when the bias is removed from the grid around the specimen. Since the secondary-

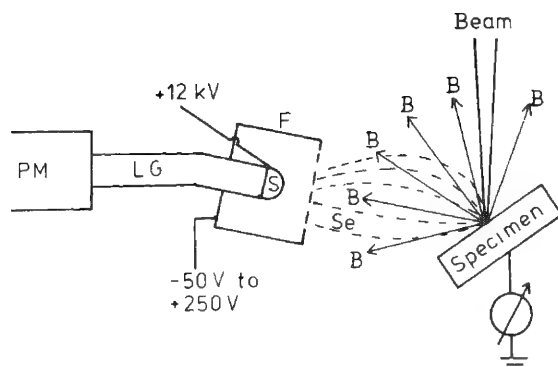


FIG. 5.--Everhart-Thornley detector for secondary and backscattered electrons; Se, secondary electrons; F, Faraday cage; S, scintillator; LG, light guide; PM, photomultiplier.^{1,5}

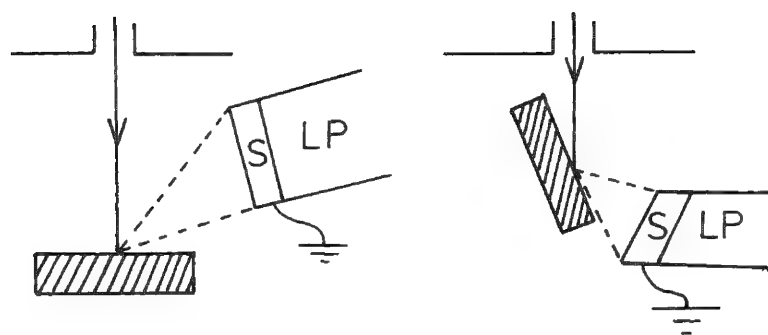


FIG. 6.--Modified Everhart-Thornley detector for collection of backscattered electrons over large solid angle, shown in position for normal incidence and for tilted specimens; asymmetric positioning relative to beam.^{6,7} S, scintillator; LP, light pipe.

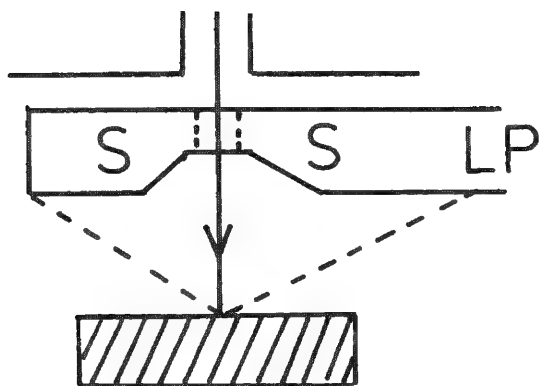


FIG. 7.--Large-solid-angle detector with symmetric positioning.⁹

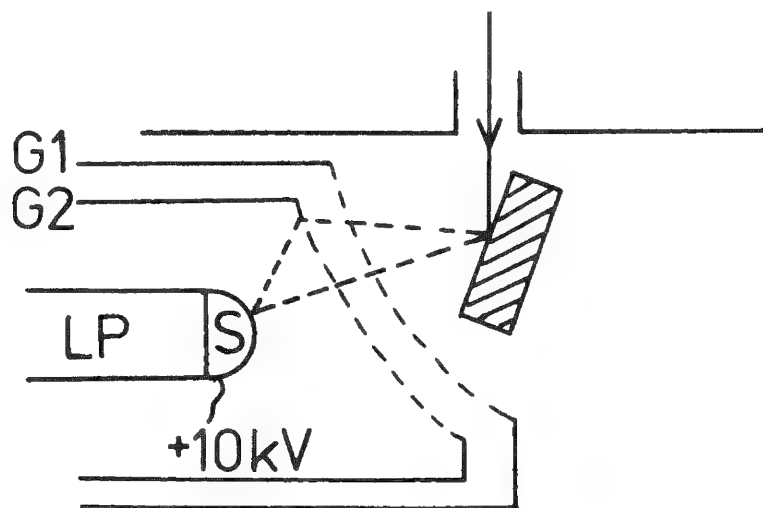


FIG. 8.--Detector for low-loss backscattered electrons.^{10,11} G1 is grid held at variable potential in range of 95-99% of accelerating potential.

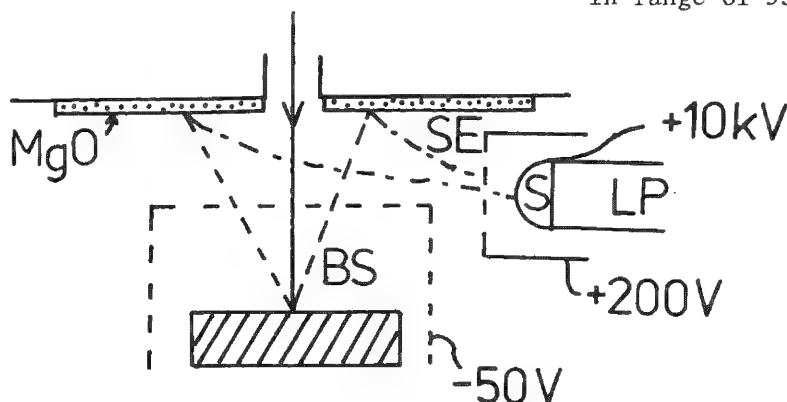


FIG. 9.--Conversion-type backscattered electron detector.^{12,13} Plate covered with MgO is placed over polepiece to enhance production of secondary electrons by backscattered electrons from specimen.

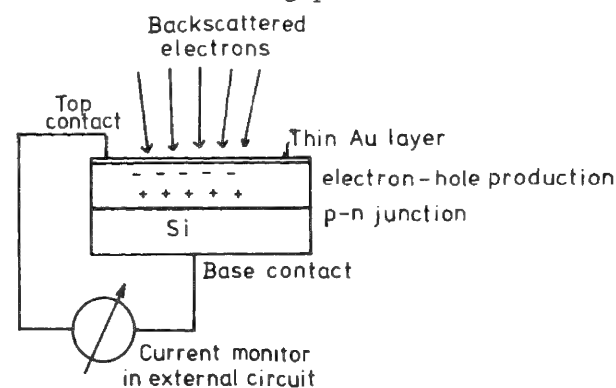


FIG. 10.--Principle of backscattered electron detection with solid-state detector.¹⁴

electron coefficient increases with decreasing primary-electron energy, the backscattered electrons of low energy are more efficient at producing a signal in a conversion detector than the high-energy backscattered electrons. Thus, the conversion detector has a negatively sloped energy response. For the same reason, the conversion detector is well suited to imaging with backscattered electrons when the incident beam energy is less than 5 keV, where other types of detectors have a poor response. Because of the large collection angle, the conversion detector has little sensitivity to trajectory effects.

Solid-state Detector

The class of solid-state detectors operates on the principle of energy-to-charge conversion due to inelastic scattering in a semiconductor crystal. When an energetic electron strikes a semiconductor such as silicon, which has a filled valence band and an empty conduction band, inelastic scattering of the energetic electron can result in the promotion of an electron from the valence band (leaving a "hole") to the conduction band (electron-hole pair). In silicon, approximately 3.6 eV is expended for each electron-hole pair. Thus, a 20keV electron creates approximately 5000 electron-hole pairs. If a potential is applied across the crystal, the electron-hole pairs can be separated without recombination to produce a flow of current in an external circuit (Fig. 10). Above a threshold which occurs because of the necessity of penetrating the inactive surface layer of the detector, the magnitude of the current is proportional to the energy of the electron striking the detector, which gives a positive energy response.

In employing the detector, the current flowing from the surface contacts must be amplified with a current amplifier.¹⁵ However, the task is somewhat easier than direct amplification of the specimen current signal (described below), since the current gain of the detector is approximately 1000. Thus, if a 2nA beam current is employed on a material such as gold with a high backscatter coefficient, the current flowing from a large solid-state detector is of the order of 1 μ A. The capacitance of the detectors and the need for long time constants in the amplifier result in a relatively slow signal response compared to a photomultiplier and set a serious limitation on rapid scan speeds. Specialty detectors have been produced with reduced capacitance to overcome this problem.¹⁴

The chief advantages of the solid state detector are:

1. *Cost.* A usable detector can be obtained for as little as a few dollars through the use of a silicon solar cell.¹⁶ Specialty detectors (size, shape, low capacitance) cost more, but are generally available for a few hundred dollars. The major investment is in the current amplifier, which averages about \$2000, although it is possible to build a suitable amplifier.¹⁵ Once the amplifier is available, detector arrays can be implemented for only the cost of additional detectors and a switching system.

2. *Size.* Detectors can be made as thin annular disk with a large collection area, or as small chips. The large annular detectors can be conveniently placed on the pole-piece symmetrically above the sample, which provides a large collection angle approaching 2π sr and does not consume much space in the sample chamber nor compromise other detectors in the system. Small detectors can be arranged in arrays or placed in special locations, such as on the snout of an energy-dispersive x-ray spectrometer to provide an electron image with the same view of the sample as the spectrometer.¹⁷

Detector Arrays

Both the solid-state detector and the scintillator detector can be used in the form of arrays of discrete detectors.^{18,19} The advantage of detector arrays is that by addition and subtraction of signals from discrete detectors placed around the sample, number and trajectory contrast effects can be selectively enhanced or eliminated.¹⁸ Thus, consider the samples and discrete detectors illustrated schematically in Fig. 11. If the beam is scanned across a simple ridge in a pure-element target, the signal from a single detector increases on the slope facing the detector because of a number effect (greater backscatter coefficient from a tilted surface compared with a flat surface) and because of trajectory effects (backscattered electrons scattered toward the detector). On the slope facing away from the detector, the signal falls nearly to zero because of trajectory effects. A second detector placed on the opposite side of the ridge produces

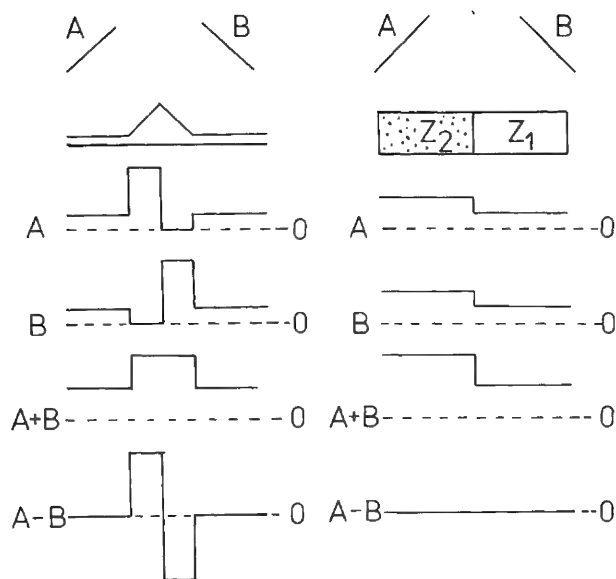


FIG. 11.--Signal profiles obtained from two-detector array (solid state or scintillator) in indicated positions from (left) single composition sample with topographic feature and (right) flat specimen with two regions of different composition. (After Ref. 18.)

the opposite response. If the signals of the two detectors are summed, the trajectory effects are eliminated, which leaves only the number effects, and the topographic contrast is reduced (although not eliminated!). If the signals are subtracted, the trajectory effects produce a large absolute difference between the signals from opposite sides of the ridge, and the topographic contrast is enhanced. For a flat two-component sample producing atomic number contrast, the signal from either detector alone will reveal the atomic number contrast. In the sum signal, the number contrast remains the same, although the total signal increases due to the larger collection angle. In the difference signal, the number effects are cancelled, the atomic number contrast is suppressed, and surface topography is enhanced.

Specimen Current

The specimen can act indirectly as a detector for backscattered electrons by measuring the specimen current signal i_{SC} , which is the difference between the beam current i_B , and the emitted currents from backscattered electrons i_{BS} and secondary electrons i_{SE} :

$$i_{SC} = i_B - i_{BS} - i_{SE} \quad (1)$$

By biasing of the specimen to +50V, the secondaries can be recollected, which effectively reduces i_{SE} to zero. The specimen current signal is then only sensitive to backscattered electron effects:

$$i_{SC} = i_B - i_{BS} \quad (2)$$

It can be shown that the contrast in the specimen current signal C_{SC} is related by a simple equation involving the mean backscattered electron coefficient to contrast in the backscattered electron signal C_{BS} :²⁰

$$C_{SC} = \frac{\Delta i_{SC}}{i_{SC}} = - \frac{\eta}{1 - \eta} \frac{\Delta i_{BS}}{i_{BS}} = \frac{\eta}{\eta - 1} C_{BS} \quad (3)$$

Besides the change in magnitude of the contrast in going from the backscattered image to the specimen current image, Eq. (3) indicates that the sense will also change, although this change can easily be modified by subsequent signal processing.

The specimen current image has several special advantages over any of the directly detected backscattered electron images.²¹

1. Contrast depends only on the number of backscattered electrons leaving the sample and not on their trajectories. Specimen current images thus show only number contrast effects and not trajectory contrast or energy effects.

2. Since all backscattered electrons leaving the sample affect the specimen current, the specimen current signal produces an image equivalent to a perfect 2π sr detector, with the contrast modified according to Eq. (3).

3. The specimen current signal can be collected regardless of the surroundings of the specimen and the fate of the backscattered electrons after they leave the sample. Thus, the presence of other objects in the specimen chamber (such as a mirror collector for cathodoluminescence) that might obstruct a conventional backscattered electron detector

causes no problem with the specimen current image.

Summary

Each of the detectors listed in Table 1 has strengths and weaknesses. From this survey, it is clear that no one detector is optimized for all backscattered electron imaging problems. Fortunately, in many cases a combination of detectors with complementary properties can be used to obtain an optimum configuration for characterizing a specimen. Several combinations are possible, but one that could be useful for general purpose microscopy of diverse samples might consist of the following: (1) A modified Everhart-Thornley detector with the Faraday cage removed and a large scintillator attached to the light pipe with provision for an accelerating bias for secondary electron detection. (2) A pair or an array of solid-state detectors for atomic number contrast and contrast manipulation. (3) Specimen current amplification for detection of pure number contrast. For special imaging problems, such as imaging at low beam energy or with environmental cells, the microscopist must be willing to implement one of the other detectors described in Table 1 to achieve useful images.

References

1. J. I. Goldstein, H. Yakowitz, D. E. Newbury, E. Lifshin, J. Colby, and J. R. Coleman, *Practical Scanning Electron Microscopy*, New York: Plenum, 1975, 110-116.
2. *Ibid.*, 149-210.
3. *Ibid.*, 49-94.
4. H. E. Bishop, "Some electron backscattering measurements for solid targets," R. Castaing et al., Eds. *X-ray Optics and Microanalysis*, Paris: Hermann, 1965, 153-158.
5. T. E. Everhart and R. F. M. Thornley, "Wide-band detector for micro-microampere low-energy electron currents," *J. Sci. Inst.* 37: 246-268, 1960.
6. O. C. Wells, "New contrast mechanism for SEM," *Appl. Phys. Lett.* 16: 151-153, 1970.
7. K. Schur, R. Blaschke, and G. Pfefferkorn, "Improved conditions for backscattered electron micrographs on polished sections using a modified scintillator detector," *SEM/1974*, 1003-1010.
8. J. B. Pawley, "Performance of SEM scintillation materials," *SEM/1974*, 27-34.
9. V. N. E. Robinson, "The construction and uses of an efficient backscattered electron detector for scanning electron microscopy," *J. Phys.* E7: 650-652, 1974.
10. O. C. Wells, "Low-loss image for surface scanning electron microscopy," *Appl. Phys. Lett.* 19: 232-235, 1971.
11. O. C. Wells, *Scanning Electron Microscopy* New York: McGraw-Hill, 1974, 139-150.
12. S. H. Moll, F. Healey, B. Sullivan, and W. Johnson, "A high efficiency nondirectional backscattered electron detection mode for SEM," *SEM/1978 I*, 303-310.
13. L. Reimer and B. Volbert, "Detector system for backscattered electrons by conversion to secondary electrons," *Scanning* 2: 238-248, 1979.
14. D. A. Gedcke, J. B. Ayers, and P. DeNee, "A solid state backscattered electron detector capable of operating at TV scan rates," *SEM/1978 I*, 581-594.
15. H. Yakowitz, C. E. Fiori, and D. E. Newbury, "Implications of specimen current and time differentiated imaging in scanning electron microscopy," *SEM/1973 I*, 173-180.
16. O. C. Wells, "Effect of collector position on Type-2 magnetic contrast in the SEM," *SEM/1978 I*, 293-298.
17. S. R. Hayashi and R. B. Bolon, "Backscatter electron detectors on energy-dispersive x-ray spectrometers," *Microbeam Analysis--1979*, 310.
18. S. Kimoto and H. Hashimoto, "On the contrast and resolution of the scanning electron microscope," *SEM/1968*, 63-78.
19. J. Jackman, "New scanning electron microscope depends on multi-function detectors," *Ind. Res. Dev.* 22: 115-121, 1980.
20. Ref. 1, 104-105.
21. D. E. Newbury, "The utility of specimen current imaging in the SEM," *SEM/1976 I*, 111-120.

TYPE-2 MAGNETIC CONTRAST: APPLICATIONS TO OBSERVING DOMAINS IN MAGNETIC MATERIALS

William G. Morris

Type-2 magnetic contrast relates to the ability of different magnetic domains to give a different number of backscattered electrons. The origin of this contrast and the development of a quantitative theory is reviewed. Important parameters in improving the contrast are specimen inclination with respect to the electron beam, and the energy of the incident electrons. Applications to studying the variation of domain wall spacing in Fe-3%Si transformer sheet have led to better understanding of magnetic losses in transformers. The magnetic domains observed in amorphous metal ribbon are discussed.

The image signal in a scanning electron microscope conveys information about how the incident electron beam has interacted with the solid sample. The most commonly used information relates to the topography or chemical composition, but electric potential differences, electron-photon conversion, and internal magnetic fields can also generate an image signal. The fact that electrons interact with magnetic fields is well known, and through careful exploitation of the various parameters in a SEM, the interactions of the incident electrons with the internal magnetic fields of a sample can be detected. If regions of different magnetization exist within a solid (magnetic domains), it is possible to form an image that distinguishes the different regions, so that one can measure domain size, shape, wall spacing, etc. This paper reviews some of the theory and applications of using an SEM to observe magnetic domains with type-2 contrast. Examples are given where macroscopic magnetic properties are related to the magnetic microstructure.

Theory of Type-2 Magnetic Contrast

Formation of SEM images of magnetic domains and understanding of the origins of the contrast in the image was first described by Fathers, Jakubovics, and Joy.¹ At approximately the same time, Newbury, Yakowitz, and Myklebust² investigated the influence of beam energy, sample tilt, and domain orientation on the magnitude of the image signal contrast. A later two-part article by Fathers et al.^{3,4} distinguished two contrast mechanisms. Type-1 had been observed earlier and appeared to originate from the interaction of low-energy secondary electrons with the fringing fields at domain walls. Type-2 could be seen in images formed from high-energy backscattered electrons. The origin of Type-2 contrast is illustrated in a schematic and exaggerated manner in Fig. 1. At normal incidence (Fig. 1a), the electrons penetrate into the sample; their range is shown as a bulb-shaped region. Where this region intersects the surface, one can expect to see backscattered electrons emitted. If the sample is inclined (Figs. 1b and c), the surface intersects more of the volume and more backscattered electrons are emitted. If a magnetic field exists within the sample, the range region can be skewed slightly off the beam axis. For regions of opposite magnetization separated by a domain wall, the range region can be skewed away from the surface (Fig. 1b) or toward it (Fig. 1c), with a corresponding effect on the number of backscattered electrons emitted. The effect is highly exaggerated in the figure; the difference in backscatter signal from one domain to an adjacent one might be 0.5%. In Fe-3%Si samples, the above-mentioned workers observed that the Type-2 contrast was relatively low, but increased with increasing beam voltage and could be optimized by variation of the specimen tilt with respect to the electron beam. At 30 kV, the contrast reached a maximum of about 0.5% at 55° for domains whose magnetization vector lay along the tilt axis. In order to make the theory more quantitative, the previous investigators²⁻⁴ and Ikuta and Shimizu⁵ used Monte Carlo calculation techniques to predict the magnitude of image contrast and the functional behavior of that important signal property on the instrument parameters. Shimizu et al.⁶ later reported the use of a 200kV SEM, and confirmed that an electron beam of higher voltage gave higher image contrast but lower resolution owing to the greater penetration and scattering of the incident electrons. The image contrast also depends on the saturation magnetization M_s , which is a measure of the strength of the magnetic field within a single domain. A comprehensive investigation of the effects of incident beam angle, backscattered de-

The author, who is with GE Corporate R & D in Schenectady, NY 12345, acknowledges many helpful discussions with J. W. Shilling, S. D. Washko, and J. D. Livingston in the preparation, measurement, and observation of domains in magnetic samples.

tector take-off angle, and accelerating voltage (up to 200 kV), was reported by Yamamoto, Nishizawa, and Tsuno in 1976.⁷ They also showed they could improve the domain image contrast by filtering out the lower energy backscattered electrons, which contained less magnetic domain information. The importance of detector type and configuration was mentioned by Shimizu et al.⁸ in a theoretical and experimental study of Mn-Zn ferrites. Although the penetration and diffusion of a 200kV electron beam limits the resolution to a few microns in Fe-3%Si, the penetration can be used to advantage to observe internal domains. Yamamoto, Tsuno, and Nishizawa demonstrated that magnetic domains in Fe-3%Si could be seen through a 4.5 μ m insulator film with a 200kV SEM.⁹ Tsuno and Yamamoto quantitatively evaluated the ability to discern subsurface domains by plating Cu over Fe-3%Si.¹⁰

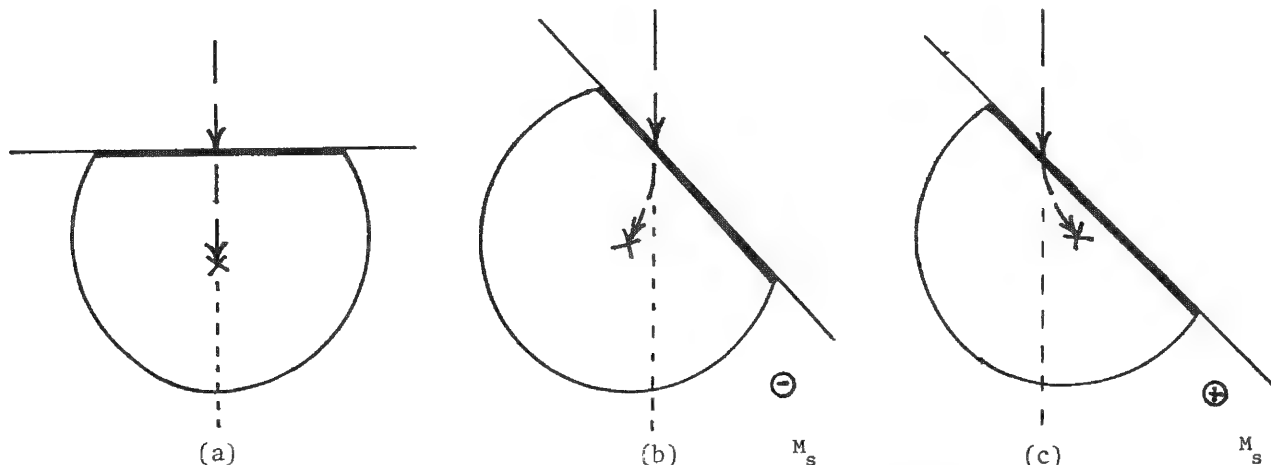


FIG. 1.--Origin of Type-2 contrast in backscattered electron images: (a) normal surface, no internal magnetic field; (b) inclined surface, negative internal magnetic field; (c) inclined surface, positive internal magnetic field.

The sensitivity of Type-2 contrast can be substantially improved by use of a lock-in amplifier. This technique was described by Wells et al.^{11,12} and applied to observing magnetic domains in thin films of permalloy.

During 1973-1976 there were many significant presentations and publications on the origin of Type-2 magnetic contrast, mainly concerned with quantitative and semiquantitative descriptions of the important experimental parameters. A primary goal was the improvement of contrast in what is inherently a low-contrast image signal. Demonstrations of the technique gradually evolved into applications where specific information about domain size and shape would be important in the understanding of magnetic behavior and the development of new magnetic materials.

Applications of Type-2 Contrast to Fe-3%Si

One of the first important applications of Type-2 contrast was the characterization of magnetic domains in grain-oriented Fe-3%Si transformer sheet. This material is processed into sheets approximately 0.3 mm thick, with a typical grain diameter of 5 to 10 mm. The grains are oriented with the (110) planes lying in the plane of the sheet and a [001] direction along the rolling direction. High-permeability, low-loss transformer laminations can be made from this sheet material. The eddy-current losses are related to the domain-wall spacing¹³; a decrease in domain-wall spacing leads to a decrease in losses and an increase in transformer efficiency. The magnetic properties and domain structure in this material have been comprehensively treated by Shilling and Houze,¹⁴ who used the magneto-optical Kerr effect to observe domains on polished surfaces. Overholt has also studied the relationship between losses and magnetic domain structure.¹⁵

In the continuing improvement of Fe-3%Si transformer sheet, a very important development was the discovery that application of a thin glass-ceramic coating could reduce the losses. This coating is formed at a high temperature; a difference in thermal-expansion coefficients induces a small tensile stress (approximately 1000 psi) in the steel when it is cooled. However, this coating prevents the use of the magneto-optical Kerr effect

to observe the domain structure. The fact that a 200kV SEM could be used to see the domains through this coating was a very important contribution by Yamamoto et al.^{9,10} In 1975 Yamamoto and Tsuno¹⁶ and Irie and Fukuda¹⁷ presented Type-2 domain images taken on coated and uncoated transformer steel, illustrating that the coating refined the domain spacing and thus reduced the losses. The coated steel is better able to maintain a desirable domain structure through processing steps such as shearing and bending, as was reported by Fukuda et al.¹⁸ A forsterite ceramic coating reduces the domain wall spacing and eliminates the aligned lancet comb domain structure, but the net effect is to increase losses because of wall pinning effects arising from the forsterite particles.¹⁹ A study of single crystals of Fe-3%Si with slightly different orientations showed that lowest losses were obtained with the [001] crystal direction tilted out of the sheet by 2°, and with an applied tensile stress of approximately 2000 psi. An increasing tilt angle reduces domain wall spacing (lower losses) but also leads to increasing flux closure structure in the domains (increased losses) with the optimum low losses being achieved around 2° tilt.²⁰ The application of coatings to single crystals also reduced their losses through the reduction of domain wall spacing.²¹

Experimental Apparatus

Since improved contrast can be obtained at higher beam energies, we chose to adapt a 200kV TEM/STEM microscope to do domain imaging. The modifications required were construction of a specimen stage, addition of a backscatter electron detector, and new deflection amplifiers and video amplifiers (Fig. 2).

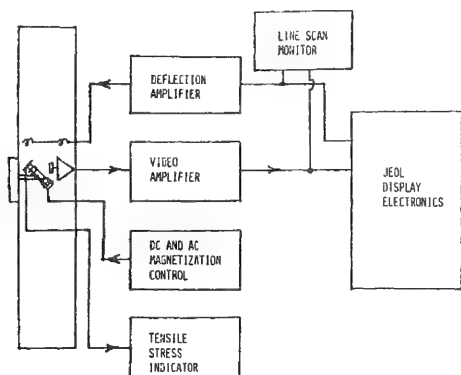


FIG. 2.--Components required to obtain Type-2 contrast in JSEM-200 STEM.

sample subjected to a uniaxial tensile stress. The Epstein strip (30 × 300 mm) represents the industry standard for measuring magnetic properties on Si-Fe steel. It was decided to approximate this standard as closely as possible for the standard microscope sample. The magnetic yoke consists of 5 laminations of Si-Fe (Fig. 3) with a portion of the center lamination removed to allow insertion of the 30 × 106mm sample. A simple tensile load frame surrounds the yoke, and the ends of the sample that protrude from the yoke are gripped for applying a tensile load. The two coils consist of 25 turns each, and give a field of approximately 10 oersted at 1 A.

The sample stage is constructed so as to give orthogonal translations ($x = \pm 1.2$ cm, $y = \pm 1.5$ cm) in the plane of the sample sheet, as well as a variable angle of incidence to the electron beam. This configuration allows access to all regions of the 2.5 × 3.0cm window between the coils on the yoke, as well as optimization of the contrast through variation of the angle of incidence. The completed stage is attached to a flange for mounting in the left 100mm-diameter part on the microscope column.

The backscatter detector, consists of a 100mm² surface-barrier silicon-charged particle detector mounted in a brass housing. The electrical connections for the detector, sample current, energizing coils on the magnetic yoke, and strain gage on the load frame are brought out through two 7-pin connections mounted in the flange.

The microscope is supplied with scanning deflection coils, which are attached to the bottom of the second condenser lens. With the anticontamination attachment removed, there is approximately 100 mm of space between these coils and the objective lens. It is in this region, which is accessible through two 100mm-diameter ports on either side of the instrument, that the specimen is mounted. A special specimen stage for holding samples of Si-Fe sheet was constructed which fits into the left port and replaces the secondary electron detector, which is not required for this application.

In addition to observing the static domain configuration in samples of Si-Fe transformer sheet, one wants to observe the domains with an applied magnetic field and with the

For operation, the gun and plate chambers of the microscope are isolated, and dry nitrogen is admitted to the column. The secondary-electron detector and anti-contamination device are removed, and the domain contrast specimen stage is inserted and secured. The automatic vacuum system usually switches from rough to diffusion pumping within 5 min, and an additional 5 to 10 min is allowed for the vacuum to improve before the gun isolation valve is opened and the beam is turned up. The apparatus has been applied to the observation of magnetic domains in a large number of Fe-3%Si samples. Figure 4 illustrates the contrast obtainable on a single crystal with the (001) direction lying in the plane of the sheet ($B = 0^\circ$). The domains are relatively large in Fig. 4(a), where the sample is in a demagnetized state. If a stress of 2000 psi is applied, and the sample is demagnetized by means of a slowly de-

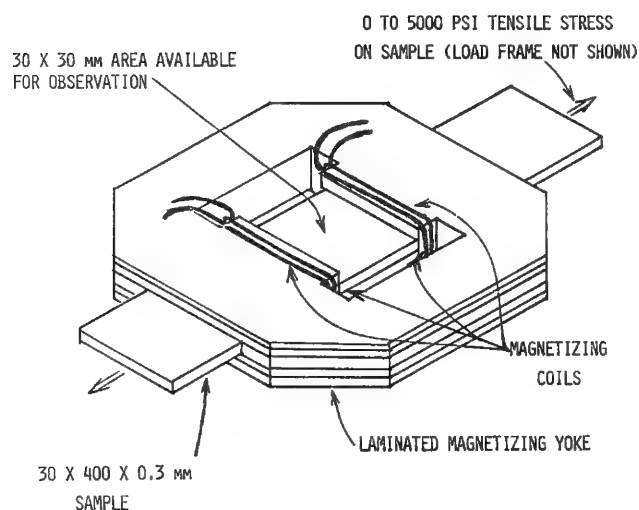


FIG. 3.--Magnetizing yoke designed to hold $30 \times 106 \times 0.3$ mm strips of Fe-3%Si.

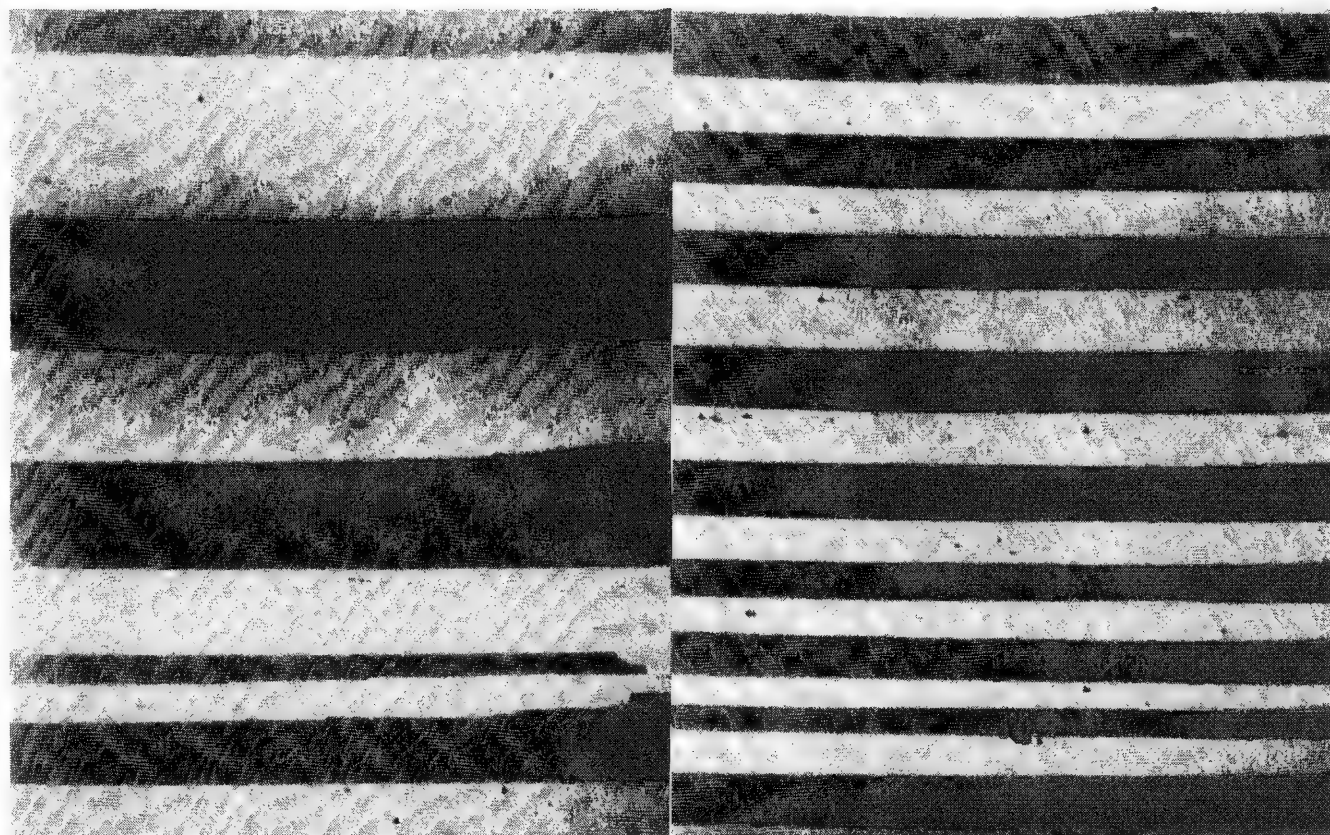


FIG. 4.--Fe-3%Si single crystal. The relatively wide domains are result of the [001] direction lying in plane of sheet ($B = 0^\circ$), and parallel to the domain walls (left). Magnification = $10\times$. Domain width and eddy current losses are reduced as result of application of 2000 psi tensile stress (right).

creasing 60Hz field, the size of the domains decreases (Fig. 4b). This observation agrees with reduced 60Hz eddy-current losses which accompany the application of a tensile stress. If the crystal is not perfectly aligned, the domain structure is altered to include closure domains. Figure 5 illustrates a grain with $B = 2^\circ$, demagnetized and no applied stress. The density of the long wedge-shaped domains varies with misorientation. At greater misorientations ($B = 5^\circ$) the domain structure becomes very complex as the supplementary fine structure becomes the dominant feature (Fig. 6). The ability to observe the domain structure in samples with a glass-ceramic stress inducing coating is shown in Fig. 7. The entire sample was initially stress coated, then the coating was etched away from the right portion. It can be seen that the contrast remains high for the domains under the coating, and stress induced by the coating does lead to a narrower magnetic domain in that region.

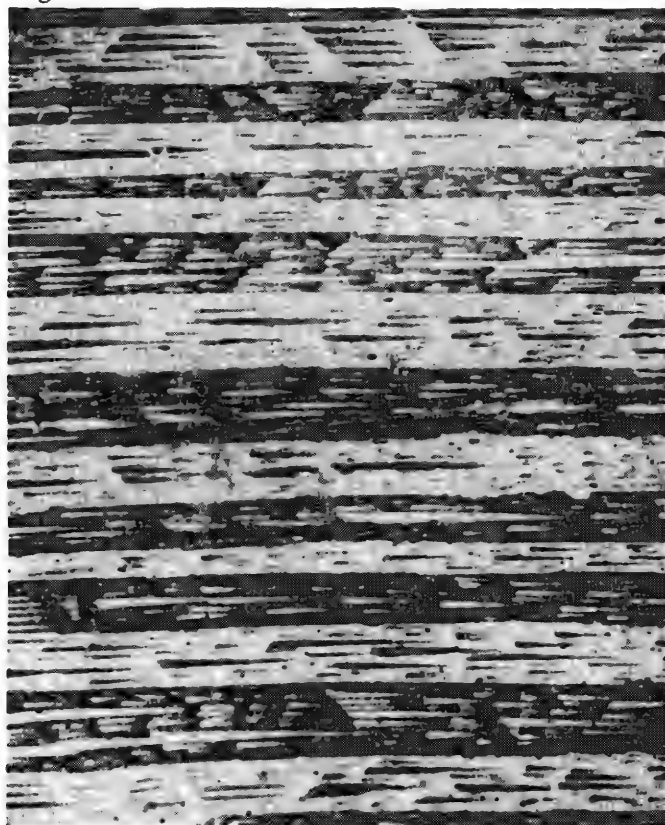


FIG. 5.--Fe-3%Si single crystal, unstressed. Domain width is reduced as [001] direction is tilted slightly out of plane of sheet ($B = 2^\circ$). Appearance of supplementary fine structure in domains partially nullifies benefit of reducing domain wall spacing.

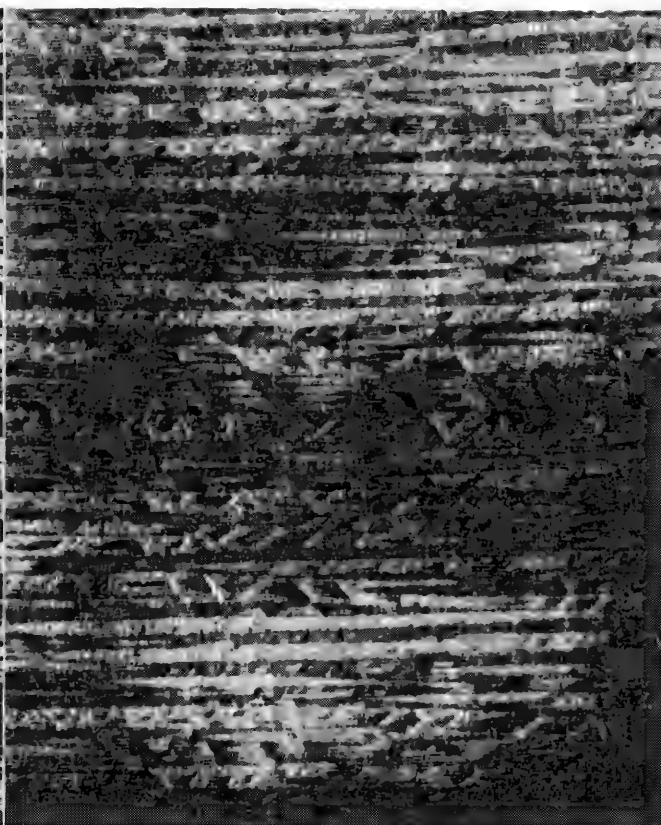


FIG. 6.--Fe-3%Si single crystal, unstressed. Domain structure becomes very complex and losses increase as [001] tilt is increased ($B = 5^\circ$).

Magnetic Domains in Amorphous Metals

The technique has been used to observe magnetic domains in amorphous Fe-B-Si-C ribbons. This material is made by rapid quenching of a stream of molten metal on a rotating wheel, which yields a continuous ribbon of a metal with no crystal structure. Since the previous work in Fe-3%Si had been designed to form grains with optimum orientation to minimize domain width and 60Hz magnetic losses, it should be interesting to observe the domain structure in a material with no grains where orientation was of no concern. Figure 8 shows the domains observed on a sample that had been annealed in a longitudinal magnetic field, then demagnetized at room temperature. The curvature of some of the domain walls suggests the presence of a residual elastic stress that may be influencing

domain configuration. If a tensile stress is applied (approximately 1000 psi) it is seen that a refinement of domain wall spacing occurs (Fig. 9). The frequency of the demagnetizing field also has an effect on the domain wall spacing. Demagnetization at 200 Hz (or above) produces approximately a two-fold reduction in average domain width as compared with a dc demagnetization. If a sample is demagnetized several times (at the same frequency) similar, but not identical, domain configurations are observed.

The mobility of domain walls is also of interest in the understanding of the nature of 60Hz magnetic losses. In Fig. 10, a small 2Hz signal is applied during the image raster scan. The line scan (perpendicular to the domain walls) is set at approximately 50 ms and is thus rapid compared with the magnetizing signal. The frame scan is parallel to the domain wall, and the wall migrates back and forth approximately 50 times while the photograph is taken, which accounts for the serrated character of the domain walls in Fig. 10. The important feature to notice is that the magnitude of the displacement of the various walls is not identical; some walls appear to have a higher mobility than others. This pinning of domain walls by surface or bulk defects can cause an increase in magnetic losses by inhibiting domain wall motion during the magnetization cycle. Additional information on domain configuration in amorphous metals will be published soon.²²



FIG. 7.--Fe-3%Si, with 3 μ m stress coating. Right half has had coating etched away. Domains are clearly visible in both regions and have finer spacing in stressed region.



FIG. 8.--Amorphous metal (Fe-B-Si-C) ribbon annealed in longitudinal field. Curvature of domains suggests local imperfections or stresses.

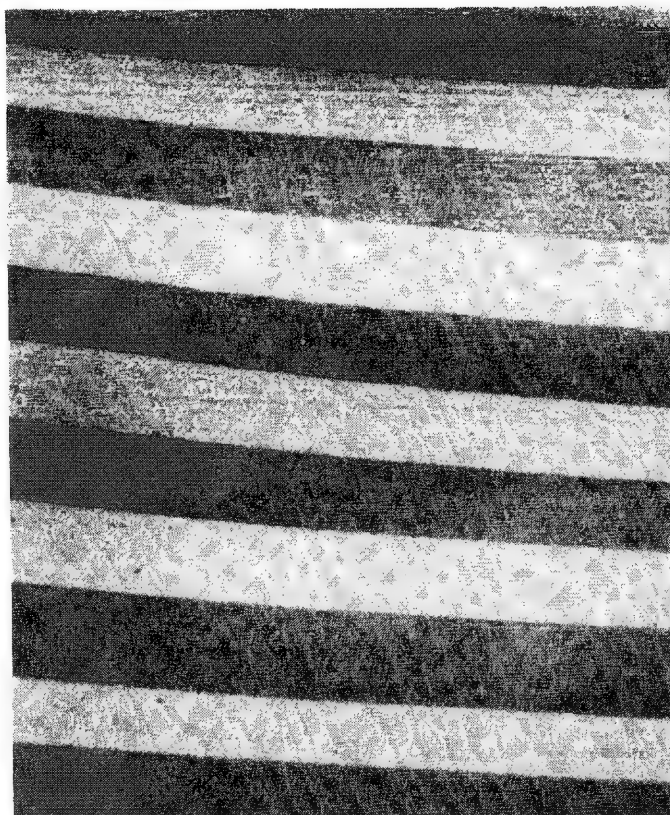


FIG. 9.--Amorphous metal ribbons. With an applied stress of 1000 psi, refinement of domain wall spacing occurs.

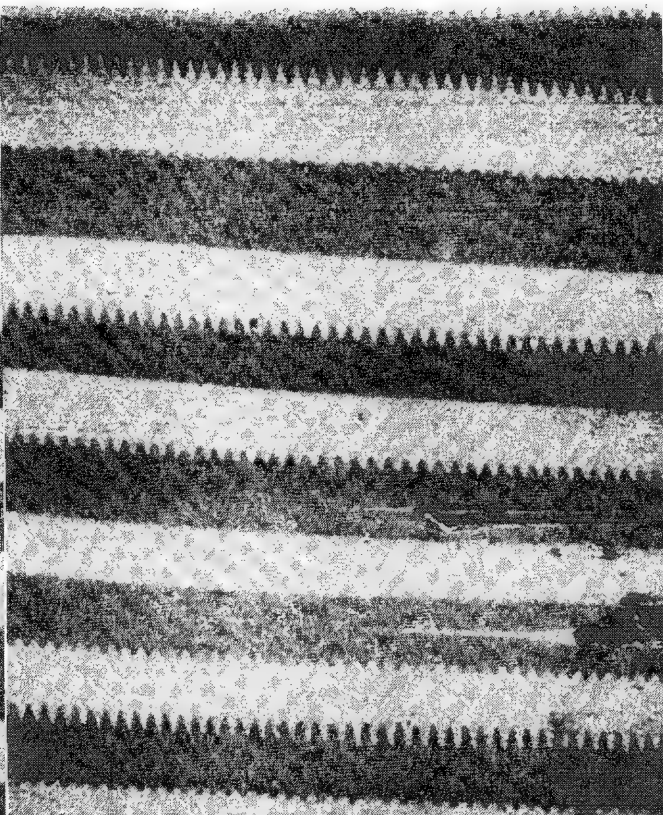


FIG. 10-Amorphous metal ribbon. Small 2Hz ac longitudinal magnetic field "wiggles" the domain walls during scanning time required to record a single frame. Some interaction with surface defects is seen.

References

1. D. J. Fathers, J. P. Jakubovics, D. C. Joy, D. E. Newbury, and H. Yakowitz, "A new method of observing magnetic domains by scanning electron microscopy," *Phys. Stat. Sol.* (A)20: 535-544, 1973; (A)22: 609-619, 1974.
2. D. J. Fathers, J. P. Jakubovics, and D. C. Joy, "Magnetic domain contrast from cubic materials in the scanning electron microscope," *Phil. Mag.* 27: 765-768, 1973.
3. D. W. Newbury, H. Yakowitz, and R. L. Myklebust, "Monte Carlo calculations of magnetic contrast from cubic materials in the scanning electron microscope," *Appl. Phys. Lett.* 23: 488-490, 1973.
4. T. Ikuta and R. Shimizu, "Magnetic domain contrast from ferromagnetic materials in the scanning electron microscope," *Phys. Stat. Sol.* (A)23: 605-613, 1974.
5. R. Shimizu, T. Ikuta, T. Yamamoto, M. Kinoshita, and T. Murayama, "Direct observation of the magnetic domain structure in Mn-Zn ferrite using the 200kV high voltage scanning electron microscope," *Phys. Stat. Sol.* (A)26: K87-98, 1974.
6. T. Yamamoto, H. Nishizawa, and K. Tsuno, "High voltage scanning electron microscopy for observing magnetic domains," *J. Phys.* D8: L13-L15, 1975.
7. T. Yamamoto, H. Nishizawa, and K. Tsuno, "Magnetic domain contrast in back-scattered electron images obtained with the scanning electron microscope," *Phil. Mag.* 34: 311-325, 1976.
8. R. Shimizu, T. Ikuta, M. Kinoshita, T. Murayama, H. Nishizawa, and T. Yamamoto, "High contrast observation of magnetic domains with the high voltage SEM," *J. Appl. Phys.* 15: 967-981, 1976.
9. T. Yamamoto, K. Tsuno, and H. Nishizawa, "High voltage scanning electron microscopy for observing magnetic domains," *Proc. 33rd Annual EMSA Meeting*, 1975, 32-33.
10. K. Tsuno and T. Yamamoto, "Observed depths of magnetic domains in high voltage

scanning electron microscopy," *Phys. Stat. Sol.* (A)35: 437-449, 1976.

11. O. C. Wells, "Isolation of Type-2 magnetic contrast in the SEM by a lock-in technique," *J. Appl. Phys.* 35: 644-646, 1979.

12. O. C. Wells and R. J. Savoy, "Enhancement of Type-2 magnetic contrast in the BSE image in the SEM by a lock-in technique," *Scanning* 21: 255-256, 1979.

13. R. H. Pry and C. P. Bean, "Calculation of the energy loss in magnetic sheet materials using a domain model," *J. Appl. Phys.* 29: 532-533, 1958.

14. J. W. Shilling and G. L. Houze Jr., "Magnetic properties and domain structure in grain-oriented 3% Si-Fe," *IEEE Trans.* M-10: 195-223, 1974.

15. K. J. Overshot, "The use of domain observations in understanding and improving the magnetic properties of transformer steels," *IEEE Trans.* M-12: 840-845, 1976.

16. T. Yamamoto and K. Tsuno, "Observation of domain structure in soft magnetic materials by means of high voltage scanning electron microscopy," *AIP Conf. Proc.* 29: 572-573, 1976.

17. T. Irie and B. Fukuda, "Effect of insulating coating on domain structure in grain oriented 3% Si-Fe sheet as observed with a high voltage scanning electron microscope," *AIP Conf. Proc.* 29: 574-575, 1976.

18. B. Fukuda, T. Irie and H. Shimanaka, "Observation through surface coatings of domain structure in 3% Si-Fe sheet by a high voltage scanning electron microscope," *IEEE Trans.* M-13: 1499-1504, 1977.

19. W. G. Morris, J. W. Shilling, D. R. Fecich, and P. Rao, "Effect of forsterite coatings on the domain structure of grain oriented 3% Si-Fe," *IEEE Trans.* M-14: 14-17, 1978.

20. J. W. Shilling, W. G. Morris, M. L. Osborn, and P. Rao, "Orientation dependence of domain wall spacing and losses in 3% Si-Fe single crystals," *IEEE Trans.* M-14: 104-111, 1978.

21. S. D. Washko and W. G. Morris, "Effects of coatings on domain wall spacing and core losses in 3% Si-Fe single crystals," *J. Mag. and J. Mag. Matl.* 19: 349-352, 1980.

22. J. D. Livingston and W. G. Morris, "SEM studies of magnetic domains in amorphous ribbons," submitted to *Trans. IEEE. Mag.* (1981 Intermag Conf.).

BACKSCATTERED ELECTRONS IN THE SEM: TECHNIQUES AND USES IN METALLURGY

D. L. Davidson

Backscattered electrons are that fraction of the illuminating beam which has been elastically scattered by the specimen through an angle of more than 90° . The magnitude of this flux may be detected by suitably placed detectors. The information derived from backscattered electrons is principally related to the atomic number and crystalline orientation of the material being observed, although surface topography may also be observed in some instances. This paper briefly reviews the techniques that accompany the use of backscattered electrons in the scanning electron microscope (SEM) on problems of materials science, and is intended for persons generally unfamiliar with the subject.

Contrast

The intensity of the backscattered electron beam can be modulated in several ways. The impinging electrons penetrate the material and are scattered by the atoms encountered along the path. The scattering event may be elastic, absorbing very little energy, or it may be inelastic, absorbing much of, or all, the electron's energies. A backscattered electron may undergo one or several essentially elastic scatterings as its path is altered through greater than 90° . This series of events is complex and difficult to quantify, but the essential aspects of simple elastic scattering events were described long ago by Rutherford. The fraction of electrons backscattered depends on atomic number of the specimen and the incident beam energy.¹ Thus, contrast is developed between two dissimilar elements in the same specimen. This contrast mechanism is the one most commonly used in the SEM, and has been demonstrated many times (see Ref. 2 for some good examples). The technique for observing atomic number contrast will be discussed subsequently, and it will be seen that the main issue is atomic number resolution, i.e., difference in atomic number, which can be resolved; differences in Z of 1 have been resolved.

In 1967 Coates discovered another mechanism by which backscattered electrons carry contrast: electron channeling.³ Channeling contrast is produced by interaction of the crystal structure with the electrons, and could as well be called diffraction contrast. As with other diffraction phenomena, Bragg's law describes electron diffraction, but a proper quantitative description of channeling contrast is mathematically complex,⁴ for it must incorporate crystallography, both lattice type and plane orientation relative to the incoming beam direction, atomic number, and electron energy effects. So complex is this contrast mechanism that consensus on mathematical description has not yet been achieved. With suitable instrumentation, channeling or diffraction contrast can be detected in the SEM, and can be very useful even if all the details of its origin are not known. The simplest use of channeling contrast is in revealing the grain structure of single phase metals (Fig. 1), something not always easily done with secondary-electron imaging. Here, each grain, being relatively small, is illuminated by the electron beam at approximately the same angle, so the backscattered electron yield from that grain will be set by the diffracting conditions relevant to the orientation of that grain to the beam; thus, each grain in general produces a different gray level on the micrograph.

When the grain size becomes large enough, the scanning beam no longer can be approximated as coming from one direction; therefore, the diffracting conditions are changing as the beam traverses the grain, which superimposes a number of bands on the micrograph that are related to satisfying the Bragg conditions, the channeling pattern. This way of making channeling patterns has some limited use.⁵ The same effect can be achieved by scanning the electron beam so that it effectively rocks about a point on the specimen surface. In this way diffracting conditions can be made to change within a single small grain, or smaller area. This technique is called selected area electron channeling (Fig. 2) and is the technique most used for making channeling patterns.

The author is with the Department of Materials Sciences, Southwest Research Institute, San Antonio, TX 78284. Continued support by the Office of Naval Research is gratefully acknowledged.

tron channeling pattern mode (SACP); thus, there is a rotation between the two which must be determined for proper use when crystallographic data are required.⁵

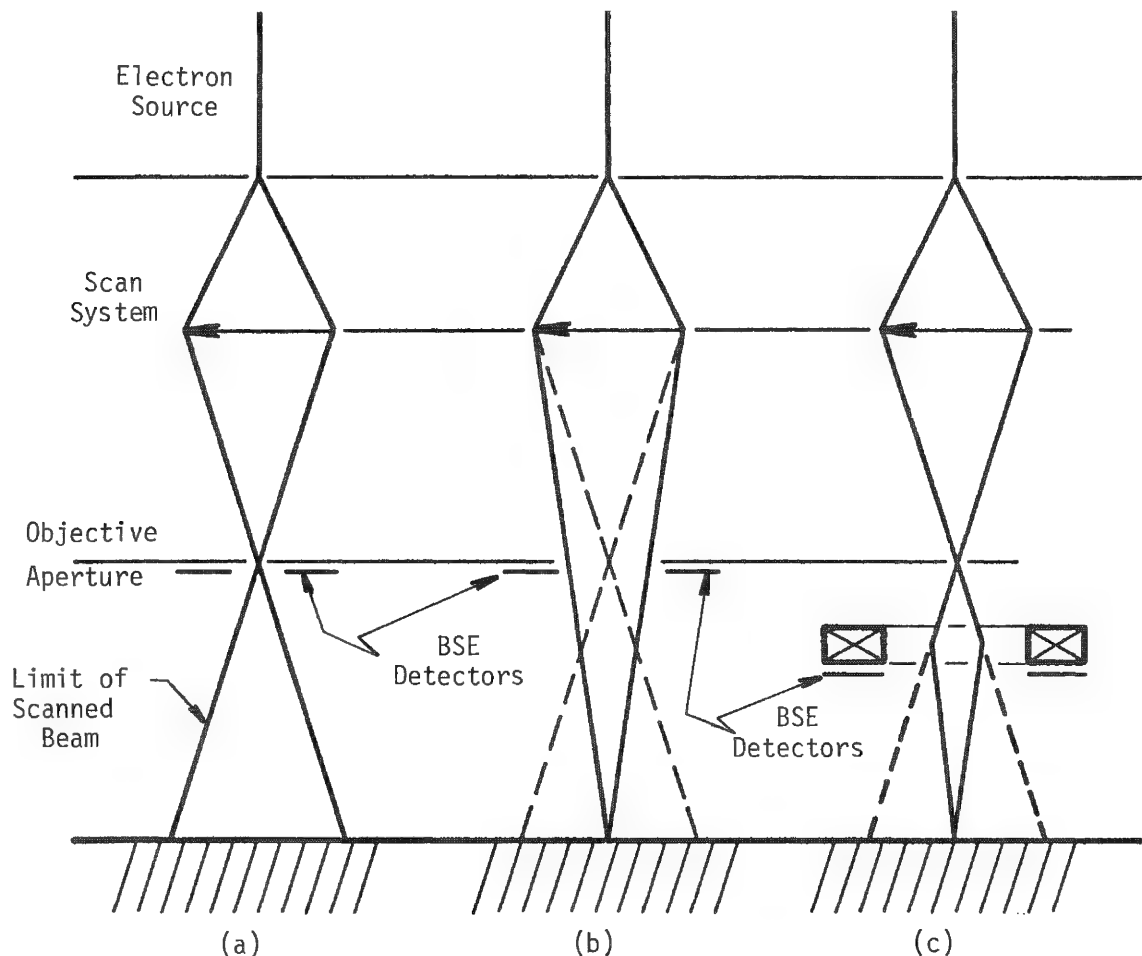


FIG. 4.--(a) best location for backscattered electron detectors and two methods of achieving selected area electron channeling patterns; (b) deflection-focus method; (c) after lens deflection method.

Specimen Preparation

Most observations involving atomic number and channeling contrast are made on flat specimens, which implies that cutting and polishing operations are required. Both operations should be carried out with a minimum of specimen damage. Since that is not possible for mechanical operations common to most materials preparation, electropolishing is usually a necessary final step, although chemical polishing is sometimes a viable alternative. This step is less critical for atomic number contrast than for channeling contrast because the latter is dependent upon crystallographic perfection, which is destroyed, at least to some degree, by mechanical polishing operations. In some materials, mainly brittle ceramics, ion etching may be substituted for chemical removal of the mechanically damaged layer. Success in obtaining channeling patterns or channeling contrast micrographs depends absolutely on the development of proper specimen preparation techniques that eliminate the damage inherent in specimen preparation procedures. Electropolishing is often a difficult operation that requires strong acids, exotic thickening agents, and very cold temperatures, and if not properly performed with the correct chemical solutions and conditions, it can lead to the formation of thick surface oxides or contamination layers, or both. Either one will prevent the development of channeling contrast, so great care must be exercised during electropolishing operations to obtain clean surfaces with thin, uniform oxide layers. In some reactive metal systems, such as zirconium and magnesium achieve-

ment of surface conditions that allow development of channeling contrast may not be feasible by ordinary chemical or electropolishing procedures.

Electron channeling patterns are very sensitive to deformation; the most common mistake made in specimen preparation from which electron channeling patterns are expected is when the material is not treated in such a way as to insure a low dislocation density in it. Many studies in which channeling was expected to be used as a tool have foundered at this point. An example is shown in Fig. 1, a low-carbon steel (0.05C) in which reasonably good channeling contrast is achieved from the individual grains. Very poor quality channeling patterns are the best that could be made from this material because in cooling, the material goes through the allotropic transformation at about 730°C, which creates a dislocation structure that is rather well pinned by carbon atmospheres, so that subsequent strain-anneal procedures are not very successful in annihilation of this dislocation structure. Fortunately, localized plasticity in this steel may be studied with channeling contrast, which reveals the formation of subgrains caused by mechanical deformation.

In summary, it cannot be emphasized too strongly that careful, methodical specimen preparation is crucial to success in studies where electron channeling is to be used.

Uses

The information contained in the backscattered electrons may be used in a number of ways; contrast developed from regions of different atomic number may be used in obvious ways, even though this technique has not been developed to the point where the atomic number can be determined from the contrast. Some examples of the uses of this contrast mechanism are found in the work of the Robinsons.²

The author is more familiar with the uses of channeling contrast, both micrographs and channeling patterns, for the study of localized plasticity.¹²⁻¹⁴ Use is made of the fact that channeling patterns are sensitive to dislocation density; thus, the plastic zone size at a crack tip can be measured, and the strain distribution within the plastic zone quantified.¹⁵ Actually, channeling patterns are sensitive to the elastic strain fields of dislocations, as well as to other elastic strains, but a quantitative relationship between channeling pattern change and elastic strain magnitude does not currently exist. An example of this use of channeling is shown in Fig. 5. To quantify strains, a calibration technique has been used,¹⁶ and to determine the accompanying dislocation density, a method has been outlined,¹⁷ although insufficient information is currently available to make the method operational.

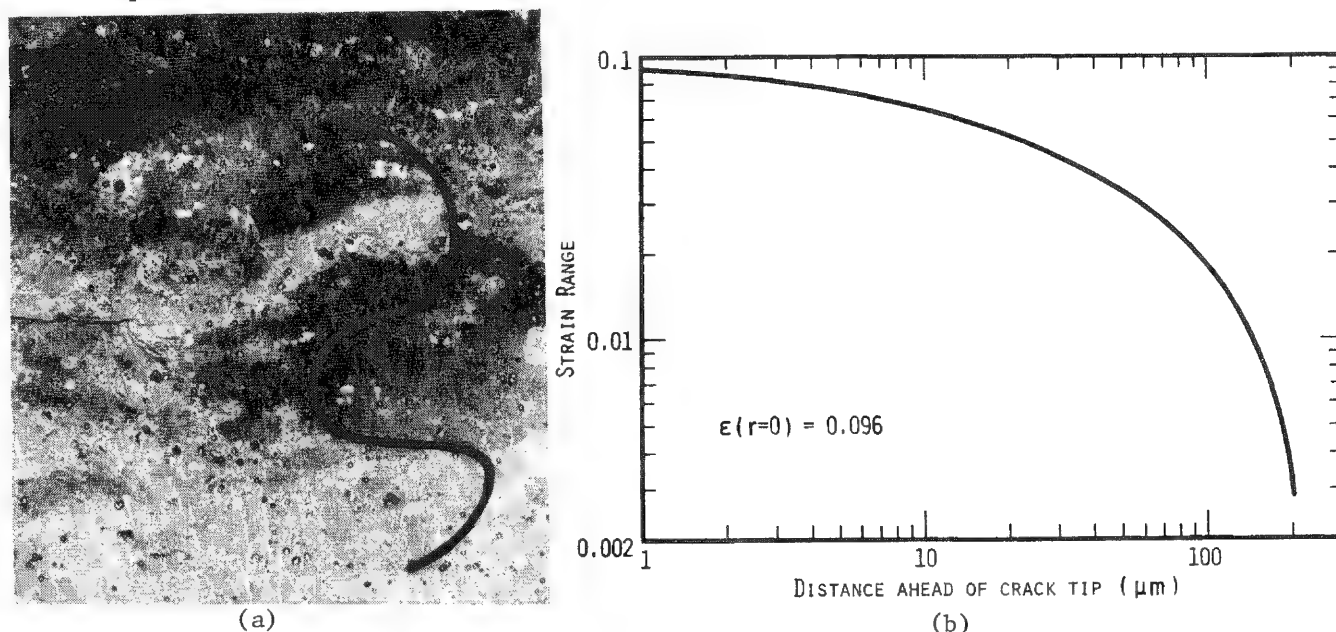


FIG. 5.--(a) plastic zone size and (b) strain range distribution ahead of crack; 7075-T6 aluminum alloy, $\Delta K = 11 \text{ MN/m}^{3/2}$, $R = 0.05$.

Channeling contrast may also be used to study localized plasticity;¹² the stresses and strains at fatigue crack tips, such as shown in Fig. 1, have been obtained by measurement of subgrain sizes in the vicinity of cracks.¹⁴ An example of this stress distribution is shown in Fig. 6. The effects of environment and crack driving force (ΔK) on stress have been studied. Alternatively, crack tip energy absorption has been measured and found to be a function of environment and driving force.

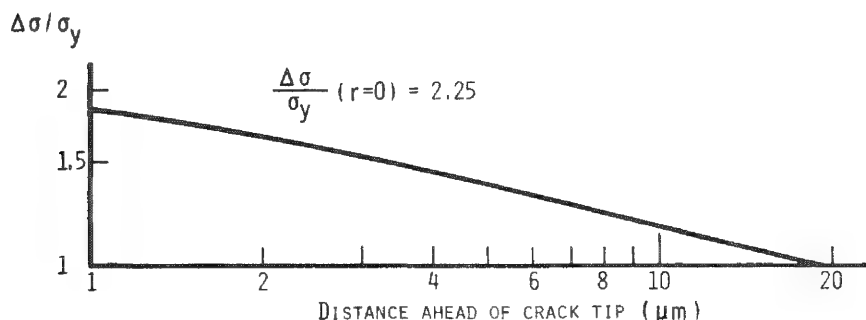


FIG. 6.--Stress range distribution ahead of fatigue crack in low-carbon steel grown in dry nitrogen, $\Delta K = 11 \text{ MN/m}^{3/2}$, $R = 0.05$, $\sigma_y = 418 \text{ MN/m}^{3/2}$.

All these uses of electron channeling have been integrated with the newer technique of stereoimaging,¹⁸ which allows surface crack tip strains to be computed directly from displacements; the combination has shown that the information deduced by electron channeling is reasonably correct, which has led to increased confidence in the results obtained by these indirect techniques, which comes directly from use of backscattered electrons.

Summary and Conclusions

The study of materials science specimens by contrast carried by backscattered electrons can yield valuable complementary information to normal secondary electron imaging. Atomic number, channeling, and magnetic contrast allow measurements on a scale of 0.5-5 μm that are virtually impossible by any other means. Successful use of these contrast mechanisms means that careful attention must be accorded material and specimen preparation, and proper backscattered electron detectors must be used.

References

1. P. R. Thornton, *Scanning Electron Microscopy*, London: Chapman and Hall, 1968, chap. 5, pp. 85-94.
2. V. N. E. Robinson and B. W. Robinson, *SEM/1978 I*, 595-602.
3. D. G. Coates, "Kikuchi-like reflection patterns obtained with the SEM," *Phil. Mag.* 16: 1179-1184, 1967.
4. J. P. Spencer and C. J. Humphreys, "A multiple scattering transport theory for electron channeling patterns," *Phil. Mag.* 42: 433-451, 1980.
5. D. L. Davidson, "Rotation between SEM micrograph and electron channeling patterns," *J. Phys.* E9: 341-343, 1976.
6. J. Lebedzik and E. W. White, "Multiple detector method for quantitative determination of microtopography in the SEM," *SEM/1975 I*, 181-188.
7. O. C. Wells, "Low-loss image for surface scanning electron microscope," *Appl. Phys. Lett.* 19: 232-235, 1971.
8. O. C. Wells, *Scanning Electron Microscopy*, New York: McGraw-Hill 1974, chap. 6, pp. 108-159.
9. D. A. Gedcke, J. B. Ayers, and P. B. DeNee, "A solid state backscattered electron detector capable of operating at TV scan rates," *SEM/1978 I*, 581-594.
10. D. E. Newbury, "The utility of specimen current imaging in the SEM," *SEM/1976 I*, 111-120.
11. L. Reimer, W. Popper, and W. Brocker, "Experiments with a small solid angle detector for BSE," *SEM/1978 I*, 705-710.

12. D. L. Davidson, "The use of channeling contrast in the study of material deformation," *SEM/1977 I*, 431-438.
13. D. L. Davidson, "The study of fatigue mechanisms with electron channeling," in J. T. Fong, Ed., *Fatigue Mechanisms*, ASTM STP-675, 1978, 254-275.
14. D. L. Davidson and J. Lankford, "The effect of water vapor on fatigue crack tip stress and strain range distributions and the energy required for crack propagation in low-carbon steel," *Intern. J. Fracture*, June 1981, in press.
15. D. L. Davidson and J. Lankford, "Fatigue crack tip plastic strain in high strength aluminum alloys," *Fatigue of Engineering Materials and Structures*, 1981, in press.
16. D. L. Davidson, "A method for quantifying electron channeling pattern degradation due to material deformation," *SEM/1974*, 927-934.
17. D. L. Davidson, "Assessment of defect density magnitude by changes in selected area electron channeling patterns," *SEM/1981*, in press.
18. D. L. Davidson, "The observation and measurement of displacements and strain by stereoimaging," *SEM/1979 II*, 79-86.

THE APPLICATION OF ELECTRON BEAM INDUCED CURRENT

J. R. Beall

Electron Beam Induced Current (EBIC) represents a valuable scanning electron microscope (SEM) application for the analysis of semiconductors. EBIC is nondestructive and easily adapted to the analysis of complex semiconductor circuits. The EBIC generation process, signal contrast formation, and video imaging techniques are reviewed. Typical examples are described to demonstrate the value and versatility of EBIC.

Introduction

The concept of detecting EBIC by means of pn junctions to separate induced electron-hole pairs was first described by Ehrenberg et al. in 1951.¹ A great wealth of information has followed that provides a better understanding of primary-electron interactions with solid surfaces, backscatter coefficients, electron penetration depth dependence, electron-hole generation, carrier lifetime, and imaging techniques. These fundamentals are reviewed to develop the basis for EBIC application techniques. A conceptual description of the electron beam processes, in conjunction with a semiconductor device, are used to provide a basic understanding of EBIC generation. This level of understanding should be sufficient to determine the feasibility of applying EBIC to different problems or applications.

Secondary electron imaging (SEI) is the principal imaging mode of the SEM. SEI contrast is developed from electron interaction with the immediate solid surface and is a function of surface topography. In comparison, EBIC is developed beneath the surface and contrast is a function of surface energy absorption and the energy loss in the active region of the underlying semiconductor. The combination of these imaging modes provides a unique capability for the analysis of semiconductor properties.

EBIC Generation

The electron beam deposits the total beam current on the specimen surface. A portion of this beam current is reflected from the specimen. An electron backscatter coefficient was derived by Bishop that provides a first-order approximation of the reflected and absorbed currents.² The backscattered coefficient depends on the atomic number of the target (density), electron beam angle of incidence, and incident electron energy. With normal beam incidence the backscattered coefficient at 20 keV is 18% for aluminum and silicon targets and 50% for gold targets.

Therefore, approximately 18% of the beam current is reflected from the surface of a semiconductor consisting of aluminum, silicon oxide, and silicon. For a beam current of 100 pA the absorbed or specimen current is about 82 pA. The EBIC level is a function of the beam current and electron energy that is lost in the active region of the semiconductor. EBIC is typically over a 1000 times greater than the current level absorbed in the active region. The electron beam loses energy through multiple scattering events. Each scattering event produces electron-hole pairs which in silicon represents a mean energy loss of 3.6 eV per pair. A 15 keV electron entering the active region provides a multiplication factor of approximately 4100. If one assumes that each electron-hole pair generated is successfully separated and measured, the EBIC level approaches 340 nA, based on an absorbed current of 82 pA. However, the measured current is modified by beam energy losses in the surface films and electron-hole recombination in the active region. The electron-hole pairs generated in the surface oxide and metal films are trapped or recombine to contribute a fraction of the total absorbed current with respect to the measured EBIC. Therefore, this contribution is negligible. As the beam energy is increased, the energy loss in the active region increases but the percentage of energy lost in the surface films decreases. Therefore, lower beam energies provide improved contrast for surface film evaluation and higher beam energies provide improved contrast for bulk evaluation.

The author is with the Parts Technology Group of Martin Marietta Aerospace, Box 179, Denver, CO 80201.

Separation and detection of electron-hole pairs generated in the active region depends primarily on the minority-carrier diffusion length of the semiconductor material and the distance from the pair generation site to the semiconductor junction. The minority-carrier diffusion length and diffusion geometries of typical semiconductor devices provide good EBIC response. The primary beam energy and atomic density of the target are the basic factors that determine the electron range in solids. Figure 1 illustrates the effect of surface film thickness on electron range and EBIC generation. Beam energy loss below the detector gate produces electron-hole pairs. This EBIC can be measured or imaged as recombination current that flows through a parallel circuit path. The EBIC signal is inversely proportional to the film thickness and density and depicts the complement of surface topography. A visual interpretation of the detected EBIC signal provides a qualitative assessment of surface topography.

Many theoretical studies and experimental measurements have been conducted to determine the electron range for various materials and beam energies. Through the evolution of these studies came expressions for deriving the electron range. The electron ranges calculated from these expressions do not generally yield the same results, in part because of the definition of electron range and the basis from which the expressions were derived. Two electron range equations are included as examples. The first equation was derived by Everhart and Hoff and is based on energy-dissipation range.³ This equation is valid for acceleration voltages of 5 to 25 keV and atomic elements 10 through 15. This range would include semiconductors employing aluminum, silicon dioxide, and silicon materials. The equation is:

$$R_G = 4.0 E_B^{1.75}$$

where E_B is the beam energy in keV and R_G is the range in $\mu\text{g}/\text{cm}^2$ (pR). This equation is plotted in Fig. 2 and shows the relationship of electron range in microns and acceleration voltage in keV for Al, Si, and SiO_2 .

The second equation, derived by Kanaya and Okayama, is based on a modified diffusion model.⁴ This equation is valid for acceleration voltages of 10 to 1000 keV for all elements. This equation applies for all semiconductor materials. The equation is:

$$\text{pR} = \frac{2.76 \times 10^{-11} A E_0^{5/3}}{Z^{8/9}} \frac{[1 + (0.978 \times 10^{-6} E_0)]^{5/3}}{[1 + (1.957 \times 10^{-6} E_0)]^{4/3}}$$

where E_0 is the beam energy in eV, A is the atomic weight in grams, Z is the atomic number, p is the density in g/cm^3 , and R is the range in cm. This equation is plotted in Fig. 3, which shows the relationship of electron range in microns and acceleration voltage in keV for Au, Cu, Al, Si, and SiO_2 . These graphs of the electron range equations show the significance of film density.

Electron range and energy dissipation profiles for Al and Au are compared in Fig. 4, which represents the respective ranges for a 15kV beam voltage. The energy dissipation profile depicts the energy-loss distribution in an Al film. The energy-loss distribution for the hemisphere is shown by the truncated Gaussian curve; the maximum occurs at the centroid of this curve.

The beam-induced electron-hole multiplication currents are separated by the semiconductor junctions. Separation occurs through minority carrier diffusion. From the point of origin the electron (in p material) or hole (in n material) drifts toward the junction depletion region. If this distance is within the minority carrier diffusion length, the carrier typically arrives at the depletion region boundary, where it is swept across the depleted region and separated. Figure 5 shows a cross-sectional view of a typical pnp transistor. Primary electrons penetrate into the regions of the transistor junctions and generate electron-hole pairs. These carriers can be efficiently separated by intrinsic and induced junction bias potentials. The holes generated in the base diffusion, which diffuse across the base-emitter and base-collector junctions produce a net electron increase in the base. One can image or measure this EBIC by connecting a current amplifier as shown in Fig. 6. The increase in electrons in the base produces a current flow through the current amplifier input and return through ground to the emitter and collector diffusions where they recombine with excess holes. Carrier separation occurs only when an electron-beam-generated bias or external reverse bias is applied to at

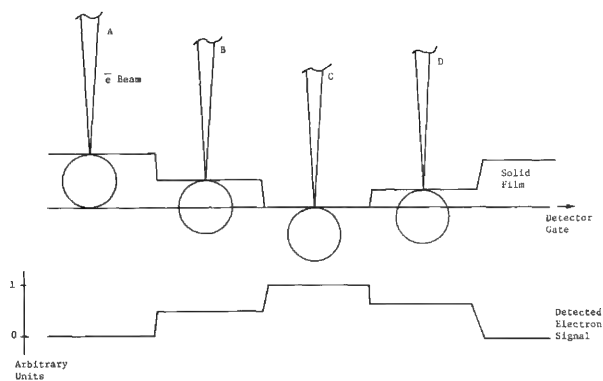


FIG. 1.--Electron range as function of film thickness.

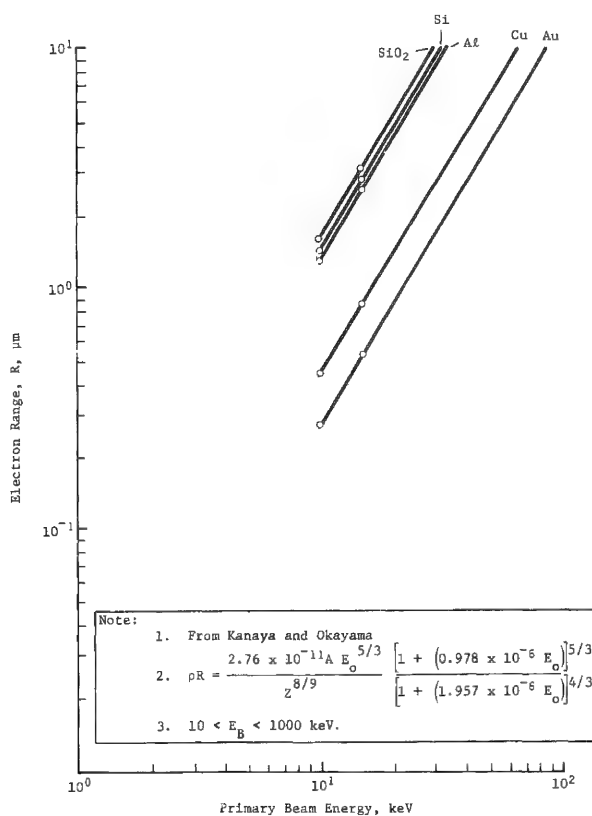


FIG. 3.--Electron range R vs primary beam energy.⁴

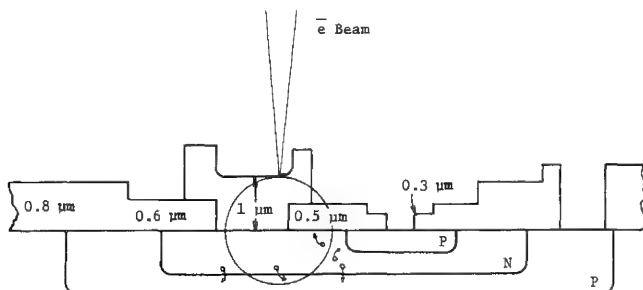


FIG. 5.--Cross-sectional view of typical pnp transistor depicting carrier generation.

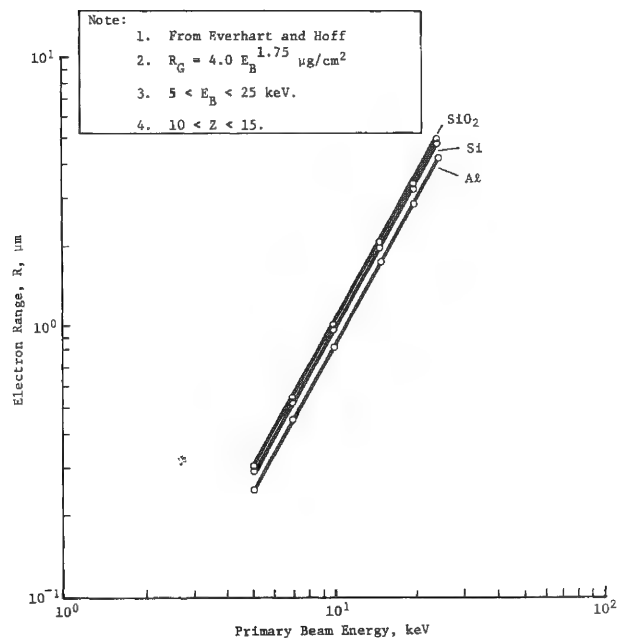


FIG. 2.--Electron range R vs primary beam energy.³

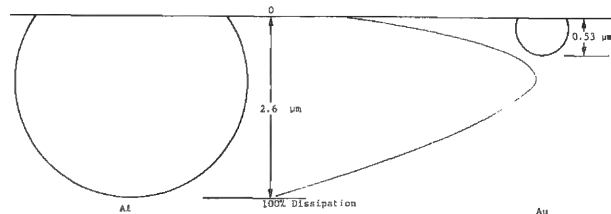


FIG. 4.--Electron range for aluminum and gold at 15 keV (Kanaya and Okayama⁴) and electron energy dissipation for aluminum (Everhart and Hoff³).

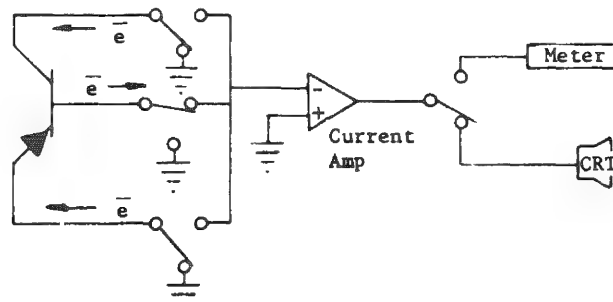


FIG. 6.--Schematic of typical specimen current amplifier interconnect circuit.

least one junction of the transistor. For example, if the emitter and collector were disconnected from ground, the current flow measured through the base connection would be the absorbed portion of the incident electron beam current.

Two factions contribute to the composite EBIC signal. One is the variance that occurs from the energy-loss differences for surface oxide and metal thin films. The contrast varies in proportion with film thickness and material density. The second faction depends on the point of origin for carrier pair generation in conjunction with the detection efficiency of the semiconductor diffusion. This contrast component depends primarily on the distance the minority carrier must travel for separation to occur, the semiconductor carrier diffusion length (parameter relating carrier recombination probability), and diffusion dopant polarity. To this extent EBIC provides applications relating to surface thin film evaluation and bulk carrier property evaluation. The image resolution for EBIC applications approaches that of the incident beam diameter for surface topography profiling and decreases to several microns for bulk property evaluation. The image resolution for EBIC applications approaches that of the incident beam diameter for surface topography profiling and decreases to several microns for bulk property evaluation.

Imaging EBIC from discrete transistors is straightforward. For integrated circuits the EBIC measurement points are not as accessible and multiple internal circuit paths are present. These parallel current paths impede external measurement of EBIC responses from these junctions. The power and ground terminals typically provide the best circuit access for EBIC imaging. Although the portion of the circuit that can be imaged is device dependent, it typically includes the major part of the circuit. The silicon-gate MOS technology is an exception. This process generally does not tolerate beam irradiation of the gate oxide. EBIC evaluation of complex integrated circuits usually requires an intimate understanding of circuit manufacturing and construction processes.

EBIC Application Examples

There are numerous applications of EBIC for measurement, evaluation, and analysis of semiconductors and their properties. EBIC applications will certainly increase as the circuit complexities grow and the defects diminish in size. EBIC provides an accurate and cost-effective solution to many problems associated with complex integrated circuits, complex integrated circuits.

The first example illustrates surface profiling by EBIC. In this example the incident beam serves as a stylus and provides a qualitative portrayal of surface topography. Figure 7 is an SEI micrograph of an aluminum conductor deposited over a silicon dioxide step on a junction FET. The micrograph contains two scan cursors and related EBIC line scan responses. The EBIC response has been inverted to portray relative surface topography. Figure 8 is an SEI micrograph of this oxide step with the specimen tilted at 75°. This micrograph provides a good topographical perspective for comparison of the EBIC line scans. An application has been reported for quantitative measurement of metallization coverage at oxide steps.⁵

The next example illustrates the location of a diffusion defect by means of EBIC. Figure 9 is a photograph of a 10 × 10 diode array. Approximately 25% of the diodes in each array exhibited excess reverse leakage. Evaluation of the leaky diodes by EBIC identified the cause of leakage. Figure 10 is an SEI micrograph of a leaky diode. Figure 11 is an EBIC micrograph of the same diode identifying a diffusion pipe located by the arrow. Once the cause of leakage was identified this failure mode was easily corrected.

An application has been reported which provides nondestructive measurement of diffusion depth.⁶ This application provides a cost-effective improvement for diffusion depth measurement.

The next example illustrates an application of EBIC for location and identification of electrostatic discharge (ESD) damage in an operational amplifier. Figure 12 is a photograph of the amplifier die with an arrow locating the transistor cell containing the ESD damage site. Figure 13 is an SEI micrograph of this cell showing the emitter, base, and collector contacts. Figure 14 is an EBIC micrograph that locates an ESD-induced filament between the emitter and base (arrow).

These examples represent a few of many EBIC applications for semiconductors. In most cases these applications represent unique solutions or cost improvements over previous methods.

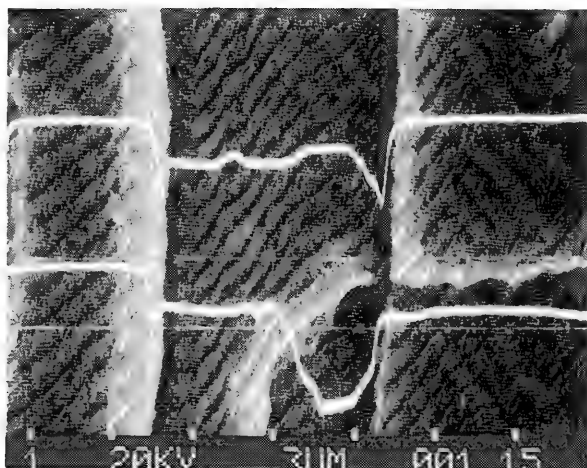


FIG. 7.--Composite SEI and EBIC micrograph showing two inverted EBIC line scans. Line scan axis is located by adjacent cursor lines; 350 \times .

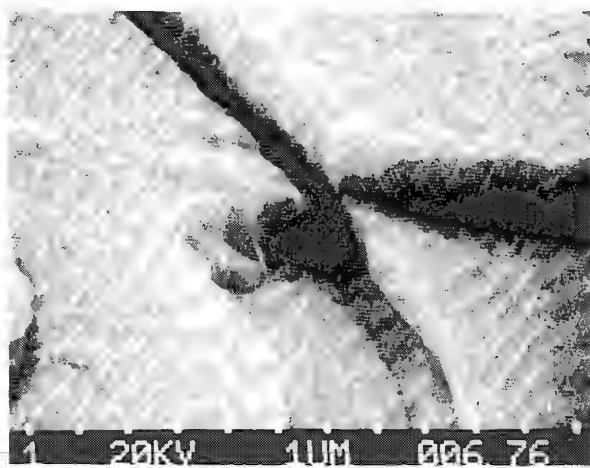


FIG. 8.--SEI micrograph of same area shown in Fig. 7; tilt angle 75 $^{\circ}$, 700 \times .

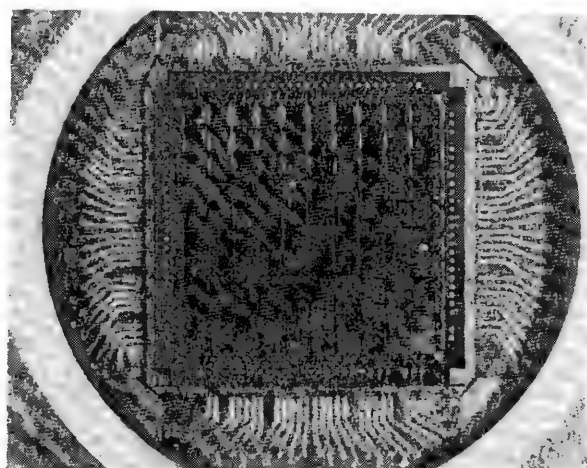


FIG. 9.--10 \times 10 photo diode array; 15 \times .

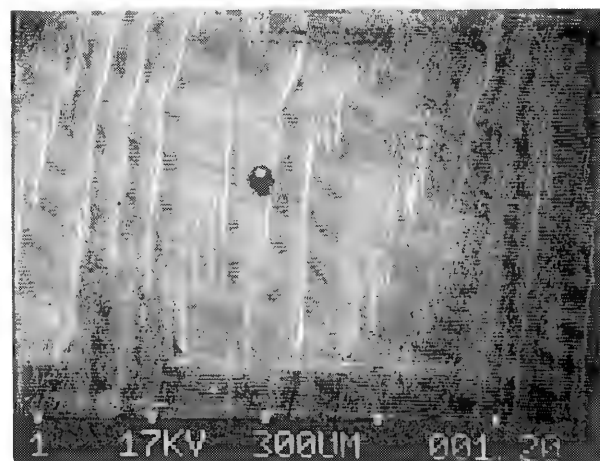


FIG. 10.--SEI micrograph of defective diode cell; 50 \times .

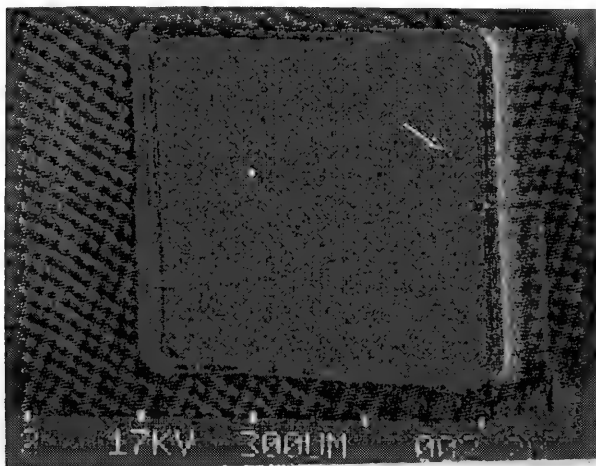


FIG. 11.--EBIC micrograph of same cell shown in Fig. 10, with diffusion pipe located by arrow; 50 \times .

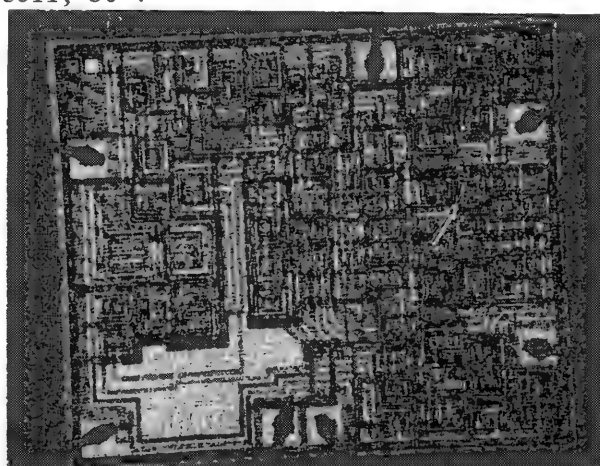


FIG. 12.--Complete operational amplifier die; arrow locates damaged transistor cell; 550 \times .

Conclusion

EBIC has many attributes that are readily adapted to the evaluation and analysis of semiconductors. These applications usually provide significant improvement over alternative methods and require less risk in performing the analysis. The inherent qualities of EBIC will likely provide solutions to problems encountered in future semiconductors.

References

1. W. Ehrenberg, C. S. Lang, and R. West, "The electron voltaic effect," *Proc. Phys. Soc.* A64: 424, 1951.
2. H. E. Bishop, "Some electron backscattering measurements for solid targets," *Fourth Cong. Int. X-Ray Opt. Mic.*, 1966, 153.
3. T. E. Everhart and P. H. Hoff, "Determination of kilovolt energy dissipation vs penetration distance in solid materials," *J. Appl. Phys.* 42: 5837, 1971.
4. K. Kanaya, S. Okayama, "Penetration and energy-loss theory of electrons in solid targets," *J. Physics* D5: 43, 1972.
5. J. Beall, "Quantitative measurement of metallization integrity using EBIC," *Adv. Tech. in Failure Analysis*, IEEE Catalog 78CH1407-6 (REG. 6), 1978.
6. J. Chi and H. Gatos, "Non-destructive determination of the depth of planar p-n junctions by scanning electron microscopy," *IEEE Trans.* Ed-24, 1977.

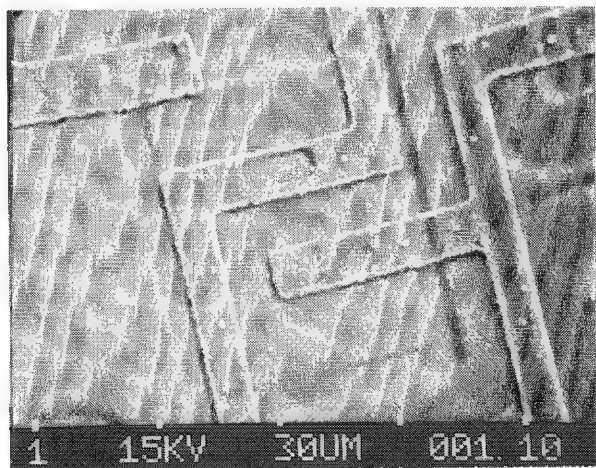


FIG. 13.--SEI micrograph of damaged transistor cell; 550 \times .

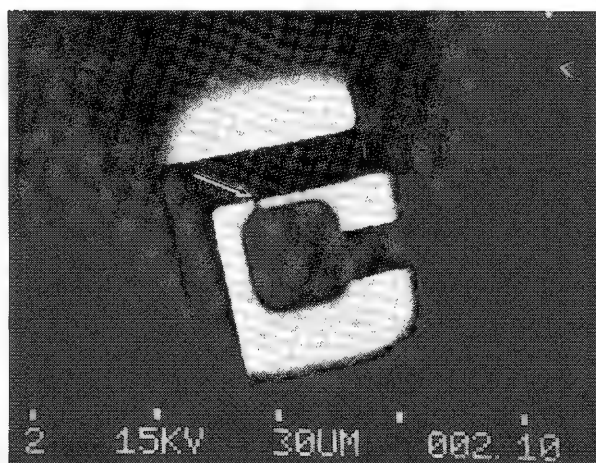


FIG. 14.--EBIC micrograph of transistor cell locating ESD damage site (arrow); 550 \times .

ACQUISITION, STORAGE, AND DISPLAY OF VIDEO AND X-RAY IMAGES

J. J. McCarthy, G. S. Fritz, and R. J. Lee

This paper describes a computer-based system that provides the capability to acquire, store, and display digital images from a scanning electron microscope (SEM). The system represents a modest expansion of a standard computer-based energy dispersive x-ray multi-channel analyzer (EDS/MCA). The additions to the normal MCA and floppy-disk subsystem consist of a digital scan generator, the interface to the SEM, and a high resolution (512 × 256 pixels) color video monitor. The software for the system can collect, store, and display both video and x-ray images. The images may be displayed as false-color gray level images, isometric contours, or as color coded maps.

Digital image recording has many advantages, particularly in the case of x-ray mapping. By placing the beam position of the SEM under direct computer control, one can avoid the problems of image registration, resolution, and count rate limitations. In addition, since image data can be obtained from several elements simultaneously, overall collection time is greatly reduced. Finally, after the data have been acquired and stored, images can be digitally processed to obtain an image that could not be obtained in any other manner.

Description of System

A simplified block diagram of the system is shown in Fig. 1. The EDS MCA is a standard TN-2000 x-ray analysis system equipped for quantitative EDS analysis. The computer chosen for the system is a PDP-11/23, configured with 64K words of solid-state memory and memory management. Special software has been written to use the extended memory as a fast input/output device to store and recall digital images. This process allows image(s) to be acquired and stored quite rapidly, and then inspected or processed before being transferred to floppy disk.

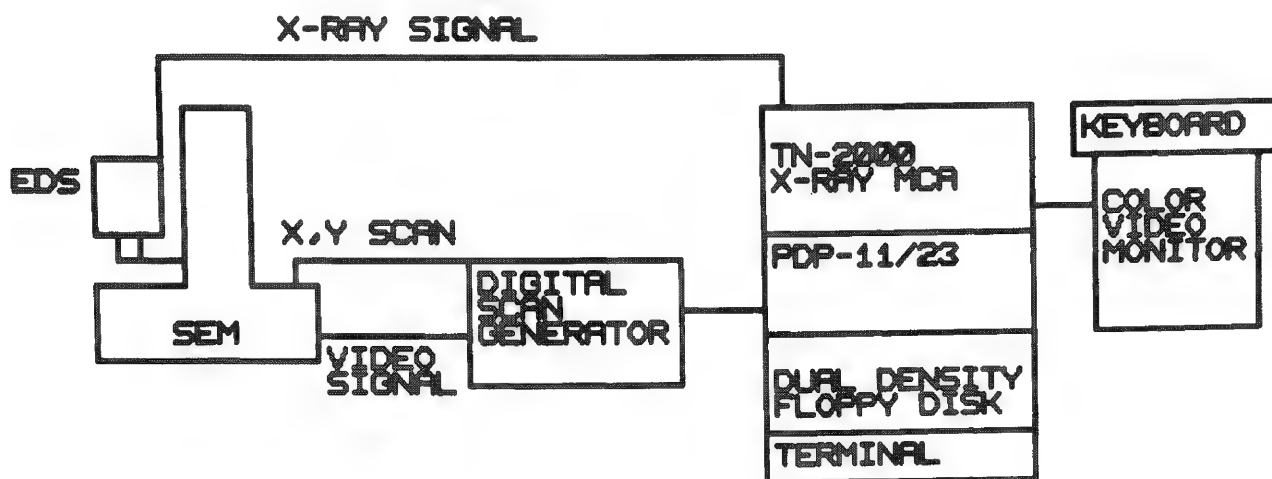


FIG. 1.--Block diagram of computer-based imaging system.

The Spectra Chrome 512 color video monitor performs a dual function in the system. In normal use the monitor provides the spectral data display for the TN-2000 with a horizontal resolution of 512 channels, and the usual complement of features expected of this type of data display. As a graphics image display, the monitor offers a resolution of 512 × 256 pixels, and the ability to select a variety of color shades to indicate intensity levels. The monitor is a complex mixture of hardware and software components and includes

Authors McCarthy and Fritz are with Tracor Northern, Inc., Middleton, WI 53562.
Author Lee is with U. S. Steel Research Laboratories, Monroeville, PA 15146.

a large image memory, a unique high-speed video refresh system, a pair of microprocessors for control, and a high resolution red-blue-green video monitor. Support software for the monitor includes routines for point and area painting, vector generation, color selection, generation of complex figures, and a number of specialized operations.

The digital scan generator consists of a video signal processor and an X-Y scan controller. The video processor includes a fast (1 μ s/sample) 8-bit analog-to-digital converter (ADC) which digitizes the SEM video signal into 256 distinct gray levels. Multiple samples may be obtained at a single pixel, and the summed result presented to the computer. A 12-bit digital-to-analog converter (DAC) allows the computer to output video signals to the SEM CRT display. Additional circuitry for use in feature analysis is not described in this paper. The feature analysis mode is described elsewhere in these proceedings.¹

The X-Y scan controller consists of two 12-bit DACs for positioning the SEM beam and a joystick module for use with an X-Y cursor. The cursor appears in the digital raster image when the SEM is under computer control. The position of the cursor can be read by the computer, which allows indexing of particular features in the image for analysis, or to record start and stop points for a digital linescan. A number of utility programs provide computer control of beam positioning, video signal acquisition, image storage, and output to the SEM CRT of image and graphics information.

Image Acquisition and Storage

In normal operation, the SEM beam is positioned in a raster fashion on a grid over a field of view. A typical grid contains 256×256 points for a video image, and 128×128 points for an x-ray image. (Point densities up to 4096 by 4096 are possible, but not particularly useful, especially for an x-ray image!) At each grid point, the beam is held stationary for a specified dwell time while a number of video samples is obtained or a set of x-ray intensities collected. Since the computer has full control of the beam, the dwell time and the number of operations performed at each grid point may be varied to obtain a desired result. For example, background subtracted x-ray intensities may be obtained "on-the-fly" during the acquisition by monitoring of specified background regions for each element. During each raster line, the data for all monitored intensities are displayed on the monitor in the form of line profiles. This procedure provides a convenient monitor of the progress of the acquisition and buffers the data before output to storage. At the end of each image line, the data are transferred to extended memory or disk storage. In normal operation, a single video image or up to eight x-ray images are collected during an acquisition. Single or dual density floppy disk drives may be used for image storage but the greater storage capacity of the dual density system recommends that device. A single-sided double-density floppy disk can store about four 256×256 video images or multiple x-ray images (depending on the number of elemental intensities recorded). Since the video monitor can display eight 128×128 images, acquisition and storage of eight elemental images at one time is a convenient match to the video display resolution. Typical dwell times of 100 to 200 ms for x-ray images yield a total collection time of about 4 min. Video image collection and dwell times are much shorter; images that average one hundred samples per pixel can be collected and stored in 70 s.

Image Display

Digital images may be read back from storage and displayed on the Spectra Chrome 512 video monitor. If the image is displayed with the highest monitor resolution, eight colors are available to code intensity information into false-color images. If a lower resolution can be tolerated, shading of each color is possible to generate a larger number of color levels. Initially, the range of intensities presented in the image is divided into eight equal gray levels and each gray level is assigned a color. The colors are selected so that low intensities are assigned "cool" colors, higher intensities are assigned "warm" colors, and the highest intensities become white. If the image obtained in this fashion is not satisfactory, a gray-level histogram can be generated with each gray level denoted by a color band. The operator may then re-define the color coding of each band and obtain a new image display. This process may be repeated until a satisfactory image is obtained.

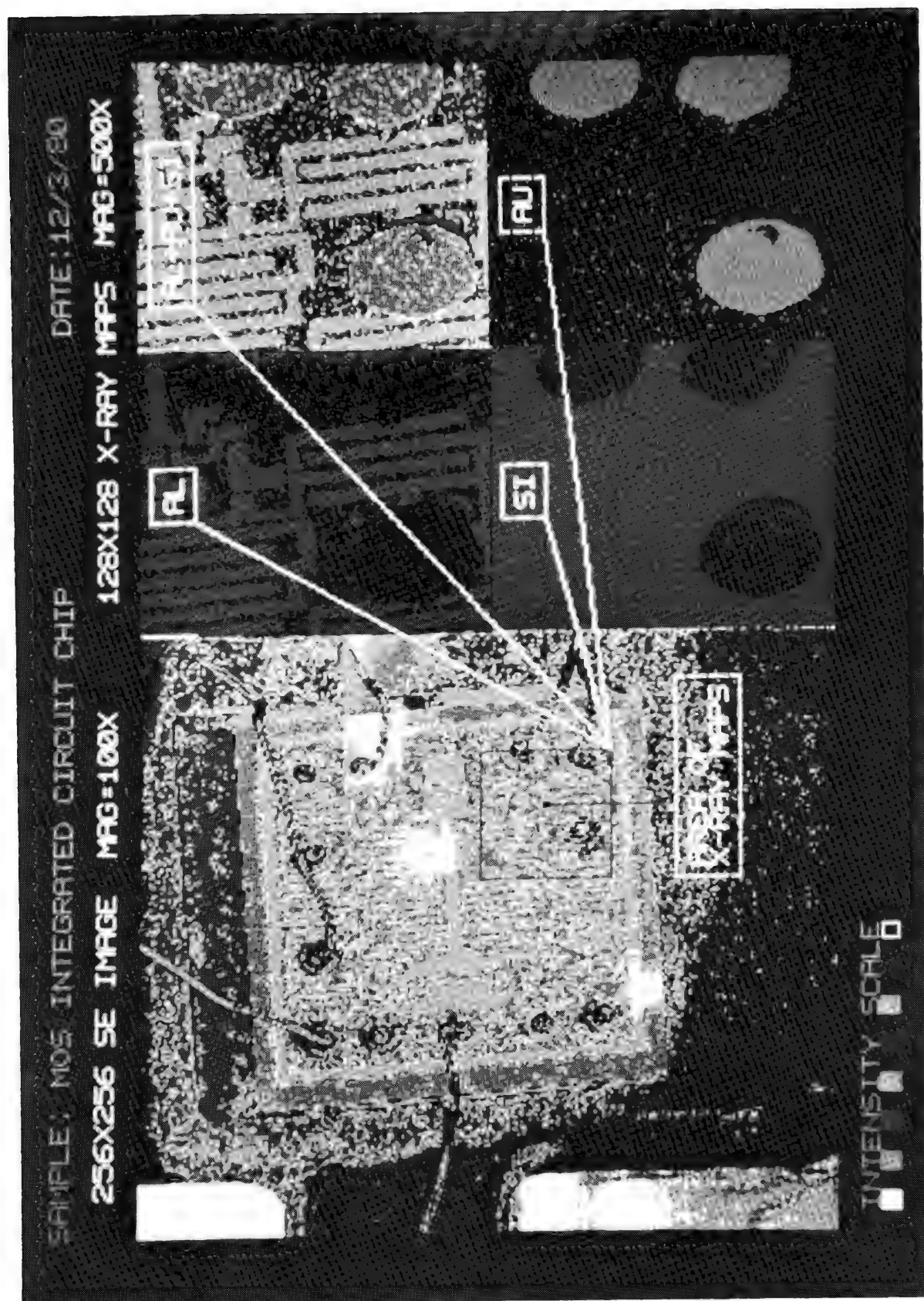


FIG. 2.--Digital secondary-electron and x-ray images of MOS integrated circuit chip. Video image illustrates use of false color for feature enhancement. X-ray image in upper right corner is composite map formed by "OR-ing" other three elemental maps into single image. (Photographed directly from video monitor.)

Although the same type of false-color image may be displayed for any of the x-ray images collected, it is often more useful to present several elemental maps in the same display with each element represented by a different color. In this format the spatial distribution of each element is revealed at a glance at the separate color-coded images. It is frequently useful to determine which elements are spatially overlapped in the field of view under examination. One can generate a display of this type by producing one multi-element image that combines several single-element images. In this display, each element is still denoted by a single color; however, where two elements occur at the same point, a new color is generated by "OR-ing" the two elemental colors. In this scheme, spatial overlaps of three or more elements appear white in the final image.

Examples and Discussion

Particularly useful is the combination of a video image with one or more x-ray images. An example of this type of display is shown in Fig. 2. The left half of the display is a 256×256 secondary electron image of the specimen (an MOS integrated circuit). The right half of the display consists of three color-coded single element maps, and a multielement composite image constructed from the other three. The image data were collected on an International Scientific Instruments (ISI) Super II Mini-SEM. With the help of the graphics included in the image, the area examined by x-ray mapping (at higher magnification) is easily discerned. This figure also illustrates the need to be able to manipulate the relationship of false color to intensity level in order to obtain a useful image. The video image portion of this display is shown with a false-color scale that is the reverse of the "cool" to "warm" scale discussed earlier. The reversed scale not only results in an image that is much more pleasing to the eye, but also calls attention to details in the image that are not as apparent when the normal color scale is used.

In addition to providing a large amount of information about the specimen in a single composite image display, digital imaging can lead to substantial reductions in the time required for analysis of a sample. By careful selection of the imaging mode and collection of selected x-ray line profiles, the spatial distribution of elements in the specimen can be determined without acquisition of a complete x-ray map, and the total observation time can be greatly reduced. Figure 3 illustrates this concept. The left half of the display is a backscattered electron image (BSE) of a multiphase inclusion found in a specimen of stainless steel; the right half shows four digital elemental line profiles taken across this inclusion. The data were taken with an ETEC Autoscan SEM equipped with a multiple segmented solid-state BSE detector. The false-color scale was carefully chosen to separate features in the inclusion. The x-ray line profile data can be used for easy identification of the elemental composition of the entire inclusion. The data were gathered in about 5 min; a complete x-ray map would have required 20-30 min.

After the data have been collected and stored, there are many interesting ways to process the image(s) to enhance the final result before display. Jones and Smith have published a comprehensive review of the field of image processing as it can be applied to scanning electron microscopy.² Image enhancement techniques in particular seem to be readily incorporated into the type of system described in this paper. The software already evolved to treat EDS spectral data is easily adapted to operations on stored images. For example, contrast and brightness changes can be effected by subtraction or multiplication of the entire image by a constant. The observed noise in an image can be reduced by operations such as filtering or nearest-neighbor averaging. Entire images may be added to or subtracted from one another to arrive at an entirely different result.

Although these techniques can be applied to both video and x-ray images, special methods can be used for processing of x-ray images. Statham and Russ have both discussed special processing techniques of interest.^{3,4} Since data can be collected from many regions of the EDS spectrum at the same time, operations based on the use of information from more than one region can be performed. An obvious example is the use of background regions adjacent to peak regions to form a background subtracted image. This method can be a great aid when elements are present in low concentration. Images formed from the ratio of different peak regions are useful in identifying particular phases. The use of peak-to-background ratios where the background region is chosen to cover a portion of the bremsstrahlung continuum provides a correction for backscatter and absorption effects.

Finally, peak overlaps may be corrected by subtraction of a fraction of the counts from an appropriate peak region from the peak counts in the region of interest.

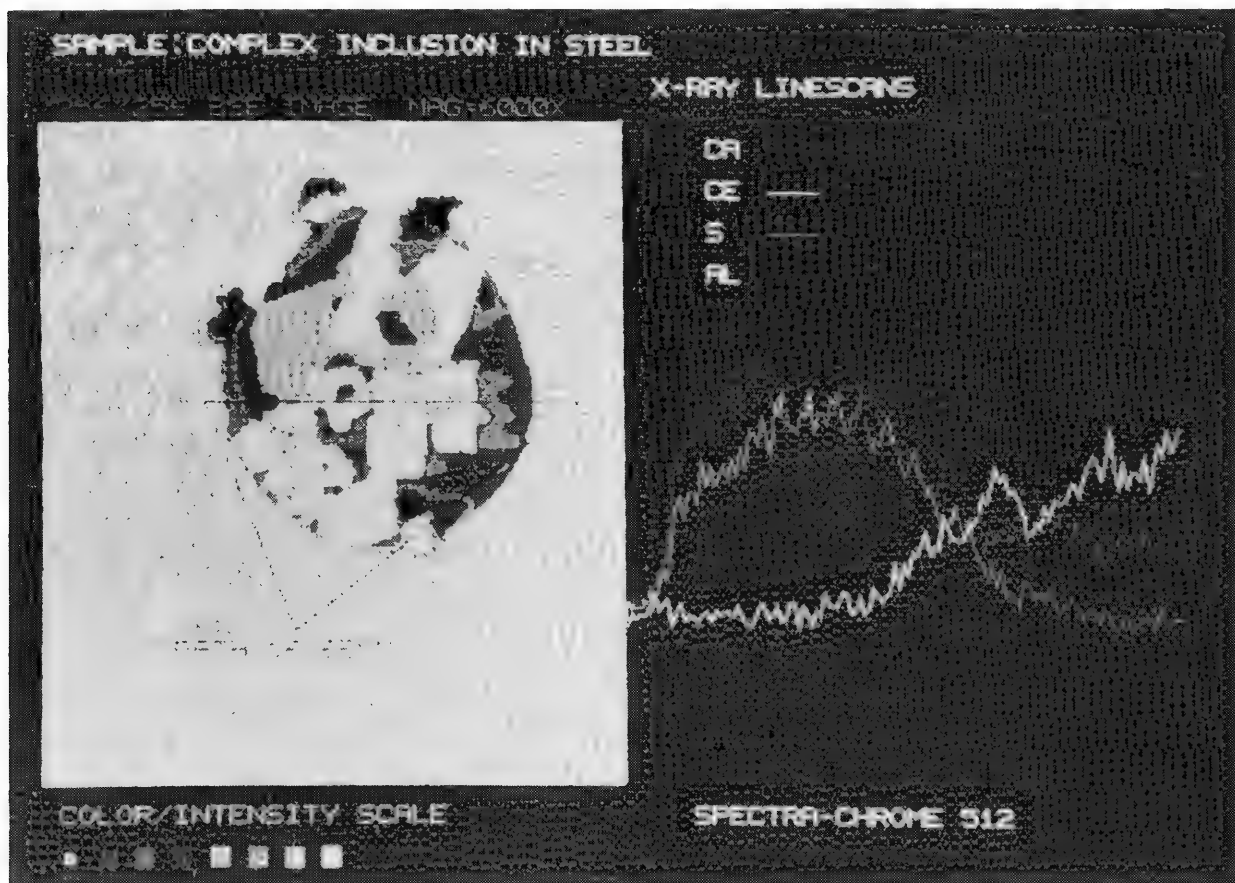


FIG. 3.--Digital backscattered electron image and x-ray line profiles of biphase inclusion in stainless-steel specimen. This figure illustrates use of carefully chosen false-color scale to separate phases visually. Composition of phases can be quickly determined from x-ray line profiles. (Photographed directly from video monitor.)

Summary

A computer-based system has been described which can acquire, store, and display digital video and x-ray images from a scanning electron microscope. The system represents a modest addition to the familiar EDS-MCS system used for analysis of x-ray spectral data.

Although digital image acquisition and processing has been in use for some time, the application of this technique to x-ray images using the scanning electron microscope is a recent development with great potential. The precise control of all phases of image accumulation and recording, the virtually unlimited dynamic range, and the ability to process image data further provides a capability far superior to the conventional photographic recording and analog electronic processing in current use.

References

1. G. S. Fritz, J. J. McCarthy, and R. J. Lee, "Interactive software for automated particulate analysis," *Microbeam Analysis--1981*, 57.
2. A. V. Jones and K. C. A. Smith, "Image processing for scanning microscopists," *SEM/1978 I*, 13-26.
3. P. J. Statham and M. Jones, "Elemental mapping using digital storage and color display," *Scanning* 3: 168, 1980.
4. J. C. Russ, "New methods to obtain and present SEM x-ray linescans," *Microbeam Analysis--1979*, 292.

SIGNAL PROCESSING TECHNIQUES IN AUGER ELECTRON SPECTROSCOPY

K. K. Smith and G. E. McGuire

Auger Electron Spectroscopy (AES) has become an extremely important tool in the analysis of thin films and surfaces owing to its high spatial resolution ($<500 \text{ \AA}$) and shallow sampling depth (about 10 \AA). Recent developments in AES hardware have been aimed at improving spatial resolution; developments in signal processing and image analysis have been aimed at faster, more accurate data acquisition and presentation. Commercial Auger spectrometers are now interfaced to microprocessors and computers that control data acquisition and display. Already several schemes have been developed for background subtraction¹ and to correct for changing secondary electron yields caused by matrix and topography effects.² Auger line shapes have been calculated³ and spectra for binary mixtures which have overlapping Auger peaks have been simulated.⁴

The options available for Auger data acquisition are reviewed: derivative, pulse counting, beam brightness modulation (BBM), and digital. The advantages and disadvantages of these techniques are discussed in terms of signal-to-noise (S/N) ratios, data acquisition time, and impact on spatial resolution.

Hardware

The most common data collection and presentation scheme used in past years has been the derivative mode first used by Harris in 1968.⁵ This approach became popular when it was realized that energy analysis of electrons in the derivative mode could be achieved by means of the retarding potential analyzer (RPA) of existing low-energy electron diffraction (LEED) systems.^{6,7}

The next major advancement in AES was the introduction of the cylindrical mirror analyzer (CMA) by Palmberg et al.⁸ With its high transmission and good resolution it quickly replaced the RPA. Except for improvements in data collection and spatial resolution of the primary electron beam, little change in the basic AES instrumentation has occurred since the incorporation of the CMA. Figure 1 shows a typical scanning Auger spectrometer. High-energy (1-10keV) primary electrons from a LaB₆ source may be focused to a point or synchronously deflected across the sample at variable raster rates. The distribution of electrons scattered by a solid is dominated by peaks from the elastically scattered primary electrons and true secondary electrons. Auger emission occurs with relatively low intensity at intermediate energies, accompanied by a high background of inelastically scattered electrons. Since the background is a smoothly varying function except for the presence of the Auger transitions, differentiation enhances the Auger signal relative to the background. One achieves this effect by ramping the voltage applied to the outer cylinder of the energy-dispersive CMA and superimposing a small sinusoidal modulation voltage on the ramped voltage. The signal from an electron multiplier placed at the end of the CMA is detected synchronously with the modulation voltage.

Electrostatic deflection analyzers have a resolution given by $R = \Delta E/E$, where R is the percent resolution when Δ is the full-width-at-half maximum for electrons of energy E . CMAs are typically used in the constant-percent resolution mode, where R is maintained at a constant value as E is increased, which means that ΔE must increase proportionately to E . In Auger spectra the background is fairly constant and the amount of background electrons that pass through the CMA and strike the detector is equal to $\Delta E \cdot N(E)$, where $N(E)$ is the background plus signal level. However, ΔE is proportional to E , so that the signal from the detector must then be proportional to $E \cdot N(E)$. The correct ordinate label for Auger data taken with a CMA should then be $E \cdot N(E)$ or $dE \cdot N(E)/dE$ versus E . When CMAs became the predominant electron energy analyzers, data were still erroneously referred to as $N(E)$ and $dN(E)/dE$ versus E , which is correct for data taken on a RPA.

The chief advantage of the derivative spectrum is its widespread use. Standard Auger spectra are reported in the derivative mode with the negative excursion used as the characteristic Auger kinetic energy.^{9,10} Derivative spectra may be used quickly for elemen-

The authors are at the Materials Analysis Laboratory of Tektronix, Inc., Box 500, Beaverton, OR 97077.

tal identification and semiquantitative analysis by measurement of the peak-to-peak height. The major problem with this approach is that peak shapes change with chemical composition and the peak-to-peak heights are no longer indicative of relative elemental abundance.¹¹ Although there is an approximately linear increase in S/N for modulation amplitudes up to a few eV,¹² overmodulation can cause significant distortion of the Auger signal and overlap of closely spaced transitions. Studies show that maximum sensitivity with minimum distortion occurs when modulation voltages of 2-4 eV are used.^{13,14}

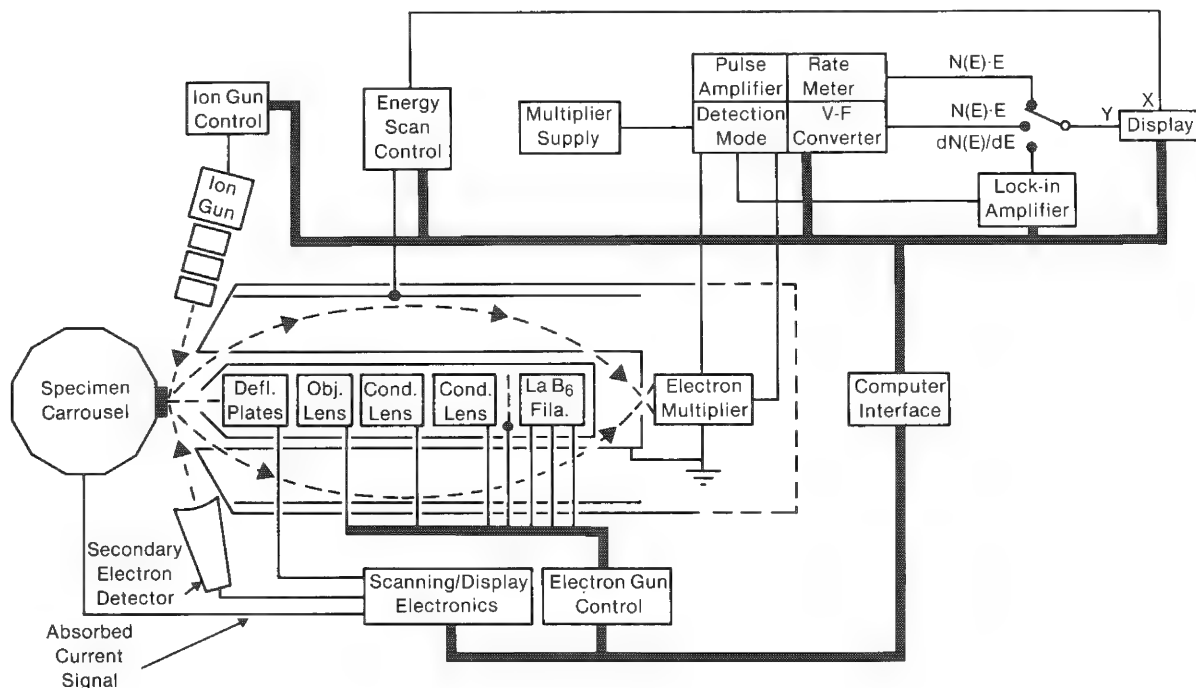


FIG. 1.--Schematic and block diagram of scanning Auger spectrometer with coaxial electron gun within single-pass cylindrical mirror analyzer.

Tailored modulation techniques (TMT) may be used to decrease unwanted modulation effects. Springer et al.¹⁵ invented a unique TMT that used positive and negative square modulations 180° out of phase. The resulting data were already background subtracted in the $E \cdot N(E)$ mode. By adding a cosine wave to the modulated signal they were able to get a background-corrected $fE \cdot N(E)$ signal. These TMTs assume a linearly varying background in the region of interest. Unfortunately, that may not be true in all cases and is certainly not true when two Auger peaks are separated by exactly the square-wave modulation voltage. This problem may be resolved if the square-wave modulation voltage is set up individually for each sample.

Another TMT consists of a waveform whose slope is initially constant and increases exponentially to a large value.¹⁶ This scheme was shown to enhance the S/N of derivative spectra by a factor of three but to introduce only minor artifacts. This TMT scheme also allowed for deconvolution due to the known instrument-response function, which gave approximately 2× better resolution. These TMTs could be implemented fairly easily with a signal generator to add a great deal of versatility to an instrument.

Many spectrometers may also be operated in the pulse-counting mode. The pulses are counted directly from the electron multiplier and displayed as $E \cdot N(E)$ vs E . The total signal from the electron multiplier is stored by pulse counting (whereas in derivative spectra, only the in-phase minus the out-of-phase portion of the signal is stored when energy modulation is used). Since S/N increases with \sqrt{t} , the S/N for pulse-counting, digital, or any continuous recording of the signal should be higher than that of derivative spectra as long as other factors are constant. The only exception occurs when the signal becomes too large to handle in the pulse-counting mode. The upper limit corresponds to a detector current of 10 μ A or count rate of 100 MHz in a high-gain (about 10^6) low-noise multiplier. The factor of 3-5 improvement in S/N of pulse counting is extremely

important in data collection, where high spatial resolution is desired.¹⁷ Under these circumstances the primary electron beam current (and subsequently the detector current) is reduced considerably as the electron-beam spot size is reduced. High spatial resolution is achieved only at the expense of data-acquisition time or S/N.

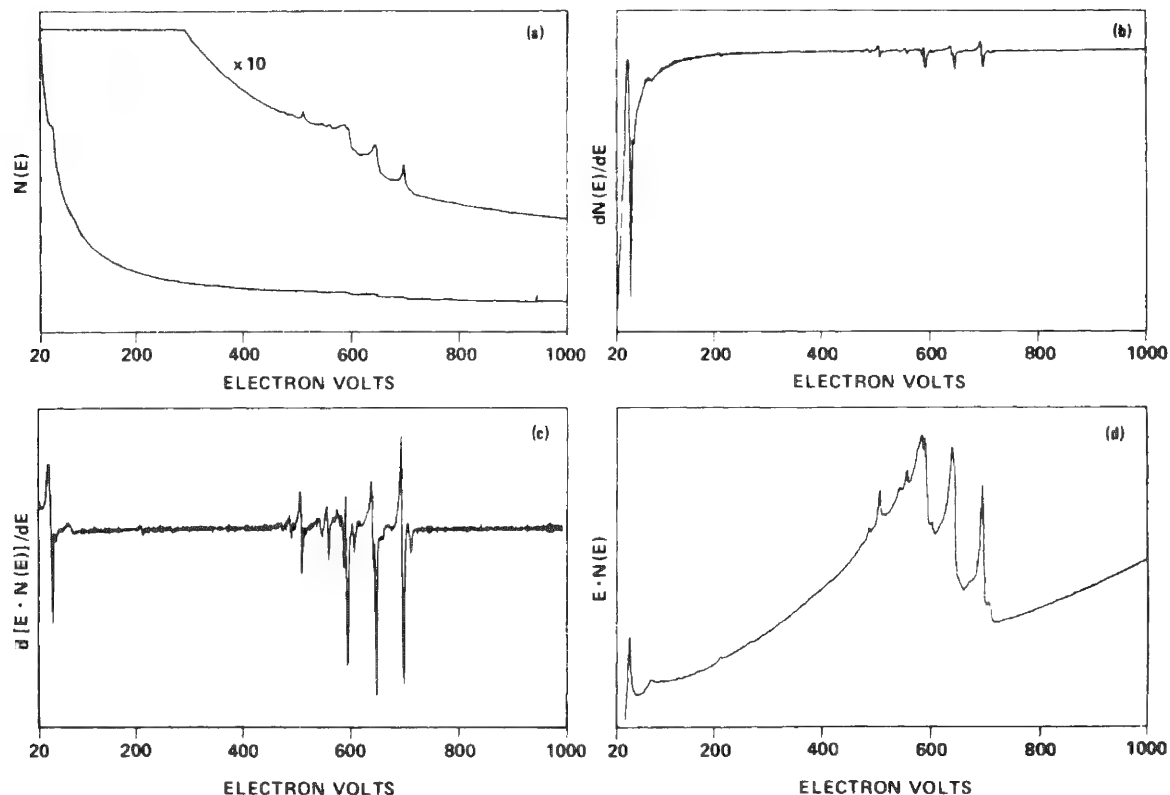


FIG. 2.--Typical Auger data taken in $E \cdot N(E)$, $dE \cdot N(E)/dE$, $N(E)$, and $dn(E)/dE$ modes. These spectra were produced from the same sample and instrument and serve as comparison of relative signal sizes for various data-acquisition modes.

Beam brightness modulation (BBM) is another technique used to obtain undistorted Auger spectra and improved S/N at low primary beam currents.¹⁸ Instead of modulating the ramp voltage on the CMA, the primary beam is modulated so that it strikes the sample while the lock-in-amplifier is accumulating data. At other times the primary beam is deflected into a beam stop. BBM was reported to improve S/N by 10 \times over energy modulation. The improved S/N allowed increased spatial resolution in a study of Ag-Cu grain boundaries.¹⁹ For equal sized beams there was a seven-fold improvement in boundary definition with BBM used over energy modulation. Although the authors have no direct experience with BBM, any S/N improvement is expected to be less than that achieved by pulse counting, where data are accumulated continuously, unless there is reduction in the background noise due to blanking of the beam.

Unfortunately BBM, as well as pulse and digital counting, does not work well for low peak-to-background (P/B) ratios. Topographical variations in secondary-electron emission yields can easily vary by more than the peak of interest and cause anomalous concentration changes. Edge-emission effects from raised surfaces may also obscure small peak signals.² Interfaces between elements with greatly different atomic numbers cause substantial changes in background emission that will alter BBM signals.

One of the most recent approaches to Auger spectroscopy has been data acquisition by a digital approach. The basic electron optics and energy analyzer are the same as in Fig. 1. Janssen et al.²⁰ used an operational amplifier followed by an optically isolated instrumentation amplifier to return the signal from the electron multiplier to low voltages. This approach eliminated the need for any modulation or pulse-counting stage that would be capacitively coupled to low potential. Varian and Physical Electronics have designed sys-

tems schematically shown in Fig. 3, which eliminates the high output noise of the optical isolation amplifier. The electron-multiplier signal is first amplified by a high-quality instrumentation amplifier floating at the anode supply voltage. This signal is then transferred to a voltage-to-frequency (V/F) converter, which is also floating. The digital pulses from the V/F converter drive an LED which is coupled through a fiber optic to a diode detector pulse counter at low voltage. This system results in minimal noise contribution to the signal by the electronics and good isolation between the high-voltage signal and the data-processing electronics. The electron multiplier voltage may be computer controlled to allow efficient use of the V/F dynamic range, which is about 100 000. The advantages of such a system are direct acquisition of $E \cdot N(E)$ vs E data that are stored for retrieval on disk.²¹ The system has reduced sensitivity to noise pickup and has sufficient dynamic range to store the largest and smallest peaks.

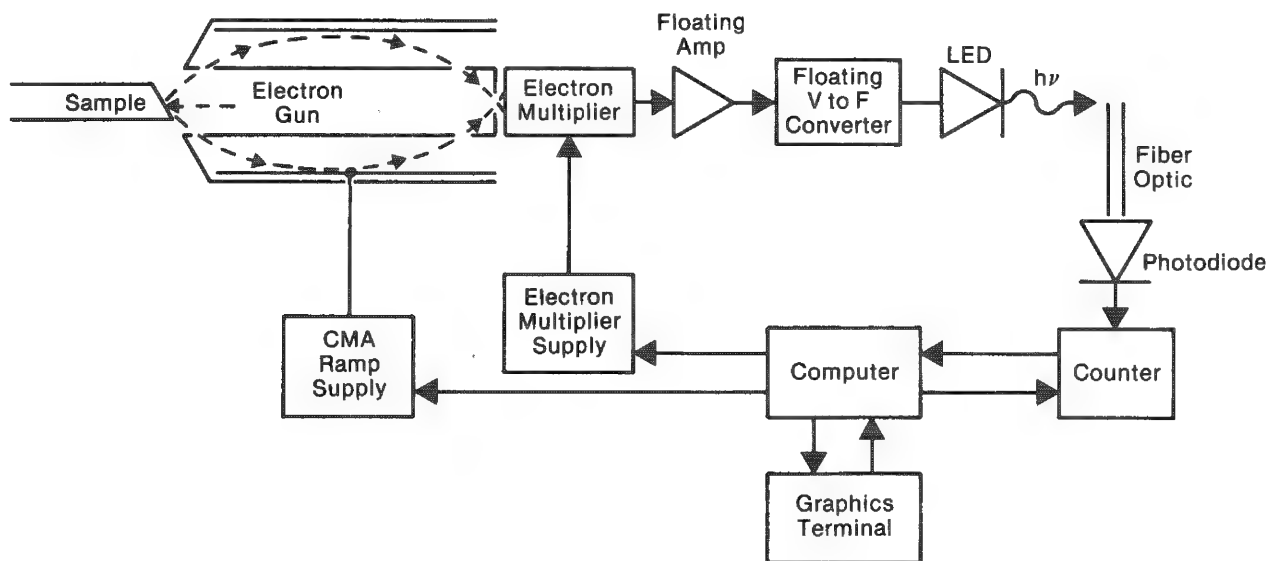


FIG. 3.--Schematic of electronics used for digital detection scheme.

Modulation effects are eliminated by collection of $E \cdot N(E)$ data directly. Differentiation routines exist to transform $E \cdot N(E)$ data into $dE \cdot N(E)/dN(E)$ for comparison with published data. Similarly, one may integrate $E \cdot N(E)$ data to get $\int E \cdot N(E) dE$ which has been shown to be representative of elemental composition. The advantages of this system over previous Auger systems are summarized in Table 1.

TABLE 1

FEATURE	Data Acquisition Mode			
	Derivative	Pulse Counting	BBM	Digital
Commercially Available	X	X	X	X
Standard Reference Spectra	X			
Modulation Distortion	X			
$E \cdot N(E)$ Directly		X	X	X
High Dynamic Range			X	X
Flexible Data Processing		X	X	X
Optimal S/N		X		X
Topographical and Edge Distortion		X	X	X

Software

Future advances in AES will probably occur in the area of data processing, since relatively inexpensive computing power is available to most laboratories. The first attempts employed dynamic background subtraction (DBS) to eliminate the slowly varying background from an $N(E)$ spectrum.²² DBS is the n -th order differentiation of the signal followed by

multiple integration of the same order. This procedure is illustrated in Fig. 4. DBS requires that the function to be recovered have a small radius of convergence, the background have a large radius of convergence, and the signal be differentiable n times, where n is the number of differentiations required to eliminate the background. This technique is quite time consuming since several differentiations and integrations must be done on the spectra under consideration. The spectra must also have fairly good S/N since differentiation routines tend to amplify noise. Data smoothing in conjunction with DBS helps decrease noise, but also increases the radius of convergence of the signal to be recovered. Application of DBS to background-subtracted TMT data should result in spectra with very low backgrounds.

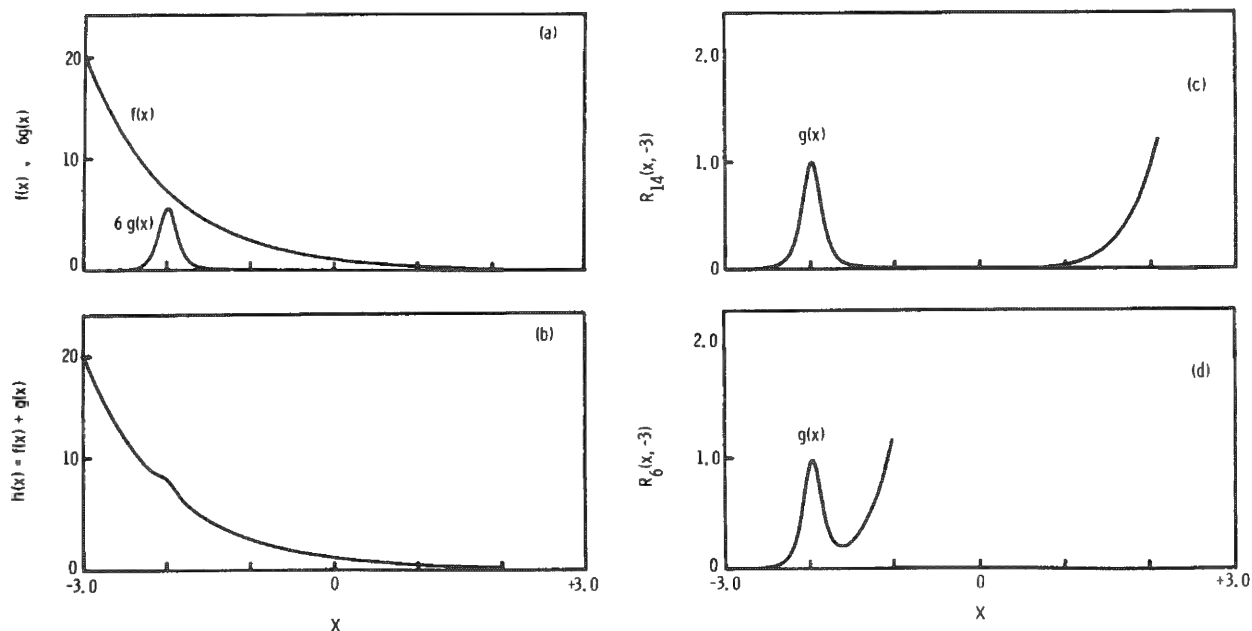


FIG. 4.--Process of dynamic background subtraction involves addition of large exponential to small Gaussian signal in (a) to give new function in (b), which is differentiated 14 times, then reintegrated; (c) and (d) show background contribution as function of number of integrations.

In a few cases Auger peaks of different elements overlap. Different chemical states of the same element also will have distinct but overlapping spectra. The ability to separate these spectra could provide useful quantitative and chemical information. One possibility for separating these closely spaced peaks is to subtract out a standard normalized spectra. This method works only when one knows the chemical species which is to be subtracted.

Deconvolution could be used to separate peaks as Mularie and Peria first demonstrated.²³ They were concerned with extracting chemical information from data obtained by use of LEED optics. The true Auger spectra was obtained from

$$A(E) = F^{-1} \frac{F N(E)}{F B(E)}$$

where A is the true Auger peak; F and F^{-1} represent the Fourier transform and its inverse, respectively; $N(E)$ is the experimentally obtained Auger peak; and $B(E)$ is the instrumental response function. $B(E)$ was determined by recording of the spectrum obtained when the sample was bombarded with primary electrons that had energies approximately equal to the Auger peak of interest. Using this approach, Mularie and Perie²³ were able to separate the $M_5N_5N_5$ and $M_4N_5N_5$ transitions in In. The deconvolution may underestimate the inelastic structure present in the Auger spectrum due to the fact that the scattering probability is higher for Auger electrons than for backscattered primaries.²⁴

Madden and Houston advanced deconvolution techniques in AES by first applying DBS to $N(E)$ data and then using an iterative (Van Cittert) deconvolution method.²⁵ This method has been successfully applied to find the valence band structure of Al,²⁶ and to examine the oxidized spectrum of Li.²⁷ The high resolution and accurate lineshape determination from this type of analysis has allowed experimental investigations of transition density of states for Si and Li.^{28,29}

Ramaker et al.³⁰ have presented a method for extracting Auger lineshapes from experimental data by using the high- and low-energy sides of the Auger peak to calculate a functional background. This background is due to scattered primary electrons and true secondary electrons. The extraction of true Auger lineshapes occurs by deconvolution of the instrument function from the background-subtracted $E \cdot N(E)$ data. Since several parameters in this method are variable, an iterative approach is necessary to find the best fit to experimental data. To implement this method one must experimentally measure the electron loss spectra of a primary beam with energy equal to the Auger peak of interest. These data are used to find the instrument response function. Every iteration includes a background calculation and subtraction and then parametric adjustment to obtain the best fit. This procedure provides accurate Auger peaks; however, it is quite time consuming.

Janssen has used an analog divider to ratio $dE \cdot N(E)/dE$ to the background level $E \cdot N(E)$ measured at a nearby level off the peak.²⁰ This ratio is shown to be $E \cdot N(E)$ or $dE \cdot N(E)/dE$. The division to display $E_p \cdot N(E)_p / E_b \cdot N(E)_b$, where p and b designate signals collected on the peak and background, respectively, could be easily done in a computer. Large angle variations or topographical differences are less likely to change the ratio signal. Application of the ratio method to line scans and maps of cleaned rough Cd showed much less signal variation than derivative spectra and gave a much better indication of the uniform Cd level.

Differential backscattering coefficients of subsurface layers have been seen to cause up to 50% variations in signal intensities.³¹ This effect was shown for Al deposited on Au stripes on Si. The Al signal over the Au stripes was about 1.5 times higher than the signal from Al deposited on Si. The ratio technique was used to examine signal variations from 0 for a sample composed of Al_2O_3 layers deposited on SiO_2 . $E \cdot N(E)$ data showed little variation in O content across the sample, whereas $dE \cdot N(E)/dE$ data had sharp spikes at the SiO_2 - Al_2O_3 interfaces. Ratioed spectra showed a distinct change in O content, without spikes, at the interface region.

Strausser has shown some simple data processing techniques that could be useful for analyzing data taken in the digital mode.²¹ One application involved analyzing a partially oxidized Al sample for Al_2O_3 content. He was able to obtain this information by subtracting a normalized pure Al spectrum from the native oxide. The remaining pure oxide spectra were integrated and ratioed to the total area under the Al peak. In another case, equal amounts of Si and SiO_2 spectra were subtracted from an $E \cdot N(E)$ curve obtained at the Si/ SiO_2 interface. This procedure revealed a new component which may be tentatively identified as an SiO type bond. These subtraction techniques using standard $E \cdot N(E)$ spectra have also been used to examine very small impurity concentrations on Al backgrounds.

Digital data acquisition is extremely useful for correcting for instrumental parameters and matrix effects, and for simulating spectra and storing standard spectra for quantitative analysis.³²

The real strength of a computer-controlled instrument is in its ability to make intelligent decisions and adjust experimental parameters on a sample-to-sample basis. In general, Auger lineshapes become broader at higher peak energies. Ramped modulation schemes have been proposed to take advantage of this phenomena. It would be fairly easy to take a survey scan to identify the elements present. The computer could then set the optimal modulation voltage for each peak of interest in subsequent scans.

Another area where computer control of experimental parameters results in increased data reliability is for the instrument shown in Fig. 3. In this case the computer controls the electron multiplier voltage. The ramp voltage is scanned to the energy where the largest signal is expected. The computer then adjusts the electron multiplier voltage until about 80% of full scale for the V/F is reached. This procedure assures maximum utilization of the full dynamic range of this instrument.

Data Display

Surface and thin-film analysis, coupled with elemental recognition and compositional analysis, are two important abilities of AES. Determination of spatial distribution and spatial relation is another important aspect of Auger spectroscopy. Mapping of impurities or species of interest often provides important clues to solving materials problems. Usually Auger maps are obtained in the derivative mode. The CMA is set to pass the energy of interest and modulated with a sine wave as the electron beam is rastered across the sample. A common problem with maps created in this manner is that they suffer from moiré patterns, which arise from the beat between scanning and modulation frequencies. A simple solution to this problem was proposed by Goto et al.³³ The clock-pulse-generator signal sent to the digital X and Y scanning controls is divided by 128 and used to modulate the ramp voltage and provide the clock for the lock in amplifiers. This arrangement was found to alleviate moiré patterns, since the map signal was then measured synchronously with the scanning signal.

Another note by the same group has pointed out the disadvantages of photographic mapping with a lock-in amplifier used to modulate the intensity of the image.³⁴ When a short time constant is used, the photographic signal is an integration of only the positive noise (Fig. 4). Lengthening the time constant enhances the contrast, but only at the expense of the resolution. One can digitally integrate the noise, which can then be transferred to a D/A converter and displayed. This digital integration results in higher S/N and higher resolution maps.

Sample imaging in Auger spectrometers is usually accomplished by measurement of the specimen or secondary electron current during rastering. Some specimens do not give high contrast images in this mode, which makes it hard to identify the areas of interest. It is possible to use the CMA to look at elastically backscattered electrons and TMT to obtain higher contrast images.³⁵ Typically one would set the CMA at the primary electron beam energy and use the sum of a square wave and a cosine wave of equal peak-to-peak heights and frequencies to modulate the amplifier by 20-100 eV from this initial value. This method results in $N(E)$ being recorded as the output of the lock-in amplifier, and in higher signal contrast over areas with different elemental compositions.

Shaffner and Keenan³⁶ acquire a standard Auger map in a 928×744 array, then plot a histogram of various intensities found in a given map. They can then expand the scale of gray levels to use the full dynamic range of their display. These data are then smoothed to reduce noise that is introduced during the rescaling operation and the final image is replotted. This scaling arrangement improves S/N at the cost of resolution. Such operations carried out on a large array are also quite time consuming and require a fairly large computer.

High-quality color terminals are becoming more available and reasonable in price. These terminals may prove quite useful for multi-element mapping. Such a system is in use at Britain's National Physical Laboratory in Teddington.³⁷ Color maps have been produced that show the relative distributions of lead and brass in tool bits. These analyses show an arrangement of brass and lead along stress-induced striations. Another analysis has examined corrosion residuals in steel. The color analysis was useful in showing that embrittlement of steel is directly related to locally high impurity concentrations.

Conclusion

The data-acquisition modes for Auger spectroscopy are rapidly evolving away from energy modulation toward digital processing techniques. Recent commercial introduction of AES systems with digital signal processing will accelerate that trend and will create a need for standard $E \cdot N(E)$ vs E spectra for data reduction. Three- to five-fold improvements in S/N will enhance the spatial resolution of AES; color CRTs will provide greater contrast for elemental mapping.

References

1. J. E. Houston, *Rev. Sci. Instr.* 45: 897, 1974.
2. J. A. Venables, A. P. Janssen, C. J. Harland, and B. A. Joyce, *Phil. Mag.* 34: 495, 1976.

3. P. J. Feibelman, E. J. McGuire, and K. C. Pandey, *Phys. Rev. B* 16: 5499, 1977.
4. K. Goto, K. Ishikawa, R. G. Wolfe, and J. T. Grant, *Applications of Surface Science* 3: 211, 1979.
5. L. A. Harris, *J. Appl. Phys.* 39: 1419, 1968.
6. R. E. Weber and W. T. Peria, *J. Appl. Phys.* 38: 4355, 1967.
7. L. N. Tharp and E. J. Scheibner, *J. Appl. Phys.* 38: 3320, 1967.
8. P. W. Palmberg, G. K. Bohn, and J. C. Tracy, *Appl. Phys. Lett.* 15: 254, 1969.
9. L. E. Davis, N. C. MacDonald, P. W. Palmberg, G. E. Riach, and R. E. Weber, *Handbook of Auger Electron Spectroscopy*, 2nd ed., Physical Electronics Division, Perkin-Elmer Corp., 1976.
10. G. E. McGuire, *Auger Electron Spectroscopy Reference Manual*, New York: Plenum, 1979.
11. C. J. Powell, "The physical basis for quantitative surface analysis by Auger electron spectroscopy and x-ray photoelectron spectroscopy," in N. S. McIntyre, Ed., *Quantitative Surface Analysis of Materials*, ASTM STP 643, American Society for Testing and Materials, 1978, 5-30.
12. J. T. Grant, T. W. Haas, and J. E. Houston, *Surf. Sci.* 42: 1, 1974.
13. D. J. Pocker, *Rev. Sci. Instr.* 46: 105, 1975.
14. G. E. McGuire and B. R. Martin, *Anal. Chem.* 51: 488, 1979.
15. R. W. Springer, D. J. Pocker, and T. W. Haas, *Appl. Phys. Lett.* 27: 368, 1975.
16. D. J. Pocker, R. W. Springer, F. E. Ruttenberg, and T. W. Haas, *J. Vac. Sci. Technol.* 13: 507, 1976.
17. C. T. Hovland, N. C. MacDonald, and R. L. Gerlach, in *SEM/1979*, I, 213.
18. A. Mogami and T. Sekine, *Proceedings 6th Europ. Cong. Elec. Micr.*, 1976, 422.
19. T. J. Shaffner, in *SEM/1979*, I, 149.
20. A. P. Janssen, C. J. Harland, and J. A. Venables, *Surf. Sci.* 63: 277, 1977.
21. Y. E. Strausser, "Applied surface analysis," ASTM STP 699, T. L. Barr and L. E. Davis, Ed., American Society for Testing and Materials, 1980, 158.
22. J. T. Grant, T. W. Haas, and J. E. Houston, *Jab. J. Appl. Phys. Suppl.* 2, Pt. 2: 811, 1974.
23. W. M. Mularie and W. T. Peria, *Surf. Sci.* 26: 125, 1971.
24. W. M. Mularie, PhD Thesis, University of Minnesota, 1971.
25. H. H. Madden and J. E. Houston, *J. Appl. Phys.* 47: 3071, 1976.
26. J. E. Houston, *J. Vac. Sci. Technol.* 12: 255, 1975.
27. H. H. Madden and J. E. Houston, *J. Vac. Sci. Technol.* 14: 412, 1977.
28. J. E. Houston, G. Moore, and M. G. Lagally, *Solid State Commun.*, 21: 879, 1977.
29. H. H. Madden and J. E. Houston, *Solid State Commun.* 21: 1081, 1977.
30. D. E. Ramaker, J. S. Marday, and N. H. Turner, *J. Elec. Spec. and Rel. Phenom.* 17: 45, 1979.
31. J. Kirschner, *SEM/1976*, I, 215.
32. P. H. Holloway, in *SEM/1978*, I, 361.
33. K. Goto, S. Ichimura, and R. Shimizu, *Rev. Sci. Instr.* 50: 46, 1979.
34. K. Goto, S. Ichimura, and R. Shimizu, *Rev. Sci. Instr.* 51: 95, 1980.
35. G. L. Jones, G. E. Hammer, T. W. Haas, and J. T. Grant, in *SEM/1979*, I, 225.
36. T. J. Shaffner and J. A. Keenan, in *SEM/1979*, I, 219.
37. E. D. Hondros, M. P. Seah, and C. Lea, *Metals and Materials*, January 1976, p. 26.

DIGITALLY CONTROLLED X-RAY MAPPING

W. F. Chambers

Traditional methods for making x-ray maps are time consuming and result in a product that can be compared only to itself. Moreover, setting exposure time and beam current for x-ray maps has been essentially an art: several exposures are often required. Despite these drawbacks, x-ray maps have been widely used because they present valuable information about the spatial distribution of elements in a form that is easily assimilated. The system described calculates and sets instrumental parameters so that the trial-and-error process is eliminated. A properly exposed x-ray map is generated every time. The system also labels the maps and incorporates the low-magnification and multi-exposure capabilities described previously.¹

TABLE 1.--Machine parameters for optimum x-ray map for Fe standard.

camera f-stop	f-11
film speed	400 ASA
frame size	110 mm x 110 mm
pulse duration	2 μ s
exposure time	80 s
beam current	40 nA
count rate	121 counts/nA-s

The generalized exposure conditions are based on the experimental parameters for an x-ray map of Fe as listed in Table 1. Use of these parameters resulted in an exposure with an intensity of about 3/4 of the saturation intensity and corresponds to a spot of pixel density of 32/mm². With this information and a table of intensities for the various elements, it is a straightforward calculation to determine a set of instrumental conditions that will bring any specified K-ratio to the reference intensity from the equation

$$K_x I_x t_x i_x = t_{Fe} I_{Fe} i_{Fe} \quad (1)$$

where K_x is the K-ratio of the element of interest which is to correspond to a 3/4 saturation level in the micrograph (roughly, the desired wt.%), I_x is the intensity (counts/nA-s) for a 100% standard of the element of interest, t_x is the exposure time (s), i_x is the beam current (nA), t_{Fe} is the exposure time for Fe (80 s), I_{Fe} is the intensity for pure Fe (121 counts/nA-s), and i_{Fe} is the beam current for the Fe map (40 nA). The values for t_{Fe} , I_{Fe} , and i_{Fe} have been obtained from Table 1.

In our system, reference intensities for various elements or compounds are stored in a table along with element names, crystal assignments, spectrometer positions and assignments, detector voltages, and pulse height analyzer windows.²

Since both t_x and i_x are independent variables in Eq. (1), there is no unique solution. In order to reach an acceptable family of solutions, we impose the following limitations in addition:

- Minimum exposure time of 40 s. This has been imposed because shorter times lead to an artifact related to rise-times in the amplifier system.
- Minimum and maximum beam current values are specified, to keep wide beam current variations from resulting in noticeable defocusing. For 100 \times maps, we commonly permit the beam current to vary between 3 and 80 nA unless the sample contains elements which are mobile or volatile. For maps of higher magnification this range must be restricted.

Combination of Eq. (1) with the restrictions above results in a procedure that is amenable to programming. We have chosen a command of the form PHOTO REF MAG CONC GRID, where

REF is the reference name for the table entry for an appropriate element. By convention, we assign a reference name by following the chemical symbol of an element by a number. If the number is 1, 2, or 3 the reference is to a pure element which is found on the corresponding spectrometer. If the number is 4, 5, or 6 the reference is to an oxide of the element which is found on spectrometer 1, 2, or 3, respectively.

MAG is the magnification. To date, MAG merely tells the computer the physical setting of the microprobe magnification control. On newer instruments it should be possible to control the magnification.

The author is a member of the technical staff at Sandia National Laboratories, Albuquerque, NM 87185, a U. S. Department of Energy (DOE) facility. This work was supported by DOE contract DE-AC04-76-DP00789.

CONC is the weight percent of the element or compound referred to by REF which should correspond to the reference intensity in the completed x-ray map. In reality, this number is directly converted to a K-ratio; however, this accuracy is sufficient for essentially all photographic situations.

GRID is a number describing the type of grid which should be drawn. If GRID is defaulted, an outline with three inner lines is drawn. If GRID is negative, the grid is suppressed. If GRID is zero or positive, an outline is drawn and the GRID number indicates the number of grid lines to draw in the outline.

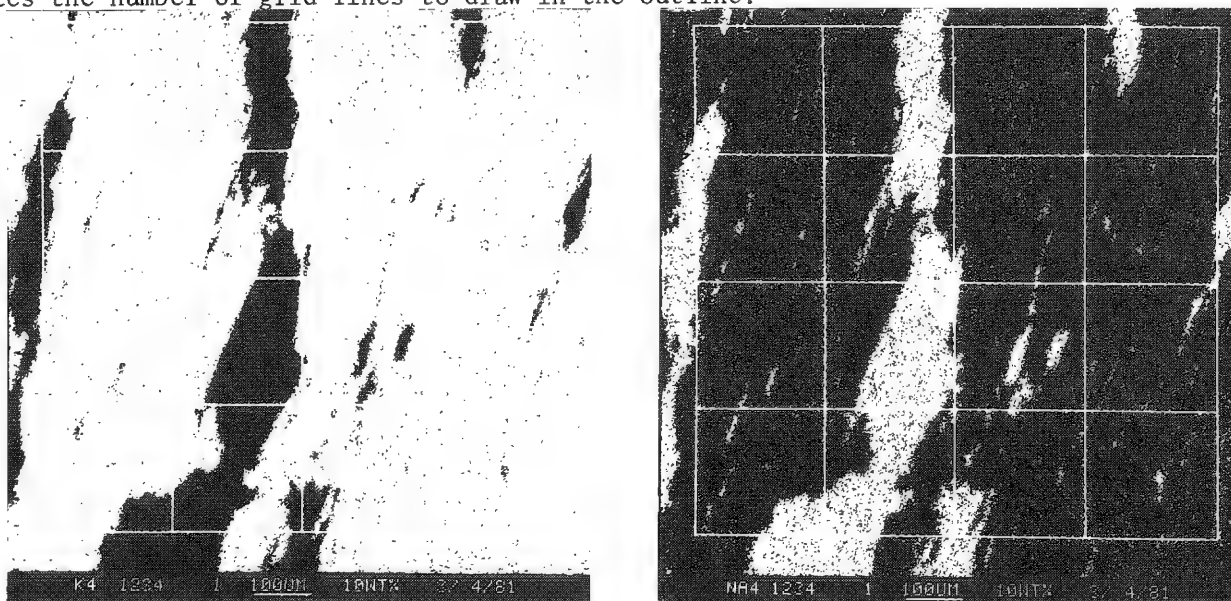


FIG. 1.--Digitally controlled x-ray maps of K (left) and Na in Perthitic feldspar. Commands used to take these maps were PHOTO NA4 100 10 and PHOTO K4 100 10.

The complete procedure is given below.

1. Read the reference name and look up the corresponding crystal, spectrometer, position, detector voltage, pulse height analyzer window, and intensity from the element table.
2. Read the magnification, calculate the spectrometer offset required to maintain x-ray focus, select the spectrometer, check the crystal and insert the proper crystal if necessary, and drive the spectrometer to the beginning position (including any offset).
3. Read the desired K-ratio and calculate the required beam current for a 40s exposure. If it is less than the minimum allowable current, set the operating current to the minimum value. If it is greater than the maximum allowable current, set the operating current to the maximum allowable current and re-calculate the required exposure time. Set these conditions into the microprobe as closely as possible and, since the time can only be stepped in increments of 4 s and the operating beam current may vary slightly from the calculated value, re-compute the actual weight percent (K-ratio) which will correspond to the reference intensity.
4. Open camera shutter, enable recording CRT, draw grid and label, start x-ray map.
5. Synchronously scan electron beam and spectrometer to maintain x-ray focus.
6. At the conclusion of the map, disable the CRT, close the shutter, advance the film if a roll film back is on the camera, and return to command mode.

This system permits the taking of high-quality x-ray maps during both attended and unattended operation. With the bulk load film transport described previously¹ it has been used to prepare x-ray maps of 35 oxides in a simulated nuclear waste sample and to prepare as many as 400 maps for a montage. The sample maps shown in Fig. 1 were used to guide the taking of quantitative analyses. Though large laminar structures show clearly in transmitted light, the smaller structures are not easily differentiated without the x-ray maps.

References

1. W. F. Chambers, "Computer controlled photography on an electron microprobe," *Proc. 13th MAS Conf.*, 1978, 84.
2. W. F. Chambers, *SANDIA-TASK '78: An Electron Microprobe Automation Program*, Sandia National Laboratories Report SAND 78-1149, 1978.

AUTOMATION SYSTEM FOR QUALITATIVE AND SEMIQUANTITATIVE ELECTRON MICROPROBE ANALYSIS WITH WAVELENGTH-DISPERSIVE SPECTROMETERS COMPARABLE IN EASE AND EFFICIENCY WITH ENERGY-DISPERSIVE SPECTROMETERS

W. J. Hamilton Jr., Ali Navapbour, and Erik Goetze

The advent of energy-dispersive detectors (EDS) in electron probe microanalysis allowed the rapid characterization of the major elements present in a material. Previously, with wavelength-dispersive detectors (WDS), a time-consuming and cumbersome "wavelength scan" was necessary, in which a crystal spectrometer was slowly moved through its entire angular range and "peaks" were characterized by reference to printed tables.

However, EDS has several significant deficiencies when used for qualitative analysis. First, counting-rate limitations of the detector electronics and inherent peak-to-background ratios can result in detection limits orders of magnitude poorer than WDS. Often, minor elements of chemical and/or physical importance remain undetected by EDS.

Second, at mid-wavelength, present EDS detectors range in resolution between 140 and 160 eV, compared to approximately 1 eV for wavelength dispersive. Overlapping peaks are therefore very common in EDS and resolving them may be critical to the analytical problem.

Third, the extremely poor performance for sodium and lighter elements restricts the use of EDS to heavier species. The presence or absence of fluorine, oxygen, nitrogen, carbon, and boron in the analyte may be knowledge of critical importance to an investigator.

The commercial success of the EDS for qualitative or semiquantitative analysis has resulted almost completely from its speed and ease of use.

We have developed an automation scheme for wavelength-dispersive electron microprobe analysis that retains all the resolution and detection advantages of WDS and is competitive in speed and ease of use with EDS. Functional analysis of the mechanisms of qualitative analysis by wavelength-dispersive spectrometers showed that the greatest inefficiencies of the conventional approach resulted from the slow motor rates and "look-up" procedures necessary to identify the multiple spectral components of each element present. We have constructed an extremely efficient system for qualitative and semiquantitative analysis which obviates both difficulties. An outline of the logic of the system is shown in Fig. 1.

To perform a semiquantitative analysis (Program: \$QUAL), the analyst/operator merely names a previously defined file containing a list of 2 to 92 elements. The elements are sorted automatically onto as many as 9 wavelength-dispersive spectrometers. A subsequent sorting algorithm assures that maximally efficient use of spectrometers is obtained. X-ray intensity data for peak and background are measured at a single predetermined position (λ) for each element. Motion of the spectrometers between peaks occurs at full slew speed of the motor, so that "dead-time" of the analysis between intensity measurements is minimized.

A printout of approximate concentration, peak-to-background ratio, and a "bar" graph of concentration is obtained. The concentrations are calculated as Castaing's First Approximation relative to disk-file intensity data.

Figure 2 shows the operator/computer dialog from a typical execution of the analytical module of this system. After specifying the crystal configuration, the operator types the name of file containing elements typically present in minerals. With minimal subsequent dialog, the computer sorts the elements and maximizes efficiency. Note in the spectrometer assignment printouts that there is an interchange of Mn and Cr, as well as the movement of Na from spectrometer 3 to 5. Note also the use of the fixed wavelength spectrometer for silicon.

With selection of the specimen location (such as an individual mineral grain) by the operator and a single push of a button, repeated semiquantitative data collection and printout occur automatically.

The authors are with Bausch & Lomb/Applied Research Laboratories, Box 129, Sunland, CA 91040.

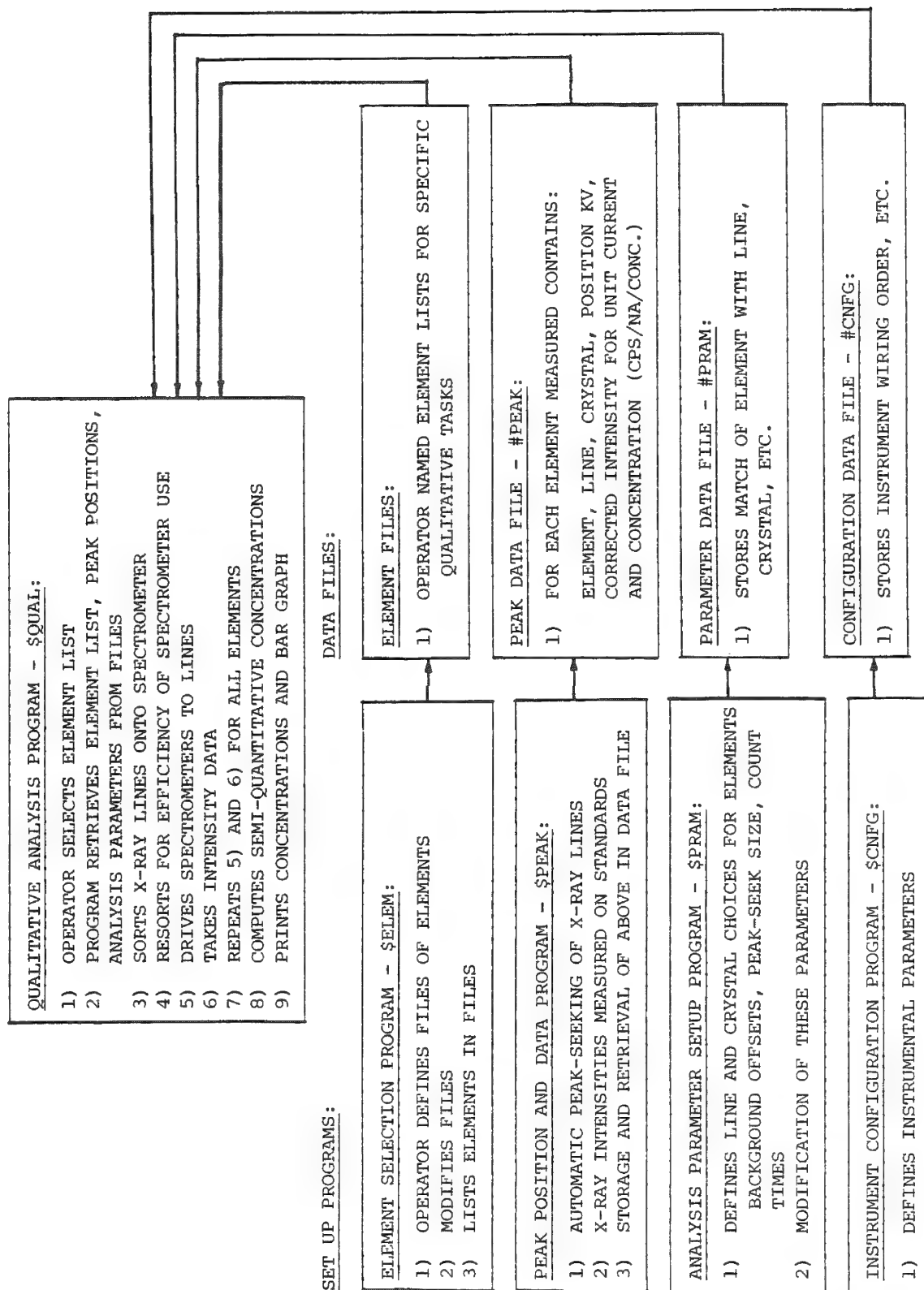


FIG. 1.--SEMQ qualitative analysis system.

A measure of the absolute accuracy of the system may be obtained by comparison of the results of the first analysis with the published composition Kakanui Horneblende, a grain of which was analyzed at that point: Na 1.93%, Mg 7.71%, Al 7.89%, Si 18.9%, K 1.70%, Ca 7.36%, Ti 2.84%, Cr 0.0%, Mn 0.07%, and Fe 7.61%. Note that the measured level of sodium is below the level easily detected by EDS.

In summary, this system has provided:

1. Ease: minimal operator input. Printout of semiquantitative results automatically; no cumbersome tables or cursor motion.
2. Speed: The slow transit of the spectrometer between putative peaks is obviated. The actual time varies with the number of wavelength spectrometers available and the element list. For general analytical work, the total time required is 1-3 min and is comparable with that required for EDS.
3. Detection limits, Resolution and Sensitivity: The system retains the significantly greater detection limits, resolution, and light-element sensitivity of WDS.

RUN #QUAL

BASIC SPECTROMETER CONFIGURATION

```

2-XTAL SCNR 1 IS LIF 1.020 ==> 3.730  ANGSTROM
2-XTAL SCNR 2 IS LIF 1.020 ==> 3.730  ANGSTROM
2-XTAL SCNR 3 IS TAP 6.560 ==> 23.99  ANGSTROM
2-XTAL SCNR 4 IS PET 2.216 ==> 8.105  ANGSTROM
2-XTAL SCNR 5 IS TAP 6.560 ==> 23.99  ANGSTROM
1-XTAL F/CH 6 IS SI  KA

```

ANY XTAL CHANGED (Y/N) [DEF=N] ? NO

ENTER ELEMENT FILE NAME & DRIVE NR ? #MNRL,0

ENTER CURRENT & VOLTAGE [NA,KA] ? 30,25

SET COMPUTER MODE FOR STAGE (Y/N) [DEF=Y] ? YES

SELECT BAR CHART SCALING: EXPANDED/DECIMAL/LOG (E/D/L) [DEF=E] ? EXPND

[#QUAL] 1ST PASS ASSIGNMENT STARTS

ELEMENT ASSIGNMENTS

```

          10000 12700 15400 18100 20800 23500 26200 28900 31600 34300 37000
XTAL SCNR!-----!-----!-----!-----!-----!-----!-----!-----!-----!-----!
-----!
LIF      1                      MN      TI
LIF      2                      FE      CR
TAP      3          AL          NA
PET      4              K  CA
TAP      5              MG
FX SI KA 6!-----!-----!-----!-----!-----!-----!-----!-----!-----!
-----!

```

FINAL ELEMENT ASSIGNMENTS.

```

          10000 12700 15400 18100 20800 23500 26200 28900 31600 34300 37000
XTAL SCNR!-----!-----!-----!-----!-----!-----!-----!-----!-----!
-----!
LIF      1                      CR      TI
LIF      2                      FE      MN
TAP      3          AL
PET      4              K  CA
TAP      5              MG  NA
FX SI KA 6!-----!-----!-----!-----!-----!-----!-----!-----!-----!
-----!

```

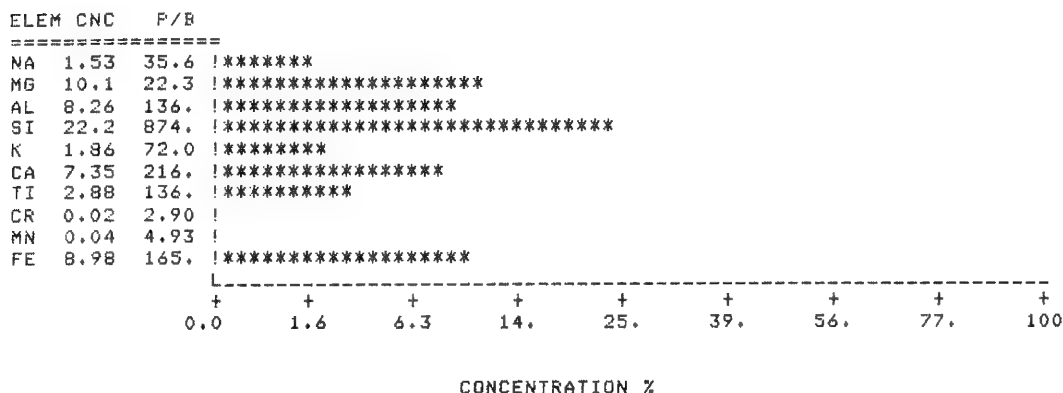
TO RUN ==> PRESS JOYSTICK BUTTON, TO RECONFIGURE ==> <CTRL X>

FIG. 2a

TO RUN ==> PRESS JOYSTICK BUTTON, TO RECONFIGURE ==> <CTRL X>

QUALITATIVE ANALYSIS STARTS

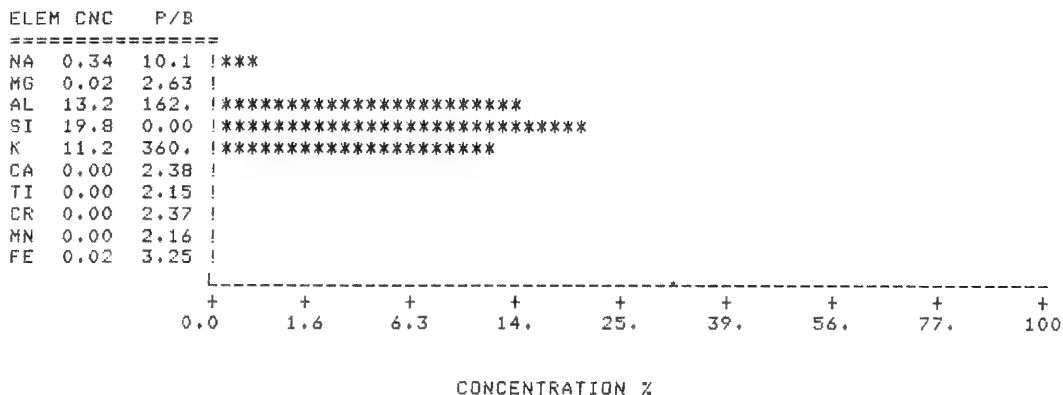
14:55:46 27-FEB-81 ELEMENT CONCENTRATION CHART



TO RUN ==> PRESS JOYSTICK BUTTON, TO RECONFIGURE ==> <CTRL X>

QUALITATIVE ANALYSIS STARTS

15:46:05 27-FEB-81 ELEMENT CONCENTRATION CHART



TO RUN ==> PRESS JOYSTICK BUTTON, TO RECONFIGURE ==> <CTRL X>

SELECT SAME OR NEW

CONF6 (S/N) ? SAME

FILE (S/N) ? SAME

KV/NA (S/N) ? NEW

ENTER CURRENT & VOLTAGE [NA,KA] ? 30,25

SET COMPUTER MODE FOR STAGE (Y/N) [DEF=Y] ? YES

SELECT BAR CHART SCALING: EXPANDED/DECIMAL/LOG (E/D/L) [DEF=E] ? EXPND

FIG. 2b

AUTOMATION OF ELECTRON-PROBE MICROANALYSIS WITH THE USE OF MICROPROCESSOR CONTROL

Alva Couch, Thomas Gantz, Clayton Lusk, and Claude Lechene

A microcomputer system for electron-probe microanalysis has been built to replace an existing minicomputer-based automation system. The availability of low-cost microprocessor systems and components has made development of custom automation systems both practical and desirable in cases where existing hardware must be integrated into the system or special user needs must be supplied. An approach relying heavily upon software has shown promise in reliability, adaptability, and ease of repair.

Our basic automation model was adapted from the previous system.¹ This model proceeds in steps within which each aspect of the automatic measurement process (job) is specified. The operator specifies test points to be counted on an automatic stage, identification labels for the points, counting times, and theoretical spectrometer settings for each pass through the test points. When all has been specified, the spectrometers are automatically tuned and the job proceeds without operator intervention, usually overnight.

Hardware Design

The major criterion for selecting a microcomputer was its ease of use as a software-development system since software architecture and quality play a greater role in system performance than hardware. Adequate development systems at the time our project began cost \$15 000 to \$20 000, which forced us to cut costs by use of the same system for development and implementation. Secondary criteria were memory-mapped input/output (I/O), a simple and versatile bus structure, and the availability of such basic system components as a small backplane, memory cards, and prototyping cards. These criteria were met by the Rockwell AIM 65 microcomputer and a line of system components manufactured by the Computerist, Inc.²

The existing instrument to be automated was a Cameca MS 46 microprobe with automatic stage and spectrometers, scalars, timer, and nanoammeter. Our interface hardware consisted of the AIM 65 microcomputer, a parallel interface for our minicomputer, a 32K dynamic random access memory (dynamic RAM or DRAM) board,³ and a video display controller with light-pen input.⁴ Three prototype boards interface with the control and measurement sections of the electron probe; another interfaces with an alphanumeric keyboard and allows us to simulate x-ray input so that the system can perform self-test diagnostics. System memory consists of 42K RAM, including two 16K overlaid banks, and 38K of ROM/EPROM, including two 8K overlaid banks. EPROM programming is provided by the DRAM board and can handle 2716, 2732, 2516, and 2532 EPROMs (Fig. 1.).

The interface cards for the electron probe communicate with the 6502 microprocessor in the AIM system via standard 6502 support devices. Six 6520 peripheral interface adapters (PIAs) and one 6522 versatile interface adapter (VIA) interface the AIM bus directly to probe functions. One card controls and reads four scalars and a timer, provides nanoammeter readings, and contains a time-of-day clock with battery backup. Another card controls the Cameca automatic stage and motors for automatic spectrometer movement. The remaining card interfaces the operator's control box, containing a three axis joystick, control switches, a six digit display, and audio annunciators.

Software Design

Initial software development began with the AIM 65, with an assembler ROM and cassette tape storage. When the parallel interface for our Hewlett-Packard 2100A minicomputer was completed we were able to marry the capabilities of mini and micro to implement a hard-disk-based development system. An improved interactive debugger was written for use with

The authors are with the National Biotechnology Resource in Electron Probe Microanalysis, Harvard Medical School, Boston, MA 02115. This work was supported in part by the National Institutes of Health grant RR 00679. We should like to acknowledge the expert work and valuable advice of Mr. Phillip Clark, who served as machinist on the project. We also thank Ms. Kathy Edgerly for her excellent art work.

Performance Evaluation

Our new system has provided our installation with many advantages not found in our older system. Probe-side interactive controls are obviously superior to the previous point input button and auto/manual switch, the only controls on the older interface. Our host minicomputer is now freed from the tasks of automation and may expend more effort in statistically manipulating the measured data. The old system was a debugging nightmare, with nine hardwired circuit boards, a handwired backplane, and a bus architecture that depended totally on the structure of the Hewlett-Packard minicomputer. Our new hardware is more compact, self testing, well documented, and easily adaptable to any host minicomputer with minor hardware changes. System expansion is now much easier than before, with free slots in the card cage already present for new functions as they become necessary. A repetitively annoying feature of the older interface was its inability to perceive operator errors during point input and the drift they generated did not allow runs of half the size usual now.

Our design approach differed from the mainstream of automation design in its selection of low-cost, readily available "hobbyist market" system modules, rather than higher-cost components with a higher entry level cost for development hardware and software. By fully utilizing our existing hardware, we avoided adding equipment superfluous to the final product while gradually building a development system on the product which can still be used after the product is completed when it is not performing its primary functions. In this way we have gained not only electron probe automation, but also cost effectiveness for future microprocessor projects in our laboratory. More extensive hardware support is now available for microprocessor design which allows a minimal amount of hardware construction and the purchase of most system components off the shelf. Thus control software becomes the major factor in system implementation.

References

1. T. Moher and C. Lechene, "Automated electron-probe analysis of biological samples," *Biosciences Communications* 1: 314, 1975.
2. AIM 65TM, Rockwell International, 3310 Miraloma Avenue, Anaheim, CA 92803.
3. DRAM PLUSTM, The Computerist, Inc., 34 Chelmsford Street, Chelmsford, MA 01824.
4. VIDEO PLUSTM, The Computerist.

SEM-BASED AUTOMATED FIBER COUNTING

W. R. Stott, E. J. Chatfield, and J. C. Méranter

Some of the advantages of automated scanning electron microscope (SEM) measurement of fibers are rapidity of measurement, reproducibility, reliability, comprehensive analysis, and the capability of identification by energy-dispersive x-ray analysis (EDXA). However, the major problem found with any fiber-counting instrument based on image analysis is the handling and counting of fibers that overlap one another in the image. An SEM-based system has been developed that can perform both image processing and x-ray compositional analysis, and has been modified to address the fiber counting problem, specifically the enumeration and classification of fibrous particulate in the workplace.¹ The automated counting of fibers requires an imaging instrument, usually an optical microscope or an SEM, and a computer to process the image which incorporates both fibrous and non-fibrous particles.²⁻⁴ To count the fibrous material in the image, we must first separate this material from the other nonfibrous debris, then distinguish any overlapping fibers, and finally count the fibers, noting their lengths and mean widths. The fibers may be then characterized by energy-dispersive x-ray analysis according to elemental composition by use of the computer to scan the electron beam over each individual fiber in turn.

A description of the instrumentation and the operation of the image-processing micro-analysis system that already exists has been published previously.¹ For the purposes of the automatic fiber counting a PDP-11/34 computer is interfaced with a Cambridge S4 SEM, which has resulted in improvements in the speed of image acquisition and also the comprehensiveness and rapidity of analysis. The new version of the system allows multiple gray levels of the image to be acquired, with analog-to-digital converters used to monitor the video signal intensity.

The initial acquisition of image data is performed by the computer, which controls the scanning of the focused electron beam via two 12-bit digital-to-analog converters. A digitized image is achieved as the electron beam is driven across the field of view in a raster pattern and the edge coordinates of features that are intersected on each line are stored. The digitized video signal intensity is used to determine the feature edges. By the technique of checks for contiguity of line segments on adjacent scan lines, the individual feature information is extracted from the digitized field of view. The total number of picture elements in a feature is used to determine the area; the perimeter is calculated by summing of the vector distances between the adjacent endpoints of the contiguous line segments. The area and perimeter of the individual lobes that constitute the whole feature are also retained for later use in the fiber analysis.

To obtain an optimized image, the threshold level must be slightly above the electronic noise level of the video signal, such that the smaller-diameter fibers are as well defined as possible. The result is that a number of very small features appear in the digitized image which are in reality generated by the noise fluctuations. Setting a lower bound on the area of individual features eliminates most of these artifacts from being analyzed further.

Since the perimeter and area of each feature are known, it is possible to eliminate features selectively on the basis of shape by use of a dimensionless ratio, perimeter squared divided by area. This ratio is larger for the fibrous particulate than for the general debris in the SEM field of view; thus, the fibers and overlapping fiber aggregates can be extracted for more detailed analysis.

Once the fibrous material in a field has been detected, each individual fiber must be described in terms of a length and a width. To do so each of the fibers is represented by a line drawn along its length (Fig. 1). For the overlapping fiber case, the fibers are mathematically broken at the junctions, and each segment thus generated is described by a skeletal line. The fibers or fiber segments are then described by their lengths,

Authors Stott and Chatfield are with the Department of Applied Physics, Ontario Research Foundation, Sheridan Park Research Community, Mississauga, Ont., Canada, L5K 1B3; Méranter is with the Health Protection Branch, Health and Welfare Canada, Tunney's Pasture, Ottawa, Ont., Canada, K1A 0L2. The significant contributions of G. P. Eastman and R. M. Clayton are gratefully acknowledged.

areas, end points, and the angular projections of the skeletal line from the two end points. In generating the skeletal line through a segment, one assumes that the image features that have remained after the preselection process have a fibrous shape; that is, the shape of the feature can be modelled in form as a rectangle or a number of interconnected rectangles. At this point, a minimum length is set and all shorter segments are discarded.

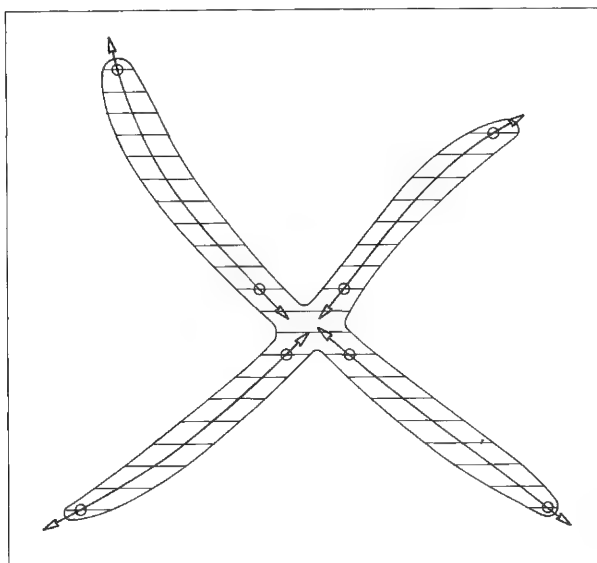


FIG. 1.--Example of crossed fibers characterized by lines for each distinctive fiber segment. Circles indicate ends of fiber segments. Arrows indicate projections of ends of segments. Length is calculated from line drawn down the middle of a given segment. Horizontal lines indicate stored image representation of crossed fibers illustrated.

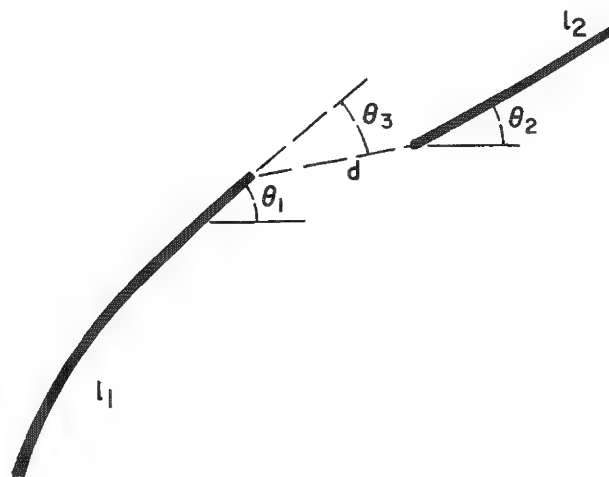


FIG. 2.--Parameters used in connectivity test of fiber segments. The tests are: (1) $d \leq 1/2 \max(\ell_1, \ell_2)$; (2) $|\theta_1 - \theta_2| \leq 15^\circ$; (3) $\theta_3 \leq 90^\circ [1 - d/\max(\ell_1, \ell_2)]^3$, where ℓ_1 and ℓ_2 are lengths of appropriate line segments, d is endpoint separation distance, θ_1 and θ_2 are angular orientations of segments, and θ_3 is angle used in kink test.

When the description of all the fibrous material has been made in terms of the skeletal line format, the segments are then connected by means of three geometrical tests, with each segment checked with every other segment. The three tests are in principle similar to the parameters outlined by Dixon and Taylor.²

1. The first test is simply the distance between two end points. If the end points are far from each other, then it is unlikely that they belong to the same fiber; if they are close it is possibly an intersection point created by the mathematical procedure that separated the lobes of the feature. It may also possibly be an artifact of the original image which gave rise to a broken fiber appearance. The distance test requires that the separation between end points must be less than or equal to half of the length of the longer segment being considered (Fig. 2).

2. The second test is the angular deviation between the angles that define the axial extrapolations from the end points. The difference in angle between the two must be less than or equal to 15° . Large angular deviations are not likely for segments which are actually parts of a single large fiber.

3. The third test is the so called kink test, a determination of how close the end of the shorter of the two segments is to the line of projection from the longer segment. An angle θ_3 is calculated and compared with a maximum acceptable value, which is a function of the endpoint separation. The idea underlying this test is that segments which have satisfied the previous two criteria (approximately parallel and close) may in fact be displaced from one another. The amount of displacement is not critical if the two segment ends are close, but with increasing separation it becomes less probable that the segments are part of a larger whole fiber. The maximum allowable angle is thus weighted by

endpoint separation. It has been determined empirically that

$$\theta_3 \leq 90^\circ [1 - d/\max(\ell_1, \ell_2)]^3$$

gives satisfactory results in eliminating unwanted segment connections (Fig. 2). The formula gives an acceptance angle of nearly 90° when the endpoint separation is small, and a value of 11.25° for the maximum allowable separation distance.

The determination of the individual fibers in the field of view is based on segment information and the appropriate connections that have been made in satisfying the three tests outlined above. A procedure is followed in which the longest path is chosen from a set of connected segments to yield the overall length of the fiber. Segments that connect to the fiber but are not part of the longest path are discarded. This process is continued until all segments have been accounted for in a fiber or have been eliminated. As well as unraveling fiber aggregates, this technique deals successfully with fibers that have multiple branches, or fibers that split into multiple ends. A table is generated at the completion of this procedure that contains the length and mean width of each fiber found. The overall length of a fiber is taken to be the sum of the lengths of all segments in the longest path through the fiber plus the distances between the adjacent endpoints of those segments; the mean width of the fiber is calculated as the total area of those segments divided by the sum of the segment lengths. Assuming that fibers are approximately rectangular in shape, the division of segment areas by segment lengths should give a good estimate of mean width. Fibers with an aspect ratio less than 3:1 are discarded.

Beyond categorization of fibers by their lengths and mean widths, a chemical identification is possible by EDXA analysis. With the line-segment information already obtained, the electron beam may be driven through the fiber from end to end for a set period of time. While the beam of electrons is scanning the fiber, the x-ray analyzer acquires its x-ray spectrum, which is then transferred automatically to the computer for analysis. The fiber may then be classified according to its composition.

In order to evaluate the effectiveness of the automated fiber counting system, a comparison was made using ten distinct SEM fields of view between a manual count and a machine count of a gold-coated sample of amosite fibers filtered onto a Nuclepore filter. At a magnification of 1100, the ten fields of view were approximately $100\text{ }\mu\text{m}$ square, having an average loading of 24.6 fibers with a standard deviation of 4.6 fibers. The manual count performed by an experienced operator and the automatic count yielded statistically identical results.

Figures 3 and 4 illustrate the performance achieved to date. Because of the long time constant of the Cambridge S4 SEM scan coils, acquisition of the SEM image (Fig. 3) required the relatively long time of 77 s; it contained 241 distinct features including fibrous material, organic debris, and noise artifacts. After selection on the basis of a maximum area of feature allowed and a perimeter squared-to-area ratio corresponding to a minimum 3:1 aspect ratio for fibers, only 28 distinct features remained. This state is illustrated in the digital representation of the fibrous particulate (Fig. 4). From this image the procedure detected 25 fibers. The total time for this example from the beginning of image acquisition to the final listing of the fibers was approximately 4 min, of which 45 s was expended in the graphical display of the images on a video terminal. A significant decrease in the image-acquisition time is expected after conversion to a SEMCO Nanolab 7 microscope, with the minimum then being determined by the analog-to-digital conversion time for the video signal digitization.

References

1. W. R. Stott and E. J. Chatfield, "A precision SEM image analysis system with full-feature EDXA characterization," *SEM/1979 II*, 53-59.
2. R. N. Dixon and C. J. Taylor, "Asbestos fibre counting by automatic image analysis," *SEM/1979 II*, 361-366.
3. E. L. Hall, G. Varsi, W. B. Thompson et al., "Computer measurement of particle sizes in electron microscope images," *IEEE Trans. SMC-6*; 138-145, 1976.
4. T. Pavlidis and K. Steiglitz, "The automatic counting of asbestos fibers in air samples," *IEEE Trans. C-27*: 258-261, 1978.

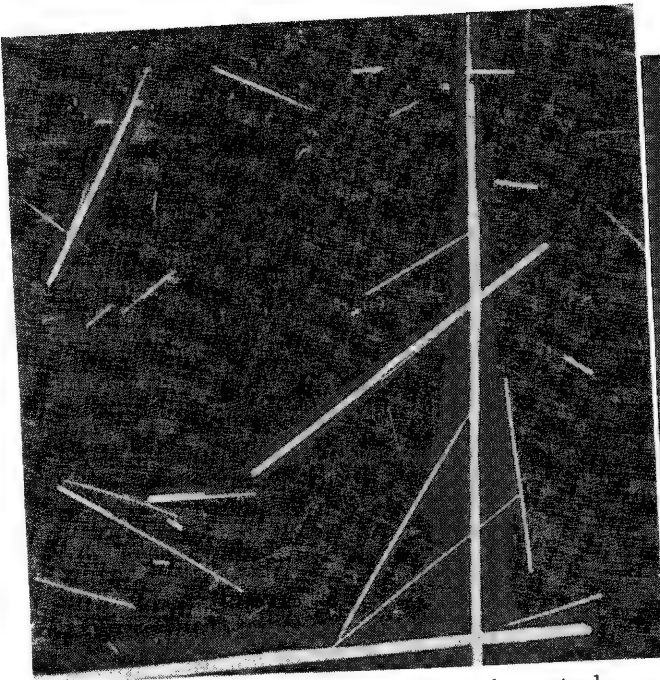


FIG. 3.--SEM micrograph of gold-coated sample of amosite fibers.

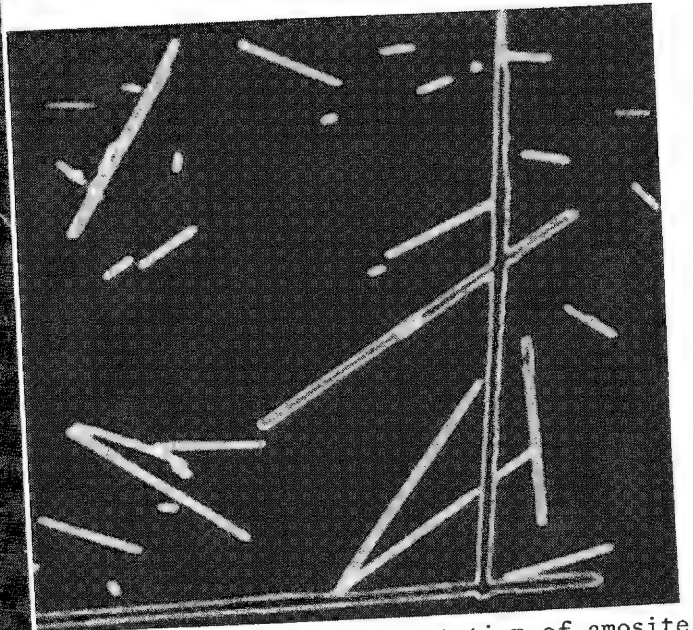


FIG. 4.--Digital representation of amosite sample illustrating particulate assumed to be fibrous. (Photograph from screen of graphics computer terminal.)

INTERACTIVE SOFTWARE FOR AUTOMATED PARTICULATE ANALYSIS

G. S. Fritz, J. J. McCarthy, and R. J. Lee

In recent years, particulate characterization has been gaining increased importance in areas such as air cleanliness, coal classification, alloy inclusion studies, and mineral analysis. Using combined facilities and resources, the authors have developed several software packages to address these problems. The software packages, which are written in FLEXTRAN, run on Tracor Northern's computer-based multichannel analyzers (MCA) and digital scan generators.¹ In each package, digital beam control is used to size the particulates while a simultaneous chemical typing is performed with the multichannel x-ray analyzer. At present, approximately 1000 particulates can be sized and typed per hour. Upon completion of the analysis, size, weight, and area distributions along with average chemistries for the chemical types are reported in tabular form.

Hardware

The basic system consists of a standard TN-2000 MCA equipped for quantitative energy dispersive spectroscopy (EDS) analysis. A video signal processor and X-Y scan controller comprise the scan generator, which is interfaced to the electron column. The video processor includes an 8-bit analog-to-digital converter (ADC) capable of dividing the SEM video signal into 256 distinct gray levels. Two 12-bit digital-to-analog converters (DACs) are used by the X-Y scan controller for positioning the SEM electron beam under computer control. A joystick module is also present in the system and is used for indexing specific features with the aid of a cursor, and for setting a video signal threshold for the detection of features. This same hardware is illustrated for image processing described elsewhere in these proceedings.²

Software

The different software systems developed use similar operating formats which employ the use of several chained programs for parameter setup; data acquisition, analysis, and storage; and listing of results. In addition, several auxiliary programs are available to access the databases and provide particle-by-particle listings, combine data sets, and re-compute results. Basic program features include:

- (a) average analysis time is less than 2 s per particle;
- (b) x-ray acquisition is performed over the entire particle during sizing operations, chemical analysis is performed while the next feature is being sized;
- (c) data collection has been designed to assure that the size and weight distributions have an absolute uncertainty which is independent of the size range selected, so that accurate reproducible results are guaranteed;
- (d) analysis time and total x-ray counts are automatically varied as a function of count rate and particle size to optimize speed and obtain constant statistical uncertainties.

These features and the program format will be illustrated by discussion of one of the packages, Air Particulate Analysis (APA), in detail.

In APA, as in all the software, the operator is led through the analysis using an English dialog. The main program allows the operator to select several different modes: calibration of the digital scan generator, data disk creation, setup of analysis parameters, analysis execution, re-list results of a previous analysis, list particle-by-particle data, combine databases, and re-analyze previously collected data. The operator need not be familiar with the various programs since they are all called from the main program. The setup and calibration parameters are stored on floppy disk; therefore, once the digital beam hardware has been calibrated and the analysis parameters have been set up, there is no need to address these modes again unless calibration is in question or a change in run parameters is necessary.

Authors Fritz and McCarthy are with Tracor Northern, Inc., Middleton, WI 53562. Author Lee is with U. S. Steel Research Laboratories, Monroeville, PA 15146.

When the run analysis mode is selected, APA automatically loads the analysis code and starts execution. Several adjustable parameters in the beam control software affect the reproducibility and precision of the results. A coarse raster scan is performed to detect features of interest. The coarse raster point spacing is automatically determined by the program on the basis of the given magnification and the size of the particulates of interest. This point spacing then determines the minimum size feature that is reproducibly detected at a given magnification. The magnification determines the area scanned per field and should be selected to optimize the analysis of features in a particular size range. The program automatically keeps track of magnification, the number of fields analyzed, and the number of particles found. Further details of this method can be found in papers by Lee and Kelly, and Kelly, Lee, and Lentz.^{3,4}

Features are detected by scanning the electron beam of an SEM under computer control and comparing the digitized video signal with a predefined threshold value. Video signals that exceed the threshold indicate the presence of a feature. The threshold, defined at the beginning of each field, is adjusted by monitoring of the digitized video signal (presented as a waveform on the TN-2000) while a series of linescans near the center of the SEM display are performed. A line depicting the threshold value is superimposed on the waveform, which can be adjusted up or down by use of the joystick. An example of the threshold setup display is shown in Fig. 1. The operator can access the threshold setup during the analysis of a field at any time by pressing an interrupt button located on the joystick. Once the threshold has been checked and/or changed, APA picks up where it left off in the field being analyzed.

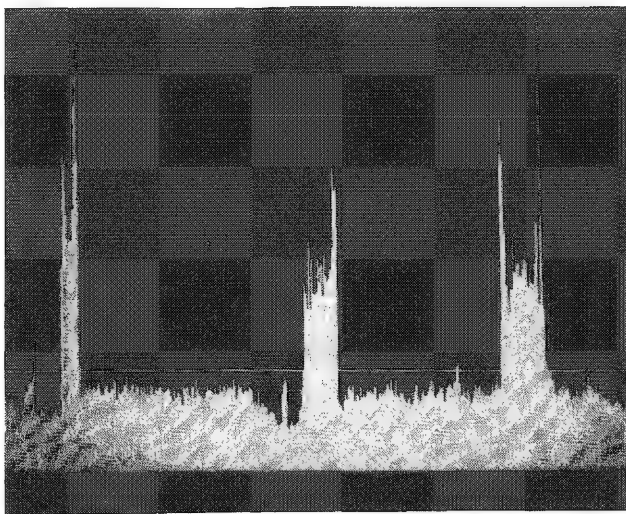


FIG. 1.--Digitized video displayed as waveform on TN-2000 console along with threshold represented as line superimposed on display.

When a feature has been detected, the resolution of the scan is increased and a sizing operation consisting of eight rotating diameters is performed. An x-ray acquisition is begun during the sizing operation and continues at the particle's center after the sizing is completed until either statistical criteria or maximum counting time have been reached.

While data are being collected for one particle, classification of the previous particle is being carried out. In APA, 20 different elemental x-ray intensities along with feature dimensions are used to classify a particle into 29 possible classes. Following sizing and typing, the program resumes the coarse-scan search for more features. During this search, features that have already been identified are excluded.

Upon completion of the analysis, size, weight, and average compositions are reported in tabular form (Tables 1-3). Elements that represent less than 5% of the total integrated peak intensities are not reported in the aver-

age chemistries. Similarly, categories that represent less than 1.5% of the total sample weight are not reported. Since data for each particle are stored on disk automatically, particle-by-particle listings, listings by category, or a re-analysis can be obtained.

Several other applications have been developed based on these basic algorithms. Coal Minerals Analysis (CMA) uses 11 elements and 29 classifications to identify mineral grains in coals. The program reports weight fractions for each mineral classification. Quantitative Metallography Analysis (QMA) is used to identify Mn-S and rare earth inclusions in steels. Density, area fractions, and cross-sectional size distributions for the various inclusions are reported. Minerals Analysis (MA) analyzes particles found in ground minerals and classifies them into 65 separate classes associated with various minerals. A selectable aspect ratio (length vs width) permits additional sorting into acicular and equiaxed categories.

TABLE 1.--Size distribution produced by APA. This table reports size distributions for each type as relative percentages with each row totaling 100%. Last column reports number of particles of each type analyzed; last row records relative distribution of all particles by bin and total number of particles analyzed.

TYPE	0.2-1	1-2.5	2.5-5	5-10	10-15	15-30	TOTAL
FLYASH	85	15	0	0	0	0	7
QUARTZ	28	69	2	0	0	0	128
CA-RICH	0	97	3	0	0	0	6
CA-S	0	0	100	0	0	0	1
MG-SI	0	100	0	0	0	0	1
MG-CA	0	95	3	3	0	0	4
MIX-CLAY	23	73	3	1	0	0	153
CA-SI	43	56	1	0	0	0	44
SI-S-CA	0	100	0	0	0	0	1
UNKNOWN	0	99	1	0	0	0	5
CARBON	0	0	67	33	0	0	3
FE-SI	0	100	0	0	0	0	2
TOTAL	28	69	2	1	0	0	355

TABLE 2.--Weight distribution produced by APA. This table reports relative weight distributions for each type as percentages. Last column gives percent contribution of each class to total weight. Particulates with sizes less than 15 μ m have been subtotaled separately to aid in distinguishing respirable and nonrespirable particulates.

TYPE	0.2-2.5	2.5-5	5-10	10-15	SBTOT	15-30	TOTAL (UG/M**3)
QUARTZ	70	18	11	0	34.9	0	34.9
CA-RICH	84	16	0	0	2.7	0	2.7
MIX-CLAY	54	20	26	0	46.6	0	46.6
CA-SI	83	13	3	0	9.7	0	9.7
TOTAL	64	18	18	0	100.0	0	100.0
				(REL %)			(UG/M**3)

TABLE 3.--Average composition produced by APA. This table provides summary of results of analysis. Average diameter, inverse aspect ratio, relative composition for ten major elements, number of particles, and relative weight percent are reported for each category. Average elemental composition of all categories is also provided as approximate bulk analysis.

TYPE	AVE	A/S	PC	MG	AL	SI	S	CL	K	CA	TI	FE	PART'S	WT%
FLYASH	0.42	0.87	8	3	14	51	0	0	9	6	0	5	7	0.3
QUARTZ	1.50	0.43	13	1	6	78	0	0	4	3	0	3	128	34.9
CA-RICH	2.13	0.39	12	1	1	12	0	0	1	78	1	1	6	2.7
CA-S	3.90	0.43	12		3	11	38		3	43		1	1	0.2
MG-SI	1.18	0.43	12	7	7	68	2	2	3	3		8	1	0.1
MG-CA	1.93	0.42	12	23	0	13	1	1	1	55	0	1	4	1.2
MIX-CLAY	1.61	0.43	11	2	16	55	1	1	10	6	0	6	153	46.6
CA-SI	1.22	0.46	11	10	5	35	1	1	4	38	0	2	44	9.7
SI-S-CA	1.56	0.58	14	2	6	18	28	2	2	38		4	1	0.3
UNKNOWN	1.83	0.46	12	9	7	47	0	1	5	14	0	13	5	1.4
CARBON	4.77	0.45	1	0	13	28	3	8	4	12	7	10	3	1.4
FE-SI	1.95	0.62	12	0	9	40	1	1	3	5	2	37	2	1.2
TOTAL				3	11	60	1	1	7	11	1	5		

Summary

A computer-based particulate analysis system for on-line sizing and chemical analysis has been discussed. The system is an extension of a normal scanning electron microscope equipped with an EDS-MCA. Applications for air particulates, coal minerals, inclusions in steel, and minerals have been realized.

References

1. F. H. Schamber, *FLEXTRAN*, Tracor Northern Report TN-1800M, 1975.
2. J. J. McCarthy, G. S. Fritz, and R. J. Lee, "Acquisition, storage, and display of video and x-ray images," *Microbeam Analysis--1981*, 30.
3. R. J. Lee and J. F. Kelly, "Overview of SEM-Based Automatic Image Analysis," *SEM/1980 I*, 303-310.
4. J. F. Kelly, F. J. Lee, and S. Lentz, "Automate Characterization of Fine Particulates," *SEM/1980 I*, 311-322.

AUTOMATION OF NBS LASER-RAMAN MICROPROBE

J. J. Blaha, R. L. Myklebust, and E. S. Etz

The automation of the NBS laser-Raman microprobe has now been completed. Several workers have described automation systems for Raman spectroscopy instruments of various types.¹⁻⁴ The NBS instrument has been automated along similar lines with the addition of the specimen stage. The software has been designed for ease of operation as well as to provide flexibility for the available options.

The instrument has been described in detail elsewhere;⁵⁻⁷ however, for easier understanding of the functions of the automation system, a brief description of the microprobe is presented below. The instrument is a monochannel Raman spectrometer of conventional design, arranged so as to permit the acquisition of analytical quality spectra from microparticles or microscopic regions of micrometer dimensions. The light from an argon/krypton ion laser is focused to a small (2-20 μ m) spot on the specimen. The light scattered by the specimen is collected by an ellipsoidal mirror in a 180° back-scattering geometry and transferred into a double monochromator. The signal is detected by a cooled photomultiplier and processed by photon-counting electronics.

The sample is supported on a substrate mounted on a stage driven by remotely controlled translators. The lateral spatial resolution of a measurement is mainly determined by the size of the beam spot on the specimen and spatial filtering elements placed in the path of the collected scattered light. Irradiance levels employed in routine probe measurements range from several megawatts/cm² to several kilowatts/cm². Measurement times for single particles of size down to 2 μ m may vary from 20 min for survey spectra to scans requiring 3-5 hr for radiation-sensitive microsamples.

All of the functions of the laser-Raman instrument except for the laser itself are controlled by a digital computer and its interface modules. The specimen is moved into the laser beam by two stage drives positioned normal to each other and controlled by the computer. The computer controls the spectrometer drive motors as well as the four spectrometer slits. The data are automatically read from the photon counter and are stored on magnetic disk, and may be displayed on the strip-chart recorder, the digital plotter, or the CRT screen.

The automation consists of a DECLAB-11/MNC system obtained from Digital Equipment Corporation.* The computer is a PDP-11/03 with 64k bytes of memory, dual 5 megabyte firm disks, and a CRT console. The console serves both as the computer terminal and as the display device for the spectra. The computer is interfaced to the laser-Raman microprobe through a series of plug-in modules (Fig. 1). Two 16-bit digital input modules and three 16-bit digital output modules have been employed in this automation system. One output module (#0) controls the stepping motors on the spectrometer and the strip-chart drive motor as well as the Burleigh* dual PZT translator stage to position the specimen. The output of the encoders on the spectrometer is read by the computer through one of the input modules (#0). The second input module (#1) reads the output from the SSR* photon counter, which is controlled by the second output module (#1) of the computer. The third output module (#2) controls the Houston Instrument* Complot digital plotter. All signals in this system are digital and no amplification outside of the SSR photon counter is required.

Every function is directed by individually controlled bit manipulation within the software, thus all motor drives are controlled by the number of steps/movement interval. A motor is selected for movement when the correct output bit in the output module is addressed. For the spectral data, the output module turns on the SSR photon counter, which

The first author is now with the U. S. Food and Drug Administration, Kansas City, Mo. The other authors are in the Center for Analytical Chemistry, U. S. National Bureau of Standards, Washington, DC 20234. The support of this work by the U. S. Air Force Technical Applications Center (AFTAC) is gratefully acknowledged.

*The commercial equipment identified in this paper serves only to more fully describe the subject discussed. In no case does this identification imply recommendation by the U. S. Government.

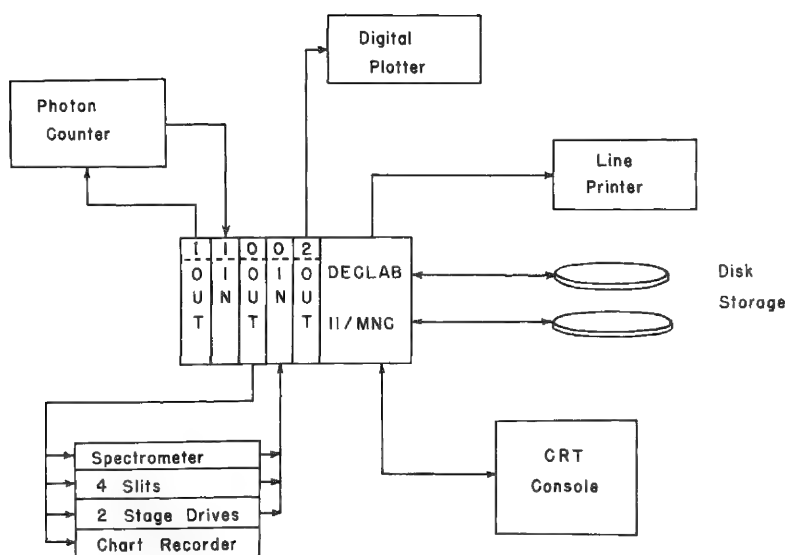


FIG. 1.--Block diagram of NBS laser-Raman microprobe automation system.

then samples for a preset time interval. The SSR sends a "ready" signal to the computer when it has finished counting and the computer then accepts the data from the SSR one digit at a time until the entire data point has been transmitted. At this time, the SSR is cleared and is ready to count more data upon a signal from the computer.

The software is divided into two parts. The first part initializes all the spectrometer functions, controls the system for data collection, and does the data acquisition. The second part controls all the data display, which consists of the CRT graphics display and the digital plotter. The first step for a data acquisition is to initialize the specimen stage and the spectrom-

eter. With prompts from the computer, the user must enter a file name, the initial wavenumber, the final wavenumber, the slit widths in wavenumbers, the time constant in seconds, the number of data points per resolution interval, and the x-y position of the sample. The increment for data sampling is then the slit width in wavenumbers divided by the number of data points per resolution interval. The data may be plotted on the strip-chart recorder while they are being collected.

The graphics programs may be used to display individual spectra or to compare two different spectra shown simultaneously on the CRT screen. It is also possible to plot one half of a spectrum in the top half of the screen and the other half of the spectrum in the bottom half of the screen, or to plot the full spectrum in the top half of the screen and a portion of the same spectrum in the bottom half. All routines allow the user to position a cursor to determine the frequency and intensity of any given data point. A hard copy of a plot may be obtained by use of the plotting program for the digital plotter. This program plots any data file in any of the ways described for the CRT graphics, including the axes and labels.

The computerized micro-Raman spectrometer system has been used for routine spectral characterization of various types of microsamples, with emphasis on the measurement and analysis of single microparticles 1 μm and larger. The automation has facilitated the acquisition of spectra and their qualitative evaluation. Among the principal benefits over manual operation are the possibilities for data manipulation and display. The software can produce modified spectra from the basic scattering data (files of intensity values vs frequency shift) by analytical manipulation within the computer. Examples include expanded spectra and difference spectra (e.g., background-corrected spectra). This capability increases the diagnostic value of the spectra.

The data-acquisition system provides for immediate display of the numerical data and the results of intermediate data processing in graphic form via a visual output on the data terminal screen. Programs have been written to display the raw data, specifying file name, spectral range, and full-scale signal intensity. The optional use of a cursor set to any frequency position provides a readout of the scattered intensity in counts corresponding to the smallest frequency interval that defines the width of the preassigned spectral element. Spectra can be scaled, subtracted, and/or ratioed (i.e., normalized) and the results displayed. Data files can be presented as one spectrum on the screen or any two spectra can be displayed for comparison although not by one-to-one superposition.

Figure 2 illustrates the graphic display function for the results from a microprobe measurement on a $\sim 5\mu\text{m}$ particle of uranium oxide (UO_2). The particles in this sample are supported by a sapphire ($\alpha\text{-Al}_2\text{O}_3$) substrate and are overcoated (i.e., embedded) by a trans-

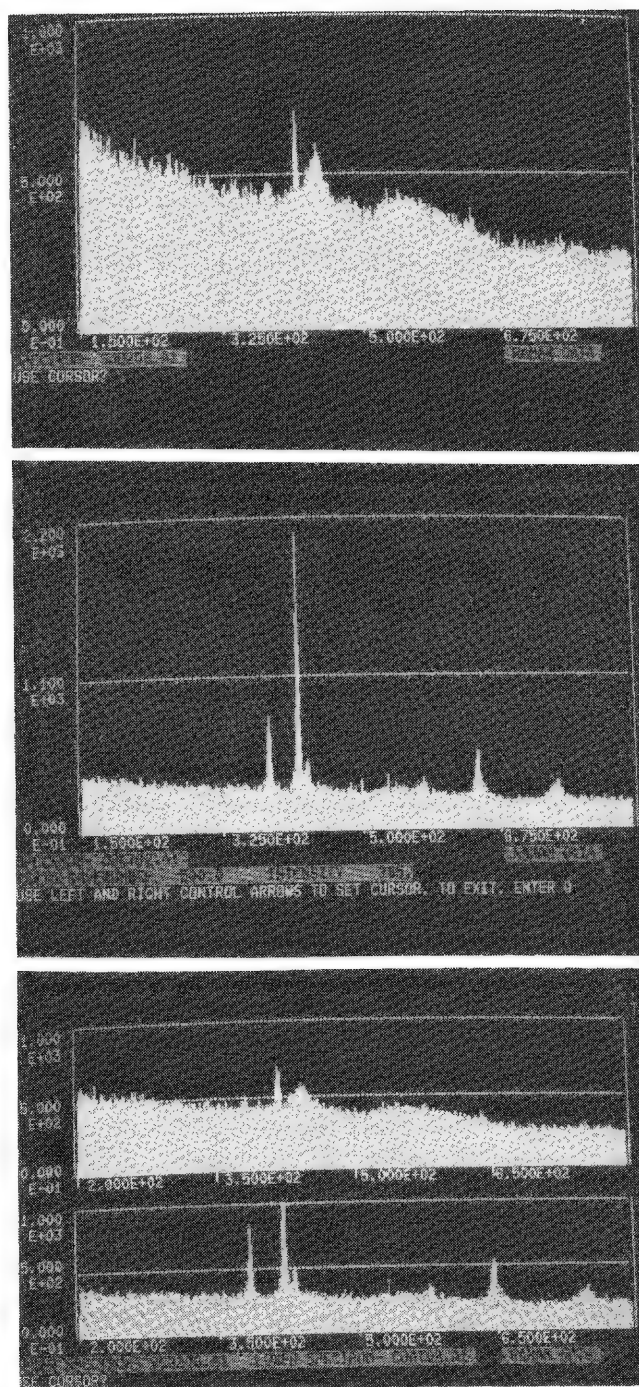


FIG. 2.--Example of Raman microprobe spectra; plot of scattered intensity (counts) vs Raman shift (wavenumbers) obtained in the characterization of microparticulate uranium oxide. Top: Spectrum ($\Delta\nu$, 50-850 cm^{-1}) of a single UO_2 particle (size, $\sim 5 \mu\text{m}$) on sapphire substrate with silicate overcoat. Middle: Corresponding spectrum of "background" arising from scattering by substrate and sample overcoat. Bottom: Comparison (expanded scale) of particle and "background" spectra in same spectral display. Measurement parameters: Laser excitation, 514.5 nm; power, 25 mW (at sample); beam spot, $\sim 20 \mu\text{m}$ diameter; spectral slit width, 5 cm^{-1} ; time constant, 3.0 s; scan rate, 13.3 $\text{cm}^{-1}/\text{min}$. Data collected at 1.0 cm^{-1} intervals with a counting time of 4.5 s per data point.

parent, noninterfering film of sodium silicate. The oxide particles are highly opaque and radiation absorbing; therefore, they cannot be analyzed successfully without a surrounding medium--or host--that effectively minimizes laser-induced sample heating. The silicate overcoat serves this function of heat-sinking the particle to the substrate. Without it, the particle would instantly be destroyed on exposure to the focused laser beam and be lost to the measurement. The particle spectrum (top) extends over the range 50-850 cm^{-1} and shows the characteristic band for UO_2 centered at about 445 cm^{-1} .⁸ The more intense and sharper feature maximizing at 418 cm^{-1} is the strongest line in the Raman spectrum of sapphire.⁹ The middle spectrum was obtained under identical measurement conditions by a translation of the particle out of the laser spot, so that the scattering from the substrate and the silicate overcoat is recorded. Several additional, weaker lines of the sapphire spectrum are detected⁹ with no bands arising from the silicate coating. The background-subtracted particle spectrum is not shown here. The bottom display of Figure 2 shows the particle and background spectrum at identical full-scale intensities with a somewhat expanded frequency scale. This mode of spectral display is useful in a simultaneous one-to-one comparison of the data.

A further important consequence of the computerization of the system is the development of a micro-Raman spectral library. We have plans for the future development of a file-searching technique using peak location and band intensity data for matching reference spectra with the spectra of unknowns.

References

1. S. Ushioda, J. B. Valdez, W. H. Ward, and A. R. Evans, "Computer controlled double-grating spectrometer system for low light levels," *Rev. Sci. Instrum.* 45: 479, 1974.
2. R. W. Chrisman, J. C. English, and R. S. Tobias, "A high sensitivity digital Raman difference spectrometer for studies on solutions of biological molecules with on-line computer control of data acquisition and reduction," *Appl. Spectrosc.* 30: 168, 1976.
3. W. F. Edgell, E. Schmidlin, T. J. Kuriakose, and P. Lurix, "A computer-spectrometer interactive system for Raman spectroscopy," *Appl. Spectrosc.* 30: 428, 1976.
4. W. H. Fletcher, J. S. Rayside, and W. B. McLendon, "A computer controlled high resolution Raman spectrometer system", *J. Raman Spectrosc.* 7: 205, 1978.
5. G. J. Rosasco and E. S. Etz, "The Raman microprobe: A new analytical tool," *Res. & Devel.* 28: 20, 1977.
6. E. S. Etz, G. J. Rosasco, J. J. Blaha, K. F. J. Heinrich, and W. C. Cunningham, "Particle analysis with the laser-Raman microprobe," *Proc. 13th MAS Conf.*, 66A, 1978.
7. E. S. Etz and J. J. Blaha, "Investigations into the critical measurement aspects of Raman microprobe analysis," *Microbeam Analysis--1979*, 173.
8. P. J. Colwell, L. A. Rahn and C. T. Walker, "Raman scattering from UO_2 ," in M. Balkanski, R. C. C. Leite, and S. P. S. Porto, Eds., *Proc. Third Intern. Conf. Light Scattering in Solids*, Paris (France); Flammarion Sciences, 1976, 239-243.
9. S. P. S. Porto and R. S. Krishnan, "Raman effect of corundum," *J. Chem. Phys.* 47: 1009, 1967.

WHAT'S NEW ABOUT THE SECONDARY ELECTRON YIELD?

R. L. Park

Techniques for the study of material properties are less frequently discovered than re-discovered. The revival of an old technique may result from technological innovations which alleviate experimental constraints or from theoretical advances which extend the usefulness of the information obtained. Both elements are present in renewed interest in the secondary-electron yield. It is now clear that the details of the secondary-electron-yield spectrum can provide information on core binding energies, surface composition, electronic structure, and surface crystallography.

The apparatus required to measure the secondary-electron yield is quite simple. It consists of a thermionic emitter and an anode with a pinhole (Fig. 1). Electrons passing through the pinhole are allowed to impinge on the sample. If the anode potential V_0 is held fixed, the current striking the sample is independent of the emitter-sample potential V . If $V_0 > V$, secondary electrons from the sample are collected on the anode. Thus, the secondary yield $Y(E)$ is just

$$Y(E) = 1 - [I_S(E)/I_p] \quad (1)$$

where $I_S(E)$ is the net sample current flowing through the measurement impedance Z and I_p is the constant primary current passing through the aperture. The primary electron energy E , relative to the Fermi energy of the sample, is given by

$$E = eV + e\phi_c \quad (2)$$

where $e\phi_c$ is the work function of the emitter.

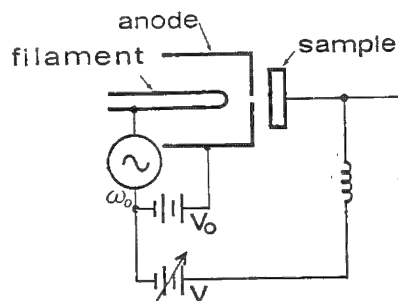


FIG. 1.--Apparatus used for Auger electron appearance spectroscopy. Electrons emitted from hot filament are accelerated past anode and impinge on sample. With constant anode voltage V_0 , current to sample is constant. Since $V_0 > V$, secondary electrons are collected by anode and sample current is constant primary current m minus secondary yield. A small modulation on filament potential is used in differentiation of sample current.

The general features of $Y(E)$ have been known for many years and are remarkable similar for metals, semiconductors, and insulators. The yield rises smoothly at low energies and reaches a maximum at several hundred electron volts, after which it slowly decreases. For most materials the yield crosses unity at an energy of 50 to 200 eV and again between 1 and 2 keV. The similarity of the yield plots for diverse materials was emphasized by Baroody,¹ who plotted so-called "reduced yield" curves in which the yield is normalized to the maximum value and the energy is divided by the energy at which the maximum occurs. The similarity of such plots for quite different materials would seem to argue that the total yield spectrum is insensitive as a means of characterizing the surface.

As early as 1926, however, Petry reported small inflections in plots of the secondary yield, which he associated with the thresholds for inelastic scattering from core states.² Not everyone was convinced. Farnsworth insisted that any agreement between the inflections he observed in the secondary yield of copper and the critical potentials for x-ray production was fortuitous, since the number of inflections greatly exceeded the number of core levels.³ He attributed the structure to changes in elastic yield produced by diffraction. By 1936 only Warnecke continued to insist that he could detect critical potentials in the secondary yield.⁴ In his detailed 1948 review of secondary electron emission, McKay managed to dismiss the whole question of critical potentials in a single para-

The author is at the Department of Physics and Astronomy at the University of Maryland in College Park, MD 20742. The work was carried out under Office of Naval Research grant NO 0014-78-C-0292.

graph.⁵ He rejected both the x-ray critical potential and diffraction explanations and suggested that the structure resulted from the desorption of contaminants.

However, recent studies of the derivative of the secondary-electron yield leave no doubt as to either the reality or the origin of these inflections.⁶ A plot of the second derivative of the secondary-electron yield of polycrystalline vanadium (Fig. 2) reveals two types of structure. At relatively high energies sharp features corresponding to the thresholds for electron excitation of the 2p core levels are evident. At energies below about 200 eV structure due to the diffraction of the incident electron beam is clearly evident. This structure damps out at high energies due to the Debye-Waller effect.⁷

To obtain the derivative spectrum, a small sinusoidal modulation is superimposed on the potential between the emitter and the sample, and the portion of the signal that varies at the same frequency is synchronously detected.⁸ The harmonics of the detected signal corresponds to the higher derivatives.

The spectrum of core excitation thresholds provides an absolute measure of core electron binding energies. Since no dispersive analyzer is required, binding energies measured in this way are not subject to error from stray fields, et . . . Moreover, the resolution is limited only by the spread in incident electron energies, which makes this the spectroscopy with the highest resolution core level. Binding energies measured in this way should provide a standard against which XPS measurements can be compared.

Distinct structure above the appearance of potential thresholds is related to the local density of unfilled states associated with the excited atom. Since there are two electrons to be accommodated in the excitation process (the incident and the ejected core electrons), the spectral shape is related to the self-convolution of the one electron density of states, modified by the matrix elements and broadened by the core hole lifetime and the spread of incident electron energies.⁶

Recently it has been shown that fine structure, analogous to extended x-ray absorption fine structure (EXAFS), extends for hundreds of electron volts above the thresholds. This structure can be invoked to obtain the near-neighbor separation of the absorbing atoms.¹⁰

Thus, the derivative of the secondary-electron yield, which is one of the simplest measurements that can be made of surfaces, can in many cases provide a remarkable complete characterization of the surface.

References

1. E. M. Baroody, *Phys. Rev.* 78: 780, 1950.
2. R. L. Petry, *Phys. Rev.* 28: 362, 1926.
3. H. E. Farnsworth, *Phys. Rev.* 31: 199, 1928.
4. R. Warnecke, *J. Phys. Radium* 7: 318, 1936.
5. K. G. McKay, L. Marton Ed., in *Advances in Electronics*, New York: Academic Press, 1948, vol. 1, p. 66.
6. R. L. Park, *Appl. Surf. Sci.* 4: 250, 1980.
7. M. L. den Boer, Ph.D. thesis, University of Maryland, 1979.
8. R. L. Park, *Surface Sci.* 48: 80, 1975.
9. P. I. Cohen, T. L. Einstein, W. T. Elam, Y. Fukuda, and R. L. Park, *Appl. Surface Sci.* 1: 538, 1978.
10. M. L. den Boer, T. L. Einstein, W. T. Elam, R. L. Park, L. D. Roelofs, and G. E. Laramore, *Phys. Rev. Lett.* 44: 496, 1980.

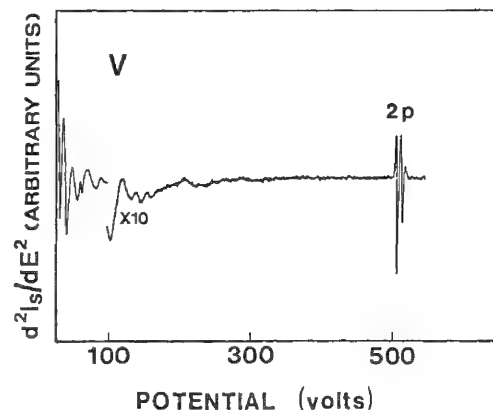


FIG. 2.--AEAPS spectrum over wide range of incident energies, showing both incident-beam diffraction structure at lower energies and 2p core appearance potential features. This spectrum was taken on a clean polycrystalline vanadium sample; second-derivative mode was used to enhance structure.

DEVELOPMENTS IN RAMAN MICROANALYSIS

Fran Adar

Subsequent to the initial description of the technological potential to develop a Raman microprobe,^{1,2} instruments were developed independently at the National Bureau of Standards in Washington³⁻⁵ and the University of Lille in France.^{6,7} The motivation for the development of a Raman microprobe was its ability to yield bonding information in condensed material--that is, molecular or chemical identification and crystal form of polymorphs. The information content available in a Raman microprobe complements the elemental information from other microprobes. With the development of this technique, the industrial laboratory can have the potential for molecular microanalysis of products and contaminants occurring in fabrication processes; and the research-oriented laboratory can characterize the molecular and/or crystalline composition of morphological features defined by the optical microscope.

Raman Microsampling

The development of Raman microprobes followed the realization that a high-aperture microscope objective is capable of focusing essentially 100% of the power in available laser beams to diffraction-limited spots of the order of 1 μm . The design of appropriate sampling optics involved a choice of method to disentangle the incident and scattered beams of large numerical aperture objectives. Classical Raman instruments use F/1 collection lenses with corresponding numerical aperture (n.a.) of 0.5. The demagnification of the 90° scattering geometry with n.a. = 0.5 lenses to microsampling geometry would place the focusing and collection lenses into physical contact.⁸ The MOLE's solution to the geometrical problem was implementation of a beam splitter above a microscope objective on a commercially available microscope.^{6,7} In the coaxial lens system in the NBS instrument,⁴ the sample is positioned at one of the foci of an elliptical reflector; the laser beam is focused by an independent microscope objective through an aperture in the elliptical mirror which images the scattered radiation at the second focus.

In designing a Raman system for microsampling, two sets of conditions determine the volume of sample detected by the instrument. Initially, the volume of irradiated sample must determine the size of the Raman source. Subsequently, the volume of sample imaged through the fore-optical system and entrance slit into the monochromator determines the portion of the source that is detected.

The size of the laser-focused volume is determined by the diffraction-limited spot produced by the focusing objective. In a classic paper describing the optical coupling between a laser, gas sample, and monochromator,⁹ Barrett and Adams present formulas for the laser focusing volume for a macrosystem. In this situation the aim is to produce a volume that can be imaged along the total length of slit; the laser-focusing lens is typically much larger than the beam and the depth of focus of the laser is much longer than the beam waist. Because the lens aperture is larger than the beam the wings of the laser Gaussian distribution are not truncated and expressions from Gaussian optics are appropriate. The minimum beam radius w_0 is given by $w_0 = 2\lambda/\pi\alpha$, where α is the focusing angle of the laser beam (defined by the $1/e^2$ points in the far field). At small angles, $\alpha = d/f$, where d is the diameter of the beam at the lens and f is the focal length of the lens. The depth of focus L of the beam describes the length over which the laser is close to being in focus; it is given by $L = 8\lambda/(\text{n.a.})^2$. They found that 90% of the Raman signal originates in a source cylinder of length L and diameter $2w_0$ at 500 nm; when $\alpha = d/f$ is 1:20, the beam waist $2w_0 = 13 \mu\text{m}$ and $L = 1.02 \text{ mm}$. In imaging this volume on a monochromator slit, advantage can be taken of the total length of cylinder.

In order to achieve the small spots required of a Raman microprobe, higher numerical aperture focusing objectives are utilized. In this case it is impractical for the objective to fulfill the Gaussian requirements. When high-n.a. objectives are used to focus a

The author is at the Applications Laboratory, Instruments SA, Inc., Metuchen, NJ 08840 and Department of Biochemistry and Biophysics, University of Pennsylvania, School of Medicine, Philadelphia, PA 19102.

laser beam the classical description of an Airy disk is more appropriate for describing the intensity profile.¹⁰ However, the Airy pattern describes the intensity distribution of a uniformly illuminated lens. An even more exact formulation was described by Innes and Bloom,¹¹ in which intensity contour diagrams are plotted and discussed for lenses with 0 to 2 wavelengths of spherical aberrations and apertures larger and smaller than the Gaussian beam. In contrast to the result of Gaussian conditions, where the focused spot has no faint rings, the case for which the spherical aberrations are zero but the aperture is twice the size of the Gaussian diameter shows minima and maxima outside the central disk. From the analytic expressions for an Airy disk, an objective with n.a. = 0.9 would focus more than 84% of the laser energy into a $2w_0 = 1.22\lambda/\text{n.a.} = 0.7\mu\text{m}$ beam spot with depth of focus (distance between axial modes) equal to $4\lambda/(\text{n.a.})^2 = 2.5\mu\text{m}$.

On the MOLE instrument a microscope is incorporated that utilizes standard microscope objectives for sample illumination and collection of scattered radiation. Observation of the spot indicates a beam waist that is indeed under $1\mu\text{m}$, with subsidiary rings containing a small amount of energy. On the NBS system one of two microscope lenses is used to focus the laser beam through the aperture in the elliptical collector onto the sample. The Beck 15 \times all-reflecting objective (n.a. = 0.28) forms a $2\mu\text{m}$ beam spot. A 5.6 \times Leitz refractive objective (useful n.a. = 0.1) forms a $6\mu\text{m}$ beam spot.

Light collected from the Raman source is subsequently imaged through a fore-optical system onto the entrance slit of a monochromator. This system is useful in limiting the volume from which signal is collected. In particular, fluorescence and Raman emission outside the volume of exact focus can be rejected. This has been treated formally in Rosasco's discussion of the design of the NBS system,^{5,12} and in Hirschfeld's original concept of that optical system² as well as P. Dhamelincourt's thesis in which the design of the MOLE is detailed.¹³ The point that was emphasized is that Raman and fluorescence radiation generated outside the laser focal volume can be blocked by a depth-of-field-limiting pinhole placed at an intermediate image plane between the Raman collecting optic and the monochromator entrance slit. The size of the pinhole for maximum suppression of signals from outside the focal volume equals the product of the beam waist at the sample and the magnification between the sample and pinhole.

The NBS system uses a $140\mu\text{m}$ pinhole to accommodate the image of the Raman source. A detailed ray trace, including aberrations, of the effective collection volume of the ellipsoid with this spatial filter shows that most of the detected radiation originates in a volume extending $6\mu\text{m}$ above and below the focal plane and $4\mu\text{m}$ around the optic axis.

The MOLE has been equipped with a variable iris diaphragm that is mounted behind the microscope. A $1\mu\text{m}$ beam spot at the sample (produced by a 100 \times objective) is imaged behind the microscope to $100\mu\text{m}$. However, the laser is quite routinely defocused to 5-10 μm at the sample in order to reduce the laser heating, in which case the diaphragm can be easily opened to accommodate the larger sample volume. Dhamelincourt's calculation shows that setting the diaphragm equal to the size of the image of the source effectively limits the volume from which the radiation is emitted to material 2-3 μm above and below the plane of focus.

Techniques for Handling Challenging Samples

A major limitation to some applications of micro-Raman spectroscopy has been laser-induced damage to samples due to high irradiance levels,¹² especially in opaque samples; and background fluorescence, alluded to above. Several techniques have been developed for dealing with these challenging samples. Andersen reports successful use of water and oil immersion to dissipate heat induced by laser irradiance.¹⁴ Etz has recently reported the use of a water glass coat for dissipation of heat away from microparticles.¹⁵ In our laboratory we have successfully used a thermoelectric cooling stage on the MOLE (supplied by Bailey Instruments, Saddle Brook, N.J.) to study organic films. Since it is the power density that is the limiting parameter in inducing sample damage, we have also found that defocusing the laser beam on the microscope reduces the chances of destruction. When the power levels drop so low that signals become too weak to detect, we find that standard practices of signal averaging (co-addition of photomultiplier pulses accumulated during multiple scans) produce quite useful spectra.

The presence of fluorescence in samples subjected to Raman microanalysis has been

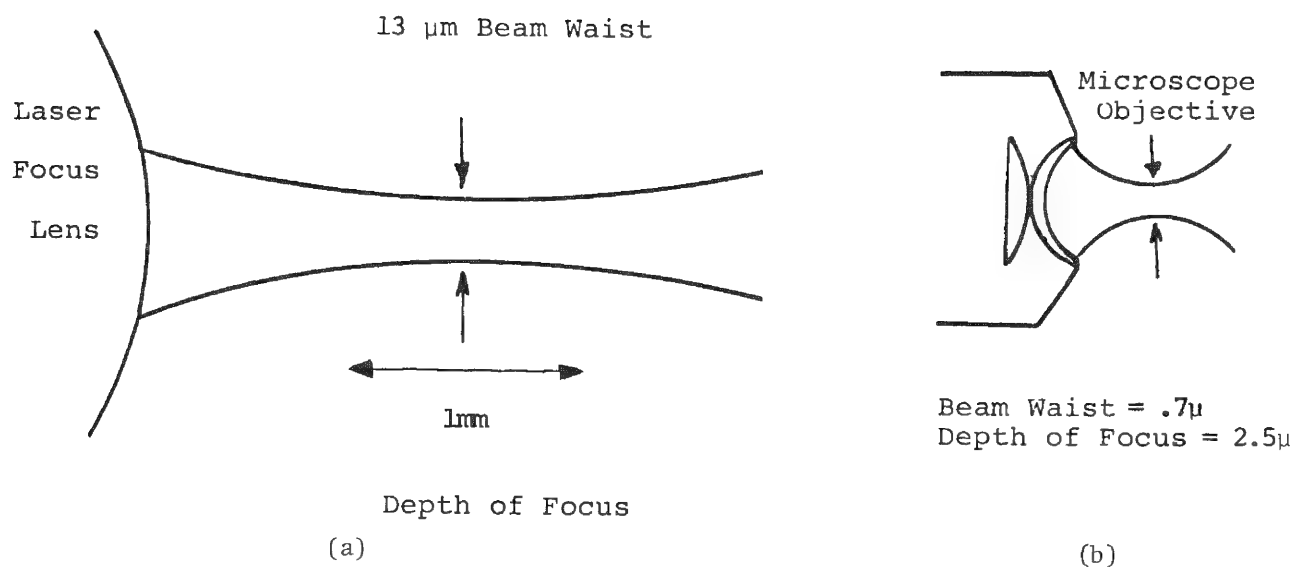


FIG. 1.--Raman sampling volume for (a) macro-optics ($F/D \approx 20$, $N.A. = 0.05$); (b) micro-optics ($N.A. = 0.9$).

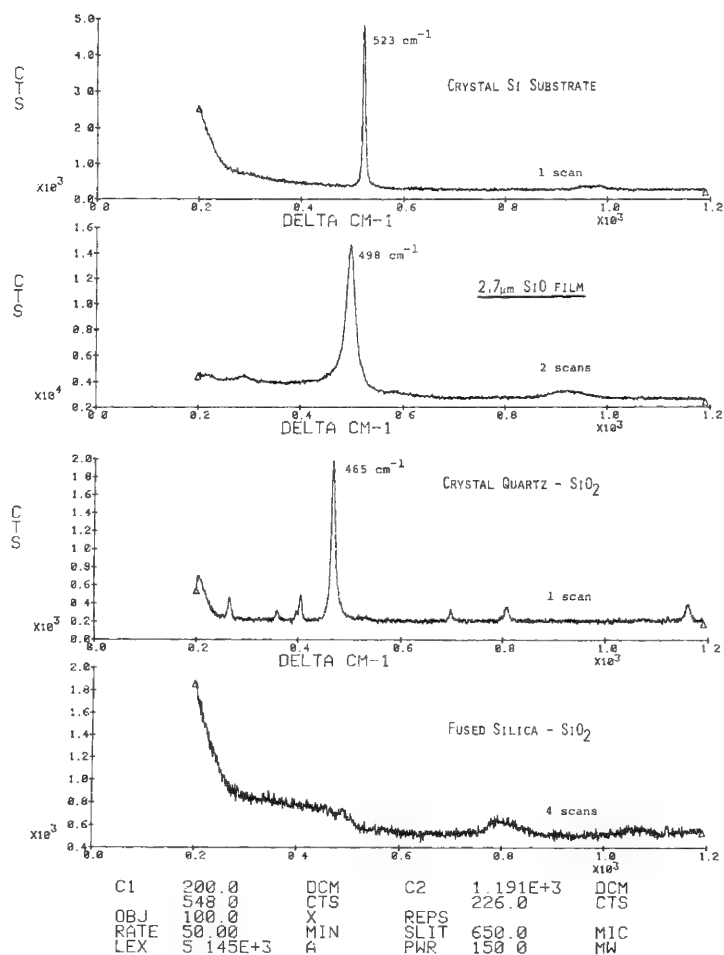


FIG. 2.--MOLE spectra of SiO compared with crystal Si and SiO₂ (quartz and fused silica).

01/14/81 11:00:09

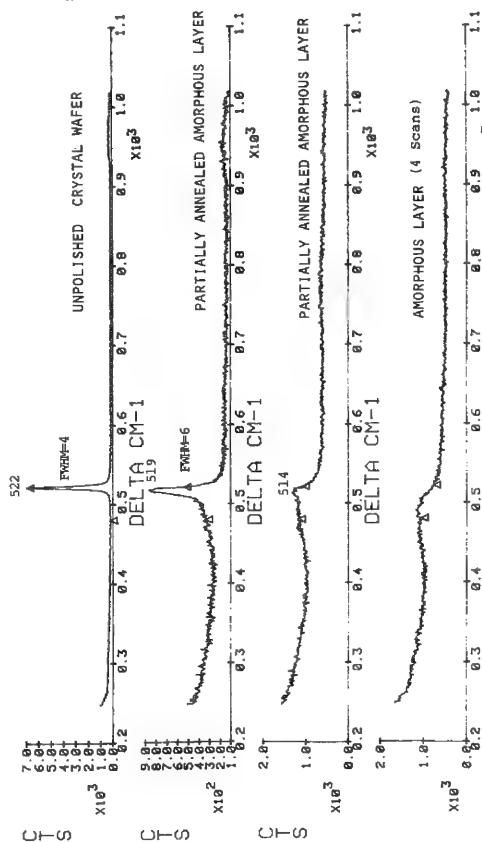


FIG. 3.--MOLE spectra of laser-annealed amorphous Si.

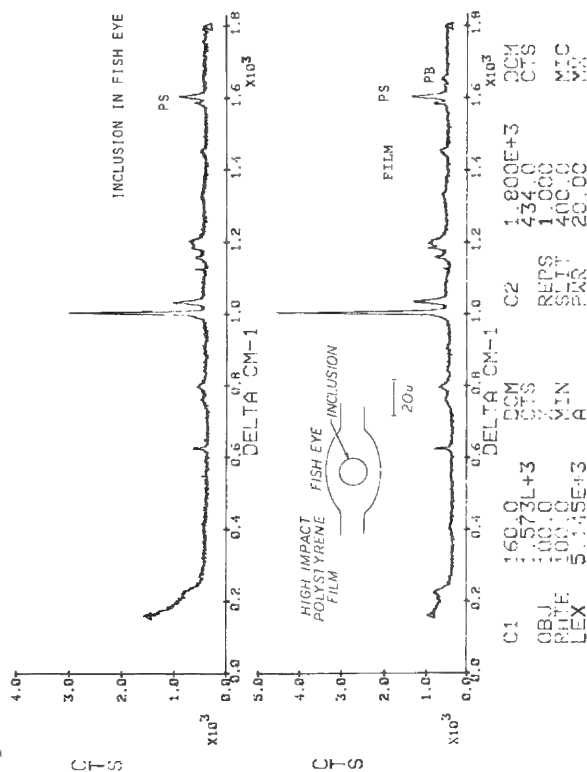


FIG. 5.--MOLE spectra of inclusion in fish-eye in high-impact polystyrene film compared with spectra of film.

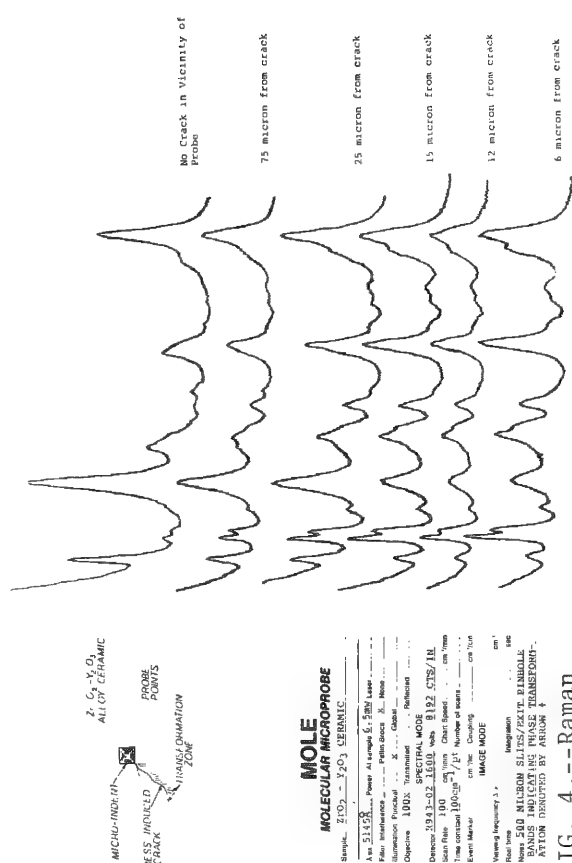
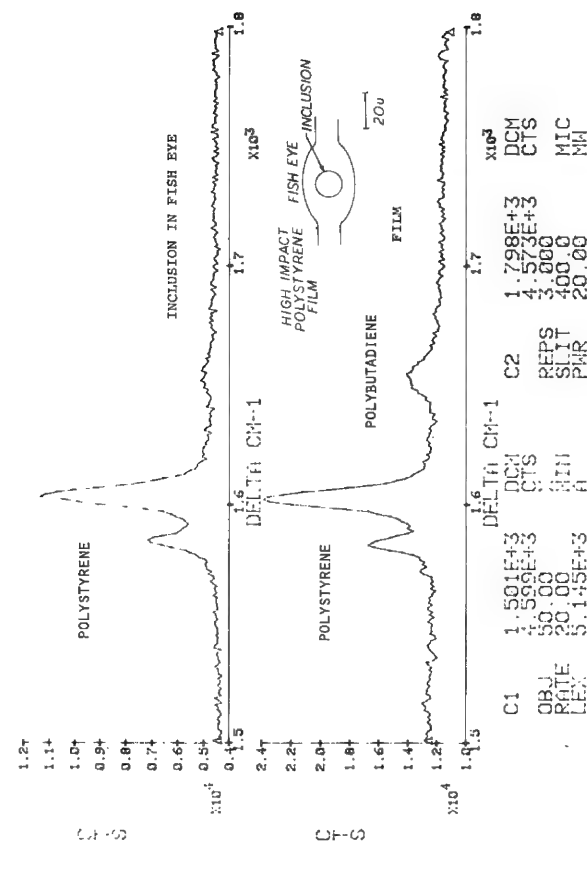


FIG. 4.--Raman

microprobe spectra of ZrO₂ ceramic as a function of distance from stress-induced crack.



found to be less of a problem on the MOLE instrument than on standard Raman instruments because of the following effects. (A) In many samples the fluorescence originates in impurities of unknown origin. These impurities tend to be inhomogeneously distributed. When a substantial amount of material is available, we find it useful to hunt for a micro-particle or microregion that fluoresces weakly. (B) Laser quenching tends to be complete within 15-30 min (presumably because of the high irradiance). (C) The iris diaphragm has been observed to block approximately 90% of the fluorescence without blocking the Raman signal. We rationalize this observation by the following argument. Fluorescence arises from excited states with finite lifetimes; these excited states can be transferred between molecules before radiative decay (exciton migration). Apparently a large percentage of the fluorescent states migrates away from the lum point of illumination before emitting photons. The Raman process, on the other hand, is essentially instantaneous, and therefore originates only in the laser illuminated volume.

To summarize, the experience of the various Raman microprobe laboratories in the last five years has demonstrated that not only is it possible to record Raman spectra of any material whose macro-Raman spectrum has been published, but that the microprobe provides capability to record spectra of some fluorescing samples that were previously unamenable to study. The examples presented below will illustrate the potential of this developing technique.

Applications

The immediate impact of Raman microanalysis has been in quality control of manufacturing processes. In particular the ability to identify organic contaminants is truly unique. During the characterization of several materials of interest to the integrated circuit industry we have found that the Raman data provide information on the coherence lengths of crystalline packing below which x-ray diffraction no longer detects "crystalline order." Because of the importance of this effect we review our observations briefly.

Because of the short focal depth of the MOLE we have been asked to examine films. One such film was the SiO film whose results were reported here two years ago.¹⁶ Another was a film of laser-annealed amorphous silicon (a-Si).

In examining the SiO film we were asked to determine whether the film had a spectrum indicative of "SiO" or could be described as a superposition of Si and SiO₂. The spectrum of the film cannot in fact be reconstructed by addition of any of the known spectra of SiO₂ and Si.

In examining the spectra of laser-annealed Si we did expect to see a superposition of the spectra of a-Si and the crystalline form. What we actually saw was a shift in the band position and narrowing of its width as the probe beam moved into more completely annealed material. At the time these measurements were taken, two Raman laboratories were reporting the same effect on macrosamples.^{18,19} By correlating with electron diffraction patterns and X-ray diffraction linewidths they were able to conclude that the Raman frequency and line width reflects the long-range order of the annealed Si.

The ability of Raman spectroscopy to monitor crystal-packing coherence lengths is somewhat surprising, but in fact has been documented previously. In a classic study of graphite it was shown that the growth of a second band in the Raman spectrum of graphite at 1360 cm⁻¹ and broadening of the 1575cm⁻¹ line correlated well with crystallite size.²⁰ In a second case, there is evidence that a high-temperature phase of ZrO₂ that was believed to be amorphous exhibits crystallinity in electron diffraction as well as Raman spectra.²¹ In this reference it is stated explicitly that "a translational repetition length of 3 to 6 units is sufficient to produce a characteristic Raman spectrum, a length shorter than that necessary to diffract X-rays" (p. 24).

The implications of this effect are important. Because a Raman microprobe has spatial resolution limited by optics, one cannot expect to probe a spot much less than a micron. However, the Raman effect is apparently sensitive to order parameters as small as 20 Å in some systems. Thus, whereas it is not possible spatially to resolve such a small region, the crystal packing is amenable to study. And a material's physical properties may be intimately related to the crystal coherence length. For example, the laser-annealed silicon mentioned above is being proposed for fabrication of solar cells and multilayered integrated circuits. The electron scattering length will depend on the crystal's long range order, and it will be the electron scattering length that will ultimately contribute to electri-

cal properties of the silicon used in manufacturing devices.

During the past year, in collaboration with David Clarke at Rockwell International, we have also examined a ZrO_2 ceramic. This material is stabilized in the tetragonal phase by alloying with Y_2O_3 or Al_2O_3 , which produces one of the toughest ceramics known. We were asked to measure the transformation zone surrounding a stress-induced crack. By monitoring Raman bands of the monoclinic and tetragonal phases, we were able to determine the extent of transformation from the metastable tetragonal form to the normally stable monoclinic form. In some cases the transformation zone was no larger than the probe (as expected), but in others it extended tens of microns from the crack. This phenomenon cannot be studied any other way. TEM does give information on crystalline phase, but sample preparation is assumed to introduce artifacts, so that the information acquired on the MOLE is truly unique.

As a final example, we have results on a fish-eye in high-impact polystyrene. Fish-eyes appeared as nodules, 300 μm in diameter, in films that were approximately 300 μm thick. High-impact polystyrene is composed of polystyrene and polybutadiene and it was suspected that the fish-eyes resulted from a higher-than-average concentration of one of the polymers. Preliminary data were taken on the surface of the film and were inclusive. Subsequently, a fish-eye was cross-sectioned with a razor blade for examination; there was a clear inclusion in the center. Examination with the MOLE clearly shows the absence of polybutadiene.

Summary

A brief history of the development of the Raman microprobe at the National Bureau of Standards and the University of Lille has been presented, with emphasis on the definition of the probe volume. Several examples of work performed in our Applications Laboratory, including organic contaminants, inorganic films, a ceramic, and a polymer fish-eye have been presented.

References

1. M. Delhay and M. Miglon, *C. R. Acad. Sci.* 262, 1966.
2. T. Hirschfeld, "Raman microprobe: Vibrational spectroscopy in the femtogram range," *J. Opt. Soc. Am.* 63: 476-7, 1973.
3. G. J. Rosasco, E. S. Etz, and W. A. Cassatt, "Investigation of Raman spectra of individual micrometer-size particles," *Appl. Spectrosc.* 29: 369, 1975.
4. E. S. Etz, G. J. Rosasco, and W. C. Cunningham, *The Chemical Identification of Airborne Particles by Laser Raman Spectroscopy: Environmental Analysis*, New York: Academic Press, 1977.
5. G. J. Rosasco, "Microanalysis by Raman spectroscopy," *Proc. 6th Intl. Conf. Raman Spectrosc.* (Bangalore), London: Heyden, 1978, 389-398.
6. M. Delhay and P. Dhamelinourt, "Raman microprobe and microscope with laser excitation," *J. Raman Spectroscopy* 3: 33-43, 1975.
7. P. Dhamelinourt, "Raman microprobe techniques," *Microbeam Analysis--1979*, 155-164.
8. D. O. Landon, "The development of instrumentation for microparticle analysis by Raman spectroscopy," *Microbeam Analysis--1979*, 185-190.
9. J. J. Barrett and N. I. Adams III, "Laser-excited rotation-vibration Raman scattering in ultra-small gas samples," *J. Opt. Soc. Am.* 58: 311-319, 1968.
10. M. Born and E. Wolf, *Principles of Optics*, Oxford: Pergamon Press, 1975, 5th ed.
11. D. J. Innes and A. L. Bloom, "Design of optical systems for use with laser beams,"
12. G. J. Rosasco, "Raman microprobe spectroscopy," in R. J. H. Clark and R. E. Hester, Eds., *Advances in Infrared and Raman Spectroscopy*, London: Heyden, 1980, vol. 7.
13. P. Dhamelinourt, "Etude et réalisation d'une microsonde moléculaire à effet Raman: Quelques domaines d'application," thesis, University of Lille, 1979.
14. M. E. Andersen, "Sample preparation and handling techniques for microanalysis with the Raman microprobe," *L'Actualité Chimique*, April 1980, 63-64.
15. E. Etz, FACCS, Sept. 1980.
16. F. Adar, M. J. Mitchell, and J. N. Ramsey, "Raman microanalysis of SiO source materials by means of MOLE," in *Microbeam Analysis--1979*.

EMPIRICAL QUANTITATION IN RAMAN MICROPROBE ANALYSIS

E. S. Etz

Raman microprobe analysis is a powerful tool for the molecular and structural characterization of microsamples, with detection limits for major scattering species frequently falling below 1 picogram.¹⁻⁷ Although the micro-Raman spectrum provides a diagnostic "fingerprint" for the qualitative identification of constituent chemical species, a quantitative treatment of the vibrational spectra has not been developed owing to the complexities of the underlying scattering phenomena and the difficulties of the experiment itself.

This paper focuses on the problems of quantitation in Raman microprobe spectroscopy. From current perspectives of the experimental and theoretical developments of the field, it is concluded that empirical approaches to quantitative analysis may provide adequate results for many solid phase scattering systems. These prospects are illustrated with a discussion of results obtained in the quantitation of carbonate contents in biological apatites,⁸ with the use of synthetic carbonate apatites as calibration standards.

Micro-Raman Scattering Characteristics

The factors that determine the quantitative analysis of micro-Raman scattering are closely associated with the microscopic dimensions of the sample (or sampling volume) and depend in large part on the fundamental properties of the scattering material and its interaction with the incident and scattered radiation field. An assessment of the technique as practiced with currently available instrumentation reveals the following principal advantages and shortcomings.³ The spectra are relatively simple and have good molecular specificity. Signal-to-background relationships are usually adequate for good discrimination, ranging from 3:1 to 100:1 depending on composition and spectral complexity. Absolute detection sensitivities for most Raman active species are in the picogram range (10-100 pg). When there are no fundamental limits to the magnitude of the laser irradiance, detection limits fall into the subpicogram range, especially for sample matrices totally transparent to the exciting radiation. Relative detection limits for good Raman scattering molecules distributed in the solid phase (e.g., microparticles) appear to be on the order of a few per cent (typically 1-5%). The effective lateral spatial resolution can be as small as a few micrometers and is principally governed by the size of the laser focal spot on the sample. Depth resolution is less well defined and depends mainly on the optical properties of the sample and the scattered-light collection geometry. In the absence of laser-induced sample heating or photodecomposition, the micro-Raman measurement is nonintrusive and nondestructive. Basic limitations result from laser-induced photo- and thermochemical sample changes and spectral interferences from sample fluorescence. Present theoretical understanding of the inelastic (Raman and fluorescence) scattering from microparticles rests on model calculations for particles of perfect geometries (e.g., spheres and cylinders) and ideal optical properties.^{1,10-12} An extension of these principles to the scattering by particles that do not fit these models (i.e., are of irregular size and shape and have complex optical properties) is not easily made and accounts for the lack of good progress in quantitation.

Relationships for Quantitative Analysis

As a first approximation, the relationships for quantitative analysis in conventional macro-Raman spectroscopy⁸ can be extended to micro-Raman scattering. The expectation is that the Raman scattered intensity is proportional to the concentration of the species that generates the line in the spectrum. This proportionality is generally observed for solution- and gas-phase scattering systems, but the same quantitative principles are as

The author is with the Center for Analytical Chemistry of the National Measurement Laboratory, U. S. National Bureau of Standards, Washington, DC 20234. He is indebted for the carbonate apatite samples to Dr. Ming S. Tung of the American Dental Association Health Foundation's Research Unit at the National Bureau of Standards, and to Dr. Marc Grynpas of the Children's Hospital Medical Center, Harvard Medical School, for providing the bone and tissue samples examined in this work.

a rule extended only with great caution to scattering from solid phases. Yet they have been found to hold true for simple solid solutions (e.g., intersubstitution compounds) and homogeneous mixtures where band intensities are linear with concentration, barring complications due to polarization effects. All reported work demonstrates that the spectra of small particles and other types of microsamples are in essential qualitative agreement with the Raman spectra of corresponding samples of macroscopic dimensions (e.g., single crystals, powders).¹⁻⁷ Although there is good theoretical understanding of the factors governing Raman intensities,⁹ the measurements of absolute band intensities present great experimental difficulties. Relative intensities, on the other hand, can be measured with good reproducibility, especially from polycrystalline samples.

For this reason, in much of contemporary Raman work (e.g., solution- and gas-phase analysis) reliable quantitation results can be obtained by reference to internal or external calibration standards.⁸ This approach compensates for differences in matrix effects (e.g., bulk optical properties), sample geometry (relative to excitation/collection configuration), and instrumental factors. However, experimenters find it difficult to apply these procedures to a microsample owing to their inability to manipulate the sample effectively.

Experience from the use of the NBS microprobe indicates that the spectrum of a micro-particle resembles that of a polycrystalline sample rather than that of an oriented single crystal. In a polycrystalline material, the information about polarization states is lost because of multiple reflections and refractions. Thus, with high aperture collection, the observed Raman intensity can be regarded the spatial average due to the randomized orientation of the particle as seen by the collector.

In utilizing the Raman effect as a diagnostic probe for molecular species in small particles, one relies on the underlying assumption that the same physical effects that occur in macroscopic samples also occur when the active molecules are distributed within particles that have dimensions comparable to the wavelength of the exciting radiation.

Current theories for Raman and fluorescence scattering predict that quantitative analysis should be more complicated because of the effects of the geometrical (e.g., size and shape) and optical properties (e.g., refractive index) of the particle, and of the distribution of molecules within the particle. These properties strongly influence the local electric field that affects the excitation of molecular transitions and the angular distribution, polarization, and intensity of the emitted radiation.^{10,11} These theories also note that the processes of inelastic scattering and optical absorption are closely related.¹⁰⁻¹² The resulting predictions of resonances in the efficiency factors for absorption have led investigators to postulate a corresponding fine structure in the Raman scattering from particles.^{1,10-12} The internal field resonance effects for weakly absorbing dielectric spheres are predicted to be a sensitive function of the absorption coefficient of the sphere, the size parameter of the particle and, for a given particle size, the wavelength of the exciting radiation. An accurate prediction of the effects of these structure resonances on the Raman spectra of particles that are of irregular size and shape is exceedingly difficult and has not been made.

The correctness of these theories for fluorescence has been borne out by the recent experimental observation of structure resonances resulting from the internal emission of inelastic radiation by fluorescing molecules embedded in microspheres.¹³ Sharp intensity peaks are observed in the fluorescence spectra from dye-impregnated polystyrene latex microspheres that are not seen in the spectra from bulk material.

To date, no conclusive experimental verification exists of these theoretical predictions for Raman scattering from small particles. Raman microprobe investigations performed at NBS of the intensity of elastic and inelastic scattering from microspheres (size 1-10 μm) of thorium oxide, have not unequivocally demonstrated the existence of these structure resonances. The scattering data are sensitively affected by a number of experimental difficulties and constraints, such as the complications arising from optical coupling to the supporting substrate (sapphire), deviations from true spherical particle geometry, and the effects from surface roughness of the particle. The data on the Raman intensities of the 467 cm^{-1} line for ThO_2 have verified only the expected signal dependence on the volume (r^3) of the particle.^{1,2}

Empirical Approaches to Quantitation

In applications of the Raman microprobe developed at NBS, various solid-phase systems have been investigated as particles in the size range 1-20 μm for which concentrations of scattering molecules have ranged from more than 1 to 5 wt% as determined by bulk chemical and electron microprobe analysis. These scattering systems have ranged in optical/spectral complexity from samples transparent to the exciting radiation to solid phases nearly opaque to the incident beam. Examples include the detection (at the 1-5 wt% level) of carbonate (CO_3^{2-}) in mineral apatite, uranium as the uranyl (UO_2^{2+}) ion in synthetic glasses, anatase (TiO_2) in microscopic polymer and carbon fibers, and thoria (ThO_2) in black urania (UO_2) microspheres. It could be shown for these systems that the distribution of the analyte of interest was uniform throughout the sample matrix.

These experimental observations suggest that the quantitation aspects of micro-Raman scattering may be tractable for a broad range of microparticulate scattering systems. To date no attempts have been reported aimed at the study of these quantitative relationships for solids, no doubt due in part to the still early stage of development of the technique.

If the concept of quantitation is applied with as much rigor as in other microprobe fields (e.g., x-ray microanalysis),¹⁴ then one is fundamentally concerned with measuring vibrational (i.e., molecular) band intensities and spectral backgrounds. One hopes that these measurements are straightforward, that the observed intensity values are statistically accurate, and that the signal-vs-background conditions permit an unambiguous, quantifiable detection of the species present in the excited sample volume. A quantitative scheme then simply requires to express this observation in relative or absolute terms.

The choice of a procedure for quantitative treatment of micro-Raman spectra is governed by the complexities at hand. As has been the practice in other microprobe fields, basically three methods may be advocated: (i) empirical procedures, (ii) semi-empirical methods, and (iii) full theoretical treatments. The advantages and pitfalls of each can be expected to be not very different from those recognized for quantitation in electron-probe microanalysis.¹⁴ Of these three methods, the first two appear to hold reasonable promise for success and may indeed furnish results quite adequate for present requirements. In any empirical approach the basic premise would rest on the first approximation that the concentration of a species is indeed related in a simple way to the ratio of the vibrational band intensity minus the spectral background to that in a pure standard. Accurate quantitative results may require more or less elaborate correction procedures, accounting for the effects of absorption of the incident and Raman-scattered radiation, sample fluorescence not present in the standard, spectral band overlap, surface scattering and sample density effects, and finally matrix effects.

Carbonate Determination in Biological Apatites

In conjunction with current studies of biological mineralization in tissues of bone and tooth¹⁵ and the interest in structural/chemical changes with age in vertebrate calcified tissues, we have examined the carbonate-hydroxyapatite mineral system as a model solid phase for micro-Raman scattering experiments to gain a preliminary understanding of empirical quantitation for small particles.

Present knowledge of the complex mechanisms of biological calcification is based on the results of light microscopy and electron beam analysis, correlated with x-ray and electron diffraction.¹⁶ However, these techniques do not discern the molecular forms of the elements present in the tissue. For example, much current interest centers on the incorporation--with age of the tissue--of carbonate phases in the biological mineral. The conventionally obtained calcium-to-phosphorus ratios (Ca/P) derived from electron probe measurements do not allow an estimation of the carbonate content.

The organic matrices of bone and dentin are known to constitute approximately 30% of their respective dry weights, consisting of collagen, proteoglycans, acidic proteins, and phosphoproteins. A solid inorganic mineral phase of a calcium phosphate salt, of which hydroxyapatite, $\text{Ca}_{10}(\text{PO}_4)_6(\text{OH})_2$, is the final form, contributes the remaining 70% dry weight. Chemical analysis of mineralized tissue shows a varying carbonate (CO_3^{2-}) content with age from 1.4 to 6.2% in mature chick bone.

The principal animal tissues examined in current studies are samples of bone and tooth, studied as powders and thin sections.¹⁵ To quantify the carbonate contents in these ma-

trices, a series of synthetically prepared minerals, calcium phosphate solids, have been obtained as standards, and these include a group of carbonate apatites with carbonate (CO_3^{2-}) contents varying from ~1.5 to ~20 wt%. These standards have all been prepared *in vitro* and characterized by powder x-ray diffraction and by wet chemical analysis.

The study of the synthetic carbonate apatites offers a means for the elucidation of the structural mechanism for the incorporation of carbonate into biological apatite.¹⁷ Infrared and Raman studies indicate that carbonate in these standards is in the type B site substitution for phosphate, rather than into the hydroxyl position, i.e., type A carbonate apatite.^{17,18}

In the micro-Raman spectra, this substitution results in the appearance of the characteristic carbonate bands of which the symmetric stretching mode (ν_1) is the most intense and found at frequency shift 1074 cm^{-1} . This band is detected from single particles (down to a few micrometers in size) at carbonate contents approaching 1 wt% in the apatite phase.

The vibrational modes of the phosphate grouping in (pure) hydroxyapatite give rise to bands with shifts 961 cm^{-1} (ν_1 symmetric stretch), 431 and 499 cm^{-1} (ν_2 modes), 581 , 590 , 610 cm^{-1} (ν_4 modes), and 1030 , 1048 , 1079 cm^{-1} (ν_3 modes).¹⁵ A logical choice for the analytical frequencies in the carbonate apatite system are the intense bands which maximize at $\sim 961\text{ cm}^{-1}$ (PO_4^{3-}) and $\sim 1074\text{ cm}^{-1}$ (CO_3^{2-}).

Microprobe measurements were performed on single particles ($5\text{--}50\text{ }\mu\text{m}$ in size) of unfractionated, mature chick bone powder known to contain 6.2 wt% CO_3^{2-} (from bulk analysis) corresponding to a carbonate content of ~4.3 wt% in the mineral phase of the bone. These results were compared with the spectra from single particles of the series of synthetic carbonate apatites. Data acquisition was made with the computerized, scanning micro-Raman spectrometer that has been described, and which allows for computer manipulation (e.g., spectral subtraction) of the digital data.^{1-4,19} Raman intensities were determined at the analytical frequencies of the peak maximum. Carbonate-to-phosphate intensity ratios were calculated from these values, with the spectral "background" taken into account at each analytical frequency. This procedure yields a calibration curve from which the composition of the solid mineral phase of the bone powder and tissue sections can be determined.

All spectra of these samples were recorded under nearly identical measurement conditions. The parameters for laser excitation and data acquisition were adjusted to yield comparable scattered intensities in the 961 cm^{-1} phosphate band in order to compensate for differences in sample scattering, sample density and particle thickness.

A result from these studies is shown in Fig. 1. Comparison of the two spectra from mature chick bone and 4.3 wt% carbonate apatite indicates that for this system the method of relative intensity measurements (in which the phosphate component may be regarded an internal standard) yields quantifiable data. The background intensities at the analytical frequencies were estimated from the intensity of the spectral background at $\sim 800\text{ cm}^{-1}$ and $\sim 1200\text{ cm}^{-1}$; in the case of the bone sample, the contributions of the organic matrix to the measured intensity were taken into account by an examination of spectra from micro-samples of (nonmineralized) collagen, the principal organic component of bone. The calculated values for the $\text{CO}_3^{2-}/\text{PO}_4^{3-}$ intensity ratio are 0.19 for both the bone sample and the carbonate apatite analog, after background corrections. The exact trend of these ratios (over the composition range of interest) with carbonate content has not been fully established, although a linear relationship with concentration is indicated. For the synthetic carbonate apatites, the increase in carbonate contents is accompanied by a decrease in the phosphate band (ν_1) intensity. Also, the Raman bands become broader with increasing carbonate content; furthermore, small shifts in the vibrational frequencies are observed.

Future Directions

Future research efforts in this field will aim at experimental verifications of the predictions made by the advancing scattering theories for small particles. This work will likely consist of a systematic investigation of several experimental/instrumental variables that have been identified as significant. Among them are the effects due to optical absorption, the contributions to the scattered intensity by "surface" and "bulk" modes of the solid phase, and the complications from optical coupling of particles to the surround-

ing medium. Scattering experiments on suspended particles (e.g., by optical/laser levitation) should prove useful in that they make possible a direct comparison with theoretical results.

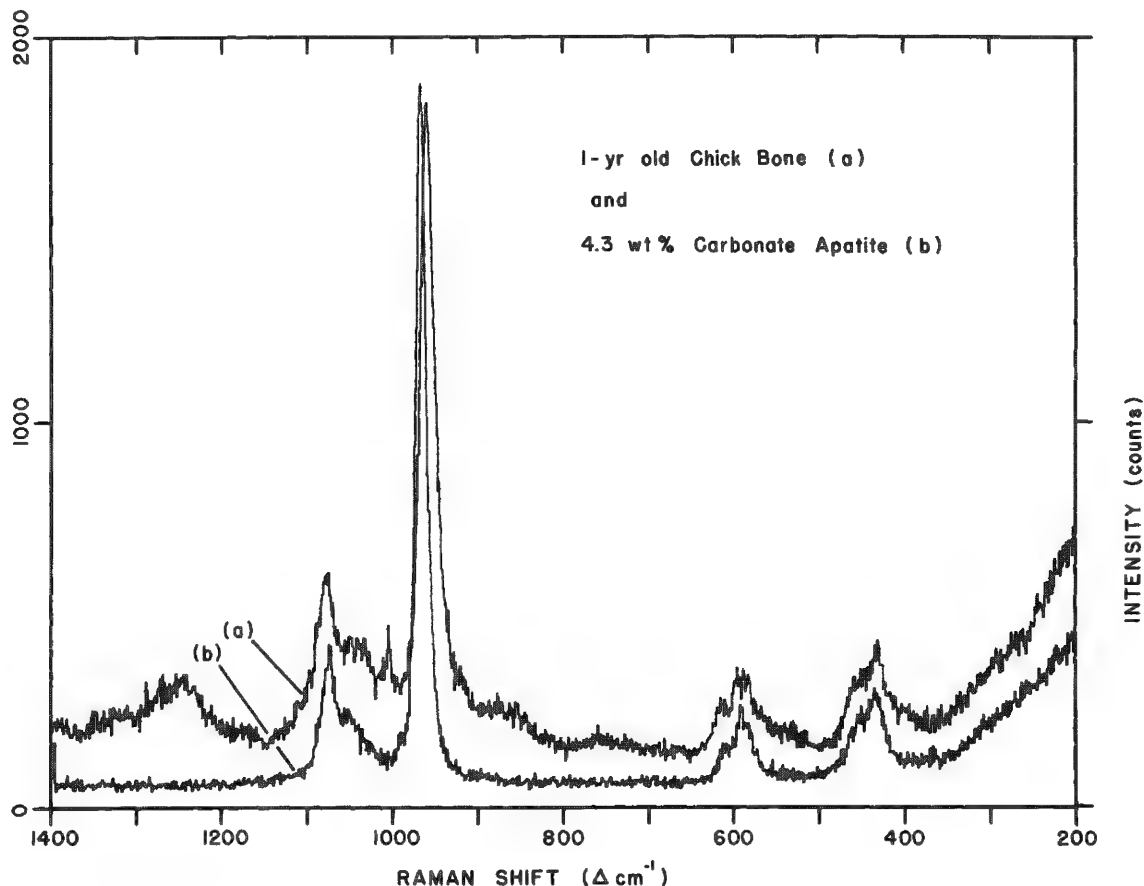


FIG. 1.--Raman microprobe spectra of single particles of (a) fully matured chick bone (powder) and (b) synthetic carbonate apatite. Spectra recorded under nearly identical conditions. Typical measurement parameters: particle size, $\sim 40\text{ }\mu\text{m}$; substrate, $\alpha\text{-Al}_2\text{O}_3$; laser excitation, 514.5 nm ; power, 50 mW (at sample); beam spot, $\sim 18\text{ }\mu\text{m}$ diameter; spectral slit width, 5 cm^{-1} ; time constant, 0.6 s ; scan rate, $28\text{ cm}^{-1}/\text{min}$. For quantitation of carbonate content in mineral phase, band intensity measurements were made at analytical frequencies $\sim 961\text{ cm}^{-1}$ (ν_1 phosphate) and $\sim 1074\text{ cm}^{-1}$ (ν_1 carbonate).

The further pursuit of empirical approaches to quantitation should in the near future provide concrete, valuable results. Measurements on particles of laboratory-generated aerosols of binary composition (e.g., the mixed sulfate/nitrate system) appear promising and have relevance to the study of "real-world" particle systems. Also of importance will be the development and characterization of micro-Raman "standards" of well-defined geometry, simple composition, homogeneous and stable under the laser beam. Forthcoming results will then encourage the development of the required empirical correction procedures.

References

1. G. J. Rosasco, "Raman microprobe spectroscopy," in R. J. H. Clark and R. E. Hester, Eds., *Advances in Infrared and Raman Spectroscopy*, London: Heyden, 1980, vol. 7 (Chap. 4), 223-282.
2. E. S. Etz and J. J. Blaha, "Scope and limitations of single particle analysis by Raman microprobe spectroscopy," in K. F. J. Heinrich, Ed., *Characterization of Particles*, NBS Special Publication 533, Washington, 1980, 153-197.

3. E. S. Etz, "Raman microprobe analysis: Principles and applications," *SEM/1979 I*, 67.
4. E. S. Etz and J. J. Blaha, Investigations into the critical measurement aspects of Raman microprobe analysis," *Microbeam Analysis--1979*, 173.
5. P. Dhamelincourt, "Developments and applications of the laser-Raman microprobe MOLE," *Microbeam Analysis--1979*, 155.
6. F. Adar, "Application of the MOLE to identification of molecular impurities and to structural characterization of microscopic samples *in situ*," *SEM/1979 I*, 83.
7. An excellent survey of the analytical versatility of the MOLE Raman microprobe/microscope can be gained from a series of research papers presented at the First International Meeting on the Applications of the MOLE, held at CNRS-Thiais (France) on December 4, 1979, and published as the proceedings in *L'Actualité Chimique*, April 1980, pp. 11-71.
8. D. E. Irish and H. Chen, "The application of Raman spectroscopy to chemical analysis," *Appl. Spectrosc.* 25: 1, 1971.
9. R. E. Hester, "Raman intensities," in Specialist Periodical Report, *Molecular Spectroscopy*, London: The Chemical Society, 1974, vol. 2, pp. 439-465.
10. M. Kerker and S. D. Druger, "Raman and fluorescent scattering by molecules embedded in spheres with radii up to several multiples of the wavelength," *Appl. Opt.* 18: 1172, 1979.
11. H. Chew, D. D. Cooke, and M. Kerker, "Raman and fluorescent scattering by molecules embedded in dielectric cylinders," *Appl. Opt.* 19: 44, 1980.
12. G. J. Rosasco and H. S. Bennett, "Internal field resonance structure: Implications for optical absorption and scattering by microscopic particles," *J. Opt. Soc. Am.* 68: 1242, 1978.
13. R. E. Benner, P. W. Barber, J. F. Owen, and R. K. Chang, "Observation of structure resonances in the fluorescence spectra from microspheres," *Phys. Rev. Lett.* 44: 475, 1980.
14. K. F. J. Heinrich, *Electron Beam X-ray Microanalysis*, New York: Van Nostrand Reinhold, 1981, chap. 12, pp. 339-413.
15. F. S. Casciani, E. S. Etz, D. E. Newbury, and S. B. Doty, "Raman microprobe studies of two mineralizing tissues: Enamel of the rat incisor and the embryonic chick tibia," *SEM/1979 II*, 383.
16. W. J. Landis, "Application of electron probe x-ray microanalysis to calcification studies of bone and cartilage," *SEM/1979 II*, 555.
17. N. S. Chickerur, M. S. Tung, and W. E. Brown, "A mechanism for incorporation of carbonate into apatite," *Calcif. Tissue Int.* 32: 55, 1980.
18. M. Nishino, S. Yamashita, T. Aoba, M. Okazaki, and Y. Moriwaki, "The laser-Raman spectroscopic studies on human enamel and precipitated carbonate-containing apatites," *J. Dent. Res.* 60: 751, 1981.
19. J. J. Blaha, R. L. Myklebust, and E. S. Etz, "Automation of the NBS laser-Raman microprobe," *Microbeam Analysis--1981*, 61.

NUCLEAR MICROPROBE ANALYSIS

B. L. Doyle, N. D. Wing, and P. S. Peercy

The use of MeV ions to probe the atomic composition in the near-surface region of materials is growing steadily. Ion-beam analysis techniques traditionally have been widely used in solid-state physics and materials science. Other scientific fields starting to use these techniques include medicine, environment, archeology, and geology. Most of the ion-beam techniques that have evolved are quantitative and many have sensitivities in the ppm range with depth resolution measured in tens or hundreds of Ångströms.

The Radiation Physics Laboratory at Sandia has a tandem Van de Graaff accelerator dedicated exclusively to solid-state physics research. The use of tandem accelerators has significant advantages over the use of the more common single-ended accelerators. The high energy (> 4 MeV) afforded by a tandem allows the use of a wide variety of nuclear reactions for analysis that cannot be achieved with accelerators of lower energy. Of particular importance is that the use of a tandem provides sufficient beam energy for depth profiling hydrogen (^1H) in solids. The behavior of hydrogen in the near surface region of solids is of metallurgical interest and is also important to semiconductor research and to controlled thermonuclear fusion materials.

The utility of these ion beam techniques has been greatly increased by the invention of lenses capable of focusing high-energy heavy-ion beams to micron dimensions. The combination of ion-beam analysis and micron-dimension ion beams yields a powerful, nondestructive new method for materials scientists which, in principle, can provide three-dimensional concentration profiles for all elements. Computer-assisted data acquisition and reduction are essential for nuclear microprobe analysis, not only to process the vast amount of information gathered, but also because of the complexity of some of the techniques.

In this paper many of the present ion beam analysis methods are reviewed and Sandia's recently constructed nuclear microprobe and its ancillary computer system are described.

Ion-beam Analysis

A wide variety of both atomic and nuclear events can occur when high-energy (MeV/amu) ions strike a target sample.¹ Atomic events include (1) the ionization of inner electron shells, which results in the generation of characteristic x rays or Auger electrons when the atom relaxes; and (2) the Coulomb-induced desorption and ionization of atoms residing on the sample surface. Some nuclear occurrences are (1) scattering of the incident particles from target atoms, (2) a target atom recoil after bombardment by an incident ion, (3) the generation of a nuclear reaction product (e.g., a γ ray) following a violent nuclear collision. All these events are useful for compositional analysis of materials with ion beams.

Atomic Signals. Particle-induced x-ray emission (PIXE)² has been proved to be a very useful composition probe of materials in which depth information is of secondary interest. In fact, PIXE is the most common analysis technique used in conjunction with a nuclear microprobe. The utility of PIXE stems from the large inner shell ionization cross sections of ion-atom collisions and the ease and efficiency with which the resultant characteristic x rays can be detected and identified with Si(Li) detectors. The cross sections for both K and L x-ray production by 3MeV protons is plotted as a function of target atomic number in Fig. 1.³ The other cross sections indicated in this figure are discussed below. The x-ray cross sections displayed in Fig. 1 reveal that the x-ray yield is quite large and therefore only a small accumulated charge (10-1000 nC) is required to obtain suitable counting statistics.

The current status of nuclear microprobes is similar to that of electron microprobes about 10-20 years ago. At present, there are only about a dozen nuclear microprobes in the world; therefore, the two fields can hardly be considered competitive. However, PIXE

The authors are at Sandia National Laboratories, Albuquerque, NM 87185, a facility of the U. S. Department of Energy; the work was done under DOE contract DE-AC-4-76-DP00789.

has a sensitivity advantage over the energy-dispersive analysis of x rays (EDAX) used with scanning electron microscopes, since there is no primary electron bremsstrahlung in a PIXE spectrum. A comparison of PIXE and EDAX is shown in Fig. 2.⁴ Sensitivities are of the order of 1 ppm for PIXE and 1000 ppm for EDAX.

Another atomic signal is the desorption or sputtering of surface atoms caused by high-energy ions.⁵ Actually it is debatable whether this event belongs under the "nuclear signal" heading because recoil collisions can produce desorption. However, since the cross section for the production of secondary ions by high-energy ion beams is of atomic dimensions, we consider this process here. Secondary-ion mass spectroscopy (SIMS) is used to obtain the mass spectrum of ions leaving the sample surface. Figure 3 shows an example of such a SIMS spectrum, taken with a slightly modified quadrupole mass spectrometer (QMS), for an Al target bombarded with a 6.4 MeV ^{19}F beam. The rich mass spectrum results from surface contamination of the Al target. It is particularly noteworthy that this technique has excellent sensitivity for hydrogen, and in fact the H^+ secondary-ion production cross section has been measured to vary from about 1 kb to 1 Mb depending on the incident projectile. This technique is too recent to have been incorporated in a nuclear microprobe. It is doubtful whether high-energy SIMS can be made as quantitative as other ion-beam analysis techniques, but it can most certainly be used to provide elemental identification for quantization by other nuclear-probe techniques. In addition, high-energy SIMS should be very useful during the focusing adjustments of nuclear microprobes because the large cross sections allow video scan rates to be used.

Nuclear Signals. Two nuclear ion-beam analysis techniques, Rutherford backscattering spectroscopy (RBS) and elastic recoil detection (ERD), are based on the simple elastic scattering that occurs during nucleon-nucleon collisions. In RBS a beam of light ions (e.g., ^1H or ^4He) strikes the sample and the energy distribution of the particles backscattered at a specific angle is measured with a Si surface-barrier detector. Consider

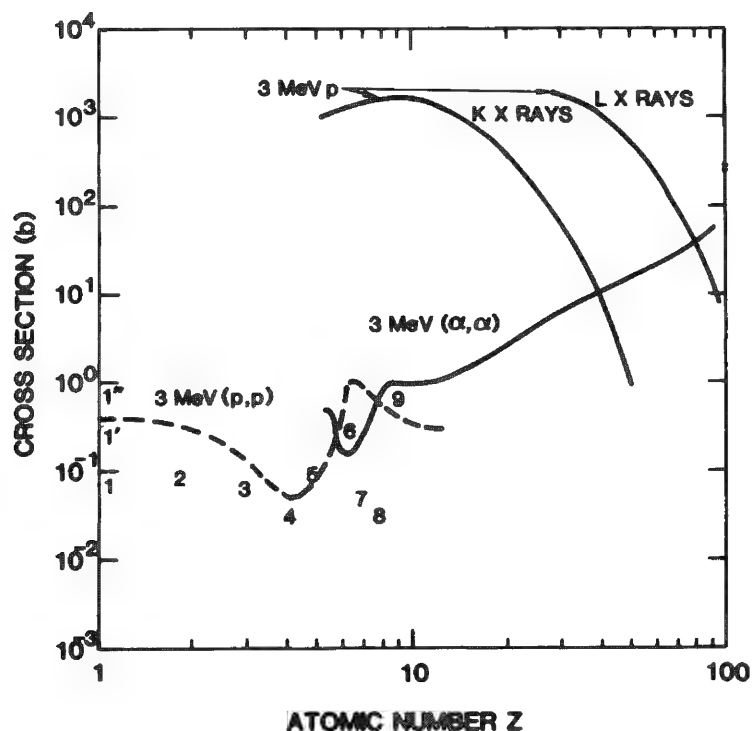


FIG. 1.--Cross sections for various ion-atom collision events as a function of target atomic number. The (α, α) and (p, p) cross sections correspond to peaks located close to 3 MeV incident energies for scattering angles of $\sim 165^\circ$. The numbered cross sections are: 1 - $^2\text{D}(^3\text{He}, p)$, 1' - $^1\text{H}(^{15}\text{N}, \alpha\gamma)$, 1'' - $^1\text{H}(^{19}\text{F}, \alpha\gamma)$, 2 - $^3\text{He}(d, p)$, 3 - $^6\text{Li}(p, \alpha)$, 4 - $^9\text{Be}(d, \alpha)$, 5 - $^{11}\text{B}(p, \alpha)$, 6 - $^{12}\text{C}(d, p)$, 7 - $^{14}\text{N}(d, \alpha_1)$, 8 - $^{16}\text{O}(d, p_1)$, 9 - $^{19}\text{F}(p, \alpha\gamma)$.

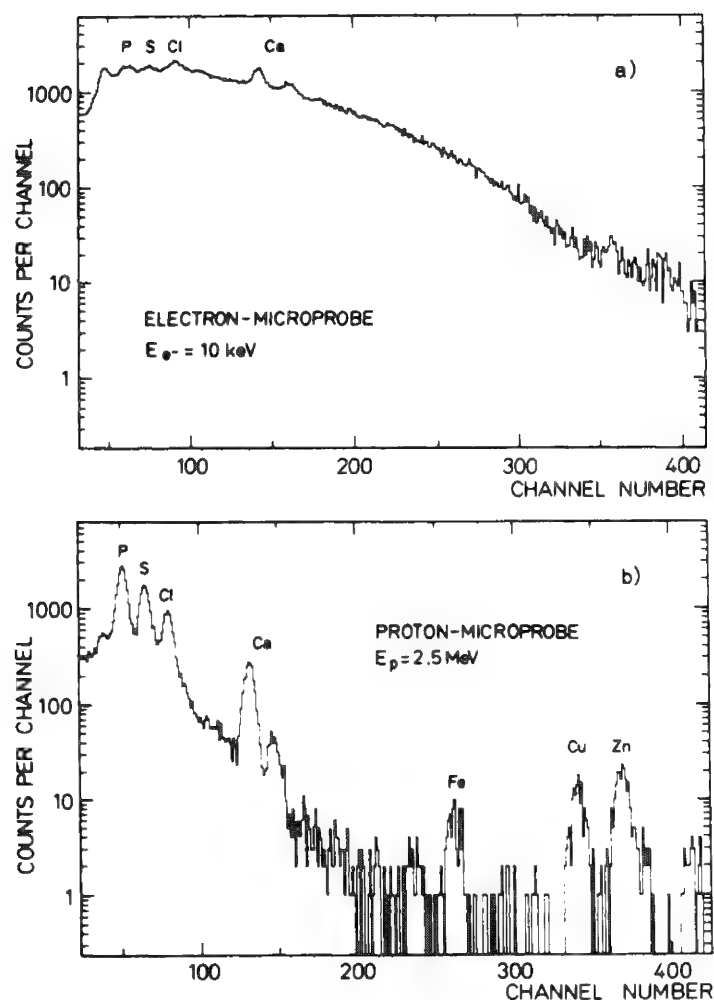


FIG. 2.--Comparison of (a) EDAX spectrum by 10keV electrons and (b) PIXE spectrum taken with 2.5MeV protons. Sample was pollen tube of a flower (after Ref. 4).

backscattering of H from Si (Fig. 4a). Hydrogen penetrates some distance into the solid, then scatters from an Si atom. Depth distribution of the Si in the solid is obtained by measurement of the energy distribution of the backscattered H and determining the rate at which H loses energy in passing through the Si. For more complicated targets, the energy spectrum of the backscattered particles is ambiguous and contains both depth and mass information; however, the interpretation of such data is seldom difficult. The RBS cross sections for 3MeV H and He are plotted vs atomic number in Fig. 1. In ERD^{7,8} the experiment is simply turned around as shown in Fig. 4b. Instead of H accelerated onto silicon, for example, silicon ions are accelerated onto a target that contains H. In this case silicon knocks the hydrogen out of the target in a forward direction. Measuring the energy distribution of the H recoiled at some well-defined angle yields the hydrogen concentration vs depth by much the same methods as RBS. In the center of mass, RBS and ERD are essentially identical experiments, and the measured spectra are similar (Fig. 4).

Two types of nuclear reactions are useful in materials studies: (1) nonresonant nuclear reaction analysis (NRA) and (2) resonant nuclear reaction analysis (RNRA).⁹ In NRA the accelerated nucleons generally have low binding energies (i.e., ²D or ³He), so that, when they collide with target nuclei, highly exothermic nuclear reactions result. The reaction products [e.g., a proton in a (d,p) reaction] therefore have high kinetic energies and are easily detected by charged particle detectors. This technique is best suited for the detection of low atomic number elements ($Z \lesssim 10$) because of low Coulomb barriers. Useful NRA reaction cross sections for $Z \lesssim 10$ are indicated in Fig. 1.

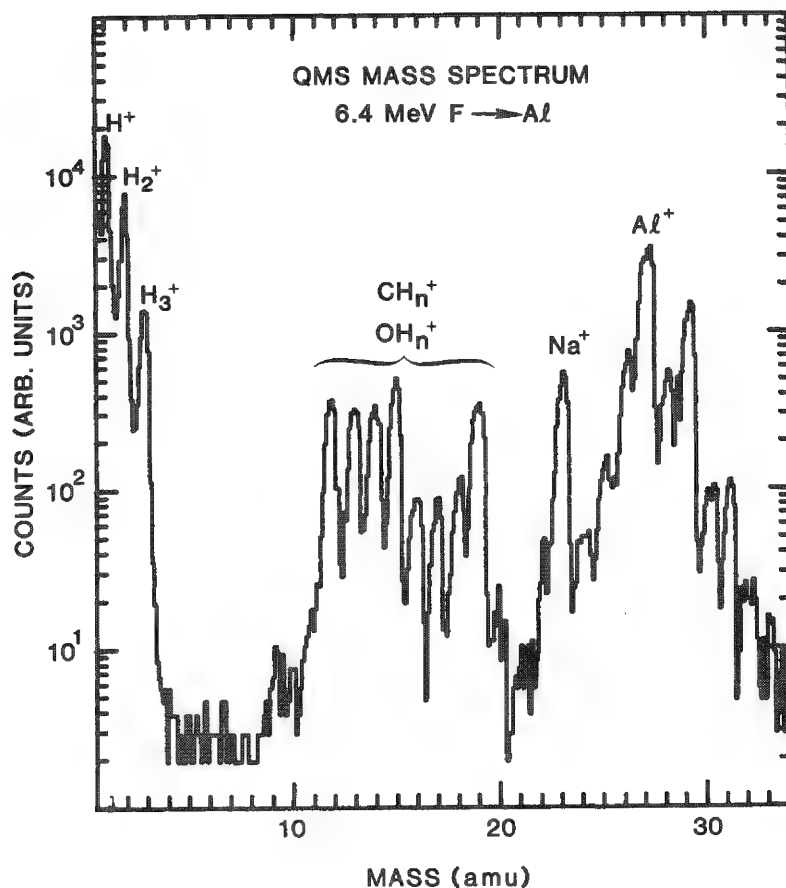


FIG. 3.--Spectrum of surface atoms desorbed by 6.4MeV ^{19}F beam.

virtually all the gamma rays are produced at the resonant energy, measurements of the γ -ray yield versus the energy of the fluorine beam directly yields the absolute hydrogen concentration vs depth in the solid from the integrated beam current, fluorine energy loss, and γ -ray production cross section.

A striking example of the combination of RBS and RNRA used to analyze silicon nitride and silicon oxynitride is shown in Fig. 6. These data were taken with 3.4MeV He backscattering and give the depth distribution of the Si, N, and O. Consider the lower trace. At the highest energies, the signal is from helium scattered from Si in SiN; at lower energy the signal from Si in the silicon substrate appears, followed by the signal from N in the SiN film. The upper spectrum shows the result of oxygen contamination. After about 2000 Å of SiN was grown, 1000 ppm of O was introduced into the carrier gas while the next 1500 Å of the film was grown. The O contamination was then removed and SiN was grown on top. The oxygen from the carrier gas replaced the nitrogen in the center region of the film, which resulted in a corresponding decrease in the silicon concentration. The high energy of the incident particles provided by a tandem accelerator is necessary for these measurements because it allows the complete separation of the oxygen signal from the region of nitrogen depletion. In addition, both the nitrogen and oxygen scattering cross sections are enhanced at the > 3 MeV energy to significantly increase the sensitivity. The inset shows an H profile of the silicon oxynitride film taken with the $^{19}\text{F}(^1\text{H}, \alpha\gamma)^{16}\text{O}$ RNRA technique. The ^1H content drops significantly in the oxide region.

Nuclear Microprobes

In the previous section, the basic principles of ion-beam analysis techniques were explained. For most of these types of experiments, the beam spot is of the order of 1 mm^2

Resonant nuclear reaction analysis (RNRA) relies on the fact that at sufficiently high energies a variety of nuclei undergo a resonant reaction with other nuclei to produce a gamma ray.¹⁰ For illustrative purposes, consider the fluorine-proton reaction (Fig. 5). There are several resonances in the cross section for the reaction between fluorine and protons to produce α particles, γ rays, and oxygen, but the one near a fluorine energy of 6.4 MeV is particularly useful. This resonance has a full width of 50 keV, and yields a depth resolution in the solid of about 140 Å without deconvolution. The concentration-vs-depth information arises because the reaction is sharply resonant. To obtain a hydrogen profile, a beam of fluorine with energy greater than 6.4 MeV is incident on the sample (Fig. 5a). As the beam penetrates the solid it slows down, and at some depth in the solid the energy of the beam is equal to the resonant energy of 6.4 MeV. At that point, there is a large cross section for γ -ray production from the fluorine-proton reaction. Since

or larger. Since the development of strong-focusing lenses for high-energy ion beams, beam-spot sizes of the order of $1 \mu\text{m}^2$ have been obtained.^{4,11-15} Small beam diameters are particularly important in experiments in which the sample is very small, as is the case for some biological studies, for studies of microelectronic circuits, or in metallurgy when individual grains are to be examined. Other areas in which one could envision the need for small analysis beams are those for which sample sizes or uniformity are limited, such as in the analysis of lunar rocks. Beam-scanning capabilities have been incorporated in many nuclear microprobes¹⁶ and have resulted in two-dimensional elemental imaging similar to that obtained on an EDAX-equipped electron microprobe, except for the improved sensitivity noted above. Beam resolution is not seriously affected by scanning. Three-dimensional profiling is in principle possible by lateral profiling while one of the depth-sensitive nuclear signals is being detected.

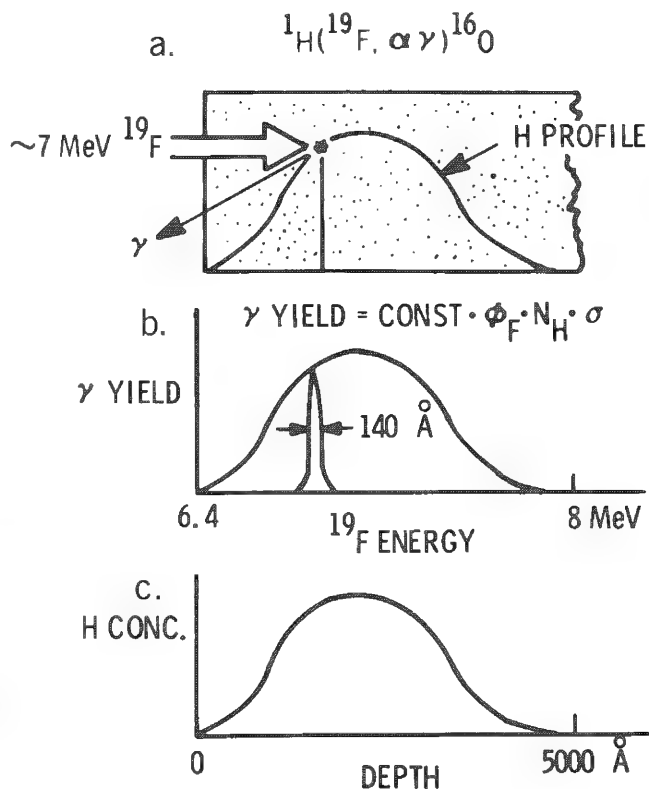


FIG. 5.--Schematic illustration of RNRA of H with ^{19}F : (a) target geometry with detection of γ rays, (b) γ ray yield measured as function of ^{19}F energy, (c) measured profile obtained from plot of γ rays vs ^{19}F energy.

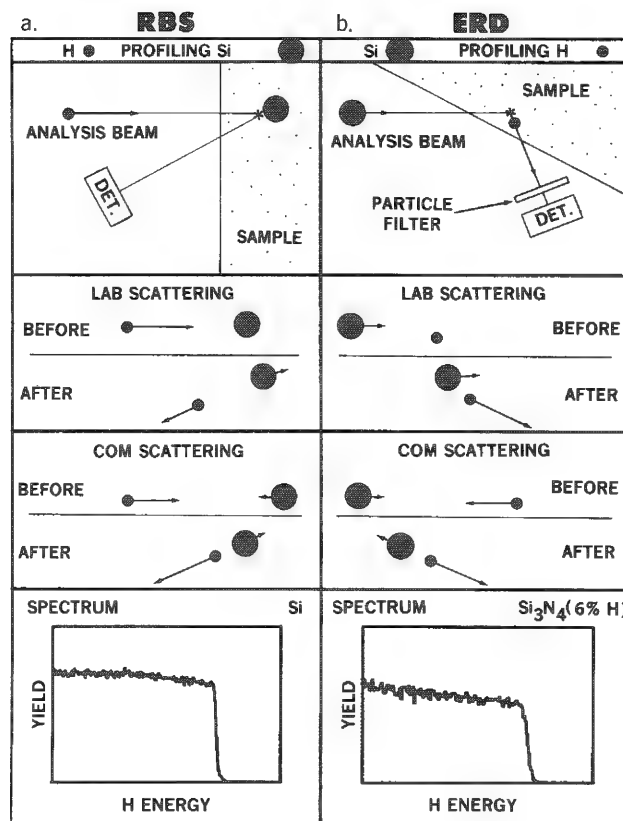


FIG. 4.--Comparison of (a) RBS and (b) ERD. Spectra in lowest panels show, respectively, Si profile taken by H RBS and H profile taken by Si ERD.

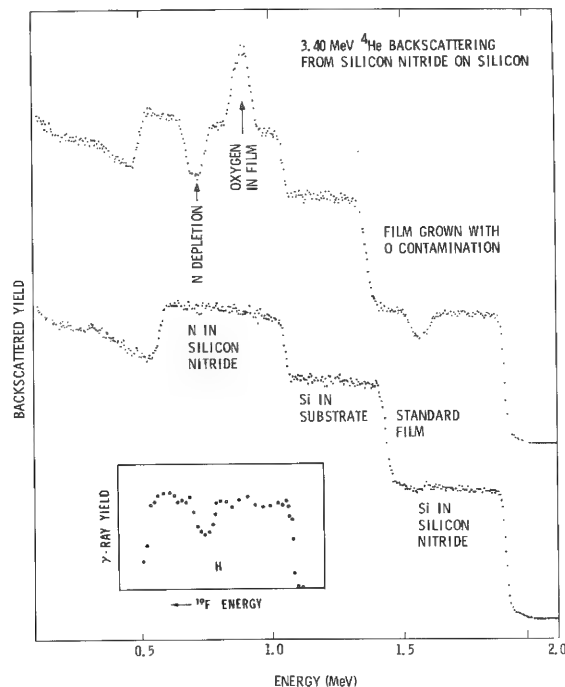


FIG. 6.--RBS and RNRA of Si_3N_4 layer (lower) and a $\text{Si}_3\text{N}_4\text{-Si}_x\text{O}_y\text{N}_z\text{-Si}_3\text{N}_4$ structure. RBS spectrum shows N, O and Si depth profile; ^{19}F RNRA provides H profile shown in inset.

Development of a nuclear microprobe is also of considerable interest because of the potential for focusing the ion beam to diameters much smaller than that of many atoms. Martin¹¹ has pointed out that because of the small De Broglie wavelength of high-energy heavy ions the diffraction limit on the resolution, of (for example) a 14 MeV ^{14}N beam, is only about 0.2 Å. The resolution record is at present held by the Heidelberg proton microprobe⁴ with a FWHM of 1.2 μm , so that the nuclear microprobe is far from its theoretical limit.

Lens types used to date include electrostatic quadrupole triplets,¹² superconducting solenoids,¹³ and magnetic quadrupole doublets,^{4,14} triplets, and quadruplets.¹⁵ A quadrupole doublet lens is used on Sandia's nuclear microprobe (Fig. 7). For scale, the track is about 3 m long. The various components of the probe are indicated in the figure; however, none of the detectors were installed at the time this photo was taken.

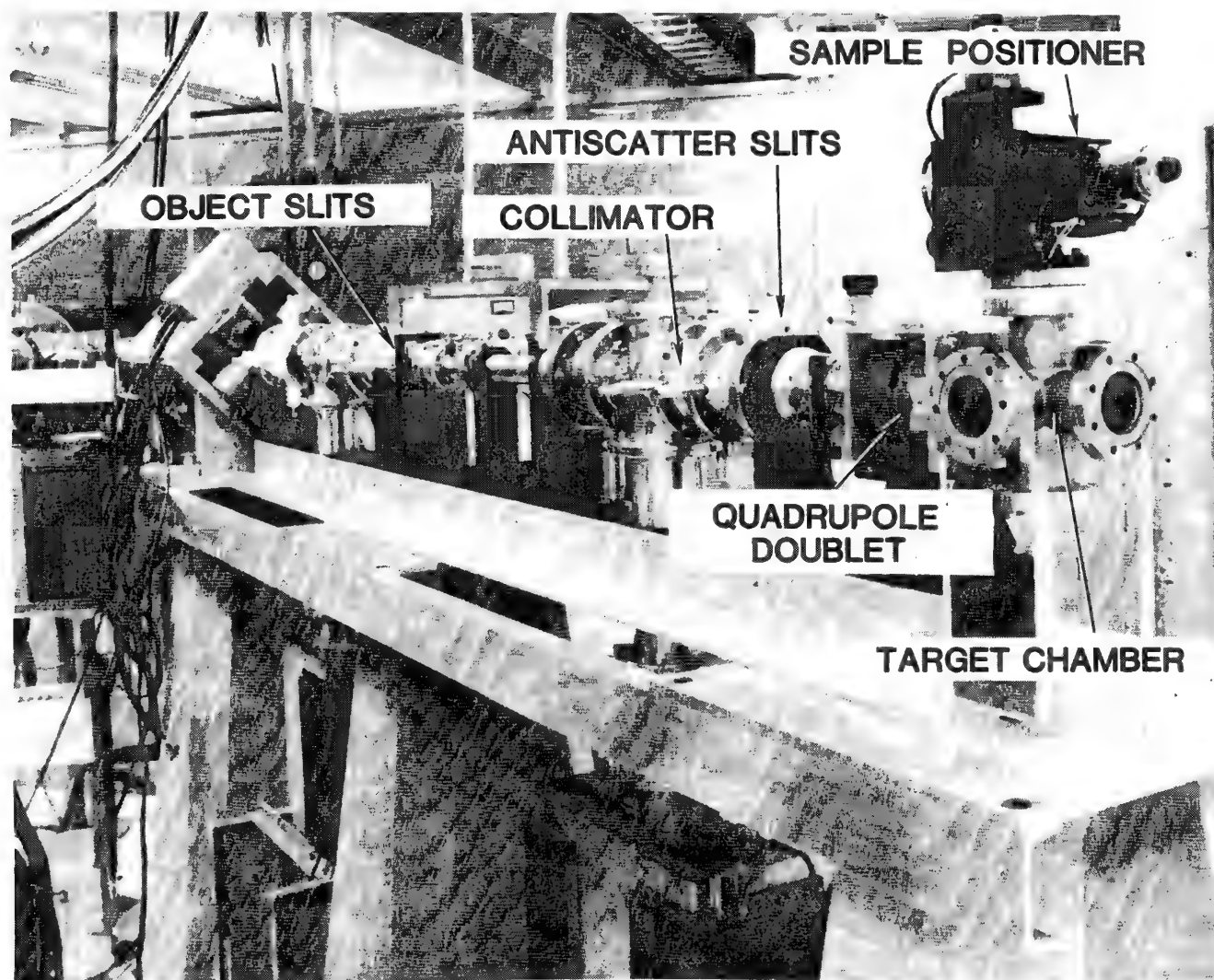


FIG. 7.--Sandia Nuclear Microprobe.

Sandia Nuclear Microprobe. The magnetic quadrupole doublet lens used in the Sandia microprobe has a small bore (3.38 mm) and each polepiece is only 6 cm long. Despite its size, this lens is capable of focusing ions with a ME/q^2 product of about 50 MeV in a distance of only 6 cm past the lens.

A unique feature of this lens is that the iron polepieces are electrically isolated and that the interior of the lens is vacuum tight. This design allows the application of voltages to each of the eight poles so as to cancel, to first order, any rotational

misalignments of the two quadrupoles elements¹⁷ and to scan the beam laterally over the target.

The principle behind our probe, and indeed most other nuclear probes, is quite simple. The beam is first spatially defined with a set of adjustable apertures (object slits) to $10\mu\text{m}$ dimensions. The beam is then allowed to drift for a length (object distance) of one or more meters before being focused onto the target (image) in a length (image distance) of about 10 cm. To first order, the demagnification is equal to the image distance divided by the object distance, which is about 0.1, so that a beam of about $1\mu\text{m}$ dimensions is provided at the target position. In practice, these simple arguments are not suitable for determining the beam-spot diameters accurately, and second-order chromatic and third-order spherical aberrations must be calculated. The trajectories resulting from such calculations for our system using the ION-BEAM program of Heck¹⁸ are shown in Fig. 8. The relevant dimensions and positions of various components are also indicated. The aberration calculations indicate that the resolution limit of our system is about $1\mu\text{m}^2$. Indeed, these calculations show that our microprobe is virtually identical, from a focusing standpoint, to the Heidelberg proton microprobe, so that similar operating characteristics are anticipated.

A wide variety of ion-induced signals can be detected in the target chamber. X rays are analyzed with a windowless Si(Li) detector with a 0.1sr solid angle. Back-scattered (or forward-recoiled) ions are detected and energy-analyzed by an annular surface barrier detector with an adjustable solid angle of up to 1 sr. Secondary electrons and ions are detected with a channeltron and QMS, respectively. A 100 \times stereo microscope is also included so that we can obtain the coarse focus by viewing the ion-induced fluorescence on quartz targets through a window in the back of the chamber.

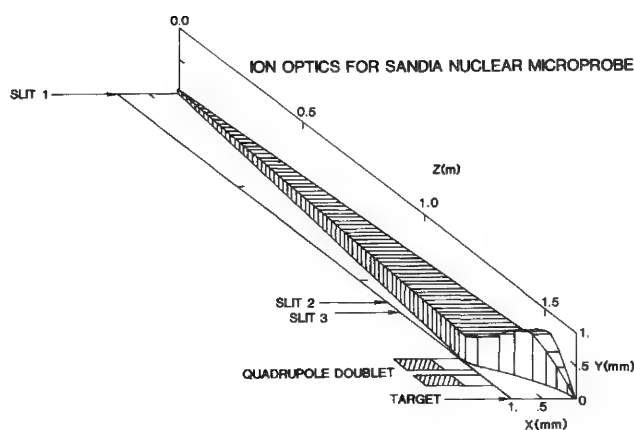


FIG. 8.--ION-BEAM calculations of particle trajectories for Sandia nuclear microprobe.

Microprobe Computer System. The data-acquisition system on the Sandia microbeam (Fig. 9) is very versatile and relies on CAMAC interfacing. The target can be scanned mechanically with computer-controlled stepping motors coupled to a three-axis manipulator geared at $2\mu\text{m}/\text{step}$, or electrically by deflection of the beam at the polepieces of the doublet. To ease focusing operations the computer control can be disconnected and the beam scanned by standard TV rastering techniques; however, the only signals bright enough for live-time video display are the secondary electrons or ions. Under computer control the x-y position of the beam is determined by either an output register or by a

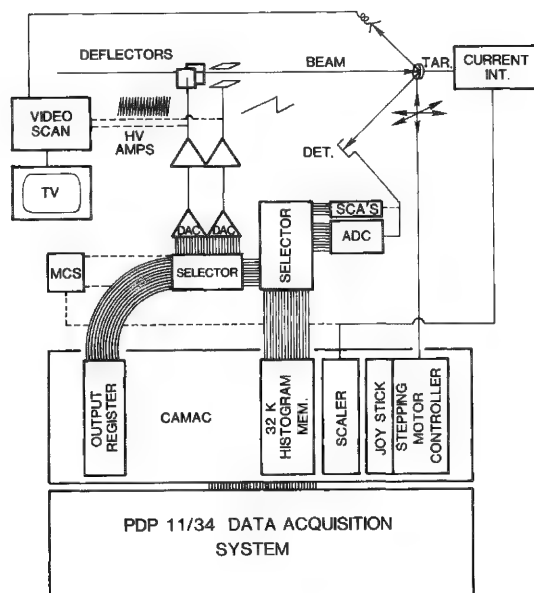


FIG. 9.--Block diagram of Sandia data-acquisition system with and without computer-controlled scanning.

multichannel scaler capable of 10 μ s timing. Detected signals can be processed by either an ADC or a series of SCAs. The address which is incremented in the 32K histogramming memory (15 bits) has its least significant bits determined by the beam position and the most significant bits determined by the signal. For example, if a 64 \times 64 xy grid is desired, the bits 1 through 12 determine the beam position and bits 13 through 15 can be used for up to eight SCA signals from x-ray or particle detectors to obtain a lateral elemental "picture" of eight different elements simultaneously. Another way the system can be used is to define a 32 \times 32 xy grid with the lowest 10 bits and define the upper 5 bits from an ADC. For charged particle analysis this results in a 32 \times 32 \times 32 three-dimensional (xyz) profile. The system is easily changed with the matrix selector boards used to route the various signals.

Display of the data is accomplished through a PDP-11/34 data-acquisition system by intensity modulation of a 64 \times 64 dot pattern or isometric display on a CRT. The data can also be transferred through a modem to Sandia's CDC-6600 computer for more sophisticated display, such as color contours.

Conclusion

Nuclear microprobe analysis is an expanding field. Although it is doubtful that this probe will become as ubiquitous as scanning electron microscopy, it is clear that many applications in materials analysis exist where ion-beam analysis is necessary. If lateral resolution is required, the nuclear microprobe can provide the required data. The applications for which nuclear microscopy is most appealing are in trace-elements analysis and the detection of elements of low atomic number such as hydrogen. The use of nuclear microprobes in microelectronics appears to be especially attractive.

References

1. J. W. Mayer and E. Rimini, Eds., *Ion Beam Handbook for Materials Analysis*, New York: Academic Press, 1977.
2. T. V. Mitchell and J. F. Ziegler, "Ion induced x rays," pp. 311-484 in Ref. 1.
3. J. A. Cookson, J. W. McMillan, and T. B. Pierce, *J. Rad. Chem.* 48: 337, 1979.
4. F. Bosch, A. El Goresy, W. Herth, B. Martin, R. Nobiling, B. Povh, H. D. Reiss, and K. Traxel, *Nuclear Science App.* 1: 1, 1980.
5. T. J. Gray, C. L. Cocke, E. Justiniano, B. L. Doyle, and P. S. Peercy, to be published.
6. G. Foti, J. W. Mayer, and E. Rimini, "Backscattering spectrometry," pp. 21-65 in Ref. 1.
7. B. Terreault, J. G. Martel, R. G. St. Jacques, and J. L'Ecuyer, *J. Vac. Sci. Technol.* 14: 492, 1977.
8. B. L. Doyle and P. S. Peercy, *Appl. Phys. Lett.* 34: 881, 1979.
9. L. C. Feldman and S. T. Picraux, "Selected low energy nuclear reaction data," pp. 109-309, in Ref. 1.
10. G. T. Clark, C. W. White, D. D. Allred, B. R. Appleton, F. B. Koch, and C. W. Magee, *Nuclear Instrum. Meth.* 149: 9, 1978.
11. F. W. Martin, *Science* 12: 173, 1973.
12. W. M. Angustyniak, D. Betteridge, and W. L. Brown, *Nuclear Instrum. Meth.* 149: 669, 1978.
13. C. J. Maggiore, "Materials analysis with a nuclear microprobe," *SEM/1980*.
14. D. Heck, Kernforschungszentrum Karlsruhe, KfK Report 2504, 1977, 109.
15. J. A. Cookson, *Nucl. Instrum. Meth.* 165 (1979) 477.
16. D. Heck, Kernforschungszentrum Karlsruhe, KfK Report 2734, 1978, 1.
17. F. W. Martin, "Electric rotation in quadrupole lens doublets," *3rd Intern. Conf. Ion Implantation Equipment and Techniques*, 1980.
18. D. Heck and E. Kasseckert, Kernforschungszentrum Karlsruhe, KfK Report 2379, 1976, 130.

SECONDARY-ION SPECTRA OF RARE EARTHS

S. J. B. Reed

The rare earth elements (REE) have atomic numbers from 57 (La) to 71 (Lu) and isotopic masses from 136 to 176. They are of interest in geology, where they occur mainly in trace concentrations, and in certain materials of technological interest. Ion-probe analysis offers the prospect of selected-area analysis for REEs with much better sensitivity than is possible with the electron probe (detection limit about 500 ppm), owing to the absence of background in the secondary ion mass spectrum. A further reason for studying the secondary-ion (SI) spectra of REEs is that these elements form a coherent group with similar, though not identical, properties and can provide valuable insights into the factors governing SI yields etc.

Interferences

Although there is no continuous background in the SI mass spectrum, the presence of interfering peaks at the masses of the isotopes of elements of interest is often a significant limitation, especially at low concentration levels. The REEs have from one to seven stable isotopes each and there is a significant probability of interference between them. However, for any REE there is at least one isotope which does not suffer such interference (Fig. 1); hence, with suitable choice of isotope, interelemental interferences do not present serious difficulties.

A feature of the SI spectra of REEs is the presence of intense monoxide peaks occurring 16 mass units above the atomic peaks (since ^{16}O is the only significant isotope of oxygen). Hence, for example, the isotopes of Gd which lie between masses 154 and 160 are subject to interference from the monoxides of the light REEs La, Ce, etc. (Fig. 1). However, the six lightest REEs (La, Ce, Pr, Nd, Sm, Eu) are free of such effects, whereas the remainder suffer interference from the oxides of lighter REEs, which cannot be avoided merely by choice of isotope. In some cases (e.g., ^{163}Dy , ^{165}Ho , ^{167}Er , ^{169}Tm) the oxide interference may be small enough for a correction to be feasible, but other elements (Gd, Tb, Yb, Lu) are not amenable to this approach.

In principle, oxide interferences could be eliminated by the use of high mass resolution: thus ^{169}Tm and $^{153}\text{Eu}^{16}\text{O}$ differ in mass by 0.0185 mass units and can be separated with a mass resolution (defined as mass divided by peak width in mass units) of > 8000 (Fig. 2). Unfortunately, the loss of intensity involved is such that this technique is of very limited use for trace REE analysis.

An alternative approach is to exploit the difference in the energy distributions of atomic and molecular SIs. In general, discrimination in favor of atomic ions can be achieved by selection of the high-energy component of the SI spectrum. However, the difference in the energy distributions of REEs and their oxides is less marked than in many cases (Fig. 3). Hence, a severe loss of intensity would occur in the process of obtaining a useful reduction in oxide/element ratio.

A possible strategy for overcoming the oxide interference problem for heavy REEs is to use their oxide peaks for analysis, so that one escapes interference from light REE monoxides. (Fortunately REE dioxide peaks are found to be of very low intensity.) The monoxide peaks of the heavy REEs Dy, Ho, Er, Tm, Yb, and Lu can be used in this way. Between this group and the six light REEs not affected by oxide interferences lie Gd and Tb, the monoxides of which coincide with Yb and Lu, and which are therefore difficult subjects for ion probe analysis.

The author is with the Department of Earth Sciences, University of Cambridge, England. He wishes to acknowledge aid of his colleagues in the ion probe unit, J. V. P. Long, M. C. Enright, R. W. Hinton, and G. C. Wilson, and of D. G. W. Smith (University of Alberta), in providing samples and stimulating discussions; and of the Natural Environment Research Council for financial support. The energy distributions in Fig. 3 were obtained with a Cameca IMS-3f instrument, thanks to the generous co-operation of H. N. Migeon and C. M. Helliwell of Cameca.

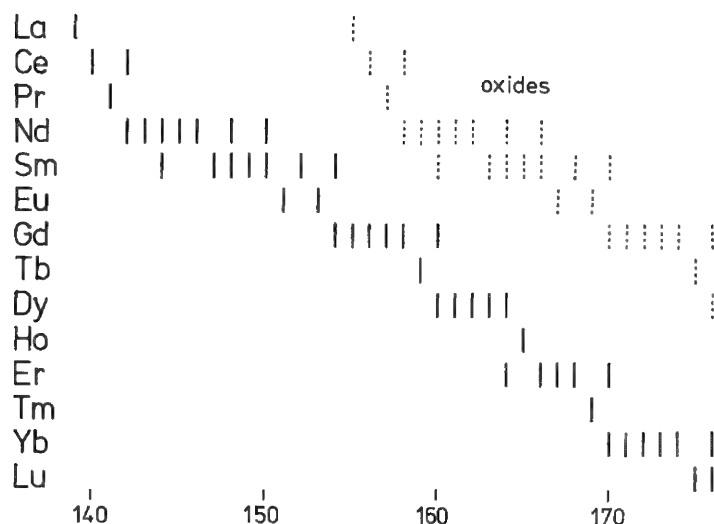


FIG. 1.--Isotopes (> 1% abundance) of REEs and their oxides, showing interelement and oxide-element interferences.

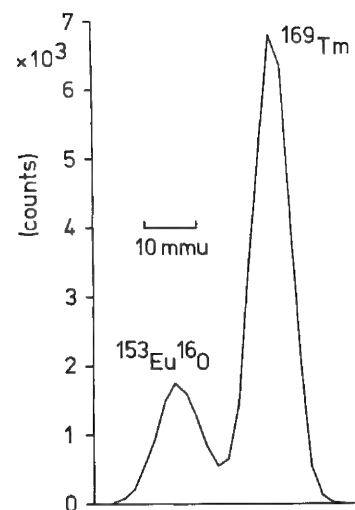


FIG. 2.--Mass 169 doublet in SI spectrum from silicate glass containing Eu and Tm, obtained with AEI IM-20 instrument (mass resolution about 12 000).

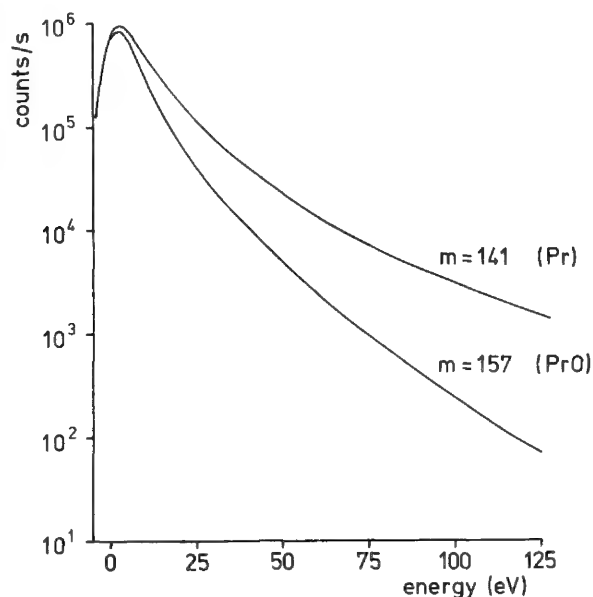


FIG. 3.--SI energy distribution of ^{141}Pr and $^{141}\text{Pr}^{16}\text{O}$ (silicate glass specimen), obtained with Cameca IMS-3f instrument.

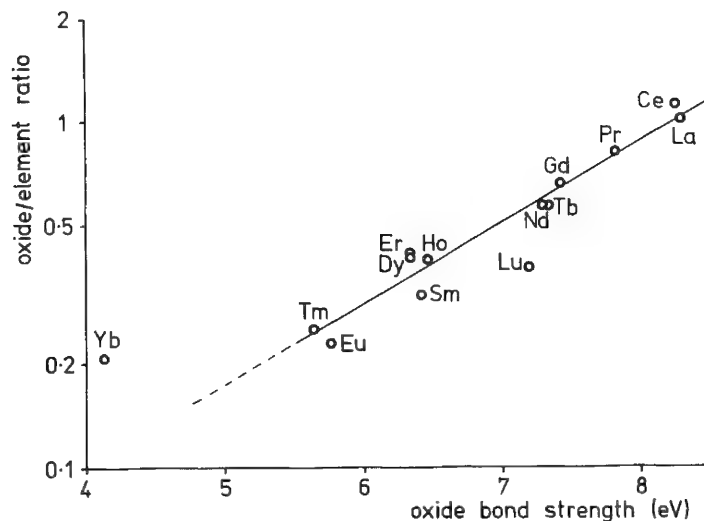


FIG. 4.--Oxide/element ratio measured with AEI IM-20 instrument on silicate glasses, showing correlation with oxide bond strength.⁷

REE Oxide Intensities

The relative intensities of oxide peaks of REEs are of interest in connection with interferences and the possible use of oxide peaks for analysis. Especially useful objects for study are the Ca-Al-silicate glasses prepared by Drake and Weill,¹ each of which contains 3 or 4 REEs with concentrations of about 4 wt.%. Thus all the REEs are available in a matrix which can be regarded as constant. (Differences in REEs are presumed to have

a negligible effect.) Measurements of REE oxide and element intensities were carried out on these samples and on certain others containing a more limited range of REEs.

The instrument used was a modified version of the AEI IM-20.² The SI extraction system, which can influence relative SI intensities, consisted of the original extraction electrode with its associated "tube einzel" lens,³ followed by a quadrupole lens designed to produce a line focus on the mass spectrometer entrance slit.⁴ The SI energy-selection properties of this system are not readily definable. However, REE oxide/element ratios are probably not seriously affected by instrumental discrimination effects, in view of the fairly flat SI energy distributions (Fig. 3). The primary beam consisted of $^{16}\text{O}^-$ ions at 30 keV, focused into a spot of about 15 μm diameter, with a current of about 15 nA. Mass spectra were recorded as follows: the field was swept through the region of interest and the output of the SI counting system was recorded via a ratemeter and chart recorder. Tests on known isotope ratios indicated reproducibility and accuracy in the region of $\pm 2\%$ by this procedure.

The oxide/element ratios in the REE glasses vary from 0.21 to 1.12 and are correlated with REE-O bond strength (Fig. 4). The dissociation constant for the reaction $\text{MO} = \text{M} + \text{O}$ can be derived from an expression closely related to the Saha-Eggert equation used in the LTE (plasma) model for predicting relative SI intensities,⁵ which leads to the following simplified expression for the oxide/element ratio:

$$\frac{\text{MO}}{\text{M}} = \text{const.} e^{E/kT}$$

where E is the oxide bond strength and T is the plasma temperature. This relationship can be applied to the SI spectrum if it is assumed that the probability of ionization of element and oxide are the same. The straight line in Fig. 4 corresponds to $T = 21\,400^\circ\text{K}$, which is somewhat higher than the values typically used in the LTE model and compares with $16\,000^\circ\text{K}$ derived from the measurements of Ishizuka⁶ on REE oxide samples by argon bombardment. The significance of these temperatures is not clear at present, since the physical basis of the LTE model is not fully understood. Factors other than oxide bond strength may be significant: thus, the oxide/element ratio for Ce is consistently higher than for La in all samples so far examined, although the reported oxide bond strength is the same for these two elements.

Argon bombardment of REE oxide samples, as carried out by Ishizuka,⁶ gives oxide/element ratios 3-10 times lower than those obtained by oxygen bombardment of silicate glasses, presumably owing to the absence of implanted oxygen from the primary beam. Measurements on pure metallic Gd, Dy, Ho, Er, and Tm by oxygen bombardment reveal oxide/metal ratios about twice those for the glasses, which is surprising in view of their zero initial oxygen content. Higher oxide intensities were also observed for light REEs in allanite (Ca-Fe-Al-silicate), monazite (REE-phosphate), and apatite (Ca-phosphate). Also exceedingly high oxide/element ratios (> 50) have been observed in the spectra of REE-containing uraninite (U-oxide). At present the factors governing REE oxide intensities are not fully understood.

Elemental SI Yields

Quantitative analysis requires the conversion of SI peak intensities into concentrations. In the absence of a universally valid theoretical model, it is necessary to resort to empirical procedures. The Ca-Al-silicate glasses were used for the investigation of the variation in the SI yields of different REEs in the same matrix. After correcting for isotopic abundance, the measured elemental REE peak intensities were divided by the ^{27}Al intensity and multiplied by the ratio of the concentrations of Al and REE to give a normalized SI yield, as plotted in Fig. 5. Usually the main factor governing SI yields is assumed to be the ionization potential, but the first six REEs (La-Eu) show a large variation in yield, though their ionization potentials are similar. As shown in Fig. 5, this variation is mirrored by an opposite trend in the oxide/element ratio, so that the total element + oxide intensity is approximately constant. The sharp drop in elemental yield from Eu to Gd is only partially explicable in terms of increased oxide intensity, but here the ionization potential jumps significantly, which probably contributes to the observed effect. The decreasing trend in the elemental yields of Dy, Ho, and Er, with a

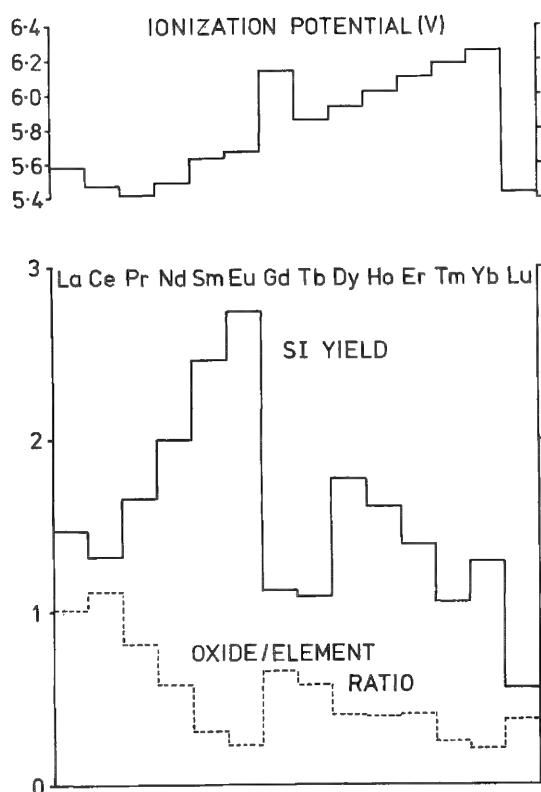


FIG. 5.--Elemental SI yields (relative to Al) and oxide/element ratios measured on silicate glasses; ionization potentials from Ref. 7.

nearly constant oxide/element ratio, can be correlated with increasing ionization potential. The remaining three REEs are somewhat anomalous: Tm fails to show an increase in elemental yield corresponding to its low oxide/element ratio; Yb has a high elemental yield along with a high ionization potential; and Lu has an unexpectedly low elemental yield in view of its low ionization potential.

Evidently the SI yields of REEs vary considerably; the assumption sometimes made that they are the same is invalid. Results for light REEs in other matrices suggest that the pattern of relative yields is fairly constant. With suitable standards quantitative REE analysis seems to be feasible. In typical silicates detection limits of a few ppm should be obtainable, depending on matrix molecule interferences.

References

1. M. J. Drake and D. F. Weill, "New rare earth element standards for electron microprobe analysis," *Chem. Geol.* 10: 179, 1972.
2. A. E. Banner and B. P. Stimpson, "A combined ion probe/spark source analysis system," *Vacuum* 24: 511, 1974.
3. I. M. Steele, I. D. Hutcheon, T. N. Solberg, J. V. Smith and R. N. Clayton, "Effect of energy selection on quantitative analysis in secondary ion microanalysis," *Int. J. Mass Spectr. Ion Phys.* 23: 293, 1977.
4. C. F. Giese, "Strong-focusing ion source for mass spectrometers," *Rev. Sci. Instr.* 30: 260, 1959.
5. C. A. Andersen and J. R. Hinthorne, "Thermodynamic approach to the quantitative interpretation of sputtered ion mass spectra," *Anal. Chem.* 45: 1421, 1973.
6. T. Ishizuka, "Secondary ion mass spectrometry of rare earth elements," *Anal. Chem.* 46: 1487, 1974.
7. *Handbook of Chemistry and Physics*, Cleveland: CRC Press, 1980, 60th ed.

APPLICATIONS OF SMALL-AREA INFRARED ANALYSIS TO SEMICONDUCTOR PROCESSING PROBLEMS

J. N. Ramsey and H. H. Hausdorff

The semiconductor industry has especially extreme requirements for cleanliness in its processing facilities. Contaminations must be analyzed, often in very small areas and on finished devices. The usual repertoire of small-area analytical techniques--electron beam (microprobe, SEM, Auger, electron diffraction in TEM, usually by extraction replication), x-ray diffraction, ion beam (SIMS)--and large-area techniques such as mass spectroscopy, plasma chromatography/mass spectroscopy, and ESCA, have been used for several years and have solved many critical problems. However, small organic particles or thin films were generally difficult or impossible to analyze. The advent of small-area Raman equipment allowed the solution of many organic and amorphous inorganic problems.¹⁻⁴ However, as there is no universal technique, some classes of materials still were difficult or impossible to analyze--those that are weakly Raman active, highly fluorescent, volatile under the laser beam, or too thin. We have applied a new complementary technique, small-area infrared, to several difficult analysis problems.

Instrumental

The infrared spectra for this study were obtained with a computerized infrared microspectrophotometer NanoSpecTM/20 IR manufactured by Nanometrics., Inc.

The outstanding feature of this system is that the specially designed microscope, with an all-reflecting optical system, is also a self-contained infrared spectrophotometer, complete with source, monochromator, and detector. This design approach provides the advantage that samples can be placed directly into the sampling area by means of a rotatable X-Y stage for direct viewing at 150× magnification and selection of small areas for transmission spectroscopic analysis. Areas as small as 20 μm^2 can be examined, which is impossible by conventional or FTIR spectrophotometers with microsampling attachments.

The optical diagram is shown in Fig. 1. Light from a bright Nernst Glower infrared source is focused with a reflecting lens onto a circular variable filter. Wavelength or frequency scanning is accomplished by its rotation through a computer-controlled, digitally stepped drive system. The beam is chopped for digital detection at 600 Hz to eliminate background radiation effects. Since chopping is done before the sampling area, hot- or cold-stage operation is possible. Underneath the microscope stage is the adjustable condenser lens. The detector is a special high-sensitivity liquid nitrogen cooled mercury cadmium telluride photodetector. A tilted variable aperture, consisting of two pairs of polished coplanar mirrors, is used to delineate the sample area of interest by means of a 10× monocular viewing system. By widening or narrowing these two reflecting slits, square or rectangular sample areas can be selected with variable area dimensions. A graduated reticule in the eyepiece permits measurements of horizontal and vertical dimensions of the target area. The smallest area which can be analyzed is determined by the wavelength range of the infrared spectrophotometer, which is from 4000 to 690 cm^{-1} (2.5-14.5 μm). Since the sample must be larger than the wavelength of radiation used, 20 μm is a natural limit of this system. Standard liquid cells can be inserted by means of a cell slide in an upright position between the source lens and the mirror which tilts the beam upwards. Standard or microgas cells for gas chromatography interfacing can be inserted vertically above the variable-filter position.

Data from the microspectrophotometer are gathered by a powerful microprocessor computer with CRT display of a large variety of operating modes and instructions. Spectra are recorded from the computer on an X-Y recorder, linear in wavelength or wavenumber, in transmittance or absorbance, as chosen by the keyboard operator. Up to eight complete

Author Ramsey is with IBM Corp.'s General Technology Division at Hopewell Junction, NY 12533; author Hausdorff, formerly with Nanometrics, Inc., at Sunnyvale, Calif., is at present with Nanometrics at Wilton, Conn. The authors acknowledge the aid of Ron Anderson and Nancy O'Neil with extraction replication and electron diffraction; of Anne Gridly Scheuer with the SEM; and of Dan Kirby, Bob Scott, and Mel Turetzky with infrared interpretation. Principal developer was Vincent J. Coates, president of Nanometrics.

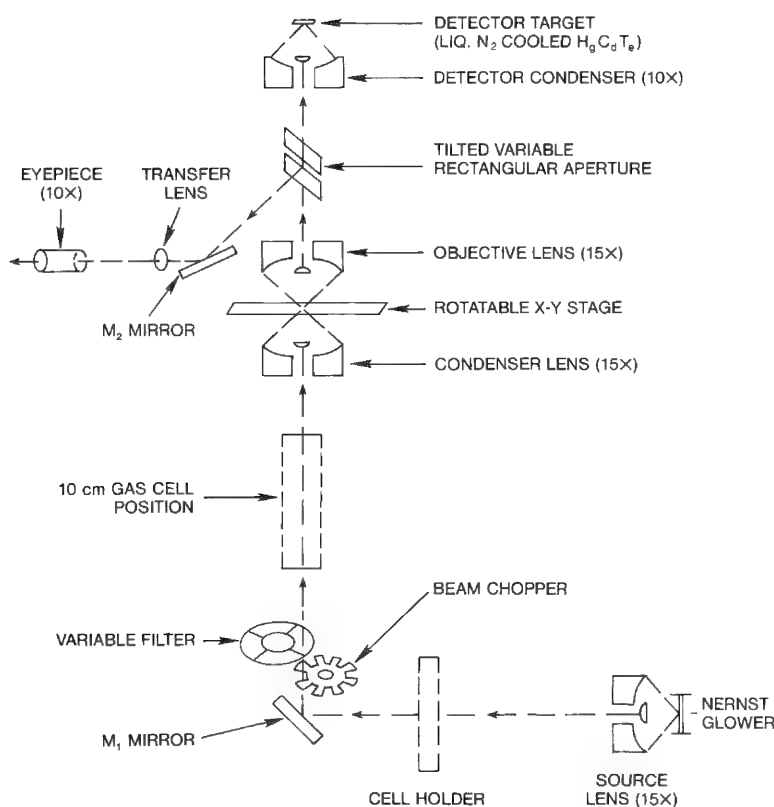


FIG. 1.--Optical diagram.

this interpretation was later confirmed by electron diffraction). As discussed earlier, the Nanospec 20 IRTM is a single-beam instrument and the specimen spectrum is referred to a background or reference spectrum, in this case air. The absorption "peak" at about 2350 cm^{-1} is due to uncompensated differences in CO_2 in the air at the times of the two measurements. (This artifact and the filter changes at about 2240 cm^{-1} and 1220 cm^{-1} are readily identifiable in many spectra.)

A contamination problem developed in a cleaning operation: particulate contamination monitors (Si wafers) showed many particles and some stains, as in Fig. 3 and 4 (inserts), with their corresponding IR spectra taken in situ. The particulate material (Fig. 3) is a corn-derived protein zein, which has many uses, including paper sizing. The source of this contaminant on the device line has not been determined at this writing. The stain material (Fig. 4) looks like an alcohol, but there are gross inconsistencies in relative intensities, possibly because the stain material is a mixture. (This is a common "real-world" analytical problem.)

Another type of stain occurred in a final device cleaning step, just prior to joining to a package module, as shown in the insert in Fig. 5 with its in situ IR spectrum. As in the previous example, this material is a mixture and we have not yet sorted out the components. As this was a finished three-level-metallurgy device, and as the IR 20 is a transmission instrument, it was necessary to find "windows" in the three layers of metallurgy in "clean" areas (for a reference spectrum) and "dirty" areas (for the unknown material).

Residual photoresist, especially in very small regions, is a common device-processing worry. There was a recent problem of the blistering of a metal film on silicon. Residual photoresist was suspected, but it was too thin to be visible. A transmission IR spectrum was run at a blistered area after the metal film was peeled back. An accumulation of five scans was sufficient to pull out a spectrum. (This spectrum is not shown because it is a proprietary formulation.)

Another class of device problem can be addressed with this small-area infrared equipment: analysis of small areas of insulating films and the relationship to device parame-

working spectra can be stored in RAM, compared by a variety of arithmetic operations, and plotted. Parameters chosen or data calculated can be printed on tape to be used with recorded spectra. Spectral data are digitized every 2 cm^{-1} over the useful range of $400\text{--}690\text{ cm}^{-1}$ ($2.5\text{--}14.5\text{ }\mu\text{m}$). A fast, wide-range A/D converter averages the detector signal at each 2 cm^{-1} increment with precise step-by-step repeatability. Electronic gain is set automatically by the computer. A dual floppy magnetic disk option allows permanent storage of spectra and data.

Applications

As part of a study of solder/flux/cleaning procedure, the residue in Fig. 2 (insert) was produced. Because the substrate was not transparent to IR, extraction replication⁵ was used to remove some of the $6 \times 10\text{ }\mu\text{m}$ leaf-like crystals. The IR spectrum is shown in Fig. 2. The absorption at 1400 cm^{-1} was interpreted as basic lead carbonate (with complementary information of lead by SEM-EDX;

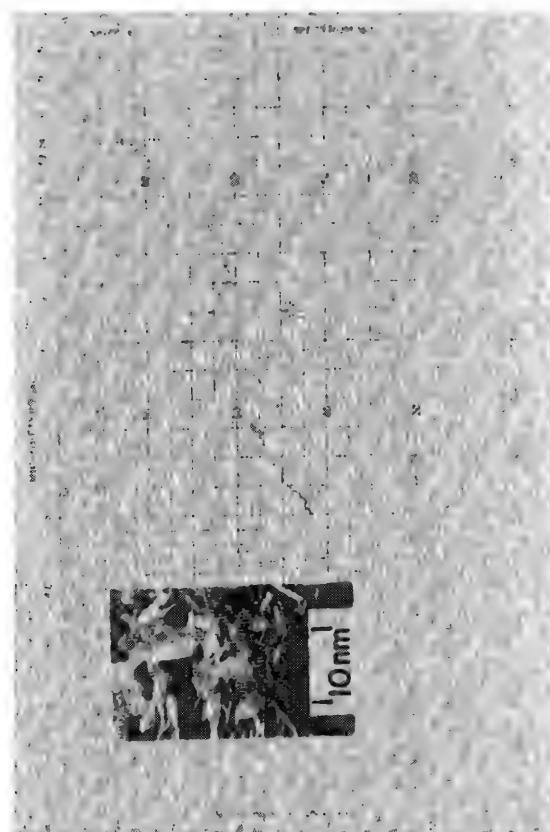


FIG. 2.--Micrograph of solder-flux residue and IR spectrum.

FIG. 3.--Particulate protein.

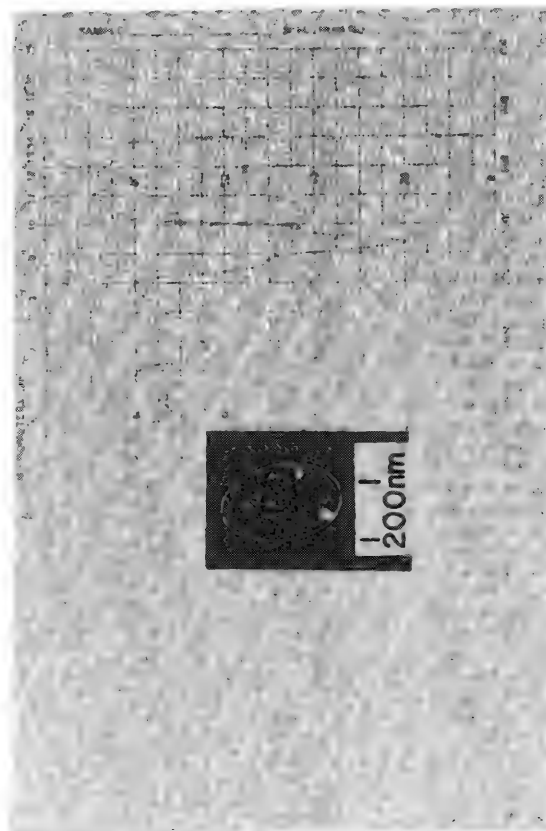
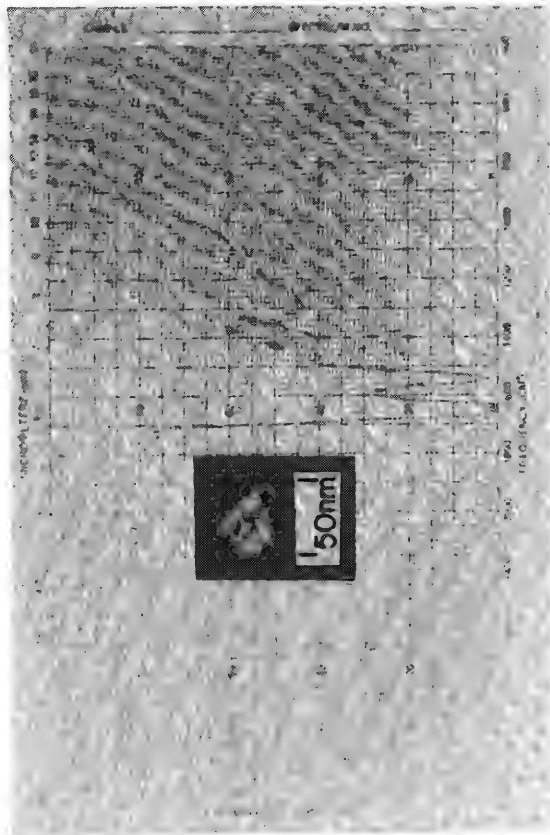


FIG. 4.--Stain material.



FIG. 5.--Unknown stain.

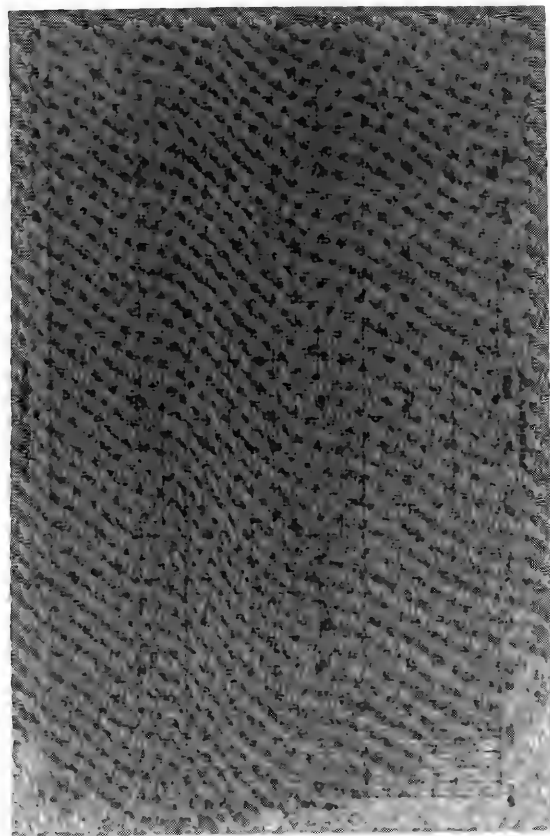


FIG. 6.--Interstitial oxygen in silicon.

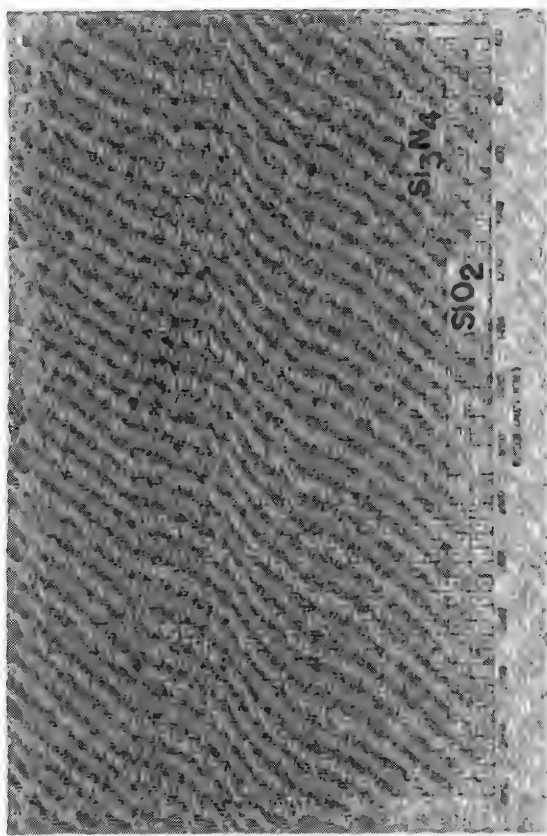


FIG. 7.--SiO₂ and Si₃N₄ films.



FIG. 8.--PSG film.

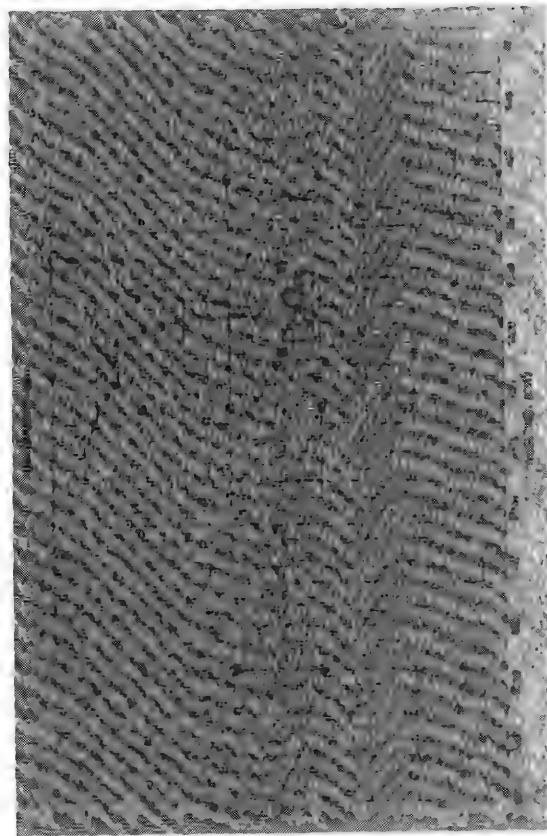


FIG. 9.--PSG, referenced to SiO₂ film.

ters. Three examples will be shown, all of which could be performed on locatable regions as small as $20 \times 20 \mu\text{m}$ (about the diffraction limit of $20\mu\text{m}$ light), maybe requiring computer averaging by accumulation. SiO_2 can be "seen" in Fig. 6. This is primarily the interstitial oxygen in the silicon, but the contribution of the native surface oxide has not as yet been sorted out. Figure 7 shows the spectrum of an 80nm SiO_2 film over 80 nm of Si_3N_4 . Figure 8 shows the absorbance spectrum of about 500 nm of 8% PSG (phosphosilicate glass), referenced to air. The main " P_2O_5 " peak is evident, but distorted due to the large overriding SiO_2 peak. The simple expedient of referencing to a 720nm SiO_2 on silicon, produces Fig. 9, in which the SiO_2 absorption has been (over) compensated, and the " P_2O_5 " peak is thereby enhanced. Such an enhancement could also be made in the arithmetic mode by subtracting out a thinner SiO_2 spectrum with the proper scale factor from the 500 nm of the PSG film.

Conclusion

The NanospecTM 20 IR microscope provides an important new versatile analysis capability for small areas and thin films so important in the semiconductor processing field.

References

1. E. S. Etz and J. J. Blaha, "Investigations into the critical measurement aspects of Raman microprobe analysis," 1979, 173-184.
2. F. Adar, "Developments in Raman microanalysis," *Microbeam Analysis--1981*.
3. C. D. Needham, "Applications of Raman microprobe analysis to the manufacture of semiconductor devices"; and J. N. Ramsey, "Raman, photoluminescence and cathodoluminescence as complementary small area analytical techniques," in *Prèmières journées d'étude sur les applications de la microsonde MOLE at CNRS, Thiais, France, 1979*, 43-44 and 47-50. (Proceedings published in *L'Actualité Chimique* for April 1980.)
4. C. D. Needham and J. N. Ramsey, "Application of Raman microprobe analysis to semiconductor materials and problem," *Semiconductor International* 4 (No. 3), March 1981.
5. D. P. Cameron, F. W. Schneider, and J. N. Ramsey, "Microbulldozing and microchiseling," *Proc. EMSA*, 1969.

SURFACE ANALYSIS BY ELS MICROPROBE

P. Demoncy

The energy loss spectrometry microprobe (ELSM) is presented for the first time. The spectra obtained by this technique are due to primary electrons which have lost a discrete amount of energy in a transition between an initial state below the Fermi level, and a vacant final state above it. The focused electron beam, which has a primary energy of less than 500 eV, is used in a reflection mode. An ultrahigh vacuum is required (10^{-9} - 10^{-10} Torr). Under these conditions, the microprobe makes micro-area and comparative surface analyses of the chemical environment possible. Elemental and chiefly chemical bonding information can be obtained for the top surface (less than 10 Å = 2 atomic monolayers) with a high sensitivity. Every element can be detected, hydrogen included, on any material, insulating or not. In-depth information and ELS imaging are also obtained. The analyses are easy, quick, clean and nondestructive. Various industrial applications, especially in the semiconductor field, are enumerated and demonstrate the utility of this analytical tool in the solution of manufacturing problems. The ELS microprobe is complementary to the scanning Auger microprobe (SAM) and electron spectrometry for chemical analysis (ESCA).

Technical Principles and Operating Conditions

Energy loss spectroscopy (ELS) was first developed for probing the bulk properties of solids. Owing to the progress of ultrahigh vacuum technology, ELS has been mainly applied in recent years to the study of surface effects. In that case the reflection mode must be considered and the energies of the electron primary beam must be less than 1000 eV. The general principle and interest of the ELS technique can be summed up as follows. The ELS peaks are due to primary electrons that have lost a discrete amount of energy in a transition between an initial state below the Fermi level and a vacant final state above it. ELS thus makes it possible to record easily the small spectrum changes corresponding to chemical modifications of a material surface. The equipment used for the experiments to be described is a scanning Auger microprobe from Physical Electronics, SAM 590. The operating conditions are chosen for practical reasons, as follows

Primary beam voltage BV = 50-500 eV
Primary intensity I_p = 10-100 nA
Modulation MOD = 1 eV
Energy resolution $\Delta E/E$ = 0.3%
Time constant τ = 1 s

In this way, we can quickly obtain an electron energy loss distribution either in the integral mode or in the first and second derivative modes. Figure 1 shows $N(E)$, the ELS spectrum of natural oxidized tantalum; Fig. 2, $dN(E)/dE$, the first derivative ELS spectrum; and Fig. 3, $d^2N(E)/dE^2$, the second derivative ELS spectrum.

A lower primary intensity (10 nA instead of 100 nA) can be used without difficulty and applied for insulators or for destructible surfaces. The energy resolution variation (0.3 to 1.2%) does not change drastically the shape of the spectra and a high $\Delta E/E$ can be sometimes taken for best detectability. But different primary beam energies affect the spectra and correspond to specific information from various depths. An ultrahigh vacuum is necessary (10^{-10} Torr) for usual recording, and profiling can be performed at an argon partial pressure of $2 \cdot 10^{-8}$ Torr with the help of a differential ion gun. The aforementioned practical values keep a balance between best possible magnification, trace detection, image visualization, and surface information and lowest possible surface modification or destruction, charge effect, and instability (for insulators and organic compounds).

Applications

Boron Nitride Disks. Comparison is essential in the ELS technique. Recordings can be made at selected point or in the "scanning mode" without critical spectrum alteration.

The author is at Compagnie IBM France, B.P. 75, F-75021 Paris.

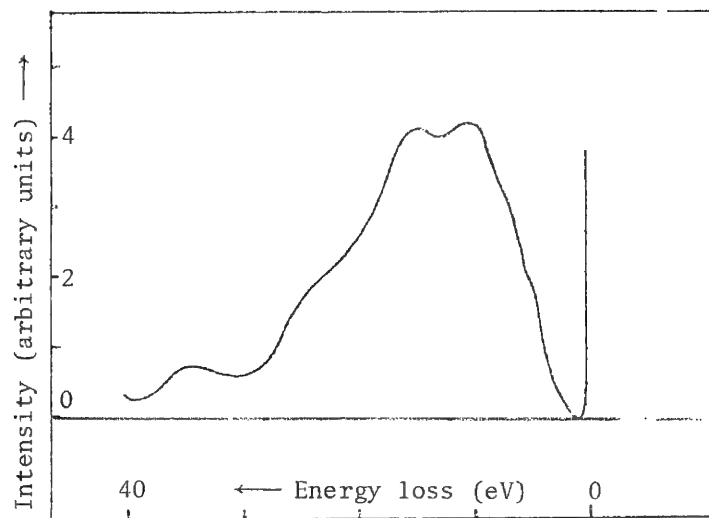


FIG. 1.-- $N(E)$ ELS spectrum of natural oxidized tantalum.

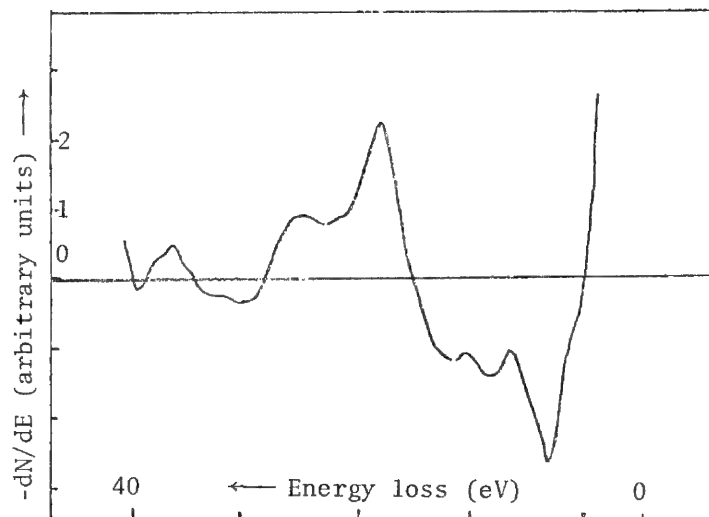


FIG. 2.--First derivative ELS spectrum of natural oxidized tantalum.

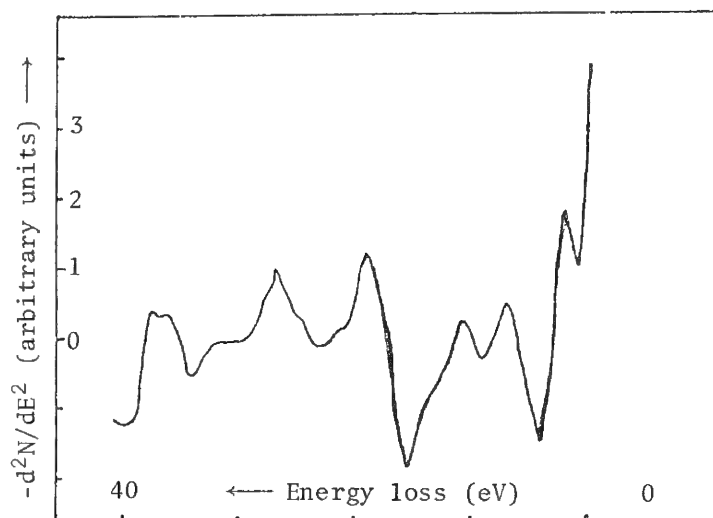


FIG. 3.--Second derivative ELS spectrum of natural oxidized tantalum.

A scanning mode is preferred when the surface is heterogeneous, rough, insulating, or organic. This is the case for the surface analysis of boron nitride samples. The various ELS spectra appear very sensitive to surface variations (Fig. 4) and correspond to different baking times under nitrogen flow. (Evaluation after 0, 10, and 50 diffusion runs of two different BN disks.) Oxidation and boron depletion appear after 50 runs. These kinds of results contribute to the general knowledge of kinetic phenomena.

Platinum Silicides in Small Contacts. ELS spectra of platinum silicides more or less oxidized are shown in Fig. 5. These analyses were made on products. The first monolayers of the natural oxidized platinum silicides after the Pt etch are evidently made up of silicon oxide and not of a Pt-Si-O compound, a result not so clearly brought out in AES. Spectra of PtSi after sputtering, PtSi just after Pt etch, and pure silicon are also shown.

Stoichiometry of Silicon Oxides. The stoichiometry of all silicon oxides can be evaluated by a consideration of the bonding energies given by ELS spectra. The position of the main positive peak on the derivative spectra yields the stoichiometry of oxides between Si and SiO (Figs. 6 and 7, SEM/Co. April 1981).

Chromium-copper Overlaps. Interesting information about the chemical compositions of Cr-Cu overlaps can be obtained. Unlike in platinum silicides, this overlap is not an alloy but a mixture of two elements, as easily seen on ELS spectra. There is no energy shift of the Cr and Cu peaks. The atomic composition of this overlap (Fig. 8) can be roughly estimated to be Cr₆₅Cu₃₅.

Unetched Copper Area on Circuits. Comparison of ELS spectra from small unetched copper areas and from photoresist immediately points to photoresist residues in these areas (Fig. 9). The ELS spectrum of resist differs slightly from an ELS spectrum of carbon contaminations. AES could not establish this difference.

Silicon Hydrides. Hydrogen absorption on metals or on silicon surface structures can be studied by ELS. Silicon covered by atomic hydrogen was in fact exposed to different partial pressures of molecular hydrogen. Figure 10 shows second-derivative ELS spectra of pure silicon and silicon exposed to hydrogen (initial pressure 2×10^{-9} Torr, final pressure 5×10^{-5} Torr; gas, argon with 10% of hydrogen). Important spectrum changes are seen as the hydrogen partial pressure increases.

Aluminum Chromium Alloy (2 hr at 450°C). The interface of the chromium-aluminum metallurgy after annealing was studied by ELS. A compound CrAl₆₋₇ can be determined after aluminum etch. This layer is not oxidized (Fig. 11).

ELS Imaging. Very small silicon oxide and silicon islands were considered for ELS imaging. Figure 12 represents the silicon oxide-silicon molecular boundary distribution. The negative peaks from the first-derivative spectrum at 17 and 10 eV, respectively, are used to obtain the SiO₂ and Si molecular boundary dispersion. The image of Fig. 12, which has been intentionally not at all optimized, is obtained in accordance with the time limitations of industrial practice. (The image is obtained in less than 2 min.) The area of the silicon oxide island is about 30 μm^2 ; and ELS line scans can be obtained, too.

Advantages and Shortcomings

From these applications, the use of the ELS microprobe appears to be a very attractive analytical tool for solving manufacturing problems. The best way of illustrating the promise of the ELS microprobe is to consider its general advantages and shortcomings. The advantages may be listed as follows.

- (1) top surface analysis
- (2) very high sensitivity
- (3) chemical bonding compounds, alloyed or nonstoichiometric
- (4) elemental and semiquantitative analysis (all elements detected, hydrogen included)
- (5) reasonable spatial resolution (microprobe: a few square microns)
- (6) low current density (insulators, organics, etc.)
- (7) in-depth information (by sputtering or with beam voltage changes)
- (8) very small contaminating film thickness (surface and volume plasmon ratio vs beam voltage)

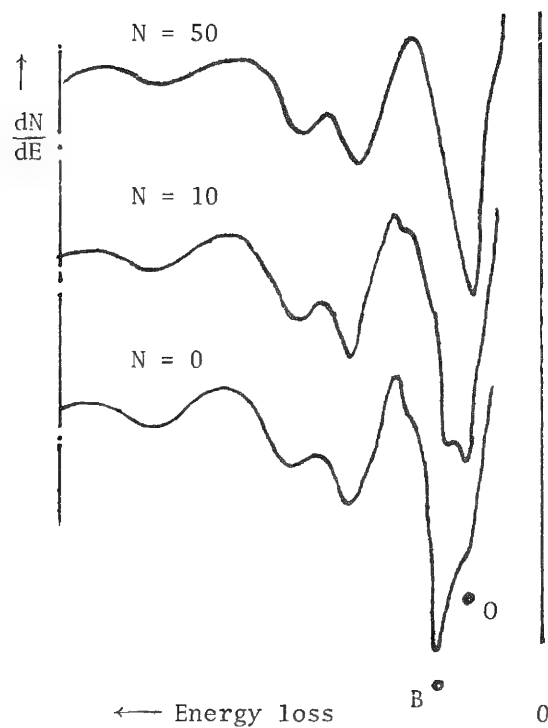


FIG. 4.--Boron nitride ELS spectra after various baking runs $N = 0, 10$, and 50 .

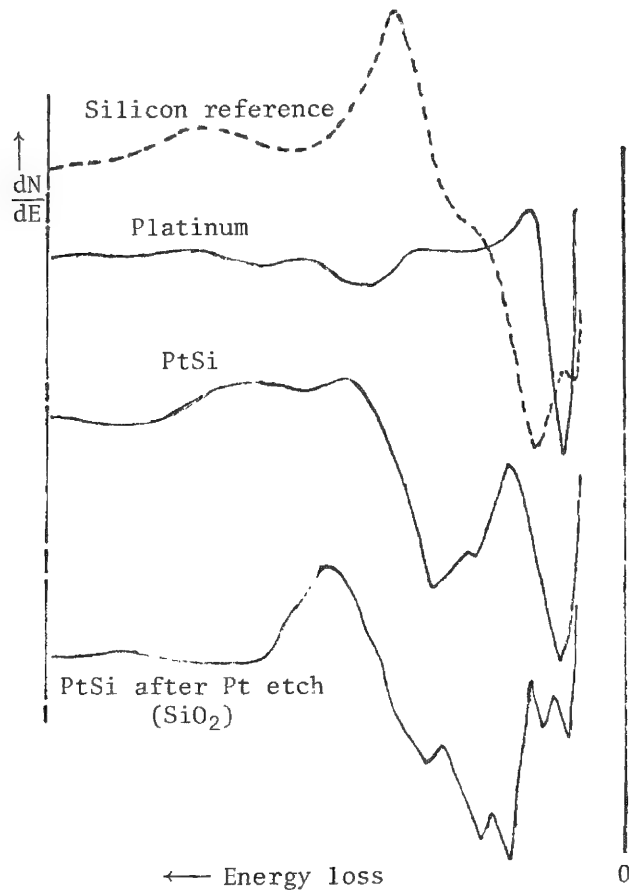


FIG. 5.--Various more or less oxidized platinum ELS spectra.

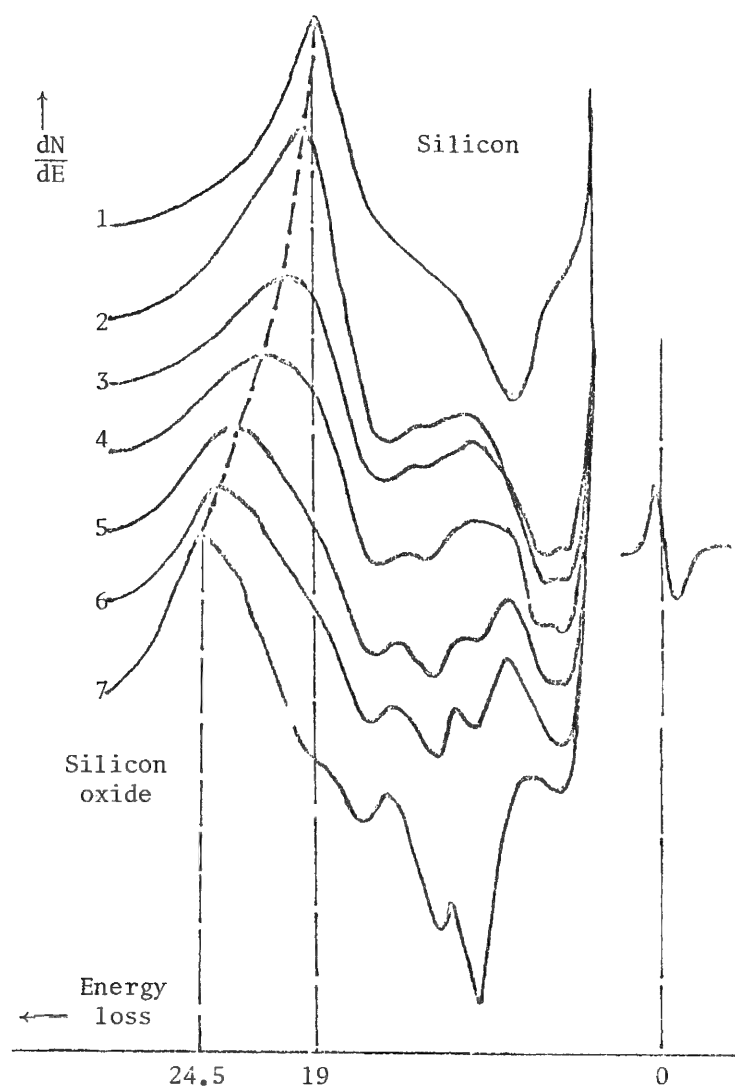


FIG. 6.--ELS spectra as oxygen coverage on silicon increases.

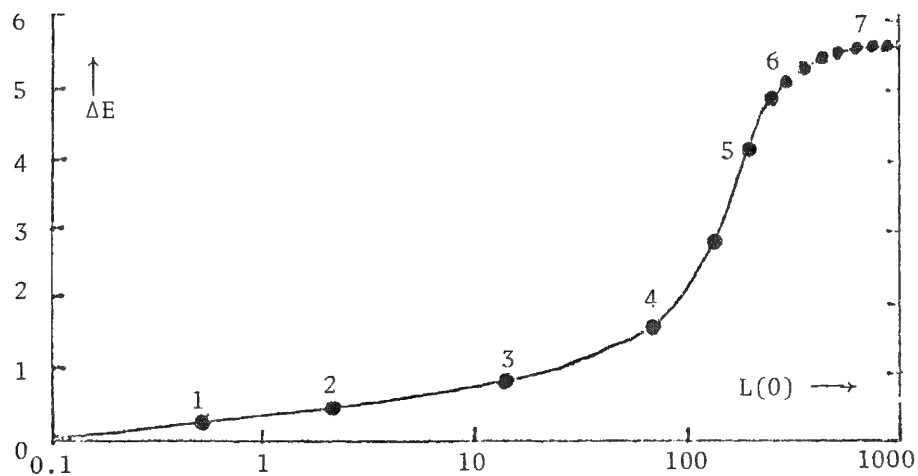


FIG. 7.--Energy shift as function of oxygen coverage exposures (in Langmuir).

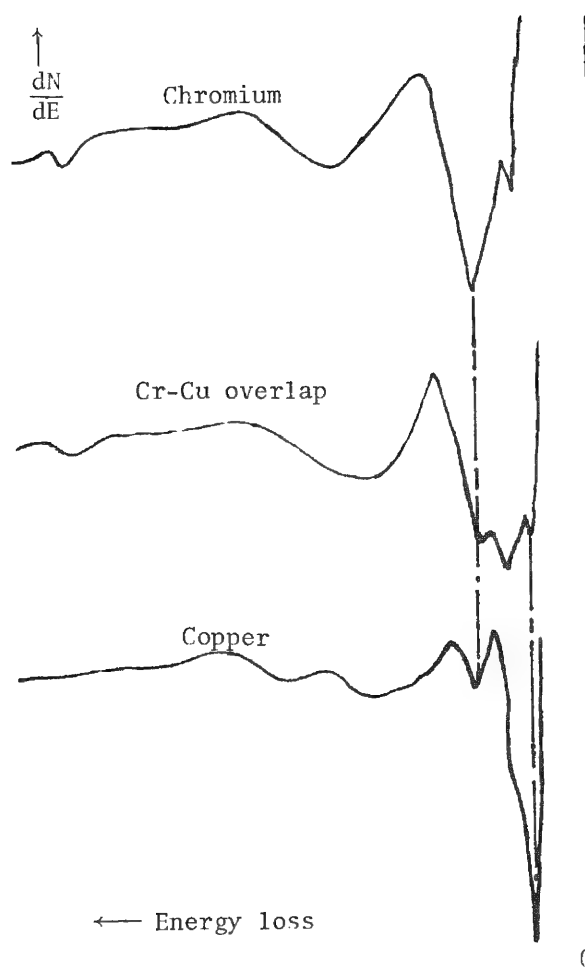


FIG. 8.--ELS spectra of chromium, copper, and the Cr-Cu overlap.

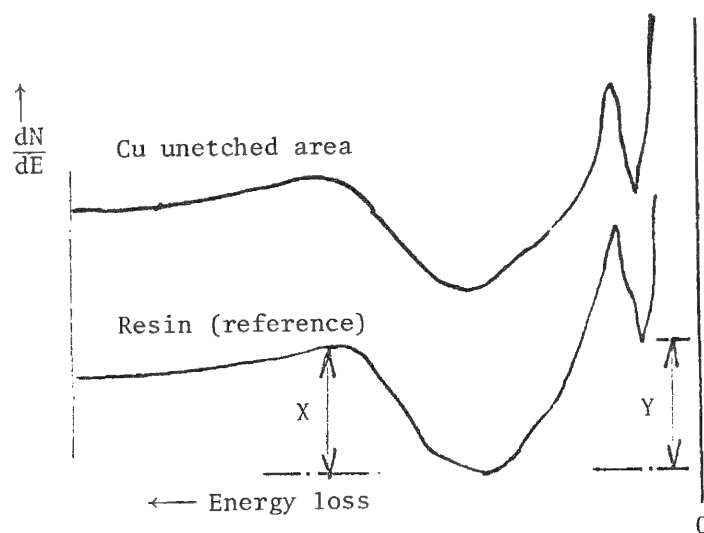


FIG. 9.--ELS spectra from Cu unetched area ($X/Y = 0.85$) and from resin ($X/Y = 0.90$); pure carbon on Si $X/Y = 1.10$.

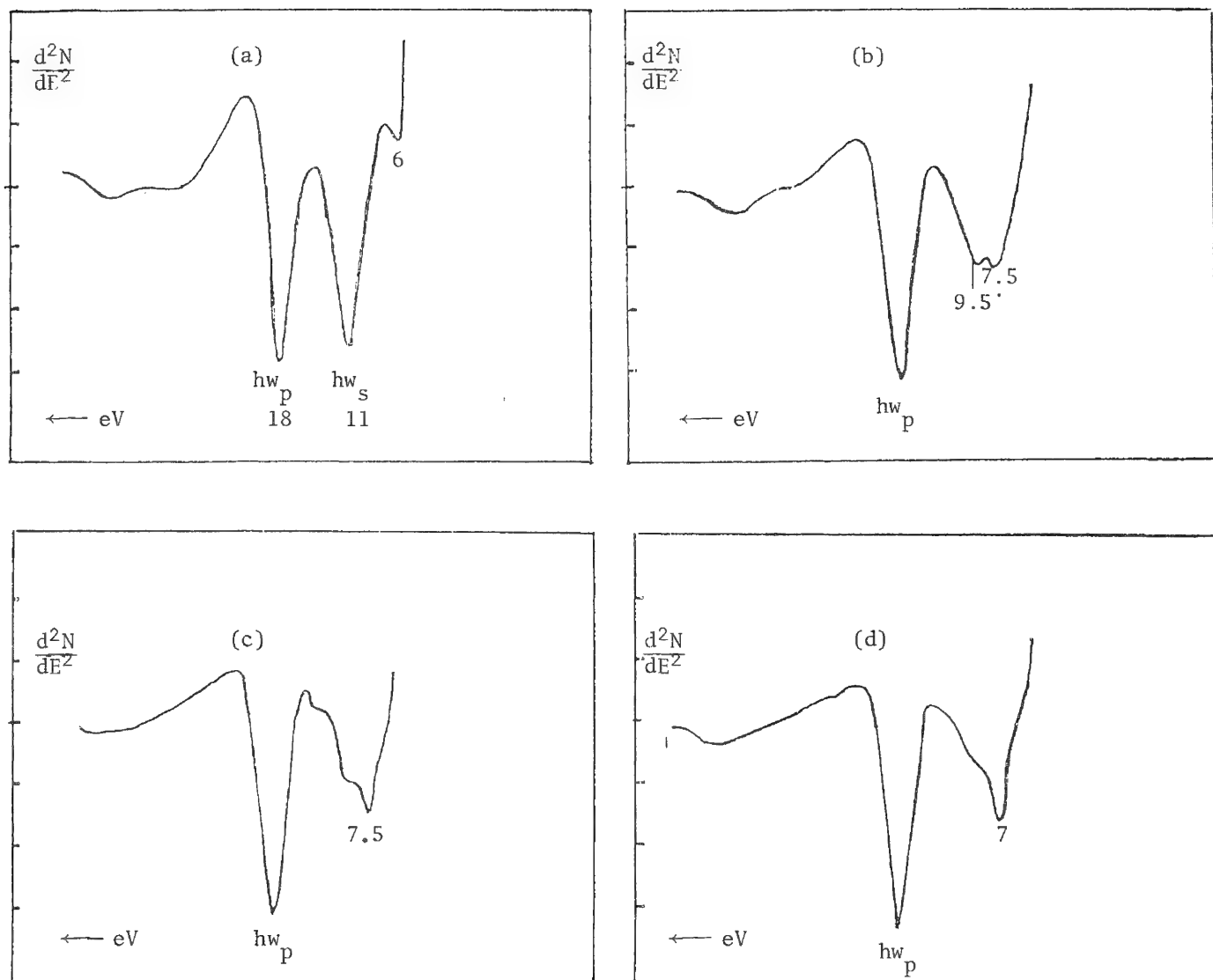


FIG. 10.-- d^2N/dE^2 ELS spectra of silicon under various hydrogen partial pressures: (a) initial pressure, 3×10^{-8} Torr; (b) Ar + H₂ pressure, 10^{-8} Torr; (c) Ar + H pressure, 10^{-7} Torr, (d) Ar + H pressure, 5×10^{-5} Torr.

- (9) some structural information
- (10) ELS imaging (chemical bonding or molecular dispersion)
- (11) quick, nondestructive, clean and easy analysis
- (12) extremely favorable for sample comparison

The shortcomings may be summed up as follows.

- (1) lack of a reference handbook of ELS
- (2) ambiguous ELS spectra for some binary or ternary compounds
- (3) necessity of fixed operating conditions. (Nonetheless, different primary electron energies are recommended for the occasional observation of additional information.)

In conclusion, the ELS microprobe permits comparative and surface analysis of the chemical environment. Any system made up of an electron beam and of the analyzer of Auger spectrometers or other similar equipment can be easily adapted to ELS. This spectrometry is complementary to Auger electron spectrometry (AES) and to electron spectrometry for chemical analysis (ESCA), as shown in Fig. 13. In addition, interesting correlations can be pointed out between ELS and SES, especially if different primary electron energies are used. AES, ELS, and SES analyses can be performed on the same area.

An optimized microprobe would be extremely valuable in semiconductor manufacture because:

- the integrated circuits give small areas of interest
- the manufacturing process uses clean materials and always of similar type
- the samples are often insulators with a rather rough surface
- the vacuum quality of the process chambers is fundamental
- the kinetic phenomena have to be understood (temperature, pressure, gas, etc.)

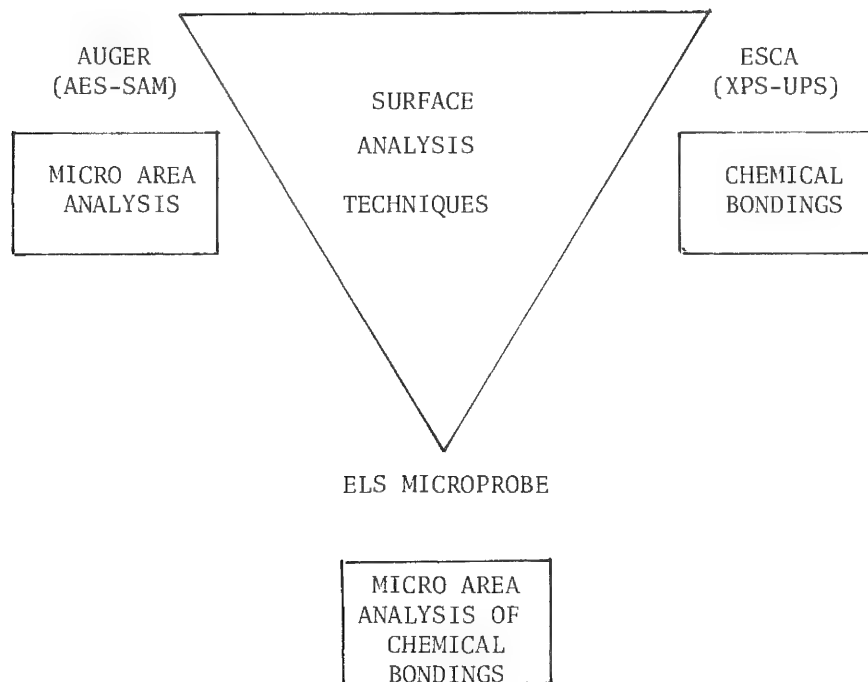


FIG. 13.--ELS Microprobe.

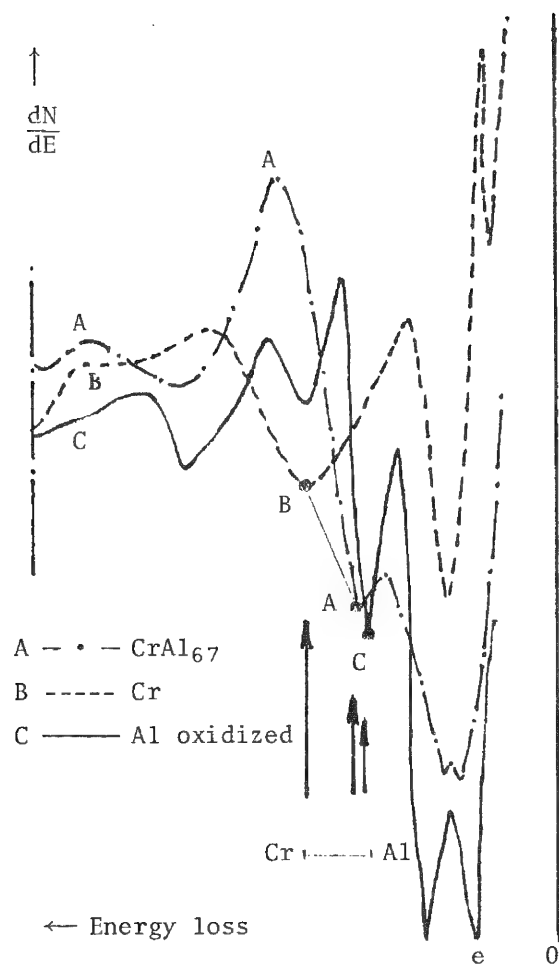


FIG. 11.--ELS spectra of chromium, aluminum, and an alloy.

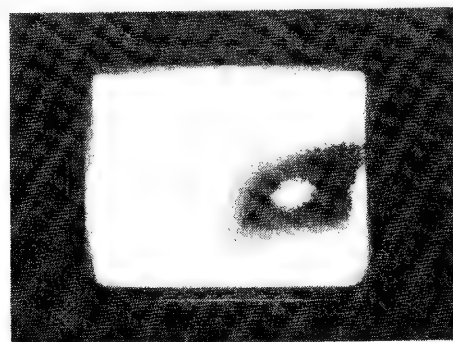
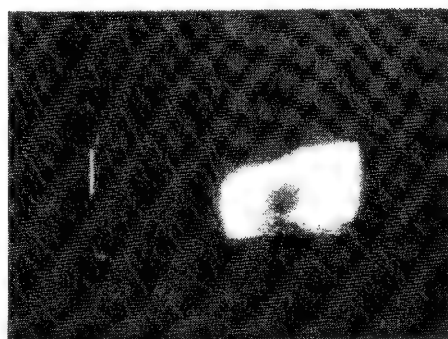


FIG. 12.--Quick ELS imaging of small silicon oxide land ($30 \mu\text{m}^2$): (a) Si-Si ELS image; (b) Si = 0 ELS image.

THERMAL-WAVE ELECTRON MICROSCOPY

Allan Rosencwaig

Imaging of microscopic features on and beneath the surface of an opaque material can be performed with a new technique, thermal-wave electron microscopy. This technique utilizes thermal waves generated by a scanning electron beam to image the features. Thermal-wave imaging bears distinctive differences from ultrasonic imaging.

There has been considerable interest lately in the unique imaging capabilities of thermal-wave microscopy. In this new technique, an intensity-modulated optical (laser) or electron beam is focused and scanned across the surface of an opaque sample. Localized periodic heating results from the absorption by the sample of the incident beam. The solution to the periodic thermal-diffusion equation for this situation is a thermal "wave,"¹ which is a wave so highly damped that it propagates no more than one wavelength. In fact, as shown in Fig. 1, this thermal wave is attenuated to e^{-1} after propagating one reduced wavelength $\mu = \lambda/2\pi$, where λ is the actual wavelength and μ is more commonly referred to as the thermal-diffusion length given by

$$\mu = \sqrt{2\kappa/\rho C\omega} \quad (1)$$

Here κ is the thermal conductivity, ρ the density, C the specific heat, and ω is the frequency at which the heating is produced. In spite of their strong damping, thermal waves have several of the characteristics of more conventional propagating waves,¹ and by analogy with optical and acoustic waves, one can, at least from a formal mathematical viewpoint, treat the interactions of thermal waves with thermal barriers or discontinuities in terms of "scattering" and "reflection" processes. The wave-like aspects of this thermal-diffusion process arise from the fact that we are dealing with harmonic single-frequency thermal flow.

Thus, the thermal waves generated in the sample through the periodic absorption of optical photons or of electrons can be considered as undergoing "reflection" and "scattering" processes at surface and subsurface thermal features, and thereby providing images of these features. In analogy with optics and ultrasonics, the resolution attainable in thermal-wave imaging is set by both the spot size of the scanning beam and by the thermal wavelength.²⁻⁴ This wavelength, as seen in Eq. (1), is in turn determined by the frequency at which the optical or electron beam is modulated. Typically, modulation frequencies in the range 200 kHz-20 MHz provide thermal resolutions in metals of 5-0.5 μm and in thermal insulators of 1.0-0.1 μm .

Since thermal waves are most difficult to detect directly because of their strong damping, thermal-wave images are generally recorded with photoacoustic techniques. In a gas-microphone photoacoustic system, the periodic surface temperature of the sample is measured through its effect on the gas in the cell. The thermal-wave images recorded in this manner can be analyzed solely in terms of thermal-wave interactions with surface and subsurface thermal features.^{5,6} Unfortunately, gas-microphone photoacoustics is limited in practice to frequencies below 10 kHz, which limits the ultimate resolution of the thermal-wave images to no better than 20 μm in most materials. To achieve higher resolution, piezoelectric photoacoustic techniques are used, in which a piezoelectric transducer in contact with the sample measures the stress-strain fluctuations in the sample produced by the localized heating from the scanning beam.^{2,7} This method permits operation at frequencies into the megahertz range, and thus resolutions into the submicron range. Electron beams, as well as laser beams, can be used to generate the thermal waves,^{2,7} and both laser and electron thermal-wave experiments have been performed by the piezoelectric method.^{4,8-10}

Some researchers have interpreted the images obtained in a thermal-wave electron microscope as electron-acoustic or ultrasonic images. In some cases, as with the normal-

Allan Rosencwaig is with the Lawrence Livermore National Laboratory, University of California, Livermore CA 94550. The work reported here was performed privately, and the opinions and conclusions are those of the author and not of Lawrence Livermore National Laboratory. The support of International Scientific Instruments, Inc., of Santa Clara, Calif., is gratefully acknowledged.

mode images in thin disks, such an interpretation is fully accurate. However, in most cases these images are more correctly interpreted as thermal-wave images, and a treatment of the thermal term as simply a diffusive source term is incomplete. Thermal-wave images obtained with the piezoelectric method bear a much closer relationship to thermal-wave images obtained with a gas-microphone method than they do to ultrasonic images. Yet, it is certainly true that piezoelectrically derived images cannot be analyzed solely in terms of thermal-wave interactions.

Following White's derivation of ultrasonic wave generation through surface heating,¹¹ we can readily show that the piezoelectric signal Q is proportional to the following integral,

$$Q \sim \int_0^\lambda B(x) \alpha_t(x) \theta(x) dx \quad (2)$$

Here, B is the elastic modulus (for simplicity here taken as the bulk modulus), α_t the thermal expansion coefficient, and θ the local temperature excursion in the sample at a distance x below the surface. This integral is over a full thermal wavelength λ . Since the scanned area is always much smaller than the dimensions of both the sample and the transducer, we need not consider the details of the ultrasonic transmission through the sample to the transducer, since these terms do not change noticeably as the beam covers the scanned area. Whereas the signal obtained in a gas-microphone system is proportional solely to the surface temperature θ_0 , the signal obtained in a piezoelectric system is proportional both to the temperature θ and to the thermoelastic product $B\alpha_t$. Thus, with piezoelectric detection, we are sensitive not only to the thermal features that perturb the thermal waves, but also to the thermoelastic features that result in changes in the local $B\alpha_t$ product. However, the most important aspects of this imaging--that is, the resolution, depth of penetration, and the depth-profiling capability--are all set solely by the thermal waves. Thus, both the resolution and the penetration depth are set by the thermal wavelength (λ or μ) and not by any elastic or ultrasonic considerations.

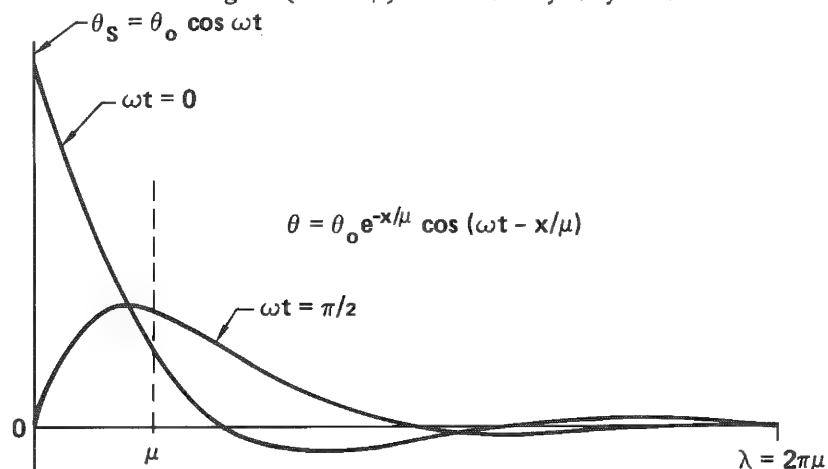
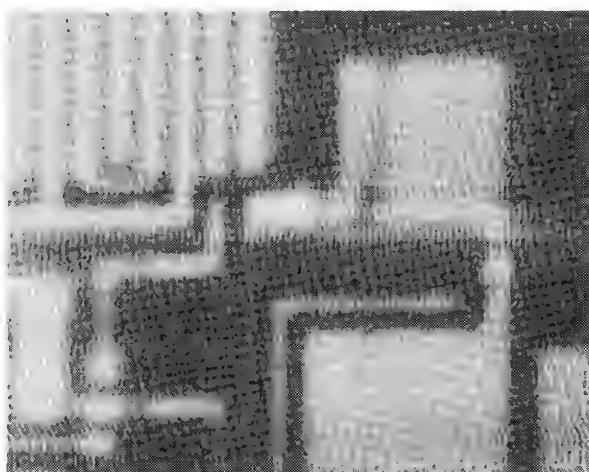


FIG. 1.--Variation of temperature with depth in solid when the surface temperature is harmonic in time. The two curves are the 0° and 90° phase curves.

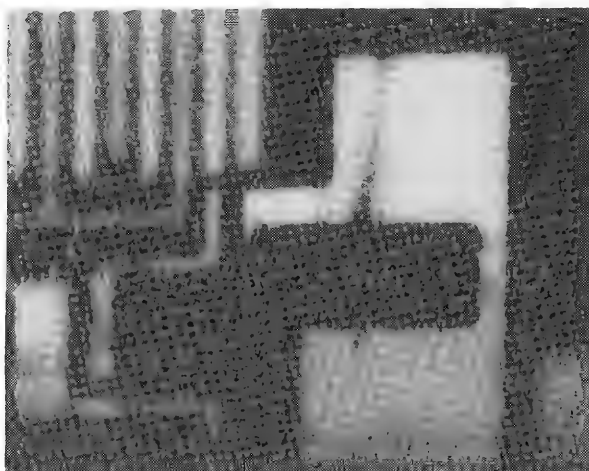
In addition, the piezoelectric thermal-wave technique permits nondestructive depth profiling, not only by changes in the depth of penetration of the thermal waves through changes in frequency, but also through changes in the phase of detection. Referring to Fig. 1, we see that at a phase of $\omega t = 0$, the major change in temperature occurs at and directly beneath the surface. Thus, the major contribution to the integral of Eq. (2) comes from this region, and the image therefore reflects the near-surface characteristics of the sample. On the other hand, at a phase of $\omega t = \pi/2$, the major temperature excursion now occurs at $x = \pi\mu/4$, and at this phase the image originates, in the main, from the part of the sample about one thermal diffusion length beneath the surface. An example of such depth-profiling is shown in Fig. 2,¹² where the 0° thermal-wave image is quite similar to the backscatter electron image of the integrated circuit, whereas the 90° thermal-wave image is quite different. This example shows that the apparently similar metallization pads in the circuit are actually quite different so far as their subsurface structure is concerned. This phase depth-profiling can be understood only if the wave-



(a)



(b)

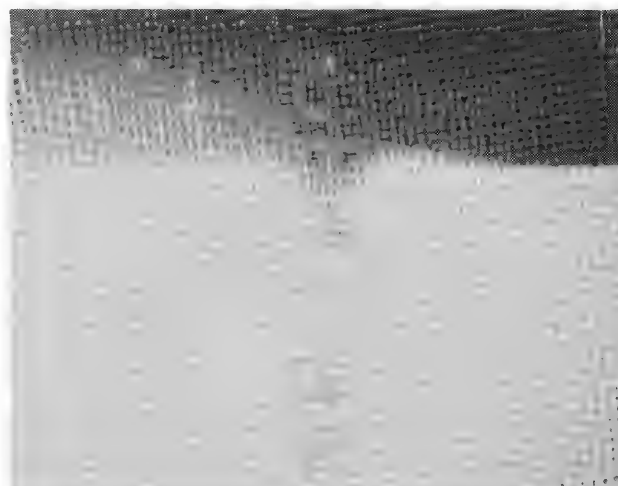


(c)

FIG. 2.--Images of an integrated circuit at 400 \times magnification (smallest detail is 5 μ m); (a) backscatter electron image; (b) thermal-wave image at 640 kHz and at 0 $^\circ$ phase setting (near-surface); (c) thermal-wave image at 640 kHz and at 90 $^\circ$ phase setting (sub-surface).



(a)



(b)

FIG. 3.--Images of a Si wafer. Silicon in upper third of each view is coated with 0.4 μ m pf SiO₂; bottom region is bare Si. Letters are 100 μ m in size. (a) backscatter electron micrograph; (b) thermal-wave image of same region at 640kHz modulation frequency.

like aspects of the thermal terms are fully appreciated.

Finally, although it is clear that the elastic contributions to the images obtained in a piezoelectric thermal-wave image cannot be ignored, for many if not most samples, the thermal features provide the dominant contributions to the image. A good example of this point is illustrated in Fig. 3. Here we have used electron thermal-wave microscopy to detect and image those regions in a silicon wafer which have undergone diffusion or ion-implantation of dopant atoms.¹³ The silicon in the upper third of each view in Fig. 3 is coated with SiO₂, and the photolithographed letters here are quite visible in the electron micrograph. The lower two-thirds of each view is of bare Si, and the letters here are ordinarily invisible since they are present only as phosphorus-doped diffusion patterns. These letters are, therefore, not visible in the electron image, but are quite visible in the thermal-wave image. At the dopant levels of 10¹⁸-10¹⁹ cm⁻³ used in this experiment (i.e., 10-100 ppm) no noticeable change in the local B₀t product can be expected. Thus, the ability to detect dopant regions in Si through thermal-wave microscopy is a result solely of the sizable changes that occur in the thermal conductivity when the single crystal lattice of Si is disrupted by the addition of other atoms, or through the presence of defects such as dislocations.¹⁴

Thermal-wave microscopy offers many new capabilities for materials evaluation and analysis. However, to utilize this new technique fully, one must understand all the processes that occur and appreciate the important differences between this type of imaging and conventional ultrasonic imaging.

References

1. H. S. Carslaw and J. C. Jaeger, *Conduction of Heat in Solids*, London: Oxford University Press, 1973, 2nd ed.
2. A. Rosencwaig, "Thermal-wave microscopy with photoacoustics," *J. Appl. Phys.* 51: 2210, 1980.
3. R. L. Thomas et al., "Subsurface flaw detection in metals by photoacoustic microscopy," *J. Appl. Phys.* 51: 1152, 1980.
4. G. Busse and A. Rosencwaig, "Subsurface imaging with photoacoustics," *Appl. Phys. Lett.* 36: 815, 1980.
5. Y. H. Wong, R. L. Thomas, and J. J. Pouch, "Subsurface structures of solids by scanning photoacoustic microscopy," *Appl. Phys. Lett.* 35: 368, 1979.
6. G. Busse, "Optoacoustic images," *Proc. Topical Meeting on Photoacoustic Spectroscopy*, 1979, Optical Society of America.
7. A. Rosencwaig, "Photoacoustic microscopy," *Am. Lab.* 11(4): 39, 1979.
8. A. Rosencwaig and G. Busse, "High-resolution photoacoustic thermal-wave microscopy," *Appl. Phys. Lett.* 36: 725, 1980.
9. E. Brandis and A. Rosencwaig, "Thermal-wave microscopy with electron beams," *Appl. Phys. Lett.* 37: 98, 1980.
10. G. S. Cargill III, "Ultrasonic imaging in scanning electron microscopy," *Nature* 286: 691, 1980.
11. R. M. White, "Generation of elastic waves by transient surface heating," *J. Appl. Phys.* 34: 3559, 1963.
12. A. Rosencwaig, "Thermal-wave imaging and microscopy," *Proc. 1980 IEEE Ultrasonic Symposium*, 1980, 600.
13. A. Rosencwaig and R. M. White, "Imaging of dopant regions in silicon with thermal-wave electron microscopy," *Appl. Phys. Lett.* 38: 165, 1981.
14. Y. S. Touloukian et al., *Thermophysical Properties of Matter, vol. II, Thermal Conductivity of Nonmetallic Solids*, New York: IFI/Plenum Press, 1970.

SEM Applications

SEM VOLTAGE CONTRAST TECHNIQUES FOR THE ANALYSIS OF MEMORY CIRCUITS

D. D. Wilson, J. R. Beall, and W. E. Echols

The current level of complexity in integrated circuits makes analysis by conventional light microscope and mechanical probing techniques extremely difficult. A study was performed on seven memory circuits to explore the feasibility of (and to develop the methodology for) producing circuit schematics, die maps, logic diagram, and bit maps, and of performing failure analysis by means of the scanning electron microscope (SEM). SEM voltage contrast was found to be practical and to provide significant improvement for the above applications in large-scale integration (LSI) circuit analysis. This paper describes the operating parameters utilized and the sample preparation necessary, and discusses typical examples.¹

SEM Operating Parameters

A Cambridge S-180 SEM was used for this study. The accelerating voltage was adjusted to obtain an acceptable image signal without damage to the circuit being analyzed. Silicon-gate NMOS circuits were found to be the most susceptible to irradiation damage and had to be operated in the 1-1.5kV accelerating range. Bipolar and metal gate MOS were found to be less susceptible and could be operated at 5 kV and in some cases up to 10 kV without significant beta degradation or threshold shifts. When the acceleration voltage was raised too high, a high-temperature bake would help in some cases to anneal the circuit damage.

The beam currents used were measured by means of a Faraday cup. At 5 kV these beam currents were in the 200-500pA range; at 1 kV, the beam current was in the 25-50pA range. These current levels did not cause any functional interference problems with the circuits and provided an acceptable signal-to-noise level.

Sample Preparation

Voltage contrast can be obtained from integrated circuits with no preparation except the introduction of the circuit into the chamber with the appropriate electrical connections. A significant improvement in the voltage contrast signal was obtained with the removal of the glass passivation layer. This removal also allows dc voltages to be observed at TV scan rates, which makes circuit organization easily discernible.

The glass removal process is a critical and difficult operation. It is critical since an adequate amount of glass has to be removed to obtain good voltage contrast sensitivity and yet the circuit has to remain functional. The principal difficulty is the wide variation in glassivation processes among different manufacturers and even among different lots for a given manufacturer.

The glass removal process was performed with 30s exposures to an etchant followed by visual examination and electrical supply current measurement. A typical etchant used was 280 ml ammonium fluoride (40%) and 35 ml hydrofluoric acid (48%). This material provided a moderate etch rate and permitted controllable removal of the glass. The visual examination checked for several conditions, including the appearance of vivid colors indicating the exposure of the thermal oxide, undercutting of the metallization, and the disappearance of the passivation line around bonding pads. If the electrical measurements indicated that the supply current was beginning to increase, the etching was stopped prior to any visual indications.

The circuit was checked at this point to determine whether voltage contrast sensitivity was adequate. Both dc and ac response was necessary to develop the circuit schematic.

General Circuit Analysis

With the glassivation removed the parts were placed in a socket in the specimen chamber. This socket was connected to a feedthrough on the front of the specimen holder. This

The authors are with the Parts Technology Group of Martin Marietta Aerospace, Box 179, Denver, CO 80201. This work was done under Contract F 30602-78-C-0354 for the Reliability Branch of Rome Air Development Center, Griffiss AFB, N.Y.

feedthrough was connected to drive circuitry which functionally operated the memory IC. The part was operated at low (1-2Hz) rate. This process produces a "functional map" of the area while it is operating. The frame period utilized was 30 s, with the film exposed from top to bottom in 800 separate line scans. The result of this process with the circuit being operated would be distinct stripes on the film related to the two states of the circuit, i.e., high and low.

The frequency of the circuit was controlled to obtain a striped pattern that allowed the metallization to be easily traced. If the frequency is too low, the metallization lines tend to segment; if too high, it becomes difficult to relate the phase in one area to the phase in another area. A stripe width slightly smaller than the line width was found to be optimum.

PROM Analysis

The remainder of this paper is concerned with one of the memory circuits analyzed, a 1024-bit Nichrome Link programmable read-only memory--a bipolar device in a 16-pin dual in-line ceramic package. This is a 256×4 bit memory; therefore there are 8 address inputs and 4 outputs. The 256 bits could be addressed in any manner desired by means of driving circuitry designed for this task. Areas of interest could therefore be operated in a manner that optimized their appearance for functional mapping.

The memory circuit was electrically tested; it was then opened and the glass passivation was removed. This procedure required approximately 3 min of etching. Circuit characterization was then performed at 5 kV in the SEM.

Schematic development for a row address buffer is typical of the method utilized for all the circuitry. The section associated with a given input is easily recognized by means of voltage contrast. Figure 1 shows a voltage contrast photograph with the individual components labeled for one input. A second input section below it is running at twice the frequency as is evident by the closer spacing of the candy-stripe pattern. Also evident in this photograph are the five other pairs of row address lines on the right-hand side, exiting into the row decode section. Each row address buffer produces two output lines at opposite phases. These are labeled A6 and A6-not for the A6 buffer. To develop this schematic, the voltage contrast photograph is compared with a light microscope photograph at the same magnification and the electrical components and interconnections are determined. Figure 2 shows a light-microscope photograph of the same area as Fig. 1. It is difficult to determine the circuitry associated with this input and the V+ and ground metallization areas are not evident. By use of both photographs the majority of the circuitry can be readily identified. If questions arise, further light-microscope or SEM voltage contrast is performed to clarify the area of concern.

The areas analyzed on this die included the row address buffer, row decode, column address buffer, column decode, data output, chip enable, and the memory array. For each of these areas a circuit schematic and logic diagram was developed.

An additional area that was identified on this die was circuitry that allowed the programmability of the chips to be tested without fusing the NiCr links on any of the 1024 bits that are normally used. Two extra columns and two extra rows can be programmed. The extra columns were labeled A and B and were easily identified by means of voltage contrast. Column A had its NiCr links tied to pin 13, CE. Column B was connected to pin 5, A0. These memory cells could be programmed by addressing each of the rows with pins 5 and 13 shorted to ground. It is necessary for each of these NiCr links to be fused open or high current will flow into a low input on pins 5 and 13.

Thirty-two rows are used in the memory array, so the extra rows were numbered 33 and 34. In row 34 alternating columns had fuses and opens and in row 33 all columns had fuses. Each of these NiCr links were fused open in row 34 to verify the programmability. The method by which these were addressed was deduced from the schematic.

A bit map was developed from a real-time voltage-contrast examination of the memory-cell array. This graphical guide identifies the physical position of the memory cell associated with each row-and-column combination. This bit map can be used to identify adjacent memory locations and is therefore useful in developing testing for pattern sensitivity.

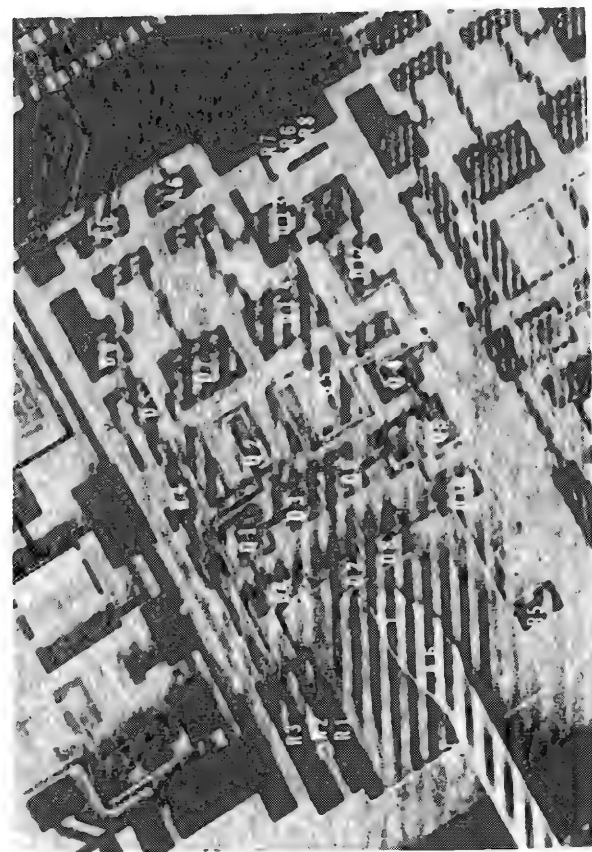


FIG. 1.--Voltage contrast micrograph of A6 row address buffer 5 kV, 275 \times .

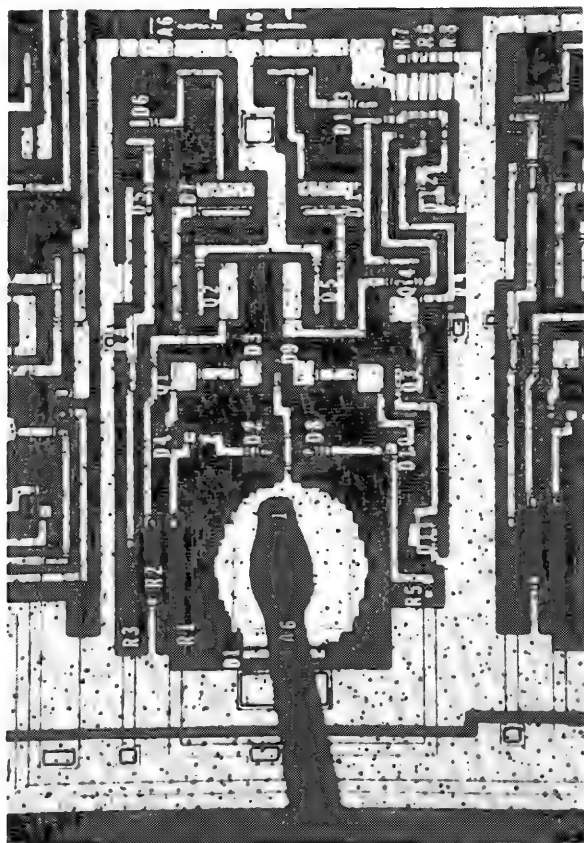


FIG. 2.--Light photograph of A6 row address buffer; 225 \times



FIG. 3.--Voltage contrast micrograph of failure in column decode circuit; 5 kV, 350 \times .

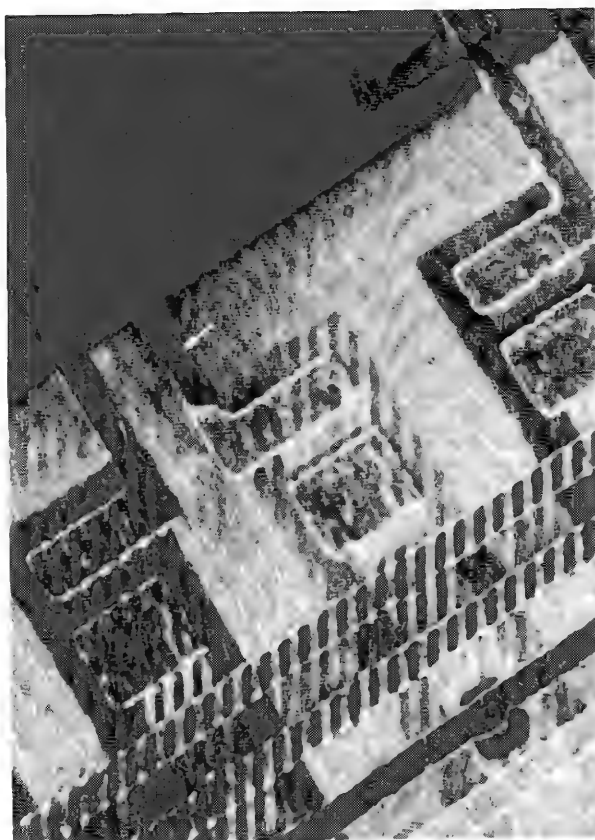


FIG. 4.--Voltage contrast micrograph of open metallization in column decode; 5 kV, 1200 \times .

Failure Analysis

The ability to perform failure analysis by means of voltage contrast was evaluated. A failure was introduced into a unit by one person and then an analysis was performed by another person.

A unit was electrically characterized and then opened, and the glass was chemically removed. The device was rechecked at this time to verify functionality. A failure was introduced as follows: the sample was coated with Tech Wax, a portion of the wax was removed by a mechanical probe, and then the part was etched by an aluminum etchant. This procedure produces a small opening in the exposed aluminum.

A connection between a pull-up resistor and the collector of a column decode transistor was etched open.

The failure would not allow the 011 code to be addressed so the associated output stayed low. This fault affected 24 words. The part was placed in the SEM and the column decode was examined with the input running at 1 to 2 Hz. The failed column was quite apparent. A photograph of the area (Fig. 3) revealed the open metallization. A higher magnification view of this is shown in Fig. 4.

Conclusion

The use of voltage contrast for memory circuit analysis was discussed. The SEM operating parameters, sample preparation, and an example of the data obtained for one memory circuit are included. The principal obstacle encountered was the nondestructive removal of the glass passivation to improve the voltage contrast sensitivity. This technique is seen to provide a significant improvement in the methods available for circuit characterization and failure isolation.

It was successfully demonstrated on seven different types of memory circuits including bipolar and SiGate MOS, PROMS and ROMS, and static and dynamic circuits ranging in complexity from 256 bits to 16K bits.

INVESTIGATION OF GATE SHORTS IN CMOS DEVICES BY ELECTRON BEAM INDUCED CURRENT AND INTERNAL SEM PROBES

R. R. Piety, E. L. Miller, K. C. Evans, and W. J. Silva

Location and characterization of gate oxide failure sites is an essential part of the failure analysis of high-reliability complementary metal oxide semiconductor (CMOS) devices. This information can indicate if the failure was caused by external overstress, such as electrostatic discharge (ESD), or by a manufacturing defect, such as an oxide pinhole. Thus, the user may be alerted to possible handling problems or to defects common to a particular group of parts. However, whereas breakdown sites at the edge of the gate metallization may be located by the scanning electron microscope (SEM), shorts beneath the metallization are not directly observable without the removal of the metallization and consequent destruction of the device. Even after metallization removal, the breakdown site may not be unambiguously located owing to its small size or the presence of other irregularities in the gate oxide.

The electron beam induced current (EBIC) mode of SEM operation, regarded as a powerful tool for the analysis and evaluation of bipolar devices, would appear to be the most likely tool for locating such shorts.¹ However, results from other failure analysis laboratories and JPL have been mixed and often unsatisfactory; the reasons include:

1. SEM/EBIC operator experience;
2. type of EBIC amplifier and method of connection to the SEM;
3. availability of EBIC signals only from the device external pins; and
4. low level of some EBIC signals owing to multiple parallel current paths on the chip.

This paper describes an extension of the EBIC technique which removes many of these limitations and permits unambiguous location of the failure site in many cases, even when the defect is hidden by gate metallization.

Description of Technique

Initially the analysis is conventional, with pin-to-pin curve tracer checks of all inputs and outputs, as well as functional and parametric testing. If a leakage path is detected, the device is delidded, examined microscopically, and then exposed to a chemical etch to remove the glassivation. The device is then retested to verify presence of the shorts.

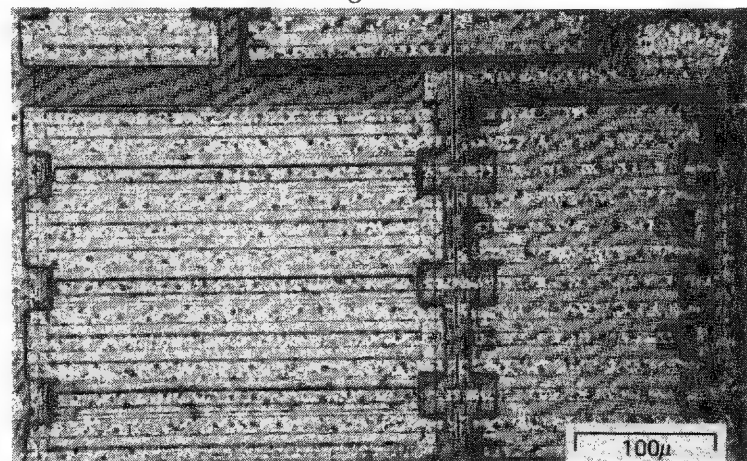


FIG. 1.--Basic CMOS inverter circuit showing isolation used to localize defect site.

The failed part is then placed in a mechanical probe station, where the short is traced to a particular transistor, and then to a particular gate stripe by a systematic scribing open of the metal lines. In the example shown in Fig. 1, a basic CMOS inverter circuit, all gate fingers and the inverter input and output may be isolated by scribing along a single line, as indicated.

Successful isolation of individual gate stripes requires a highly stable probe station and probe manipulators with linear motion and a minimum of backlash or wandering. For this work, three-axis, micrometer-driven manipu-

The research described in this paper was carried out at the Jet Propulsion Laboratory (JPL), California Institute of Technology, Pasadena, CA 91109, under NASA Contract NAS7-100. The authors, who are with the JPL Electronic Parts Engineering Department, would like to thank Dr. Alex Shumka for reviewing the paper and for his many helpful suggestions; and Mr. James Beall, for his advice and encouragement.

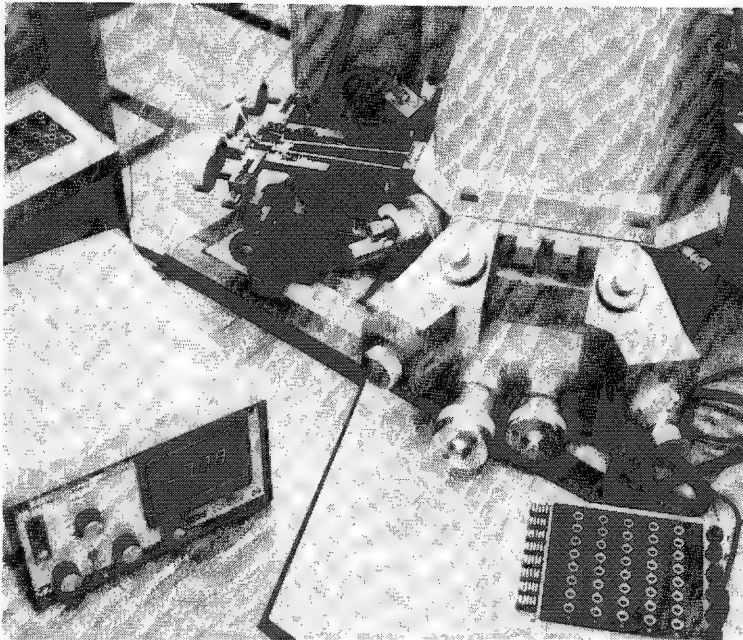


FIG. 2.--Probe system, amplifier, and breakout box shown attached to Cambridge S4-10 SEM.

lators made by Kulicke and Soffa Manufacturing Co. were used, with probe carriers from Alessi Industries.

The part is then mounted in the SEM for EBIC examination. Internal probes are positioned on the suspect gate metallization and an adjacent source line while the normal SEM image is observed. The EBIC signal obtained from these probes is utilized to pinpoint the failure site and document its location. The EBIC image, superimposed on a secondary electron image, can then be used to identify the actual oxide breakdown site after the metallization has been chemically removed.

The SEM equipment is shown in Fig. 2. Internal probing is accomplished with the use of an Ernest F. Fullam two-probe micromanipulator mounted to the side port of a Cambridge S4-10 SEM. The two probes are connected through shielded leads to the input of a GW Electronics digital specimen current amplifier, type 9DM.

Results

The examples that follow are of gate shorts in the n-channel transistor of an aluminum gate CMOS inverter. However, the techniques developed and the interpretations discussed in the following paragraphs may be readily applied to p-channel transistors and more complex circuits. Results obtained on both n-channel and p-channel transistors may vary, depending on the probe contact points, as discussed later in this paper.

The two most common types of shorts encountered were gate-to-source and gate-to-channel. Gate-to-source shorts had a diode curve tracer characteristic between the input and V_{SS} (Fig. 3a). Gate-to-channel shorts produced a resistive characteristic to V_{SS} (Fig. 3b). These short characteristics are explained by the fact that the aluminum gate material alloys with the underlying silicon through an oxide pinhole or ESD site and produces a p+ region at that point. Thus, the contact would be resistive to the p-type channel material and rectifying to the n-type source or drain diffusions. After removal of the glassivation and scribing to isolate the shorted gate stripe from all other circuitry, probing confirmed the short characteristics (Fig. 3c and d). Figures 4(a) and (b) show EBIC images for the two types of shorts commonly encountered. Note that the rectifying short to the source stands out clearly as a small bright spot (Fig. 4a), whereas the resistive short to the channel is revealed as a diffuse bright area surrounding the shorting site. A proposed explanation for this difference follows in the discussion section. Final examination of these shorting sites was readily accomplished, using the SEM/EBIC micrographs as maps to locate the sites after metallization removal. Figures 4(c) and (d) illustrate these typical shorting sites, revealed as oxide defects.

Results such as those in Fig. 4 have been readily attainable at moderate gain settings of the amplifier (10^{-8} to 10^{-9} A range). When these areas were examined by conventional EBIC (without scribing, and with the amplifier connected to the external device pins), the shorting sites were generally revealed poorly or not at all, even at the maximum amplifier gain (10^{-11} A range). Thus, in most cases, the technique has greatly enhanced the detectability of shorting sites. For complex circuits with transistors not directly accessible to the external pins, it may be the only way to locate such failure sites.

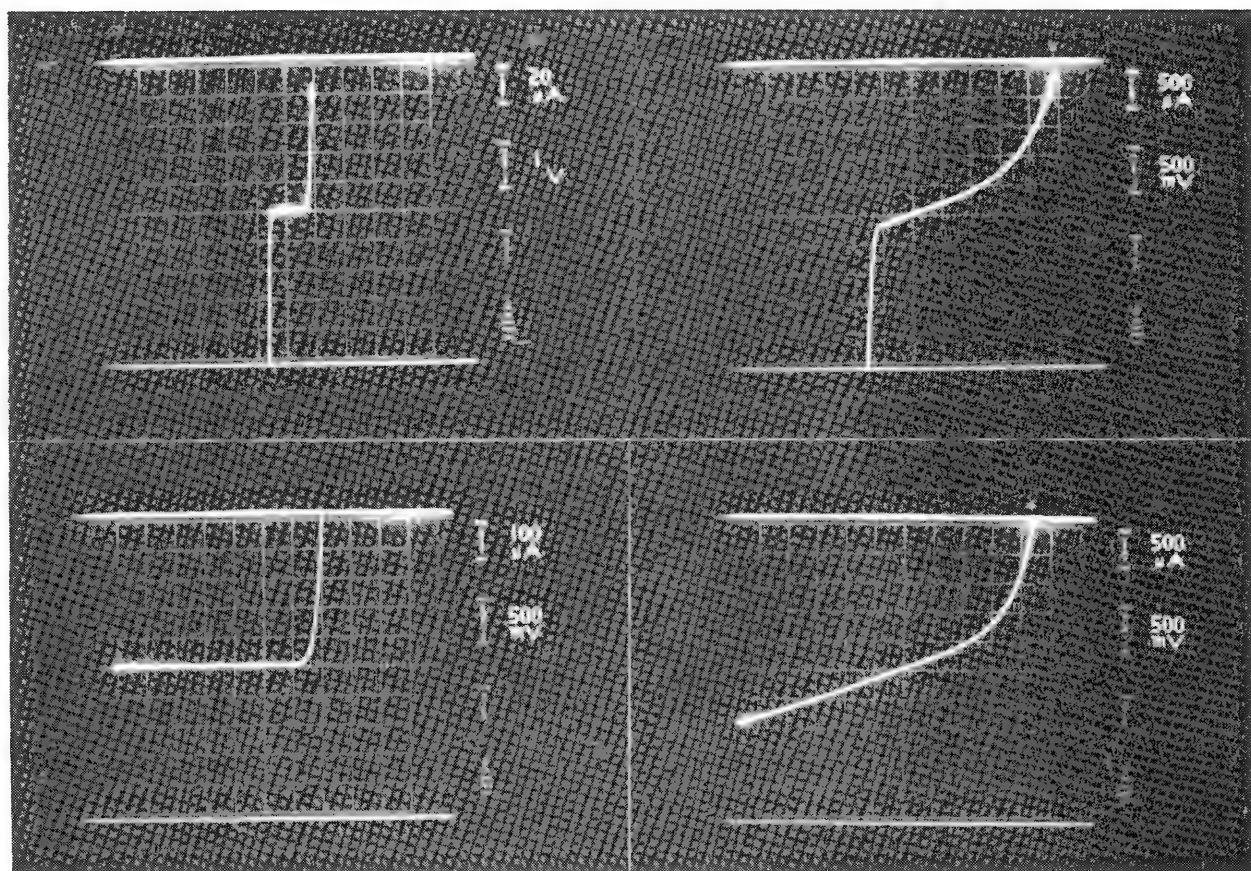


FIG. 3.--Curve tracer photographs: (a) intact device with gate-to- V_{SS} (source) short, connections between input and V_{SS} (source); (b) intact device with gate-to-channel resistive short, connections between input and V_{SS} (source); (c) isolated device with gate-to- V_{SS} (source) short, connections between isolated gate stripe containing short and V_{SS} (source); (d) isolated device with gate-to-channel resistive short, connections between isolated gate stripe containing short and V_{SS} (source).

Discussion

The two examples exhibited distinctly different types of EBIC images. The small bright spot observed at rectifying gate-to-source or gate-to-drain shorts was expected, as the junction formed by alloying of the gate aluminum at the shorting site produces a normal EBIC signal when the SEM electron beam approaches within the diffusion length for electrons or holes. Gate-to-channel shorts do not produce such junctions (n-channel transistors), and should not themselves produce an EBIC signal, but an EBIC response was observed over a relatively large area surrounding the shorting site. The explanation may be found by consideration of the internal construction of the device. The source and drain diffusions are in intimate contact with their respective metallizations along their entire length. However, the channel region makes contact with the source metallization only at each end of the source diffusion. Thus, the channel may be represented schematically as a distributed resistance and diode network (Fig. 5). For a resistive gate-to-channel (short), the shorting resistance R_s makes contact to the channel at some point along this distributed network, and permits a portion of the EBIC signal generated by the source-to-channel junction to be sensed by the EBIC amplifier. The resultant signal behavior may be predicted from the equivalent circuit (Fig. 6) if it is assumed that the voltage generated across the source-channel junction is insufficient to forward bias the distributed diodes. Thus, the observed diffuse region of EBIC signal around the non-rectifying gate-to-channel short actually is derived through a resistive divider network from the source-to-channel junction.

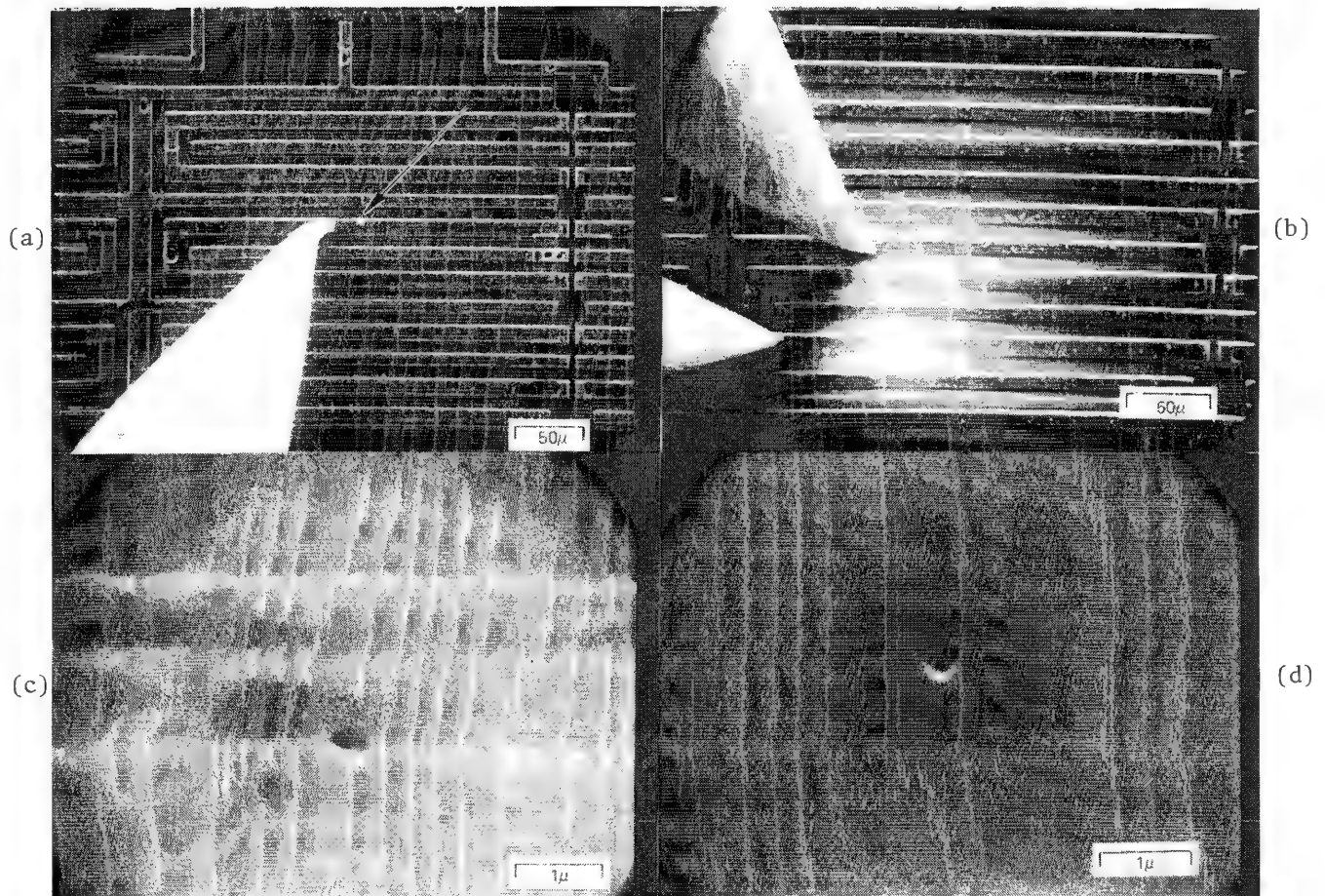


FIG. 4.--SEM micrographs: (a) gate-to- V_{SS} (source) short (arrow), mixed EBIC and secondary emission signal, note scribed isolation at right; (b) gate-to-channel short, mixed EBIC and secondary emission signal, note scribed gate isolation at right; (c) gate-to- V_{SS} (source) leakage site following metallization removal; (d) gate-to-channel leakage site following metallization removal.

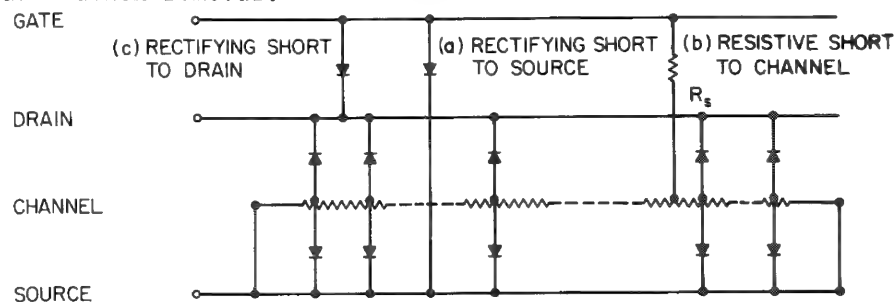


FIG. 5.--Distributed resistor/diode representation of n-channel transistor with three possible types of gate shorts.

For this simple treatment, it is possible to show that the EBIC signal E varies according to the following formula as the SEM electron beam is scanned along the source-to-channel junction.

$$E \propto I_0 R_c (X_s)(1 - X_s) X_B$$

where X_s = normalized position of short along the channel ($0 \leq X_s \leq 1$), X_B = normalized position of electron beam between end of channel and short ($0 \leq X_B \leq 1$), R_c = total channel resistance $R_1 + R_2 + R_3$, and I_0 = beam-induced current at the point on the junction excited by the electron beam

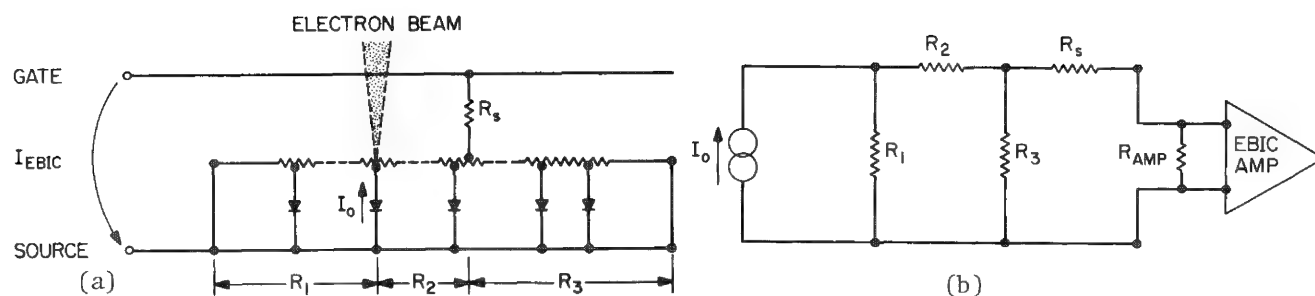


FIG. 6.--(a) Distributed network representation: I_0 is current generated by SEM electron beam impinging on source-to-channel junction; (b) resistive divider network derived from distributed network, R_{AMP} is input impedance of EBIC amplifier, may be $\gg R_1, R_2, R_3$ (R_{AMP} is 27 K Ω for this work).

Therefore, the EBIC signal would vary linearly from zero at each end of the channel to a maximum at a point on the junction nearest the shorting site. Also, shorts occurring near the ends of the channel would generate only a very weak EBIC signal, and would be difficult or impossible to detect.

From similar considerations of the equivalent circuit of the isolated n-channel and p-channel transistors, it is possible to predict which junctions should be observed on EBIC images. These junctions differ for various types of shorts and according to how the probes are connected to the transistor. These results are summarized in Table 1.

TABLE 1.--Expected EBIC images of transistor and gate short junctions.

EBIC AMPLIFIER CONNECTION	N-CHANNEL TRANSISTOR			P-CHANNEL TRANSISTOR		
	SHORTING SITE JUNCTION	SOURCE TO CHANNEL JUNCTION	DRAIN TO CHANNEL JUNCTION	SHORTING SITE JUNCTION	SOURCE TO CHANNEL JUNCTION	DRAIN TO CHANNEL JUNCTION
Gate to Source	A-Strong C-Weak	B-Strong Near short; Weak near ends of channel	C-Weak	E-Strong	E-Strong near short; Weak near ends of channel F-Weak	F-Strong
Gate to Drain	C-Strong	A-Weak	*B-Strong near short	E-Strong	D-Weak	D-Strong E-Strongest near short
Source to Drain	No Image	Weak Image	Strong Image	No Image	Weak Image	Strong Image

A - Rectifying Short to Source
B - Resistive Short to Channel
C - Rectifying Short to Drain

D - Resistive Short to Source
E - Rectifying Short to Channel
F - Resistive Short to Drain

NOTE: Table lists relative strength of EBIC signal from various junctions, for different amplifier connections (left column) and types of gate shorts (aluminum gate transistors). Example (*): For amplifier connected between gate and drain, the drain to channel junction of an n-channel transistor will be imaged strongly if a type "B" short exists, but not for type A or C shorts.

The EBIC signal is generated only by the p-n junctions inherent in the transistor structure and by junctions resulting from rectifying-type shorts. Thus, Table 1 tells which of these junctions will appear on an EBIC image of the transistors, for any combination of short type and amplifier connection. Multiple shorts, nonaluminum gate devices and closed-cell geometry (i.e., C²L* construction) are not considered. By study of Table 1, or construction of a similar table for other geometries, it should be possible to choose the optimum points for placing the probes onto the transistor circuit lines.

Some limitations in detectability of shorting sites result from the structure of the transistors. As already noted, gate-to-channel shorts may not be detectable if they occur near either end of the channel, because the EBIC signal is shorted out by the source-to-channel contacts at each end. Also, for p-channel transistors, gate-to-source and gate-to-drain shorts (both nonrectifying) would not result in localized EBIC signals, and thus the technique would not permit exact localization of these types of shorting sites.

Conclusions

The results indicate that the scribe, isolation, and internal SEM probe technique is a valuable tool for the failure analysis of CMOS devices. The technique eliminates parallel paths, provides a stronger EBIC signal and avoids confusion by removal of other transistor junctions. It also permits EBIC examination of internal transistors of complex devices when no direct access is provided by external pins.

It has also been shown that some nonrectifying types of gate shorts can be localized by their effect on the EBIC signal generated in nearby junctions.

Reference

1. J. R. Beall, *Study of SEM Induced Current and Voltage Contrast Modes to Assess Semiconductor Reliability*, Final Report NASA/MSFC NAS8-31567, 1976.

*RCA Trademark.

BACKSCATTERED ELECTRON CHANNELING CONTRAST APPLIED TO LASER-ANNEALED POLYSILICON

R. H. Geiss, T. Sedgwick, V. E. Hanchett, and S. W. Depp

Technologically there is great interest in the development of methods for growing single-crystal silicon on amorphous substrates. A successful processing technique would give the device designer the potential for building CMOS, MESFET, or other devices on an insulating layer or even multilevel devices on a silicon substrate while reducing the capacitance and improving isolation between devices separated by buried insulating regions in the silicon matrix. Many different experimental approaches are being pursued at present in hope of achieving this special form of crystal growth. These approaches include graphoepitaxy,¹ small island growth,² "explosive crystal growth,"³ and nucleated lateral crystal growth.^{4,5}

Conventional monitoring of the growth progress is by optical microscopy after "Secco" etching⁶ the wafers to delineate the grain boundaries. Crystallographic information is not readily available through optical microscopy and there is an undesirable fundamental limitation to the image resolution.

Occasionally, thin films are prepared and studied in the transmission electron microscope⁷; however, here it is almost impossible to prepare specimens to study very large areas. Also, both etching and thinning are destructive tests and eliminate any further processing of the sample.

To surmount these problems, the technique of observing backscattered electron (BSE) channeling contrast and diffraction patterns in the SEM and S(TEM) provides for both single crystal growth observation and crystallographic orientation evaluation. Although the technique of BSE channeling has been widely studied,⁸ this is the first time it has been applied to the problem of laterally nucleated silicon single-crystal growth on insulating substrates. In this paper, the experimental details are presented along with results that show some very large ($> 50\mu\text{m} \times 1\text{mm}$) single-crystal overgrowths obtained by nucleated crystal growth.

Experimental

Nucleated lateral crystal growth involves the melting and subsequent crystal growth of a deposited polysilicon film, first vertically over a base silicon substrate seed region and then laterally up over an amorphous film in an adjacent region (Fig. 1). Energy for the local melting and lateral growth is provided by a laser beam scanned in a serpentine pattern.⁵

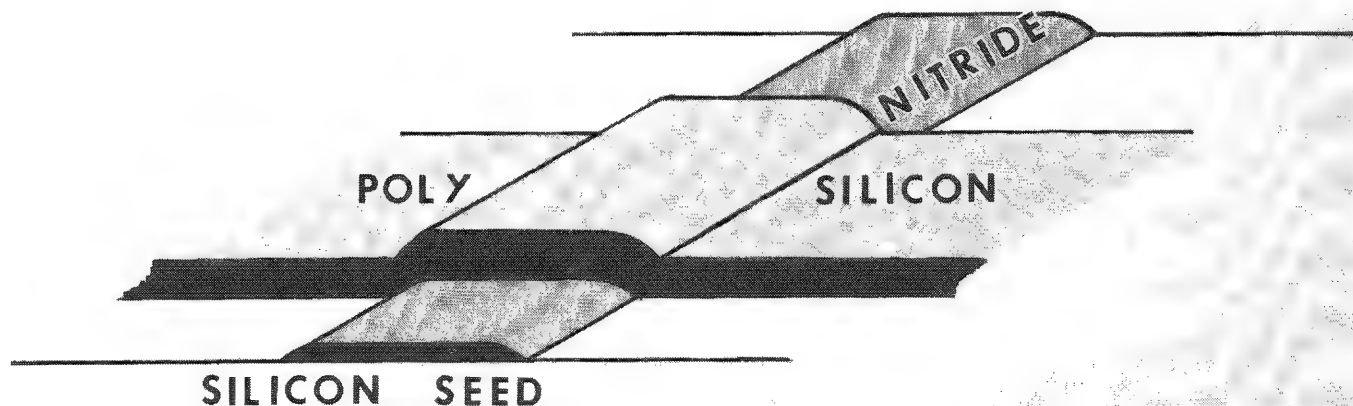


FIG. 1.--Schematic representation of polysilicon film, amorphous silicon nitride film, and silicon seed single-crystal substrate showing relative orientation.

The authors are at the IBM Research Division, San Jose, CA 95193.

The basic sample structure is shown in Fig. 1; a wide range of nitride and polycrystalline silicon (poly Si) linewidths were used for the crystal growth experiments. Nitride lines were initially formed on an Si (001) wafer along the [100] direction by LPCVD and RIE. Poly Si lines orthogonal to the nitride lines and in [010] directions were then formed by a vapor deposition process and subsequent etching. Finally, the samples were either coated with Si_3N_4 or SiO_2 , or left uncovered prior to laser scanning.

Samples for crystal growth were held by vacuum on a hot stage and scanned with an argon ion laser beam. The beam was focused with a 90mm f/1.0 lens and the sample was positioned 3 mm from the focal plane. The width of a single melted line was 50-100 μm . The scanning apparatus used two galvanometer-driven mirrors controlled by a microprocessor.

After annealing, the resulting single-crystal growth was studied by observation of crystallographic contrast in the BSE-channeling mode. In this mode, crystalline regions, or small grains, oriented with a major axis deviating less than the Bragg angle from the incident electron beam backscatter strongly and thus appear bright in the image. A qualitative explanation follows from consideration of the two-beam dynamical theory of electron diffraction. According to the theory, an electron inside a crystal may be described in terms of two Bloch waves: Type I, with antinodes coinciding with the atomic planes; and Type II, with antinodes located between the atomic planes. When the angle of incidence of the electron beam θ with respect to the atomic (reflecting) planes is less than the Bragg angle θ_B , it can be shown that Bloch wave I is preferentially excited. The Bragg angle for low index planes in silicon at 25 keV is typically about 1° . On the other hand, for $\theta > \theta_B$, Bloch wave II is dominant. Consequently, when $\theta < \theta_B$, the incident electrons are very strongly backscattered and crystalline regions in this orientation appear brighter in the image. Crystalline regions, or small grains, not so favorably oriented appear with varying shades of gray. A more complete discussion may be found in Ref. 9.

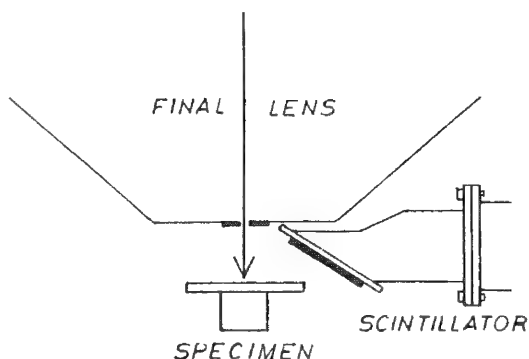


FIG. 2.--Schematic of final lens, BSE detector, and specimen position in SEM.

The experimental configuration for observing the BSE channeling contrast in the Hitachi S-500 SEM is shown schematically in Fig. 2. The working distance was varied between 10 and 15 mm depending on the specimen size. Images were taken over a magnification range of $100\times$ to $18\,000\times$. In the latter case, individual grains in the polysilicon as small as 500 \AA in diameter could be identified. The BSE detector is a scintillator/photomultiplier with an active area of about 250 mm^2 . Specimens for oriented near normal with the channeling contrast optimized for the single crystal silicon overgrowth.

Channeling diffraction patterns were obtained from large (approximately 25mm^2) areas of the silicon wafer with the SEM, operated in a very low magnification mode ($< 50\times$), with the specimen positioned at 10-15 mm working distance and the objective lens current as low as possible. Smaller-area (less than 5 μm in diameter) channeling diffraction patterns were obtained by means of a Philips 301 S(TEM) in the SEM mode at various accelerating voltages. The detector was a surface barrier diode placed as close to the specimen as possible. The small rocking probe was obtained from a highly excited objective lens and the patterns were focused by means of the second condenser lens. Since the specimens are in the center of the strong magnetic field of the objective lens, some curvature of the patterns was observed, especially for wide-angle patterns at low accelerating voltages. These patterns were used to characterize the silicon overgrowth and defect regions.

Results

Figure 3 is a BSE channeling micrograph showing a 5-10 μm single-crystal growth over the right-hand edge of the nitride film. The uniformly bright region shows the single-crystal growth and the darker contrast region suggests the formation of many large grains.

Finally, near the left-hand side of the micrograph, individual grains of the original polysilicon can be distinguished. Selected area backscattered electron channeling diffraction patterns (BSE-CDP) from similar specimens support this analysis, showing there is no change in the diffraction pattern of the silicon overgrowth from the seed area onto the nitride film until the boundary where the large grains nucleated is reached. Careful study of the micrograph shows there are many differently oriented large grains that nucleate at the terminus of the single crystal region. The fact that the contrast of these grains is quite different from that of the single-crystal growth region, which is [001] oriented normal to the surface, indicates that the misorientation is at least a few degrees and could be quite large, perhaps many tens of degrees.



FIG. 3.--BSE-channeling micrograph showing results of early experiments at laterally nucleated silicon crystal overgrowth. Bright area is single-crystal silicon growth; darker regions are variously oriented grains in polysilicon.

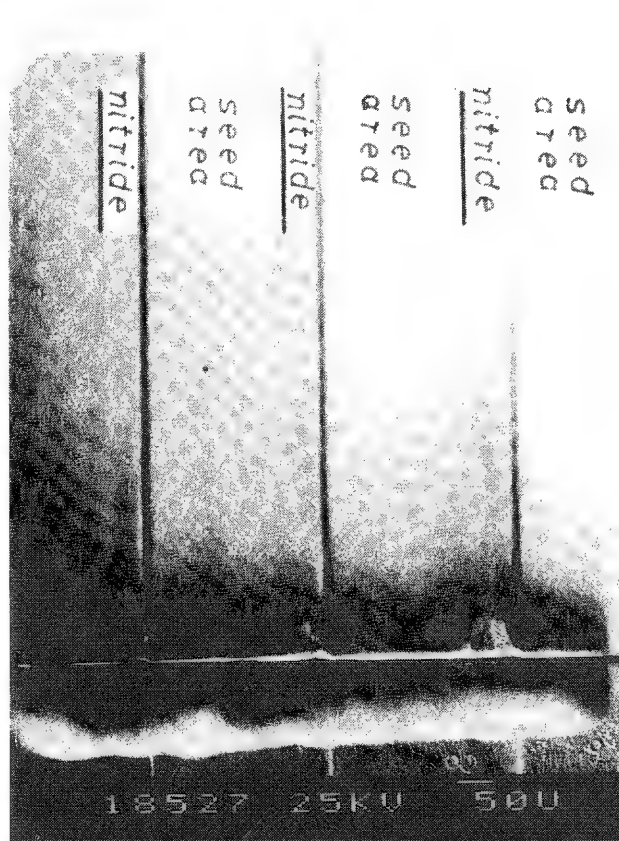


FIG. 4.--BSE-channeling micrograph showing successful laterally nucleated overgrowth over very large area.

Near-perfect overgrowth has been obtained over large areas, except for occasional small defects at various interfaces of the overgrowth regions. Figure 4 shows three near-perfect stripes extending 60-75 μm wide and over 1 mm long, with only slightly defective ends where there is some pullback of the melted silicon. The dark line on the right side of each stripe is a morphology change. BSE-CDP from the seed and overgrowth areas are identical (Fig. 5), which means perfect registry between the seed and the laterally nucleated overgrowths. The orientation of these defects relative to the single crystal region is being studied by means of BSE-CDP and will be discussed in detail in a forthcoming publication.

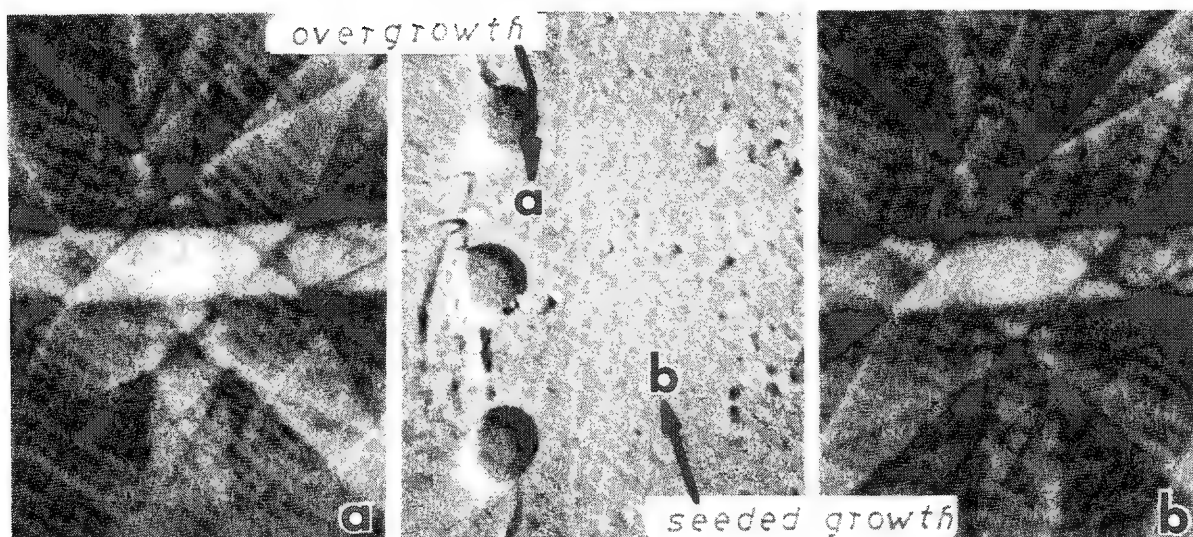


FIG. 5.--BSE-CDP from (a) laterally nucleated overgrowth and (b) seeded growth regions showing that identical crystalline orientation is maintained in overgrowth.

Conclusions

Backscattered electron channeling contrast and diffraction patterns have been shown to be superior to the conventional methods of etching/optical microscopy and transmission electron microscopy for studying laser annealing of polysilicon. The extent of the silicon single-crystal overgrowth and details of other grain growth can be easily observed by means of BSE-channeling contrast. Crystal orientation of any component of the annealed silicon may be obtained from the BSE-CDP. Proper utilization of these techniques has helped speed a successful study of nucleated lateral crystal growth.

References

1. M. W. Geis, D. C. Flanders, and H. L. Smith, *Appl. Phys. Lett.* 35: 71, 1979.
2. J. F. Gibbons, K. F. Lee, T. J. Magee, J. Peng, and R. Ormond, *Appl. Phys. Lett.* 34: 831, 1979.
3. H. J. Leamy, W. L. Brown, G. Celler, G. Foti, and G. H. Gilmer, *Appl. Phys. Lett.* 38: 137, 1981.
4. H. W. Lam, R. F. Pinizzotto, and A. F. Tasch Jr., *Electrochem. Soc.* (in press).
5. T. O. Sedgwick, B. G. Huth, S. W. Depp, R. H. Geiss, V. E. Hanchett, and V. J. Silvestri, *Proc. Fifth International Conf. Vapor Growth and Epitaxy and Fifth Am. Conf. on Crystal Growth*, Coronado, Calif., 1981.
6. F. Secco d'Aragona, *J. Electrochem. Soc.* 119: 948, 1972.
7. A. Gat, L. Gerzberg, J. F. Gibbons, T. J. Magee, J. Peng, and J. D. Hong, *Appl. Phys. Lett.* 33: 775, 1978.
8. D. G. Coates, *Phil. Mag.* 16: 1179, 1967.
9. J. I. Goldstein and Harvey Yakowitz, Eds., *Practical Scanning Electron Microscopy*, New York: Plenum Press, 1975, chap. 5, 149-210.

MONTE CARLO SIMULATION OF SUBMICROMETER LINEWIDTH MEASUREMENTS IN THE SCANNING ELECTRON MICROSCOPE

G. G. Hembree, S. W. Jensen, and J. F. Marchiando

A computer program has been developed which models, by a Monte Carlo procedure, electron-specimen interactions involved in the generation of backscattered electron (BSE) profiles of submicrometer line objects in a scanning electron microscope (SEM). Such a predictive model is necessary to determine signal levels in a BSE profile which correspond to the edges of the line feature for various line and substrate compositions, line geometries, and SEM operating parameters. These signal levels are edge-location thresholds for experimental measurements of linewidths made by a piezoelectrically scanned stage whose displacement is measured by laser interferometry.¹ This project is part of a continuing effort to establish a national calibration facility for reference artifacts in the 0.1-100 μ m range.²

Monte Carlo Method

Monte Carlo simulation of both the BSE and the secondary electron profiles of micrometer-size objects has been reported previously by several authors. George and Robinson have calculated the image profiles expected for various small topographic and atomic-number variations in SEM specimens.³ Stephani and Lin et al. computed registration mark BSE profiles for electron-beam lithography applications.^{4,5} Of these three groups only Stephani included the detector acceptance solid angle and energy response in his model.

The specific Monte Carlo procedure followed here is similar to that described by Curgenven and Duncumb and incorporates the modifications suggested by Love et al.^{6,7} Each electron trajectory was divided into 100 steps of fixed length equal to 1/100 of the Bethe range for the incident beam energy. The form of the Rutherford law used for the distribution of polar scattering angles included an adjustable maximum impact parameter. This parameter was varied until the Monte Carlo program reproduced the experimental backscatter coefficient from a smooth surface of a single material to within the standard deviation of the simulation. Normally 20 000 electron trajectories were calculated and the resulting standard deviation was a few per cent. The experimental backscatter coefficients used for impact parameter determination were those of Hunger and Kuchler.⁸

The topography of the symmetric line object is specified by four parameters in the computer program. These values determine the line height, width, and edge angle and the distance from the incident beam impact point to the left line edge. The transition from line material to substrate material was taken as the z-axis zero point. Stepping of the incident beam across the edge creates the simulated BSE profile.

The SEM system characteristics included in the model are the electron beam size and energy and the parameters of the BSE detector. To account for the finite probe size a Gaussian random-number generator is used to produce a distribution of electron impacts about the nominal point of incidence. The response of a split-annular silicon diode BSE detector is allowed for by a procedure that counts only electrons scattered into the solid angle subtended by the detector and linearly weights the detected electrons by their energy.

Results

The experimental situation of immediate interest involves the measurement of photo-mask linewidth calibration artifacts such as NBS Standard Reference Material (SRM) 474.⁹ The total BSE profile resulting from an approximate model of the 0.5 μ m-wide line on this artifact is shown in Fig. 1. The geometric parameters of the line are nominally the same in both the model and the artifact; the material parameters are different. The actual substrate material is borosilicate glass instead of pure silicon and the chromium lines are thinly coated with chromium oxide on the SRM. Despite these differences the computed profiles are useful as indicators of the effect that variation in the model parameters

The authors are at the National Bureau of Standards, Washington, DC 20234.

have on the BSE signal level at the edge location. As shown in Fig. 1, the given model parameters result in a computed BSE profile in which the line material edges, as marked by the arrows, correspond quite closely to the break in slope at the bottom of the rise the BSE signal.

Of the SEM parameters included in the simulation only the incident beam energy when varied causes dramatic changes in the BSE profile. This behavior is demonstrated by the profiles of the line edge region that appear in Fig. 2. We see that we can gain a substantial increase in BSE contrast by lowering the incident electron energy while all other parameters remain constant. However, this beneficial effect is

countered by the increase in electron-beam diameter and the decrease in both the beam current and the sensitivity of the electron detector at lower energies. The results shown in Fig. 2 were obtained for a 10nm incident beam and total BSE collection. Further modeling shows that an increase to a 50nm beam diameter is required before statistically significant changes are produced in the BSE profile. The only change noted due to this beam-diameter increase was a slight broadening of the region of transition from substrate to line signal levels. For the object with 70° line edge slopes inclusion of the detector characteristics in the model does not change the BSE profile shape. In addition, the right and left detector halves produce the same BSE signal so that a difference (topographic) image would be of no use for the situation modeled.

Changes in the parameters of the line object have a more direct effect on the BSE profile than do changes in the parameters of the SEM system. Increasing the ratio of the atomic number of the line material to that of the substrate material increases the contrast available from a given line geometry. This behavior is clearly demonstrated in Fig. 3. Figure 4 shows that for an increase in edge slope from 60° to 80° there is little change in the BSE profile except for a shortening of the transition region, which is directly attributable to the physical change in line shape. However, for an edge slope of 90° the BSE profile exhibits a rise from the substrate level well before the actual material edge and an overshoot to signal levels above that of the line material. As a consequence of this sudden rise in signal levels, the level corresponding to the line material edge is much greater for the 90° edge slope than the level for a 70° edge slope. As shown in Fig. 5, these edge effects vary with line thickness; in particular, the maximum of the overshoot first increases and then decreases slightly as the thickness is increased.

The Monte Carlo modeling results described above lead to a number of insights with respect to the accurate assignment of the BSE signal level which corresponds to the actual edge of the line material. Obviously, any change that improves the contrast between the substrate and line makes the break in slope in the BSE profile (corresponding to the line edge) more clearly visible. The parameters that affect contrast most significantly are incident electron energy, line-to-substrate atomic number ratio, line thickness, and edge slope. Of these factors only the first is easily controllable by the SEM operator and it must be balanced against increases in beam diameter and decreases in beam current and detector sensitivity needed if a reasonable signal-to-noise ratio in the experimental BSE profile is to be achieved. The effect of the remaining, specimen-related parameters should be used as a guide in the fabrication of linewidth calibration artifacts so that optimum measurement conditions can be maintained. For example, the line edge slope should ideally be about 70° if one is to avoid the ambiguities that result from edge effects near 90° while a narrow transition region from substrate to line signal levels is maintained;

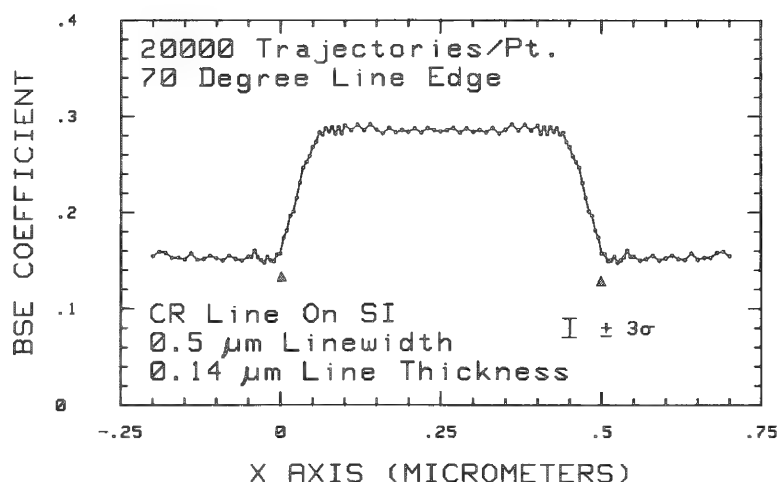


FIG. 1.--Total backscattered electron coefficient profile generated by a 20keV, 10nm-diam. Gaussian electron beam simulated by Monte Carlo procedure; error bar indicates size of 99% confidence interval of calculation.

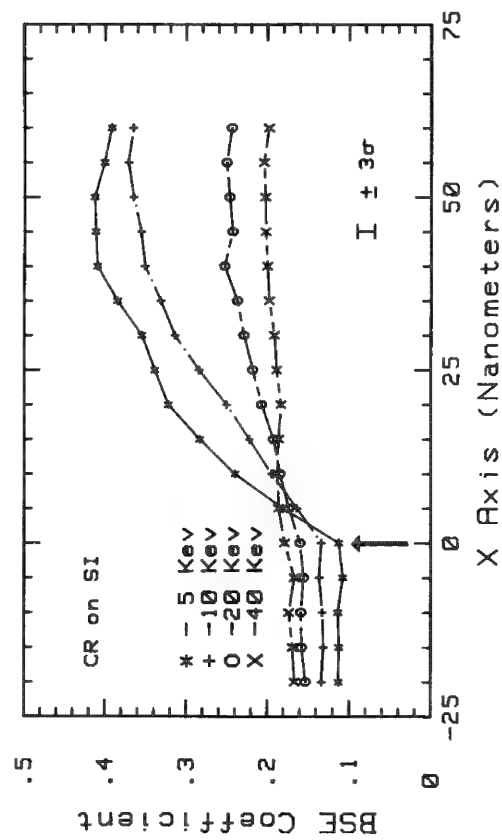


FIG. 2.--Change in calculated BSE profile at material line edge with varying incident electron beam energy; 30 000 trajectories per point, all other parameters same as in Fig. 1.

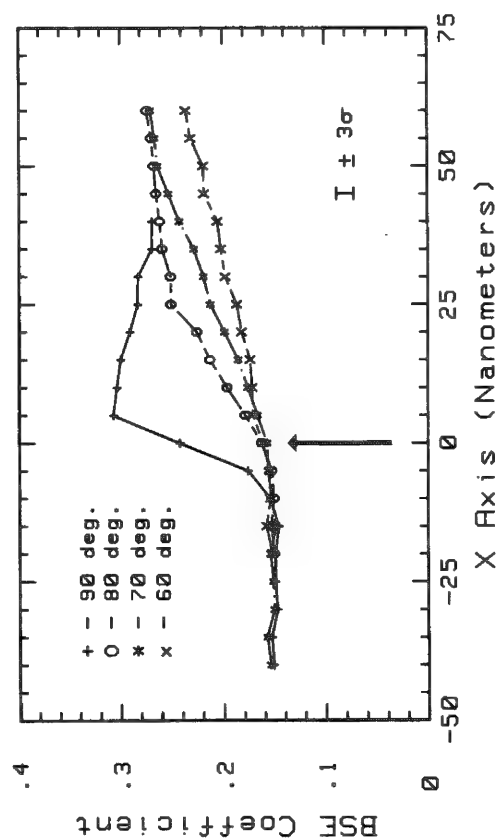


FIG. 4.--Variation in calculated BSE profile caused by changes in line edge slope angle; all other parameters same as in Fig. 1.

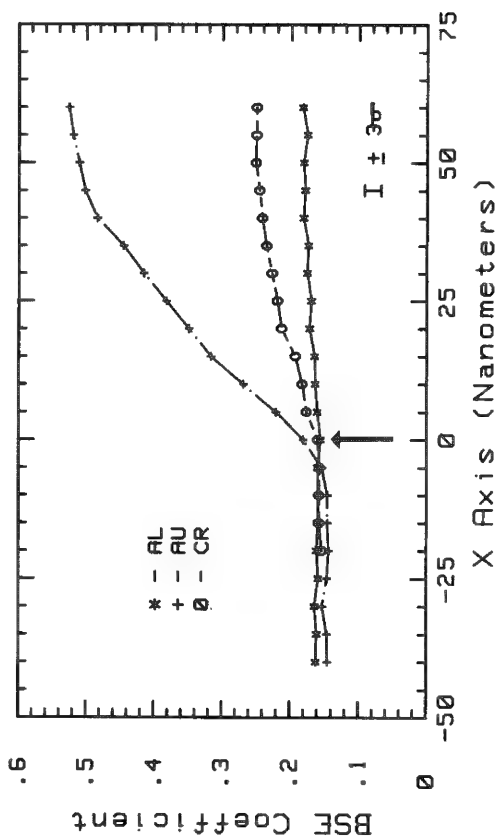


FIG. 3.--Calculated BSE profiles of various line materials on a silicon substrate; all other parameters same as in Fig. 1.

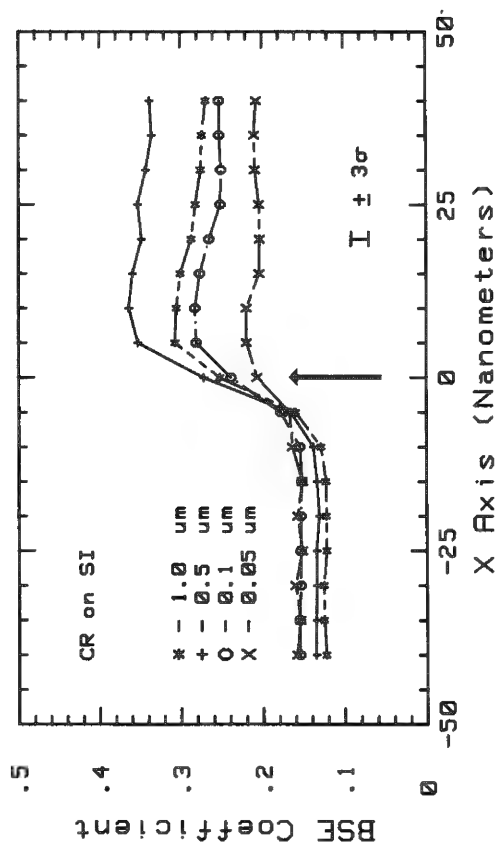


FIG. 5.--Calculated BSE profiles at material line edge for lines of different thickness; 90° edge slope, all other parameters same as in Fig. 1.

and in the case of chromium lines on a silicon substrate, the line material should be somewhat thicker than the 140nm-thick lines now available in order to maximize the available contrast.

References

1. S. W. Jensen, "Planar micrometrology in the SEM," *Microbeam Analysis--1980*, 77.
2. D. A. Swyt and S. W. Jensen, "An electron-microscope-based system for accurate microdimensional measurements," *Precision Engineering* 3: 11, 1981.
3. E. P. George and V. N. E. Robinson, "The dependence of SEM contrast upon electron penetration," *SEM/1976* I, 17.
4. D. Stephani, "Monte-Carlo calculations of back-scattered electrons at registration marks," *J. Vac. Sci. Technology* 16: 1739, 1980.
5. Yi-Ching Lin, I. Adesida, and A. R. Neureuther, "Monte Carlo simulation of registration signals for electron beam microfabrication," *Appl. Phys. Lett.* 36: 672, 1980.
6. L. Curgeven and P. Duncumbe, "Simulation of electron trajectories in a solid target by a simple Monte Carlo technique," *Tube Investments Research Reports* 303.
7. G. Love, M. G. C. Cox, and V. D. Scott, "A simple Monte Carlo Method for simulating electron-solid interactions and its application to electron probe microanalysis," *J. Phys. D10*: 7, 1977.
8. H. J. Hunger and L. Kuchler, "Measurements of the electron backscattering coefficient for quantitative EPMA in the energy range of 4 to 40 keV," *Phys. Stat. Sol. A* 56: K45, 1979.
9. D. A. Swyt, "Design of a pattern on a photomask-like physical standard for evaluation and calibration of linewidth-measuring systems," *Solid State Technology*: 35, January 1978.

CALCULATION OF TYPE-1 MAGNETIC CONTRAST IN THE SCANNING ELECTRON MICROSCOPE

Oliver C. Wells

Type-1 magnetic contrast arises in the scanning electron microscope (SEM) because the secondary electrons (SE) are deflected between the specimen and the collector by the fringing fields above the surface of the specimen.¹⁻⁸ This paper contains a simplified derivation of the magnitude of this contrast.

Parallel Stripe Domains

A specimen that contains parallel stripe domains can be approximated by the two-dimensional situation shown in Fig. 1. The z axis is at right angles to the surface of the specimen, the x axis is in the paper plane, and the y axis is at right angles to the plane of the paper. The incident electron beam is in the xz plane.

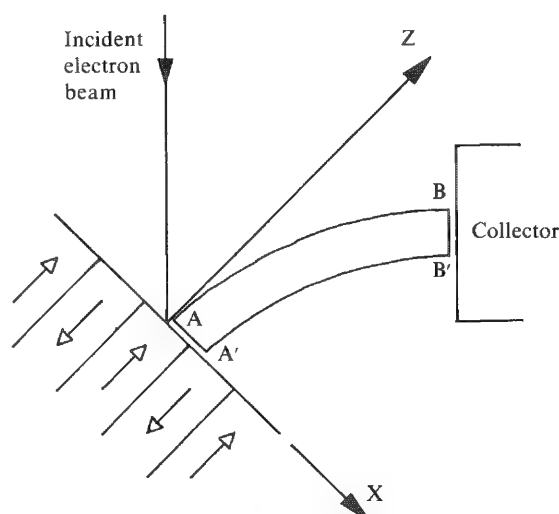


FIG. 1.--For two-dimensional magnetic field, integral of $B_z dl$ around contour ABB'A' is zero.

point on the surface of the specimen, and then expressed the expected magnetic contrast in terms of this amount.

To avoid the complications of the mathematics, Wells et al.⁷ wrote: "With some specimens the magnetic field has a peak flux of H G which is reversed at distances that are approximately uniform across the surface. If this distance is L cm, then the secondary electrons can experience a deflecting field that in most cases will be of the order of HL G-cm." It is the purpose of this paper to point out that under certain two-dimensional situations to be specified, the above approximation is exact.

Flux-times-distance Integral (FDI)

In many of the published analyses, it is assumed that the SEs move at constant velocity v through the fringing fields. The deflection θ of a SE in a small section of the trajectory in a two-dimensional situation such as is shown in Fig. 1 is then given by either

$$d\theta = \frac{e}{mv} B_z ds \quad (1)$$

The author is at the IBM Thomas J. Watson Research Center in Yorktown Heights, NY 10598. Helpful discussions with B. E. Argyle and D. C. Joy are gratefully acknowledged.

or

$$d(\sin \theta) = \frac{e}{mv} B_{\perp} dl \quad (2)$$

where θ is measured up or down from the xz plane in Fig. 1; ds is the element of path length measured along the SE trajectory; dl is the projection of the element ds into the xz plane; B_{\perp} is the (signed) component of B in the xz plane perpendicular to ds or dl ; and e and m are the charge and mass of the electron. If the SE is initially emitted in a direction in the xz plane, then the total deflection of a SE in moving from A to B is given by

$$\sin \theta = \frac{e}{mv} \int_A^B B_{\perp} dl \quad (3)$$

where the integral is calculated along the projection of the electron trajectory into the xz plane. It is convenient to define the flux-times-distance integral (FDI) along a line in the xz plane as

$$\text{FDI} \equiv \int B_{\perp} dl \quad (4)$$

The FDI has the following property. In the general case, the integral $\oint B \cdot dA$ is zero over a closed surface that does not contain magnetic poles. For a two-dimensional magnetic field, this is the same as saying that $\oint B_{\perp} dl$ is zero round a closed contour in the plane of the field.

In Fig. 1, an SE emitted from the specimen at A in a direction that initially lies in the paper plane follows a trajectory to the collector that projects into the line AB in that plane. Consider also the projection A'B' of the trajectory from a second point A' to the collector. If the FDI is different for AB and A'B', then the collected current will be different if the detector is sensitive to the fraction of the SE that arrive either above, or below, the paper plane. This difference can be calculated from the fact that the FDI around the contour ABB'A' is zero. In the situation shown in Fig. 1, the field at infinity above the specimen surface is zero. Thus, if the magnetic field B at the entrance of the collector is also zero, then it follows immediately that:

- (1) if SE are emitted from a point A in various different directions in the plane of the paper in Fig. 1, then the FDI between the specimen and the collector is the same for all of the trajectories that are so generated;
- (2) for two points A and A' as shown in Fig. 1, the *difference* in the FDI for AB and A'B' is numerically equal to the FDI along the line AA' between them, and for points that are close together, this is given by the product of the distance AA' and the z component B_z of the fringing field close to the surface of the specimen;
- (3) if the sample is symmetrical so that the FDI can be seen to be zero along a particular line between the specimen and the collector, then this method gives an absolute value for the FDI, and not just the difference between the FDI for two points; and
- (4) although the entire space in Fig. 1 is shown as being two-dimensional, in practice it might be expected that the deflection of the SE will be localized quite close to the specimen surface; thus, if the stripe domains are sufficiently long in relation to their width, then it is to be expected that these results will hold in the more general case also.

Mathematically, if the origin is at the center of a domain in Fig. 1 so that the FDI is zero by symmetry when $x = 0$, then between the origin and the domain wall,

$$\text{FDI} \equiv \int_A^B B_{\perp} dl = xB_z \quad (6)$$

where B_z is the z-component of the flux close to the surface of the specimen.

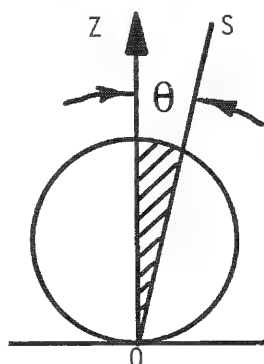
For an infinitely thick sample as shown in Fig. 1, the fringing flux B_z just above the surface of the sample should be equal to the saturation flux density $4\pi M_s$. If $4\pi M_s$ is substituted for B_z in Eq. 6 above, then this result is consistent with Eq. 3 in Yamamoto and Tsuno.⁸

Image Contrast

The image contrast C is defined as

$$C \equiv \frac{S_{\max} - S_{\min}}{S_{\text{average}}} \quad (6)$$

where S_{\max} and S_{\min} are the collected current as increased or as reduced by magnetic contrast, and S_{average} is the average collected current.



The change in the collected current S caused by the deflection θ of the SE is shown in Fig. 2. For a cosine angular distribution of SE, the average signal is proportional to half the volume of the sphere shown. The change in collected current is proportional to the region between the Z axis OZ and the line OS inclined at an angle θ to OZ . According to the present analysis, the deflection θ of the SE away from the xz plane is independent of the angle of emission of the SE from the specimen in that plane. The appropriate volume to represent the change in the collected current is therefore a cone defined by rotation of the line OS around the y axis in Fig. 2. For small values of θ this gives

$$S = 1 + \frac{16}{3\pi} \sin \theta \quad (7)$$

from which

$$C = 3.40 \sin \theta \quad (8)$$

FIG. 2.--Part of sphere between OZ and OS corresponds to change in collected current caused by deflection θ of SE.

Joy and Jakubovics⁶ and Wells et al.⁷ used different assumptions for the part of the sphere that corresponds to the signal; and these give values of 2.54 and 2.50 for the numerical coefficient in Eq. 8.

Cylindrical Symmetry

In the case of cylindrical symmetry, the integral that gives the deflection of a SE is no longer zero around a closed path. If we write down the condition that the total flux into the appropriate solid of revolution is zero, it follows that the maximum value of the FDI for a bubble (as calculated along a line parallel to the axis of symmetry of the bubble) is 0.25 times the diameter of the bubble times the fringing flux. These arguments can be used to justify the approximation that for a real sample, the peak-to-peak variation in the FDI between different points on the specimen and the collector might reasonably be expected to lie somewhere between 0.25 (for a bubble) and 1.0 (for a parallel-sided domain) times the domain width D or L multiplied by the fringing field.

References

1. D. M. Cort and J. W. Steeds, "A liquid helium cooled stage for the scanning electron microscope," *Proc. 5th Eur. Cong. Electron Microsc.*, The Institute of Physics, London and Bristol, 1972 376-377.
2. J. R. Dorsey, "Scanning electron probe measurement of magnetic fields," in L. L. Marton, Ed., *1st Nat. Conf. Electron Probe Microanalysis* (College Park, Md.), 1966, Paper 10.
3. J. R. Dorsey, "Scanning electron probe measurement of magnetic fields," in A. J. Tousimis and L. Marton, Eds., *Advances in Electronics and Electron Physics*, New York: Academic Press, 1969, Suppl. 6, 291-312.
4. D. J. Fathers, D. C. Joy, and J. P. Jakubovics, "Magnetic contrast in the SEM," *SEM/1973*, 242, 259-262.
5. G. A. Jones, "Magnetic contrast in the scanning electron microscope: An appraisal of techniques and their applications," *J. Magnetism & Mag. Mat.* 8: 263-285, 1978.

6. D. C. Joy and J. P. Jakubovics, "Scanning electron microscope study of the magnetic domain structure of cobalt single crystals," *Brit. J. Appl. Phys.* D2: 1367-1372 and 3 plates, 1969.
7. O. C. Wells, A. Boyde, E. Lifshin, and A. Rezanowich, in *Scanning Electron Microscopy*, New York: McGraw-Hill, 1974, 1978, 34-36 and 202-207.
8. T. Yamamoto and K. Tsuno, "Magnetic contrast in secondary electron images of uniaxial ferromagnetic materials obtained by scanning electron microscopy," *Phys. Stat. Sol.* A28: 479-487, 1975.

USE OF A MODULATED SEM BEAM FOR SOLAR CELL DIAGNOSTICS

S. Othmer and M. A. Hopkins

In this paper, a diagnostic technique for solar cells that uses a modulated scanning electron microscope (SEM) beam is described. With this technique, solar cell junction properties may be investigated with high spatial resolution and at injection levels appropriate to solar cell operation. Direct detection of the modulated component of the electron beam, without interception, is provided for, with a sensitivity of 2 pA. Faraday cup measurements of the modulated component of the beam current, and measurements of solar cell current, may be made with a resolution of 0.2 pA. Operating frequency range extends from 100 kHz to 50 MHz. With this technique, solar cell terminal currents have been measured over a range of beam energies from 3 to 33 keV, and the results analyzed to yield carrier collection efficiency as a function of depth into the cell.

Introduction

The scanning electron microscope has been used for solar cell diagnostics for some years and the utility of the SEM in this application is becoming more widely recognized. Direct measurements of bulk minority-carrier diffusion length are possible when the SEM is utilized as a point source of excess carriers. In such experiments, the electron-beam-induced current (EBIC) is measured as the beam is swept away from the periphery of a junction. In this manner, diffusion lengths ranging from 1 to 100 μm have been measured in silicon.¹ Use of special configurations has permitted measurements of submicron diffusion lengths in direct-gap materials.² Alternatively, analysis of the beam-induced current for direct injection into the junction has permitted diffusion lengths to be estimated which are small compared with the dimensions of the energy deposition volume of the SEM beam.³ More refined analysis of beam-induced current measurements based on different assumptions of energy-deposition profiles have recently been reported.^{4,5} The SEM has also been used in qualitative studies of recombination properties of grain boundaries in polycrystalline solar cells.^{6,7} In a similar manner, the SEM has been used to examine spatial fluctuations in surface recombination velocity,⁸ and to examine the oxygen distribution in Czochralski-grown silicon on the microscopic scale.⁹

In all these studies, the SEM has been employed essentially without modification, which entails a number of compromises when quantitative measurements of cell parameters are required. In the first place, the electron beam current is typically of such a magnitude (10^{-10} to 10^{-8} A) that high injection conditions prevail within the energy deposition volume. It has been customary to use defocused beams in order to reduce the injection level below that at which Auger recombination dominates.^{2,4,5} In the Auger regime, the induced excess density is nonlinearly related to the incident beam current. At injection ratios of the order of unity, the transport parameters (diffusivity, mobility) are those applicable to ambipolar conduction. Even at injection ratios considerably below unity, the minority-carrier diffusion length may exhibit a strong dependence on injection level.¹⁰ It is therefore important to perform quantitative studies at an injection level appropriate to the application; if the inherent spatial resolution of the SEM is to be maintained, reduction in beam current by factors of up to 10^3 over those used previously are required.

There are other motivations for such a reduction in probe current. The surface recombination velocity in a solar cell may be affected by the presence of the beam, which may serve to charge up metastable interface states in any insulating layer coating the cell, such as an antireflection coating. It is possible to generate sufficient positive trapped charge in a native oxide layer on silicon to invert the surface of p-type material, which may lead to misinterpretation of EBIC data. For the determination of intrinsic cell properties it is therefore essential that the SEM beam be minimally perturbing.

Authors Othmer and Hopkins are with Northrop Research and Technology Center, One Research Park, Palos Verdes Peninsula, CA 90274. The work was supported by the Solar Energy Research Institute, a prime contractor to the U. S. Department of Energy, under Subcontract XS-9-8313-1, Prime Contract EG-77-C-01-4042.

Reduction of beam current requires comparable improvement in signal recovery capability, and to this end we have employed a modulated beam which permits phase-sensitive detection with arbitrarily small noise bandwidths. Use of any convenient frequency would permit discrimination against the quiescent junction leakage current, so that measurements may be made as a function of applied bias. However, use of modulation frequencies in excess of 100 kHz also discriminates against the $1/f$ noise that strongly prevails in the large-area, unpassivated solar cell junctions being tested. Use of a modulated beam permits measurement of information in the time domain as well and makes it possible to determine bulk transport parameters such as minority-carrier drift mobility. Finally, use of a modulated beam permits detection of the beam intensity by sensing of the ac magnetic field, which makes it possible to measure the actual beam intensity impinging on the sample without interception or significant perturbation. This feature in turn permits stabilization of the beam intensity at a given level for the purpose of long-term measurements.

With the rationale just described, a modulated beam capability that approaches theoretical limits of detectability of beam and sample current, in both amplitude and phase, has been established. Direct detection of the modulated component of the beam at the level of a few pA has been achieved. Induced solar cell currents are likewise detectable at that level. A time resolution of 50 ps has also been realized. A SEM thus augmented is capable of yielding considerable information on solar cell properties that are not accessible by other techniques. Such a capability is also useful in the study of MOS devices, where total ionizing dose to gate insulators must be severely limited. Furthermore, it facilitates study of semiconductor devices such as infrared detector arrays operated at cryogenic temperatures, where spot scans can be made under conditions of low incident power levels. The modulated beam technique has been subjected to two critical tests. The first utilizes the high spatial resolution in depth of the carrier collection efficiency and is described in the section entitled *Experimental Test of the Modulated Beam System*. The second utilizes information in the time domain to yield values of minority-carrier drift mobility, as reported in Ref. 11.

Description of the Experimental Facility

A schematic diagram of the experiment approach is shown in Fig. 1. The modulated component of the magnetic field of the electron beam is sensed by a ferrite core transformer. The beam constitutes a one-turn virtual primary of that transformer, as shown in the accompanying equivalent circuit. The beam is shown impinging on a solar cell junction. In practice, the system is calibrated with respect to a miniature Faraday cup which is connected to the sample current amplifier, so that precise gain calibrations are obviated.

High detectivity requires signal recovery with small noise bandwidths, which has recently become practical with commercially available high-frequency lock-in amplifiers. A previous effort in the determination of minority-carrier drift mobility in solar cells by means of a network analyzer was hampered by the necessarily larger noise bandwidths.¹² A schematic diagram of the complete experimental facility is shown in Fig. 2. Identical Princeton Applied Research Model 5202 lock-in amplifiers were employed for recovery of the beam current and sample current signals.

The modulated beam is obtained by deflection past the final aperture, using deflection plates placed within the drift space beneath the anode. A review of the considerations that bear on this approach is given in Ref. 13. A combination of sinusoidal and dc deflection yields an approximate half sine wave at the sample. In the present implementation, the dc deflection signal is under servo control to stabilize the beam current by adjustment of the duty cycle. The deflection plates were placed far apart (4 mm initially, 10 mm ultimately) to minimize perturbation of the beam by image forces and to avoid gradual buildup of hydrocarbons abetted by beam impact. Large deflection voltages (~100 V p-p) were therefore required. A 3W broadband power amplifier was used in conjunction with a step-up transformer. The requisite deflection angle for beam cutoff was found to be about 0.5° , by virtue of the demagnification of the electron lens system.¹⁴

Direct beam detection is accomplished by means of a ferrite toroidal transformer placed beneath the final aperture. Amplification is by means of a preamplifier with a

dual-gate MOSFET input gain stage and two follower stages for impedance match to 50 ohms. Under conditions of the high MOSFET input impedance, the "unloaded" or resonant characteristics of the ferrite core are observed and give peak conversion constants of about 1 nV/pA. The limiting noise source is the Johnson-Nyquist noise of the effective shunt resistance, or about 10^4 ohms. With a 10s time constant (effective noise bandwidth of 25 mHz), and with rejection of quadrature noise in the phase-sensitive detector, the detection limit is 1.4 pA. Lateral deflection of the beam due to the presence of the circuit should not occur as long as axial symmetry is maintained. In practice, some degradation of focus is observed, so that the beam detection circuit must be removed if the SEM is to be used in the conventional viewing mode at high magnification.

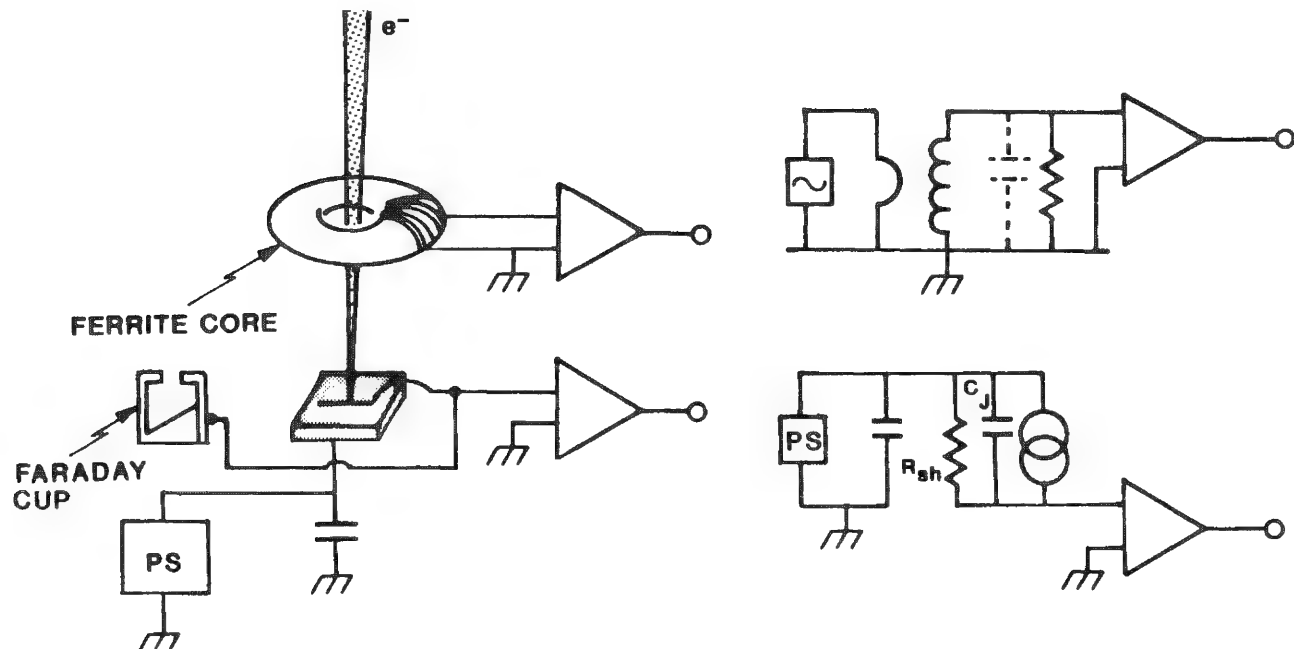


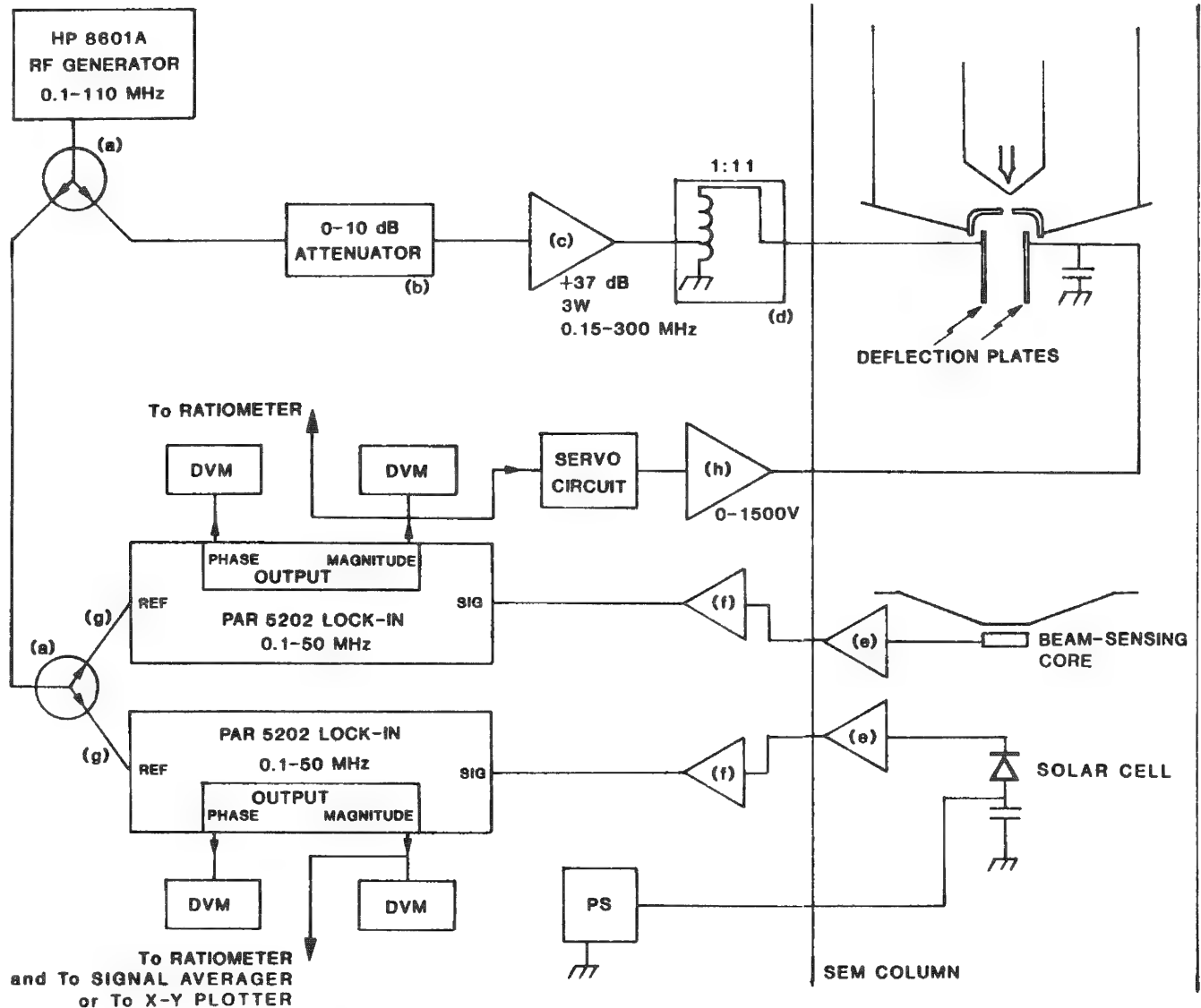
FIG. 1.--Experimental method of characterizing junction properties with modulated electron beam. Left, beam current is detected by means of magnetic core and solar cell current is measured under bias; in equivalent circuits (right) R_{sh} and C_j refer to shunt resistance and junction capacitance of solar cell specimen.

Preamplification of the solar cell terminal current is accomplished with amplifiers matched to the application. Typically, the amplifier is identical to the one used for beam detection. For broadband applications, a step-up transformer is used to impedance-transform the low junction reactance. Measurements of large area junctions, on the other hand, are made at low frequency with a conventional current-to-voltage converter.

Sensitivity to low signal levels requires a high degree of isolation (in excess of 200 dB) from the power amplifier. This requirement makes it necessary for preamplification to be performed within the SEM. Signals are then conducted out of the SEM column with flexible 50-ohm cables, where they are further amplified in matched low-noise broadband amplifiers (labeled "f" in Fig. 2). Thus amplified, the signals are phase-sensitively detected in the lock-ins, which provide for display of either phase and magnitude or in-phase and quadrature signals. The magnitude response of the beam detection circuit is used for servocontrol of the beam intensity and the specimen signal is displayed ratio-metrically with respect to the beam signal.

The detection sensitivity of beam current with use of the Faraday cup (and concomitantly of the sample current) is greater than that of the beam detection circuitry if no step-up transformer is used. In practice, a sensitivity to 0.2 pA has been achieved. Practical limitations on the signal detection sensitivity include, in addition to the fundamental noise limits, the coherent pickup from the power amplifier, the rf source, and the lock-in amplifiers themselves. Up to now, this pickup has been taken into account by

vectorial subtraction. A preferable solution would be to buck out the offending signal or to perform second detection at low frequency by superimposing a second square-wave modulation signal on the beam. Moreover, the beam detection circuit is affected by secondary electrons passing near it. The ferrite core therefore needs to be carefully shielded from such effects.



(a) POWER SPLITTER, 6 dB insertion loss (not 3I): HP 11625-60009.

(b) 10-dB ATTENUATOR, 1-dB steps: Alan Industries 50V10.

(c) RF POWER AMPLIFIER, 37 ± 1 dB gain, 3W linear output power, 0.15-300 MHz: Electronic Navigation Industries 403LA.

(d) STEP-UP AUTOTRANSFORMER, 1:11 turns ratio.

(e) PREAMPLIFIER, 3-stage, MOSFET input, 50Ω output.

(f) POST-AMPLIFIER, 43 dB gain.

(g) MATCHED CABLES: HP 11652-60002.

(h) VOLTAGE-PROGRAMMABLE POWER SUPPLY, 0-1500V: Kepco ABC-1500M.

FIG. 2.--Experimental facility for characterizing solar cells as function of beam energy and modulation frequency.

Experimental Test of the Modulated Beam System

A first test of the modulated beam facility was performed by determination of carrier collection efficiency as a function of depth into a solar cell by analysis of measurements of solar cell currents over a wide range of beam energies or, equivalently, penetration depth. In this application, low-energy electron excitation serves as a useful complement to optical excitation because the former is more highly localized, and is moreover dependent only on material parameters such as density and atomic number of the constituent species. Such measurements have been previously made by others.^{4,5} The salient difference in the present instance is that the use of a modulated beam makes possible measurements with a focused beam at low intensity and a variable dc bias.

Results are shown in Fig. 3, where the ratio of measured specimen current to beam current is presented as a function of beam energy. Beam currents employed ranged from about 3 to 20 pA. The solar cell was maintained at 1V reverse bias, yielding about 200 nA leakage current.

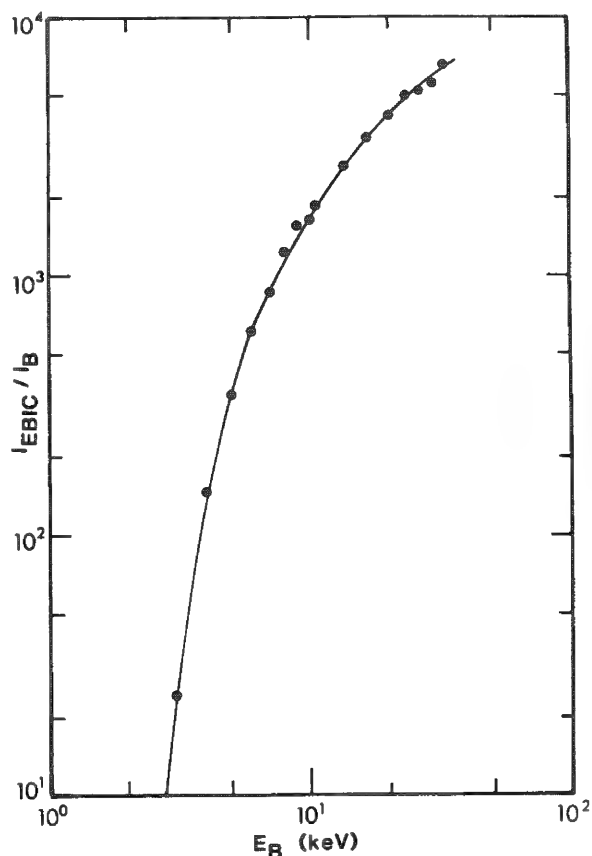


FIG. 3.--Ratio of electron-beam-induced current (EBIC) to incident beam current, as function of beam energy, for high-quality, conventional solar cell.

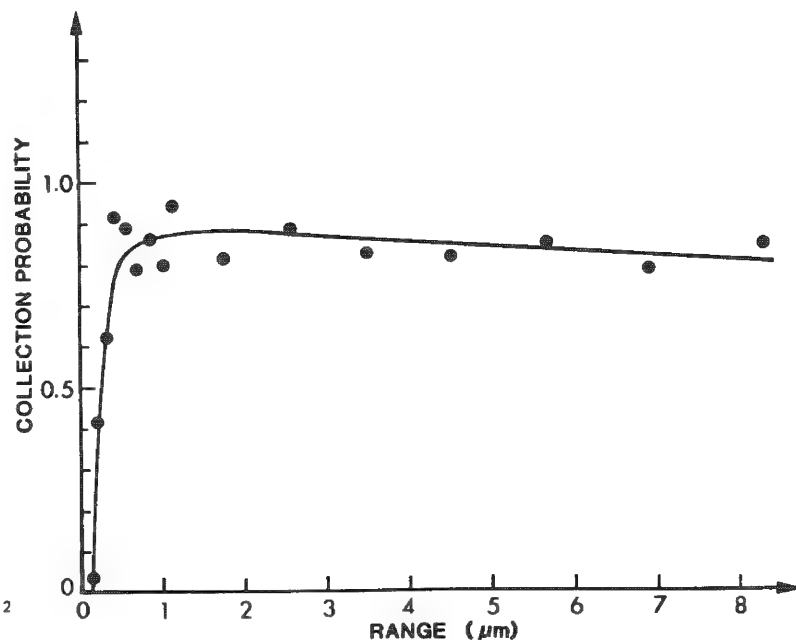


FIG. 4.--Carrier collection probability as function of depth into crystal under assumptions in terms of pair generation energy, range-energy relationship, and energy deposition profile discussed in text.

The carrier collection efficiency is determined by following the formalism of Everhart and Hoff.¹⁵ The sample current I_s is given by

$$I_s = \frac{I_B f E_B}{E_p} \int_0^1 P(y) \lambda(y) dy$$

where y is the depth within the solid normalized to the range $R(E)$. For silicon we assume

$$R(E) = 0.0184 E_B (\text{keV})^{1.75} (\mu\text{m})$$

where E_B is the beam energy; I_B is the beam current and f is the fraction of energy deposited in the solid, taken to be 0.9,¹⁶ E_p is the pair creation energy (for this case, 3.65 eV), $P(y)$ is the carrier collection probability, and $\lambda(y)$, given by $(fE_B)^{-1}(dE/dy)$, is the normalized energy loss parameter. According to Everhart and Hoff, $\lambda(y)$ can be expressed as a third order polynomial,

$$\lambda(y) = 0.60 + 6.21y - 12.4y^2 + 5.69y^3$$

The above integral was evaluated numerically for the data at hand. To simplify the analysis, the total range was divided into a number of bins equal to the number of energies at which data were taken. Each bin was defined in terms of the range for a given energy. Thus the width of the first bin was coincident with the range of the lowest beam energy used. The width of the second bin was the range of the next energy minus the range of the first, etc. Thus, a matrix equation could be defined, given by

$$\begin{pmatrix} I_1 \\ I_2 \\ \vdots \\ I_n \end{pmatrix} = \begin{pmatrix} a_{11} & a_{12} & \cdots & a_{1n} \\ a_{21} & a_{22} & \cdots & a_{2n} \\ \vdots & \vdots & \ddots & \vdots \\ a_{n1} & a_{n2} & \cdots & a_{nn} \end{pmatrix} \begin{pmatrix} P_1 \\ P_2 \\ \vdots \\ P_n \end{pmatrix}$$

where I_n is the sample current measured at beam energy n , and P_n is the carrier collection probability in the corresponding bin. The matrix is conveniently triangular and can be solved trivially by substitution. Results are shown in Fig. 4. Considerable scatter is evident. This scatter is partly the result of the particular method of solution we employed. That is, the solution is forced so that any error, either in the data or in the dose-deposition profile, must be accommodated fully in the choice of P for the particular bin. Any resulting underestimate of P in one bin then must be compensated for by an overestimate in the next bin. Thus, the deviation of data points from the curve (Fig. 4) is seen to have an oscillatory character. Clearly, the method needs to be augmented so that a best fit may be found.

A second test of the modulated beam facility was performed via the determination of minority-carrier drift mobility in a space-quality silicon solar cell that had been subjected to unconventional processing sequences. Drift mobilities in agreement with expected values were found, which negates the hypothesis that the drift mobility might have been degraded as a result of processing.¹¹

In summary, modulation of a SEM beam provides a unique, powerful analytical technique. By use of a low-current focused beam, inherent spatial resolution is maintained, which makes it a useful tool in any quantitative experiment where carrier injection is required. Semiconductor junctions and MIS structures are two classes of devices particularly suited to this technique. The present facility at Northrop Research and Technology Center is now being used in several experiments involved with basic device physics.

References

1. S. Othmer and O. L. Curtis Jr., "Scanning electron microscope measurements of diffusion length in neutron-irradiated silicon," *IEEE Trans.* NS-20: 204, 1973.
2. W. H. Hackett Jr., "Electron-beam excited minority-carrier diffusion profiles in semiconductors," *J. Appl. Phys.* 43: 1649, 1972.
3. J. J. Oakes, I. G. Greenfield, and L. D. Partain, "Diffusion length determination in thin-film $\text{Cu}_x\text{S}/\text{CdS}$ solar cells by scanning electron microscopy," *J. Appl. Phys.* 48: 2548, 1977.
4. G. E. Possin and C. G. Kirkpatrick, "Electron beam depth profiling in semiconductors," *SEM/1979 I*, 245.
5. C. J. Wu and D. B. Wittry, "Investigation of minority-carrier diffusion lengths by electron bombardment of Schottky barriers," *J. Appl. Phys.* 49: 2827, 1978.
6. G. H. Schwuttke, T. F. Cizek, and A. Kran, Quarterly Report 5, JPL Contract 954144, 1976.

7. T. Daud, K. M. Koliwad, and F. G. Allen, "Effect of grain boundaries in silicon on minority-carrier diffusion length and solar-cell efficiency," *Appl. Phys. Lett.* 33: 1009, 1978.
8. H. C. Gatos, M. Watanabe, and G. Actor, "Surface recombination velocity and diffusion length of minority carriers in heavily doped silicon layers," Conference Record, Solar Cell High Efficiency and Radiation Damage, *NASA Conference Publication 2020*, 1977, 59. (Also *IEEE Trans.* ED-24: 1172, 1977.)
9. A. Murgai, J. Y. Chi, and H. C. Gatos, "Microdistribution of oxygen in silicon," *J. Electrochem. Soc.* 127: 1182, 1980.
10. J. R. Srour, "Stable damage comparisons for neutron-irradiated silicon," *IEEE Trans.* NS-20: 190, 1973.
11. S. Othmer and M. A. Hopkins, "Measurement of minority-carrier drift mobility in solar cells using a modulated electron beam," Conference Proceedings, Space Photovoltaic Research and Technology, *NASA Publication 2169*, 1980, 61.
12. S. Othmer, "Determination of the diffusion length and drift mobility in silicon by use of a modulated SEM beam," *SEM/1978 I*, 727.
13. E. Menzel and E. Kubalek, "Electron beam chopping systems in the SEM," *SEM/1979 I*, 305.
14. A. Gopinath and M. S. Hill, "Deflection beam-chopping in the SEM," *J. Phys. E: Scientific Instruments* 10: 299, 1977.
15. T. E. Everhart and P. H. Hoff, "Determination of kilovolt electron energy dissipation versus penetration distance in solid materials," *J. Appl. Phys.* 42: 5837, 1971.
16. H. E. Bishop, "Electron scattering in thick targets," *Brit. J. Appl. Phys.* 18: 703, 1967.

A MICROPROBE STUDY OF CRYSTALLIZATION TRENDS OF FELDSPARS IN SILICATE LIQUIDS

W. Ian Ridley

Carmichael (1963)¹ suggested that the crystallization of feldspars from salic liquids involved a two-feldspar liquidus surface which allowed the equilibrium coexistence of two feldspars of disparate composition. One feldspar would be a plagioclase or "ternary" feldspar; the other, a potassium-rich variety (sanidine, microcline, or orthoclase depending on the conditions of crystallization). The approximate topology of the liquidus surface was illustrated *schematically* for the system $\text{CaAl}_2\text{Si}_2\text{O}_8\text{-NaAlSi}_3\text{O}_8\text{-KAlSi}_3\text{O}_8\text{-SiO}_2$ in which quartz, plagioclase, and K-feldspar are possible crystallizing phases. This system, sometimes referred to as the "salic tetrahedron" (Fig. 1), demonstrates possible phase relations between salic liquids and their co-existing feldspars. The salic tetrahedron is a useful model for crystallization of quartz-normative silicate liquids found in nature and the phase relations suggested in Fig. 1 may be tested by the detailed examination of feldspar compositions during crystallization of natural melts. Changes in composition of the melt should be reflected in variations in composition of co-existing feldspars, which can be measured by microprobe techniques. In the present study, we show that Fig. 1 is indeed a useful guide to feldspar crystallization trends in natural quartz-normative melts.

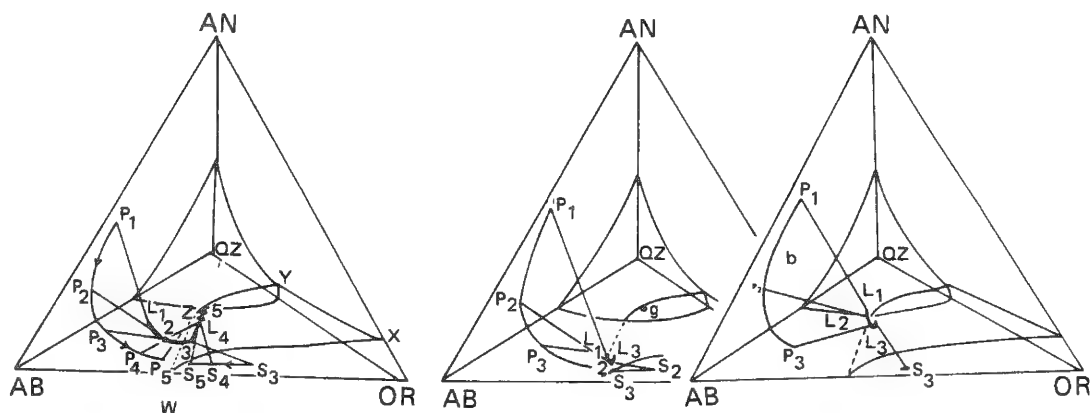


FIG. 1.--Proposed phase relations in salic tetrahedron An-Ab-Or-Qz. Two-feldspar liquidus surface is shown by W-X-Y-Z and terminates above anorthite-free system Ab-Or-Qz. Three liquid lines of descent are shown (L_1 - L_2 - L_3 etc.) for melt systems with differing quartz-normative characteristics. Plagioclase solidus path is P_1 - P_2 - P_3 , etc., and K-feldspar solidus is S_2 - S_3 - S_4 , etc.; hence at left, liquid L_3 is in equilibrium with plagioclase P_3 and alkali feldspar S_3 . Position of solidus curves and quartz saturation surface is a function of vapor pressure.

A detailed microprobe examination has been made of feldspars crystallized from members of a continental andesite-latite-quartz latite-rhyolite association. The association is part of the Mount Taylor region, a volcanic complex of Plio-Pleistocene age, near Grants, New Mexico. Independent evidence indicates the association is of crustal origin and can be distinguished from another geographically related association of basinite-hawaiite-soda hawaiite forming the surrounding volcanic plateau.

Feldspars have been analyzed with an ARL-SEM microprobe with KRISEL automation located at Lamont-Doherty Geological Observatory of Columbia University. Analysis conditions were $E_0 = 15$ kV, $S_c \approx 20$ nA, with Hakone anorthite, Hohenfels sanidine, Nunivak Island anorthoclase used as standards. Data were reduced by means of an empirical Bence-Albee matrix correction program. The bulk composition of individual samples discussed in the text were determined by classical techniques.

The bulk compositions of aphyric or weakly porphyritic members of the association define a trend shown in Fig. 2, which approximates the liquidus line of descent. Figure 2

is a projection from quartz into the ternary system anorthite-albite-orthoclase and also shows the projected position of the two-feldspar liquidus surface. Note that the liquid line of descent is toward the two-feldspar surface from anorthite-rich to anorthite-poor compositions, which is also the direction of falling temperature in the feldspar system. The bulk compositions lie above the surface, which suggests that in nature the two-feldspar liquidus surface is a low-temperature region that controls the direction of liquid fractionation. Once a melt has fractionated to this surface, further fractionation must take place on the surface with residual liquids moving toward more silica rich compositions.

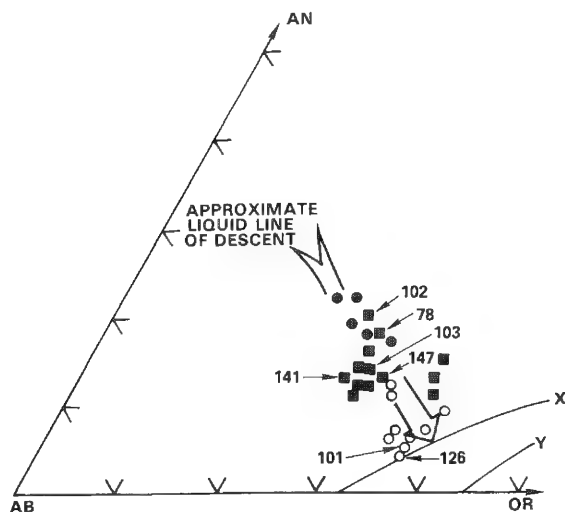


FIG. 2.--Projection of members of andesite-latite-quartz latite-rhyolite association from quartz into ternary feldspar system anorthite (AN)-albite (AB)-orthoclase (OR). Approximate position of two-feldspar liquidus surface for quartz-free compositions is at X and projection of intersection of two-feldspar surface with quartz saturation surface is at Y. ● andesites, ■ latites, ○ quartz latites.

Since most of the bulk compositions lie *above* the two-feldspar surface we would predict that the initial liquidus feldspar would be a plagioclase. However, fractionation *within individual melts* (e.g., internal fractionation within a small magma body) would result in a residual-liquid trend towards the two-feldspar surface and in some cases interstitial melt may intersect this surface. In this case, internal fractionation should be reflected in systematic changes in feldspar compositions (shown as internal zoning) and ultimately the precipitation of two feldspars. Obviously, the closer the initial bulk composition is to the two-feldspar surface the greater the probability that internal fractionation will result in crystallization of two feldspars. If the bulk composition lies *upon* the two-feldspar surface (e.g., sample 126 in Fig. 2), then the melt initially crystallizes two feldspars and the residual liquid migrates along the surface towards the quartz saturation surface (Fig. 1). Only the rhyolitic samples have bulk compositions lying on the quartz saturation surface, but several quartz latites carry interstitial quartz, which indicates that internal fractionation has produced interstitial melt on this surface.

Analysis of feldspars in individual samples confirm the crystallization trends proposed above. The mineral data have been recalculated into stoichiometric end-members albite, anorthite, and "K-feldspar" and plotted in the ternary feldspar system in Fig. 3. The crystallization paths of feldspars trace out the feldspar *solidus* path in contrast to the bulk rock compositions which define the *liquidus* path. The feldspar trends are unique to this particular association since the solidus position is a function of both bulk composition and vapor pressure. Use of an independent estimate of paleotemperature from co-existing Fe-Ti oxides and utilization of the plagioclase thermometer data³ suggests a partial pressure of water of 2-4Kb during crystallization of this association.

Evidence for extensive internal fractionation within samples of andesitic composition is lacking and only very rarely have they crystallized two feldspars. That is also the case for latites that have cooled rapidly and whose bulk compositions lie above the two-feldspar liquidus surface (e.g., samples 78, 102 in Fig. 2 and 3). However, coarsely crystallized samples (e.g., 103 in Figs. 2 and 3) show protracted internal fractionation

and eventually the precipitation of both anorthoclase and K-feldspar. Some of the quartz-latites lie upon the two-feldspar surface (e.g., sample 126 in Figs. 2 and 3) at their liquidus temperatures and phenocrysts of anorthoclase and alkali feldspar are found even in the most glassy samples (e.g., 101 in Fig. 3). Once two feldspars begin to crystallize the movement of the residual liquid along the two-feldspar surface is reflected in the changing composition of individual feldspars. Plagioclase feldspars are

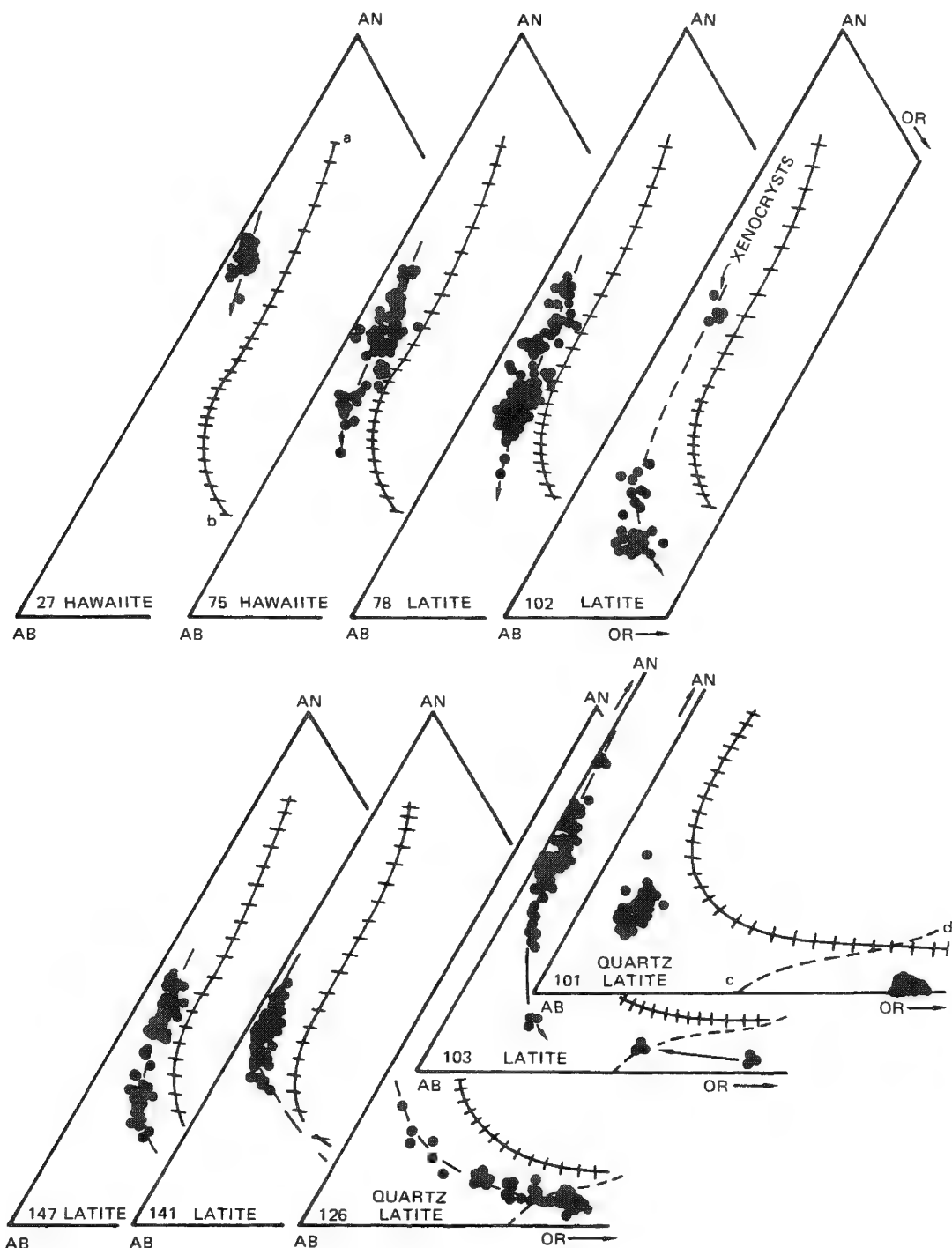


FIG. 3.--Microprobe analyses of feldspars in andesites, latites, and quartz latites plotted in ternary feldspar system AN-AB-OR. Curve a-b is limit of ternary solid solution in natural feldspars; curve c-d is two-feldspar liquidus surface.

initially zoned to more albitic compositions but then become enriched in the orthoclase component. Concomitantly, the K-feldspar becomes progressively enriched in the albite component. Hence, fractionation results in the two feldspars approaching each other in composition. Slowly cooled quartz-latites, besides containing plagioclase and K-feldspar phenocrysts, also contain an abundance of crystals with compositions around $\text{Ab}_{73}\text{Or}_{27}$ (e.g., sample 126 in Fig. 3). This is also the composition attained on the *outer* rims of strongly zoned plagioclase and K-feldspar. We suggest that the crystallization of two feldspars is eventually replaced by precipitation of a single feldspar having a composition of the feldspar minimum in the binary Ab-Or system. This conclusion is consistent with the two-feldspar surface terminating prior to reaching the base Qz-Ab-Or, as required by phase relations in the anorthite-free system.

The observed phase relations for the rhyolitic samples is also consistent with the topology shown in Fig. 1. Rhyolites plot on the intersection of the quartz-feldspar cotectic at $P_{\text{H}_2\text{O}} \approx 4\text{Kb}$ and the two-feldspar surface (Fig. 4) but are displaced towards the orthoclase corner, relative to the polybaric ternary minima and the 5Kb eutectic. Large blocks of granite gneiss are found as xenoliths within the rhyolites; the composition of these granites is also shown in Fig. 4. Granite gneisses contain both plagioclase ($\text{An}_{16}\text{Ab}_{84}$) and alkali feldspar ($\text{Or}_{96}\text{Ab}_4$) and partial melting of such an assemblage would produce liquids in equilibrium with two feldspars and constrained to lie on the intersection of the quartz saturation surface and two-feldspar surface; i.e., having the composition of the analyzed rhyolites. The latter have also crystallized two feldspars as liquidus phases along with quartz, a plagioclase ($\text{An}_9\text{Ab}_{81}\text{Or}_{10}$ zoned to $\text{An}_3\text{Ab}_{73}\text{Or}_{24}$) and a K-feldspar ($\text{An}_1\text{Ab}_{52}\text{Or}_{47}$). Hence the observed feldspar relations are consistent with a genetic relationship between the rhyolitic rocks and their granitic xenoliths.

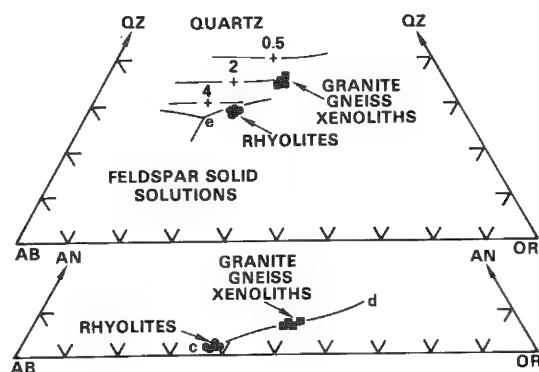


FIG. 4.--Rhyolites (●) and granite gneiss xenoliths (■) projected into ternary systems AB-AN-OR and AB-OR-QZ. Curve c-d is two-feldspar liquidus surface. Also shown are traces of quartz-feldspar field boundary for $P_{\text{H}_2\text{O}} = 0.5, 2, 4\text{ Kb}$, the position of ternary minimum (+) and the ternary eutectic (e) at 5 Kb.

In summary, a detailed microprobe study of feldspar compositions in a sequence of quartz-normative rocks has demonstrated the utility of proposed liquidus phase relations in the quaternary system Qz-An-Ab-Or. These phase relations closely correspond to those observed in natural salic melts and may be usefully employed for a better understanding of petrogenetic relations between associations of quartz-normative igneous rocks.

References

1. I. S. E. Carmichael, "The crystallisation of feldspar in volcanic acid liquids," *Quart. Jour. Geol. Soc.* (London) 119: 95-131, 1963.
2. I. S. E. Carmichael, F. J. Turner, and J. Verhoogen, *Igneous Petrology*, New York: McGraw-Hill, 1974.
3. E. A. Mathez, "Refinement of the Kudo-Weill plagioclase thermometer and its application to basaltic rocks," *Contrib. Mineral. Petrol.* 41: 61-72, 1973.

DETECTION OF SMALL, SYSTEMATIC COMPOSITIONAL VARIATIONS IN PERIDOTITE BY AUTOMATED ELECTRON MICROPROBE POINT COUNTING ANALYSIS (PCA) WITH AN ENERGY DISPERSIVE DETECTOR

J. E. Quick, A. A. Chodos, and A. L. Albee

Automated electron microprobe point count analysis (PCA) may be used to determine average compositions of inhomogeneous phases in complex aggregates. The procedure is to analyze for 10 elements with an energy dispersive detector for 5s counts at about 2500 grid points on polished thin sections. A computer identifies the mineral at each point from the K-values, stores these data, and calculates the average k-values for each mineral type. The accuracy of the average mineral compositions is limited by the ability to identify minerals accurately by computer, the counting time at each point, and the total number of times a mineral is encountered in a point count. We report the results of a study to determine average compositions of primary minerals by PCA in rocks from the Trinity peridotite, northern California. The samples are complex in that they are composed of 2-5 different, zoned, primary minerals and up to 6 alteration products. Somewhat to our surprise, we detected systematic variations in major elements (>1% abundance) as small as 1%, and even systematic variations in minor elements (<1% abundance). Although the variations are extremely small, they are in excellent agreement with average mineral compositions determined by averaging of high quality analyses. Apparently, PCA, in analyzing large numbers of points, can detect even small variations in mineral compositions and is probably superior to averaging fewer but higher quality analyses to determine average phase compositions in complex aggregates.

We have described previously the use of point counting by automated electron microprobe, or point count analysis (PCA), as a method for studying phase aggregates.^{1,2} The technique utilizes computer-automated control of the electron microprobe sample stage and energy dispersive analyzer to collect x-ray data at discrete grid points on a probe mount. The computer identifies the phase at each grid point from calculated K-values and stores these data plus the location of the grid point. This technique results in simultaneous determination of:

- (1) the abundance of each phase,
- (2) the average composition of each phase,
- (3) the range and distribution of compositions of each phase, and
- (4) spatial controls on the distribution of phases and phase compositions.

Furthermore, the first two sets of data allow calculation of the bulk composition of the entire aggregate. Our laboratory has successfully applied PCA to a large number of rocks that encompass a wide range of phase and bulk compositions. In rocks for which XRF data are available for comparison, the calculated bulk compositions agree well with whole-rock XRF data.²

PCA is a very powerful analytical technique and experimentation with it continues to impress us. PCA analysis of samples from the Trinity peridotite dramatically illustrates the utility of PCA for determining average phase compositions and detecting small differences in this parameter among samples. The rocks are extremely complex in that they are composed of 2-5 inhomogeneous, primary minerals and up to 6 alteration products, and, therefore, constitute a difficult test of PCA. Initially, the goal of this investigation was to measure mineral abundances in each of 5 samples of peridotite using PCA, and to search for small compositional variations by averaging large numbers of high-quality wavelength-dispersive analyses (WDA). To our surprise, PCA was able to detect very small variations in oxide abundances.

Analytical System

Our laboratory is equipped with a MAC-5-SA3 electron microprobe interfaced to a PDP-8L computer for control of spectrometers and sample stage and for on-line data processing. Energy-dispersive analysis is performed with an ORTEC 161eV Si(Li) detector interfaced to

The authors are at the Division of Geological and Planetary Sciences of the California Institute of Technology in Pasadena, CA 91125.

a Tracor Northern NS-880 multichannel analyzer with 24k of memory and a DSD-210 dual floppy disk. The Si(Li) detector is mounted approximately 18 cm from the sample analysis point and collimated so that the counting rate is less than 3000 cps on brass. Stage and spectrometer control programs are written in FOCAL (Digital Northern Corp.) for the PDP-8L; energy-dispersive programs are written in FLEXTRAN (Tracor Northern) for the NS-880. These systems are linked via the interrupt "flag" on the scaler-timer and also via a modem interface.

Basic Approach

The automated point count procedure is described in detail by Albee et al.² The underlying philosophy is as follows. The composition of any phase may be represented by either (1) the abundance of each element or oxide, or (2) the abundance of theoretical end-member compositions. The former may be thought of as representing the composition in element or oxide space and the latter as representing it in phase space. These equivalent representations are related by simple linear transformations that represent the stoichiometric constraints of the mineral structure. In practice it is faster and more convenient in the point count to substitute K-values for actual abundances, a procedure that may be thought of as representing the composition of the phase in K-value space. A computer is programmed to examine an energy-dispersive spectrum collected at a single point on the sample. Background-subtracted K-values are calculated, and the identity of the phase is determined by simple matrix transformation from K-value space to phase space. The stage is moved so that a polished probe mount is sampled by the beam at discrete grid points with counting time at each point routinely set at 5s. Approximately 2500 grid points spaced at distances equal to the average grain size were found to be statistically adequate for characterizing most thin sections.^{1,2}

Sample Description and Analysis

Five samples were collected from the Trinity peridotite³ within 1 m of each other in an outcrop where systematic variations in mineralogy were observable. The sample numbers, rock type, and mineralogy of the samples in sequence are listed in Table 1.

TABLE 1.--Sample number, rock type, and point count data for rocks used in this investigation.

Sample	Rock Type	Primary Mineralogy					Alteration	Sum
		ol	sp	opx	cpx	plag		
9W2	Plagioclase lherzolite	1164	1	412	23	5	740	2345
9W3	Lherzolite	1381	24	305	55		682	2447
9W4	Harzburgite	1450	10	648	47		753	2908
9W5	Dunite	1555	17	4			606	2182
9W6	Dunite	1658	18				847	2523

ol, olivine; sp, spinel; opx, orthopyroxene; cpx, clinopyroxene; plag, plagioclase.

In thin section, the samples were seen to be complex, composed of 2-5 inhomogeneous, primary minerals and up to 6 alteration products. The primary mineral assemblages were: olivine + spinel ± orthopyroxene ± clinopyroxene ± plagioclase. Individual primary grains were concentrically zoned in composition. Furthermore, compositions of minerals in each probe mount were found to be dependent on grain size and proximity to other minerals. The primary assemblages were about 20-30% altered to the assemblage serpentine ± magnetite ± brucite ± talc ± chlorite ± clinozoisite. Therefore, successful PCA of these samples required accurate identification of the phase at each grid point, and taking into account of compositional variation in phases and effects of alteration.

Identification of phases showing compositional zonation was performed by bracketing of a given solid solution series with end-member phases as outlined by Albee et al.² For example, a typical olivine composition is bracketed by Mg_2SiO_4 and Fe_2SiO_4 , and identification of an olivine is accomplished by successful transformation from K-value space into

these end-members.

The extensive alteration of primary minerals in these rocks made PCA more difficult than in unaltered rocks. An implicit assumption of the matrix calculation is that there are no compositional degeneracies between the constituent phases; i.e., the compositions of all phases in the aggregate are linearly independent. This assumption is equivalent to the observation that inspection of an x-ray spectrum cannot distinguish between excitation of phase C or the grain boundary between phases A and B if the compositions of the phases are related by $A + B = C$. In the specific case of the Trinity peridotite, serpentine is the most abundant alteration product and, in terms of the x-ray spectrum, serpentine = olivine + orthopyroxene. Fortunately, the petrography of the rocks provides some constraints. Essentially all the alteration products are concentrated along grain boundaries, and in most places, primary phases are not in contact. Therefore, spectra produced during a point count fall into one of three categories:

- (1) excitation of a single primary phase
- (2) excitation of a grain boundary between a primary phase and alteration phase(s)
- (3) excitation of alteration phase(s)

Cases (2) and (3) were discriminated from (1) by a series of branching statements prior to the matrix calculations.

In addition to PCA, 264 analyses by crystal spectrometer, with longer counting times, were performed on representative grains of each primary phase. These analyses will be referred to as wavelength-dispersive analyses (WDA) and were performed using the methods of Chodos et al.⁴ Each analysis was made for 9-15 elements under operating conditions of 15 kV accelerating voltage and 0.5 μ A sample current on brass. These analyses have the advantage over PCA of longer counting times (15-90 s/element) and higher counting rates--and therefore greater analytical precision at each point. However, they constitute a limited and more subjective sampling of each phase.

Results

Representative WDA analyses for pyroxenes, olivine, and spinel are presented in Table 2 to illustrate the approximate order of abundance of the oxides of interest in these phases. A comparison of WDA and PCA results is summarized in Fig. 1-4, for the following parameters, selected for their geologic significance and plotted as a function of distance from sample 9W2: Mg/Mg + Fe and weight percent CaO and NiO in olivine; Mg/Mg + Fe and weight percents Al_2O_3 , Cr_2O_3 , and TiO_2 in ortho- and clinopyroxene; and Al/Al + Cr and weight percent TiO_2 in spinel. The WDA results are also summarized in histogram form at the bottom of each diagram, showing the real variation within each sample.

TABLE 2.--Representative wavelength-dispersive analyses.

	Olivine	Orthopyroxene	Clinopyroxene	Spinel
SiO_2	40.76	55.68	51.65	0.09
TiO_2	0.01	0.10	0.30	0.25
Al_2O_3	0.00	3.44	3.55	33.09
Cr_2O_3	0.05	0.53	1.06	33.94
MgO	48.90	33.20	17.90	15.34
CaO	0.04	0.54	22.31	--
MnO	0.14	0.19	0.07	0.22
FeO	9.71	6.26	2.68	16.03
NiO	0.33	--	--	--
Na_2O	--	0.06	0.26	--
Sum	100.04	100.00	99.78	99.27

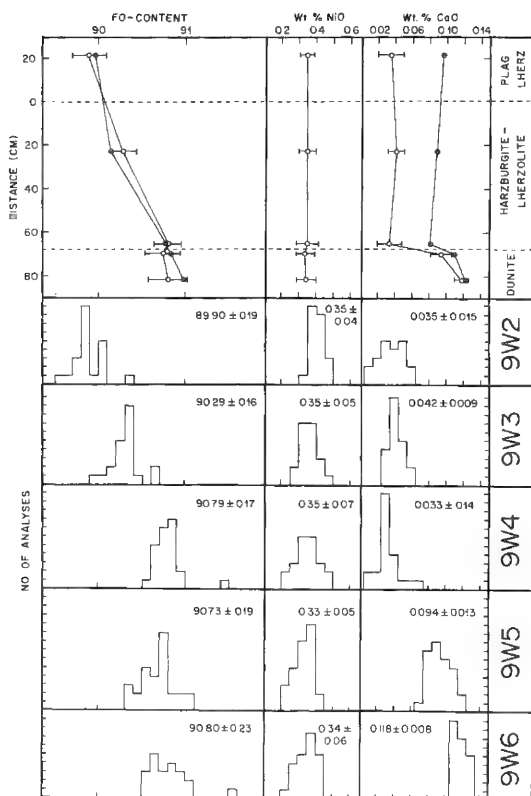


FIG. 1.--Compositional variations in olivine vs distance between samples (top to bottom) 9W2, 9W3, 9W4, and 9W5. Approximate boundaries between rock types shown in dashed lines. Fo-content is defined as $Mg/Mg + Fe$, where Mg and Fe are in catatom abundances. Solid points are results of PCA. Open circles are averaged results of WDA. Complete results of WDA for each sample shown in histograms in lower half of diagram.

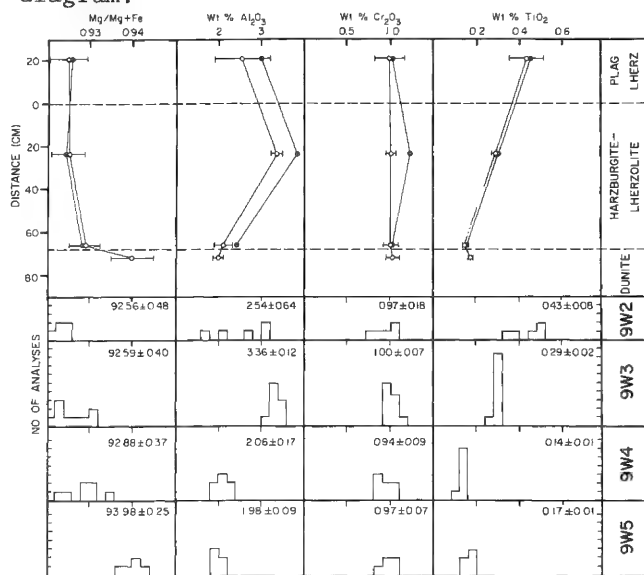


FIG. 3.--Compositional variations in clinopyroxene vs distance between samples. Construction same as Fig. 2.

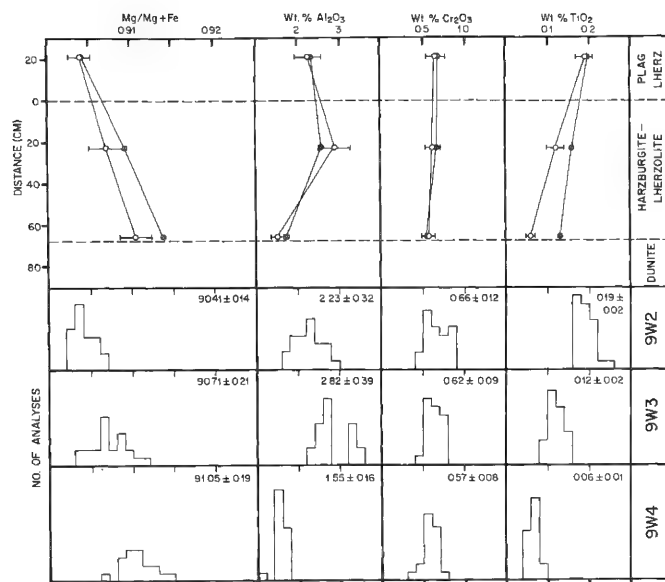


FIG. 2.--Compositional variations in orthopyroxene vs distance between samples. Solid points are results of PCA. Open circles are averaged results of WDA showing ± 1 s.d. Complete results of WDA for each sample shown in histograms in lower half of diagram.

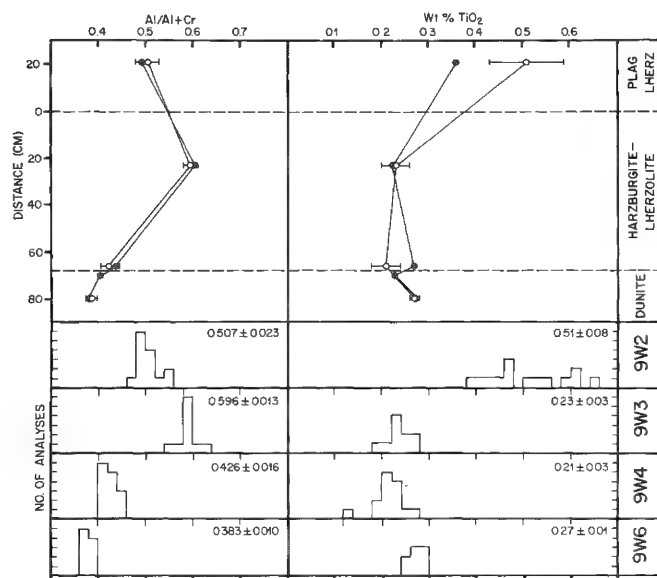


FIG. 4.--Compositional variations in spinel vs distance between samples. Solid points are results of PCA. Open circles are averaged results of WDA showing ± 1 s.d. Complete results of WDA for each sample shown in histograms in lower half of diagram.

Discussion

Several observations may be made from Figs. 1-4. First, the results of PCA and WDA are very similar for oxides that range in abundance in their host phases from <1 to >40%. Second, very small variations in abundance were determined by PCA for oxides that comprise large amounts of their host phase. The most extreme cases are the systematic variations of only 1% found for Mg/Mg + Fe for olivine, orthopyroxene, and clinopyroxene. Although very small, these variations appear to be real based on the agreement between PCA and WDA and the parallel variation in the three phases. Third, some variations were even detected for oxides that are only present in minor (<1%) amounts. For example, with increasing distance from 9W2, TiO₂ decreased 50 percent in spinel, orthopyroxene, and clinopyroxene.

These results demonstrate the validity of PCA as a technique for determining average mineral compositions. Phases were properly identified during PCA. Although the counting time at each grid point during PCA was only 5s, the cumulative effect of large numbers of 5s analyses resulted in a high degree of precision in the determination of an average analysis. This effect may be appreciated if we consider the results for olivine. During a 5s count on the olivines in this study, approximately 18 000, 1100, and 7 counts are collected for MgO, FeO, and CaO respectively, with standard deviations of 0.8, 3.0, and 38%. At any given point, the uncertainty in Mg/Mg + Fe can be no better than about $\pm 3\%$. However, the standard deviation of the total counts for each element, as more and more olivine grains are analyzed, decreases proportionally to the square root of the number of analyses. After 1000 analyses of olivine, we have effectively sampled for 5000 s, and 18×10^6 , 1.1×10^6 , and 7000 counts would have been accumulated for MgO, FeO, and CaO, and counting statistic errors for these determinations will be 0.02, 0.09, and 1.2%, respectively. Therefore, the observed variations of 1% for Mg/Mg + Fe and 30-50% for CaO are well within the range of detectability.

Unfortunately, systematic errors tend to be compounded. Systematic errors in background subtraction are unavoidable in our point count procedure. In order to save time, a fixed "shape" is subtracted from all analyses. The resulting errors would have the greatest impact on oxides in low abundance, and compounding of those errors could result in discrepancies between WDA and PCA results such as for CaO in olivine (Fig. 1) or TiO₂ in orthopyroxene (Fig. 2). However, relative variations in these oxides were still detected, which indicates a high degree of precision. We conclude that PCA may be less accurate than WDA, but, if large numbers of analyses are made, PCA will be very precise.

PCA appears to be superior to using fewer numbers of WDAs for determination of average phase compositions in complex aggregates. PCA analysis of the five samples required 25-30 hr of instrument time compared to about 45 hr to obtain the WDA results. Furthermore, PCA was essentially autonomous, so that the operator is freed for other tasks. Sampling was more statistically meaningful; PCA collected a sample of each phase that was free of operator biases that might be introduced during selections of points for WDA analysis.

References

1. A. J. Gancarz and A. L. Albee, "Microprobe analysis of the bulk composition of phase aggregates," *Proc. 8th Natl. Conf. on Electron Probe Analysis*, 1973.
2. A. L. Albee, A. A. Beaty, A. A. Chodos, and J. E. Quick, "Quantitative analysis of petrographic properties and of mineral compositions with a computer-controlled energy-dispersive system," *12th Natl. Conf. on Electron Probe Analysis*, 1977.
3. J. E. Quick, *Petrology and Petrogenesis of the Trinity Peridotite, Northern California*, Ph.D. dissertation, California Institute of Technology, 1980.
4. A. A. Chodos, A. L. Albee, A. J. Gancarz, and J. Laird, "Optimization of computer-controlled quantitative analysis of minerals," *Proc. 6th Natl. Conf. on Electron Probe Analysis*, 1973.

ORGANIC OXYGEN AND SULFUR ANALYSIS OF VARIOUS COAL MACERALS

J. J. Friel and G. D. Mitchell

The elemental composition of coal is usually determined chemically by the ASTM standard procedure known as ultimate analysis.¹ In this technique, C, H, N, and total S are analyzed chemically, and oxygen is reported by difference. Ash and moisture are determined separately, and the data, thus corrected, may be reported on a dry ash-free (DAF) basis. In the determination of oxygen by difference, all the errors in the analysis of each of the other elements and errors attributable to interference by mineral matter are summed in the oxygen value.² Neutron activation analysis has been used to determine oxygen directly, but this technique requires accurate knowledge of the inorganic component if the data are to be reported on a dry mineral-matter-free (DMMF) basis.³

In the standard procedure for determining organic sulfur in coal one chemically determines total sulfur and then subtracts the sulfates extracted in hydrochloric acid and the pyrites dissolved in nitric acid.¹ The principal error in this procedure results from the incomplete dissolution of pyrite in nitric acid; thus, the value reported for organic sulfur is too high. Besides these potential sources of error, the standard methods of oxygen and organic sulfur analysis are not microtechniques and therefore do not permit analysis by maceral.

In contrast, electron microprobe analysis of these elements, when combined with chemical analysis of C, H, and N, does permit comparison of one maceral with another. Raymond and Gooley have previously used the microprobe to analyze organic sulfur in numerous coals.⁴ We included the measurement of sulfur in this study to see how it was distributed among macerals. Moreover, sulfur can be analyzed simultaneously and with essentially no more effort than is required for oxygen alone. Although the electron microprobe is able to analyze oxygen and organic sulfur directly and is thus free from most of the errors associated with standard techniques, electron-beam instruments are still subject to the usual problems of light-element and trace-element analysis. Our approach to these problems is the subject of the following section.

Method

A well-characterized Elkhorn No. 3 coal from Eastern Kentucky was chosen for analysis by an ARL-EMX automated microprobe. An RAP crystal was used for oxygen and focused on the oxygen peak. An ADP crystal was used for sulfur. Other elements were monitored with the energy-dispersive detector, and analyses showing iron or silicon were discarded as contaminated by adjacent or subsurface minerals. A homogeneous natural magnesite specimen (MgCO_3) was used as the standard for oxygen. This standard was chosen because the oxygen peak was found at the same wavelength as oxygen in coal ($\text{O K}\alpha = 23.568 \text{ nm}$), and atomic number differences were minimized. Anhydrite (CaSO_4) was used as the sulfur standard ($\text{S K}\alpha = 0.53775 \text{ nm}$). For comparison, $\text{S K}\alpha = 0.53833 \text{ nm}$ in pyrite, and $\text{O K}\alpha = 23.708 \text{ nm}$ in Al_2O_3 . All standards and unknowns were coated with aluminum at the same time to insure an identical coating. Aluminum was chosen to minimize absorption of oxygen x rays. The accelerating voltage was set at 12 kV to produce a sufficiently high peak to background ratio yet minimize the absorption correction for oxygen x rays by carbon.

The data were reduced by the ZAF method, in which carbon concentration was fixed at 86% for vitrinite, 90% for fusinite, and 80% for sporinite. The first two values were determined by chemical analyses of vitrinite and fusinite concentrates. The value for sporinite was estimated. Nitrogen was determined by chemical analysis of vitrinite and fixed at 1.5% for all macerals. An error of 1% absolute in the value chosen for carbon results in an error of approximately 0.1% in the absolute concentration of oxygen. The specimen current was 0.2 μA , which resulted in a count rate of about 100 counts per second of oxygen in MgCO_3 and about 5000 counts per second of sulfur in CaSO_4 . Such a current produced a count rate that was stable over time, but it was feared that higher currents might damage the sample. Counting times varied but were of the order of 60 s, and an air jet was

The authors are engineers with Bethlehem Steel Corp. at the Homer Research Laboratories, Bethlehem, PA 18016.

used to minimize contamination. These operating conditions resulted in a relative precision of about 10% for both oxygen and sulfur in a typical analysis. The mass absorption coefficients for light elements used in the ZAF calculation were those of Henke and Ebisu.⁵ The analysis of a typical vitrinite area is given in Table 1, from which it can be seen that the ZAF factors for oxygen and nitrogen are by no means insignificant. The difference between the total of 93.6% and 100% is presumably due to hydrogen.

TABLE 1.--Typical vitrinite analysis showing effect of Z, A, and F factors individually.

Element	K	Z	A	F	ZAF	Conc.
O	0.017	0.937	3.403	0.999	3.190	0.0555
S	0.006	0.987	0.993	1.000	0.981	0.0063
N	0.002	0.962	7.599	0.999	7.311	0.0150F
C	0.799	1.005	1.069	0.999	1.075	0.8600F
					TOTAL	0.9368

F = fixed

Discussion

Polished sections of coal mounted in epoxy either as blocks or as ASTM standard petrographic samples were analyzed. The resulting organic oxygen and sulfur concentrations are plotted in Fig. 1. These data points resulted from the analysis of several different coal macerals: 27 areas identified as vitrinite, 10 as fusinite, and 9 as sporinite. Since the paleobotanical origin of these components as well as the physical and chemical processes that might have affected their development are discussed in detail elsewhere, we need only mention that vitrinite derives predominantly from the cell walls of plants fusinite is the charred remnants of the original plant cells after oxidation, and sporinite is the outer wall, or exine, of a spore.⁶

The order of decreasing oxygen content from fusinite to vitrinite to sporinite may well relate to the original organic materials from which they were formed. Vitrinite results from the coalification of cellulose and lignin, both of which contain more than 50% oxygen by weight. Even if most of the hydroxyl oxygen is lost during coalification, the remaining bridging oxygen is more than enough to account for the 2-8 wt.% organic oxygen observed in this sample. Fusinite results from oxidation in the coal swamp; thus, hydrogen is lost and the remaining carbon-rich material is higher in oxygen than is vitrinite. Sporinite is derived from sporopollenin, which contains roughly half the oxygen in cellulose. Although the composition of the original materials from which coal was formed probably varied widely in composition, the oxygen measured in this sample follows the trends known about the geochemistry of coal.

Organic sulfur is highest in sporinite, possibly owing to the action of bacteria that fixed sulfur in this maceral. Sulfur is lowest in fusinite, probably resulting from the oxidation of sulfur along with hydrogen. The organic sulfur content of vitrinite is intermediate between those of the other two macerals and varies most widely.

The values shown in Fig. 1 represent only *organic* oxygen and sulfur. Any inorganic component in an amount > 0.1% would be seen in the energy-dispersive spectrum and thus be discarded. The average concentration of organic oxygen and sulfur in each maceral is given in Table 2. The values of C, H, N, and total S in vitrinite and fusinite were measured chemically by means of hand-picked concentrates of these macerals. The values for the same elements in sporinite were estimated because it was not possible to separate a sufficient quantity of this maceral. When the analyses are recombined on the basis of the petrographic composition of the coal, an average for the entire coal can be calcu-

lated. In this coal it is evident that the composition of vitrinite, which comprises about 56% of the coal, is representative of the entire coal. A comparison of the petrographically weighted average with the composition determined by ultimate analysis shows greater oxygen and organic sulfur determined by electron microprobe. This result is to be expected if mineral matter and incompletely removed pyrite affects the ultimate analysis.

TABLE 2.--Elemental composition of Elkhorn No. 3 coal (wt.%).

	<u>C</u>	<u>H</u>	<u>N</u>	<u>S_{inorg}</u>	<u>S_{org}</u>	<u>O</u>	<u>Total</u>
Vitrinite	85.41 ^a	5.74 ^a	1.92 ^a	1.00 ^d	0.71 ^e	5.07 ^e	99.85
Fusinite	89.76 ^a	3.40 ^a	0.44 ^a	1.04 ^d	0.44 ^e	6.03 ^e	101.11
Sporinite	80.00 ^b	10.00 ^b	1.50 ^b	1.00 ^b	1.33 ^e	3.32 ^e	97.15
Weighted Avg	85.80	5.74	1.44	1.01	0.73	5.07	99.79
Ultimate Analysis	83.70 ^a	6.63 ^a	1.55 ^a	0.27 ^a	1.15	6.70 ^c	100.00

^a determined chemically, ^b estimated, ^c by difference,

^d total S - org S, ^e electron microprobe

In conclusion, the advantages of the microprobe technique are that it: (1) determines organic oxygen as well as sulfur directly, (2) does not permit contamination by inorganic species, and (3) makes it possible to analyze individual macerals and even to examine homogeneity within a maceral.

References

1. ASTM *Annual Book of ASTM Standards*, Part 26, "Gaseous fuels; coal and coke; atmospheric analysis," Philadelphia: Am. Soc. Test. Mater., 1979.
2. P. H. Given and R. F. Yarzab, in C. Karr Jr., Ed., *Analytical Methods for Coal and Coal Products*, New York: Academic Press, 2: 3, 1978.
3. A. Volborth, G. E. Miller, C. K. Garner, and P. A. Jerabek, "Material balance in coal: 2. Oxygen determination and stoichiometry of 33 coals," *Fuel* 57: 49, 1978.
4. R. Raymond Jr. and R. Gooley, "A review of organic sulfur analysis in coal and a new procedure," *SEM/1978*, 93.
5. B. L. Henke and E. S. Ebusu, "Low energy X-ray and electron absorption within solids," in G. L. Grant, Ed., *Advances in X-Ray Analysis*, New York: Plenum Press, 17: 150, 1974.
6. M. Teichmuller and R. Teichmuller, "Fundamentals of coal petrology," in E. Stach, Ed., *Coal Petrology*, Berlin: Gebrüder Borntraeger, 1975, 5.

THE POLYBARIC HISTORY OF FAMOUS BASALT 527-1-1: EVIDENCE FROM TRACE ELEMENTS IN OLIVINE

P. I. Nabelek, C. H. Langmuir, and A. E. Bence

Olivine plays a major role in the petrogenesis of oceanic basalts erupted at active spreading centers. It is the major mineralogical constituent of the source and of the residuum after partial melting and is a liquidus or near-liquidus phase over a very wide range of pressures (0 to as high as ~15 kb). Thus it controls the liquid line of descent of ascending basaltic liquids over a considerable depth range. It is thus not surprising that olivine phenocrysts and microphenocrysts are ubiquitous in fresh basalt glass collected along mid-ocean ridges.

The composition of the olivine is determined by the bulk composition of the liquid from which it crystallized and the intensive thermodynamic (T, P, fO_2 , PH_2O , etc.) and kinetic parameters operating at the time of crystallization.

The transition metals Cr, Mn, Co, and Ni that occur in trace concentrations in mid-ocean ridge basalts are, to varying degrees, preferentially incorporated into the olivine, and thus can be sensitive recorders of olivine crystallization. The abundances of the transition metals in ocean floor basalts have been used to constrain models for their petrogenesis.¹⁻⁹ Experimental studies of the partitioning behavior of the transition metals between olivine and basaltic liquids¹⁰⁻¹² constrain the temperature-composition dependence of the partition coefficients and permit numerical modeling of olivine fractionation.^{3,11,13-15}

The application of the partitioning behavior of trace transition metals to the modeling of the petrogenesis of natural basalt systems has been hampered by the difficulty of obtaining precise analyses with high spatial resolution. The electron microprobe provides the needed spatial resolution (2-3 μm^3) but trace element analysis is a painstaking procedure that can be applied to only a few of the elements of interest. Bence et al.¹⁶ discuss some of the problems encountered in the determination of trace element concentrations by electron microprobe and describe a procedure by which these measurements can be made for selected trace elements in specific systems with high degrees of precision. Nabelek¹⁷ used this procedure to measure the partitioning of nickel between olivine and basaltic liquid in reversal experiments conducted on FAMOUS basalt, 527-1-1. Preliminary measurements on selected olivines in that basalt indicated that the partitioning was not simple, prompting the present study to investigate, in some detail, the characteristics of the Ni distribution in olivines from 527-1-1. We have used the technique described by Bence et al.¹⁶ to determine the distributions of Ca, Mn, Cr, and Ni in selected olivines and observe zoning trends that are inconsistent with normal fractional crystallization at low pressure but that may be explained by a polybaric crystallization history.

Analytical Procedures

Major and trace-element analyses of the coexisting olivines and glass of basalt 527-1-1 (~96% glass, ~3% olivine, <1% spinel, and trace plagioclase) were obtained on an automated 4-spectrometer ARL-EMX-SM electron microprobe. Major element oxide compositions were calculated by the technique of Bence and Albee¹⁸ and an a-matrix modified from that given by Albee and Ray.¹⁹ Trace-element concentrations, detectability limits, and precision were determined by the procedures described by Bence et al.¹⁶ The run conditions for the trace-element determinations were: accelerating potential, 30 kV; specimen current (on brass), 0.015 μA (standards) and 0.15 μA (unknowns). Ten 30s replications were obtained for each point analyzed. Background intensities were obtained on both sides of the peak and were redetermined for each point. Errors and detectability limits are cal-

Author Langmuir is at the Lamont-Doherty Geological Observatory, Palisades, N.Y.; Bence, at the Exxon Production Research Company, Box 2189, Houston, TX 77001; and Nabelek, at the SUNY Department of Earth and Space Sciences at Stony Brook, NY 11794, where this work was carried out under NSF Grant OCE-78-20058 (Oceanography Section, Submarine Geology and Geophysics).

culated for the 99% confidence level.

Preliminary major element and Ni concentrations were obtained for the cores and rims of approximately 40 olivines and the adjacent glass in four separate thin sections of 527-1-1. From these data eight olivines chosen to represent the total variability in the sample were selected for detailed analysis.

Results and Discussion

The microprobe analyses of the eight olivine crystals reveal rather complex zoning profiles for Ni, Mn, Ca, and Cr in relation to the major element zoning. Markedly different trace-element distributions occur in immediately adjacent olivines. Examples of the two extremes observed are shown in Figs. 1 and 2. "Normal" zoned olivines have generally uniform $Mg/(Mg + Fe)$, but have cores with higher Cr and Ni and lower Mn and Ca than the rims (Fig. 1). "Inverse" zoned olivines have high $Mg/(Mg + Fe)$ and Mn cores but Ni, Cr, and Ca are lower relative to the rim (Fig. 2). The latter type is frequently rimmed with olivine having "normal" zoning. Zoning in the glass at the glass/olivine

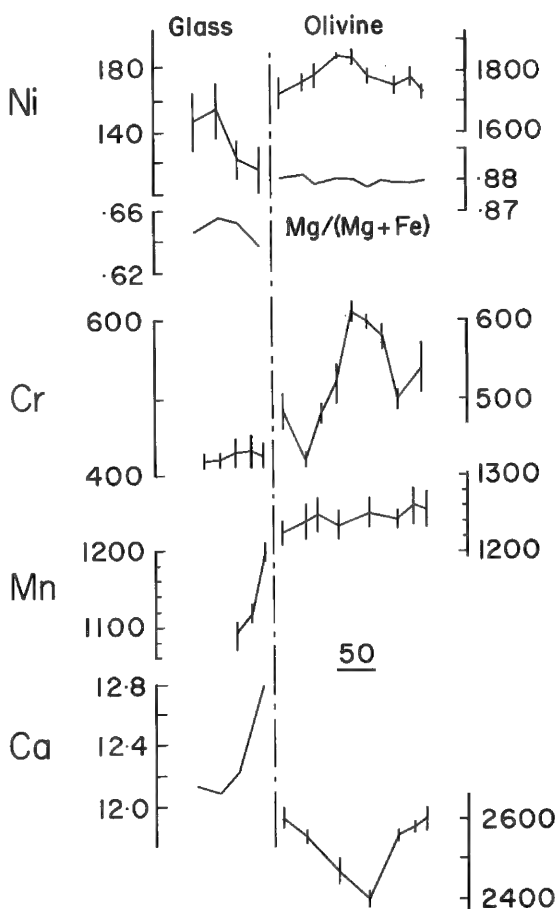


FIG. 1.--Electron microprobe traverse across "normal" zoned olivine phenocryst into adjacent glass. Error bars are calculated from the counting statistics for 99% confidence level. All concentrations in wt.ppm except Ca in glass which is wt.% CaO. $Mg/(Mg + Fe)$ is atomic ratio. Scale bar in micrometers.

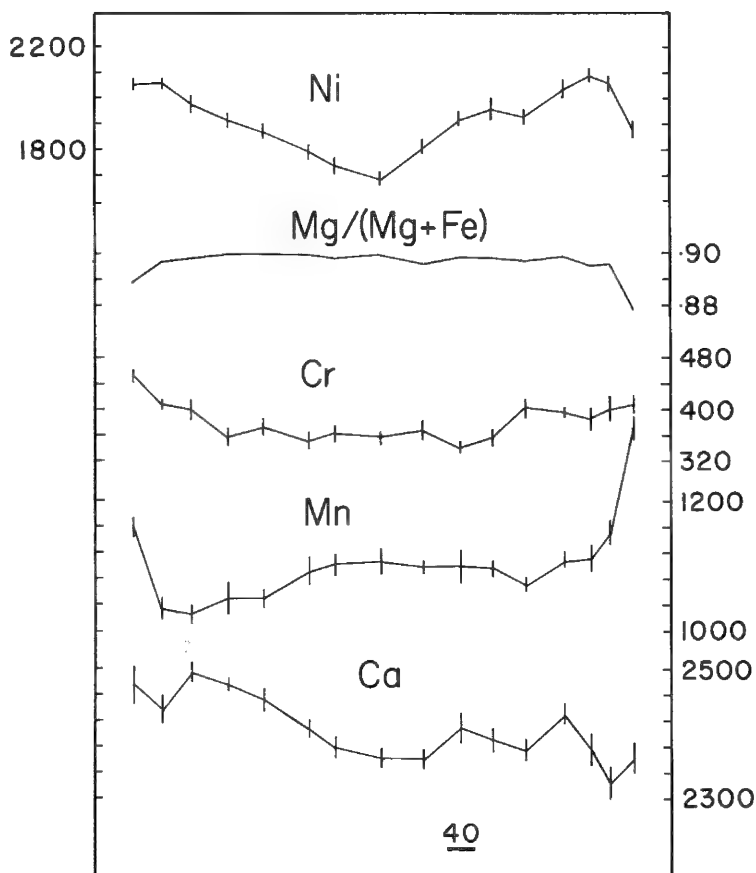


FIG. 2.--Electron microprobe traverse across "inverse" zoned olivine phenocryst. Error bars as for Fig. 1.

interface (Fig. 1) is the result of the quench growth of olivine on an olivine nucleus when the basalt came in contact with seawater. Controlled cooling experiments conducted on a Project FAMOUS basalt glass²⁰ that used the depletion and enrichment zones around phenocrysts as a means of calibration indicate that the melts were quenched at rates in excess of 150°C/hr. In these zones Ni is depleted because it is strongly partitioned into the olivine and Ca and Mn are enriched at the growing face because they are preferentially excluded from the olivine.

A plot of Ni concentration vs Mg/(Mg + Fe) (Fig. 3) reveals that the "normal" zoned olivines follow a calculated one atmosphere fractionation path. This path was calculated from the equations of Leeman¹⁰ and Hart and Davis¹¹ by the type of calculation employed by Hanson and Langmuir.²¹ Rayleigh fractionation is assumed. "Inverse" zoned olivines follow a different path and have core Ni concentrations that are lower than those predicted by low pressure fractionation. However, their rim compositions approach those defined by the 1-at. fractionation paths. We suggest that the "normal" zoned olivines record a low-pressure crystallization history at the time of eruption. The "inverse" zoned olivines record a high-temperature--high-pressure crystallization history followed by low-pressure crystallization.

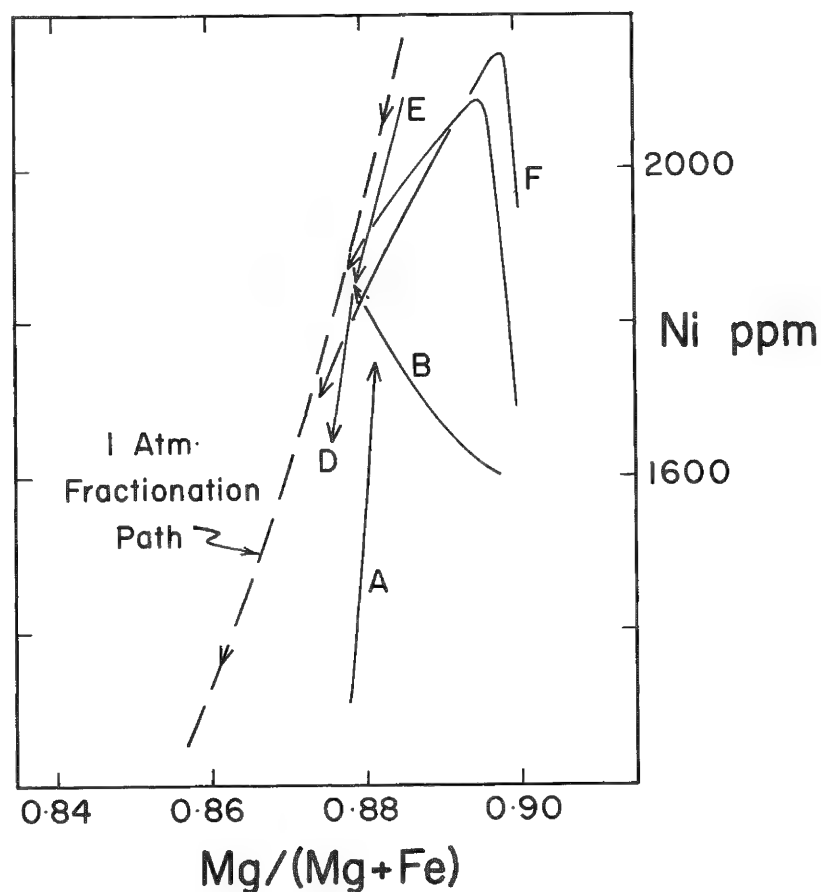


FIG. 3.--Ni vs Mg/(Mg + Fe²⁺) for "normal" (D, E) and "Inverse" (A, B, C, F) zoned olivines. Olivines C and F have "normal" zoned rims.

At 10 kb the liquidus temperature for 527-1-1 is 1310°C. At 1310°C, $k_d^{Ni}(Ol/L) = 9.07$ and at 1268°C (low pressure liquidus), $k_d^{Ni} = 11.22$. Thus if a magma forms at depth and crystallizes olivine on its way to the surface, the nickel content of the olivine should change to reflect the changing bulk composition and changing (increasing) K_d . These effects should tend to cancel each other. Therefore, the fact that the olivine Ni content increases from core to rim in the "inverse" zoned crystals is convincing evidence that changing K_d is the dominant process.

The experiments of Leeman,¹⁰ Hart and Davis,¹¹ and Bickle et al.²³ indicate that $K_d^{Ni}(Ol/L)$ is largely temperature- rather than pressure-dependent. Thus we conclude that we are seeing the pressure effect indirectly through the changing liquidus temperature as a

melt is brought up from depth. This conclusion is substantiated by the Cr data, which correlate with Ni. The increase of Cr from core to rim is consistent with a K_d^{Cr} (O/L) increase as temperature decreases.

References

1. F. A. Frey, W. B. Bryan, and G. Thompson, "Atlantic ocean floor: Geochemistry and petrology of basalts from Legs 2 and 3 of the Deep-Sea Drilling Project," *J. Geophys. Res.* 79: 5507, 1974.
2. H. Sato, "Nickel content of basaltic magmas: Identification of primary magmas and a measure of the degree of olivine fractionation," *Lithos* 10: 113, 1977.
3. H. Bougault, P. Cambon, O. Corre, J. L. Joron, and M. Treuil, "Evidence for variability of magmatic processes and upper mantle heterogeneity in the axial region of the mid-Atlantic Ridge near 22° and 36° N," *Tectonophysics* 55: 11, 1979.
4. W. B. Bryan, G. Thompson, and P. Michael, "Compositional variation in a steady-state zoned magma chamber: Mid-Atlantic Ridge at 65°51' N," *Tectonophysics* 55: 63, 1979.
5. W. B. Bryan and J. G. Moore, "Compositional variation of young basalts in the mid-Atlantic Ridge rift valley near Lat. 36°49' N," *Geol. Soc. Amer. Bull.* 88: 556, 1977.
6. M. J. O'Hara, "Are any ocean floor basalts primary magma?" *Nature* 220: 683, 1968.
7. M. J. O'Hara, "Geochemical evolution during fractional crystallization of a periodically refilled magma chamber," *Nature* 266: 503, 1977.
8. E. Stolper, "A phase diagram for mid-ocean ridge basalts: Implications for petrogenesis," *Contrib. Min. Petrol.* 74: 13, 1980.
9. C. H. Langmuir and G. N. Hanson, "An evaluation of major element heterogeneities in the mantle sources of basalts," *Phil. Trans. Roy. Soc.* A297: 383, 1980.
10. W. P. Leeman, *Experimental Determination of Partitioning of Divalent cations Between Olivine and Basaltic Liquid*, Ph.D. thesis, University of Oregon, 1974.
11. S. R. Hart and K. E. Davis, "Nickel partitioning between olivine and silicate melt," *Earth Planet. Sci. Lett.* 40: 203, 1978.
12. E. Takahashi, "Partitioning of Ni^{2+} , Co^{2+} , Fe^{2+} , Mn^{2+} , and Mg^{2+} between olivine and silicate melts: Composition dependence of partition coefficient," *Geochim. Cosmochim. Acta* 42: 1829, 1978.
13. L. Glitsch and C. J. Allegre, "Determination of crystallization temperatures in fractional crystallization series by nickel partitioning equations," *Earth Planet. Sci. Lett.* 44: 105, 1979.
14. D. B. Clark and M. J. O'Hara, "Nickel and the existence of high MgO liquids in nature," *Earth Planet. Sci. Lett.* 44: 153, 1978.
15. D. Elthon and W. I. Ridley, "Comments on 'The partitioning of nickel between olivine and silicate melt' by S. R. Hart and K. E. Davis," *Earth Planet. Sci. Lett.* 44: 162, 1979.
16. A. E. Bence, S. Brande, G. J. Indelicato, and F. Allen, "Analysis of trace and minor elements in rock-forming minerals using an automated electron probe," in D. R. Beaman, R. E. Ogilvie, and D. B. Wittry, Eds., *Eighth International Congress on X-ray Optics and X-ray Microanalysis*, 1980, 238-248.
17. P. I. Nabelek, "Nickel partitioning between olivine and liquid in natural basalts: Henry's law behavior," *Earth Planet. Sci. Lett.* 48: 293, 1980.
18. A. E. Bence and A. L. Albee, "Empirical correction factors for the electron microanalysis of silicates and oxides," *J. Geol.* 76: 382, 1968.
19. A. L. Albee and L. Ray, "Correction factors for electron probe analysis of silicates, oxides, carbonates, phosphates, and sulfates," *Anal. Chem.* 42: 1408, 1970.
20. S. Rice, *Diffusion and Olivine Growth in FAMOUS Glasses*, unpub. M.S. thesis, State University of New York at Stony Brook, 1978.
21. G. N. Hanson and C. H. Langmuir, "Modelling of major elements in mantle-melt systems using trace element approaches," *Geochim. Cosmochim. Acta* 42: 725, 1978.
22. J. F. Bender, F. N. Hodges, and A. E. Bence, "Petrogenesis of basalts from the Project FAMOUS area: An experimental study from 0 to 15 kbars," *Earth Planet. Sci. Lett.* 41: 277, 1978.
23. M. J. Bickle, C. E. Ford, and E. G. Nisbet, "The petrogenesis of peridotitic komatiites: Evidence from high-pressure melting experiments," *Earth Planet. Sci. Lett.* 37: 97, 1977.

PETROGRAPHY OF THE U-BEARING MINERALS IN GRANITIC ROCKS: TECHNIQUES AND RESULTS

J. A. Speer and T. N. Solberg

The difficulty of studying the spatial distribution and mineralogy of U in most crustal rocks is its low concentrations. For example, the average U content of 215 samples of late Paleozoic granite of the southeastern USA is 7.3 ppm. A succession of macro- and microanalytical techniques were used to study increasingly smaller areas to record the location of U and to identify and characterize U-bearing minerals.

The topics of uranium location in rocks and its mineralogy and migration are central to several areas of current interest: (1) Weathered granites may provide the source of U for sedimentary U deposits. Determining which rocks are most susceptible to U loss could aid in locating depleted granite source regions and potential adjacent sedimentary U deposits. (2) Effective and economic solution-mining of granites for U requires understanding of the mechanisms of U retention. (3) The same knowledge can be applied toward locating long-term radioactive waste depository sites. The behavior of U in granites over geologic time will provide a model for the behavior of actinides in the earth's crust, which can be used to design a containment system that minimizes transport of radioisotopes. (4) Variation in crustal abundance of radioactive elements is largely responsible for the lateral variation in surface heat flow in the eastern USA. Potential geothermal resources in an area of otherwise normal geothermal gradients depend on the added radiogenic heat from elevated U, Th, and K contents. Nearly half of this added heat is derived from U, and the ability to identify which rocks can retain U will help to locate areas of high heat flow.

The rocks are first screened in the laboratory or field for further study by γ -ray spectrometry measurements for U. Concentrations of γ -emitting parent or daughter isotopes are determined to calculate U, Th, and K contents. Measurements are made on either powdered surface or drillcore samples, or on rocks in place by airborne, hand-held, or in-borehole instruments (Fig. 1A). Small areas for detailed work are located by radioluxographs,¹ which give a graphical look at the distribution of the α -producing elements (Fig. 1B). Polished petrographic thin sections are made of these areas and are used to identify the larger, discernible U-bearing minerals by transmitted or reflected optical petrography (Fig. 1C). The same thin sections are used for U-mapping by induced fission by means of a muscovite detector to record the fission particle tracks (Fig. 1D and E). Fission track work is specific for U when a thin section is irradiated with thermal neutrons and the recording is made with a muscovite detector. A fluence of 10^{17} n/cm² can reveal U levels as low as 3 ppm on a microscopic scale. The fission track work is essential for locating the U present in indiscernible minerals and as a trace component of the major minerals.

Once the U location has been documented by optical petrography and fission track U mapping, point analyses and area scans for U, as well as other elements, are done by electron microprobe (Fig. 2). The electron microprobe helps to identify the U-bearing and associated minerals, and allows study of chemical substitutions and elemental distribution at greater magnifications than the fission track work. For the final step, the U-bearing minerals are examined by ion microprobe for light and trace-element chemistries (Fig. 3) as well as isotopic compositions for age determinations.

In order of abundance, U occurs (1) in accessory minerals, with U concentrations decreasing in the order uraninite, coffinite, thorite, zircon, monazite, titanite, allanite, apatite, zeolites; (2) on altered surfaces of Fe²⁺- and S-bearing minerals; (3) at microcracks filled with carbonate, zeolite, and Fe-Mn-Ti oxyhydroxide minerals; (4) on clay minerals of altered feldspars; and (5) in major minerals as a widely dispersed minor component.

Author Speer is with the Orogenic Studies Laboratory and Solberg is with the Molecular Structures Laboratory of the Department of Geological Sciences, Virginia Polytechnic Institute and State University, Blacksburg, VA 24061. This work was partially supported by the U.S. Department of Energy under contract DE-AC05-78ET27001.

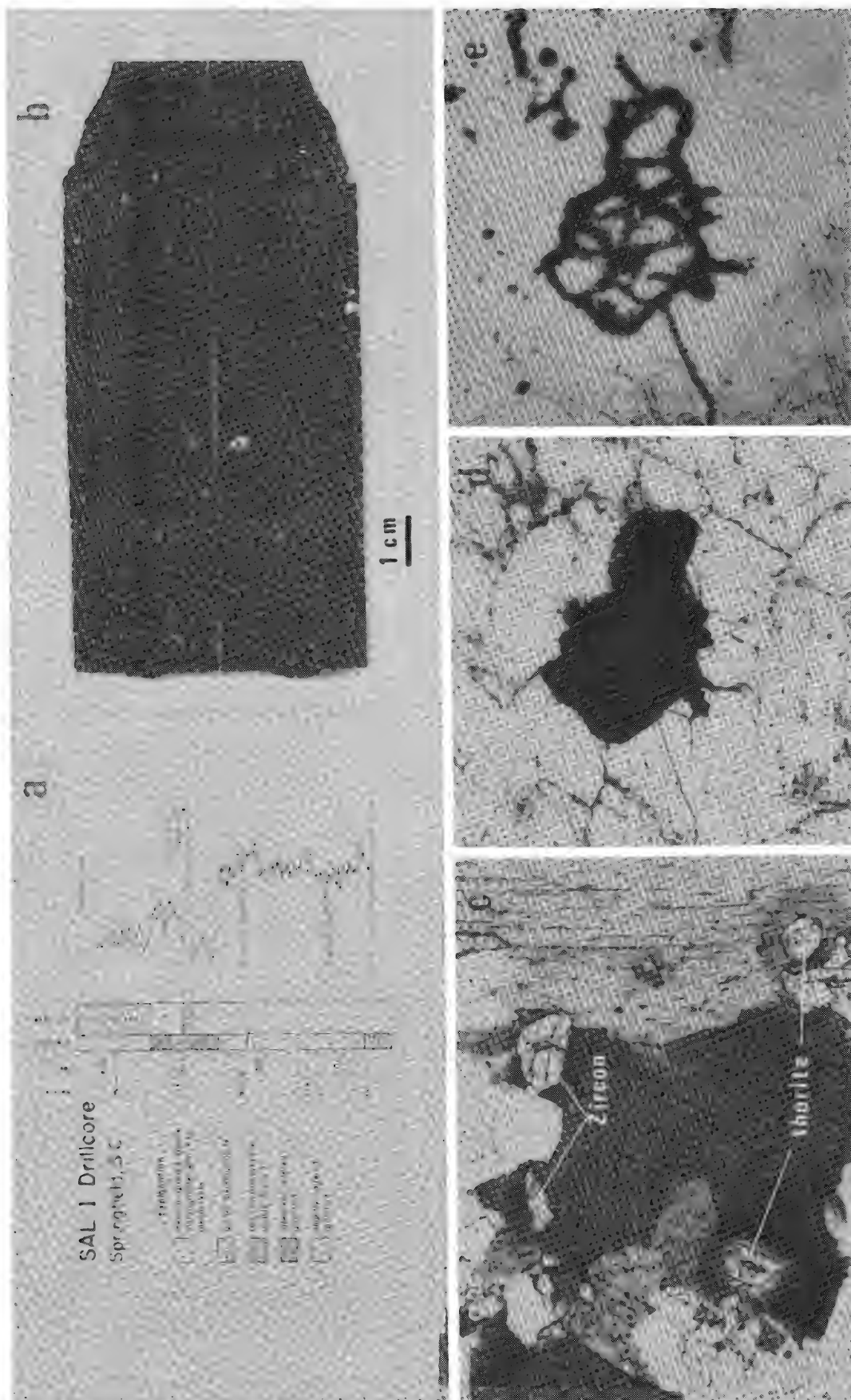


FIG. 1.--A. Lithologic and γ -ray log of drillcore in granite beneath Atlantic coastal plain at Springfield, S.C. The γ -log shows that U and Th contents of fresh and slightly altered granite is uniform. The intensely altered granite is depleted in these elements but a cross-cutting microcrystalline, brecciated quartz vein is enriched in U. B. Radioluxograph¹ of sectioned core sample from Petersburg granite (Va.) showing location of α -emitting elements U and Th which are primarily located in uraninite, thorite, zircon, and titanite. C. Thorite and zircon crystals included in biotite of Liberty Hill granite (S.C.). Photomicrograph of polished thin section. These two thorites are compositionally zoned and contain up to 9.5 wt% UO_2 . D. Photomicrograph of a magnetite grain. E. Same specimen showing increased fission track densities associated with the surfaces of the grain boundaries and cracks.

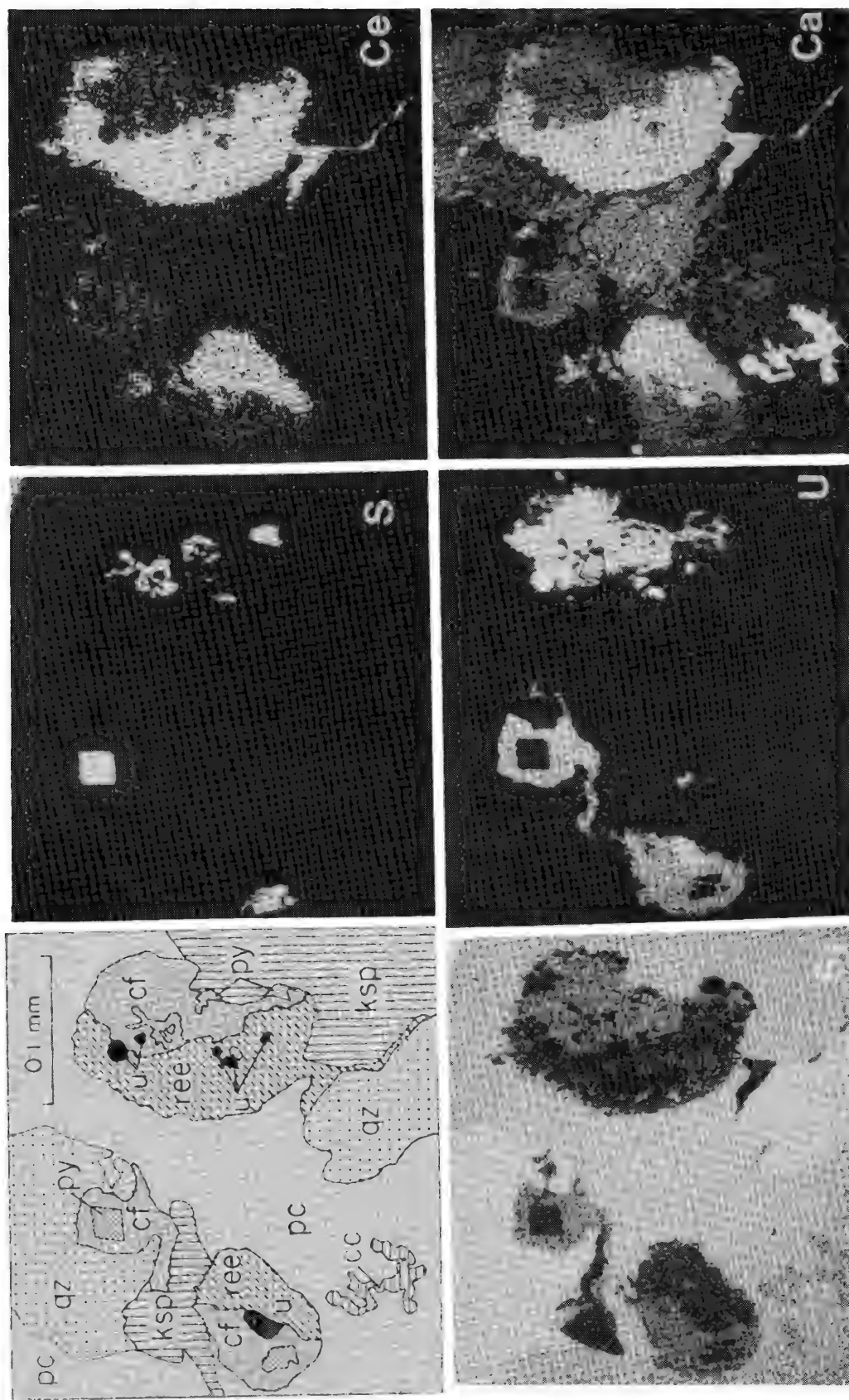


FIG. 2.--Sketch and electron beam scanning images for S, Ce, Si, U and Ca showing the distribution of minerals associated with an U-silicate (coffinite ?) by their characteristic elements: U = uraninite (U), cf = coffinite (U + Si), REE = Ca + Ce + La fluorocarbonate (bastnaesite ?), py = pyrite (S), cc = calcite (Ca), pc = plagioclase (Ca + Si), qz = quartz (Si), Ksp = alkali feldspar.

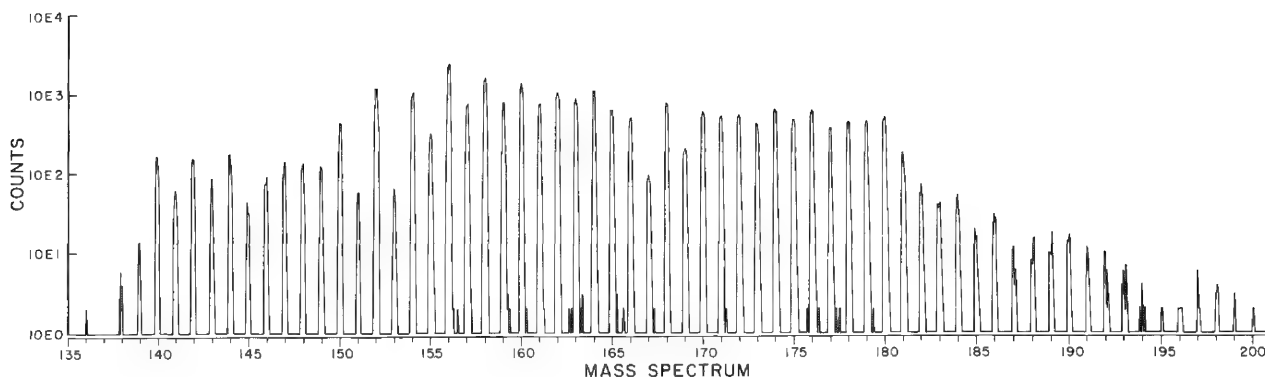


FIG. 3.--Mass spectrum obtained by ion microprobe in the region of the rare earth elements on uraninite from Spruce Pine, N.C. Ratios of the counts for the rare earths show the uraninite to be heavy RE-enriched.

U distribution in the accessory minerals uraninite, uranoan thorite, zircon, monazite, titanite, allanite, and apatite is believed to be of magmatic origin. They occur as euhedral crystals included in the major magmatic minerals. Electron microprobe analyses of the uraninites reveal up to 4 wt% ThO_2 and 10 wt% RE_2O_3 , chemical evidence of magmatic origin.² Determination of the uraninite Pb isotopic composition by ion microprobe yield isotopic ages approaching whole rock Rb-Sr isotopic ages, further evidence of their magmatic origin. The ion microprobe also revealed a variety of trace elements present in the uraninite with minor solid solutions (in addition to ThO_2 and REE) with CaO , ZrO_2 , HfO_2 , UF_4 . The uraninites have heavy rare earth element enrichment. The thorites are zoned and contain up to 20 mol% USiO_4 , and lesser amounts of PbO and RE_2O_3 . The remaining primary accessory minerals contain less than 0.01 wt% U.

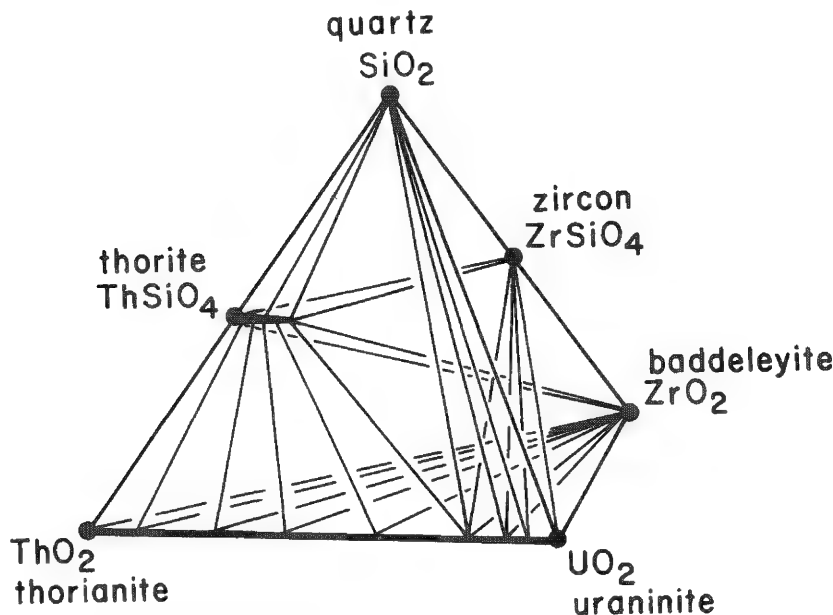


FIG. 4.--Subsolidus phase assemblages in the system $\text{SiO}_2\text{-ThO}_2\text{-UO}_2\text{-ZrO}_2$.³

Within the $\text{UO}_2\text{-ThO}_2\text{-ZrO}_2\text{-SiO}_2$ system (Fig. 4), the U-bearing phase assemblages of the southeastern United States granites are:

uraninite + thorite + zircon + quartz
thorite + zircon + quartz

In rocks with $\text{U}/(\text{U} + \text{Th}) < 0.25$, U is incorporated into the thorites with much smaller amounts in the other minerals. The thorites in these rocks contain less than 15 mol% USiO_4 . In rocks with $\text{U}/(\text{U} + \text{Th}) > 0.25$, the amount of U present exceeds that which can be incorporated in the thorite and the excess U forms uraninite. Thorites coexisting with uraninite are the most U-rich, containing about 20 mol% USiO_4 , comparable to the maximum amount found experimentally.³

Mineralogical and textural evidence suggests that the remaining occurrences of U in coffinite, zeolites, and indiscernible U-bearing phases result from postmagmatic fixation of U migrating by way of fractures and microcracks. Fixation of the redistributed U can be attributed to either (1) reactions involving Fe, Mn, S, or Ca that can consume the oxidizing-complexing agents of U; or (2) ion exchange or sorption of U by zeolite, clay, or Fe-Mn-Ti oxyhydroxides. These processes of U retention demonstrate the microscale mechanisms which give the rocks the ability to buffer

chemical conditions and prevent U loss.

References

1. J. R. Dooley Jr., "The radioluxograph: A fast, simple type of autoradiograph," *Second UN Internat. Conf. Peaceful Uses Atomic Energy*, 3: 550-553, 1958.
2. C. Frondel, "Systematic mineralogy of uranium and thorium," *U.S. Geological Survey Bull.* 1064, 1958.
3. F. A. Mumpton and R. Roy, "Hydrothermal stability studies of the zircon-thorite group," *Geochim. Cosmochim. Acta* 21: 217-238, 1961.

GRAPHICAL PROCEDURES FOR THE REFINEMENT OF ELECTRON MICROPROBE ANALYSIS OF FINE-GRAINED PARTICLES

Todd N. Solberg, Jürgen Abrecht, and David A. Hewitt

Precise stoichiometry of fine-grained particles, especially of experimentally synthesized minerals, is a difficult analytical problem for the electron microprobe because the sample size is commonly insufficient to contain the analytical volumes for the elements present. Theoretical approaches as well as some specialized technical approaches to this problem have been well described and offer solutions but are either unavailable to or beyond the scope of existing equipment in the majority of present-day facilities.¹⁻³ This paper is a progress report on some simple experimental and graphical procedures that have allowed us successfully to analyze synthetic mica particles with widths of 1-10 μm and thicknesses of a few microns or less.

To determine how the composition of a homogeneous material appears to change as the sample becomes thinner than the beam excitation depth, the following experiment was performed. A cleavage flake of natural biotite was ion-thinned (Fig. 1) to produce a low angle wedge tapering in thickness from a few hundred microns to zero. Analyzing along this taper from the thick portion towards a thinned edge in 1 μm steps yields analyses with sums of $\sim 96\%$ (plus $\sim 4\%$ H_2O) as long as the sample thickness is greater than the effective excitation depth.⁴⁻⁷ As the sample becomes thinner than the effective excitation depth, the analytical sums monotonically decrease to zero.

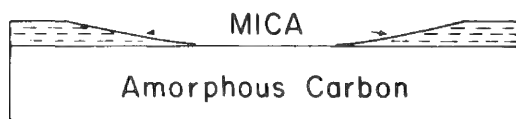


FIG. 1.--Ion-thinned biotite mounted on a carbon substrate as used for electron microprobe analysis: 10 kV, 10 nA, 20 s, 1 μm steps.

Figure 2 shows the results of a single scan of the thinned biotite at a beam voltage of 10 kV. The data are plotted in terms of analytical sum versus the occupancies of the biotite calculated on the basis of 22 oxygens. If one assumes the density for this biotite to be 3 g/cm^3 , and uses the critical excitation potential of Mg $K\alpha$ (which is the lowest energy x-ray line used for this analysis), then the effective excitation depth as described by S. J. B. Reed is approximately 2.7 μm . Plots of the Mg $K\alpha$ x-ray line counts versus distance showed that the effective excitation depth was reached 20 μm from the edge of the thinned biotite sample. Therefore each 1 μm step represented a change in thickness of ~ 1500 Å. An analogous procedure with the Fe $K\alpha$ x-ray counts (the highest energy x-ray line used for analysis) gave the same changes in thickness. Several important features should be noted. First, the sample is homogeneous, as shown by the tight clusters of data points at $95 \pm 1\%$ analytical sum. Second, the trends of the calculated occupancies are smooth and have relatively gentle slopes. Note, however, that the slopes vary both in sign and amount, which shows that significantly different "apparent" compositions are obtained when grain thicknesses are less than excitation depths. Finally, note that the plots appear to behave nicely down as far as $\sim 30\%$ analytical sum. The same experiment has been run at voltages ranging from 7 to 30 kV and yielded similar results each time.

This experiment suggests that fine-grained particle analysis can be obtained by analysis of a spectrum of particles of various sizes yielding analytical sums in the range of 50-100%. Plots of these data and extrapolation to 100% or some other ideal total can yield consistent and reliable analyses. The technique is obviously improved if a relatively large number of analytical points are used and if data in the range of high analytical sums are widely spread.

These techniques have been tested by analysis of some hydrothermally grown fine-grained biotite. The particles are subhedral to euhedral flakes with widths of 1-10 μm

The authors are with the Department of Geological Sciences, Virginia Polytechnic Institute and State University, Blacksburg, VA 24061.

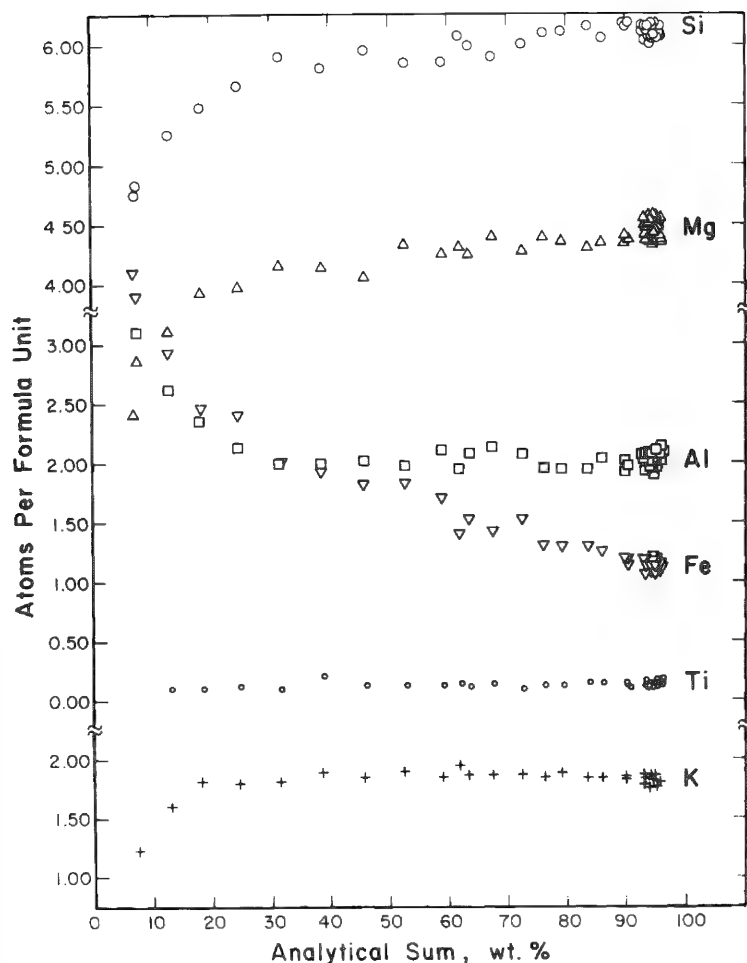


FIG. 2.--Plots of the atoms per formula unit vs analytical sums of the ion-thinned natural biotite show smooth monotonic variations.

Although many more experiments remain to be performed in order to establish clearly the procedure under a variety of conditions and with a variety of materials, the present results suggest that the techniques are promising as a simple and relatively quick method for fine-particle analysis.

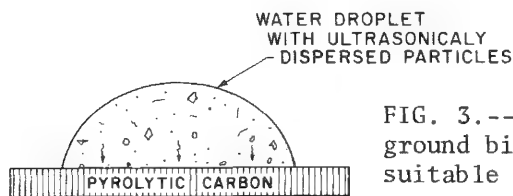
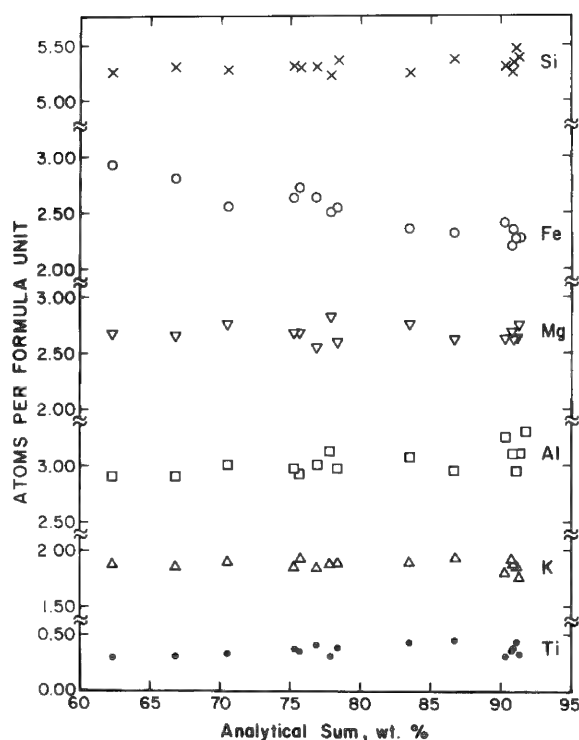


FIG. 3.--Samples of small particles to be analyzed or of ground biotite standards are dispersed ultrasonically in suitable liquid; after a droplet of liquid was slowly evaporated, sample was carbon coated for electron microprobe analysis.

and thicknesses of a few microns at most. The sample was prepared by ultrasonic dispersion of a small amount of the material in water (or alcohol); a droplet of the dilute mixture is then placed onto a polished plate of pyrolytic carbon oriented normal to the C-axis (Fig. 3). The sample was allowed to dry slowly and was then carbon coated in the normal manner for electron microprobe analysis.

During analysis, backscattered and/or secondary electrons were used to image the sample and to select isolated single grains with a range of sizes. The grains were analyzed for Si, Fe, Mg, Al, K, and Ti, with samples of orthoclase, fayalite, Mg-olivine, and rutile used as standards. The data are plotted in Fig. 4. Note again that the variations are smooth and nearly linear over the range of 60-92%. We obtained the final analysis for the material by fitting lines to the data and extrapolating to 96%. The reliability of this analysis and many others on similar synthetic biotites can be attested to by the self-consistent substitution models for Ti-biotites that have been developed from these data.⁸ An additional advantage of the method is that it provides a way to check whether the population of fine-grained particles is truly homogeneous in composition.



ELECTRON MICROPROBE ANALYSIS ON

on SAMPLE B 114

10 KV 10 na 10 sec

STARTING BULK COMPOSITION:



RUN DATA:

T = 800°C P = 1 Kb Run Duration = 7d

Graphite - Methane Buffer

PRODUCT:

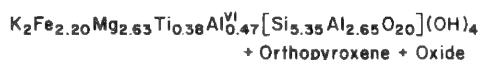


FIG. 4.--Typical plot of analysis of hydrothermally grown biotite used for estimation of its true composition. Note the smooth nature of plots.

References

1. J. T. Armstrong and P. R. Buseck, "Quantitative chemical analysis of individual microparticles using the electron microprobe," *Anal. Chem.* 47: 2178, 1975.
2. J. T. Armstrong, *Quantitative Electron Microprobe Analysis of Airborne Particulate Material*, Ph.D. Thesis (Arizona State University), Ann Arbor, Mich.: Microfilms International, 1978.
3. J. A. Small, D. E. Newbury, and R. L. Myklebust, "Analysis of particles and rough samples by Frame P, a ZAF method incorporating peak to background measurements," *Microbeam Analysis--1979*, 243.
4. T. O. Ziebold and R. E. Ogilvie, "An empirical method for electron microanalysis," *Anal. Chem.* 36: 322, 1964.
5. A. E. Bence and A. L. Albee, "Empirical correction factors for the electron microanalysis of silicates and oxides," *J. Geol.* 76: 382, 1968.
6. A. L. Albee and L. Ray, "Correction factors for electron probe microanalysis of silicates, oxides, carbonates, phosphates, and sulfates," *Anal. Chem.* 42: 408, 1970.
7. S. J. B. Reed, *Electron Microprobe Analysis*, London: Cambridge University Press, 1975, 217.
8. J. Abrecht and D. A. Hewitt, "Ti-substitution in synthetic Fe-biotites," *Geol. Soc. Am. Abstr. Progr.* 12: p. 377, 1980.

CHEMICAL VARIATIONS IN GOLD FROM THE CENTRAL APPALACHIANS OF VIRGINIA

T. N. Solberg and J. R. Craig

Compositional variations of lode samples and placer gold nuggets from the Central Appalachians of Virginia are defined in terms of gold, silver, mercury, and copper contents. These data provide potential signatures of gold from different deposits and define thin surficial compositional changes that result from weathering by oxygenated waters and from contamination by mercury released in previous recovery attempts.

The nature and variations of chemical composition of small gold particles either *in situ* in lode deposits or as loose "nuggets" in placer ores is poorly known because the conventional assay techniques of bulk samples mask individual grain identities. The electron microprobe is ideally suited for the analysis of individual grains because of its resolution in spot analysis and the ability to define the distribution of elements by x-ray mapping. The present investigation, the first microanalytical study of gold from the once prosperous deposits along the Piedmont region of the Appalachians, is part of a continuing investigation into the nature and mineralogy of Appalachian gold.

Samples, Preparation, and Analytical Procedures

Gold mining in Appalachia goes back to Colonial times¹ and some production continues to the present day.² The areas in Virginia in which gold occurrences have been reported are noted in Fig. 1 and have been described by Sweet.³ The best-known and largest zone is the gold-pyrite belt extending in a north-northeast trend for more than 100 miles in the Virginia Piedmont, which contains scores of minor gold-bearing quartz veins. Similar occurrences of gold-bearing quartz veins are present in the Virgilina district and in central Virginia near the North Carolina border. Localized placer deposits are known from streams draining the areas of the gold-bearing veins and in scattered localities.

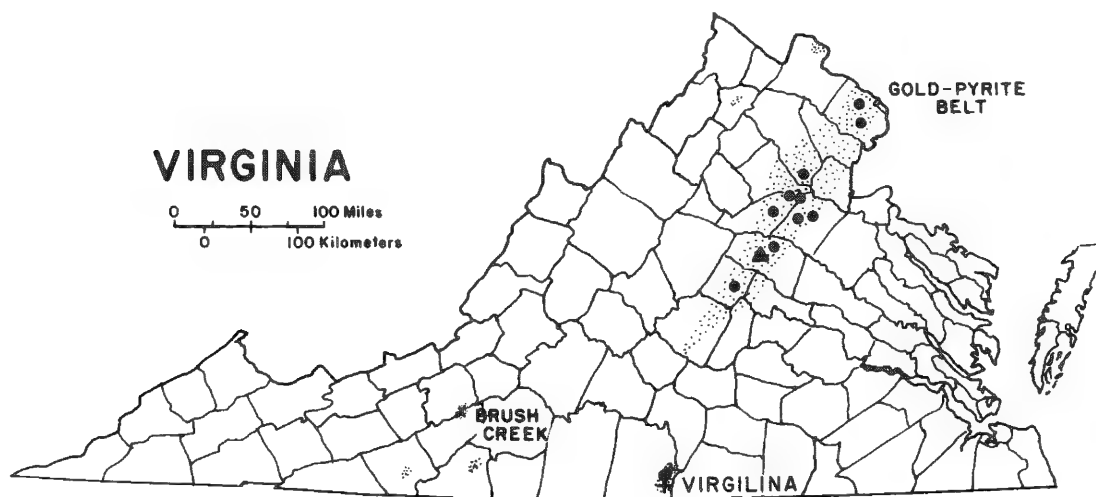


FIG. 1.--Gold occurrences in Virginia: quartz vein sites (●), place sites (x and +), sulfide ore sites (▲).

The samples examined in the present study included (1) gold-bearing quartz vein specimens from several of the deposits in the gold-pyrite belt (●), (2) gold-bearing massive sulfide ores from the Mineral District in Louisa County (▲), and (3) placer samples panned from streams in the Brush Creek and Virgilina areas (x and +). We are indebted to the

The authors are with the Department of Geological Sciences, Virginia Polytechnic Institute and State University, Blacksburg, VA 24061. The support of the VPI&SU Mining and Minerals Resources and Research Institute and of National Science Foundation grant EAR-8011-418 is gratefully acknowledged.

National Museum of Natural History of the Smithsonian Institution and to the Mineralogical Museum of Harvard University for providing quartz-vein samples from the gold pyrite belt.

Gold-bearing quartz-vein samples and massive sulfide samples were cut with a slow-speed thin blade diamond saw, cast in a cold-setting epoxy resin, and polished in the routine manner employed in the examination of ore samples.⁴ Placer samples were separated from their host sands and gravels by panning and the use of heavy liquids. Individual grains were hand picked from heavy mineral concentrates, mounted in cold-setting epoxy resin, and polished in the conventional manner.

Analysis was carried out by an ARL-SEMQ electron microprobe operated in conventional fashion with pure metals as standards. Data reduction was carried out by the Bence-Albee and Magic Schemes.

Results and Discussion

Electron microprobe analysis has revealed significant compositional variations in gold, silver, copper, and mercury (Figs. 2-5). It is apparent from Fig. 4 that gold from

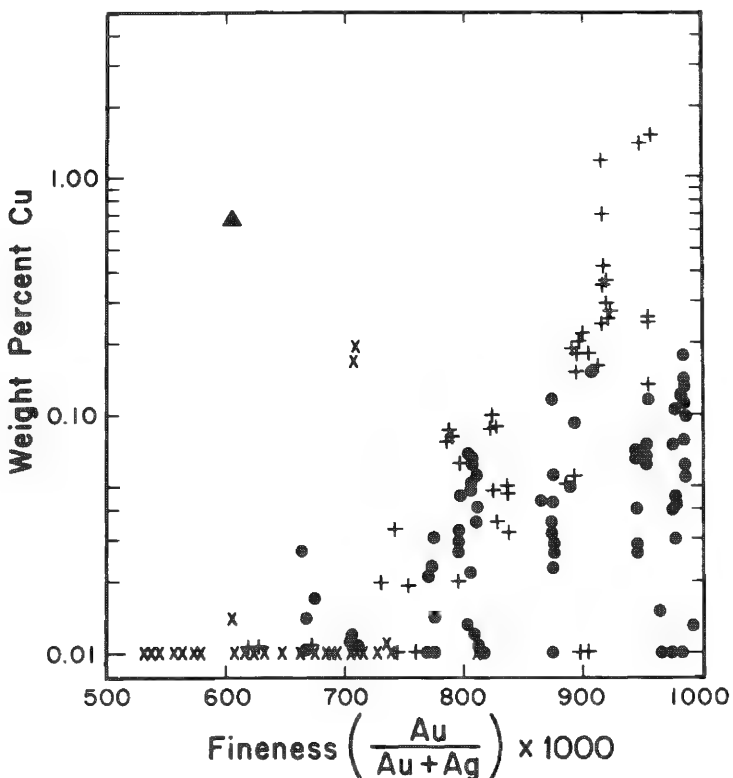


FIG. 2.--Compositional ranges of gold in terms of fineness and copper content. (Symbols as in Fig. 1.)

tions of gold from different areas and environments. Microprobe analysis has permitted definition of the degree of homogeneity within individual grains and between isolated grains in individual samples of quartz-vein material. Spot analysis on individual gold grains up to 200 μm wide revealed that the compositions varied by less than 1%. Step scans at 17 μm intervals on grains up to 350 μm across showed the same degree of homogeneity and the absence of any grain boundary variations.

In contrast to the homogeneity of quartz-vein gold and most placer grains, some placer samples from the Brush Creek area revealed marked heterogeneity at grain margins. Two effects are illustrated in Figs. 2-5. The first effect is the presence of a 5 μm -thick gold-rich rim (95-98 atomic % gold = 972-991 fine) on grains with homogeneous interiors ranging from 40 to 41 atomic % gold (= 550-562 fine). (Atomic % is used in Figs. 3 and 4 merely for clarity of presentation.) This rim is visible under the ore microscope as a

quartz-vein deposits is generally purer and contains more copper than does gold from placer or stratabound massive sulfide deposits. The quartz-vein gold ranges from 665 to 991 fine with copper contents up to 0.18 wt.%. The vein gold samples from eight localities along the gold-pyrite belt ranged only from 875 to 991 fine; samples taken from the residue in an old stamp at the Red Bank Mine in the Virgilina District, which are presumed to represent pulverized quartz-vein samples, have fineness values ranging from 665 to 805.⁵ In contrast, the placer gold ranges from 530 to 950 fine with copper contents reaching a maximum of 1.5 wt.%. The placer samples from the two major districts sampled have significant but only partly overlapping ranges: Brush Creek samples range from 532 to 739 fine (and a single grain of 914 fineness) and Virgilina District samples range from 620 to 958 fine. Gold from a stratabound massive sulfide ore has a fineness of 605 and a copper content of 0.68 wt.%. There thus appear to be significant differences, albeit somewhat overlapping, in the composi-

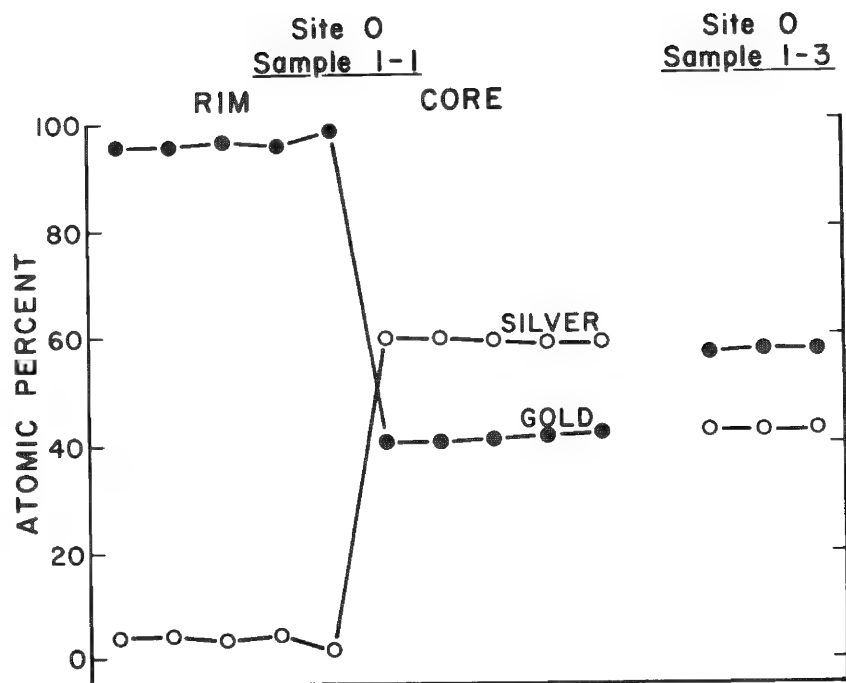


FIG. 3.--Step scan across gold grains in 1µm intervals shows gold-rich rim on one sample and homogeneous nature of another grain.

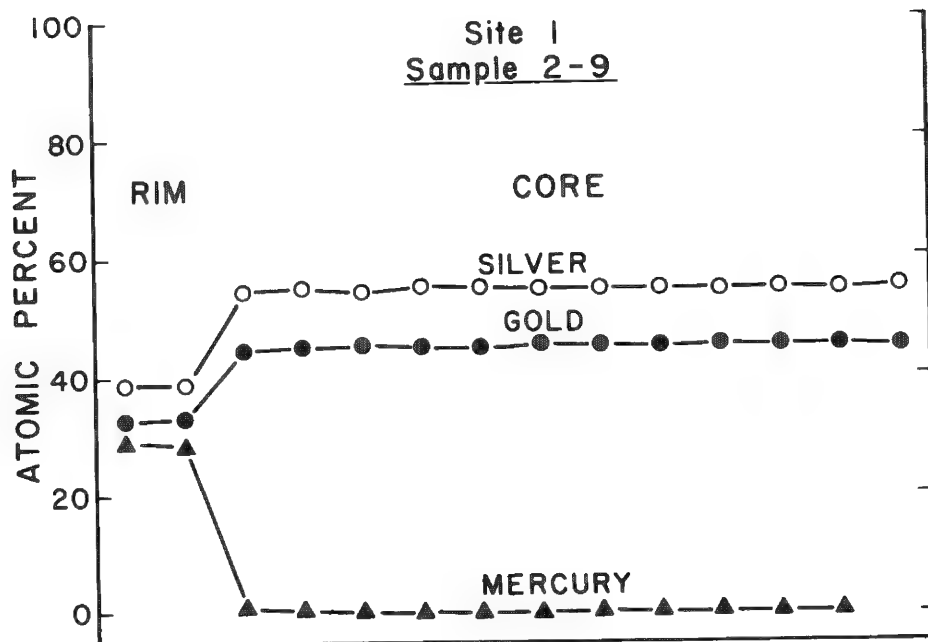


FIG. 4.--Step scan across gold grain in 1µm intervals shows mercury contamination along rim.

distinctly more yellow zone and has been ascribed by Desborough, who observed a similar effect in some placer gold from the western USA, to the leaching of the more soluble silver by oxidizing stream waters.⁶ Although this study is the first to quantify this alteration effect in Appalachian gold, credit for its first observation and proper interpretation must go to Fontaine, who noted it in 1882.⁷ Figure 5 shows that silver depletion has also occurred along internal grain margins, presumably as the result of grain boundary diffusion.

The second effect, illustrated in Figs. 4 and 5, is the localized surficial presence of mercury on some grains. These grains, which are often distinctly silvery in appearance, have been found by microprobe analysis to contain regions containing up to 29 atomic % mercury. Although generally confined to small exterior regions of grains, mercury has also been found concentrated along fractures in the interiors of some grains. Because most grains contain no detectable mercury, because the mercury is very localized

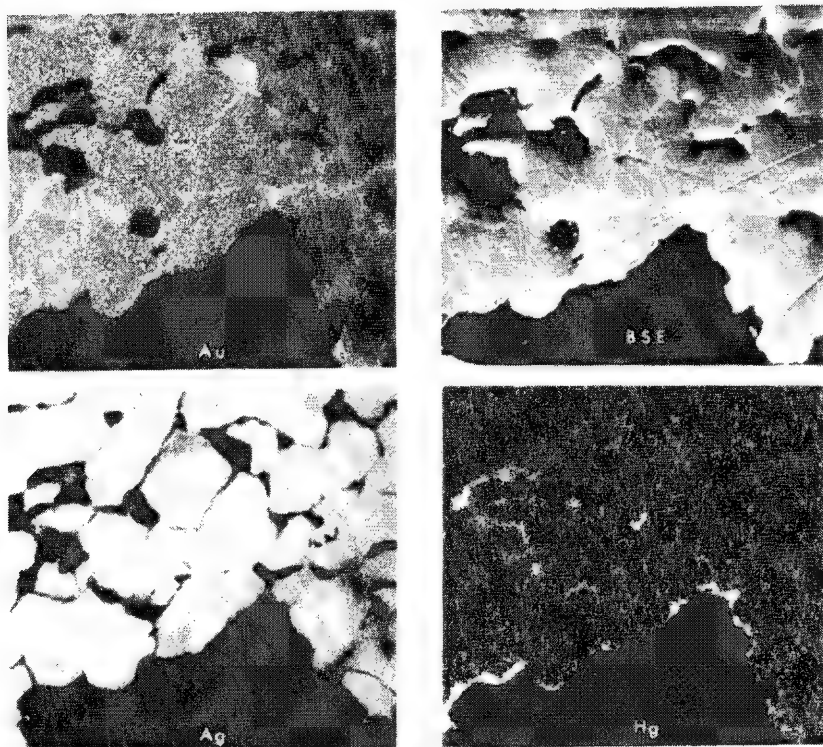


FIG. 5.--Backscattered electron (BSE) image and select element scans for gold (Au), silver (Ag), and mercury (Hg) illustrate compositional variations in placer gold grain from Brush Creek area of Montgomery and Floyd Counties. (Field of view = 200 μ m.)

even on the richest of grains, and because numerous old records note the frequent use of mercury as an amalgamating agent in stamps and in gold pans, we believe that the mercury is a contaminant. It is likely that the mercury found in some grains was lost during prior gold recovery attempts. The same conclusion was reached by investigators who recently reported a similar occurrence of mercury-bearing placer gold from the Johnsville District of California.⁸

The electron microprobe is thus a powerful tool, perhaps the only tool today, that may be used to define compositional variations in, and characterize the signatures and history of, gold grains in several types of deposits.

References

1. Thomas Jefferson, *Observations sur la Virginie*, Paris, 1786, 64-65; *Notes on the State of Virginia*, 1st Am. ed., 1787, 38; 2nd Am. ed., 32.
2. G. F. Becker, *A Reconnaissance of the Gold Fields of the Southern Appalachians*, Washington: U.S. Geological Survey, 16th Ann. Rept., 1894-95, Pt. III, 251; T. L. Watson, *Mineral Resources of Virginia*, The Virginia Jamestown Exposition Commission, Lynchburg, Va.: J. P. Bell Co., 1907; A. H. Koschmann and M. H. Bergendahl, *Principal Gold-producing Districts of the United States*, U.S. Geological Survey Prof. Paper 610, 1968; J. T. Pardee and C. F. Park, *Gold Deposits of the Southern Piedmont*, U.S. Geological Survey Prof. Paper 213, 1948.
3. P. C. Sweet, *Gold in Virginia*, Virginia Division of Mineral Resources Publication 19, 1980.
4. J. R. Craig and D. J. Vaughan, *Ore Microscopy and Ore Petrography*, New York: Wiley, 1981.
5. M. A. Linden, *Gold Mineralization in the Virgilina District, Halifax Co., Va.*, M.S. thesis, Virginia Polytechnic Institute and State University, Blacksburg, Va., 1981.
6. G. A. Desborough, "Silver depletion indicated by microanalysis of gold from placer occurrences, western United States," *Econ. Geol.* 65: 304, 1970.
7. W. M. Fontaine, "Notes on Virginia geology: The Brush Creek, Va., gold district," *The Virginias* 3: 108, 1882.
8. R. L. Foster, E. E. Foord, and P. E. Long, "Mineralogy and composition of Jamison Creek particulate gold, Johnsville Mining District, Plumas Co., Calif.," *Econ. Geol.* 73: 1175, 1978.

SEM AND CHEMICAL EVALUATION OF COAL ASH AND RELATED EROSION AND CORROSION FROM SOME WESTERN COALS

M. Mitchell and P. Ludi

This paper concerns the analysis of mineral matter and fouling products associated with a Western coal from the San Juan Basin of New Mexico, which is currently used in large electric generating plants. On burning, the mineral matter becomes the bottom ash, fly ash, and slag in the furnace. It also contributes volatile elements that deposit with the ash on cooler portions of the combustion unit or exit with the hot gases. The gases and fouling deposits contribute to corrosion, and the moving particulates are responsible for metal erosion. The SEM and EDX have been used to examine the surfaces and deposits in a furnace. In addition, x-ray diffraction and fluorescence and optical (metallographic) analyses have been used in the study. The primary difference between the analyses of the raw mineral matter and the fly ash are the volatile materials that exit with the combustion gases or redeposit in the cooler regions of the furnace and cement fly ash into the fouling material. These deposits include NaCl and sodium sulfite, as well as glass and mullite, which are the primary components of the fly ash.

As the problems associated with energy production and use become more severe, research in the development of low-grade and low-rank coals becomes more important. Since electricity, investigations concerning combustion and generator efficiency are of interest.

Fireside problems are associated with incomplete combustion and smoking, usually eliminated by use of excess air for combustion, 15-20% over that required for complete theoretical combustion. Other problems include high-temperature corrosion in the combustion region and low-temperature corrosion in other regions of the combustor. Figure 1 is a typical combustion unit as used in power generation. The third group of problems is associated with fouling ash removal in the combustor and inorganic particulates generated during combustion. The last two groups of problems are associated with the composition of the particular coal being burned and are the concerns of this study.

Coal is a highly variable material in both its organic structure and in the associated inorganic minerals. It is the mineral matter that results in the ash that is removed from the bottom of the furnace, the fly ash (Fig. 2), which can erode the furnace walls and tubes--the material that adheres to the furnace walls and decreases the heat flow to the steam and thus reduces the efficiency of the system. Volatile elements that form part of the minerals and the organic fraction of the coal are responsible for corrosion.

The gases leaving the combustion section of the furnace are usually between 1650 and 1775°F. Those leaving the economizer are between 600 and 700 F. Exact temperature cannot be given even for a specific unit because a unit is run at various loads depending on the power load expected in the service area of the generating plant.

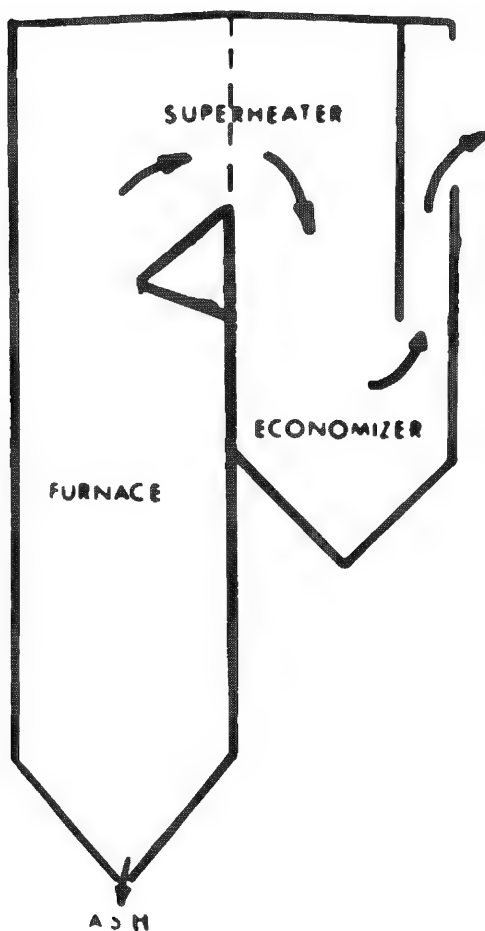


FIG. 1.--Typical coal-fired furnace for steam electric generation.

The authors are at the Department of Metallurgy, New Mexico Institute of Mining and Technology, Socorro, NM 87801.

Approximately 100 minerals have been identified in coal. However, clays (often kaolinite), quartz, pyrite, calcite, and sulfates are the most common in Western coals. The Eastern coals are usually associated with higher sulfur and iron content than Western coals. Of the Western coals, the lignites of the Great Plains are noted for their high sodium content.^{1,2} The coals studied in this project are primarily from the San Juan Basin of New Mexico and are not particularly high in sulfur nor sodium, the elements often associated with corrosion. The coal averages 18% ash and is often classified as sub-bituminous. Recent analysis indicates that the coal is actually bituminous. The ash is particularly acidic, and the primary minerals are kaolinite and quartz. Analyses of the ash from the coal and of the fly ash are given in Table 1. Figure 2 is an SEM photo of a typical fly ash generated from this coal.

Analytical Techniques

Samples of the tube walls of the combustion area and of the superheater tubes were used in this analysis along with the fly ash from the plant's electrostatic precipitator. Chemical analyses of ash from various coals are given in Table 1.

The furnace wall tubes are smooth and those of the superheater have a spiral fin for improved heat transfer. This fin is eroded by the fly ash and the combustion gases, and the tube is eventually thinned enough so that it fails. In some areas, the fin becomes a site for fouling deposit formation. A section of superheater tubing and its deposit are shown in Fig. 3. SEM analysis indicated a variety of structures present, including areas with large amounts of material grown from the vapor phase. Areas from the superheater are shown in Figs. 4, 5, and 6. The x-ray diffraction analysis confirms that the high sulfur content in many of these samples is part of $\text{CaSO}_3 \cdot 0.5\text{H}_2\text{O}$ crystals. This type of deposit has been described in simulated magnetohydrodynamic systems.⁶ The cubic crystal in Fig. 5 is NaCl.

The material deposited on the boiler tube wall (as shown in Fig. 7) is thinner and appears smoother and harder. This material is more like the fly ash when viewed at high magnification but still contains many blade-like crystals and the encrusting material cementing the material together is high in both sulfur and calcium. Quartz and mullite are the primary crystalline components of the fly ash as identified by x-ray diffraction.

The fouling deposits contain the elements usually associated with corrosion. On the surfaces in postcombustion regions of the furnace, the primary failure modes are those of erosion.

Conclusion

The primary problems associated with the life of superheater tubes are erosion in high-gasflow regions and fouling in low-gasflow regions. Fouling deposits are formed by fly ash and calcium sulfite deposits when cooling fin construction causes eddy currents in low-gasflow regions. Slag corrosion takes place on the tubes forming the boiler walls where iron is dissolved by the slag. The problems associated with boiler life differ widely in nature from area to area within a boiler. Boilers cannot be characterized by one set of physical parameters.

References

1. W. A. Selvig and F. H. Gibson, *Analyses of Ash from United States Coals*, U. S. Bureau of Mines Bulletin 567, 1956, 1-33.
2. R. S. Mitchell and H. J. Gluskoter, "Mineralogy of ash of some American coals: Variations with temperature and source, *Fuel* 55 (No. 2): 90-96, 1976.
3. Frank Campbell, private communication, New Mexico Bureau of Mines and Mineral Resources, Socorro, N.M., 1980.
4. Stephen Benson, private communication, Grand Forks Energy Technology Center, Grand Forks, N.D., 1980.
5. P. H. Tufts and W. Beckering, "A proposed mechanism for ash fouling burning northern Great Plains lignite," ASME Paper 74-WA/CD-3, presented at the Winter Meeting, ASME, New York, 1974.
6. D. Bienstock et al., "Corrosion of heat-exchange tubes in a simulated coal-fired MHD system," *Trans. ASME Engineering for Power*, April 1971, 249-256.

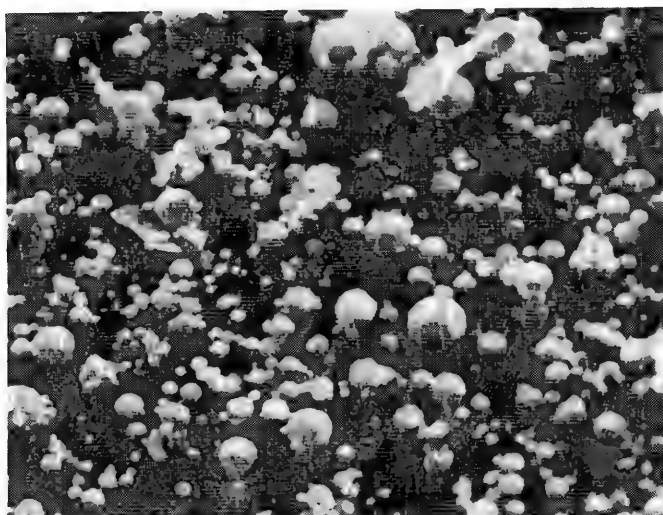


FIG. 2.--Fly ash generated from northern New Mexico coal.

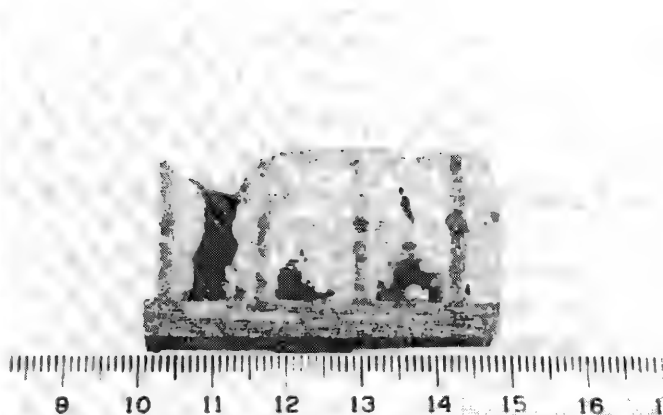


FIG. 3.--Section of superheater showing fin and fouling deposit.



FIG. 4.--Deposit on superheater: blade-like crystals are high in Ca and S.

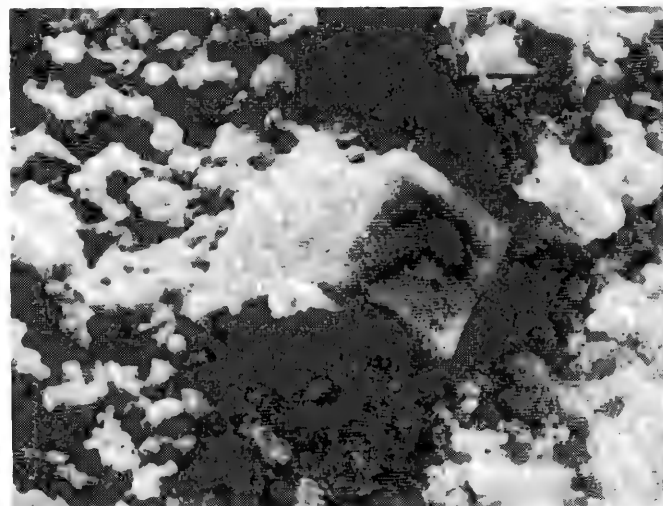


FIG. 5.--View of NaCl crystal of tube often found in fouling deposit on superheater.

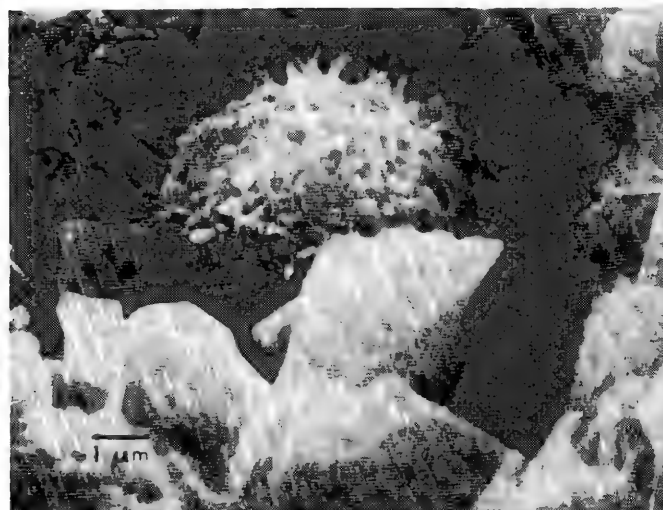


FIG. 6.--Superheater deposit with material re-deposited on fly ash.

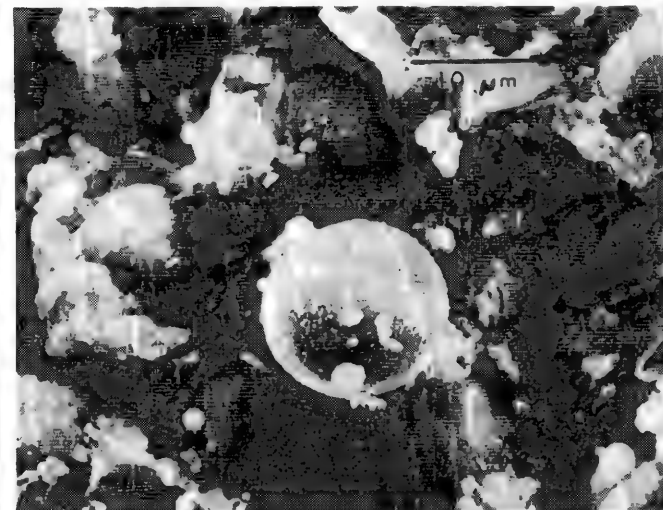


FIG. 7.--Typical deposit found on boiler-tube walls.

TABLE 1.--Ash analysis: Major components reported as oxides (wt.%).

	NM Bituminous (3)	NM Fly Ash (4)	PA Bituminous (1)	N. Great Plains Lignite (5)
SiO_2	22.0-78.5	51.	43.	19.
Al_2O_3	8.6-31.2	22.	33.	11.
CaO	0.6-37.0	5.2	1.9	20.
Fe_2O_3	1.1-23.0	4.2	15.	11.
TiO_2	0.6-1.0	1.1	1.3	0.4
SO_3	0.1-7.9	1.1	2.5	22.8
MgO	0.5-4.7	2.1	0.3	8.
Na_2O	0.2-2.8	2.7	0.3	7.
P_2O_5	0.1-1.0	0.1	0.1	0.5
K_2O	0.3-1.5	1.2	1.0	0.3

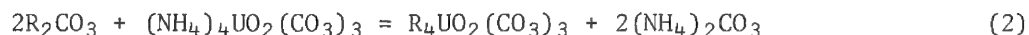
ANALYSIS OF ION EXCHANGE RESIN USED IN URANIUM SOLUTION MINING: AN SEM AND EDS STUDY

V. K. Berry and Velu Annamalai

In situ leaching, also called solution mining, is one of the leaching methods used in the mining industry to recover metals from low-grade ores found in several parts of this country. IEC Corporation is recovering uranium by this technique at their Zamzow site in south Texas. An oxidative lixiviant with ammonium carbonate and hydrogen peroxide is injected into the subsurface ore strata according to a defined wellfield pattern. The resulting uranium-enriched leachate solution is pumped out of the ground and brought to the recovery plant. Uranium is recovered from this solution by an ion-exchange process. The final product of yellow cake (U_3O_8) is produced by steam precipitation and vacuum drying. The uranium-free barren solution is reinjected into the ore body after the necessary make-up chemicals are added.¹ The overall leaching reaction is:



The uranium-enriched pregnant solution consists of uranyl tricarbonate ion, $UO_2(CO_3)_4^{4-}$. The chemical reaction to exchange this complex with the resin in the ion exchange column can be written as:



where R denotes the resin exchange site. In this process S, Cl, Si, and Mo are some of the elements present in the form of anions which foul the resin. The fouling is indicated by a marked reduction in the loading of uranium on the resin, which greatly reduces the life of the resin. The SEM study is aimed at an understanding of the IX loading process and the presence and the levels of various fouling agents, with a view to preventing fouling and hence extending the usable life of the resin.

The IX resin used in the operation is Ionac A-641 made by Sybron Corporation, Ionac Chemical Division, New Jersey. The resin has styrene divinyl benzene copolymer as the base. It has symmetrical arrangements of side chains around the quarternary ammonium exchange site.² The three resin samples examined are from the plant columns through which uranium-enriched pregnant solution with 15-20 ppm H_2O_2 is fed in. The samples were taken from Column 2C (used 3 months), Column 4C (used 5 months) and Column 1A (used 8 months) after uranium was chemically stripped from the loaded resin. Air drying of the samples was followed by vacuum drying. The dry samples were mounted on a carbon planchet with colloidal carbon paint and coated with about 100 Å carbon in an evaporating unit. The samples were examined in JEOL JSM-35 SEM fitted with a Nuclear Semiconductor Si(Li) energy-dispersive x-ray detector and Tracor Northern NS-880 analysis system. The microscope was operated at 25kV accelerating voltage in the secondary-emission mode. The energy dispersive x-ray spectra were taken in 0-20keV range with a count time of 100 s. The three samples were also examined after a column wash with 1N $NaNO_3$.

Figure 1(a) shows a bead of new Ionac A-641 resin (as received) along with an x-ray spectrum of the area. The new resin is in chloride form; thus, a strong chlorine peak is seen. The resin is changed to carbonate form by treatment with ammonium carbonate solution before it is put into use (Fig. 1b). The unconverted chloride (Fig. 1b) is removed from the resin during the uranium loading process. Figure 2(a) shows the spectrum and micrograph of a resin bead from col. 1A. Mainly two types of crystal formations were noted. A flat rectangular type of crystal has strong Ca and S peaks (Fig. 2b) and needle-like crystal with only a large S peak (Fig. 2c). The x-ray spectrum of a barren area void of any crystal formations on the surface (Fig. 2d) shows a strong S peak. Figure 3 shows resin specimen from col. 4C along with the micrograph of the corresponding area and Fig. 4 is of the resin specimen from col. 2C. The three resin samples examined were subsequently washed with 1N $NaNO_3$, to strip the anions which are reversibly held and are not responsible in fouling the resin. All the fouling ions are held both reversibly and irreversibly; it is the latter ones which permanently foul the resin. Figure 5 shows the

Author Berry is at the Department of Anatomy of the University of Texas Health Science Center in San Antonio, TX 78284; author Annamalai, at IEC Corp., Three Rivers, TX 78071. The partial support by IEC Corporation is gratefully acknowledged.

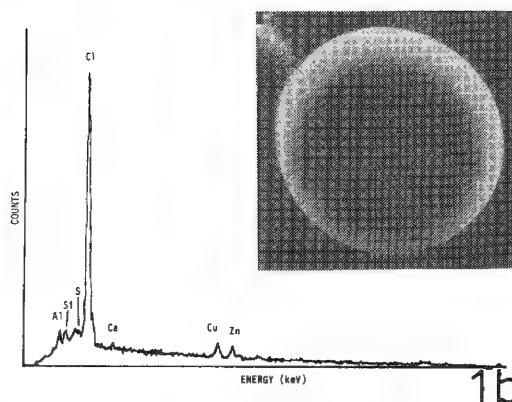
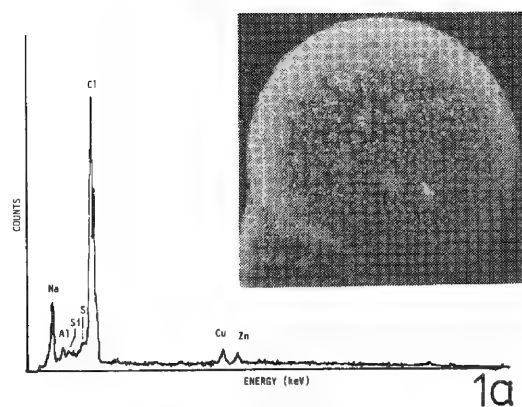


FIG. 1.--Micrographs and x-ray spectra of new resin A-641: (a) bead as received in chloride form; (b) after treatment with $(\text{NH}_4)_2\text{CO}_3$, before resin is put into use.

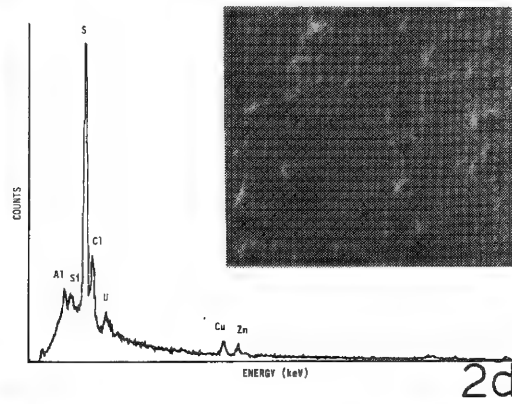
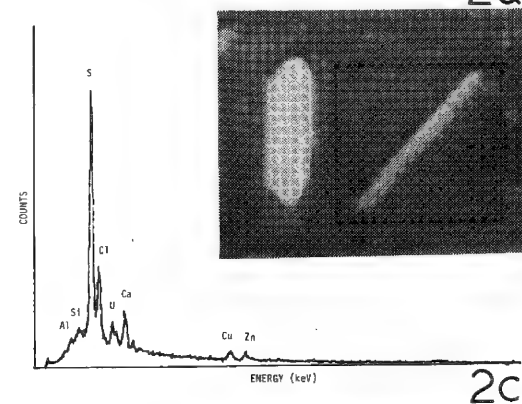
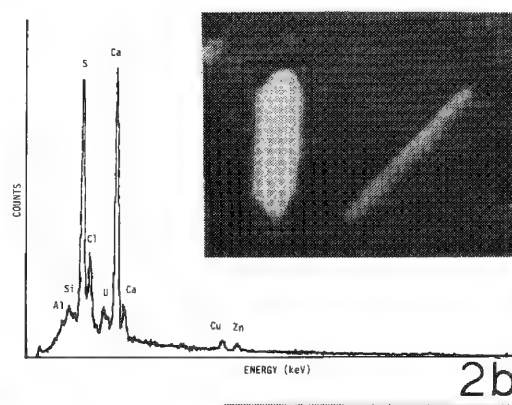
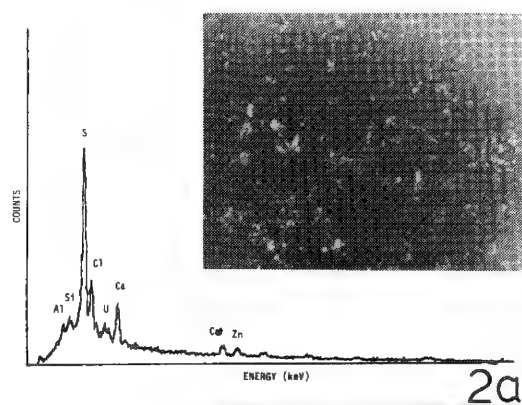


FIG. 2.--Used resin from column 1A: (a) spectrum and corresponding area, 90 \times ; (b) spectrum from rectangular crystal on resin surface and crystal; (c) spectrum from needle-shaped crystal and crystal; (d) spectrum from area with no crystal formations and corresponding area. Magnification: (b) and (c), 4300 \times ; (d) 9000 \times .

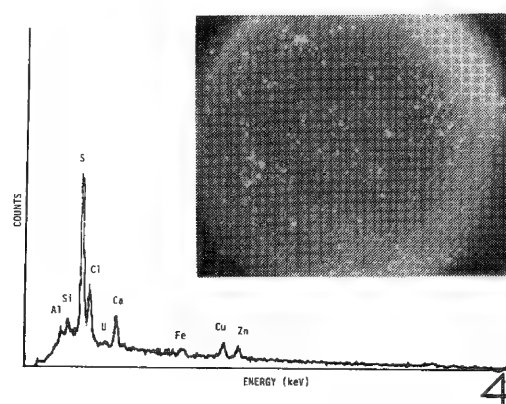
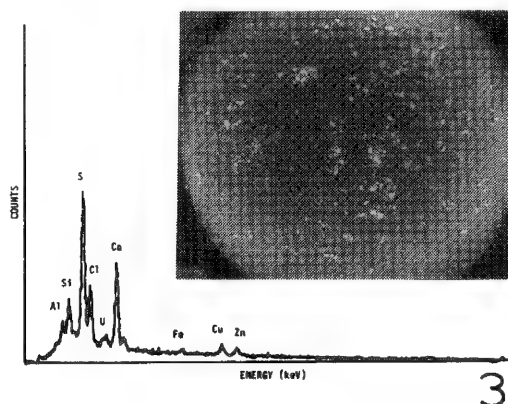


FIG. 3.--Used resin from col. 4C, mag. 75 \times . FIG. 4.--Used resin from col. 2C, mag. 75 \times .

spectra of the three resin samples after the NaNO_3 wash.

Two types of crystal formations are seen on the resin surface in all three samples before the NaNO_3 wash. The rectangular type of crystals are possibly CaSO_4 and the needle type crystals are possibly $(\text{NH}_4)_2\text{SO}_4$. The strong S peak from the barren area void of any visible crystal formations indicates that S is finely dispersed inside and outside the bead. The 1N NaNO_3 wash is supposed to wash off all the irreversibly held ions. The spectra of samples after the wash show reduced amounts of S, which means that the remaining S

is permanently held by the resin and is responsible for the fouling action. The crystal formations observed in the samples before the wash may physically or chemically inhibit the loading process. A comparison of the three samples after NaNO_3 wash (Fig. 5) shows that col. 1A has the highest amount of irreversibly held ions. However, of the columns 2C and 4C, sample from col. 2C has more sulfur; it is the same for the unwashed samples (Figs. 3 and 4). The reason is that the leach liquor fed to col. 2C comes from a mine area newly opened to leaching and thus has more S in the ore-body; the other columns are fed from areas that have been mined for a few years. The fact that higher amounts of Si are seen in sample from col. 4C than in the samples from cols. 1A and 2C needs further investigation. The amount of S held in the three samples shown in Fig. 5 by relative peak heights is a direct indication of the useful life of the resin, which corresponds well with the length of time the three resin samples were in use; the longer the usage the more the accumulation of fouling ions. It is believed that S held in resin irreversibly is in the form of polythionates (S_xO_y). Hydrogen peroxide oxidizes the polythionates to noninterfering sulfates.¹ Normally the life of the resin is about 2-3 months without any treatment. Addition of 15-20 ppm H_2O_2 to the feed solution, as practiced by IEC, extends the life of the resin to 8-10 months.

The study reported here is preliminary in nature and is first of its kind ever attempted. Far more information is obtained by the EDS analysis than by the conventional wet-analysis techniques in

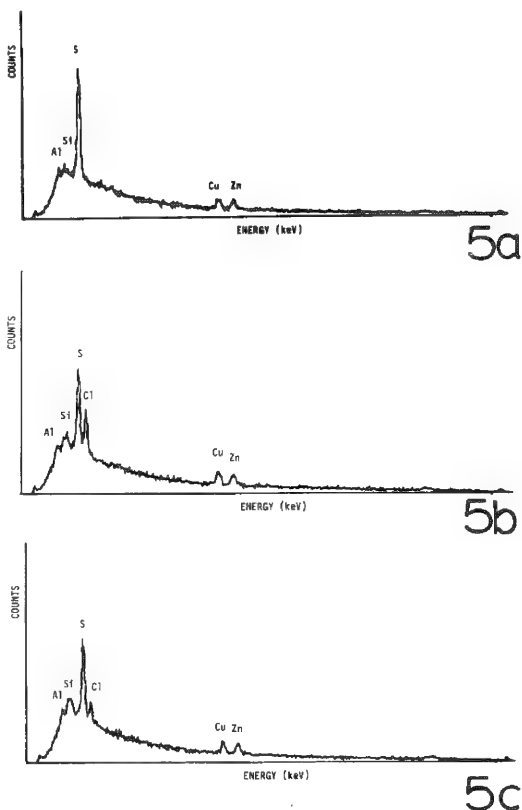


FIG. 5.--Spectra of the three samples after wash with 1N NaNO_3 : (a) spectrum of sample from col. 1A; (b) from col. 4C; (c) from col. 2C.

a short period of time. The high cost of IX resin makes it imperative to find means to extend the useful life of the resin. Any increase in the usable life of the resin will be a tremendous advance for the uranium-solution mining industry. This study has contributed toward that goal by identifying the various ions reversibly and irreversibly held and thereby their functions in the IX process.

References

1. Velu Annamalai and F. X. McGarvey, "Operating experience in the recovery of uranium at the Pawnee and Zamzow sites," paper presented at the 55th annual meeting of AIME Soc. Petroleum Eng. (Dallas), 1980.
2. F. X. McGarvey and J. Unger, "Influence of the ion exchange functional group on uranium recovery," paper presented at the Symposium of Ion Exchange and Solvent Extraction in Mineral Processing (Randburg, South Africa), 1980.

QUANTITATIVE ELECTRON PROBE MICROANALYSIS WITH GAUSSIAN EXPRESSION FOR $\phi(\rho z)$ CURVES

J. D. Brown, R. H. Packwood, and K. Milliken

A Gaussian expression centered at the surface of the sample had been derived to describe the depth distribution of x-ray production curves [$\phi(\rho z)$ curves],¹ of the form

$$\phi(\rho z) = \gamma_0(1 - qe^{-\beta\rho z})e^{-\alpha^2(\rho z)^2}$$

where α , β , and γ_0 could be derived on the basis of theoretical arguments concerning electron interaction, backscattering, and ionization cross sections; q can be shown to be equal to $[\gamma_0 - \phi(0)]/\gamma_0$, where $\phi(0)$ is the value of $\phi(\rho z)$ at the surface. Hence q is not a separate independent parameter.

In this equation, the term involving α determines the shape and extent of the tail of the x-ray production curve, γ_0 directly affects the magnitude of the area under the curve (the atomic number effect), and the term involving β establishes the slope of the initial rise from $\phi(0)$ to the maximum value of $\phi(\rho z)$ and to a large extent the position of that maximum with respect to depth in the sample. These characteristics allow a critical examination of the theoretically derived values² with respect to the known shape of measured $\phi(\rho z)$ curves and those calculated by Monte Carlo programs.

The particular values for calculating the $\phi(\rho z)$ curves depend on choices of certain parameters used in those calculations. For $\phi(0)$ the expression of Reuter³ was used initially and the value of Berger and Selzer⁴ for the average ionization potential. Further, Bethe's law⁵ was used for the rate of energy loss, an expression by Newbury and Myklebust⁶ for the mean free path for Rutherford scattering, and Bishop's expression⁷ for the atomic screening factor. With these values in hand, a computer program based on the Gaussian equation to relate measured intensities to compositions was written and was used to construct a histogram for the 430 cases of Poole.⁸ This initial histogram, although encouraging in that about one-third of the results lay within $\pm 1.5\%$ of the amount present, did show that for systems in which a large atomic number correction was necessary, a significant and residual error remained. This error suggests that the values of γ_0 and β need some adjustment.

$\phi(\rho z)$ curves were calculated and plotted for a number of systems, in particular for the $CK\alpha$ line in a number of carbide matrices at electron energies from 4 to 10 keV. In this region, particularly for large Z matrices, the $\phi(\rho z)$ curves were found to rise rapidly from $\phi(0)$ to the maximum value within a few $\mu\text{g}/\text{cm}^2$ of the surface. This finding suggests that the value of β is too large in that region.

The effect of changes to the $\phi(\rho z)$ equation, such as use of the expression for backscatter coefficient due to Love and Scott⁹ and Ruste's value¹⁰ for the average ionization potential, are being investigated to improve the agreement of calculated and known compositions from standard specimens and the shape of the predicted $\phi(\rho z)$ curves.

References

1. R. H. Packwood and J. D. Brown, in *Microbeam Analysis--1980*, 45.
2. R. H. Packwood and J. D. Brown, accepted for publication in *X ray Spectrom.*, 1981.
3. W. Reuter, *Sixth Intern. Conf. X-ray Optics and Microanalysis*, University of Tokyo Press, 1972, 121.
4. M. J. Berger and S. M. Seltzer, NASNRC Publication 1133, Washington, 1964, 205.
5. H. A. Bethe, *Handbuch der Physik* 24: 519, 1933.
6. D. E. Newbury and R. L. Myklebust, *Ultramicroscopy* 3: 391, 1978.
7. H. E. Bishop, *Brit. J. Appl. Phys.* 18: 703, 1967.
8. D. M. Poole, in *Quantitative Electron Probe Microanalysis*, NBS Special Publication 298, Washington, D.C., 1968, 93.
9. G. Love and V. D. Scott, *J. Phys.* D-11: 106, 1978.
10. J. Ruste, in F. Maurice et al., Eds., *Microanalyse microscopique électronique à balayage*, Orsay, 1978, 308.

Author Brown is at the University of Western Ontario in London; authors Packwood and Milliken are with the Department of Energy, Mines, and Resources in Ottawa.

MONTE CARLO ELECTRON TRAJECTORY CALCULATIONS OF X-RAY GENERATION IN TILTED, SOLID SPECIMENS

Dale E. Newbury and Robert L. Myklebust

Monte Carlo electron trajectory calculations provide a useful technique for obtaining information on electron-beam interactions in solids in situations in which direct experimental measurements are difficult or impossible. In the present work, electron interactions have been simulated in solid specimens tilted at various angles to the incident beam. Parameters which describe certain aspects of x-ray generation, including the characteristic/bremsstrahlung ratio (peak-to-background), loss of generation due to electron backscattering, and the x-ray absorption effect, have been determined in support of the development of methods for quantitative x-ray microanalysis of tilted samples.

The Monte Carlo electron trajectory simulation which was used was of the hybrid single/multiple elastic scattering type and has been described in detail elsewhere.^{1,2} The Bethe cross section for inner-shell ionization and the Kirkpatrick-Wiedmann cross section for bremsstrahlung were used for the x-ray calculations.^{3,4} For the low overvoltage regime appropriate to x-ray microanalysis, $1 \leq U \leq 5$, where U is the overvoltage ($U = E_0/E_c$), the optimum choice of the cross section for inner shell ionization is not obvious.^{5,6} However, for the present calculations, relative rather than absolute calculations are required, and so the exact form of the cross section is less important. At each tilt angle, 5000 electron trajectories were calculated which yielded a precision of better than $\pm 2\%$ in calculated x-ray parameters, as confirmed by replicate calculations with different random number sequences.

Characteristic/Bremsstrahlung (Peak-to-background Ratio)

Recently, modified matrix correction methods have been proposed for x-ray microanalysis which extend quantitative analysis to the difficult case of particles and rough surfaces. These methods are based on measurements of the characteristic and bremsstrahlung x rays at the same energy.⁷⁻⁹ Experimental observations suggest that the peak-to-background ratio is approximately the same regardless of the geometry of the target and the orientation of the x-ray detector. For each characteristic x-ray energy, the measured bremsstrahlung background is used to scale the characteristic intensity to eliminate geometric effects on x-ray generation and absorption. The method is based on the fact that x rays of the same energy, whether characteristic or bremsstrahlung, are similarly affected by beam-specimen parameters. To study the relationship of the generated and emitted characteristic and bremsstrahlung x rays, calculations were made for targets of Al, Cu, and Au for tilt angles ranging from 0 to 80°. The x-ray emergence angle was taken as 40°.

Results are plotted in Figs. 1 and 2 for aluminum and gold targets. The peak-to-background value at a particular angle is normalized to the value obtained at 0° tilt. Also plotted in Fig. 1 and 2 is the peak intensity normalized to the peak intensity at 0° tilt. The peak-to-background ratio is found to change with tilt, decreasing by about 7% at a tilt of 80° in an aluminum target. By comparison, the peak intensity changes by a much greater amount, decreasing by about 50% at a tilt of 80°. These calculations suggest that the corrections to characteristic intensities based upon bremsstrahlung measurements can indeed eliminate a large fraction of the geometric effects, but the correction will not be perfect. However, at a given tilt, all the elements tested were similarly affected, which indicates that a simple final normalization may suffice to eliminate the discrepancy. The origin of the deviation of the peak-to-background at high tilts can be understood in terms of the backscattered electron energy distribution. At high tilt, more electrons are scattered out of the specimen at high energies, which both raises the energy and relative intensity of the peak in the energy distribution. The characteristic and bremsstrahlung cross sections behave differently with overvoltage near the excitation energy, with the characteristic cross section falling sharply near $U = 1$ while the brems-

The authors are with the Center for Analytical Chemistry, National Bureau of Standards, Washington, DC 20234.

strahlung cross section is rising in this overvoltage region. The increased loss of high energy electrons from the sample at high tilt predominantly affects the characteristic generation. Thus, the peak-to-background tends to fall relative to an untilted specimen.

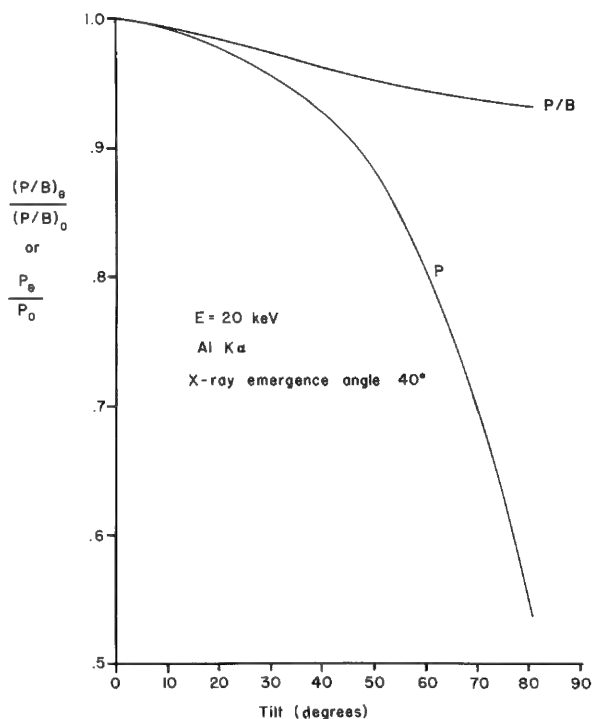


FIG. 1.--Peak-to-background and peak intensity normalized to values at 0° tilt as function of tilt angle. Target: aluminum; $E_0 = 20$ keV, x-ray detector 40° above surface. Radiation: P = Al K (1.49 keV); B = 1.49 keV bremsstrahlung.

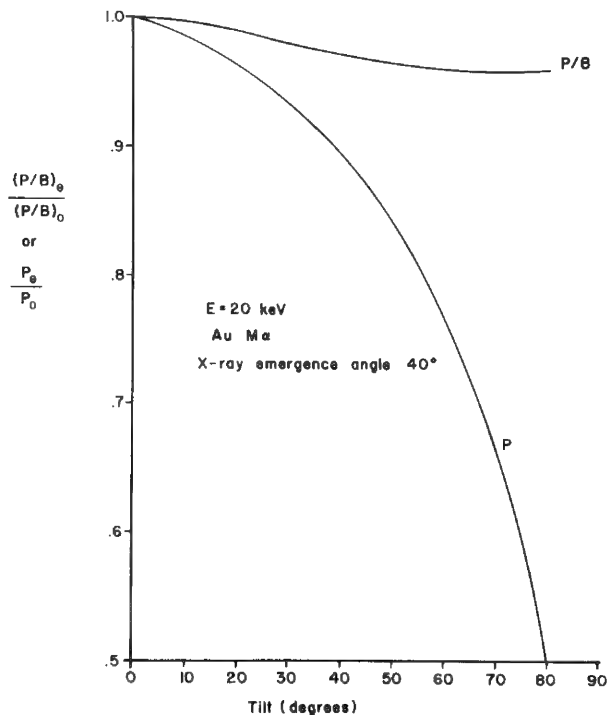


FIG. 2.--Same conditions as Fig. 1, except target: gold; P = Au M (2.12 keV); B = 2.12 keV bremsstrahlung.

Backscatter Loss

The backscattering of electrons from the sample results in a loss of x-ray generation, as shown in Fig. 1 and 2. This loss is described by the backscatter loss parameter $1 - R$, where R is the fraction of the total possible ionization actually produced in the sample. The backscatter loss is an important parameter in quantitative x-ray microanalysis by the ZAF method. Evaluation of R requires knowledge of the number of backscattered electrons and their energy distribution, which is readily available in the Monte Carlo simulation. X-ray production X_i along the path within the target is calculated for each incident electron. For each backscattered electron, the additional x-ray production X_e possible after backscattering is separately calculated in a hypothetical external target of the same material. The R parameter can then be directly calculated as $R = X_i / (X_i + X_e)$. R has been calculated as a function of specimen tilt for both characteristic and bremsstrahlung x-ray production in Fig. 3 for copper and gold targets. A general decrease in R is observed with increasing tilt, which is similar for the two different types of x-ray generation. A family of such curves could be used to modify conventional ZAF matrix correction schemes for the analysis of flat, tilted specimens, which is the common configuration in the SEM, particularly if the standards and unknowns are measured at different tilts.

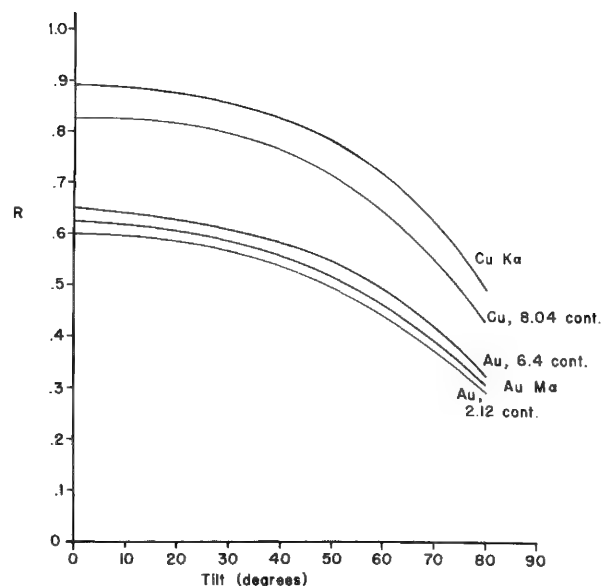


FIG. 3.--Fraction R of total possible x-ray generation actually produced in specimen as function of tilt. $E_0 = 20$ keV.

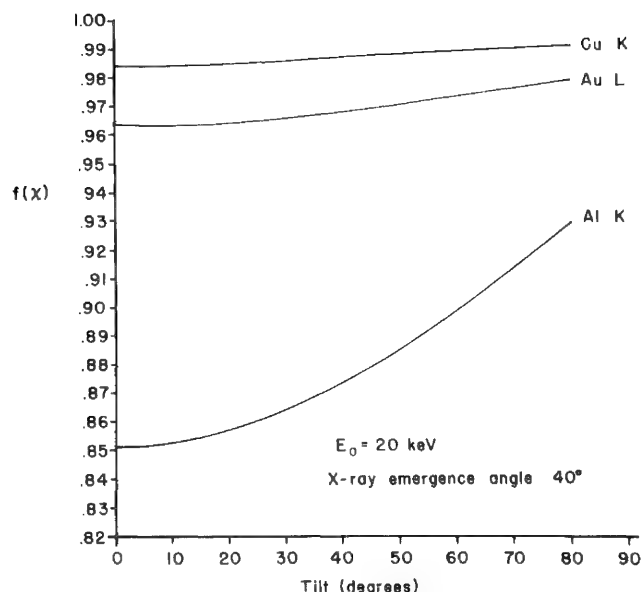


FIG. 4.--Absorption parameter $f(\chi)$ as a function of specimen tilt; x-ray detector 40° above specimen surface.

Absorption Parameter

The matrix absorption correction, denoted by the parameter $f(\chi)$, which gives the fraction of emitted x rays relative to generated x rays, is also modified in a tilted specimen compared to a specimen set normal to the beam, since the x rays are produced nearer to the surface in a tilted specimen and consequently undergo less absorption. The $f(\chi)$ parameter can be calculated in the Monte Carlo procedure since the x-ray depth distribution histogram is directly available. Examples of $f(\chi)$ curves as a function of sample tilt are shown in Fig. 4. For convenient incorporation of this information into a ZAF routine, we shall have to derive the functional dependence for various x-ray emergence angles in order to establish a general formula.

References

1. R. L. Myklebust, D. E. Newbury, and H. Yakowitz, "The NBS Monte Carlo electron trajectory calculation program," in K. F. J. Heinrich, D. E. Newbury, and H. Yakowitz, Eds., *Use of Monte Carlo Calculations in Electron Probe Microanalysis and Scanning Electron Microscopy*, National Bureau of Standards Special Publication 460, Washington, 1976, 105.
2. D. E. Newbury, R. L. Myklebust, and K. F. J. Heinrich, "A hybrid Monte Carlo procedure employing single and multiple scattering," in D. R. Beaman, R. E. Ogilvie, and D. B. Wittry, Eds., *8th Int'l. Cong. X-ray Optics and Microanalysis*, 1980, 57.
3. H. Bethe, *Ann. Physik* 5: 325, 1930.
4. P. Kirkpatrick and L. Wiedmann, *Phys. Rev.* 67: 321, 1945.
5. C. J. Powell, "Evaluation of formulas for inner-shell ionization cross sections," in Ref. 1, 97.
6. D. E. Newbury and R. L. Myklebust, "Monte Carlo calculations of absolute x-ray generation from solid targets," *Microbeam Analysis--1979*, 51.
7. J. A. Small, K. F. J. Heinrich, C. E. Fiori, R. L. Myklebust, D. E. Newbury, and M. F. Dillmore, "The production and characterization of glass fibers and spheres for microanalysis," *SEM/1978 I*, 445.
8. P. J. Statham and J. B. Pawley, "A new method for particle x-ray microanalysis based on peak-to-background measurements," *SEM/1978 I*, 469.
9. J. A. Small, K. F. J. Heinrich, D. E. Newbury, R. L. Myklebust, and C. E. Fiori, "Procedure for the quantitative analysis of single particles with the electron probe," in K. F. J. Heinrich, Ed., *Characterization of Particles* National Bureau of Standards Special Publication 533, Washington, 1980, 29.

DETERMINATION OF COMPOSITION AND THICKNESS OF ZINC SULFIDE FILMS DOPED WITH Cu AND Mn, BY MEANS OF ELECTRON PROBE DATA AND MONTE CARLO CALCULATIONS

N. C. Miller

The Monte Carlo electron scattering model of Kyser and Murata, combined with experimental electron probe measurements of x-ray intensity ratios, has been used to predict the composition and thickness of a four-element system: zinc sulfide films doped with both manganese and copper.¹⁻⁴ Dopant concentrations vary from 0.05 to 3 wt.%; and film thickness varies from 0.1 to 1.7 μm . Predicted film compositions are in good agreement with low-voltage bulk electron probe measurements. Since the films are not necessarily stoichiometric, there are four independent variables: three element concentrations and film mass thickness. For a bulk density of 4 gm/cm^3 for ZnS, the thickness range corresponds to a mass thickness from 40 to 720 $\mu\text{g}/\text{cm}^2$. (Films thinner than 0.1 μm could also have been treated.)

In the Monte Carlo simulations, it was assumed that copper and manganese atoms substitute for zinc atoms. Stoichiometric ZnS is used as the experimental standard for zinc and sulfur. One thousand electron trajectories are simulated for each calibration point.

The Monte Carlo calibration curves for sulfur and zinc, at 20 and 30 keV, are shown in Figs. 1 and 2, for stoichiometric ZnS films on silicon. Complete sets of sulfur and zinc calibration curves were calculated and plotted for zinc sulfide films with dopant concentrations at the low, middle, and high end of the range. One set of calibration curves appears in Fig. 3 and 4.

The Monte Carlo calibration curves for copper, at 20 and 30 keV, are given in Figs. 5 and 6. A similar set of calibration curves has been calculated for manganese at 20 keV and at 30 keV, from 0.01% to 3% Mn. Since deviations of zinc sulfide from stoichiometry of ± 10 wt.% of sulfur change the copper or manganese x-ray intensity by less than 2%, the calibration curves for copper and manganese can be used for all films independent of the sulfur concentration.

The following procedure is used to determine the film composition. The sulfur and zinc experimental x-ray intensity ratios (k ratios) are fitted to the theoretical curves of the stoichiometric ZnS films (Figs. 1 and 2). Thus $(\rho Z)_S$ and $(\rho Z)_{Zn}$ are determined. The average of $(\rho Z)_S$ and $(\rho Z)_{Zn}$ is used with k_{Cu} to determine the approximate weight percent copper from Fig. 5 or 6. Similarly the approximate manganese concentration is determined from the average ρZ and k_{Mn} . These copper and manganese concentrations represent the "zeroth iteration."

Another iteration, the "first iteration," provides more accurate results. Once the approximate copper and manganese concentrations are determined, the appropriate set of precalculated complete sulfur and zinc calibration curves is chosen (e.g., Figs. 3 and 4). The sulfur and zinc concentrations, as well as ρZ , are then determined by the usual convergence procedure.¹ From the unique ρZ , more accurate values of copper and manganese concentrations are selected.

In practice, the accelerating voltage was chosen so that k_S and k_{Zn} would lie on the linear portion of the calibration curves if possible. Therefore films up to 0.8 μm are measured at 20 keV, whereas films up to 1.8 μm are measured at 30 keV.

Experimental

For these films compositions were checked by low-voltage bulk electron probe measurements by use of the ZAF correction model of the Magic IV computer program.⁵ At 14 keV, all four $K\alpha$ x-ray lines were used; at lower voltages, the Zn $L\alpha$ was chosen.

The electron probe measurements were made on a Philips 4500 electron probe. The Monte Carlo simulations were carried out on an IBM 3033/168 computer. The copper and manganese doped zinc sulfide films were rf cosputtered onto silicon substrates. Carbon-coated polished single crystals of ZnS were used as standards in the experimental measurements.

The author is a Member of the Technical Staff of GTE Laboratories Incorporated, 40 Sylvan Road, Waltham, MA 02254.

Results

The calculated compositions of undoped or very lightly doped zinc sulfide are given in Table 1. Also included in Table 1 is the zinc and sulfur composition determined by low-voltage (6keV) bulk electron probe measurements. (At 6 keV, the x-ray generation depth is 0.3 μm , from the bulk Monte Carlo simulation.) The agreement between calculated and measured compositions is very good: sulfur concentrations are within 0.3% S at 30 keV and 0.5% S at 20 keV.

TABLE 1.--Composition of undoped and very lightly doped ZnS films on Si. S, Zn, Mn, Cu are in weight percent; ρZ is in $\mu\text{g}/\text{cm}^2$.

Film	E_0 (KeV)	S	Zn	Mn	ρZ	$(\rho Z)_{\text{Si}}$
Undoped	30	33.4	66.6	--	100	114
	20	33.9	66.1	--	98	112
	6	33.3	66.7			
1	30	32.6	67.4	ND	240	228
	20	33.7	66.275	.025	262	256
	6	33.0	67.0			
2	30	33.4	66.57	0.03	430	390
	20	34.0	65.975	.025	340	408
	6	33.4	66.6			
3	30	33.0	66.94	0.06	342	318
	20	33.8	66.15	.05	350	337
	6	33.3	66.7			
4	30	31.9	67.92	0.18	205	191
	20	33.0	66.81	.19	220	202
	6	32.8	67.2			

The predicted compositions of films with higher dopant concentrations are shown in Table 2, along with compositions determined by bulk measurements at low voltages (10-16 keV). At 30 keV, the predicted and measured copper concentrations agree within 11% on the average; for manganese, the concentrations are within 20%. Statistical measurement error (twice the standard deviation) nearly accounts for copper (7.6%) but only partially accounts for manganese (9.0%). The four films with the lowest manganese concentrations have much larger differences between predicted and measured concentrations than films with larger manganese concentrations ($\text{Mn} > 0.3\%$). In summary, the agreement between Monte Carlo calculated and bulk measured dopant concentrations is reasonably good, and improves as the dopant concentration increases.

For the films listed in Table 2, the zinc and sulfur concentrations predicted at both 30 and 20 keV are in very good agreement with the values measured at low voltages. In this case, predicted and measured sulfur concentrations agree to 0.3% S at 30 keV, and to 1.0% at 20 keV, on the average.

If one chooses a set of zinc and sulfur calibration curves with dopant concentrations

not closest to the dopant concentrations predicted in the "zeroeth iteration," the predicted sulfur concentration differs by only 0.1-0.4% S from the sulfur concentration predicted from the best choice of zinc and sulfur calibration curves. Therefore, only a few calibration curves are necessary for zinc and sulfur.

TABLE 2.--Composition of Cu, Mn doped ZnS films on Si. S, Zn, Mn, Cu are in weight percent; ρZ is in $\mu\text{g}/\text{cm}^2$.

Film	E_0 (KeV)	S	Zn	Mn	Cu	ρZ	$(\rho Z)_{\text{Si}}$
R170	30	33.0	65.0	.60	1.4	750	812
	14	33.1	64.6	.70	1.6		
R168	30	33.6	63.5	1.7	1.2	700	776
	14	33.3	63.3	2.1	1.4		
R129	30	33.5	65.41	.24	.85	740	720
	16	33.6	65.3	.34	.77		
R158	30	33.5	65.03	.37	1.1	740	
	14	33.2	65.3	.43	1.1		
R166	30	33.5	64.29	.81	1.4	685	675
	14	33.4	64.5	.90	1.3		
R123	30	33.2	66.38	.11	.31	615	640
	14	33.4	66.0	.17	.50		
R127	30	33.7	65.83	.068	.40	495	480
	20	33.5	66.04	.10	.36	500	487
	12	32.7	66.7	.14	.47		
R148	30	32.6	66.36	.22	.82	350	416
	20	34.0	64.89	.20	.91	410	435
	10	32.4	66.5	.28	.76		
R141	30	32.2	66.86	.24	.70	405	370
	20	34.2	64.98	.26	.56	385	377
	11	33.6	65.4	.40	.59		

Dopant concentrations calculated after the zeroeth iteration were compared with those calculated after the first iteration. For the films listed in Table 2, the copper and manganese concentrations change by only 1-4% when the first iteration is carried out. The change is larger the higher the concentration and the smaller ρZ (Figs. 5 and 6). The improvement in including the first iteration is less than or equal to the statistical error of the electron probe data.

It has been shown previously from the substrate k ratio can be used to predict film mass thickness.³ From k_{Si} and the silicon calibration curve, $(\rho Z)_{\text{Si}}$ is determined, and is in good agreement with ρZ (Tables 1 and 2).

Summary

The composition and thickness of zinc sulfide films doped with both copper and manganese have been predicted by means of the Monte Carlo model. Calculated dopant concentrations are in satisfactory agreement with those measured by low-voltage bulk electron probe microanalysis. Predicted sulfur and zinc concentrations are in very good agreement with low-voltage measurements.

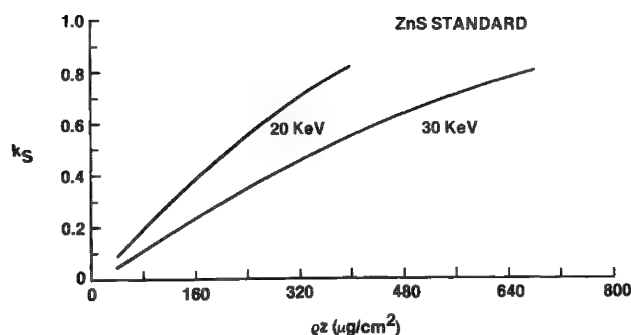


FIG. 1.--Theoretical S x-ray intensity ratio vs mass thickness of stoichiometric ZnS (32.9 wt.% S) film on Si.

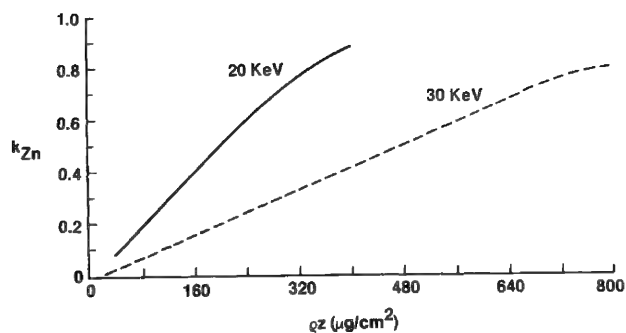


FIG. 2.--Theoretical Zn x-ray intensity ratio vs mass thickness of stoichiometric ZnS film on Si.

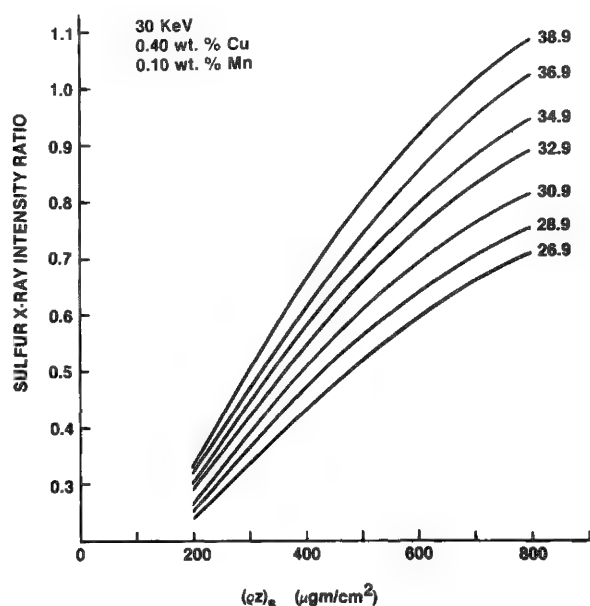


FIG. 3.--Theoretical S x-ray intensity ratio vs mass thickness for ZnS film, doped with 0.40% Cu and 0.10% Mn, on Si, at 30 keV. Weight percent S is the parameter for each curve.

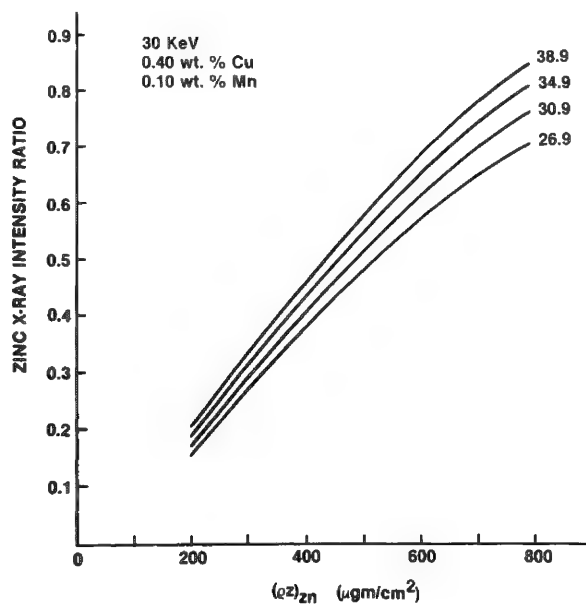


FIG. 4.--Theoretical Zn x-ray intensity ratio vs mass thickness for ZnS film, doped with 0.40% Cu and 0.10% Mn, on Si, at 30 keV. Weight percent S is the parameter for each curve.

The procedure for predicting film composition and thickness is straightforward and rapid. Copper and manganese concentrations can be calculated by only a zeroth iteration, whereas sulfur and zinc concentrations require a first iteration. Only a few sets of sulfur and zinc calibration curves are necessary, corresponding to judiciously chosen intervals in dopant concentrations.

References

1. D. F. Kyser and K. Murata, "Quantitative electron microprobe analysis of thin films on substrates," *IBM J. Res. and Dev.* 18: 352, 1974.
2. S. Cvikevich and C. Pihl, "Application of the Monte Carlo simulation to quantitative electron microprobe analysis of refractory thin films," *Proc. 12th MAS Conf.* 1977, 116.
3. N. C. Miller and D. M. Koffman, "Determination of thin-film composition or thickness from electron-probe data by Monte Carlo calculations," *Microbeam Analysis--1979*, 47.
4. C. Pihl and S. Cvikevich, "Monte Carlo simulation approach to quantitative electron microprobe analysis of ternary alloy thin films," *Microbeam Analysis--1980*, 157.
5. J. W. Colby, "MAGIC IV: A new improved version of MAGIC," *Proc. Sixth Nat. Conf. Electron Probe Analysis* (Pittsburgh), 1971, 17A-17B.

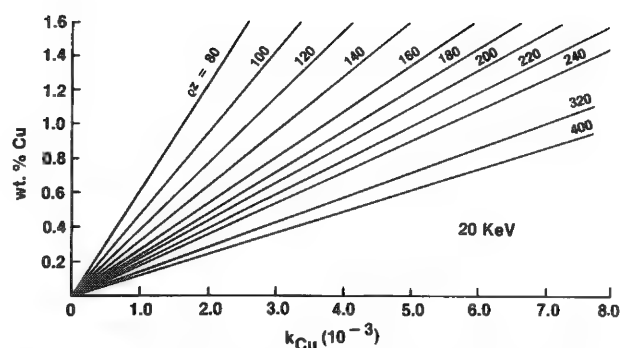
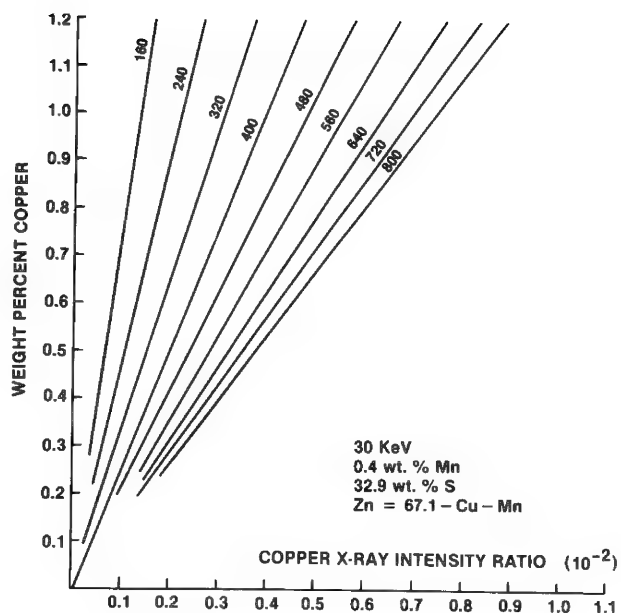


FIG. 5.--Weight percent Cu vs Cu x-ray intensity ratio for Cu, Mn doped ZnS film on silicon, 20 keV. Each line refers to different film mass thickness.

FIG. 6.--Weight percent Cu vs Cu x-ray intensity ratio for Cu, Mn doped ZnS film on silicon, 30 keV. Each line refers to different film mass thickness.



ACCURACY OF PEAK-TO-BACKGROUND METHOD FOR QUANTITATIVE ANALYSIS

John F. Konopka and Peter Rez

The analysis of particulate matter has become important in many pollution-control studies. The problem in particle analysis is that the electrons can be scattered outside the particle, which of course affects the number of characteristic x rays generated. Conventional methods of analysis such as ZAF all assume a bulk sample with a flat surface and in their unmodified form do not give good results for particles.¹ Attempts have been made to take account of particle-size effects by classification of the particles by shape and application of appropriate correction procedures.² However, a general method of analysis should be independent of particle geometry; the peak-to-background method has been suggested^{1,3} as any absorption effects apply equally to characteristic and continuum x rays. The peak-to-background ratio is assumed to be equivalent for a particle and a bulk specimen, which enables bulk correction procedures to be applied to a derived peak intensity if the bulk continuum can be estimated.^{1,3,4} This procedure implies that the peak-to-background ratio is independent of geometry. The purpose of this investigation is to test this assumption.

It is assumed that the background is due to bremsstrahlung and the peak is due to characteristic x rays. If the peak-to-background ratio is to be truly independent of geometry, not only must the absorption paths be the same but also the cross sections for bremsstrahlung and characteristic x-ray production must vary the same way with electron energy. The number of characteristic x rays observed X_C for a beam current I is

$$X_C = I \int \Phi(r, E) \sigma_C(E, E') \exp[-\mu(E')|r - r'|] d^3r dE \quad (1)$$

where $\Phi(r, E)$ is the probability of finding an electron at a position r in the specimen, $\mu(E')$ is the absorption coefficient for x rays of energy E' , $\sigma_C(E, E')$ is the cross section for production of characteristic x rays of energy E' by electrons of energy E , and r' is the position of the detector. If the cross section for bremsstrahlung production is $\sigma_B(E, E')$ the number of background x rays X_B is

$$X_B = I \int \Phi(r, E) \sigma_B(E, E') \exp[-\mu(E')|r - r'|] d^3r dE \quad (2)$$

If both the characteristic and bremsstrahlung cross sections can be written as products of a term dependent on the electron energy and a term specific to the process,

$$\sigma_C(E, E') = f(E)g_C(E') \quad \sigma_B(E, E') = f(E)g_B(E') \quad (3)$$

the integration over the specimen and electron energies at all points in the specimen can be performed and the peak-to-background ratio is

$$\frac{X_C}{X_B} = \frac{g_C(E')}{g_B(E')} \quad (4)$$

A reasonable form for the characteristic cross section is⁵

$$\sigma_C = \frac{6.51 \times 10^{-14} b_c Z}{EE'} \ln(c_c E/E') \quad (\text{cm}^2) \quad (5)$$

and for the bremsstrahlung cross section is

$$\sigma_B = \frac{7.88 \times 10^{-22} Z^2 dE'}{EE'} \ln[(\sqrt{E} + \sqrt{E - E'})/\sqrt{E'}] \quad (\text{cm}^2) \quad (6)$$

A further complication is that the characteristic radiation is relatively isotropic, whereas the bremsstrahlung is peaked in the forward direction, although that will not be too serious a problem at typical SEM electron energies. Equations (5) and (6) evidently do not satisfy the criterion that the cross sections must show the same behavior with

The authors are with Kevex Corp., 1101 Chess Drive, Foster City, CA 94404.

electron energy except when the logarithmic terms vary slowly at high electron energy and low photon energy.

The variation of the peak-to-background ratio can be determined with flat polished specimens if we take EDX spectra at different accelerating voltages and specimen tilts. The measurements were performed on a Hitachi S-550 microscope with a Kevex detector and 7000 analyzer; for each case the acquisition live time was 200 s. Spectra from copper, aluminum, gold, and alumina were taken at accelerating voltages of 5, 10, 15, 20, 25 and 30 kV and tilts of 0, 10, 20, 30, and 40°. The x-ray take-off angle was 38.5° in all cases. The background was fitted by a low-order polynomial in regions on either side of the peak. The errors for the peak were estimated from the square root of the number counts. The background error was estimated from the difference between fitted and observed background in the regions outside the peaks normalized to the size of the peak region. The peak-to-background ratios were plotted as a function of overvoltage and angle of incidence. For gold this plot was done for both L and M lines (Fig. 1).

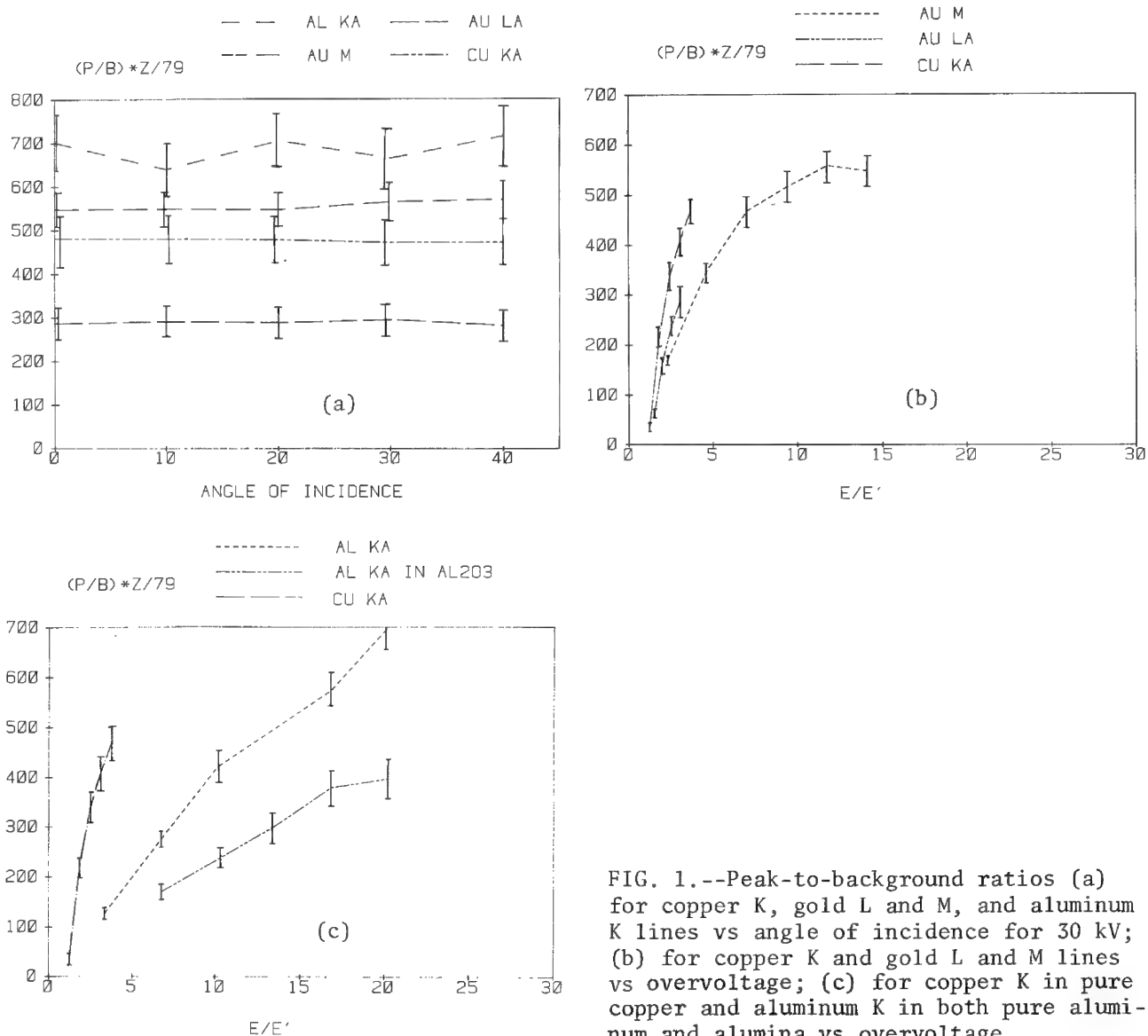


FIG. 1.--Peak-to-background ratios (a) for copper K, gold L and M, and aluminum K lines vs angle of incidence for 30 kV; (b) for copper K and gold L and M lines vs overvoltage; (c) for copper K in pure copper and aluminum K in both pure aluminum and alumina vs overvoltage.

As can be seen the peak-to-background ratio approaches a constant value as the overvoltage E/E' increases, in agreement with theory. It is interesting to note that the gold

M and L ratios fall on similar curves; the determining factor for the peak-to-background ratios is evidently the electron distribution in the solid. The approach to a constant is much slower for the lighter elements, probably because the electron distribution in aluminum is more spread out and any differences are more pronounced. In all cases the peak-to-background ratio did not vary with incidence angle within experimental error. The plots for 30 kV are shown as examples. As a test of quantitative analysis procedures the peak-to-background ratio for alumina was also measured and the stability of the ratio of the aluminum to alumina peak-to-background ratios calculated for various accelerating voltages (Table 1. This value can be calculated from Eqs. (5) and (6) as 0.64. The reason for any errors is the slight difference in average Z, which means that the electron distributions are sufficiently different to cause changes in the characteristic and bremsstrahlung yields in the two samples. The stability shown in this case does not insure it will hold when particles of different sizes are analyzed with respect to a bulk standard.

TABLE 1.--Peak-to-background ratios of alumina and aluminum compared as measure of stability of procedure..

<u>Accelerating voltage (kV)</u>	<u>Ratio of peak-to-background for alumina to peak-to-background for aluminum</u>
30	0.57
25	0.66
20	0.59
15	0.59
10	0.62

Another problem with the peak-to-background method is caused by fluorescence. There is no easy way to correct for it but there should be an additional voltage dependence in the peak-to-background ratio associated with the increase in characteristic fluorescing radiation with voltage.

In summary, the peak-to-background method can be truly independent of geometry only if the cross sections for characteristic and bremsstrahlung production have the some dependence on electron energy, which is only true at high overvoltages. This effect will be worse for light elements, where the electron range is greater and the electron energy distribution more spread out. In practice one might want to work at low voltages to minimize the interaction volume so that the particle size is greater than the x-ray generation volume, but that might not always be feasible.

References

1. J. A. Small, D. E. Newbury, and R. L. Myklebust, "Analysis of particles and rough samples by FRAME P, a ZAF method incorporating peak-to-background measurements," *Microbeam Analysis--1979*, 243.
2. J. T. Armstrong and P. R. Buseck, "Quantitative chemical analysis of individual microparticles using the electron microprobe: Theoretical," *Anal. Chem.* 47: 2178, 1975.
3. P. J. Statham and J. B. Pawley, "A new method for particle analysis based on peak-to-background measurements," *SEM/1978*, I, 469.
4. P. J. Statham, "A ZAF procedure for microprobe analysis based on measurement of peak-to-background ratios," *Microbeam Analysis--1979*, 247.
5. C. J. Powell, "Cross sections for ionization of inner shells by electrons," *Rev. Mod. Phys.* 48: 33, 1976.
6. W. Heitler, *Quantum Theory of Radiation*, London: Oxford University Press, 1959.

CHARACTERIZATION OF HETEROGENEOUS POLYCRYSTALLINE MATERIALS

J. C. Russ and T. M. Hare

Classical quantitative microanalysis is by definition intended for the determination of the composition of homogeneous specimens or of single regions within materials. We report here a new technique that deals in a statistical way with heterogeneous materials, composed in our case of a variety of fine-grained individual phases that also have broad ranges of composition from grain to grain, owing to solid solution or substitutional effects. The method requires no presumptions by the user about the composition of the individual phases, nor even about the number of such phases that may be present.

The Analytical Problem

SYNROC is a generic name for a family of polyphase ceramic materials being tested for possible use for long-term storage of radioactive waste from power-generating reactors and other sources.^{1,2} These wastes typically contain 31 or more radioactive or toxic elements, and it is necessary to design a matrix of phases that will incorporate them in stable lattice sites to prevent their leaching out into ground water for geologically long periods. The materials currently under test contain from three to five different host phases, all complex oxides, whose relative amounts are chosen based on the composition of the anticipated waste. Each has been chosen based on its presumed ability to offer favorable sites for some of the waste ions, as well as suitability for ceramic processing and sintering.

The finished form of the material is a technically dense, very fine grained (1-3 μ m) ceramic containing a mixture of phases. However, because of the random nature of the mixing process of the raw materials and the waste, the waste ions are not dispersed uniformly in the host material; in other words, some grains of one host phase contain one waste ion, and some grains contain little of that ion but large amounts of several others.

Our microanalytical problem is to characterize this material. We need specifically to know which waste ions end up in which host phases, in what amounts, and in place of what elements (or together with what elements). The substitutions make the phases nonstoichiometric, and indeed alter the lattice parameters so that x-ray diffraction patterns are difficult to interpret. There may even be new phases formed or stabilized by the presence of the waste, which are not present when only the host raw materials are fabricated. In addition, the fine grain size makes selective analysis of individual grains difficult, and it is clear that classic quantitative analysis of the thousands of grains needed to determine overall composition is not practical. Simple summation of known phases using a least-squares addition of individual spectra³ works fine for the host phases by themselves, but is not possible when the composition of the constituent phases varies.

The problem described clearly requires a statistical approach, which we anticipate will be applicable to many other, less exotic heterogeneous materials as well.

Analyzing method

Samples are analyzed in our SEM (JSM--2) on polished but unetched surfaces, lightly carbon coated for conductivity. The electron beam (usually operated at 15 kV and a beam current of about 10 nA) is positioned by a microcomputer (Apple II) interfaced to the scan coils with 8-bit digital-to-analog converters (DAC). The beam is stepped across as a regularly spaced grid of points, with spacing at least as great (usually 5-10 times) as the typical grain size of the material, so that thousands of "random" points can be sampled in the microstructure. Analysis at each point is carried out for times ranging from 10 to 100 s (depending on the elements of interest) under control of the microcomputer's clock. Unattended overnight runs can be made and the resulting data stored on floppy disk for subsequent analysis.

The authors are in the Engineering Research Services Division, North Carolina State University, Raleigh, NC 27650. The work was partially supported by the U. S. Department of Energy under Contract No. DE-RP09-80ET41902.

The generated x rays are detected by a Si(Li) detector, whose amplified pulses are fed to a multichannel analyzer (MCA Nucleus 1024D) for operator inspection or when complete spectra are to be transferred to the computer for classic quantitative microanalysis, but also go to a specially designed interface card in the computer. This card contains eight DACs and comparators, which function as four single-channel analyzers (SCA) and feed four 16-bit counters. The result is to allow the computer to set upper and lower energy bounds for each of four pulse counters, and for the scalars to count the x rays in discrete energy windows for four elements, or combinations of elements or backgrounds, at a time. The counting process is controlled by the microcomputer, and the scalars are read by it. The data can be read far more quickly than by transfer of data from the MCA (transfer time is 20 μ s). The computer has seven interface slots (four are occupied by the beam-control DACs, the master clock, a printer interface, and the disk drive controller), and multiple-SCA counter boards can be used to obtain data for more elements.

The raw intensities (peak plus underlying background) can be used in three different ways, in an attempt to obtain values insensitive to long-term instrument beam current drift, minor topographic relief of the surface, and so on: (1) normalized intensities (each value divided by the sum of all values recorded); (2) peak-to-background ratios (with channels set to nearby energies to get the background); and (3) intensities normalized by the backscattered electron signal (which is also read by the computer by means of the same interface that controls the beam position).

The first method has the drawback that it introduces an anticorrelation effect in the intensities; that is, if one element's intensity rises, it automatically forces the normalized values for the others down. The normalization scheme also forces the assumption that all significant elements are being counted.

The second method has the advantage of being substantially independent of topographic effects, as well as beam-current fluctuations,⁴ but in this case it allows the counting of fewer elements (since up to half the channels must be devoted to background). Also, and more important, the counting statistics of the background values are generally rather poor for these short-time counts, and so the standard deviation of the P/B ratio becomes unacceptably large.

The third method, which we generally favor, is particularly attractive with a large-solid-angle annular detector such as ours (G&W Model 40). The signal is statistically better than any x-ray count value, and is largely independent of minor topographic relief. Since the backscattered electron fraction is a function of average atomic number, the use of these ratios causes some bias or nonlinearity in the relationship between normalized intensity and actual concentration, but that is not troublesome in our application.

Data Presentation

Several methods of analysis and data presentation were utilized to determine the number of phases, approximate phase composition and abundance, and a semiquantitative description of grain size effects and the presence of solid solutions. A computer-generated set of elemental intensities for a wide variety of experimental conditions was employed to aid in the design of the various algorithms.

From the series of measurements, we have for each point on the sample a set of N elemental intensities, normalized in one or another of the ways described. Each point may thus be plotted in an N-dimensional intensity space, in which we would expect to find clusters of points for each distinguishable phase. If the distribution is viewed as a histogram of point density along a one-dimensional (one element) axis, or if a plot of points is viewed in a two-dimensional projection (as a plot of one element vs another), these clusterings are not always apparent. The multidimensional nature of the problem causes overlaps in the projections, which compound the naturally broad nature of these distributions because of counting statistics, the natural range of composition of the phases, and surface topographic effects. In addition, depending on the grain size, we expect a fair number of the measured points to have more than one grain included partially in the analyzed volume, either because the lateral spread of the electrons covers more than one grain (the flat unetched surface analyzed does not show grain boundaries well, and in any case the computer is choosing points without looking at the image), or because the depth of penetration of the electrons may carry through to an underlying grain not visible on

the surface.⁵

Analyses of Distributions

Two distinct methods were evaluated to characterize the data clustering: a multiple-centered chi-squared minimization method designed to work with an unknown number of cluster centers, and a novel peak sharpening algorithm which assigns "mass" to the points in intensity space and then employs "gravity" to condense the clusters.

The first method uses a straightforward statistical approach to find the overall standard deviation in intensity space and then does a search in which increasing numbers of cluster center points are used to find significant decreases in the average deviation. With this method it is not always clear when the addition of another cluster center is producing a real improvement (i.e., postulating another phase present).

In the second method, for each point in the distribution, a small motion is applied with a vector determined by the summation of vectors toward each point with a magnitude determined by the inverse square of the distance to the point. The points are moved a short distance in each such step, but are not allowed to build up a velocity. The repeated application of such movements causes points in clusters to attract each other so that the comparatively diffuse clouds of points fuse into dense, massive clusters. There is some tendency for neighboring clusters to attract each other, and obviously if the process were repeated indefinitely all the points would end up at one common location, but in the first stages of this attractive process, after a small number (5-20, depending on the "gravitational constant") of cycles, only local clustering takes place. The sharpness of the resulting point distributions is then easily seen in one-dimensional histograms along each elemental axis. Contour plots of point density on two-dimensional projections both show the cluster locations and give information about their shapes, which are mentioned below.

As a calculational device, the stepwise application of small vector motions, which requires the repeated summing over all the point locations in the distribution, is very slow (although not in proportion to the time required for the measurements). Single-step calculations of N-dimensional gravitational potential functions can also identify cluster sites in many cases.

Phase Descriptions

From the location of peaks in one-dimensional histograms, detected by a simple peak-to-background criterion, one can calculate the centroid locations of the clusters in a straightforward manner, using simple logic to handle overlaps in one projection that are resolved by differences in another element or elements. This is a combinatorial problem that can be calculated exhaustively, since few cluster locations are involved. The centroids of these clusters give us the intensity values that characterize each phase and may be subsequently converted to approximate concentration by conventional standardless (normalized) ZAF calculation. The number of points (the "mass" of the cluster) gives the relative abundance of the phase. The limiting contour for each cluster is somewhat arbitrarily set where the point density drops to 10% of the peak density. Points that lie far from cluster centers and are isolated in space are presumed to result from overlap of two (or more) grains in a single point analysis, and are ignored.

The relative abundance of phases is taken as the number of points in each cluster as a fraction of all the clusters. The shape of the clusters, given by the standard deviation of concentration in the various elemental directions, gives valuable information about the degree of composition variation. Orientation of a major axis of a nonspherical cluster may identify the substitution of one element for another. These cluster-shape effects are particularly evident in two-dimensional contour plots, which show the strong elemental correlations present in our SYNROC materials.

Conclusion

By locating clusters of points in the N-dimensional distribution of measurements of x-ray intensity values from a large number of "randomly" located points on the surface of fine-grained heterogeneous materials, we can identify the mean compositions and rela-

tive abundance of the phases present. No presumptions about these parameters, or even the number of phases, need be made. From the shape of the clusters of points, conclusions may be drawn about the extent of solid solution or substitutional effects among the elements in each phase. This is a practical method for characterization of heterogeneous, unknown materials which do not lend themselves to classic quantitative x-ray microanalysis, and for which bulk analytical methods are also inappropriate because they do not describe the heterogeneity.

References

1. A. E. Ringwood, *Safe Disposal of High Level Nuclear Reactor Wastes: A New Strategy*, Australian National University Press, 1978.
2. A. G. Solomah, T. M. Hare, and H. Palmour III, "Demonstration of the feasibility of subsolidus sintering of radwaste containing SYNROC-B composition," *Nuclear Technology* 7: 183, 1980.
3. J. C. Russ, "Quantitative analysis of multiphase samples," *Microbeam Analysis--1979*, 259-264.
4. J. C. Russ, "New methods to obtain and present SEM x-ray line scans," *ibid.*, 292-304.
5. J. C. Russ, T. M. Hare, and A. G. Solomah, "Selective x-ray analysis of individual fine grains for phase identification in SEM," *Canadian J. Spectroscopy* 25: 64-69, 1980.

DEPENDENCE OF ZAF CORRECTIONS ON TILT AND AZIMUTH

M. A. Parker

The literature has been reviewed to determine the dependence of the ZAF corrections on tilt and azimuth. The validity of the assumption that the atomic number correction Z is independent of these geometric parameters has been examined. The effective take-off angle, a function of tilt and azimuth, has been shown to be appropriate only to the absorption correction A . Finally, the fluorescence correction F has been shown to depend on two separate geometric parameters (which in turn depend on tilt and azimuth) that affect a foreshortened mean depth of x-ray production and a decreased x-ray absorption pathlength.

With the advent of scanning electron microscopes (SEMs) equipped with energy-dispersive x-ray (EDX) spectrometers, analysts have employed a number of unusual analysis geometries for quantitative microprobe analysis (QMPA).¹ These systems often employ glancing electron beam incidence on tilted samples, and detectors mounted with nonzero azimuth.^{2,3} In addition, analysts purposely choose high tilt angles for sample analysis to minimize x-ray absorption effects. Under these nonstandard conditions, a danger inherent in analyses performed on SEM-EDX systems is the use of inappropriate geometric models for calculating ZAF corrections. For example, there is confusion regarding the dependence of the atomic number correction on tilt due to the variation of the backscattering coefficient R with tilt. Also, the multitude of expressions available for the effective take-off angle offers a difficult choice in the appropriate expression for use in the absorption correction. Finally, analysts can inappropriately employ values of the effective take-off angle, which is a concept relevant to the absorption correction in the fluorescence correction.

*Dependence of ZAF Corrections on Geometry under Standard Conditions*⁴

Under standard conditions, the electron beam impinges perpendicularly the surface of flat, well-polished specimens (Fig. 1). Also for standard conditions, the take-off angle ψ is the angle α_0 determined by elevation of the detector and does not depend on the detector azimuth ω . Under these conditions, the concentration C depends on the x-ray take-off angle ψ as follows:

$$C = ZA(\psi) F(\psi)k(\psi)$$

The ZAF corrections are necessary to adjust the intensity ratio for differences between the unknown and the standard for the absorption of x rays by the specimen, fluorescence excitation by line radiation, and the effects of backscattering and stopping power on the electron beam. ZAF corrections depend on the interrelationships of three x-ray intensities associated with each of these effects:

- (1) the generated intensity I_g due to primary beam excitation,
- (2) emitted intensity I_e due to the absorption within the specimen of the generated intensity, and
- (3) the contribution to detected intensity I_f due to fluorescence by discrete x-ray lines (Table 1).

The dependence of the ZAF corrections on the geometric parameter ψ and, in general any other geometric parameters, is determined by the dependence of these x-ray intensities on Lambert's law and Lenard's law, which determine the effect the path lengths traversed by various radiations have on the x-ray intensities.

Dependence of X-ray Intensities on Geometry under Standard Conditions

The generated intensity I_g is independent of ψ and is obtained from the function $\phi(\rho z)$, which is the x-ray distribution in depth. To obtain I_g , we perform an integration over

The author, formerly with the Department of Metallurgical Engineering at the Illinois Institute of Technology in Chicago, is now a materials scientist at IBM Information Systems Division, Rochester, MN 55901. The support of IIT is gratefully acknowledged.

$\phi(\rho z)$ that extends below the surface of the specimen to the depth of complete electronic diffusion, ρz^* (Fig. 2). Castaing proposed and Philibert⁵ later modified an expression for $\phi(\rho z)$ based directly on Lenard's law for electron penetration.

The incorporation of the geometric parameter for classical analysis conditions, ψ , is immediately apparent from the definition of the primary emitted intensity I_e derived by Philibert (Fig. 2). The differential primary-generated intensity of a line element $d(\rho z)$ in the x-ray distribution in depth is given by $dI_g = \phi(\rho z) d(\rho z)$. On passage through the intervening material to the specimen surface, x rays of this intensity travel a mass-path length $\rho z \csc \psi$. The differential primary-emitted intensity at the specimen surface is given by Lambert's law:

$$dI_e = dI_g \exp[-(\mu/\rho)\rho z \csc \psi]$$

Integration over the entire length of the line source determines the total primary emitted intensity I_e that reaches the detector. The form in which the geometric parameter enters is $\csc \psi$.

The secondary fluorescent x-ray intensity I_f accounts for the enhancement of low-energy x-ray lines of an A-type atom in the fluoresced volume by higher energy x-ray lines of a B-type atom of the primary volume. The secondary fluoresced x-ray intensity I_f arises in the following fashion: The electrons penetrate to some depth z and cause the generation of x rays in the line element $d(\rho z)$. From this point, the generated x rays travel in all directions in the surrounding material. Some of these x rays are absorbed; a few produce ionizations in the companion atomic species of the sample with subsequent fluoresced x-ray emission. Lambert's law for x-ray absorption must be considered along the pathlength with absorption coefficient μ_B of the fluorescing x rays en route to the location of the ionization event, and along the path length with absorption coefficient μ_A of the resulting fluoresced x rays en route to the detector.⁶

Expressions for the Geometric Dependence under Standard Conditions

The atomic number correction Z is independent of the geometric parameter ψ , as is evident from the definition of Z in terms of the generated intensities I_g and their independence of ψ . Hence the backscattered electron factor R and the material stopping power S , both independent of ψ , give Z (Table 1).

The absorption correction A depends heavily on the geometric parameter ψ . The absorption correction is expressed in terms of $f(\chi)$, where $f(\chi)$ is the fraction of the generated intensity that is emitted; $f(\chi)$ clearly depends on ψ through the χ term discussed in conjunction with I_e (Table 1).

The fluorescence correction F also depends on ψ . Wittry derived an expression for F based on the integration of the x-ray distribution in depth $\phi(\rho z)$ of Castaing, which gives I_f and I_e (Table 1). Clearly, F depends on χ , hence ψ , through the u term; the v term is independent of ψ , and K is a constant.

Note that σ , χ , u , and v are expressions that contain the absorption coefficients for the various radiations, as well as the various geometric parameters.⁷ These expressions may be viewed as the effective absorption parameters for the various radiations of the excited analysis volume in the specimen.

Dependence of the ZAF Corrections on Geometry under Nonstandard Conditions

Under nonstandard conditions, the ZAF corrections depend on a number of other geometric parameters, specimen tilt θ , and detector azimuth ω , which are determined by the specimen geometry and instrument design (Fig. 3). For nonstandard conditions of analysis, it is useful to employ the effective take-off angle ϵ , the x-ray take-off angle ψ , and the effective tilt angle λ , which are functions of tilt and azimuth (Table 1). Moll⁸ has defined λ through the equation $\tan \lambda = \tan \theta \cos \omega$. Under nonstandard conditions, the concentration C depends on ϵ , ψ , and λ as follows:

$$C = ZA(\epsilon) F(\psi, \lambda) k(\psi, \lambda)$$

Expressions for the Geometric Dependence under Nonstandard Conditions

Jones and Abelmann,⁹ studying the effect of tilt on the backscattering factor R , found that there was an effective backscattering factor R^* , which depended on tilt. From their data it may be concluded that the dependence of R^* is approximately: $R^* = g(\lambda)R$. The consequence of this result is that the atomic number correction to the intensity ratio Z is nearly independent of tilt (Table 1).

All the various models that have been developed for the geometric dependence of the absorption correction on tilt and azimuth assume that the mean depth of x-ray production is foreshortened by some geometric parameter $g(\lambda)$ with tilt.¹⁰⁻¹² The mean depth of x-ray production decreases by some unknown amount dependent on the specimen tilt to $g(\lambda)\rho z$. The x-ray absorption pathlength is given by $g(\lambda)\rho z \csc \psi$, where ψ is increased to $\alpha_0 + \lambda$, with tilt of the specimen (Fig. 4). The meaning of the effective take-off angle becomes clear upon evaluation of $f(\chi)$; $\csc \epsilon$ is no more than the algebraic simplification of the angular dependence of the mean depth of electron penetration and the x-ray absorption path length that is possible because χ^*/σ^* appears as a ratio in Philibert's expression for $f(\chi)$ (Table 1). It is thus an accident of the analysis that one may employ $\csc \epsilon$ as a substitution for the $\csc \psi$ of normal electron-beam incidence, a result of the algebraic simplicity of Philibert's approximation.

The expression for the effective take-off angle is:

$$\csc \epsilon = g(\lambda) \csc \psi$$

Inspection of this expression for $\csc \epsilon$ makes clear the motivation analysts have for tilting the specimens under analysis in the SEM (Fig. 4): namely, a reduction in the magnitude of the absorption correction and its associated uncertainty. The resulting error in analysis decreases since $\csc \psi$ decreases with increasing λ as:

$$\csc \psi = \csc(\alpha_0 + \lambda)$$

Any error in analysis due to absorption is reduced still further by a mean depth of x-ray production nearer the surface, given by $g(\lambda) < 1.0$; so that with tilt

$$\csc \epsilon = g(\lambda) \csc(\alpha_0 + \lambda) << \csc \alpha_0$$

The concept of a foreshortening factor $g(\lambda)$ may be extended to the fluorescent intensity through its dependence on $\phi(\rho z)$. Wittry has suggested that the fluorescence correction F changes with tilt so that the term affecting the mean depth of electron penetration, $\sec \lambda$, and that related to the x-ray absorption path-length, $\csc \psi$, are split; the effective takeoff angle is no longer an appropriate concept (Table 1). However, Wittry made the same geometric simplification Green and Moll made in their treatment; that is, he assumed that

$$g(\lambda) = \cos \lambda = \sin \beta$$

for the altered electron beam pathlength (β is the electron beam incidence angle). It is more appropriate to leave $g(\lambda)$ in this expression as some arbitrary function of λ . It is suggested that if the analyst wishes to correct F properly for tilt, he should estimate $\csc \psi$ and obtain a value for $g(\lambda)$ in the fluorescence correction from

$$g(\lambda) = \csc \epsilon / \csc \psi$$

where $\csc \epsilon$ is the calibrated effective take-off angle based on absorption within a standard.¹³

This result clearly shows that substitution of $\csc \epsilon$ for $\csc \psi$ in the fluorescence correction not only leads to errors in overcorrecting u^* , but also in an error from failure to correct v^* entirely. Neglecting $g(\lambda)$ in the v^* term is equivalent to neglecting the reduced fluorescence of material resulting from a mean depth of x-ray production nearer the specimen surface with increasing tilt. Thus, tilting the specimen reduces the magnitude of the fluorescence correction and its associated uncertainty.

TABLE 1.--Summary of expressions for ZAF corrections under various conditions of analysis.

Correction	Z	A	$f(\chi)$	F
Definition [†]	$\frac{I_g^0 C}{I_g'}$	$\frac{I_e^0 I_g'}{I_e' I_g^0}$	I_e'/I_g	$\frac{I_e'}{I_e' + I_f'}$
Standard Form _{III}	$\frac{R^0/S^0}{R^1/S^1}$	$f(\chi)^0/f(\chi)'$	$\frac{1+h}{(1+\chi/\sigma)(1+h(1+\chi/\sigma))}$ $\sigma = \sigma$ $\chi = (\nu/\rho)\csc\psi$	$\frac{1}{1+K[\frac{1}{u} + \frac{\ln(1+v)}{v}]}$ $u = \frac{\mu_A \csc\psi}{\mu_B}$ $v = \frac{\sigma\rho}{\mu_B}$
Nonstandard Form _{III}	$\frac{R^{0*}/S^0}{R^{1*}/S^1}$	$f(\chi^*)^0/f(\chi^*)'$	$\frac{1+h}{(1+\chi^*/\sigma^*)(1+h(1+\chi^*/\sigma^*))}$ $\sigma^* = \sigma/g(\lambda)$ $\chi^* = (\nu/\rho)\csc(\alpha_0+\lambda)$	$\frac{1}{1+K[\frac{1}{u^*} + \frac{\ln(1+v^*)}{v^*}]}$ $u^* = \frac{\mu_A \csc(\alpha_0+\lambda)}{\mu_B}$ $v^* = \frac{\sigma\rho}{\mu_B g(\lambda)}$

[†] α_0 is used to designate intensity of x-ray line from pure element standard and λ the intensity, from unknown specimens.

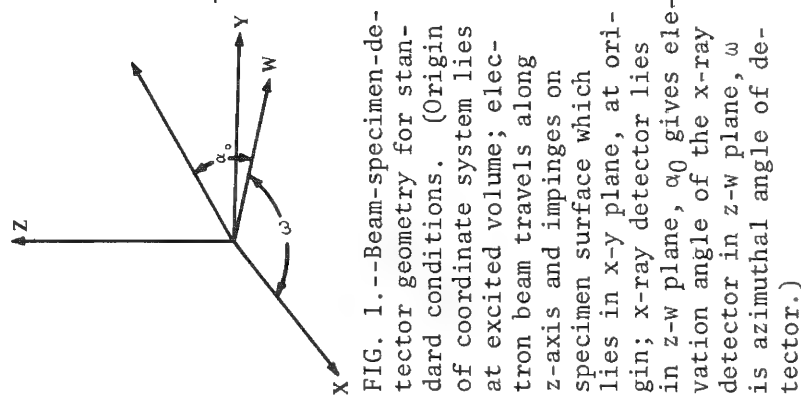


FIG. 1.--Beam-specimen-detector geometry for standard conditions. (Origin of coordinate system lies at excited volume; electron beam travels along z-axis and impinges on specimen surface which lies in x-y plane, at origin; x-ray detector lies in z-w plane, α_0 gives elevation angle of the x-ray detector in z-w plane, ω is azimuthal angle of detector.)

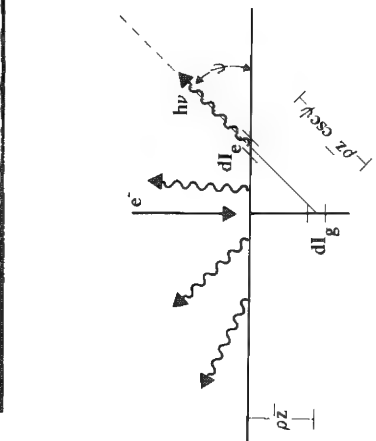


FIG. 2.--Geometry for x-ray generation and absorption for standard conditions. (Electrons produce x-rays along line source; a segment of line source gives rise to intensity dI_g , which is attenuated along path-length $\rho z \csc \psi$; attenuation results in lessened emitted intensity dI_e for segment of line source; ρz designates mean depth of x-ray production for line source.)

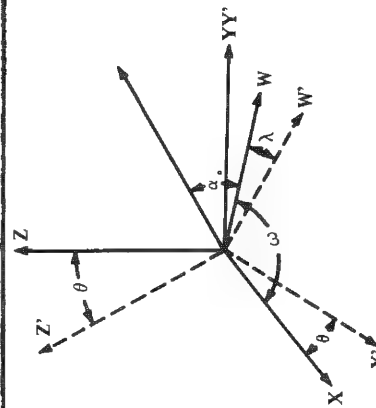


FIG. 3.--Beam-specimen-detector geometry for nonstandard conditions. (Specimen is tilted by angle θ about tilt axis, the y-axis; specimen surface is thus rotated in-plane to x'-y' plane; normal to specimen surface z' no longer lies along path of electron beam z ; x-ray take-off angle ψ now becomes sum of α_0 and λ , which is effective tilt angle in plane of detector and electron beam; effective tilt angle λ depends on the detector azimuth ω and specimen tilt θ .)

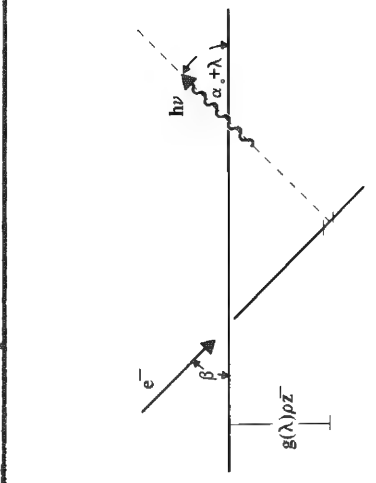


FIG. 4.--Geometry for x-ray generation and absorption for non-standard conditions. (Electron beam impinges on specimen at incidence angle β in z-w plane due to effective tilt of the specimen, λ ; mean depth of x-ray production is lessened by geometric parameter $g(\lambda)$; x-ray take-off angle is increased to $\psi = \alpha_0 + \lambda$.)

References

1. E. Lifshin, "Quantitative microprobe analysis with energy dispersive detectors," Syracuse, N.Y.: *General Electric Technical Information Series*, 75 CRD 253, 1975.
2. H. Yakowitz et al., *Practical Scanning Electron Microscopy*, New York: Plenum Press, 1975, 327-372.
3. L. S. Birks et al., "X-ray absorption and emission," *Analytical Chemistry* 46: 360R, 1974.
4. D. R. Beaman, *Electron Beam Microanalysis*, Philadelphia: American Society for Testing and Materials, 1972, STP-506.
5. J. Philibert, "A method for calculating the absorption correction in electron-probe microanalysis," *X-Ray Optics and X-Ray Microanalysis*, New York: Academic Press, 1963, 378-392.
6. D. B. Wittry, "Methods of quantitative electron probe analysis," *Adv. X-Ray Analysis* 7: 397, 1963.
7. M. A. Parker, *The Effective Takeoff Angle for Quantitative Electron Probe Microanalysis*, Thesis, IIT, 1978.
8. S. Moll, "Geometrical considerations for ZAF corrections in the SEM," Technical Bulletin 111-277, Advanced Materials Research Corp., 1977.
9. R. A. Abelmann and R. Jones, "X-ray spectrometer performance as a function of electron probe geometry," *J. Appl. Phys.* 37: 4507-4510, 1966.
10. H. E. Bishop, "The absorption and atomic number corrections in electron probe microanalysis," *Brit. J. Appl. Phys.* 1: 673, 1968.
11. M. Green, "The angular distribution of characteristic X radiation and its origin within a solid target," *Proc. Phys. Soc.* 83: 435, 1964.
12. N. Gennai et al., "The $f(\chi)$ -curves for Fe K α and Al K α x-rays in the inclined EPMA targets of Fe, Al and Fe-Al alloy," *Jap. J. Appl. Phys.* 10: 491, 1971.
13. M. A. Parker, "Determination of the effective take-off angle on scanning electron microscope energy dispersive x-ray analysis systems," *Microbeam Analysis--1980*, 65.

METHOD OF ZAF ANALYSIS IN THE SEM IN CASES IN WHICH THE TAKE-OFF ANGLE IS UNKNOWN

P. B. De Groot

One of the problems arising in x-ray fluorescence analysis in the scanning electron microscope (SEM) is the uncertainty in the x-ray take-off angle ψ in the analysis area. On rough or irregular surfaces, ψ often cannot be defined geometrically. In the present work, the take-off angle is determined from intensity changes in two spectra obtained at initially unknown angles a known increment apart. Preliminary results suggest this method will be useful for both planar and rough surfaces.

The absorbance correction, and to some extent the fluorescence correction applied in ZAF (atomic number, absorbance, fluorescence) and similar matrix-correction schemes can vary greatly with ψ . Several methods have been used to try to minimize this problem. Bomback¹ showed that determining the local take-off angle from stereo photomicrographs improved analysis accuracy, at least for approximately planar regions. Small et al.² and Statham³ have shown that peak-to-background ratios vary less than peak intensities for irregular surfaces, and have used this fact to improve analysis accuracy. Recently, Russ and Hare⁴ presented a method based on data from spectra at two different beam voltages. An iterative solution of ZAF corrections was used to find the ψ giving the same concentrations at the two voltages. Parker and Warke⁵ have developed a method which uses an "effective ψ " calibration curve generated from standards. In the present method, spectra are obtained at two initially unknown angles differing by a known amount. Calculation of concentrations from these spectra by the ZAF method will in theory yield identical results for the two spectra only at the correct take-off angles. The approach, then, was to devise a scheme for producing a rapidly converging series of ZAF analyses to find these angles.

All these methods, including the present one, have produced substantially improved analyses on some types of samples. It would be of future interest to have a systematic comparison of the limitations of these methods on samples of varied composition and surface topography.

Experimental Methods

Specimens were analyzed in an AMR 1000 SEM equipped with a Tracor-Northern NS-880 x-ray fluorescence system. The SEM was operated at 30 kV. Beam current was adjusted to give convenient x-ray count rates.

The ZAF matrix correction program used was a modified version of the program furnished by the x-ray equipment manufacturer. For some of the analyses, a modified version of the fundamental parameters program SSQ (Standardless Semi-Quantitative), also furnished by the x-ray equipment manufacturer, was used. This program uses ZAF along with calculated pure-element intensities to determine concentration.

Zinc sulfide (Fisher, reagent grade) was used as an analytical standard to test the method of take-off angle determination. It was pressed to a smooth-surfaced pellet in a conventional KBr infrared pellet press. A 2024 aluminum alloy was also used to test the method. A smooth surface was produced by polishing, using standard metallurgical methods. Rough surfaces were produced in ZnS by fracturing, and in the Al alloy by cutting with a hacksaw.

Results and Discussion

Development of Method. As noted in the introduction, the problem of finding an unknown take-off angle, given spectra obtained at ψ 's a known angle $\Delta\psi$ apart, reduces to finding the two angles ψ and $\psi + \Delta\psi$ that yield the same ZAF-corrected concentrations. It is unlikely, owing to other experimental uncertainty, for these two ZAF calculations to yield identical results for all elements in the sample. Therefore, we shall adopt the criterion that one selected element should give the same concentration at both angles.

The author is with the Celanese Chemical Company Technical Center, Box 9077, Corpus Christi, TX 78408.

The x-ray emission of the selected element should be at relatively low energy, since absorption varies most strongly with ψ in this region.

To determine how the calculated concentrations vary with ψ , a hypothetical 50/50 by weight Zn/Al alloy was analyzed by ZAF methods at various values of ψ and $\Delta\psi$. A true ψ of, say, 30° , and $\Delta\psi$ of 10° was first assumed, and the k-ratios that would be observed were calculated by ZAF. These k-ratios were then put into a series of ZAF calculations throughout the range of $\psi = 10-80^\circ$. If we ignore the fluorescence correction, the form of the absorbance correction suggests that $\ln(C_\psi/C_{\psi+\Delta\psi})$ vs $\Delta\text{cosec } \psi$ should be roughly linear. (C is the ZAF-calculated concentration of the element of interest; in this case, Al.) Such plots are shown in Fig. 1 for several values of "true" take-off angles.

The point at which a plot crosses the x axis represents the solution for the correct ψ and $\Delta\psi$. Since these curves are only very approximately linear, an iterative method of finding the correct $\Delta\text{cosec } \psi$ (and then the correct ψ) is necessary. First, $\ln(C_\psi/C_{\psi+\Delta\psi})$ is calculated at $\psi = 90^\circ - \Delta\psi$ and $\psi = 90^\circ - 2\Delta\psi$. The intersection of the straight line through these points and the x axis gives an estimate, $\Delta\text{cosec } \psi'$, of the correct $\Delta\text{cosec } \psi$.

Unfortunately, if $\Delta\psi$ is a finite increment, there is not a simple relationship between $\Delta\text{cosec } \psi'$ and ψ' . Therefore another iterative method is used to find ψ' . This method begins by assuming that

$$\Delta\text{cosec } \psi' \approx d(\text{cosec } \psi') \approx -\text{cosec } \psi' \cdot \cot \psi' \cdot \Delta\psi'$$

and solving for ψ' . The $\Delta\text{cosec } \psi'$ at this estimate of ψ' is evaluated, compared to the "target" $\Delta\text{cosec } \psi'$, and a correction applied. The process is repeated until ψ' is found.

With this estimate of ψ' , the ZAF analysis is repeated at ψ' and $\psi' + \Delta\psi$. A straight line is drawn through this point and the previous ZAF-determined point to yield a new estimate of the true take-off angle, and the process continues. Convergence to two concentrations differing by less than one part in 10^4 usually occurs in 2-5 iterations.

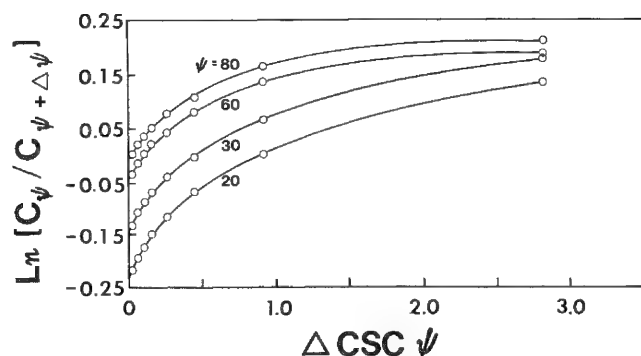


FIG. 1.--Relationship between difference of the cosecants of two assumed take-off angles and logarithm of ratio of Al concentrations calculated by ZAF at these angles for 50/50 Zn/Al alloy.

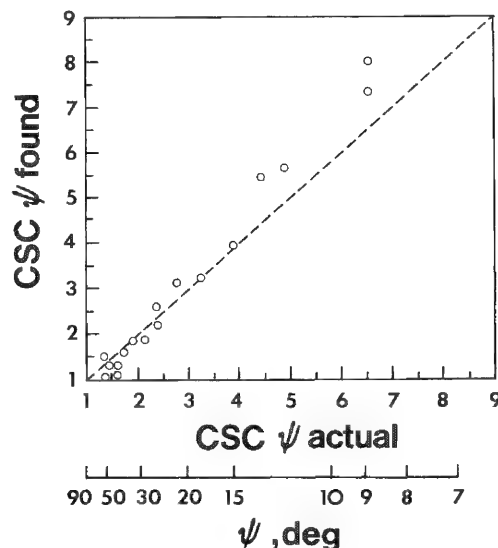


FIG. 2.--Determination of cosec ψ of smooth ZnS samples by SSQ/dual take-off angle method.

Testing the Method at Known ψ . to test the method, the spectra of smooth-surfaced ZnS samples at known ψ and $\psi + \Delta\psi$ were obtained, and subjected to the above procedure to determine the take-off angle. The change in ψ was made by changing the tilt angle of the specimen. For these analyses, the fundamental parameters method SSQ was used, as it had previously been shown to give reasonably accurate results for ZnS. Figure 2 shows a plot of the true cosec ψ vs the cosec ψ found by this method. The results are quite encouraging and show that cosec ψ can be determined to within about 20% in the range $\psi = 10-60^\circ$.

The scatter in the data appears to be about that expected from the statistical precision of measurement of the S $K\alpha$ peak used as the convergence criterion. Calculations based on the data obtained at $\psi = 30^\circ$ show that the variance in the S k-ratio, when prop-

agated through the calculations of the method, produces a variance in $\csc \psi$ which is about ten times greater than that of the k-ratio. The systematic error evident in the results of Fig. 2 may be due partly to inaccuracies in the ZAF or SSQ methods. At low ψ , the complicated geometry of the sample and detector positions in the AMR instrument also makes the determination of the true ψ difficult.

Application to Irregular Surfaces. The above experiments showed that this method can be applied to the determination of the take-off angle of planar surfaces. The question remains as to whether a useful "effective" take-off angle for irregular surfaces can be defined by these means. Strictly speaking, the method compensates correctly only for planes oriented parallel to the tilt axis of the sample. Surface regions not so oriented will have only partial correction for take-off angle effects. Nevertheless, it seemed worthwhile to determine what sort of improvement of analysis of rough surfaces could be obtained.

It is important to produce rough or irregular surfaces that are known to have the same composition as the bulk sample. The first of these surface was obtained by fracturing the pressed ZnS pellet, and mounting a broken piece at an arbitrary orientation on a sample stub. An area of this fracture surface with a steep ridge and other irregularities (Fig. 3) was chosen for analysis. Analysis was done by the ZAF method, with the analysis of a smooth specimen of ZnS at $\psi = 39.2^\circ$ used as a standard. Results are given in Table 1. They illustrate the ability of the method to find an effective take-off angle which gives quite reasonable analytical results on a nonplanar surface of unknown orientation.

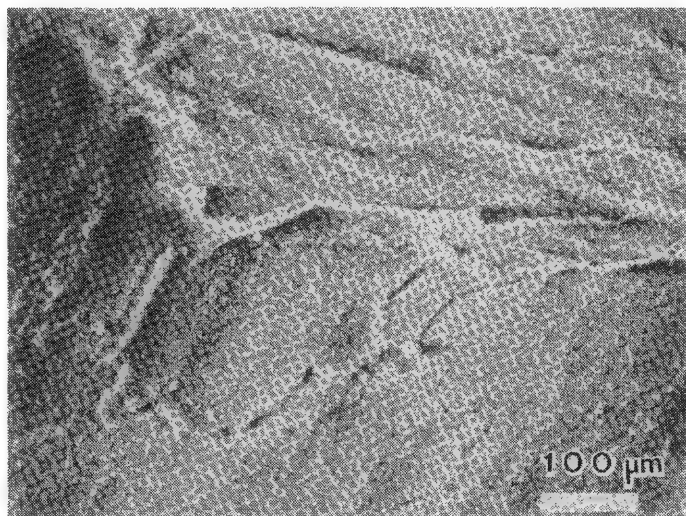


FIG. 3.--Area of fracture surface of ZnS.

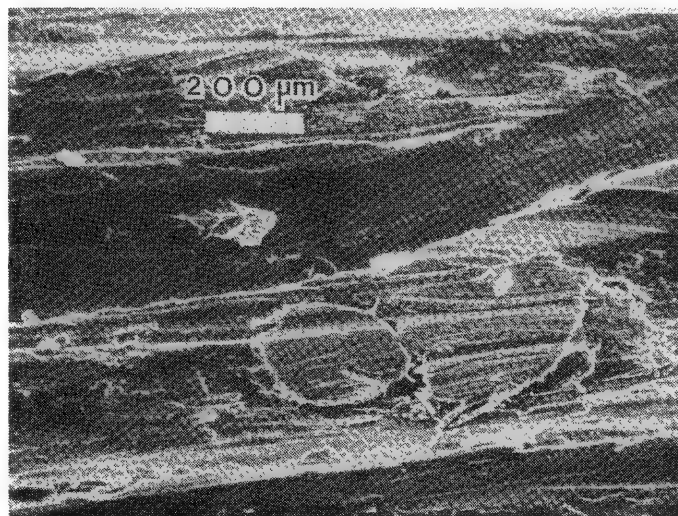


FIG. 4.--Area of rough surface of Al alloy.

Another application to rough surfaces involved the sawed surface of a 2024 Al alloy (Fig. 4). The sample was mounted in the SEM with the sawed surface parallel to the sample stub surface. Results of ZAF analyses for Al are given in Table 2. The "nominal" take-off angle was that calculated for the plane of the saw cut. Clearly, the results obtained for Al at the calculated effective ψ are much better than those obtained at the nominal ψ , especially at low take-off angles. As expected, the results calculated from the relatively high energy Cu $K\alpha$ line show little dependence on ψ in either case. The mean Cu concentration found at the nominal ψ was $5.02 \pm 0.14(2\sigma_{\text{mean}})$ and that found at the effective ψ was 5.04 ± 0.14 , compared to the actual concentration of 5.15%.

TABLE 1.--Results of ZAF analyses of fracture surface shown in Fig. 3.

TILT, DEG.	ψ EFF., DEG.	WT.% (RELATIVE ERROR, %)	
		ZINC	SULFUR
30	29.2	69.7 (+3.9)	30.6 (-7.0)
40	35.8	68.5 (+2.1)	
45	29.8	68.1 (-1.5)	33.1 (+0.6)
55	37.1	67.1 (0.0)	
60	41.0	69.6 (+3.7)	32.7 (-0.3)
70	49.2	68.0 (+1.4)	

TABLE 2.--Results of ZAF analyses of rough surface of Al alloy shown in Fig. 4.

ORIENT- TATION	ψ , DEG.		WT.% Al (REL. ERROR, %) ^a	
	NOMINAL	EFFECTIVE	AT ψ NOMINAL	AT ψ EFFECTIVE
(b)	18.0	5.9	77.9 (-15)	93.7 (+1.9)
	24.6	12.5	84.4 (- 8.2)	
(b)	22.7	9.1	77.4 (-16)	90.0 (-2.1)
	29.8	16.2	81.9 (-11)	
(c)	22.7	10.6	82.5 (-10)	92.7 (+0.8)
	29.8	17.7	86.0 (- 6.4)	
(b)	39.2	31.6	90.1 (- 2.0)	92.3 (+0.4)
	47.4	39.9	90.6 (- 1.4)	

(a) Rel. error with respect to value obtained by ZAF analysis of polished section. (Al-91.9%, Cu-5.15%). Sample also contains small amounts of Mg, Si, Fe, Mn, not analyzed.

(b) As shown in Fig. 4. (Grooves parallel to tilt axis)

(c) Rotated 90° from above. (Grooves perpendicular to tilt axis.)

Conclusions

The method of determining ψ from ZAF analyses at two take-off angles a known increment apart has been shown to provide rapid, improved quantitative and semiquantitative ZAF analyses on some irregular surfaces and surfaces of unknown orientation. Analyses can be obtained rapidly because the sample orientation need not be known or fixed beforehand.

References

1. J. L. Bomback, *SEM/1973*, 98-104.
2. J. A. Small, D. E. Newbury, and R. L. Myklebust, *Microbeam Analysis--1979*, 243-247.
3. P. J. Statham, *ibid.*, 247-253.
4. J. C. Russ and T. M. Hare, *Microbeam Analysis--1980*, 62-64.
5. M. A. Parker and W. R. Warnke, *Ibid.*, 65-67.

EMPIRICALLY DETERMINED DEPENDENCE OF EFFECTIVE TAKE-OFF ANGLE ON TILT AND AZIMUTH

M. A. Parker

Empirically determined values of the effective take-off angle, which were obtained by use of a calibration standard, were fitted to various expressions for the effective take-off angle as functions of tilt and azimuth. Best fit was found to an expression that incorporated the effect of multiple electron scattering based on the Monte Carlo model.

In recent years, energy dispersive x-ray (EDX) detectors have made possible the use of the scanning electron microscope (SEM) for quantitative microprobe analysis (QMPA).¹ A problem of specimen-detector geometry exists on such systems, since these detectors are mounted at vacant ports of the SEM with undefined azimuths, and analysts often tilt their specimens to obtain conditions of lessened x-ray absorption at higher take-off angles.^{2,3} Many expressions for the effective take-off angle, ϵ , have been posited on the basis of theoretical models as adjuncts to work on the absorption correction.⁴ Currently disagreement exists as to the correct expression to employ (Table 1).⁵⁻¹⁰ Furthermore, these expressions are difficult to relate to systems with a complicated geometry, such as that encountered on contemporary SEM-EDX systems. Thus, the choice of the correct expression for the effective take-off angle is a difficulty that confronts many analysts. It is important to use the correct expression since the accuracy of the absorption correction depends on the correct value for the effective take-off angle.

Experimental Setup

A JEOL U3 SEM, Canberra Si(Li) detector and amplifier, and Tracor Northern NS 880 spectral analysis system constituted the analytical system. Chamber peaks were eliminated by use of a polepiece shield and a collimator over the EDS detector. Other precautions were taken to assure satisfaction of the conditions for quantitative analysis.

The calibration standard was the W-20% Mo alloy standard reference material, SRM480, which can be obtained from the National Bureau of Standards. The $L\alpha$ and $L\beta$ lines of Mo were chosen because they required a large absorption correction and the fluorescence correction factor was essentially unity.

Calibration Method

The absorption factor for the Mo $L\alpha$ and $L\beta$ lines was determined by $A = C/kZ$.¹¹ The composition C was known; the intensity ratio k was measured; and the atomic number correction Z was calculated. Since there was a negligible fluorescence correction for the Mo x-ray line the resulting empirically determined value of the absorption correction depended directly on the specimen orientation with respect to the detector, given by α_0 , and the tilt of the specimen relative to the electron beam θ . There is a simple dependence of the absorption correction on the effective take-off angle ϵ , which is a function of α_0 and θ . Using Philibert's expression for the absorption correction, and solving for $\csc \epsilon$, we obtained a simple quadratic equation for $\csc \epsilon$ in terms of the empirical absorption correction. In a sense, the calibration was the converse of quantitative analysis.

Derivation of the Calibration Equation

The absorption correction is given by Philibert in terms of $f(\chi)$, from which one obtains

$$Af(\chi)' - f(\chi)^0 = 0 \quad (1)$$

Since χ is just the product of the mass-absorption coefficient μ/ρ and $\csc \epsilon$, we can rewrite Eq. (1) as a quadratic in $\csc \epsilon$,

$$a \csc^2 \epsilon + b \csc \epsilon + c = 0 \quad (2)$$

The author, formerly with the Department of Metallurgical Engineering at the Illinois Institute of Technology in Chicago, is now a materials scientist at IBM Information Systems Division, Rochester, MN 55901. The support of IIT is gratefully acknowledged.

where

$$a = \frac{1}{\sigma^2} \left[A^* h^0 \left(\frac{\mu}{\rho} \right)^0 - h' \left(\frac{\mu}{\rho} \right)' \right]$$

$$b = \frac{1}{\sigma} \left[A^* \left(\frac{\mu}{\rho} \right)^0 (1 + 2h^0) - \left(\frac{\mu}{\rho} \right)' (1 + 2h') \right]$$

$$c = A^*(1 + h^0) - (1 + h')$$

A^* is given in terms of the experimentally determined absorption correction by $A^* = A(1 + h')/(1 + h^0)$. Equation (2) has the solution

$$\csc \epsilon = \frac{-b + \sqrt{b^2 - 4ac}}{2a} \quad (3)$$

Determination of Beam-specimen-detector Geometry

To verify theoretically the form of the dependence of $\csc \epsilon$ on the tilt of the specimen, one must be able to define the geometry of the specimen, electron beam, and x-ray beam. Three angles are required to specify the effective take-off angle precisely enough so that a least-squares fit of the various expressions for the effective take-off angle to the calibrated values of $\csc \epsilon$ can be performed.

The three angles on which the effective take-off angle depends are the stage tilt θ , the detector azimuth ω , and the detector elevation angle α_0 (take-off angle for untilted samples). The plane in which the x-ray emergence angle ψ is measured is that defined by the electron beam and the detector. The x-ray emergence angle ψ is then the sum of α_0 and λ , where α_0 is the take-off angle for perpendicular electron beam incidence given by the elevation angle of the detector, and λ is the effective tilt angle of Moll defined in terms of θ and ω (Table 1). The plane in which the angle of electron beam incidence β (the complement of λ) is determined is also the plane that contains both the electron beam and the detector.

The angle θ was then incremented in 5° steps from -7° to 43° , and spectra were acquired of the W-20% Mo calibration standard over the range of θ angles for a flat mount and a 30° wedge mount of the standard; i.e., $\theta_0 = 0^\circ$ and 30° . Thus, calibrated values of $\csc \epsilon$ were obtained from -7° to 73° tilt angles θ for a 20° detector elevation angle α_0 and a 17° detector azimuth angle ω .

Results of Curve Fitting $\csc \epsilon$ to Theoretical Expressions

These calibrated values of $\csc \epsilon$ were plotted versus the specimen tilt angle θ , so that the behavior of $\csc \epsilon$ with tilt might be compared with the behavior predicted by models which assumed no geometric foreshortening of the mean depth of x-ray production, a simple geometric foreshortening, and a mean depth lessening, based on the Monte Carlo model. The effect of detector azimuth ω on the lessening of the mean depth of x-ray production in these models was compensated for by using Moll's effective tilt angle λ instead of θ in these expressions.

On inspection of these plots it was seen that the data followed rather well the curve predicting the behavior of $\csc \epsilon$ with tilt derived from Bishop's model for electron penetration (i.e., the Monte Carlo model) when the effect of azimuth was incorporated. The differences in the behavior of $\csc \epsilon$ with tilt between the various models was also indicated. At high tilt angles, estimation of $\csc \epsilon$ by $\csc \psi$, based on Gennai's model which relies on the x-ray emergence angle only, gave values of $\csc \epsilon$ that were too high compared with the empirical values obtained by calibration. Also, at high tilt angles estimates of $\csc \epsilon$ based on Moll's model, derived from Green's simple geometric foreshortening model when the effect of azimuth was incorporated, gave estimates of the value of $\csc \epsilon$ too low compared with the empirical values. The best agreement with a theoretical model for the effective take-off angle dependence on tilt was given by the expression derived from Bishop's theory based on the Monte Carlo theory of electron penetration when compensated for the effect of azimuth. However, at high values of θ the empirical data indicated a slightly higher value of $\csc \epsilon$ than Bishop's theory might predict.

TABLE 1.--Principal expressions for effective take-off angle.

Author	Formulae	Remarks
Wittry ⁵ and Green ⁶	$\text{csc} \epsilon = \cos \theta \text{ csc} \psi$	simple geometric model, based on foreshortened mean depth of production, azimuth neglected
Bishop ⁷	$\text{csc} \epsilon = 1/2(1 + \cos^2 \theta) \text{csc} \psi$	Monte Carlo model, empirical fit to Green's data, based on shallower mean depth of production, azimuth neglected
Gennai ⁸	$\text{csc} \psi^* = \frac{1}{\sin \alpha_0 \cos \theta + \cos \alpha_0 \sin \theta \cos \omega}$	simple geometric model, foreshortened mean depth of production neglected, azimuth effect incorporated
Moll ⁹	$\text{csc} \psi = \text{csc}(\lambda + \alpha_0) = \frac{1}{\sin \alpha_0 \cos \lambda + \cos \alpha_0 \sin \lambda}$ $\tan \lambda_0 = \tan \theta \cos \omega$ $\text{csc} \epsilon = \cos \lambda \text{csc}(\lambda + \alpha_0)$	simple geometric model, based on foreshortened mean depth of production analogous to Green's model, azimuth effect incorporated
Parker ¹⁰	$\text{csc} \psi = \text{csc}(\lambda + \alpha_0) = \frac{1}{\sin \alpha_0 \cos \lambda + \cos \alpha_0 \sin \lambda}$ $\tan \lambda_0 = \tan \theta \cos \omega$ $g(\lambda) \equiv \text{csc} \epsilon / \text{csc}(\lambda + \alpha_0)$ $\text{csc} \epsilon = g(\lambda) \text{csc}(\lambda + \alpha_0)$	empirical model, standard used to determine lessened mean depth of production, azimuth effect incorporated

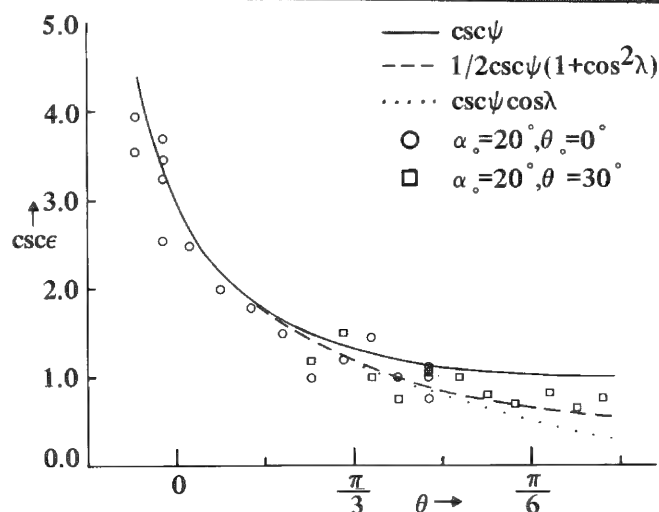


FIG. 1.--Plot of empirically determined values of effective take-off angle compared with curves for various theoretical expressions for the effective take-off angle as a function of tilt θ ; α_0 = detector elevation angle, θ_0 = specimen wedge angle, λ = effective tilt angle, ψ = x-ray emergence angle.

The expressions of Green and Bishop suggested that the mean depth of x-ray production was $g(\lambda)$, a trigonometric series in $\cos \lambda$ and $\sin \lambda$. In order to determine the best form of $g(\lambda)$, the empirically determined values of $\text{csc} \epsilon$ were fitted to a variety of functions of λ and ψ , as well as a power series in $\cos \lambda$ and $\sin \lambda$. Since the regression was nonlinear it was necessary to fit $\text{csc} \epsilon / \text{csc} \psi$ to various expressions for $g(\lambda)$.

The best fit was to the expression for $g(\lambda)$ developed from Bishop's¹² theory based on the Monte Carlo model:

$$g(\lambda) = 1.025 \frac{1}{2} (1 + \cos^2 \lambda)$$

The standard error in $g(\lambda)$ was 0.180 for the expression based on Bishop's theory. The fit to the expression for $g(\lambda)$ given by Moll and developed from Green's theory gave

$$g(\lambda) = 1.117 \cos \lambda$$

with a standard error in $g(\lambda)$ of 0.344. This result was in poor agreement with the experimental data. The fit to a constant for $g(\lambda)$ independent of λ suggested by Gennai's theory gave

$$g(\lambda) = 0.859$$

with a standard error in $g(\lambda)$ of 0.151. Although the standard error in $g(\lambda)$ was the least for a constant independent of λ , the constant was far from unity; there was considerable divergence from the expected theoretical result (predicted by Gennai) of identification of $\csc \epsilon$ with $\csc \psi$. The small error may have resulted since the principal dependence of $\csc \epsilon$ was on $\csc \psi$, and the dependence of $g(\lambda)$ on λ could be ignored if the entire $\csc \psi$ curve was scaled down to overlap the empirical data. The results of the fit to power series in $\sin \lambda$ and $\cos \lambda$ were inconclusive owing to the complexity of the expressions. On the basis of the preceding, it was concluded that the expression derived from Bishop's theory employing the Monte Carlo model and the effect of azimuth most accurately depicted the empirically found dependence of $\csc \epsilon$ on λ with tilt angle θ .

References

1. E. Lifshin, "Quantitative microprobe analysis with energy dispersive detectors," *General Electric Technical Information Series* 75 CRD 253, Syracuse, N.Y., 1975.
2. H. Yakowitz et al., *Practical Scanning Electron Microscopy*, New York: Plenum Press, 1975, 327-372.
3. L. S. Birks et al., "X-ray absorption and emission," *Analytical Chemistry* 46: 360R, 1974.
4. J. Philibert, "A method for calculating the absorption correction in electron-probe microanalysis," *X-Ray Optics and X-Ray Microanalysis*, New York: Academic Press, 1963, 378-392.
5. H. E. Bishop, "The absorption and atomic number corrections in electron probe microanalysis," *Brit. J. Appl. Phys.* 1: 673, 1968.
6. D. B. Wittry, "Methods of quantitative electron probe analysis," *Adv. X-ray Analysis* 7: 397, 1963.
7. M. Green, "The angular distribution of characteristic x radiation and its origin within a solid target," *Proc. Phys. Soc.* 83: 435, 1964.
8. N. Gennai et al., "The $f(\chi)$ -curves for Fe K α and Al K α x-rays in the inclined EPMA targets of Fe, Al and Fe-Al alloy," *Jap. J. Appl. Phys.* 10: 491, 1971.
9. S. Moll, "Geometrical considerations for ZAF corrections in the SEM," Technical Bulletin 111-277, Advanced Materials Research Corp., 1977.
10. M. A. Parker, *The Effective Take-off Angle for Quantitative Electron Probe Microanalysis*, Thesis, IIT, 1978.
11. M. A. Parker, "Determination of the effective take-off angle on scanning electron microscope energy dispersive x-ray analysis systems," *Microbeam Analysis--1980*, 65.
12. H. E. Bishop, "A Monte Carlo calculation on the scattering of electrons in copper," *Proc. Phys. Soc.* 83: 435, 1964.

ROLE OF INTRACELLULAR MEMBRANES IN TRANSCELLULAR CALCIUM TRANSPORT

J. R. Coleman, L. B. Young, and P. C. Wade

Calcium absorption is one of the most important functions of small intestine: calcium is essential for normal functioning of nerve and muscle, and it is involved in the control of such processes as secretion, hormone response, and enzyme regulation. Recently, electron probe analysis has shown that the Golgi membranes of the intestinal absorptive cells play a major role in moving calcium from mucosal to serosal surfaces.¹ Based on this information, models for transcellular transport involving intracellular membranes were proposed.^{2,3} Subsequent investigations have shown that Golgi membranes isolated from intestinal cells sequester calcium in an energy-dependent fashion.^{4,5} These findings formed the basis for a more detailed model for transcellular transport. This model involved diffusion of calcium into the absorptive cells, across the brush border, driven by an electrochemical gradient. The calcium is sequestered in the Golgi membranes in an energy-dependent fashion. The calcium sequestered in the Golgi cisternae is moved to the basolateral surface of the absorptive cell and extruded to the extracellular space, which completes the transcellular transport process. In this model, mitochondria do not participate in transcellular transport, but serve in a standby mode to sequester calcium if the concentration of free calcium in the cytoplasmic space should rise above homeostatic levels.

Fortunately, this model can be tested through the use of various agents that affect different portions of the overall mechanism. The calcium ionophore A23187 can be used to increase the rate of calcium entry through the brush border, effectively removing diffusion through the brush border as a rate-limiting step. It would be expected that treatment with A23187 would thus increase the overall rate of calcium transcellular transport. In contrast, chlorpromazine has been shown to inhibit *in vitro* calcium uptake by Golgi membranes. Consequently, if the model is correct, treatment with A23187 and chlorpromazine would tend to raise the cytoplasmic calcium concentration, since the Golgi membrane uptake mechanism would be inhibited, and calcium would accumulate in mitochondria with little or no increase in transcellular transport. Finally, Golgi membranes have been shown to release calcium in response to ATP. Sodium azide inhibits ATP generation and calcium uptake by mitochondria. Thus, treatment with A23187 and sodium azide should cause accumulation of calcium in the Golgi membranes, if the proposed model is correct.

The purpose of this investigation was to use coordinated electron probe x-ray microanalysis and transmission electron microscopy to test the response of the intestinal absorptive cells to the agents mentioned above.

Strips of duodenum from rats weighing approximately 100 g were incubated (as in Ref. 1) in a buffered saline solution containing 2 mM CaCl_2 labelled with ^{45}Ca (curve labelled Normal in Fig. 1). Some strips were incubated in solutions that also contained (a) 10 nM A23187 (curve A23187, Fig. 1); (b) 10 nM A23187 plus 0.5 mM chlorpromazine (curve Chlor); and (c) 10 nM A23187 plus 0.5 mM sodium azide (curve Azide). The effects of these agents were determined by scintillation counting of ^{45}Ca . Some of these strips were fixed with glutaraldehyde and oxalate⁶ and prepared for coordinated electron probe analysis and transmission electron microscopy.⁷

Figure 1 shows the normal uptake of calcium (Normal) by the small intestine. The uptake is increased by treatment with A23187 (curve labelled A23187) as the model predicts. However, both chlorpromazine (curve labelled Chlor) and sodium azide (curve labelled Azide) inhibit this increased uptake due to A23187, as is also predicted by the model.

Most important, these changes in transport capability are accompanied by noticeable changes in calcium distribution within the cells, as shown by electron probe microanalysis and transmission electron microscopy. Electron probe microanalysis was employed in the analysis of the elemental composition of the electron dense deposits seen by transmission electron microscopy. In the normal tissue, calcium is found in the Golgi membranes and extracellular spaces,¹ as has been described (Fig. 2). When intestine is exposed to A23187, the extracellular spaces between cells become dilated and calcium accumulates

The authors are at the Department of Radiation Biology and Biophysics, University of Rochester Medical Center, Rochester, NY 14620. This report, which is based on work done under U.S. Department of Energy contract DE-AC02-76EV03490, has been assigned Report number UR-3490-1991.

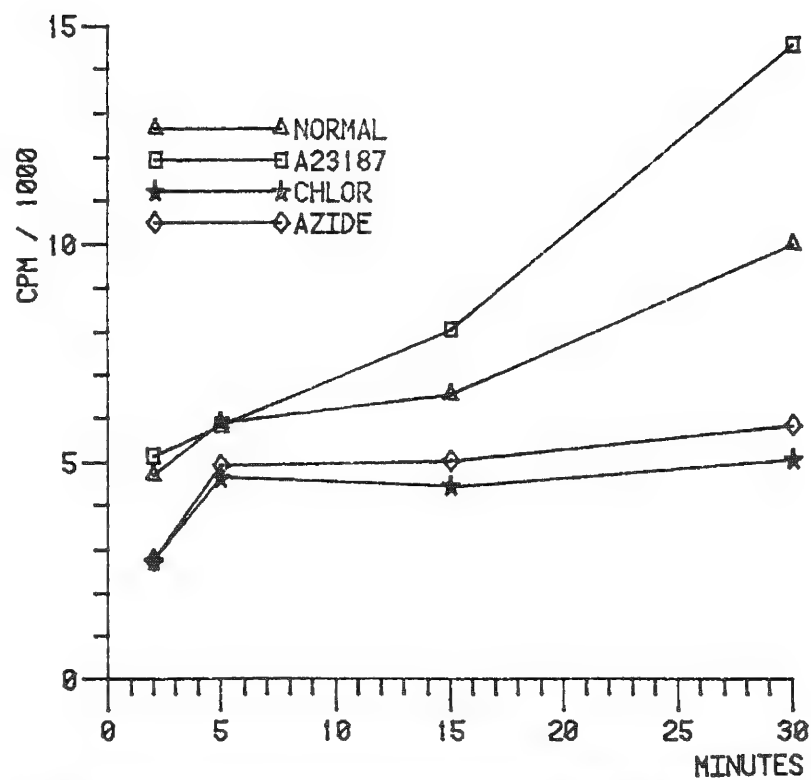


FIG. 1.--Calcium uptake by isolated duodenum strips from rat intestine.



FIG. 2.--Calcium accumulation in extracellular space close to tight junction in absorptive cells incubated under "Normal" conditions.



FIG. 3.--Calcium accumulation in mitochondria in absorptive cells treated with chlorpromazine.

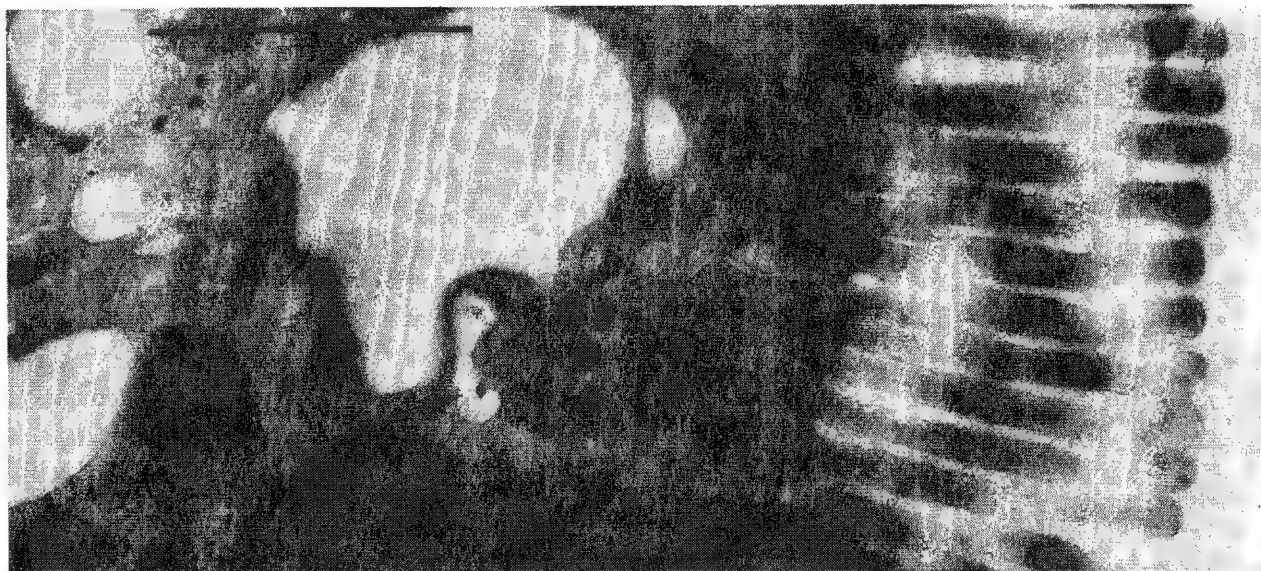


FIG. 4.--Calcium accumulation in Golgi membranes in absorptive cells treated with sodium azide.

within these spaces. When intestine is exposed to chlorpromazine and A23187, the extracellular spaces are again dilated and calcium accumulates within these spaces, but mitochondria are now seen to contain calcium deposits as well (Fig. 3). In contrast, when sodium azide is added to the A23187, the swollen extracellular spaces are again seen, but the mitochondria no longer accumulate calcium (Fig. 4). Instead, calcium is now found within smooth membrane vesicles, presumably of Golgi origin.

These findings provide additional insight into the calcium transport process. The fact that A23187 increases uptake rate strongly suggests that the normal rate-limiting step for absorption rests in the brush border membrane. Chlorpromazine binds calmodulin and prevents calcium binding by this molecule. Other studies have shown that chlorpromazine prevents calcium uptake by isolated Golgi vesicles. This information suggests that calmodulin may be involved in the overall transport process. Finally, the observation that sodium azide interferes with transport and permits accumulation of calcium within Golgi membranes indicates that oxidative phosphorylation is necessary for extrusion of calcium at the basolateral membrane, but not for uptake by Golgi vesicles. This result is also consistent with unpublished information that ATP is responsible for calcium extrusion from Golgi membranes. Consequently, it is now possible to refine the original model of calcium transport, and include a definite role for mitochondria, perhaps through the generation of ATP, whereas chlorpromazine inhibits uptake by Golgi vesicles which is necessary for the transport process. Finally, treatment with A23187 alone shows that the brush border membrane is the rate-limiting step in transport, and the calcium transporting cells may have sufficient reserve capacity to transport much greater amounts of calcium than ordinarily diffuses into the cytoplasm through the brush border. That might explain how increased transport can result from the change in membrane permeability that results from 1,25(OH)₂ cholecalciferol.

References

1. R. R. Warner and J. R. Coleman, *J. Cell Biol.* 64: 54, 1975.
2. R. H. Wasserman and F. A. Kallfelz, in H. Schraer, Ed., *Biological Calcification: Cellular and Molecular Aspects*, New York: Appleton-Century-Crofts, 1970, 313-345.
3. A. R. Terepka, J. R. Coleman, H. J. Armbrecht, and T. E. Gunter, in *Calcium in Biological Systems, 30th Symp. Soc. Exp. Biol.*, Cambridge University Press, 1976, 117-140.
4. R. A. Freedman, M. M. Weiser, and K. J. Isselbacher, *Proc. NAS* 74: 3612, 1977.
5. R. A. Freedman, J. A. MacLaughlin, and M. M. Weiser, *Arch. Biochem. Biophys.* 206: 233, 1981.
6. J. R. Coleman and A. R. Terepka, *J. Histochem. and Cytochem.* 20: 401, 414, 1972.
7. B. P. Halloran and J. R. Coleman, *Proc. 11th MAS Conf.*, 1976, 62A.

ULTRASTRUCTURAL EXAMINATION OF URINARY AND BILIARY CALCULI WITH PROTON-INDUCED X-RAY EMISSION AND X-RAY MICROANALYSIS

B. E. McConville

Several methods of analysis have been employed, with little success, to determine the formation and growth mechanisms of biliary (gall) and urinary (kidney and bladder) stones.¹ Because ordinary chemical analysis alone does not give any indication of either of these two mechanisms, other techniques have been employed.² The scanning electron microscope (SEM) has been used to examine the ultrastructure within the stones and particular attention has been given to the central or nuclear region. Detailed analyses have indicated distinct mechanisms of stone growth. Accompanying x-ray microanalysis has revealed several interesting and unexpected trace elements present in these regions. This trace-element examination has been continued and extended by use of proton-induced x-ray emission (PIXE), where the limits of detection are in parts per million. These low levels of trace elements have been undetectable by previous methods of analysis.

Many theories have been propounded to explain the mechanisms of stone formation and growth.³ However, none has satisfactorily accounted for all aspects of the problem. The simplest hypothesis proposes that stone formation takes place in four stages. First, there is a *nucleation* phase during which crystallites are formed in a supersaturated solution (i.e., in the urine). Second, there is a period during which the initial embryos *grow* and *aggregate* to form larger particles. Third, one of the secondary particles becomes large enough to be *trapped* at some narrow point in the urinary or biliary tract. Fourth, this trapped particle acts as a *nidus* or *nucleus* for the formation of a stone.

One of the main problems has been in determining whether the nucleation is essentially homogeneous (i.e., takes place spontaneously from highly saturated urine) or whether it is heterogeneous (i.e., is initiated by some other agents such as trace elements). The present-day theory is the latter: it is now believed that the matrix is likely to be a secondary inclusion adventitiously adsorbed on the faces of growing crystals.⁴

Experimental Procedure

Interior and exterior calculi sections were coated with carbon prior to the x-ray microanalysis, which was undertaken on a Cambridge S4 SEM equipped with an energy-dispersive x-ray analysis system. The calculi sections were later coated with gold for a detailed ultrastructural examination on the SEM.

Further sections of calculi were coated with aluminum prior to the PIXE analyses. Birmingham Radiation Centre's Dynamitron was used to produce a beam of 2.5 MeV protons incident on the stone sections with a beam current of 10-20 nA. Counting time varied depending on the beam current but was of the order of 20 min with a charge of 10 μ C. The x rays produced were determined by means of a Si(Li) detector on line to the computer.

Aluminum sheet absorbers (5-50 μ m thick) were used (to absorb x-rays) in certain analyses to prevent pulse "pile-up." The aluminum absorbers were placed between the Si(Li) detector and the stone sections.

Results

The results of the analyses in which the complementary techniques were used on sections of the same stones were compared and have provided evidence in support of the recent formation and growth theory. For example, a calcium oxalate kidney stone provided by the Queen Elizabeth Hospital in Birmingham was shown to exhibit a considerable degree of crystallinity in the SEM (Fig. 1). Calcium oxalate dihydrate crystals (bipyramid structures) are clearly seen in bunches or clusters, varying in size, in the central or nuclear region of this stone. From the x-ray microanalysis spectra of this region, no unexpected trace elements were found. However, from the PIXE spectra of this stone (Fig. 2), the elements P, Ag, Ca, Cu, and Zn were identified without an absorber. With 40 μ m of aluminum absorber, Fe was also identified.

The author is in the Department of Physics of the University of Birmingham, England B15 2TT.

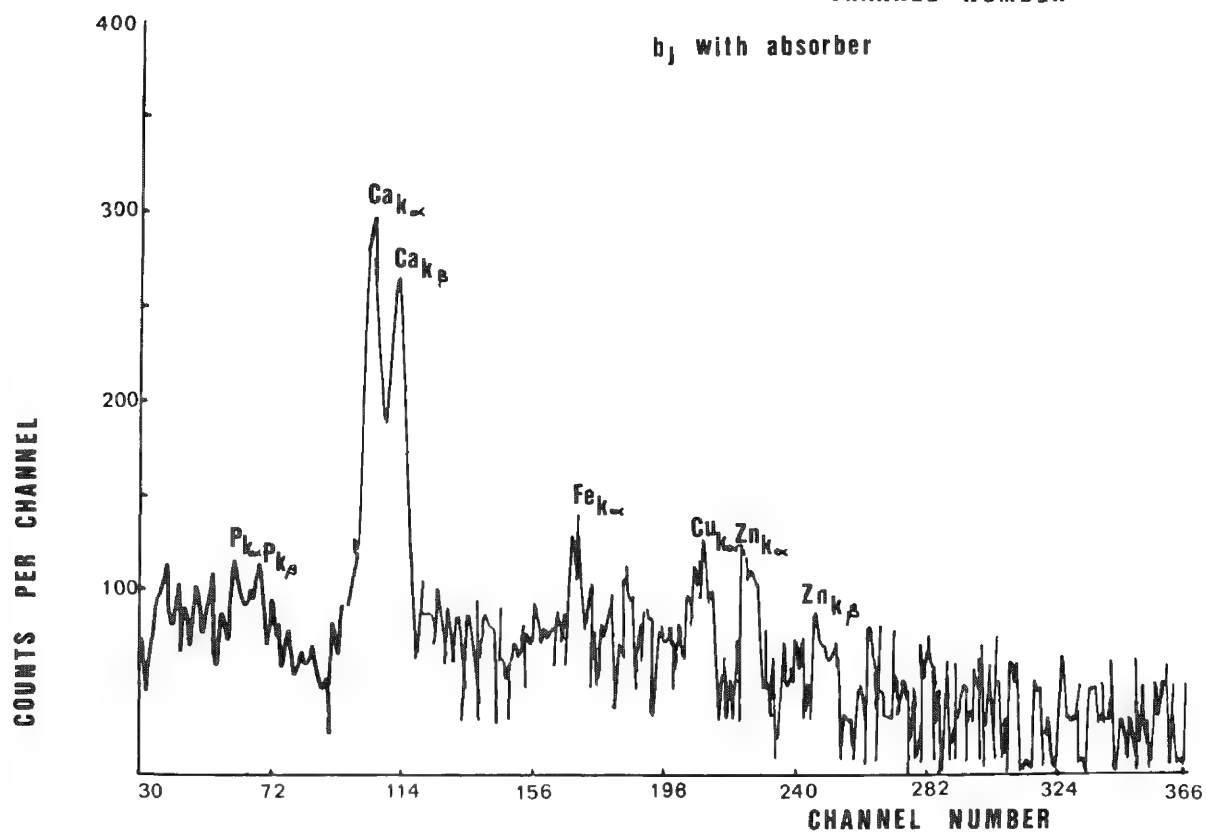
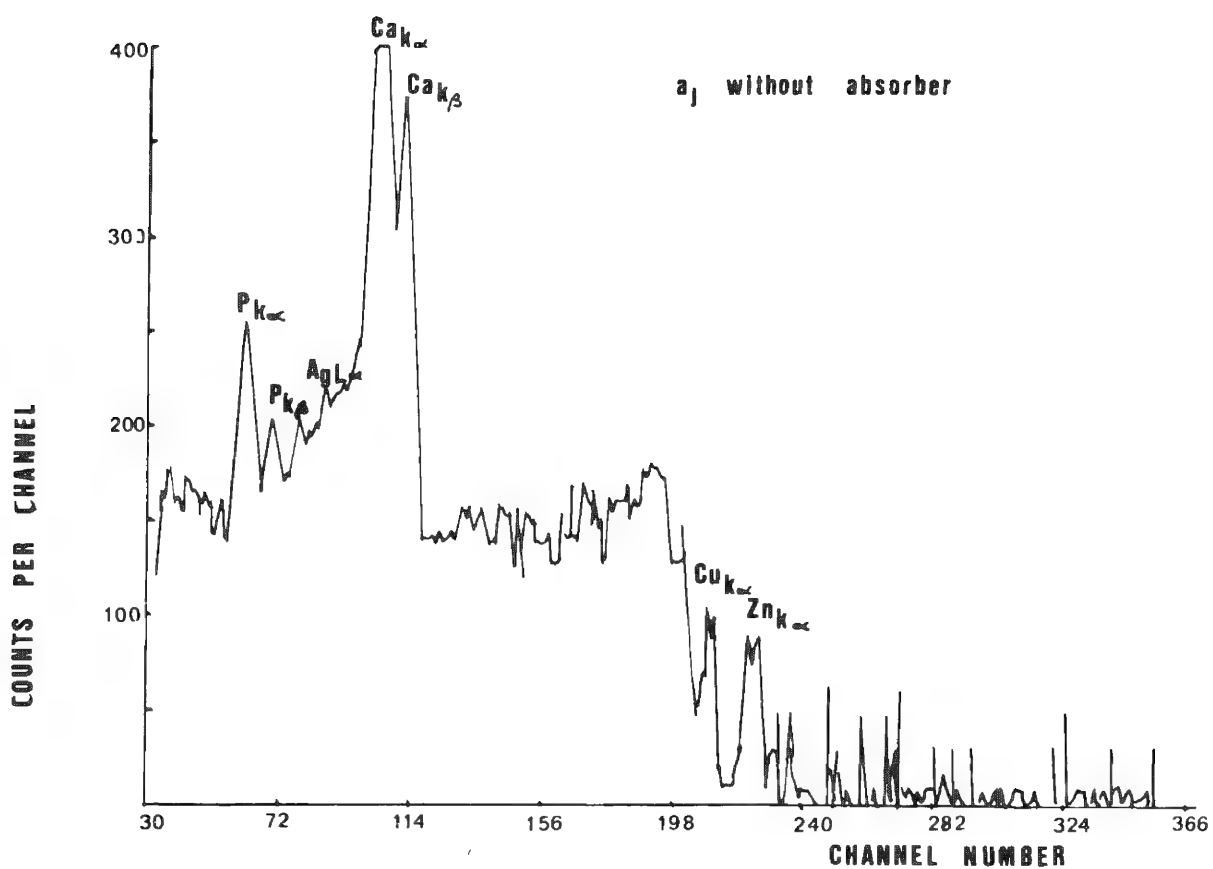


FIG. 2.--Proton-induced x-ray spectra of calcium oxalate kidney stone.

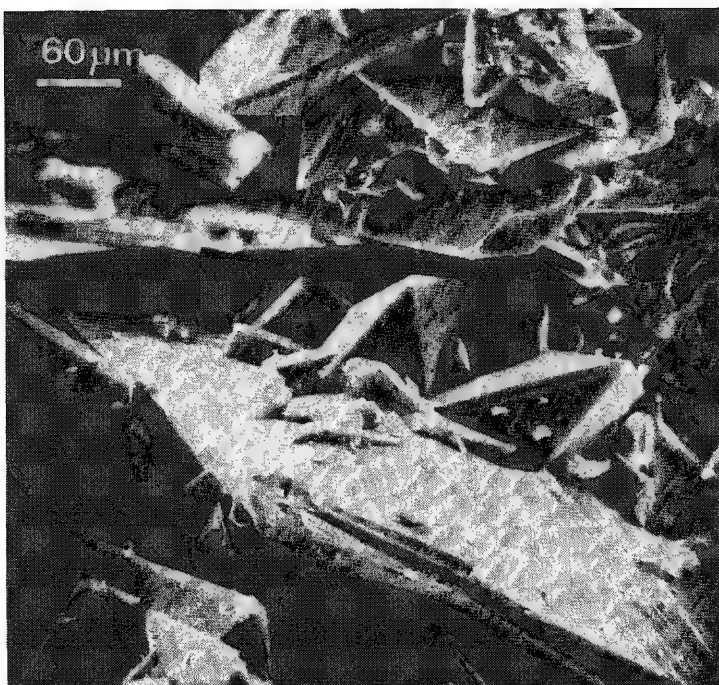


FIG. 1.--Electron micrograph of calcium oxalate kidney stone.

The problem of pulse "pile-up" caused by the predominance of one element (in this case calcium), which causes close elements (i.e., iron) to be masked in the PIXE analysis, is a limitation of the technique. However, there is a marked improvement in the background with the reduction of this "pile-up" by the introduction of an absorber (in this case 40 μm of aluminum) when iron is clearly identified (Fig. 2b); nevertheless, the introduction of the absorber does reduce the resolution of the lower atomic number elements. However, the calcium oxalate stone analyzed was predominantly calcium and was included here to illustrate some of the difficulties encountered and their resolution.

References

1. E. L. Prien and C. Frondel, *J. Urol.* 57: 949, 1974.
2. B. E. McConville, "Physical investigations of urinary calculi," *Urolithiasis*, New York: Plenum, 1981 (in press).
3. J. L. Meyer and L. H. Smith, *Invest. Urol.* 13: 36, 1975.
4. W. G. Robertson, *Urolithiasis Research* New York: Plenum, 1976, 5-25.

The masking by pulse "pile-up" was extremely rare, as can be seen in Fig. 3 of the PIXE spectra of a so-called "pure" organic kidney stone, where the elements S, Cl, Ag, K, Ca, Ti, Fe, Co, Cu, and Zn are clearly resolved without the use of an absorber.

Conclusion

The ultrastructural analysis has supported the present theory of formation and growth since it is possible that for some time during precipitation, new nuclei and the growth of existing ones occur simultaneously and lead to a variation of size distribution of particles. Also, calculi are clearly seen to be heterogeneous systems with secondary inclusions adsorbed on the faces of growing crystals. The limitation of the x-ray microanalysis, with sensitivity of the order of 0.5%, is emphasized by comparison with the more sensitive PIXE technique, where trace elements are determined in parts per million.

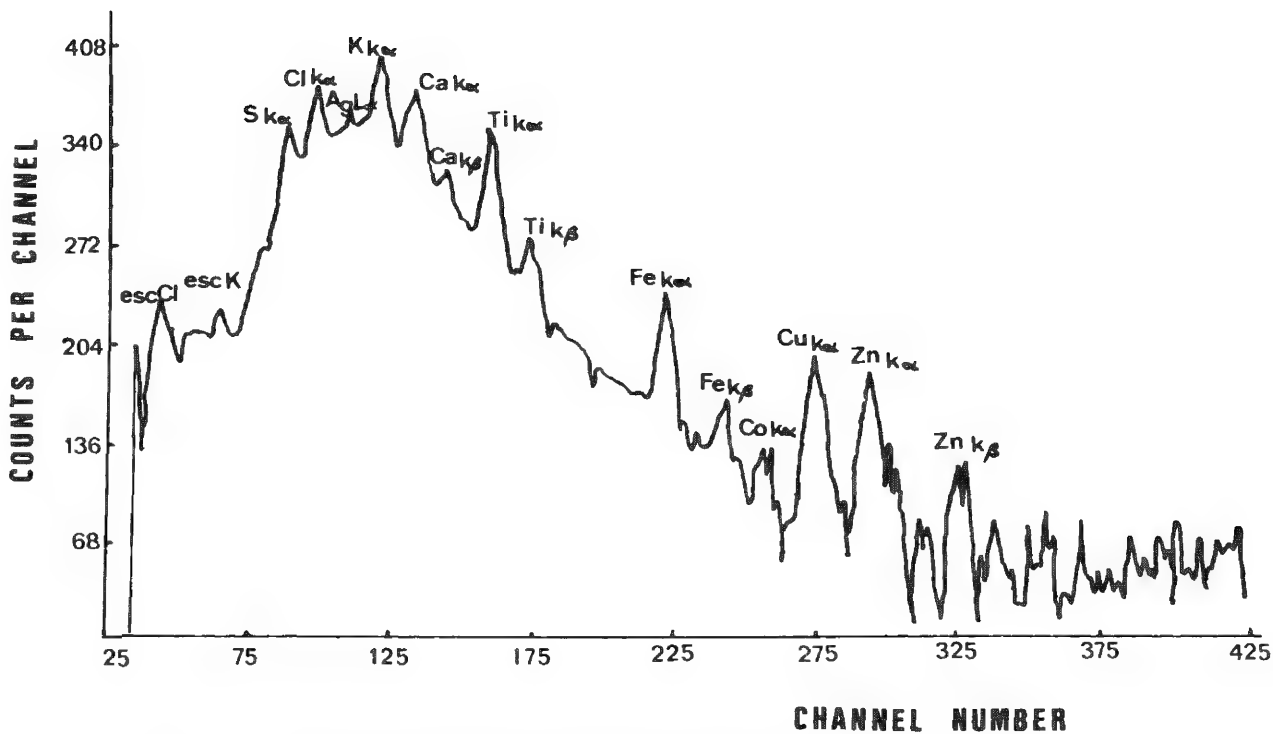


FIG. 3.--Proton-induced x-ray spectra of organic kidney stone.

ULTRASTRUCTURAL DISTRIBUTION OF SULFUR IN HUMAN HAIR

M. C. Myers, J. Van, and R. R. Warner

Human hair and other keratinized tissues are biologically distinct in that they contain high concentrations of the sulfur-containing diamino acid cystine. Cystine disulfide linkages in keratin give hair durability, insolubility, and stability in harsh environments. Chemical analysis of hair subfractions, electron histochemistry, and electron-probe analysis have shown that sulfur (cystine) is not distributed uniformly in hair; the outer cell layers (cuticle) contain more sulfur than the core (cortex).¹⁻⁶ However, the precise distribution of this sulfur in morphologically distinct regions of a hair is controversial; for example, a recent electron-probe study of bulk hair indicated that the outer subcellular layer (A-layer) of cuticle cells is particularly high in sulfur (11.8% by weight),³ contrary to earlier evidence from a chemical analysis of hair subfractions and a histochemical study.^{2,7} We report here our preliminary observations using histochemical techniques and the analytical microscope to measure directly the subcellular distribution of sulfur in hair.

Methods

One-inch lengths of the root ends of chemically untreated hairs were prepared by two different techniques. Hair was flash-frozen in liquid nitrogen slush, mounted in an LKB cryoultramicrotome, sectioned at a nominal thickness of 0.5 μm at -90°C , and freeze-dried in the cryochamber. Alternatively, hair was embedded directly in Spurr's epoxy resin and 0.5 μm sections were cut dry at room temperature. Sections were transferred to carbon-coated formvar films mounted on 100 mesh copper grids. Sulfur standards were prepared by sprinkling of finely ground bovine serum albumin crystals (dialyzed and lyophilized) onto a grid. All specimens were coated with 20 nm of evaporated carbon.

Specimens were analyzed with an Hitachi H500 transmission electron microscope equipped with a scanning attachment and a Kevex 7000 series energy-dispersive x-ray system. Data were acquired with a 20nm static beam, a 100kV accelerating potential, and a cold stage at -100°C . Data acquisition time was 300-500 s, during which the beam position was checked at 50s intervals. Specimen current was kept low (10^{-11} A) in order to avoid mass loss; mass loss was evaluated for each data point by linear regression analysis of the counting rate. Although a low beam current was used, sufficient contrast was present in the STEM image to enable precise positioning of the electron beam. It was thus possible to analyze the 0.1 μm -wide A-layer of the cuticle cells as shown by the micrograph in Fig. 1.

Quantitation was by the Hall continuum method.⁸ The continuum was monitored from 4-7 kV and was corrected for extraneous background.⁹ Background was subtracted from the sulfur characteristic peak by the Kevex background modeling routine. The value for Z^2/A required in the Hall continuum method was calculated from an amino acid analysis of whole hair¹⁰ and was found to be 3.6. This value was assumed to be constant throughout the hair, which is a reasonable assumption considering the uniform appearance of unstained hair sections in the TEM and the constant values we obtained for continuum counts in the various cell layers.

For histochemical studies, plastic-embedded hairs were sectioned using conventional procedures and stained with Gomori's silver methenamine reagent² following prior reduction of the hair sulfur with 1% Na borohydride.

Results

Two cell types are apparent in cross sections of hair (Fig. 2). The inner region, composed of one cell type and comprising 80% of the hair fiber, is the cortex. Completely enclosing the cortex are 5 to 10 layers of stratified cells that comprise the cuticle. Each cuticle cell is 0.3 to 0.5 μm thick and contains three morphological regions: the

The authors are at the Miami Valley Laboratories of Procter & Gamble Co., Box 39175, Cincinnati, OH 45247.

A-layer, the exocuticle, and the endocuticle (Fig. 2).

The electron histochemical stain results in metallic silver deposition that is presumed to indicate the location of cystine in hair.² As seen from Fig. 3, there is a relatively heavy deposition of silver in the A-layer, a similar amount in the exocuticle, a moderate amount in the cortex, and negligible staining in the endocuticle. This staining is consistent with a previous investigation.²



FIG. 1.--STEM image of three 350s analyses of A-layers (arrows) done with cold stage at -100°C . Magnification 30 000 \times .



FIG. 2.--Transmission EM image of hair thin section showing partial view of five cuticle cell layers and small portion of cortex (C). Each cuticle cell contains three ultrastructural regions: A-layer (arrows), exocuticle (Ex), and endocuticle (En). Magnification 21 000 \times .

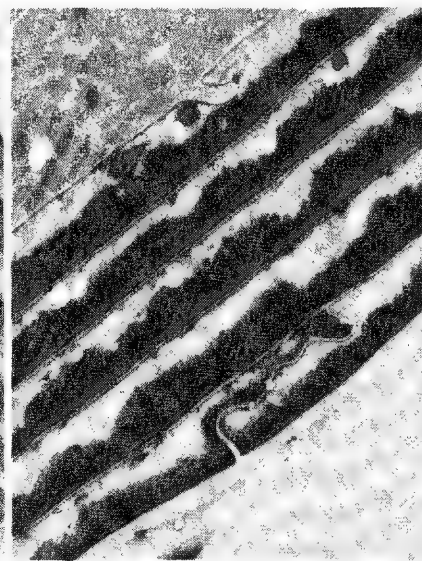


FIG. 3.--Hair section similar to Fig. 2 except stained histochemically with silver methenamine for cystine. Silver deposition is greatest in A-layer and exocuticle, moderate in cortex, and minimal in the endocuticle. Magnification 26 000 \times .

The sulfur concentrations obtained by analytical microscopy on either cryosectioned or resin-embedded hair were not different; consequently we have analyzed primarily resin-embedded hair. The average sulfur weight fractions and their standard deviations for different ultrastructural regions in hair are reported in Table 1. These values are based on the analysis of a very small number of hairs. Although there was variation in the absolute sulfur concentration between hairs, the relative distribution of sulfur between the various subcellular regions in a single hair section was constant, with the A-layer > exocuticle >> endocuticle \approx cortex. This relationship was invariant, although that is not evident from the Table 1 values owing to statistical averaging.

TABLE 1.--Sulfur weight fractions in hair.

	% Sulfur (mean \pm standard deviation)	Number of observations
Cuticle cells		
A-layer	6.0 \pm 1.4	9
Exocuticle	5.9 \pm 1.3	16
Endocuticle	3.3 \pm 0.9	20
Cortex	3.9 \pm 0.6	31

Discussion

It was necessary to use a low-temperature stage in our studies to minimize mass loss¹¹ and contamination. However, at temperatures less than -100°C, ice formed on the sample and interacted with the electron beam to produce excessive mass loss at any operating current, similar to the observations of Shuman et al.⁹ Even at temperatures of -100°C when sample icing was not detected, beam currents commonly used (1 nA) resulted in sulfur and continuum mass loss. Only by lowering the beam current to a very low value of 10⁻¹¹ A could we avoid mass loss.

Our values for the exocuticle and endocuticle (Table 1) are in basic agreement with the sulfur concentrations that can be calculated from the amino acid composition determined from cuticle cell subfractions (obtained by enzymatic digestion), in which the sulfur concentrations for exocuticle and endocuticle were 6.9 and 1.7%, respectively.⁵ Our values are also in good agreement with the average sulfur concentration measured for whole hair, 4.6%.¹² We are in disagreement with a previous electron probe study of bulk hair that indicated a very high (11.8%) sulfur concentration in the A-layer.³ We attribute this disagreement to problems of mass loss and sample charging that can occur in bulk tissues as used in the previous study.

Although our results remain preliminary, our analytical measurements indicate that the sulfur concentrations in the endocuticle and cortex are not markedly different (Table 1). This is in contrast to histochemical staining for sulfur (cystine), which is moderate in the cortex but negligible in the endocuticle (Fig. 3 and Ref. 2). This discrepancy could be explained by the presence of large concentrations of methionine in the endocuticle⁵ and/or by reagent diffusion delays in the endocuticle.

We have directly measured the sulfur concentration at an ultrastructural level in hair by employing a cold stage and very low beam currents to minimize mass loss and contamination. Our preliminary values are compatible with those obtained by less direct techniques. Our determinations have helped to resolve controversies regarding the distribution of sulfur in hair.

References

1. L. J. Wolfram, and M. K. O. Lindemann, "Some observations on hair cuticle," *J. Soc. Cosmet. Chem.* 22: 839-850, 1971.
2. J. A. Swift, "The electron histochemistry of cystine-containing proteins in thin transverse sections of human hair," *J. Royal Microscopical Soc.* 88: 449-460, 1968.
3. J. A. Swift, "Minimum depth electron probe x-ray microanalysis as a means for determining the sulfur content of the human hair surface," *Scanning* 2: 83-88, 1979.
4. J. A. Swift and B. Bews, "The chemistry of human hair cuticle: I. A new method for the physical isolation of cuticle," *J. Soc. Cosmet. Chem.* 25: 13-22, 1974.
5. J. A. Swift and B. Bews, "The chemistry of human hair cuticle: III. The isolation and amino acid analysis of various subfractions of the cuticle obtained by pronase and trypsin digestion," *J. Soc. Cosmet. Chem.* 27: 289-300, 1976.
6. P. Kassenbeck, H. Marfels, and H. Meichelbeck, "Quantitative determination of sulfur on cross sections of keratin fibers by x-ray fluorescence analysis," *Deutsches Wollforschungsinstitut Aachen* 2: 162-172, 1975.
7. J. A. Swift and B. Bews, "The chemistry of human hair cuticle: II. The isolation and amino acid analysis of the cell membranes and A-layer," *J. Soc. Cosmet. Chem.* 25: 355-366, 1974.
8. T. Hall, in K. F. J. Heinrich, Ed., *Quantitative Electron Probe Microanalysis*, National Bureau of Standards, Special Publication 298, 1968, 269-229.
9. H. Shuman, A. V. Somlyo, and A. P. Somlyo, "Quantitative electron probe microanalysis of biological thin sections: Methods and validity," *Ultramicroscopy* 1: 317-339, 1976.
10. C. R. Robbins, *Chemical and Physical Behavior of Human Hair*, New York: Van Nostrand-Reinhold, 1978.
11. T. A. Hall and B. L. Gupta, "Beam-induced loss of organic mass under electron-microprobe conditions," *J. Microsc.* 100: 177-188, 1974.
12. B. Barman and R. Wickett (Procter & Gamble Co., Cincinnati), personal communication.

ELECTRON MICROPROBE ANALYSIS OF CULTURED (LLC-PK₁) RENAL EPITHELIAL CELLS

J. V. Bonventre and C. A. Rabito

Studies of multiple cellular functions--e.g., transport, volume regulation, hormonal responsiveness--and examination of the role played by intracellular electrolytes in these functions, rely critically on the accurate determination of intracellular elemental composition. Assessment of intracellular composition is frequently hampered by cellular heterogeneity, inadequate washing of extracellular fluid, and uncertainty in the determination of extracellular space by cellularly impermeant markers. Cell culture techniques that have provided important insight into mechanisms of cellular function in multiple organ systems¹ offer many advantages in the study of the relationships between intracellular electrolytes and cellular function. In the kidney--a very heterogeneous organ with various epithelial structures involved in many varied functions--the use of these techniques permits the study of a relatively homogeneous population of epithelial cells under carefully controlled environmental conditions. We have developed techniques to determine intracellular elemental composition in isolated cultured kidney epithelial cells and have applied these techniques to the study of the effect of ouabain on intracellular elemental composition.

While classical approaches can be applied to the determination of intracellular elemental composition in cell cultures,² frequently, for example with primary cultures, the amount of cells is limited or there may be functional heterogeneity that may not be appreciated purely on morphological examination. This functional heterogeneity, as might for example exist among similar cells in various stages of the cell cycle, cannot be established by classical techniques, since only mean values of elemental content in large populations of cells are established by these techniques.

Electron microprobe analytical techniques offer the opportunity to measure intracellular composition in individual cells and provide a large amount of data on a limited number of cells exposed to various experimental conditions. If the cells are prepared isolated from each other then uncertainty regarding trapped extracellular media is reduced.

We have analyzed the elemental composition of LLC-PK₁ cells, a continuous cell line derived from pig kidney,³ maintained under normal culture conditions and compared them with cells exposed to ouabain, a potent inhibitor of the Na, K-ATPase enzyme. In epithelial cells this enzyme plays important roles in the regulation of intracellular electrolyte composition and in the transepithelial transport of solutes and water, and has been postulated to be an important factor in the maintenance of cell volume regulation.

Cells were maintained in polystyrene tissue culture dishes with Dulbecco's modified Eagle's medium containing 10% fetal calf serum. Cultures were incubated at 37°C in an atmosphere of 95% air-5% CO₂. Cell passages were made with trypsin (0.5 g/L)-EDTA (0.2 g/L) solutions. Prior to the experiments cells growing in monolayer culture were lifted off the polystyrene supports with trypsin-EDTA. They were then plated onto pyrolytic graphite supports and maintained under standard culture conditions for at least 27 hr. Groups of cells were then exposed to culture medium containing ouabain at a concentration of 10⁻⁴M. After 2.5 hr of exposure to ouabain the graphite disks were removed from the culture medium and washed with lithium chloride, choline chloride, or distilled water at 4°C for 15 s. The samples were then quench-frozen in isopentane, previously cooled with liquid N₂ to -159°C, and freeze-dried. Analysis was performed with a Cameca MS-46 microprobe. The pyrolytic graphite supports were cut so that supports with control populations of cells as well as supports with ouabain-exposed cells could be mounted simultaneously in the microbeam column. Both control cells and ouabain-treated cells could be therefore examined under identical microprobe analytical conditions.

The authors are with the Renal Unit and Departments of Medicine, Massachusetts General Hospital, Boston, MA 02114, and Harvard Medical School. They acknowledge the guidance of Dr. C. Lechene and help from the staff of the National Biotechnology Resource in Electron Probe Microanalysis, Harvard Medical School. This work was supported by NIH grants HL0664 and PR00679, and a Young Investigator Research Award AM 27957 to J. V. Bonventre.

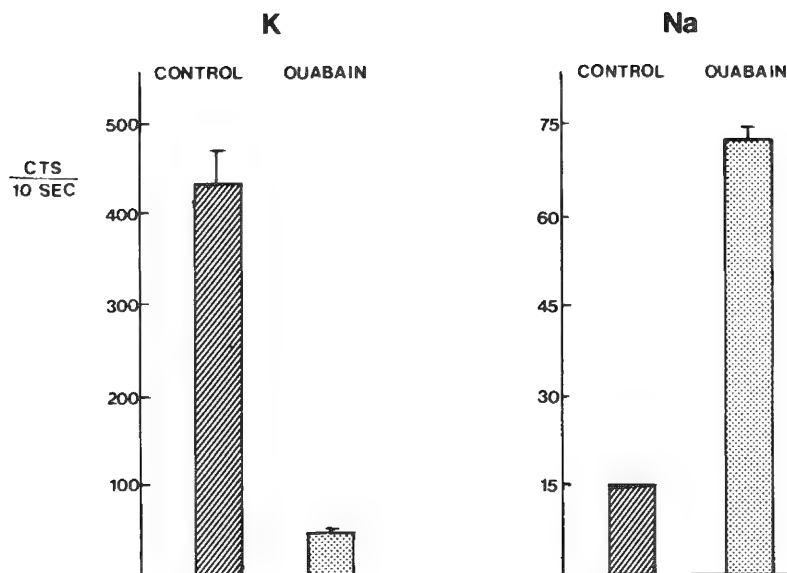


FIG. 1.--Sodium and potassium x-ray signals obtained from cultured renal epithelial cells. In this representative experiment forty-one cells exposed to ouabain ($10^{-4}M$) were compared with forty-two control cells. Mean values \pm S.E.M. are shown. The standard error of sodium counts in the control population of cells was too low to be depicted in the figure. Cellular phosphorus signal was not statistically different between the two populations of cells.

The results of a representative experiment are depicted in Fig. 1. In this study the cells were washed with 150 mM lithium chloride. The beam current was 200 nA; the accelerating voltage, 11 kV; and the beam diameter, 18 μm . The beam diameter was chosen so that the entire cell would be within its boundaries. As shown in Fig. 1, in cells exposed to ouabain for 2.5 hr there was a marked decrease in potassium signal and marked increase in sodium signal as compared with the control cells. There was no difference in phosphorus signal in either population of cells. The absence of a sodium signal above background adjacent to the cells on the graphite support confirmed the efficiency of washing of the medium to which the cells are exposed, a medium that has a high sodium concentration.

These results are consistent with those of Mills et al.,² who studied electrolyte changes in LLC-PK₁ cells after exposure to ouabain using flame photometry. They measured a fall in intracellular potassium and increase in intracellular sodium (measured as mmol/kg dry wt.) when cells in suspension were incubated with $10^{-3}M$ ouabain for 60 min. The changes we have found in elemental x-ray signal represent a greater change in intracellular composition than that found by Mills et al. This result may be due to our longer exposure time or to a different level of sensitivity to ouabain of plated cells as compared with cells in suspension.

In summary, we have developed techniques for determining intracellular composition of isolated cultured renal epithelial cells. With these techniques, we have demonstrated that ouabain, a potent inhibitor of the Na, K-ATPase enzyme, results in marked reduction in intracellular potassium and marked increase in intracellular sodium. These techniques of electron microprobe analysis as applied to cultured epithelial cells will likely provide new insight into the understanding of epithelial cell transport processes, cellular metabolic processes, and cell volume regulation.

References

1. C. C. Harris, B. F. Trump, and G. D. Stoner, "Normal human tissue and cell culture," *Methods in Cell Biology* 21, 1980.
2. J. W. Mills, A. D. C. MacKnight, J.-M. Dayer, and D. A. Ausiello, "Localization of [3H] ouabain-sensitive Na⁺ pump sites in cultured pig kidney cells," *Am. J. Physiol.* 236: C157-C162, 1979.
3. R. N. Hull, W. R. Cherry, and G. W. Weaver, "The origin and characteristics of a pig kidney cell strain, LLC-PK₁," *In Vitro* 12: 670-677, 1976.
4. E. H. Abraham et al., (Children's Hospital Medical Center, Boston, Mass.), "Electron probe analysis of tissue culture shells on cleaved pyrolytic discs" (in preparation).

AN ELECTRON-PROBE ADAPTATION FOR BIOLOGY

F. D. Ingram, M. J. Ingram, and B. L. Nichols

Electron probe microanalyzers are commonly designed for metallurgical applications. Software for computer automated systems is directed toward ZAF-type correction schemes based on pure-element standards, and the general configuration is adapted to bulk sample studies rather than to thin-section work. Biological tissue studies require good imaging, spatial resolution as high as the combination of sample and electron-beam parameters permits, and x-ray discrimination that unequivocally identifies and counting efficiency that quantitates trace elements. Although modern electron-probe microanalyzers can meet basic requirements, some modification is necessary to make an instrument useful for the biologist, and special modes and data-handling techniques are found to be helpful. Our modifications of an Applied Research Laboratories SEMQ, Model 131000-76 (Applied Research Laboratories, Sunland, Calif.) for use in biological studies is described below. Particular emphasis is given to developing the features required for analysis of freeze-dried, plastic-embedded tissue.¹

Instrumentation

The SEMQ is a computer-automated, four spectrometer electron microprobe with KEVEX 7000 Si(Li) energy detector system (Kevex Corporation, Foster City, Calif.). The spectrometers, sample stage, counting electronics, and electron beam blanking and positioning all can be controlled by a computer. As configured presently, the 28K DEC PDP 11/04 computer (Digital Equipment Corp., Maynard, Mass.) is available for use either with the electron probe and ARLEB (ARL Extended BASIC), or with the Si(Li) energy detector and FORTRAN. The computer cannot support both systems simultaneously with the present software; although both are RT-11 based, each contains unique features that complicate interaction with other systems or computers. However, simultaneous operation is realized by coupling of the output of painted regions in the energy spectrum to the electron probe counting electronics. Care must be taken to allow for the large differences in dead time between the two types of detectors.

Most electron microprobes can be supplied with transmitted electron detectors for STEM operation, but we have found it quite useful to construct our own STEM detector after the designs of Murphy and Metzger² and Coleman et al.³ Such a device is useful for work with freeze-dried, cryosectioned samples or with thin sections of embedded materials in high-resolution studies. As the direct electron signal from a carbon stub is sent to the video electronics, that signal also can be used for microdensitometry.

A digitized signal that delineates prominent features of tissue morphology is of great importance to the biologist, but is not commonly provided on electron probes. We have added this feature to our present instrument by digitizing the video signal with a suitable analog-to-digital converter using a circuit based on a Type 9400 voltage-to-frequency converter. The output is counted with a scaler in the x-ray counting electronics. With the ARL-SEMQ it is possible to mount the video digitizer on a printed circuit card and plug it into an unused slot in the video console. Power is obtained from existing $\pm 5V$ lines in the video console.

The SEMQ has been provided with 8 scalers which can be interchanged, but which are commonly configured so that one is dedicated to the timer and one each to the four wavelength-dispersive spectrometers. The remaining scalers are used for any three of the following: electron beam current integrator, digitized video signal, and x rays counted in regions painted on the energy detector spectrum. The timer scaler is the only scaler that occupies a unique position. Input to all the other scalers can be interchanged freely, although in practice consistency of use decreases confusion.

Because x-ray counting rates are typically quite low, it is important to have long-term stability in counting conditions. The digitized current integrator output provides a means for monitoring electron-beam current drift with the SEMQ. However, current inte-

The authors are with the USDA Children's Nutrition Research Center, Department of Pediatrics, Baylor College of Medicine and Texas Children's Hospital, Houston, TX 77030.

grators are sometimes not as stable against long-term drift as is the electron column; thus, we find it more advantageous to use a Keithley 480 Picoammeter (Keithley Instruments, Cleveland) at the current monitor aperture.

Software

It is unfortunate that manufacturers have not developed software in industry-compatible form. Modular construction is common practice in the electronics industry. In the case of NIM bins, for instance, one can plug in any manufacturer's circuit and expect it to function. This concept has yet to find acceptance in software development. We seem to have regressed in this aspect as manufacturers attempt to optimize performance of their software and to capitalize on investment in computer programming for a particular device; the user is permitted only minor latitude in modification of the basic software package, and it is uncommon for a computer-controlled device to be supplied with the necessary source listings and operating system so that drastic changes in software are possible. For example, although a computer software package may be written in a common language such as FORTRAN, there is no way the user can modify or add to the software unless he has a source listing of the programs and the necessary editor, compiler, linkage, and operating system for his particular computer. This information is normally not provided; the potential user who is unfamiliar with computer operation or the fine points of drawing up sales agreements may not recognize the need for investing additional funds at the time of purchase to obtain this capability.

A computer system based on an interactive, immediate-mode language such as BASIC provides an advantage to the user in that he can completely rewrite the computer operation package. The adaptation of an electron probe for use in biology does in fact require such a major programming effort. Although BASIC is in many ways not a sophisticated language, it is flexible, easy to use, and of adequate speed, and it contains all the essentials for effecting instrument control and data manipulation. ARLEB (ARL Extended Basic), the language that has been used for the ARL-SEMQ, is RT-11 BASIC modified to include special functions required for device handling and machine operation. This modification has been made at the expense of a few features common to most BASIC languages, but the result is entirely acceptable.

We have written our ARLEB operating programs in modular form as a series of subroutines, each called by a single word entered on the system keyboard. The details concerned with spectrometer positioning, electron-beam positioning, electron-beam blanking, data collection, storage, and analysis are all handled by the computer, so that the operator is free to concentrate on the biology.

Data Collection

Damage to fragile organic samples is an ever-present problem that places demands on electron probe design and operation.⁴ There appear to be two components to the damage. One is a dose-related phenomenon that is a function primarily of the number of electrons that have interacted with the sample. The other component is a function of sample thermal conductivity and the rate at which heat is delivered to the sample.

When some types of samples are analyzed with high accelerating voltage, sample mass loss is the most obvious manifestation of the dose-related component of sample damage. When high accelerating voltages are used, the effects of mass loss may be minimized by cooling of the sample with a suitable cold stage in the electron probe.^{5,6} Fortunately, there are types of samples and operating conditions that permit operation without the need for a cold stage. We have found that analysis of embedded samples at relatively low accelerating voltage, 8-10 kV, can be made without cooling of the sample. Under these conditions, mass loss as monitored by K α signals from the elements of interest is constant over long periods of time after an initial, rapid increase in signal rates of about 5%. For such analyses, computer-directed electron beam positioning is best;⁷ it permits counting from one location with a focused electron beam for 1 s or less, leaving that spot for 10-100 s, then returning to the original location for another brief data-collection interval. This procedure greatly reduces thermal damage on samples that are poor thermal conductors.

Another method of data collection that is commonly used in biology involves reducing the scanning electron beam area while observing the image on the video display screen.

A few potential problems with this mode of analysis with the ARL-SEMQ may also occur with other instruments. First, if TV scan rates are used, the high and rapidly changing currents in the beam scan coils tend to couple noise into the Si(Li) energy detector and cause peak broadening and spectral distortion. (That is not a problem at lower scan rates.) Second, and of more significance, the electron beam is parked at the beginning of each scan for a brief period before it crosses the sample--a common feature introduced for noise cancellation. The effect is not obvious to the operator since the video display is blanked off during this period. The result is a nonuniform excitation of the region that appears on the video display. A third and by far the most important difficulty is lack of precise knowledge concerning the region excited by the electron beam. For bulk samples, it is well understood that the spatial resolution of imaging is much better than the x-ray resolution,^{8,9} and the same is probably true for thin sections as well.^{10,11} We have found a more accurate means of analysis in the use of line-scan profiles. Not only is the difference in spatial resolution between imaging signals and x-ray excitation volumes graphically demonstrated, but the difference in spatial resolution among the various x-ray signals is also immediately obvious. Decisions concerning boundaries of analyzed structures can be made with considerable confidence on the basis of line-scan profiles; thus, contamination of data with signals from undesired sources is diminished.

The ARL-SEMQ was delivered with the necessary D/A converters and control subroutines for electron-beam positioning. We have written the required ARLEB programs for the simultaneous collection of eight line-scan profiles using computer controlled, interlacing electron-beam positioning. An auxiliary Tektronix Model 608 Monitor screen (Tektronix, Inc., Beaverton, Ore.) has been mounted in the video display console on which the line-scan profiles are imaged. Two bright bugs can be positioned at different locations on the display to delineate regions of interest for data reduction. These electronic bugs are used to identify boundaries of biological structures and to define unequivocally the region in a cell from which quantitative measurements are obtained. They document the spatial relationships between the imaging signal and the various x-ray signals for the permanent record.

Data are stored on floppy disk for later, off-line analysis. A region of continuum measured with the Si(Li) detector provides a signal that can be calibrated to produce a reliable indication of off-peak background for each spectrometer. Through secondary standards, x-ray counting rates on tissue samples are compared with counting on prepared standards of 20% albumin solutions containing known concentrations of the elements of interest.¹² Counting rates on NaCl, KCl, and PbS crystals entered on the computer terminal are combined with stored calibration information to convert data into numbers representing physiological concentrations. These counting rates are appropriate, of course, only with data collected from samples in which prescribed electron beam parameters of 8 or 10 kV and freeze-dried, plastic-embedded tissue are used.¹³

Conclusions

Computer control of an ARL-SEMQ electron-probe microanalyzer adapted for use as a biological research instrument permits data collection in a manner that both minimizes sample damage and presents data in a form that portrays spatial relationships among signals graphically. Simultaneous Si(Li) energy detector and wavelength dispersive spectrometer counting permits data collection under conditions that exploit the excellent signal-to-background ratios of wavelength spectrometers while providing x-ray continuum measurement necessary for immediate background determination. All aspects of data management and computations are handled by the computer to provide rapid, orderly manipulation of the large data arrays encountered in data collection, storage, and on-line reduction. The instrument permits quantitative measurement of intracellular distributions of important biological elements with accurate spatial definition.

References

1. F. D. Ingram and M. J. Ingram, "Freeze-dried, plastic-embedded tissue preparation: A review," *Scanning Electron Microsc.* 4: 147-160, 1980.
2. A. P. Murphy and C. A. Metzger, "Transmission electron microscopy with an ARL microprobe," *Rev. Sci. Instr.* 39: 1705, 1968.

3. J. E. Coleman et al., "A simple transmitted electron detector (TED) for thin biological samples," *Proc. 10th MAS Conf.*, 1975, 45A-45G.
4. J. W. Edie and P. L. Glick, "Electron irradiation products from organic materials and implication for microanalysis of biological sections," *Microbeam Analysis--1979*, 81-84.
5. T. A. Hall and B. L. Gupta, "Measurement of mass loss in biological specimens under an electron microbeam," in T. Hall, P. Echlin, and P. Kaufmann, Eds., *Microprobe Analysis as Applied to Cells and Tissues*, New York: Academic Press, 1974, 147-158.
6. H. Shuman, A. V. Somlyo, and A. P. Somlyo, "Quantitative electron probe microanalysis of biological thin sections: Methods and validity," *Ultramicroscopy* 1: 317-339, 1976.
7. F. D. Ingram and M. J. Ingram, "Quantitative x-ray microanalysis of bulk specimens," in M. A. Hayat, Ed., *X-ray Microanalysis in Biology*, Baltimore: University Park Press, 1980, 367-399.
8. D. R. Beaman and J. A. Isasi, "Electron beam microanalysis: The fundamentals and applications," ASTM STP 506, American Society for Testing and Materials, 1972, 1-80.

SIMPLE MICROFORGE FOR PICOLITER PIPET CONSTRICTIONS

Mary Jo Ingram and F. Duane Ingram

Electron probe analysis of dried residues from picoliter volumes of liquid has proved to be an important method for measuring a variety of elements in samples too small for conventional chemical analysis. Although preparative techniques have taken different courses, the common factor in all these approaches is the use of a micropipet for reproducible delivery of fluid in aliquots of constant volume.¹⁻⁶

It is common practice to pull pipets from glass capillary tubing and then break or grind the resulting tip to a lumen of 2 μm or less. A fiducial mark is made at a suitable location to produce aliquots of constant volume. However, it is far easier to use a pipet with a constriction that allows the fluid sample to seek its own level, which permits easier operation.⁷ The use of a constriction in the pipet also reduces operator fatigue, an important consideration for studies involving pipetting of large numbers of samples. In our experience, comparable reproducibility of pipetting is obtained with both methods, around 2%.

The pipet constriction is most commonly formed by means of a microforge.^{7,8} The asymmetric heating used with many microforges, however, causes severe bending of the pipet, so that additional straightening steps are required. To overcome this problem we have devised a simple and inexpensive apparatus for producing the constriction. In this device the pipet is inserted through a small hole drilled in a thin, flat platinum filament and heated.

Constriction

A 0.3mm-diameter platinum filament wire is flattened between two smooth surfaces by hammer blows, and a hole 0.1 to 0.2 mm in diameter is drilled in the flattened wire, with a fine pin used as a drill. The filament is clamped firmly between the electrodes of a spent ARL filament support (Applied Research Laboratories, Sunland, Calif.; Fig. 1). Other means of mounting the filament could be devised to work as well.

It is convenient to mount the filament on a base with adjustable height. With the help of a microscope, the pipet is inserted and positioned within the hole by a micromanipulator (Fig. 2). The filament, heated by a variable 6V ac power supply, requires very little current to obtain the dull red heat needed for constricting the glass.

A slight amount of bending occurs if the pipet is not well centered in the filament hole (Fig. 3). This feature is not objectionable, as a slight curve makes it somewhat easier to observe the meniscus.

The diameter of the lumen at the constriction should be nearly as small as the lumen at the tip. If it is smaller, the flow of oil and fluid is impeded; if it is too large, the reproducibility of pipetting suffers. The amount and duration of heat necessary for suitable constrictions can be readily judged with a small amount of practice.

Results

A pipet constructed in this fashion was used to deposit droplets of standards solutions to establish a standard curve. Five microdrops each of six different solutions of sodium, potassium, and chloride were deposited under water-saturated paraffin oil onto a quartz slide. The oil was washed away with xylene, and the slide was plunged into nitrogen slush and then freeze-dried in a vacuum. The dried residues, circular and with uniformly small crystals, were coated with a thin layer of carbon and analyzed with a defocused 15kV 100nA electron beam in an ARL-EMX Serial No. 59 electron probe microanalyzer. Wavelength dispersive spectrometers fitted with PET diffraction crystals for each of K-K α and Cl-K α , and RAP for Na-K α were used for the analysis.

The authors are with the USDA Children's Nutrition Research Center, Department of pediatrics, Baylor College of Medicine and Texas Children's Hospital, Houston, TX 77030. The work was supported by NIH program project grant HL 14388 while the authors were with the Cardiovascular Center, Department of Medicine, University of Iowa, Iowa City, IO 52242.



FIG. 1.--Glass micropipet tip is shown positioned through approximately 0.2mm-diameter hole in flattened platinum filament. Filament is clamped in spent ARL electron probe filament mount.

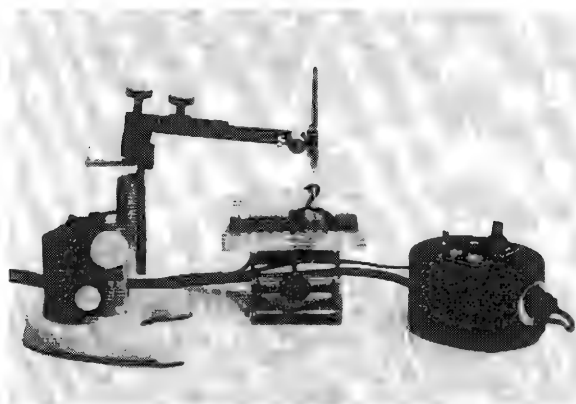


FIG. 2.--Apparatus for making constriction in micropipet. Actual positioning of pipet and heating process are monitored with microscope (not shown).

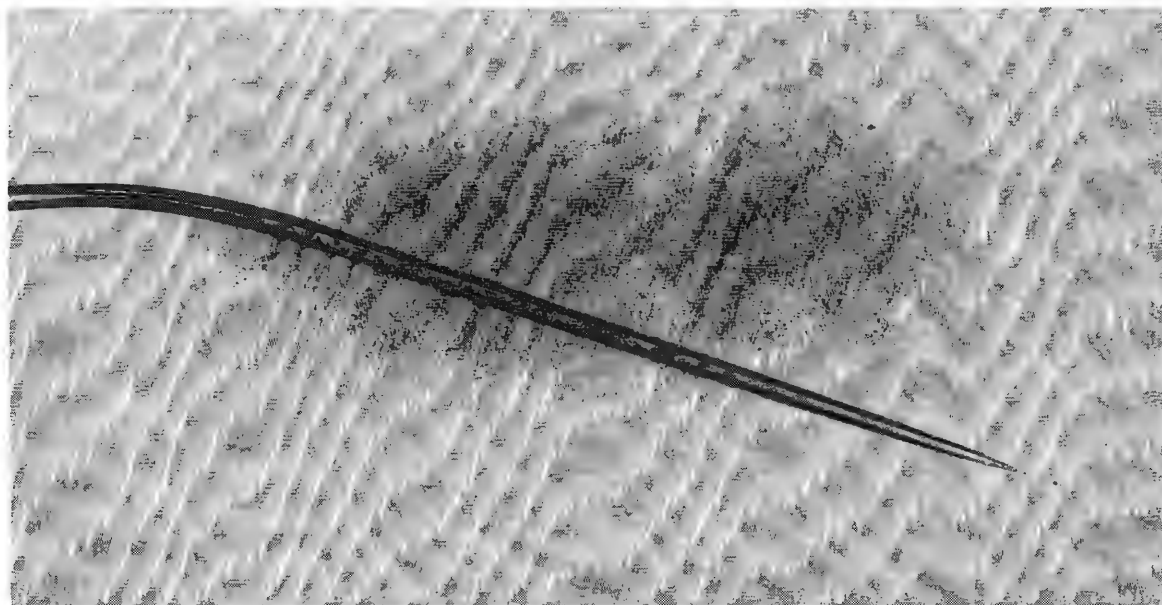


FIG. 3.--Micropipet tip displaying constriction approximately 1 mm from tip. Pipet is shown magnified about 150x.

The data were fitted with a straight line, which served as a calibration curve for subsequent analysis of renal samples. Such a calibration curve was established for each occasion on which samples were prepared for analysis. Calibration lines from 28 different sets of data were studied in order to discuss the reliability of the pipets. Correlation coefficients averaged 0.9965 ± 0.0023 , 0.9983 ± 0.0009 , and 0.9982 ± 0.0012 for K, Cl, and Na respectively. Estimates of the standard deviation of slope (expressed as percentage of slope) averaged $1.4\% \pm 0.58$, $0.88\% \pm 0.32$, and $0.71\% \pm 0.40$ for the same elements. Sources of scatter in the data include microdrop preparation and electron probe analysis as well as pipetting. These levels of uncertainty in data are entirely adequate for studies of renal fluids.⁹

Some idea of the reproducibility of the pipet can be obtained by examination of the agreement in counting rate among the five measurements in each group of samples examined. Among twenty-four groups of measurements, the average and standard deviation of the fractional standard deviation was 0.012 ± 0.0055 for Cl-K α x-ray counting. As that also includes scatter induced both by subsequent steps in the preparation and by the analysis, the scatter evident in these data places an upper limit on the scatter introduced by any

problems of pipetting reproducibility.

Conclusion

It is generally agreed that the use of a constricted pipet makes pipetting for microdrop analysis easier, faster, and more reproducible. Since the use of microdrop analysis in biological experimentation requires arduous effort in each step to produce useful data, any means of simplifying the procedure should be adopted. The simple device described here can be assembled in any laboratory, operation is straightforward, and reproducibility of pipetting with the resultant pipet is extremely good.

References

1. M. J. Ingram and C. A. M. Hogben, "Electrolyte analysis of biological fluids with the electron microprobe," *Anal. Biochem.* 18: 54, 1967.
2. M. A. Cortney, "Renal transfer of water and electrolytes in adrenalectomized rats," *Am. J. Physiol.* 216: 589, 1969.
3. F. Morel, N. Roinel, and C. Le Grimellec, "Application de la microsonde électronique à l'analyse élémentaire quantitative d'échantillons liquides d'un volume inférieur à 10^{-9} l.," *J. Chim. Phys.* 66: 1084, 1969.
4. C. Lechene, "The use of the electron microprobe to analyze very minute amounts of liquid samples," *Proc. 5th MAS Conf.*, 1970, 32A.
5. R. Rick et al., "Determination of electrolytes in small biological fluid samples using energy dispersive x-ray microanalysis," *Pflügers Arch.* 369: 95, 1977.
6. P. M. Quinton, "Energy dispersive x-ray analysis of picoliter samples of physiological fluids," *Proc. 10th MAS Conf.*, 1975, 50A.
7. P. De Fonbrune, *Technique de micromanipulation*, Paris: Mason, 1949.
8. J. V. Bonventre, K. Blouch, and C. Lechene, "Liquid droplet preparation techniques," in M. A. Hayat, Ed., *X-ray Microanalysis in Biology*, Baltimore: University Park Press, 1980.
9. J. B. Stokes et al., "Heterogeneity of the rabbit collecting tubule: Localization of mineralocorticoid hormone action to the cortical portion," *Kidney International* (in press, 1981).

SEM/EDX ANALYSIS OF GRANULAR ACTIVATED CARBON FROM A WATER TREATMENT FACILITY

N. M. Perrins, K. Alben, and E. Shpirt

Granular activated carbon (GAC) is being evaluated as an adsorbent for organic pollutants in water treatment facilities. Elemental compositions of GAC determined by scanning electron microscopy/energy-dispersive x-ray analysis (SEM/EDX) may help to monitor the efficiency of the carbon filters. For this project samples of GAC were taken from pilot columns designed to treat potable water from the Hudson River in New York State. In the samples analyzed Al, S, K, Ti, and Fe were uniformly distributed and had concentrations similar to those in virgin GAC. Calcium and chlorine decreased monotonically on samples collected downstream of the outlet to the system and eventually reached the background levels of virgin GAC.

Experimental

Results in this paper are for GAC samples from four pilot columns connected in series and operated for 26 weeks at Waterford, New York. Methods of sampling and design and operation of the pilot columns are described elsewhere.^{1,2}

For SEM/EDX analysis the GAC samples were dried to constant weight, powdered, mounted on graphite planchettes, and examined in an ETEC SEM with a PGT detector, coupled to a Tracor-Northern 880 for data reduction. The samples were not coated. Reagent-grade inorganic minerals were used as reference materials for quantitation. Elemental concentrations were calculated by peak deconvolution techniques with background levels subtracted. The results were not corrected for matrix effects, neither in the standard reference materials nor in the GAC samples.

To explain the results of analyses of the Waterford samples test columns were run in the laboratory on columns of Calgon F400. For these experiments 1.9 L of synthetically prepared solutions were passed through a column (1 cm ID, 20 cm long) at a rate of 5 ml/min. After the test solution was eluted, each column was washed with 1.9 L of distilled water unless otherwise noted. Samples of GAC were taken from the inlet and outlet of each column and processed for SEM as previously described. The concentration reported is the difference between the concentrations at the inlet and the outlet. Since breakthrough did not occur, the outlet concentration represents the background level.

Results and Discussion

Figure 1 shows typical spectra for Waterford GAC samples from the inlet and outlet of the system, compared to the spectrum of virgin GAC. The distribution of the major elements in the GAC columns is given in Fig. 2. Each data point represents the result of three determinations.

The elements are divided into two groups. The first group consists of elements in the virgin GAC: Al, Si, S, Fe, K, and Ti. The distribution of these elements in the Waterford samples is essentially uniform. Concentrations of these elements calculated without matrix corrections are in agreement with the manufacturer's data.³ The second group consists of Ca and Cl. Their concentration is at a maximum at the inlet to the system and decreases downstream, eventually reaching the background level of virgin GAC.

Results of additional experiments give insight into the chemical identity of the Cl and Ca found on the GAC. The Cl is considered to result both from adsorbed halogenated organics (such as PCBs) found on the samples² and from the reaction of hypochlorous acid (HOCl) with GAC. Hypochlorous acid is routinely added for bacterial disinfection of the raw water source prior to GAC treatment, which removes organic contaminants. The results of experiments summarized in Table 1 indicate that HOCl can readily attach itself to the surface of a GAC particle. Although HOCl and GAC react to produce chloride ion and sur-

The authors are research scientists at the Division of Laboratories and Research, New York State Health Department, Albany, NY 12201. Dr. Alan Stevens, Office of Research and Development, U. S. Environmental Protection Agency, offered helpful suggestions for the planning of experiments to explain results obtained for GAC samples from Waterford, N.Y.

face oxides on the GAC,⁴ experiments 1 and 2 show that chloride ion alone does not attach itself to the GAC surface. Experiments 3 and 4 show that after exposure to HOCl a significant amount of Cl (about 50 mg/g GAC) remains on the GAC and is not removed even by washing with distilled water. These results suggest that the reaction of GAC with HOCl forms not only chloride ion, the predominant product, but also chemically bound Cl as a secondary product.

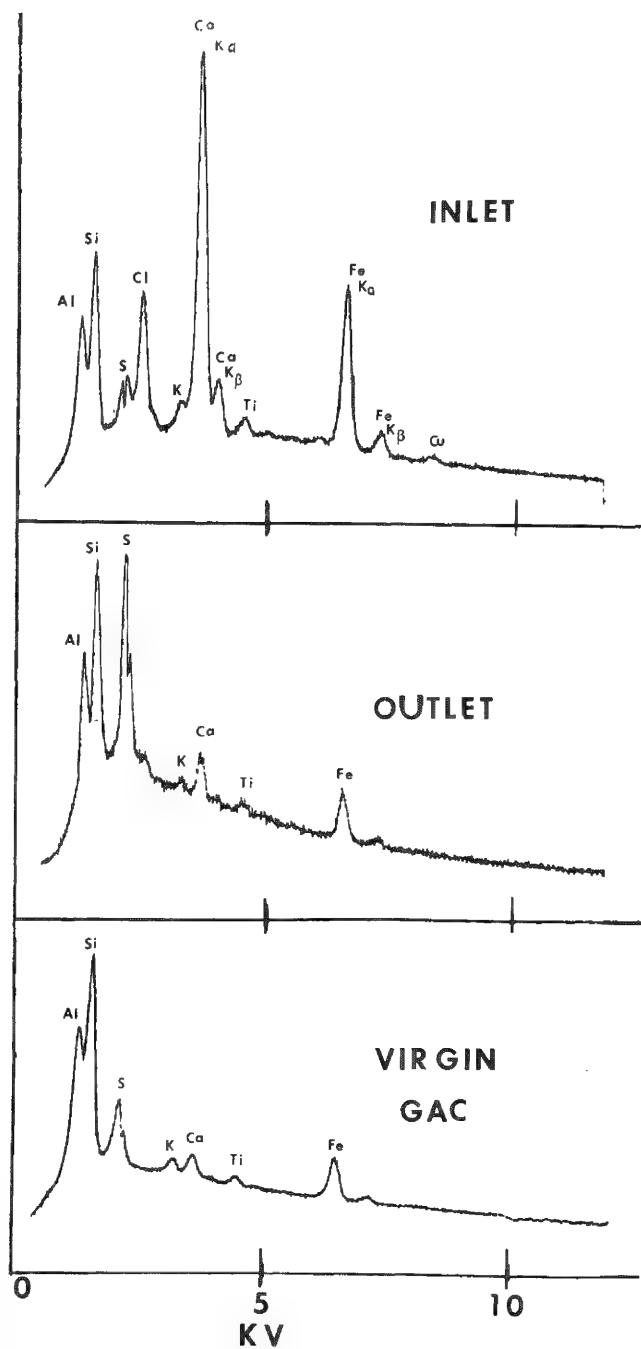


FIG. 1.--SEM/EDX spectra for GAC samples from Waterford and virgin GAC.

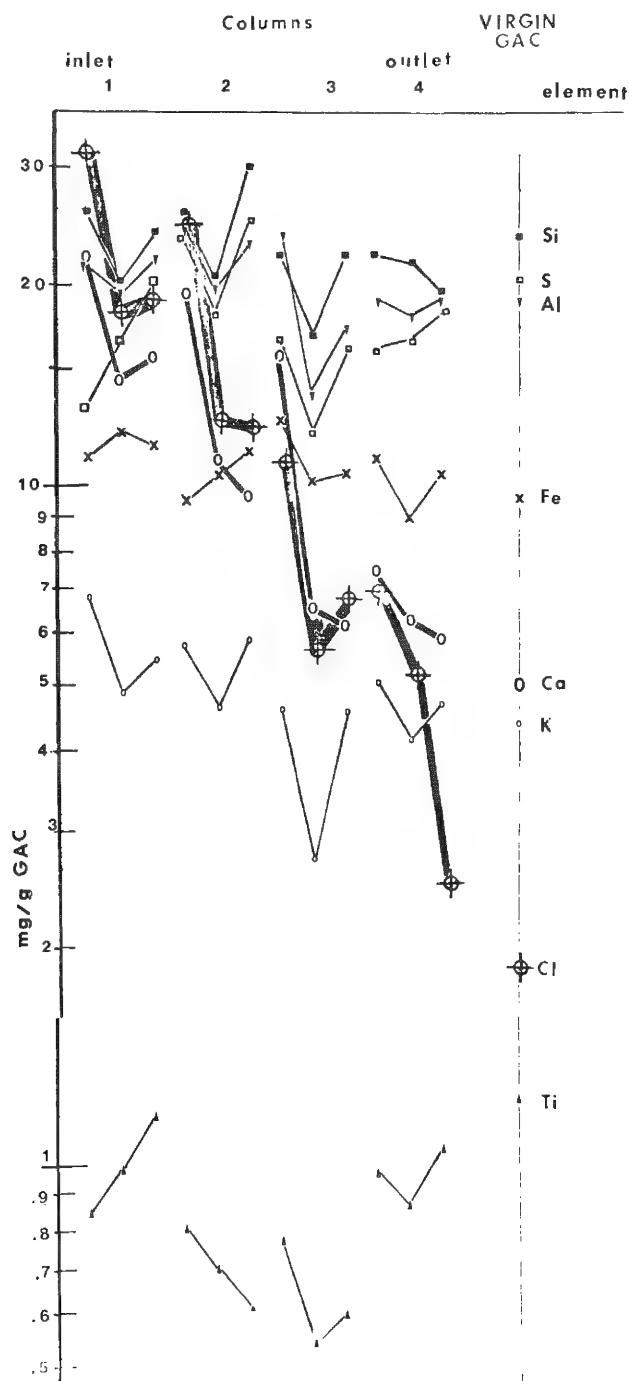


FIG. 2.--Distribution profiles for elements found on Waterford GAC.

TABLE 1.--Results of experiments to study uptake of inorganic Cl and Ca by virgin GAC.

Expt no.	Treatment*	Concen (mg/g GAC)	
		Cl	Ca
1	Distilled water	2.0	-
2	NaCl, 20 mg/L	0.8	-
3	HOCl, 20 mg/L No DW wash	54.0	-
4	a) HOCl, 20 mg/L b) Distilled water	48.0	-
5	a) HOCl, 20 mg/L b) NO ₃ , 5000 mg/L	0.07	-
6	CaCl ₂ , 20 mg/L	-	1.4
7	a) HOCl, 20 mg/L b) CaCl ₂ , 20 mg/L	-	-0-
8	HOCl, 20 mg/L + CaCl ₂ , 20 mg/L	-	-0-
9	CaCO ₃ , 20 mg/L, buffered at pH 9.6 with NaOH/NaHCO ₃	-	3.0

* a and b denote solutions were added sequentially

In further experiments it was found possible to displace bound Cl from the GAC by use of a high concentration (5000 mg/L) of nitrate ion. Elsewhere nitrate ion has been used to displace inorganic Cl from GAC to determine low concentrations of organic halogens in water samples.⁵ In experiment 5, after the nitrate wash, essentially no Cl was found on the GAC. A tracing of the chloride ion concentration for this experiment (Fig. 3) shows that it evolves while HOCl is pumped through the GAC column (A) and decreases when the column is washed with distilled water (B). The residual Cl is finally displaced by nitrate (C). Integration of the small final peak of chloride ion indicated that about 10% of the Cl added as HOCl was retained on the GAC as a result of the reaction. To calculate this value it was necessary to correct the area of the large peak for the background chloride ion in commercial solutions.

Experiments are now being performed on Waterford samples that utilize the ability of nitrate to displace Cl bound from reaction with HOCl. It may be possible by this technique to resolve the fraction of organically bound Cl.

Finally it was noted that the Cl concentration that could be accumulated on virgin GAC from reaction with HOCl was about twice as high as the Cl on the Waterford samples. The test columns may be exposed to higher concentrations of HOCl than the columns in the treatment plant.

Thus far experiments to account for uptake of Ca on the Waterford GAC columns have been only partially successful. It was not possible to bind calcium ion to the GAC surface (experiment 6), nor was adsorption enhanced by the presence of HOCl added either simultaneously or sequentially (experiments 7 and 8). Deposition of calcium carbonate, added as a suspension, was also ineffective (experiment 9). Experiments are being performed to determine if the calcium ion is scavenged by organic molecules adsorbed to the GAC.

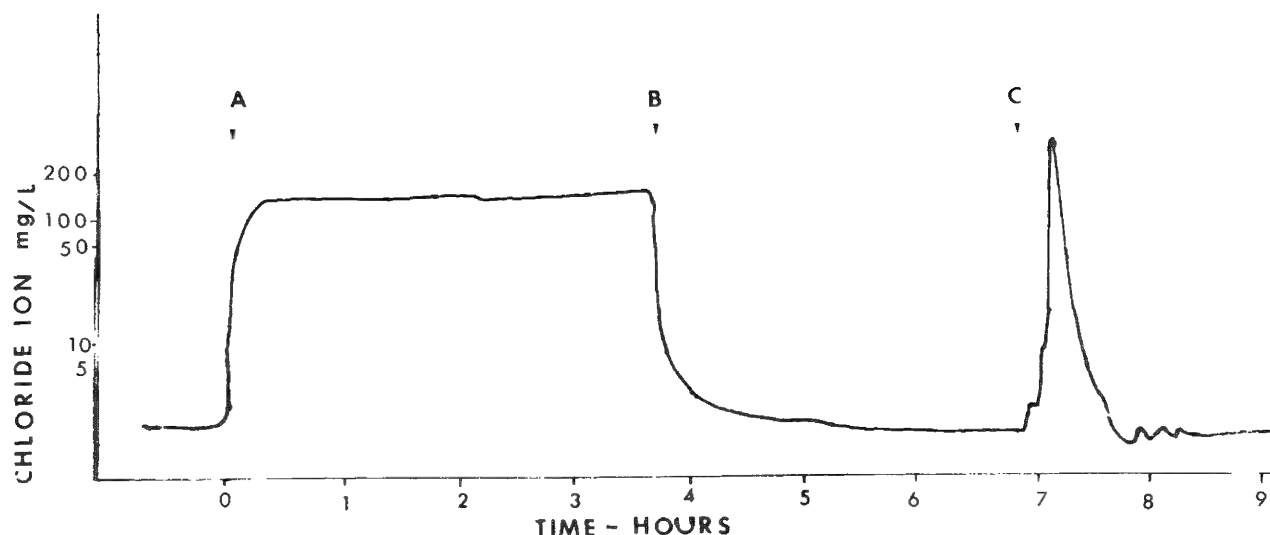


FIG. 3.--Chloride ion concentration in effluent from column of virgin GAC. Influent were (A) HOCl , 20 mg/L; (B) distilled water; (C) NaNO_3 , 5000 mg/L.

References

1. K. Alben and E. Shpirt, "Applications of thermal desorption-gas chromatography and mass spectrometry to monitor dynamic adsorption in activated carbon," in William Cooper, Ed., *Chemistry in Water Reuse*, Ann Arbor, Mich.: Ann Arbor Science, vol. 2 (in press).
2. K. Alben and E. Shpirt, "Competitive adsorption of chloroform, weak organic acids and PCBs on granular activated carbon," submitted for publication in *Environ. Sci. and Tech.*
3. Calgon Corporation, *Ash and Ash Constituent Analyses for Fitratorb Carbons (F400, F300, F200, F100)*, August 1978, Calgon Corp. (Activated Carbon Division), Box 1346, Pittsburgh, PA 15230.
4. M. T. Suidan, V. L. Snoeyink, and R. A. Schmitz, *J. Envir. Engr. (ASCE)* 103: EE4: 677, 1977.
5. Y. Takahashi, *Preliminary Instructions for TOX-1 Adsorption Module for total Organic Halides in Water*, Dohrmann, Envirotech, 3420 Scott Boulevard, Santa Clara, CA 95050.

EFFECT OF STEROL STRUCTURE ON INTRACELLULAR SODIUM AND POTASSIUM IN MYCOPLASMA CAPRICOLUM

E. D. Waitzkin and E. H. Abraham

Among prokaryotes, mycoplasmas are unusual in their absolute sterol nutrient requirement and their absence of a cell wall. Membranes of these organisms have been shown to incorporate, unmodified, a variety of different sterol molecules.¹ We have therefore selected *M. (Mycoplasma) Capricolum* as a model system to study the possible role of membrane sterols in an important physiological function, ion transport. A method has been developed to prepare *M. Capricolum*, cultured on various sterols, for measurement of intracellular sodium (Na) and potassium (K) concentrations by electron-probe microanalysis and the microdroplet technique. Change in the membrane sterol component was found to have striking effects on intracellular Na and K concentrations in *M. Capricolum*.

Materials and Methods

M. Capricolum (California Kid Strain 14, ATCC 27342) was cultured on delipidated Modified Edward Medium.¹ Thallium acetate was omitted, and the serum fraction was replaced by essentially fatty acid free bovine serum albumin (Sigma, Fraction V), 5 µg/ml (micrograms/milliliter) palmitate (Sigma), 6.5 µg/ml elaidate (Sigma), and either 1.5 or 15 µg/ml of various sterols in ethanolic solution (final ethanol 0.5% by volume). Cholesterol, lanosterol, cholesteryl methyl ether, and cycloartenol were gifts of Dr. K. Bloch. The first three sterols were 99% pure by gas-liquid chromatography, but cycloartenol used in this study contained some trace impurities.

Cells were incubated statically at 37°C and growth was monitored by absorbance at 640 nm on a Gilford spectrophotometer and by pH of the medium. At mid-log phase growth (pH of culture = 7.0), 1.0 ml aliquots of culture were centrifuged through silicone oil (70% Dow Corning No. 550, specific gravity 1.07; 30% Dow Corning No. 510, specific gravity 1.00) at 15 000 g, 37°C for 2 min in a Beckman microfuge. This process resulted in density separation of a cell pellet from its growth medium supernatant. Supernatants were transferred for storage at -70°C and silicone oil above the pellets was replaced with hydrated mineral oil. Pellets were then lysed by addition of 1 µl distilled deionized water. A mixture of silicone oils (60% Dow Corning No. 550; 40% Dow Corning No. 510) was introduced into the tubes and the samples were centrifuged for 5 min, which resulted in a clear cell lysate solution at the interface between silicone and mineral oils, and in a pellet of cell membranes at the tube bottom. Cell lysate solutions were stored under hydrated mineral oil at -70°C.

Samples of supernatant media and cell lysates were prepared for analysis by the microdroplet technique.³ Sample size was 50 to 100 pl. Analysis was performed on a Cameca MS 46 electron probe, with an accelerating voltage of 11 kV, a beam diameter of 80-100 µm, and a beam current of 200 nA. Characteristic K α x-ray lines were analyzed for K with a penta erythritol crystal, and for Na with a potassium acid phthalate crystal. Automated analysis was carried out under computer control (Hewlett Packard 2100A).

Determination of the volumes of (a) total cell pellet water and (b) extracellular water trapped in the pellet respectively was carried out by means of markers ³H₂O and ¹⁴C-carboxy-Inulin (New England Nuclear) counted on a Beckman Model 700 scintillation counter. Correction for quenching was made with a calibrated external standard.

The authors are with the National Biotechnology Resource in Electron Probe Microanalysis, Harvard Medical School, Boston, MA 02115. E. D. Waitzkin is also with the James Bryant Conant Laboratories at Harvard University; Dr. Abraham is also with the Division of Metabolism, Department of Medicine, Children's Hospital Medical Center and the Department of Pediatrics, Harvard Medical School. This work was supported in part by NIH grant RR-00679 and an NSF grant. The authors are indebted to Prof. Konrad Bloch and Dr. Claude Lechene for their guidance and generosity, to Dr. Ronald Warner for many helpful discussions, and to Ms. Kathy Edgerly for her excellent technical assistance.

To calculate intracellular ion concentration, we employed the following equation:

$$C_i = \frac{C_1(V_t + V_w) - C_0V_0}{V_t - V_0}$$

where C_1 = measured ion concentration of the cell lysate, C_0 = measured ion concentration of the growth medium supernatant, V_t = total pellet water volume, measured by $^3\text{H}_2\text{O}$ and calculated as $V_t = ^3\text{H}_{\text{pellet}} / (^3\text{H}/\text{ml of medium})$, V_0 = extracellular space trapped in the pellet, measured by ^{14}C -inulin and calculated as $V_0 = ^{14}\text{C}/\text{ml medium}$, and $V_w = 1 \mu\text{l}$ of water added to lyse the pellet.

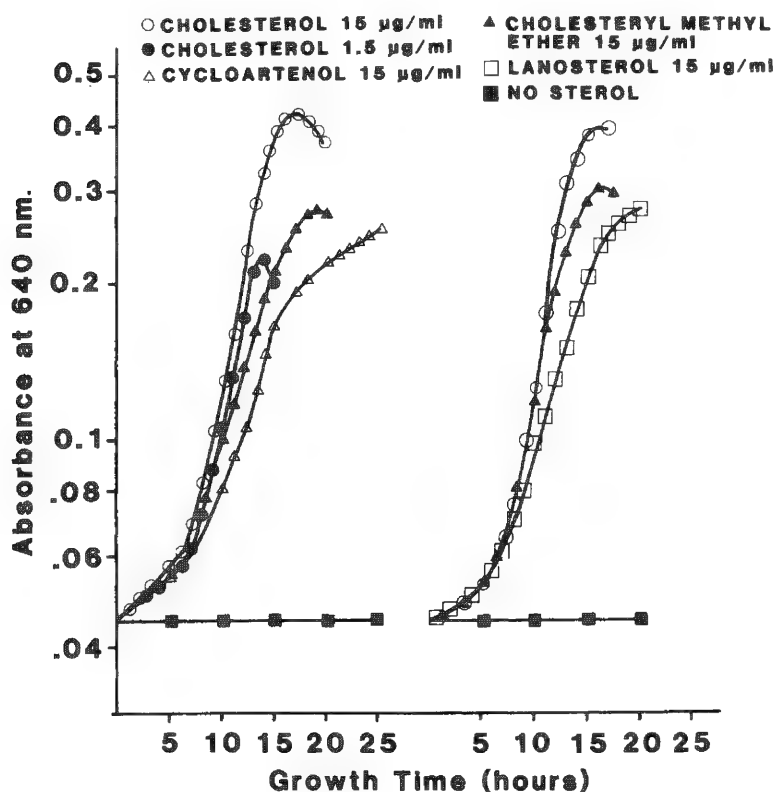


FIG. 1.--Growth of *M. Capricolum* on various sterols at 37°C, measured by absorbance at 640 nm.

With replacement of cholesterol by cycloartenol, cholesteryl methyl ether, and lanosterol, there is a progressive rise of intracellular sodium with concomitant loss of potassium. While maintaining low levels of intracellular Na, cells cultured on 1.5 µg/ml of cholesterol appear to have a lower intracellular K ($K_i = 150 \text{ mM}$) in comparison to cells supplied with ten times more cholesterol ($K_i = 234 \text{ mM}$). Changes of intracellular ion content with changes in membrane sterol composition are most strikingly demonstrated by calculation of the mean intracellular ratios of Na/K, which follow in the order 0.07 (high cholesterol), 0.12 (low cholesterol), 0.49 (cycloartenol), 1.03 (cholesteryl methyl ether), 1.15 (lanosterol).

Discussion

Our approach for preparation of cell samples circumvents washing. This approach minimizes possible artifact introduced by differential leakage of ions from cells with various membrane sterols in response to a washing solution. We have shown that cells cultured on all test sterols retain viability after centrifugation through silicone oil. Electron probe analysis has allowed us to investigate sterols which are difficult to obtain, and thus result in limited amounts of cell culture for sample measurement.

Results

The sterols, in the order of their efficacies as growth factors, are cholesterol > cholesteryl methyl ether > cycloartenol > lanosterol (Fig. 1 and Table 1). This hierarchy has been reported in previous studies with the exception of cycloartenol, which usually resides between cholesterol and cholesteryl methyl ether. We have attributed the present relatively slower growth rate of cells on cycloartenol to the trace impurities which were present in our sterol preparation. Cells grown on low amounts of cholesterol (1.5 µg/ml) had the same doubling time but reached a lower maximum cell culture density, as measured by optical absorbance, compared with cells supplied with high amounts of cholesterol (15 µg/ml) (Fig. 1, Table 1).

Alteration in membrane sterol structure greatly affects the intracellular concentrations of sodium and potassium, as shown in Table

TABLE 1

Sterol	Cholesterol	Cholesterol	Cycloartenol	Cholesteryl methyl ether	Lanosterol
Concentration ($\mu\text{g/ml}$)	15	1.5	15	15	15
Doubling time: (hr)	2	2	5	4	6
Maximum absorbance of culture	0.45	0.25	0.25	0.30	0.27
Na_i	15.3	12.6	91.5	126	143
K_i	234	150	199	130	154
Na_e	79.5	70.2	74.1	82.2	89.5
K_e	28.2	27.9	30.7	31.5	36.2
Mean ratio of intracellular Na/K	0.07	0.12	0.49	1.03	1.15
Number of experiments (number of total replicate samples)	2 (24)	2 (20)	2 (26)	2 (28)	2 (14)

i = intracellular concentration (mM); e = extracellular concentration (mM)

Our value of intracellular K concentration in *M. Capricolum* cultured on high cholesterol concentrations is equivalent to the intracellular K concentration measured by atomic absorption in a related strain, *M. Capri* (where $\text{K}_i = 208 \text{ mM}$).⁵ Increasing K leakiness of mycoplasma membranes adapted to grow in low cholesterol has been reported,⁶ a finding that may explain the reduced internal K concentration which we observe when cells are grown on small amounts of cholesterol.

Substitution of different sterols into the cell membrane of *M. Capricolum* has a striking effect on the intracellular concentrations of Na and K. Changes in the intracellular Na and K concentrations appear to parallel the effects of the test sterols on growth characteristics and, with the exception of cholesteryl methyl ether, on membrane microviscosity in *M. Capricolum*.² However, since cholesteryl methyl ether and cholesterol produce equivalent values of microviscosities in *M. Capricolum* membranes,⁴ membrane fluidity per se probably does not entirely account for the observed effects of the different sterols on ion distribution in this organism.

References

1. J. M. Odriozola et al., "Sterol requirement of mycoplasma capricolum," *Proc. Natl. Acad. Sci. USA* 75: 4107, 1978.
2. C. E. Dahl, J. S. Dahl and K. Bloch, "Effects of cycloartenol and lanosterol on artificial and natural membranes," *Biochim. Biophys. Acta* 92: 221, 1980.
3. J. V. Bonventre, K. Blouch, and C. Lechene, "Liquid droplets and isolated cells," in M. A. Hayat, Ed., *X-ray Microscopy in Biology*, Baltimore: University Park Press, 1980, 307.
4. A. K. Lala, T. M. Buttke, and K. Bloch, "On the role of the sterol hydroxyl group in membranes," *J. Biol. Chem.* 254: 10 582, 1979.
5. U. Schummer et al., "A novel method for the determination of electrical potentials across cellular membranes: II. Membrane potentials of acholeplasmas, mycoplasmas, streptococci and erythrocytes," *Biochim. Biophys. Acta* 600: 998, 1980.
6. C. LeGrimellec and G. LeBlanc, "Effect of membrane cholesterol on potassium transport in mycoplasma mycoides var. capri (P63)," *Biochim. Biophys. Acta* 514: 152, 1978.

INVESTIGATION OF FLY ASH PARTICLES WITH RESPECT TO THE MORPHOLOGY AND SURFACE ENRICHMENT OF MATRIX AND TRACE ELEMENTS

A. J. Gay, A. P. von Rosenstiel, and P. J. van Duin

In this investigation a fly ash was used originating from a U.S. bituminous coal of relatively high ash content (17.9%) and low sulfur content (1.52%), burned in a pulverized coal-fired power plant. Four sized fractions were obtained by means of a Bahco Micro-particle Classifier.¹ This paper is the first in a series reporting results of an investigation of the distribution, concentration and nature of toxic compounds on small fly ash particles (respirable range).

The eight most important matrix elements (Al, Ca, Fe, K, Mg, Na, Si, Ti) and sulfur, as well as fifteen arbitrarily chosen toxic trace elements (As, B, Be, Cd, Co, Cr, Cu, Mo, Ni, Pb, Sb, Se, Tl, V, Zn) were analyzed in an as-received (AR) sample and four sized fraction samples by scanning electron microscopy (SEM)/energy dispersive spectroscopy (EDS), atomic absorption spectrometry (AAS), emission spectrometry (ES), and instrumental neutron activation analysis (INAA). Surface analysis and depth profiling were performed by electron spectroscopy for chemical analysis (ESCA), Auger electron spectroscopy (AES), and secondary ion mass spectrometry (SIMS). Furthermore, trace element concentrations of individual single particles were analyzed by laser microprobe mass analysis (LAMMA).

Morphologically the fly ash presents a standard appearance, of predominantly spherical particles with some irregular ones. A typical SEM micrograph is presented in Fig. 1.

The trace element content as determined by AAS and INAA in relation to the mean particle size is given in Fig. 2. The results for Cd, Co, and As are in general agreement with those of Smith et al.¹ and show a leveling effect with decreasing particle size. However, no leveling was observed for Zn, V, Pb, Cu, Cr, and Se. As an indication of enrichment of these elements the data for the AR sample are included in Fig. 2. The concentrations of the major elements as determined by EDS, INAA, and classical chemical analysis are presented in Table 1. There is remarkable enrichment in S and C on the smaller particles, with more or less constant composition for the other elements.

TABLE 1.--Elemental concentrations of major elements in four fractions and AR sample.

Fraction size (microns)	Al	Ca	Fe	K	Mg	Na	Si	Ti	S	C
1	14.9	1.15	5.68	1.7	1.0	0.32	28	0.91	0.41	2.87
4	12.9	1.0	4.85	1.6	0.75	0.27	32	0.73	0.3	-
8	13.3	1.0	4.4	1.7	0.79	0.27	29	0.72	0.2	-
15	12.4	0.9	4.5	1.7	0.65	-	29	0.67	0.1	0.62
AR(.5-250)	13.0	0.9	5.6	1.5	0.65	0.23	35	0.82	0.15	-

Authors Gay and van Duin are with the Department of Chemistry, Division Mt-TNO, P.O. Box 217, 2600 AE Delft, The Netherlands; A. P. von Rosenstiel is with the Department of General Metallurgy, Division B&M-TNO, P.O. Box 541, 7300 AM Apeldoorn, The Netherlands. The valuable help and skillful work of TNO colleagues during this investigation are gratefully acknowledged. (TNO is the Dutch Organization for Applied Scientific Research.) The authors wish to thank the following specifically: Prof. Dr. K. Spurny, FHG Institut für Toxikologie und Aerosolforschung in Graftschaft for the preparation of SIMS specimens and the optical and aerodynamic particle size determinations; Dr. S. Storp of Bayer AG in Leverkusen and Dr. H. Goretzky of Perkin-Elmer GmbH for the ESCA and AES analysis; Dr. H. J. Heinen of Leybold-Heraeus in Cologne for the LAMMA determinations; KEMA in Arnhem for the supply of the fly ash sample; and BEOP in Petten for their permission to publish these results within the framework of the Dutch national research program on re-introduction of coal (NOK).

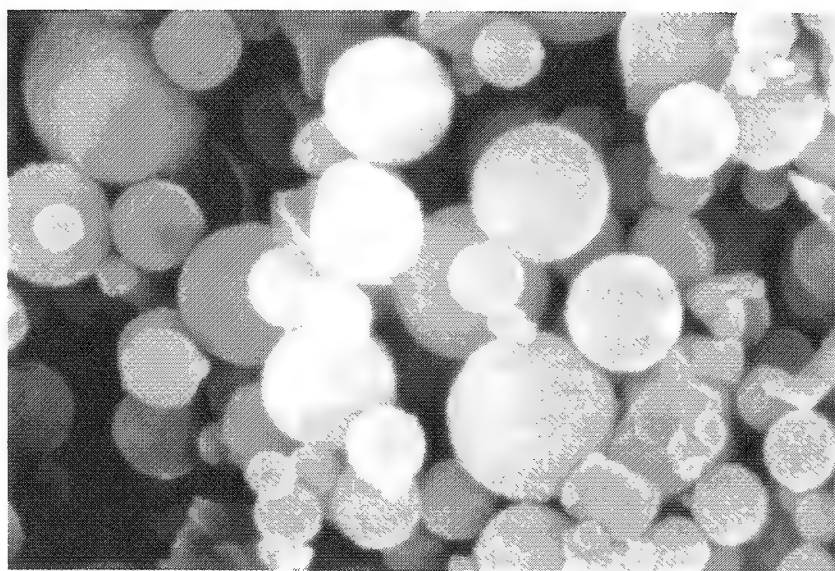


FIG. 1.--SEM micrograph of AR fly ash fraction.

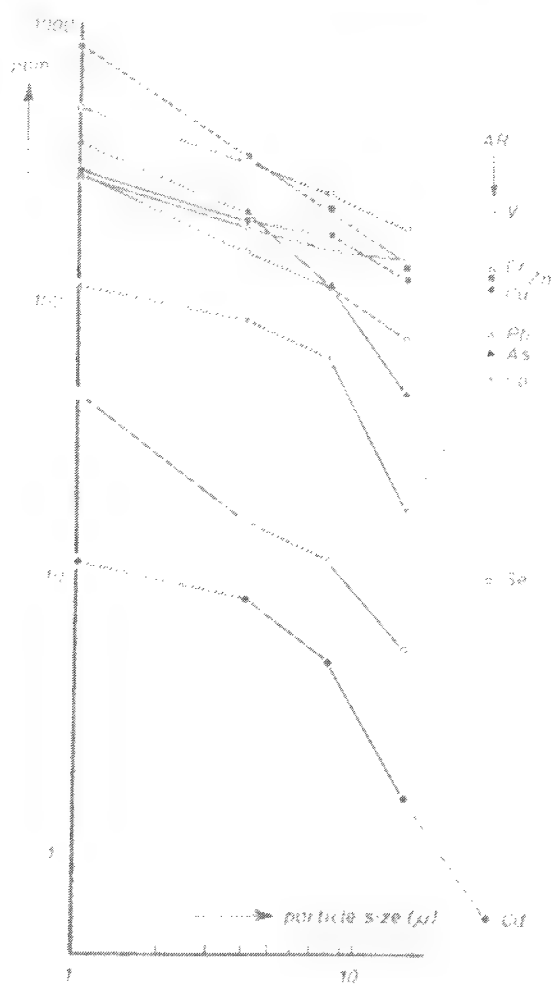


FIG. 2.--Trace element concentration vs particle size.

TABLE 2.--Quantitative surface analysis of major elements by ESCA (recalculated to weight %).

Fraction size (microns)		Al	Ca	Fe	Si	S	C	O
1	surface	7.1	1.4	2.2	16.8	6.4	20.5	45.6
	50 $\overset{\circ}{\text{Å}}$ sputtered	10.8	2.2	2.4	21.1	1.6	16.0	45.8
	350 $\overset{\circ}{\text{Å}}$ sputtered	14.9	1.7	3.2	21.7	0.5	17.8	46.6
8	surface	6.7	1.3	1.9	17.7	6.5	17.6	48.1
	50 $\overset{\circ}{\text{Å}}$ sputtered	10.2	1.6	3.4	21.2	1.6	19.0	43.0
15	surface	9.3	1.3	1.5	18.0	5.9	16.1	47.8
	50 $\overset{\circ}{\text{Å}}$ sputtered	13.7	1.4	5.2	21.5	1.2	8.6	48.8
AR 0.5-250	surface	7.7	1.8	2.8	17.0	6.5	15.2	49.0
	50 $\overset{\circ}{\text{Å}}$ sputtered	12.2	1.7	4.2	19.3	1.6	16.0	44.9

The elemental concentrations as obtained by ESCA on the surface² and after successive sputter etching of 50 and 350 Å are given in Table 2. These results show the high surface concentration of S and C and the increase of the matrix element concentrations of Al, Ca, Fe, and Si with increasing depth. Most remarkable are the nearly constant *surface concentrations* for all fractions, despite the large difference in *bulk concentrations* (Table 1). Also, evidence was found for the presence of Pb and Cd in the surface layer of the fly ash fractions, which means that these elements are present on the surface at concentrations of at least 1% (atomic).

Further attempts were made by ESCA to obtain additional information on the chemical state of a number of selected matrix, minor, and trace elements such as Al, Si, Ca, Fe, S, Pb, and Cd. High-resolution spectra of the S 2p peak revealed clearly the presence of sulfate, most probably Fe(III) sulfate.² However, with decreasing particle size an increasing side peak was found (Fig. 3). Although our data do not definitively identify it, this side peak is probably an organic S-compound in the C-rich "soot like" surface layer as shown by a 1000kV transmission electron microscope (TEM) micrograph (Fig. 4).

For a more detailed characterization of the C- and S-rich surface layer of the 1 and 15 μm fractions, AES analyses were performed on several individual fly ash particles (Fig. 5). These AES spectra³ clearly show the high surface concentration of C, S, and O. With increasing depth the C and S intensities decrease rapidly, whereas the matrix elements Si, Al, Ca, and Fe increase.

Most obvious is the marked difference in the thickness of the C- and S-rich surface layer between the fine (1 μm) and the coarse (15 μm) fly ash fraction. For the fine fraction a large thickness of 300-350 Å was found; for the coarse, the surface layer was much thinner (50-80 Å). These results are in good agreement with the ESCA results of constant surface concentrations despite the large difference in bulk concentrations of the fly ash fraction.

Data obtained by SIMS on specially prepared specimens of these fly ash fractions showed a thin surface layer that contained a number of trace elements such as As, Ba, Cd, Cr, Cu, Mo, Ni, Pb, V, and Zn.³ Typical depth profiles for some selected toxic elements such as Pb, As, Cr, V, and Zn vs Al as "internal standard" are given in Fig. 6. Some indication of the chemical state of some trace elements could be obtained, for example the presence of Pb in oxydic form due to the strong appearance of the PbO mass peak with respect to the weaker Pb peak during the SIMS analysis.

A larger number of individual particles were analyzed by LAMMA and showed largely differing trace element concentrations of Ba, Cr, Cu, V, and Zn, and incidentally also of As, Co, Pb, and Tl.⁴ Typical examples are given in Fig. 7. Negative secondary ion LAMMA

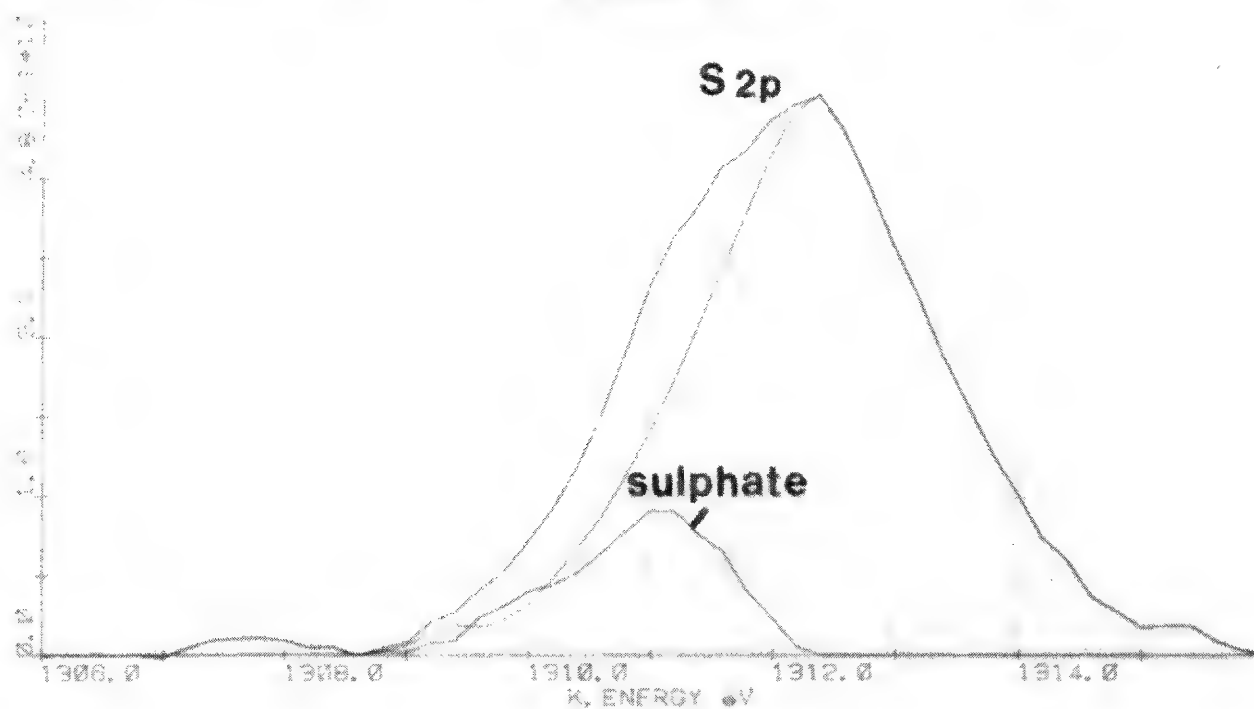
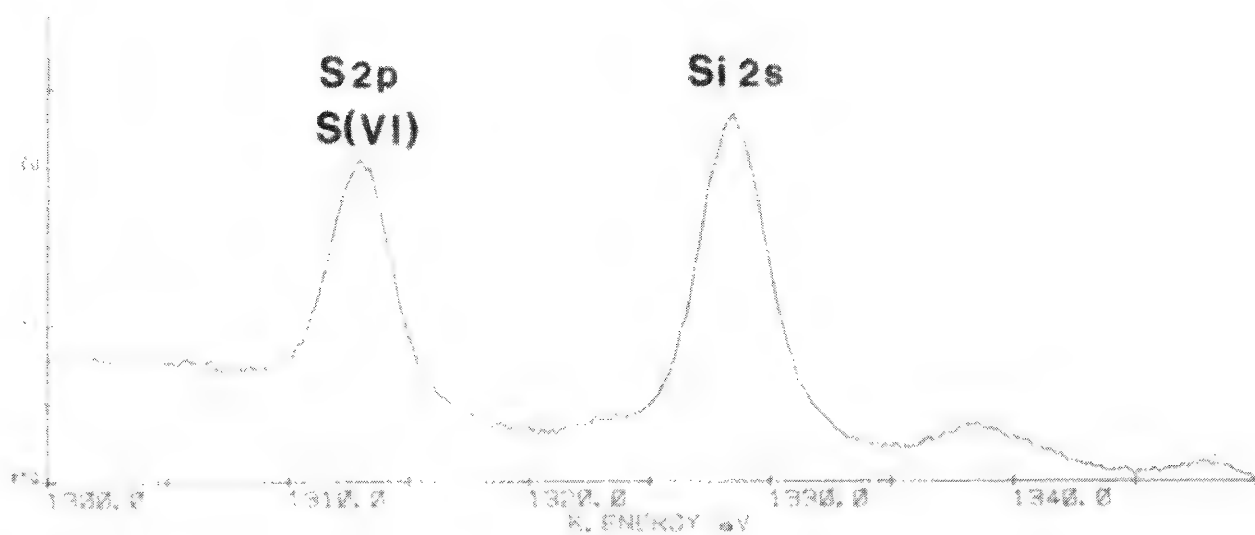


FIG. 3.--High-resolution S 2p ESCA peak (1 μ m fraction).

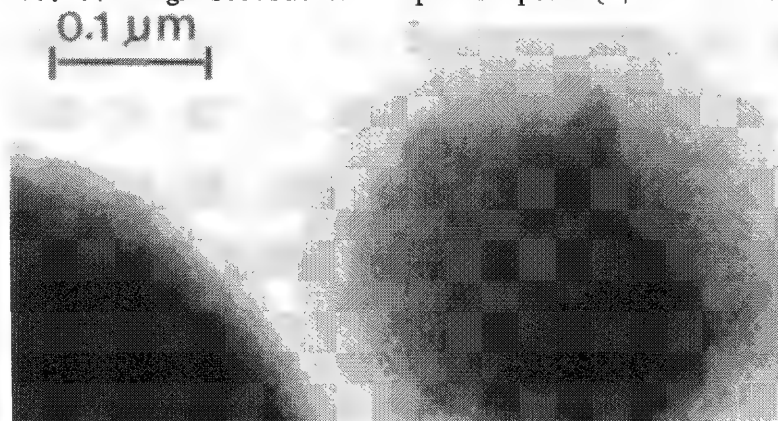


FIG. 4.--1000kV TEM micrograph of 0.3 μ m fly ash particle.

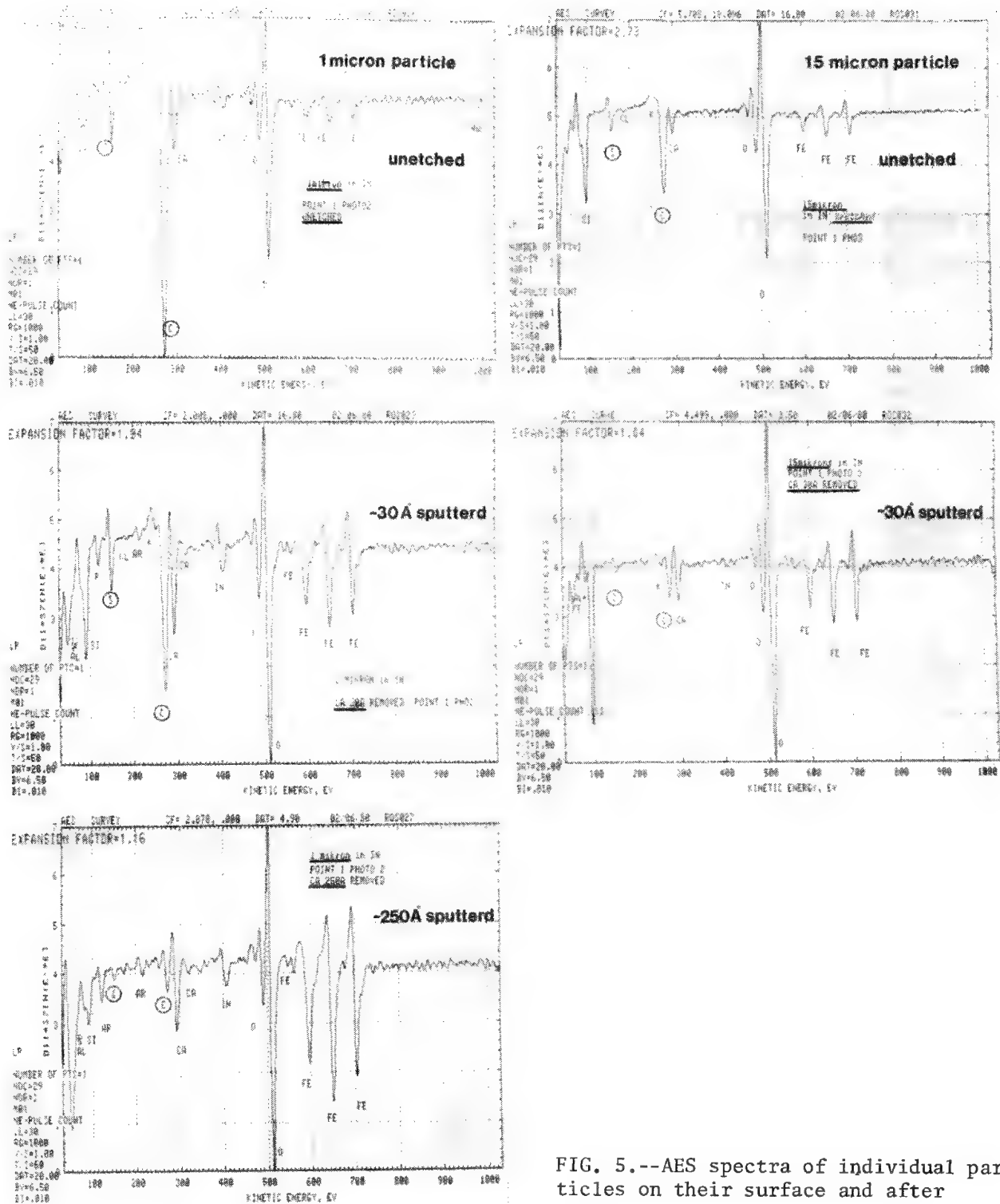


FIG. 5.--AES spectra of individual particles on their surface and after sputter etching.

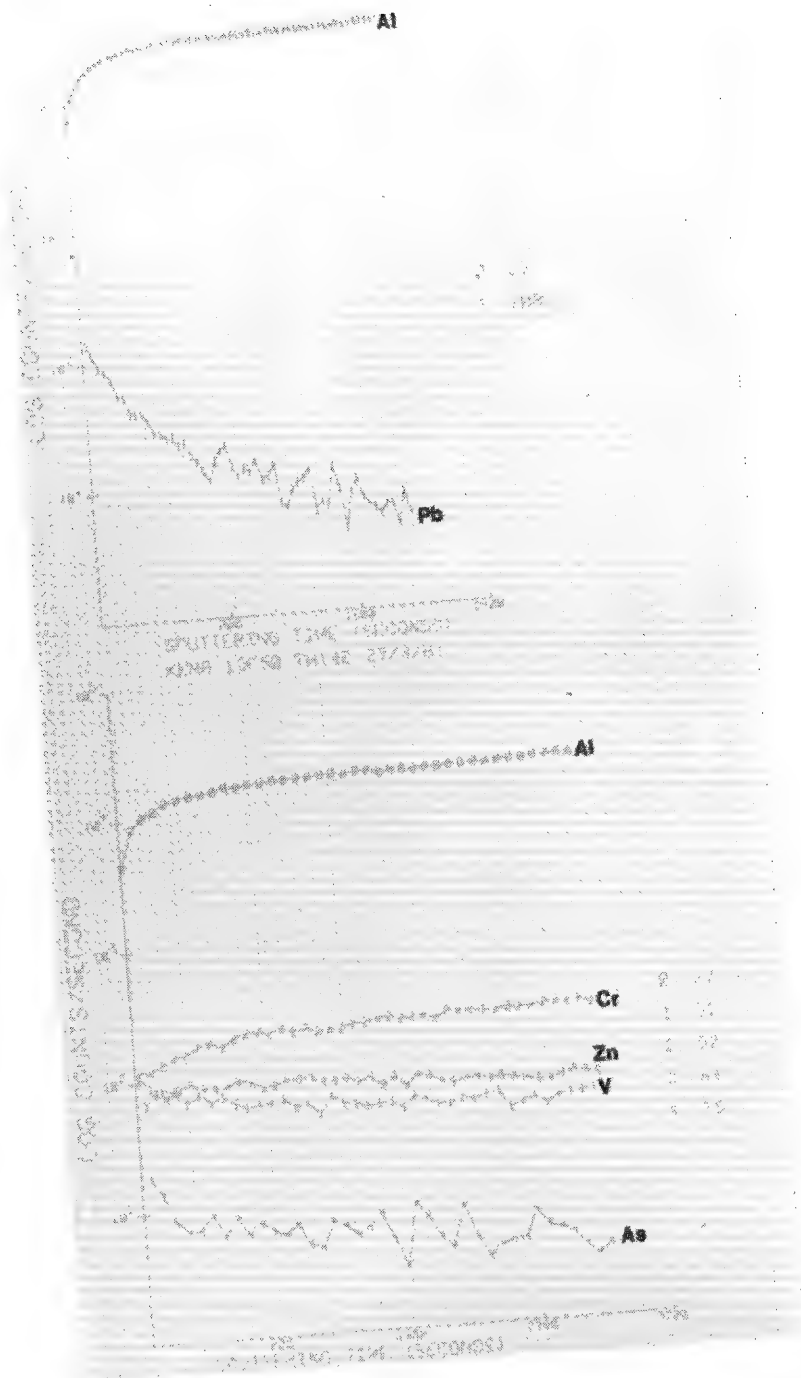


FIG. 6.--SIMS depth profiles of some selected trace elements (4 μ m fraction).

spectra showed the presence of larger amounts of F, Cl, P, and S as well as hydrocarbons, PO_2^- , PO_3^- , SO_2^- , SO_3^- , SO_4^- , and HSO_4^- (Fig. 8).

References

1. R. D. Smith et al., "Characterization and formation of submicron particles in coal fired plants," *Atm. Env.* 13: 607, 1979.
2. S. J. Rothenberg et al., "Coal combustion fly ash characterization: ESCA, EDS and SEM," *Appl. Spectr.* 34: 549, 1980.
3. R. W. Linton et al., "Determination of the surface predominance of toxic elements in airborne particles by ion microprobe mass spectrometry and Auger electron spectrometry," *Anal. Chem.* 49: 1514, 1977.
4. K. F. J. Heinrich, Ed., *Characterization of Particles*, Special Publication 533, U.S. National Bureau of Standards, Washington, D.C., 1980.

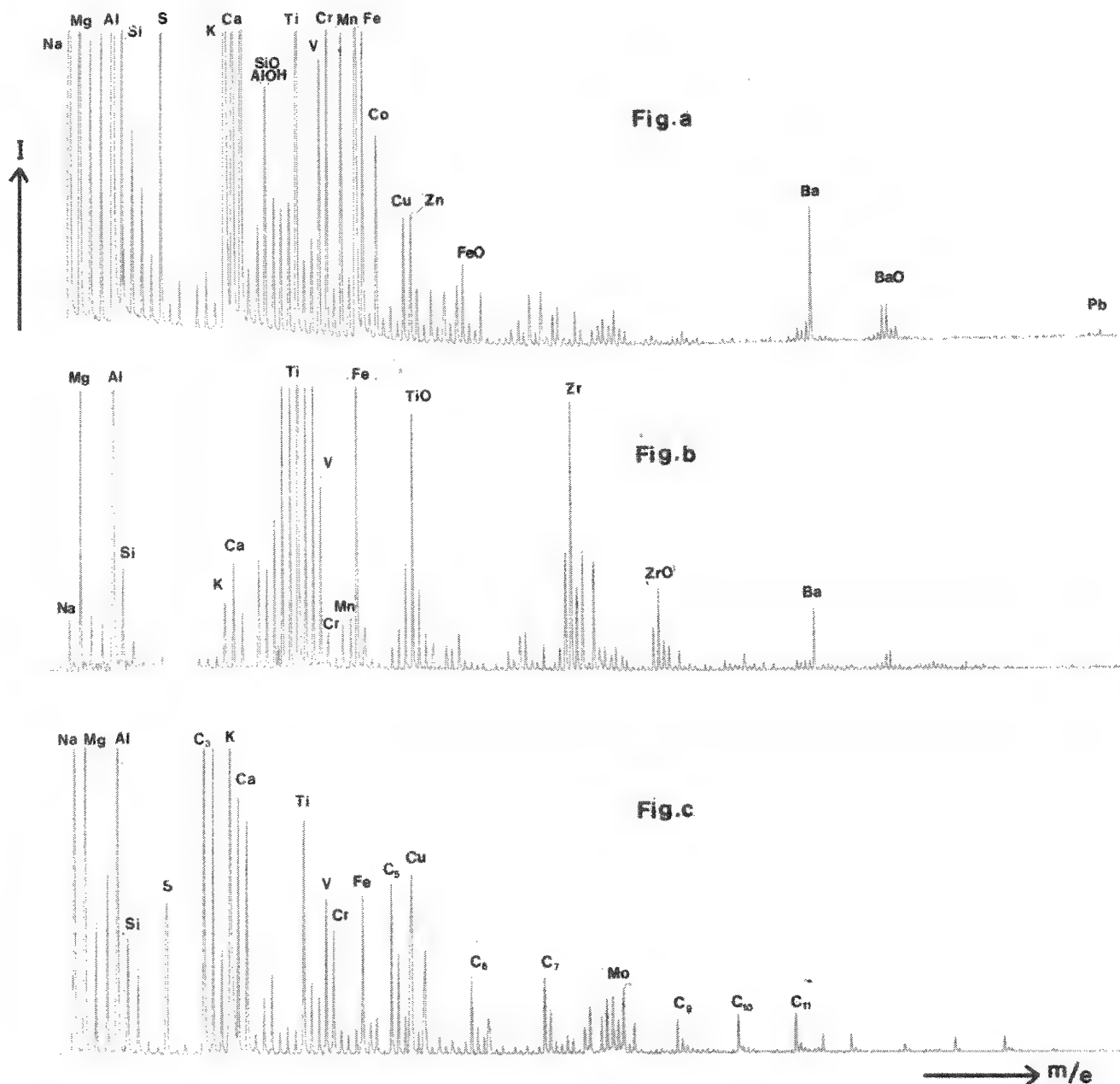


FIG. 7.--Positive secondary ion LAMMA spectra from three individual 1 μm fly ash particles.

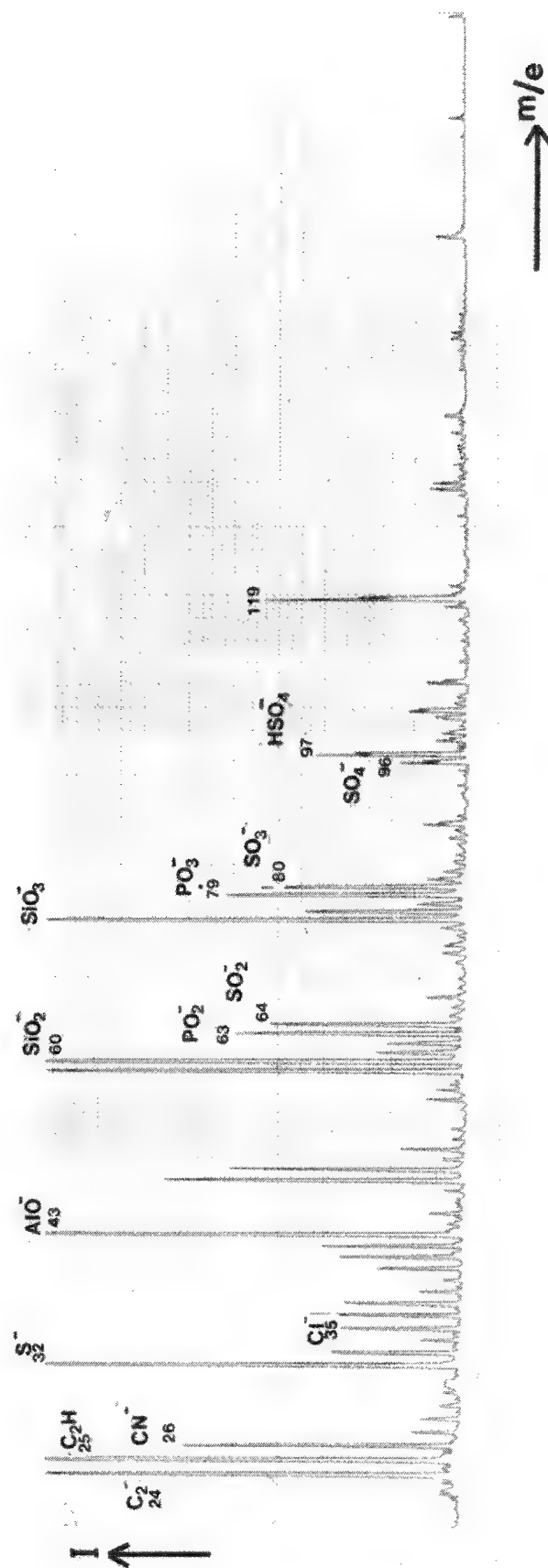


FIG. 8.--Negative secondary ion LAMMA spectrum from a lum fly ash particle.

XPS ANALYSIS OF FLYASH CHANGES DUE TO GUINEA PIG ALVEOLAR MACROPHAGE EXPOSURE

D. L. Davidson and E. M. Gause

Alveolar macrophages are involved in one of the first mechanisms used by the body to take action against a foreign body inhaled into the lungs. When a foreign particle is deposited in the lung, the primary mechanism possessed by the macrophage for reducing its possible toxicity is phagocytosis (the process of ingestion, digestion, and finally elimination of the residual). This paper examines the changes in flyash particles that have been exposed to live alveolar macrophages in culture by measurement of particle surface chemistry by x-ray photoelectron spectroscopy (XPS). The purpose of the work reported was to gain an understanding of the mechanism by which macrophages are killed by flyash.

Experimental Procedure

The flyash particles were collected near a coal-burning facility by the U.S. Department of Energy (designated EP-12) by electrostatic precipitator and sized so that all of the particles used in this study were smaller in diameter than 3.4 μm . Other details are unknown. Particles of this size are inhaled into the deep lung region inhabited by macrophages.

Macrophages were obtained from Strain 13 random-bred guinea pigs. The animals were killed by a drug overdose (nembutal) and then bled. Lungs and trachea were excised and the macrophages washed out of the lungs (lavaged) immediately by accepted methods, then centrifuged and resuspended in a biologically acceptable fluid medium for culture, which kept them alive until exposure to flyash; cells attached to culture flask surfaces in 10-20 minutes. Macrophages were incubated with flyash particles at a concentration of 97 particles per cell for 1 hr at 37°C.

In the experiment (Fig. 1), one portion of flyash was incubated with live macrophages once, which resulted in the death of nearly all of the cells; this flyash was then recovered by centrifuging, washed twice with deionized water and partitioned: one part went for XPS analysis and the other part for incubation a second time with live macrophages from another guinea pig. A concentration of 97 particles per cell was used again.

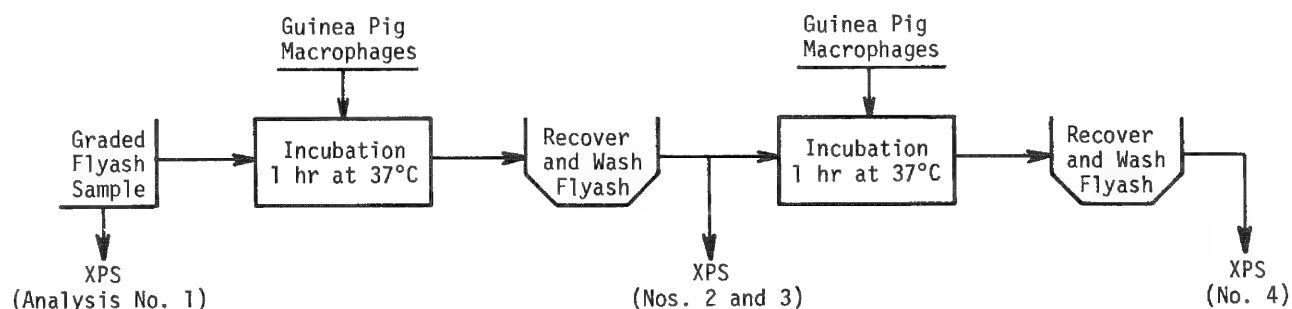


FIG. 1.--Design of flyash exposures to macrophages, showing when XPS analysis was performed.

For control and comparison, flyash samples were also immersed in (1) BSA extraction (aqueous bovine serum albumin solution at a concentration of 2 mg/ml), (2) benzene (organic and inorganic solvents), and (3) culture medium, for 60 hr at 37°C, then recovered and prepared for analysis in the same way as all other samples. Longer culture time was used to amplify any solvent extraction that might occur.

For spectroscopy, flyash particles were slurried in 25% isopropyl alcohol in water and flooded onto sintered silver filters (0.25 μm pore size from Selas, Inc.). XPS was

Author Davidson is a materials scientist and author Gause, a biochemist with Southwest Research Center, San Antonio, TX 78284. The technical assistance of Physical Electronics is gratefully acknowledged, as is the financial assistance of both Southwest Research and Physical Electronics.

performed by Physical Electronics Division of Perkin-Elmer Corp. The x-ray source used had an aluminum target and was operated at 10 keV, 50 mA.

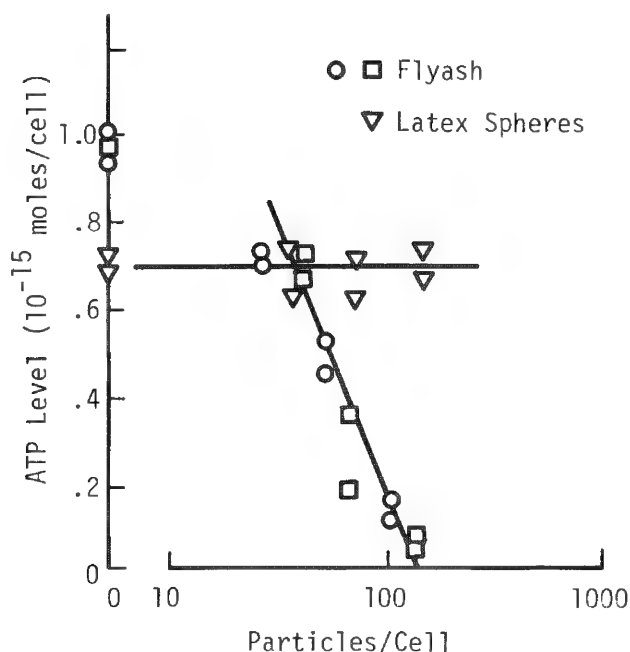


FIG. 2.--ATP level of macrophages after one exposure to flyash at different concentrations.

the presence of small amounts of arsenic and (probably) selenium, with the latter not definite because of interferences from the other elements present in larger quantity. Comparison of this analysis with the composition of other flyash indicates similar, but fewer constituents.² Although it is well known that some elements segregate to the surface of flyash,³ that this segregation is size dependent,⁴ and that flyash is very heterogeneous when analyzed particle by particle,⁵ these factors are not considered here; XPS analysis gives a surface analysis averaged over thousands of particles. The lack of other trace heavy metals is surprising, and taken together with the lack of Ti, Fe, and K may indicate that the sample was derived from a fluidized bed combustor.⁶

After one exposure to macrophages, the two trace element peaks are gone (No. 2), and the removal of approximately 50 Å of surface (No. 3) does not show them up again. Comparison of the high toxicity of macrophages with the disappearance of these elements implies that they were removed by the macrophages, and were the cause of death. Another effect of one incubation is the shift of the phosphorus 2s line to a higher energy level, which is consistent with phosphorus becoming bound organically; note that the phosphorus 2p line does not shift (reason unknown). A nitrogen peak (near 402 eV) appeared after incubation (Table 1). Surface removal restored the silicon, oxygen, and aluminum peaks, but left residual increases in carbon, nitrogen, and phosphorus. The shift in energy of the nitrogen peak was consistent with it being bound organically. These changes in concentration suggest surface deposition of organic molecules during removal of arsenic and selenium. The increases in carbon and change in phosphorus suggest products from macrophage lysosome (digestive enzyme) release during phagocytosis.

After immersion in the control/comparison media, some differences are apparent, but they are different from those arising from incubation with macrophages. Benzene appears to have altered the arsenic, selenium, and phosphorus peaks; sodium and chlorine were picked up from BSA; culture medium caused no change.

Conclusions

Alveolar macrophages are killed by incubation with flyash particles. XPS indicates that a loss of arsenic and selenium accompanies this process. There are some indications

At each step in the experiments, the recovered macrophages were analyzed for ATP (adenosine triphosphate, the cellular energy carrier), as one way of monitoring the level of cellular mortality. The measurement method was that described by Lundin and Thore.¹ Since dead macrophages produce no ATP, this level may be used to supplement visual observation of the effects of flyash on cell mortality. An inverse relation was found between ATP activity and the flyash concentration (Fig. 2), with no ATP being produced at 150 particles per macrophage; no change in ATP level was found when macrophages were exposed to latex spheres. ATP level therefore appears to be a sensitive measure of macrophage cytotoxicity.

Results

Figures 3 and 4 and Table 1 give the spectrographic findings. This flyash is made principally of aluminum silicate, with traces of sodium and iron (Analysis No. 1). Removal of approximately 25 Å of surface by argon ion bombardment resulted in a nearly identical spectrum. These analyses showed

that phagocytosis is also occurring and might be responsible for the flyash toxicity; however, since a variety of organic compounds are also known to exist on flyash,⁶ it is not possible to determine conclusively from this data the mechanism by which flyash kills macrophages. Immersion of the flyash in solvents and culture medium does not cause similar effects.

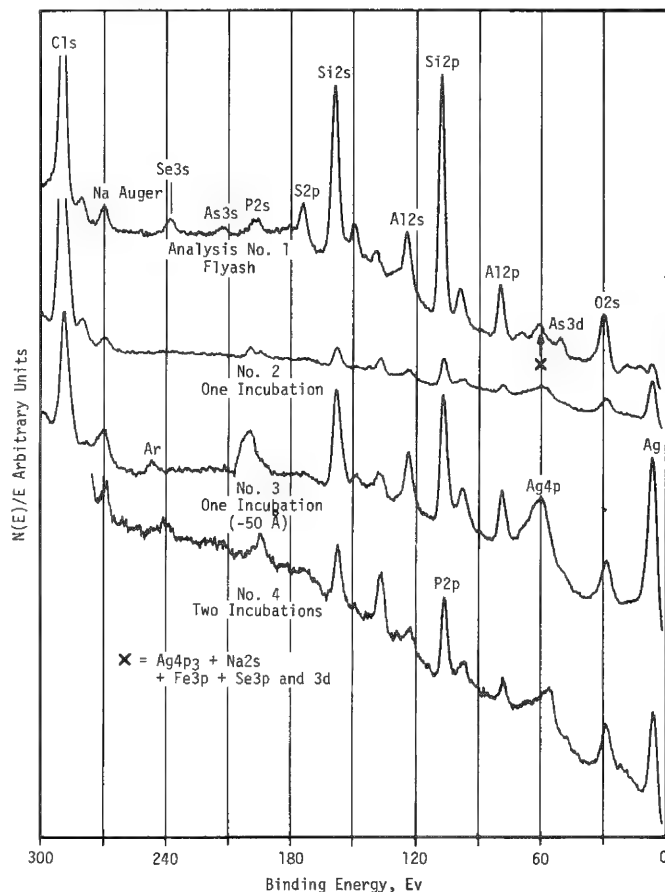


FIG. 3.--XPS spectra of as-received flyash (No. 1); flyash after one incubation (No. 2); same, but with about 50 Å removed by argon sputtering (No. 3); and flyash after two incubations (No. 4). Unlabelled peaks are x-ray satellites of intense peaks nearby.

References

1. A. Lundin and A. Thore, "Analytical information obtainable by evaluation of the time course of fire fly bioluminescence in the assay of ATP," *Analytical Biochemistry* 66: 47-63, 1975.
2. G. L. Fisher et al., "Physical and morphological studies of size-classified coal fly-ash," *Environ. Sci. and Tech.* 12: 447-451, 1978.
3. R. W. Linton et al., "Surface predominance of trace elements in airborne particles," *Science* 191: 852-854, 1976.
4. G. L. Fisher and D. F. Natusch, "Size dependence of the physical and chemical properties of coal fly-ash," in C. Karr, Ed., *Analytical Methods for Coal and Coal Products* New York: Academic Press, 1979, 3.
5. T. L. Hayes et al., "The effect of chemical variability of individual fly ash particles on cell exposure," *SEM/1978 I*, 239-244.
6. C. H. Hobbs and R. L. Carpenter, Eds., *Fluidized Bed combustion Emissions Toxicology Program Status Report--July 1980*, LMF-83, VC-48, Lovelace Inhalation Toxicology Research Institute. (Available from NTIS, 5285 Port Royal Road, Springfield, VA 22161.)

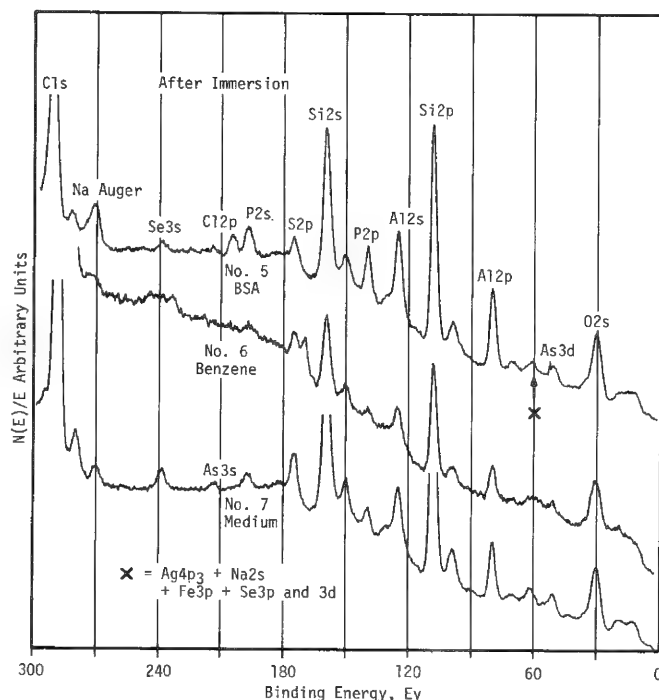


FIG. 4.--XPS spectra of flyash after immersion in solvents and incubation medium for comparison and control.

TABLE 1.--Surface chemistry of flyash particles (atomic per cent).

	Flyash as received	One Incubation		Two incubations	Solvents		Medium only
		as recovered	50 Å removed		BSA only	Benzene	
Analysis No.	1	2	3	4	5	6	7
Silicon	22.8	8.8	18.4	4.5	6.2	20.2	17.6
Aluminum	10.4	4.8	11.6	3.2	3.8	6.2	10.0
Oxygen	49.8	28.3	45.9	18.8	25.0	46.0	48.7
Carbon	8.9	42.0	15.6	63.1	46.8	20.9	13.6
Nitrogen		10.8	2.0	7.2	15.2		
Phosphorus	1.5	5.4	6.5	3.3	0.8	1.6	3.1
Selenium	1.6				2.1	2.0	1.4
Arsenic	2.0					1.8	2.2
Iron	1.4					0.8	0.7
Fluorine	1.6					0.6	1.9
Chlorine							0.8

ANALYTICAL ELECTRON MICROSCOPY AT MIT

A. J. Garratt-Reed, J. B. Vander Sande, and D. Imeson

The Center for Materials Science and Engineering at MIT, part of the NSF-MRL program, provides various services and equipment for sponsored research programs through several central facilities; one is the central facility for transmission electron microscopy, which possesses a VG HB5 dedicated scanning transmission microscope as well as three conventional instruments. By the nature of the facility, these microscopes are applied to a wide variety of topics by many users. It is the purpose of this paper both to mention some of the successful applications of analytical electron microscopy in this laboratory, and to share some of our experience in the operation of such a facility. The research results are, or will be, discussed in full in places appropriate to the topics mentioned. The material is subdivided according to various types of applications of STEM. Often, of course, applications are not well categorized; these divisions are for descriptive purposes only.

Thin-film X-ray Microanalysis

The single greatest use of the STEM in this facility is for compositional analysis at high spatial resolution by means of x-ray spectrometry. The following subsections illustrate such use through descriptions of several of the applications being pursued at MIT at the present.

Analysis of Precipitates and Other Particles. The properties of high strength low alloy (HSLA) steels are to a large extent determined by a dispersion of small precipitates formed during the hot-rolling process. A combination of thin-foil and extraction replication measurements enables one to measure not only the size and spatial distribution of these precipitates but also their composition. Measurements of light-element content will be mentioned later, but even without them it has been possible to relate the precipitation kinetics to the mechanical properties in a vanadium HSLA steel. Figure 1 shows a replica (in this case, an aluminum extraction replica) on which several precipitates are seen. They are found to be rich in vanadium and no other heavy element. These precipitates can be measured and incubation times and growth rates determined for various mechanical and thermal treatments, and for various alloys.

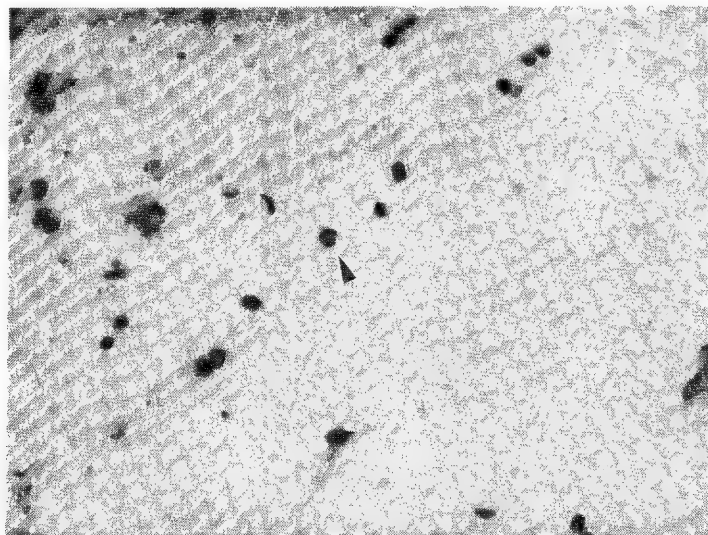


FIG. 1.--Precipitates containing vanadium (dark spots) extracted onto aluminum replica from vanadium HSLA steel. In this example specimen was aged for 3300 s at testing temperature after hot compression. Precipitate indicated by arrow is the one from which spectrum of Fig. 6 was obtained.

The authors are at the MIT Center for Materials Science and Engineering, Cambridge, MA 02139. They acknowledge those who have kindly permitted quotations from their work (Mr. T. Kelly, Mr. G. DiFilippo, Prof. T. Grove, and Dr. E. Hall), as well as financial support from the National Science Foundation under block grant DMR 78-24185.

An extension of this method is to study particles such as may be collected, say, from the atmosphere. For instance, carbon support films may be placed in an electrostatic precipitator and collect directly ash particles from flue gases. Information so obtained not only identifies the ash particles being emitted, it allows optimization of the furnace operating conditions and gas cleaning systems for both efficient and environmentally sound operation.

In this mode, essentially free from effects such as beam broadening and bremsstrahlung background, the energy-dispersive x-ray analyzer can be exceedingly sensitive. For example, it has been estimated that for vanadium nitrides, one can identify a precipitate 1.5 nm in diameter, which contains about 100 vanadium atoms (less than 10^{-20} g of vanadium).

Concentration Variations at Interfaces. High spatial resolution composition profiles are being generated in a number of materials. The goal of this research is to develop a quantitative analysis of the degree of elemental segregation or depletion that can occur at interfaces in multicomponent materials systems. To this end an interface is chosen for analysis, properly oriented with respect to the foil thickness variation, the electron probe, and the x-ray detector. The probe is stepped in appropriate intervals along a line normal to this interface and an analysis is obtained at each position. It is important to consider possible effects of beam spreading and other factors that depend on the foil thickness in this type of analysis, as discussed further in the section on the determination of foil thickness.

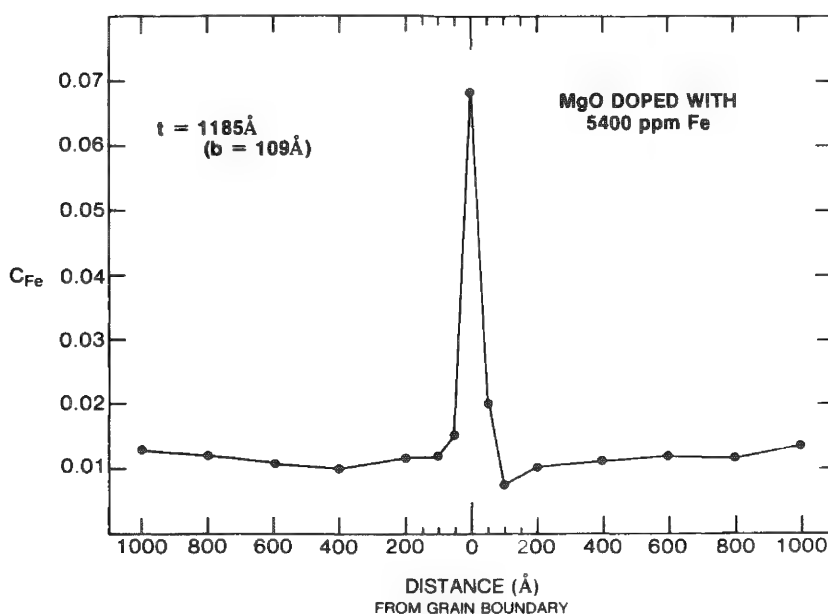


FIG. 2.--Plot of iron content as function of position near grain boundary in Fe-doped MgO.

Figure 2 shows a typical result from an analysis done on a grain boundary in MgO doped with Fe. Strong Fe segregation to the boundary is observed, with the enhanced Fe signal extending less than 100 Å into the matrix. In addition, Ca segregation is observed, even though Ca is a trace impurity in this MgO sample. Knowledge of the composition variation at grain boundaries in materials such as MgO can lead to a better understanding of the physical properties of these materials.

Another materials problem of a different nature can be approached with this instrumental technique. Sensitization of stainless steels, where time at elevated temperature can lead to Cr depletion at grain boundaries, is an important technological problem. The

amount of Cr depletion and the Cr depletion profile at a grain boundary can determine the stress corrosion cracking resistance of an alloy. To study this problem, Cr content as a function of distance from a grain boundary can be monitored in the same way as Fe was monitored in the above case. Such Cr depletion profiles can then be related to the macroscopic behavior that the alloy exhibits.

Analysis of Rapidly Solidified Steels. Rapid solidification processing has shown high potential for producing improvements in physical and mechanical properties of steels. Analytical microscopy is being used to study the way in which high cooling rates affect the solidification of steels to produce the microstructural refinements generally responsible for the improved properties. The foils studied are prepared from a composite sample of metal powder particles embedded in electrodeposited nickel and significant thickness varia-

tions occur in the foil on a small scale (about 1 μm). As a result, annular dark-field imaging in the STEM has been an extremely useful tool.

Composition profiles of these fine-scale solidification structures, with cell spacing of about 1 μm , are generated by point-by-point x-ray analysis. An example of segregation at a dendrite cell wall in a 303 stainless steel is shown in Fig. 3. Comparison of composition profiles from specimens processed at various cooling rates yields information on the effect of high cooling rates on microsegregation. Because of the rapid changes in foil thickness, thickness measurements at each analysis point are particularly important. Such measurements can be carried out simultaneously with the acquisition of an x-ray spectrum by means of the convergent-beam diffraction technique described in the next section. The very small probe diameter of the dedicated STEM makes it possible for acceptable convergent-beam patterns to be obtained, which would otherwise suffer critically from effects of "averaging" over the larger volume of the complex material being sampled.

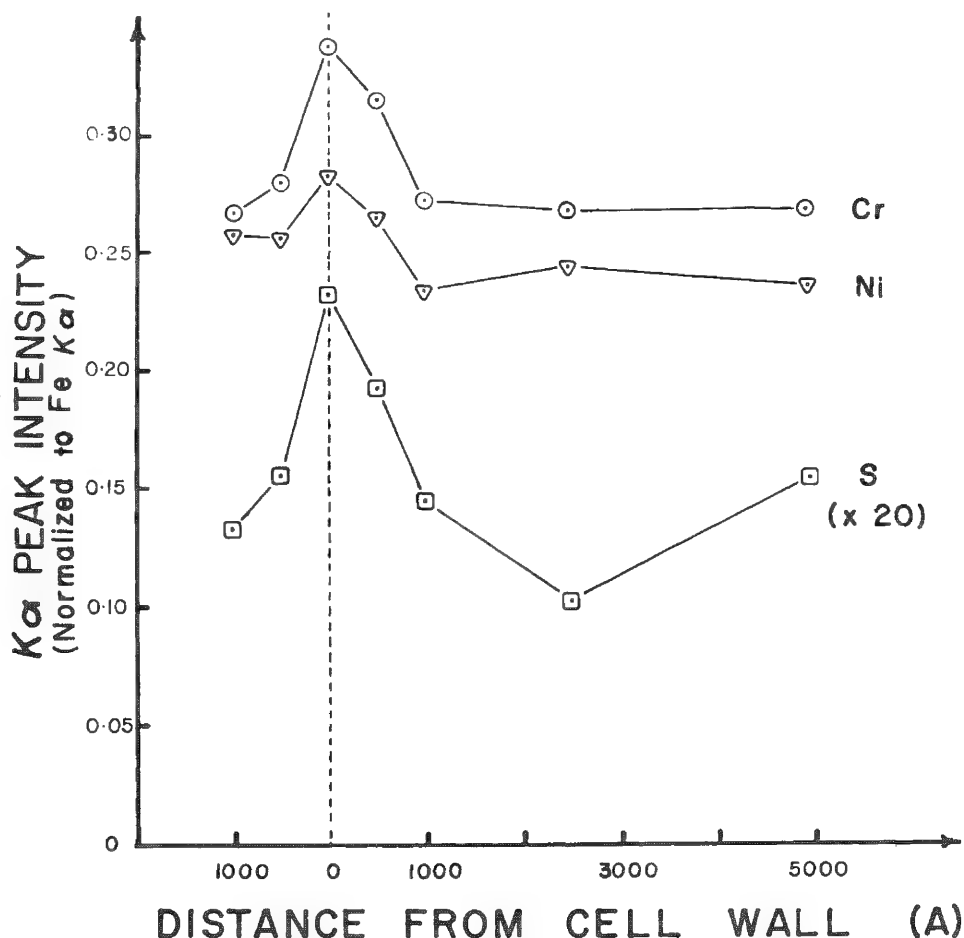


FIG. 3.--Composition profile obtained across dendrite cell wall in rapidly solidified 303 stainless steel powder particle with cellular solidification structure.

Analysis of Mineral Specimens. This research, part of an investigation of lunar rock samples, involves a class of silicate minerals that contain 50% SiO_2 , with the balance composed of a mixture of magnesium, calcium, and iron oxides, plus trace elements. X-ray spectrometry is being used to determine the Mg:Ca:Fe ratio in a variety of microstructural features, including an antiphase domain structure produced by an ordering transition, and a very fine lamellar structure (Fig. 4) produced by phase separation in a region of immiscibility. By the study of samples prepared and treated in the laboratory, a knowledge of the phase diagram is being obtained. The intent is then to use the microstructural and microchemical data obtained from actual samples to determine their probable thermal histories, a rich source of geological information.

The Technique and Use of Foil Thickness Determination

As mentioned previously, when one is attempting to do quantitative x-ray analysis in the STEM, it is often of considerable importance to know the thickness of the sample at

the analysis point, so as to account for possible absorption of the x-ray signal of interest in the sample. The foil thickness plays a further role in situations in which it is desirable to take beam spreading in the sample (which is strongly dependent on the thickness) into consideration. The segregation/depletion studies described above are an important example, especially when the spatial extent of the segregation is limited to the order of a few tens of nanometers. The procedure for correcting for absorption effects, when they have been identified as important, has been adequately described¹ and will not be discussed further here. To include beam spreading in the analysis requires some knowledge or model of the extent of the spreading. We have developed a simple approach to the problem, discussed below.

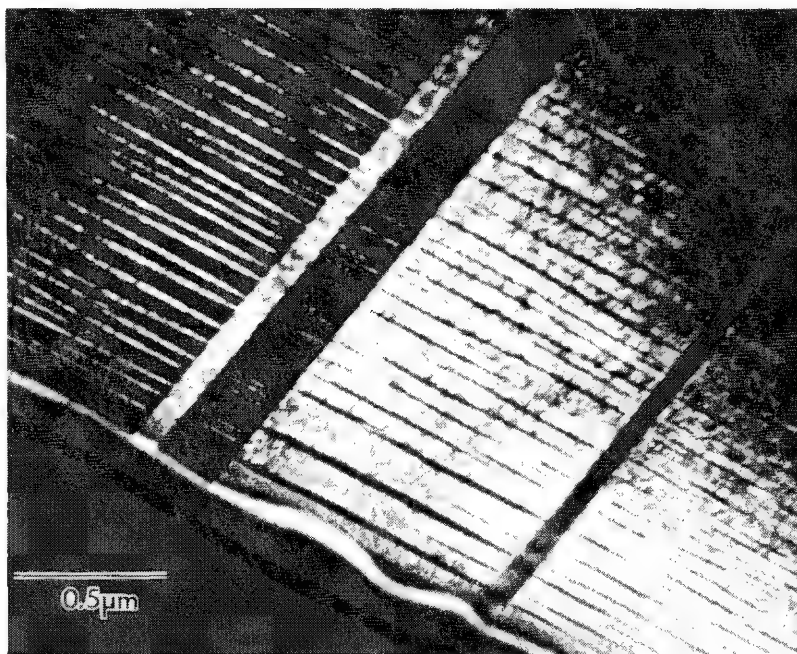


FIG. 4.--Dark-field conventional TEM micrograph showing typical microstructure of mineral specimens being analyzed. Of particular interest is compositional analysis of the two lamellar phases.

Accurate measurement of foil thicknesses has long been recognized as a major problem in all areas of electron microscopy. The STEM configuration, where a small electron probe is focused onto the sample, is particularly suitable for the convergent-beam diffraction technique for measuring thickness, provided of course that the material is crystalline. In this technique the three-dimensional diffraction information that distinguishes convergent-beam diffraction from "normal" diffraction is used to obtain a measurement of the foil thickness. The theory and application of the technique are particularly simple for a crystal set in a "two-beam" diffracting condition, as has been described in detail elsewhere.^{2,3} The technique is relied on quite heavily in the work at MIT, as it can be very precise, with accuracies better than 5% achievable in many cases. There is a limitation: for given conditions there is a thickness range outside of which analysis is not feasible because of a combination of factors both instrumental and intrinsic to electron diffraction processes. However, by a considered choice of the reflecting vector \bar{g} the maximum determinable thickness can be made large enough for most applications. To obtain a good convergent-beam pattern requires a locally near-perfect crystal structure; hence it is sometimes difficult to apply the technique to, for example, heavily dislocated foils. In such cases, and in some others involving complex materials or complex materials processing, the addition of a large elastic diffuse component to the intensity within the convergent beam disk sharply reduces the fringe contrast and hence the maximum foil thickness that can be determined. Thus, although a very useful and accurate technique, convergent-beam diffraction should not be regarded as a complete solution to the problem of thickness measurement.

To take some account of the effect of beam spreading, we have developed the use of a

parameterized function to model the electron intensity distribution, where the parameters can be varied to achieve best-fit theoretical or experimental values for the spreading. An analytic expression for the x-ray emission from a region of known or modeled composition variation can then be obtained. We have considered in detail the problem of segregation to a grain boundary using this type of analysis, described elsewhere.⁴ The result is that by a computationally simple calculation, one can reveal in some detail the expected consequences of substantial beam broadening in a given experimental situation. This capability allows better experimental insight and hence experiment design, as well as the possibility of better data interpretation. An example of the use of such calculations, referred to the problem of segregation to a grain (or dendrite cell, or other) boundary, is illustrated in Fig. 5. These calculated curves clearly explain the general features of observed profiles, especially the changes resulting from increased foil thickness. In addition, the experimental importance of retaining a sufficiently small incident probe, even when substantial beam spreading occurs, is demonstrated.

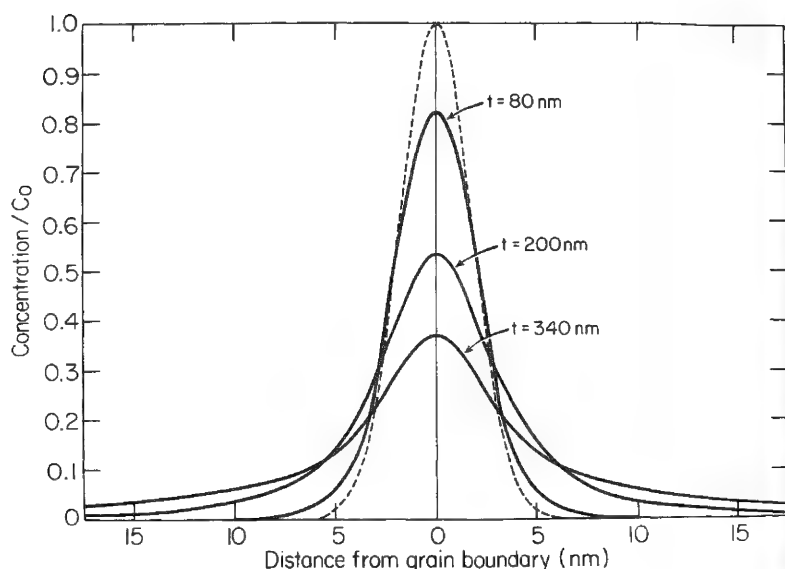


FIG. 5.--Calculated profiles of concentration variation near grain boundary normalized to true peak value C_0 that would be determined from experiment, for various values of foil thickness t . Dashed curve shows true concentration variation. Beam was assumed to be Gaussian with half-width of 1 nm.

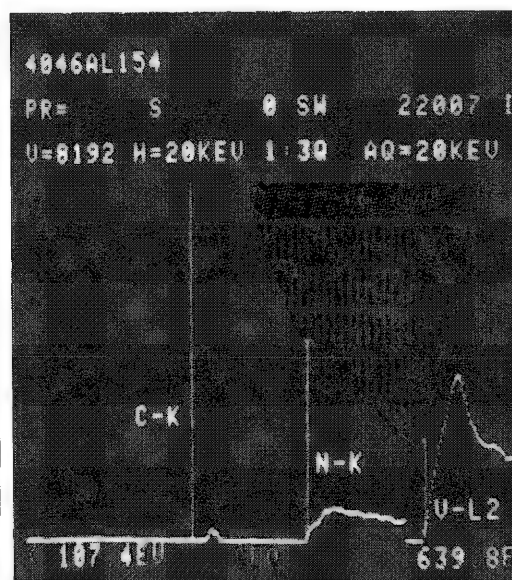


FIG. 6.--Electron energy-loss spectrum from precipitate indicated in Fig. 1. Upper curve, separating gray area from black area, is raw spectrum. Lower, white curve shows spectrum with background stripped for regions near carbon-K, nitrogen-K, and vanadium- L_{2-3} edges.

Electron Energy Loss Spectroscopy

Electron energy loss spectroscopy (EELS) can potentially convey a wealth of information about a specimen. This field is rapidly developing as workers strive to perfect spectrometers with improved transmission and resolution. Even a modest system can yield most useful and otherwise unobtainable results. The spectrometer system on the HB5 at MIT falls into this category. At present its use is exclusively the detection of light ($3 < Z < 9$) elements in specimens. By sacrificing resolution to sensitivity, and by interfacing the spectrometer to a commercial multichannel analyzer and computer, supplied with commercial spectrum manipulation software, one can now routinely perform qualitative analysis for boron, carbon, nitrogen, and oxygen. Elemental overlaps do occur, as with any analytical technique, but combination of EELS with energy-dispersive x-ray analysis can often resolve them. Typical specimens to which EELS is applied are steels containing precipitates. The metallic content of the precipitate may be determined from the x-ray spectrum, and EELS used to ascertain the light-element constituents.

It is often necessary to take precautions against contamination buildup on the speci-

men, particularly if carbon analysis is desired. In the HB5, with a vacuum in the specimen chamber better than 2×10^{-9} torr, contamination is never observed on a specimen that was known to be clean prior to insertion. Contamination is evidently a problem of specimen preparation, and precautions are taken at the preparation stage; for instance, a gentle bake in a moderate vacuum is frequently found to be very helpful in eliminating contamination.

Many precipitates can be observed in thin foils of the material of interest. In the case of particularly small particles, however, it is usually necessary to extract them onto a replica for analysis. Carbon extraction replication is a standard technique, but the deliberate introduction of carbon prevents analysis for that element. Instead, aluminum extraction replicas may be made. Figure 1 is a photograph of such a replica. As has been described earlier, the dark spots are vanadium precipitates. Thermodynamics predicted that with the history of this particular specimen these precipitates should be vanadium nitride, but mechanical testing, and in particular the observation that the properties of this steel seemed quite independent of the nitrogen content, had cast doubts on this prediction, and the presence of carbon was suggested. Figure 6 shows the EELS spectrum from the indicated precipitate. Strong vanadium L_{2-3} and nitrogen K absorption edges are seen, but there is only a small suggestion of a signal near the carbon edge. In fact, it is concluded from the average of the results from many specimens that the carbon level is below the limits of detection, and that the composition of the particle is $V(C_{<0.1}, N_{>0.9})$. Thus the thermodynamic prediction appears to be verified, and the explanation of the properties of the steel must be sought elsewhere.

Polymers Research by Means of the STEM

A further strength of scanning transmission electron microscopy is the ability of the instrument to allow for the combination of various signals electronically in an effort to enhance contrast. The argument of Crewe et al.⁵ is that the annular detector collects a signal that arises primarily from elastic scattering which, when combined by a ratio technique with the energy loss signal associated with inelastic scattering, provides enhanced contrast from samples containing elements of differing atomic number. Applications of this technique include single-atom images and detailed observations on supported catalysts.⁶

Contrast and sample stability in the beam are a major concern in the study of polymers. To improve contrast in polymer thin sections the usual technique is to stain the polymer selectively with a heavy metal. Figure 7 shows a normal bright-field image of a deformed polystyrene/polybutadiene high-impact polystyrene that has been stained with osmium tetroxide. It can be seen that the rubbery phase (polybutadiene) has been stained selectively in this way. In the ratio image from the same area, a shear band has been delineated. It is easily seen that the amount of stain in this feature produces sufficient contrast to yield a quality image in the ratio imaging mode, but insufficient contrast for bright-field observation.

An effort is under way to develop a staining technique based on differences in diffusion rates of uranyl acetate between more and less dense regions in polymers. Cured epoxies and semicrystalline polyethylene exhibit these density variations in the microstructure, and uranyl acetate will diffuse to a greater extent in the less-dense regions. The relative difference in number of uranium atoms is sufficient to yield the contrast shown in the ratio images of Fig. 8 for a semicrystalline polyethylene sample stained in this way.

Ultra-thin Window Detector

The standard energy-dispersive x-ray detector employs a lithium-drifted silicon crystal to convert the x-ray energy into an electric charge of proportional magnitude. The physics of the crystal itself imparts a lower limit of about 300 eV on the range of measurable x-ray energies. However, the dirty vacuum of most detectors makes it necessary to protect the crystal with a thin beryllium window, which has the undesired effect of absorbing x rays with energies below about 1.5 keV. In microscopes such as the HB5, with excellent specimen chamber vacuum, this window is not necessary, and manufacturers are now offering "windowless" or "ultra-thin window" detectors and promising use of energy-dispersive x-ray analysis to measure elements with $Z \geq 6$. Such a detector has been purchased at MIT, and its

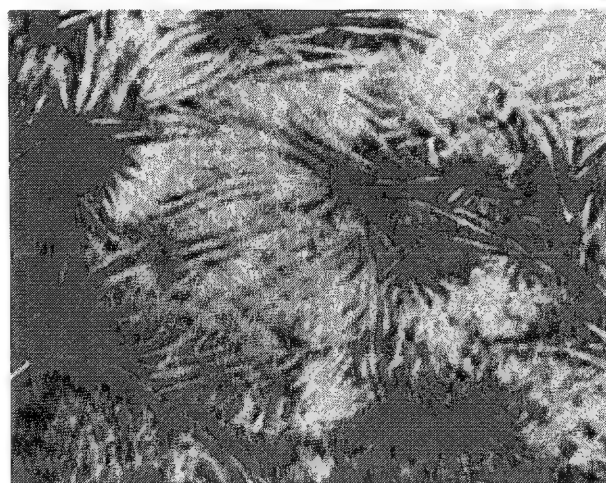
usefulness is being urgently evaluated, for it is hoped that the disadvantages of EELS (thickness limitations of the specimen, and inconvenience) may be partially overcome by use of this device.



BF

0.4 μm

FIG. 7.--STEM-image of polystyrene-polybutadiene. In lower, unprocessed image, only polybutadiene islands are seen, but after image processing (upper image) a shear band, other invisible, is seen.



0.2 μm

FIG. 8.--STEM-image with processing of semi-crystalline polyethylene stained with uranyl acetate.

Operation and Education

Our policy in the operation of the analytic microscopy capability is based on making a high level of expertise available to all users, from encouragement and advice through to complete technical assistance when appropriate, rather than an extensive "blanket" training program. Such a service, for a staff already heavily involved in research and in developing the research capabilities further, does mean that an important part of our effort is educational. Our purpose is both to create some general awareness of the capabilities and limitations of analytical electron microscopy among the materials science community here, and to provide detailed information to those who are especially interested. We also try not to add to an already considerable burden of formal courses for most students, and to include nonstudent members of the community. The result is coverage in a well-attended, informal seminar series that discusses all aspects of the practical application of electron microscopy in materials science; in the case of AEM, we also offer a short, intensive lecture course once a year (during MIT's pre-spring-semester Independent Activities Period, a time ideally suited for our purpose). This arrangement covers the general educational need quite well, and (together with a limited academic

course coverage) leaves only the in-depth training of those people who will become skilled users of the machines themselves. Such training applies to relatively few people at any one time, and is hence done by a combination of small group sessions and individual, guided experience.

Conclusion

The HB5 at MIT was purchased as a tool. It has proved to be an extremely valuable one. As more members of the faculty and research staff appreciate the information that can be obtained by focusing a small intense beam of electrons onto their samples and studying the products of the resulting interaction, ever more ingenious experiments are devised. Already much of the sense of "wonder" about the instrument has faded. Workers in many fields, not themselves skilled electron microscopists, reserve time as a matter of course to study their various problems.

Using the full potential of STEM is a complicated endeavor. However, with a mix of professional advice, education--both direct and practical and broad and conceptual--and technical help, a wide range of otherwise intractable problems is being solved routinely and without fanfare.

References

1. J. J. Hren, J. I. Goldstein, and D. C. Joy, *Analytical Electron Microscopy*, New York: Plenum Press, 1979, chaps. 3 and 4.
2. P. M. Kelly, A. Tostsons, R. G. Blake, and J. G. Napier, *Phys. Stat. Sol.* A31: 771, 1975.
3. S. M. Allen, *Phil. Mag.* 43: 325, 1981.
4. E. L. Hall, D. Imeson, and J. B. VanderSande, *Phil. Mag.* (in press).
5. A. V. Crewe, J. P. Langmore, and M. S. Isaacson, in B. Siegel and D. Beaman, Eds., *Physical Techniques of Electron Microscopy and Microbeam Analysis*, New York: Wiley, 1975.
6. M. M. J. Treacy, A. Howie, and C. J. Wilson, *Phil. Mag.* 38: 569, 1978.

QUANTITATIVE X-RAY MICROANALYSIS OF U-Nb ALLOYS WITH THE SCANNING TRANSMISSION ELECTRON MICROSCOPE

A. D. Romig Jr.

The transmission electron microscope (TEM) and scanning transmission electron microscope (STEM) are currently being used to study phase transformations in uranium rich U-Nb alloys. To perform quantitative STEM x-ray microanalysis successfully, several problems must be solved. One problem is sample preparation since these alloys react strongly to most chemical solutions and oxidize readily in air. In addition, the high average atomic number of this material requires characterization of electron penetration, x-ray absorption, and electron-beam spreading within the foil. It is the objective of this paper to describe the techniques developed to make quantitative x-ray microanalysis on these alloys possible. Included are the experimental determination of the Cliff-Lorimer k_{NbU} factor at 100 and 200 kV and an examination of the limitations of this analysis technique, including x-ray spatial resolution and x-ray absorption, as applied to U-Nb alloys.

Background

The characteristic x-ray spectra for U and Nb are quite complex. Each element produces many characteristic x-ray lines below 20 keV, which can be detected with solid-state x-ray detectors. In many cases several characteristic lines are separated by energy differences that are smaller than the resolution of the energy-dispersive x-ray spectrometer (about 150 eV). The detector cannot resolve these lines. Table 1 summarizes the characteristic x-ray lines for U and Nb. Owing to the resolution limit of the detector, the Nb $L\alpha_1$, $L\beta_1$, $L\beta_2$, $L\gamma_1$, and $L\gamma_3$ lines merge into one large peak. The Nb $L\alpha_1$ line is by far the most intense; hence this peak will be simply called $\text{Nb}_{L\alpha}$. Similarly, the $\text{Nb}_{K\alpha_1}$ and $\text{Nb}_{K\alpha_2}$ lines cannot be resolved. For U, the M_α , M_β and M_γ lines merge, as do the L_α and L_{α_2} lines. For quantitative analysis the $\text{Nb}_{L\alpha}$ or $\text{Nb}_{K\alpha}$ lines and the $\text{U}_{L\alpha}$ or $\text{U}_{M_{\alpha+\beta+\gamma}}$ lines may be used. If the $\text{Nb}_{K\alpha}$ peak is used, several interfering U lines must be stripped from the $\text{Nb}_{K\alpha}$ lines since the spectrometer cannot resolve the $\text{U}_{L\beta_2}$ and $\text{U}_{L\beta_4}$ lines from the $\text{Nb}_{K\alpha}$ line. The $\text{U}_{M_{\alpha_2}}$ line is too weak to interfere with the Nb_L lines.

Elemental C_2 compositions can be calculated from x-ray intensity data with the Cliff-Lorimer standardless ratio technique. The Cliff-Lorimer relation for U-Nb is given by:

$$\frac{C_{\text{Nb}}}{C_{\text{U}}} = k_{\text{NbU}} \frac{I_{\text{Nb}}}{I_{\text{U}}} \quad (1)$$

where C_{Nb} and C_{U} are the weight fraction of Nb and U, respectively, and I_{Nb} and I_{U} are the Nb and U intensities, respectively. The Cliff-Lorimer k-factor k_{NbU} can be calculated from first principles or it can be determined experimentally.

Experimental determination of the k-factor requires homogeneous single phase alloys. Figure 1 shows the U-Nb phase diagram.¹ Above 800°C the uranium-rich alloys (≤ 10 w/oNb) exist as γ_1 -phase (bcc) solid solutions. If quenched from 800°C to room temperature these alloys transform martensitically to a single metastable phase in which all the niobium is retained in a supersaturated solid solution suitable for determining k-factors.

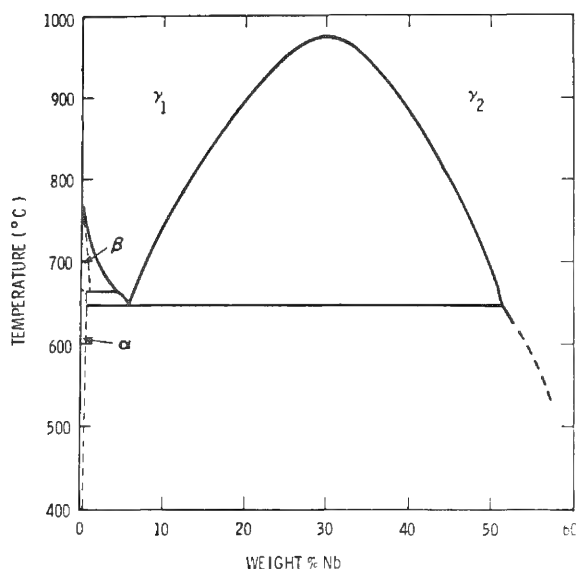
X-ray spatial resolution also is an important consideration in the study of phase transformations with STEM techniques. A fine two-phase structure is a suitable sample with which to investigate x-ray spatial resolution.² The solid solution (γ_1) which exists at 800°C in the U-Nb system (Fig. 1) presumably transforms during slow cooling by monotectoid decomposition into the equilibrium two-phase α (orthorhombic) and γ_2 (bcc) below 647°C. Such decomposition transformations usually produce a fine two-phase lamellar structure.

The author is at the Sandia National Laboratories, Albuquerque, N.M. Sandia National Laboratories is a U. S. Department of Energy facility; the work was supported by DOE under contract DE-AC04-76DP00789. The assistance of W. R. Sorenson in the experimental work and the careful manuscript review by K. H. Eckelmeyer are sincerely appreciated.

TABLE 1.--Observed characteristic x-ray lines.

Uranium		Niobium	
Line Energy (keV)	Line(s)	Line Energy (keV)	Line(s)
2.51	M_{ζ_2}	1.91	L_{ℓ}
3.17	M_{α}	2.00	L_{η}
3.34	M_{β}	2.16	L_{α_1}
3.56	M_{γ}	2.26	L_{β_1}
4.40	M_{η}	2.36	L_{β_2}
11.62	L_{ℓ}	2.46	L_{γ_1}
13.44	L_{α_2}	2.66	L_{γ_3}
13.62	L_{α_1}	16.52	K_{α_2}
15.40	L_{η}	16.61	K_{α_1}
16.43	L_{β_2}	18.62	K_{β_1}
16.58	L_{β_4}	18.95	K_{β_2}
17.22	L_{β_1}		
17.46	L_{β_3}		
20.17	L_{γ_1}		

*Peaks as resolved.

FIG. 1.--U-Nb phase diagram.¹

Experimental Procedure

The Cliff-Lorimer factor k_{NbU} was determined experimentally with homogeneous single-phase alloys (U-2.3w/oNb, U-4.2w/oNb, U-6.0w/oNb, U-7.9w/oNb). The alloys were vacuum homogenized (10^{-4} Torr) at 850°C for 10 days. Following homogenization the alloys were water quenched so that the γ_1 transformed martensitically to a metastable single-phase supersaturated solid solution.

The samples used for the x-ray spatial-resolution experiments were produced by slow cooling (0.04°C/sec) a U-6w/oNb alloy from the γ_1 field into the $\alpha + \gamma_2$ field. A fine $\alpha + \gamma_2$ two-phase lamellar microstructure resulted. X-ray diffraction was used to verify that the sample indeed contained an orthorhombic (α) and a bcc (γ) phase. The constituent α and γ_2 laths were less than 2000 Å wide. Figure 2 shows the lamellar microstructure as observed with the SEM and the TEM.

The alloys were heat treated in bulk form. Samples were then sliced ($\sim 375 \mu\text{m} \approx 0.015 \text{ in.}$) on a slow-speed diamond saw and ground to a thickness of approximately 250 μm (0.01 in.).

Disks 3 mm in diameter were cut with a mechanical punch. The disks were ground to a thickness of approximately 50 μm (0.002 in.). The edges of the foils were painted with microstop. The thin foils were prepared by the window technique with a solution (-10 to -15°C) containing 150 ml of methanol, 50 ml of butyl cellusolve, and 4 ml of perchloric acid employing a stainless-steel cathode. Thinning was done with a potential of 20 volts. Ion-beam thinning or cleaning was not possible because enough residual O_2 remained in the ion thinner chamber to cause excessive oxidation. The foils were analyzed with a JEM 100C STEM/TEM and a JEM 200 CX TEM. The 100C was equipped with a Kevex detector and multichannel analyzer (MCA) and the 200 CX was equipped with a Nuclear Semiconductor solid-state detector and a Tracor Northern MCA.

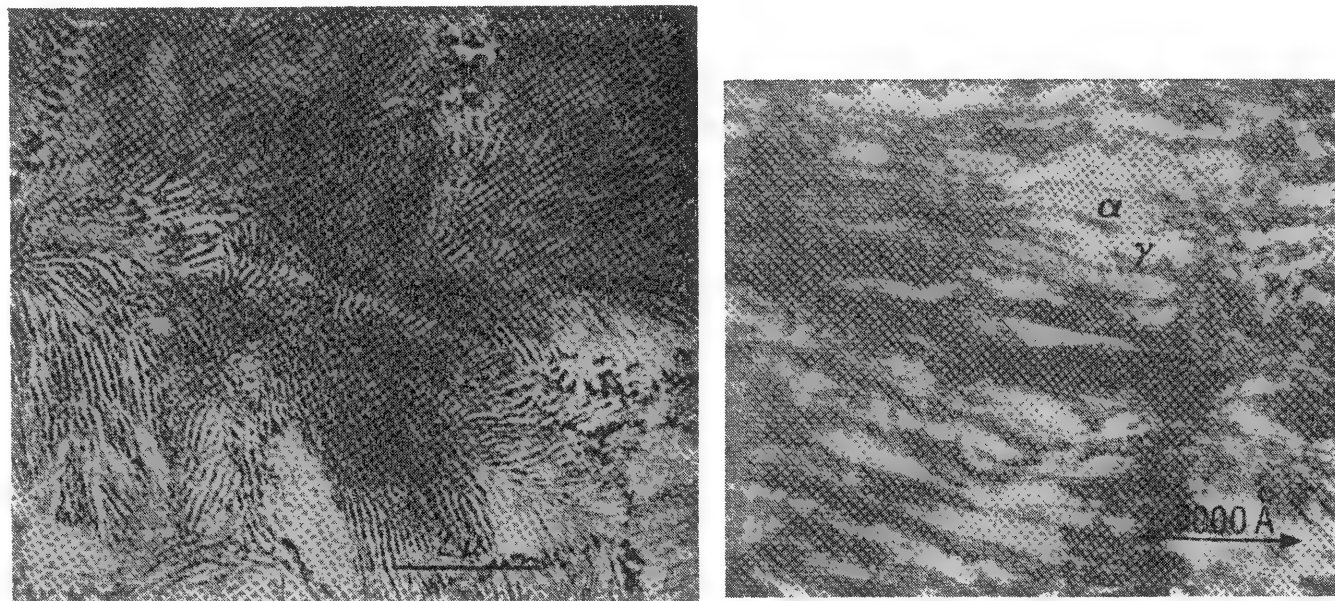


FIG. 2.--(Left) SEM micrograph of U-6 w/oNb alloy cooled from 800°C to room temperature at 0.040°C/s; two-phase structure $\alpha + \gamma$; scale bar = 2 μm . (Right) TEM bright field micrograph of U-6 w/oNb alloy cooled from 800°C to room temperature at 0.040°C/s; two-phase structure of $\alpha + \gamma$; scale bar = 5000 \AA .

Results and Discussion

Determination of k_{NbU} . To improve the statistical quality of the data used to calculate k_{NbU} the total number of accumulated counts must be maximized.² The data used to calculate k_{NbU} at 100 and 200 kV were obtained in the TEM mode with a focused beam approximately 2 μm in diameter. This large spot size produced a high x-ray intensity. However, the spot was still small enough so that all the x-rays were generated in thin regions of the foil. Four combinations of characteristic Nb and U lines were used to calculate four different k_{NbU} factors: $\text{Nb}_{\text{K}\alpha} - \text{U}_{\text{L}\alpha}$, $\text{Nb}_{\text{L}\alpha} - \text{U}_{\text{L}\alpha}$, $\text{Nb}_{\text{K}\alpha} - \text{U}_{\text{M}\alpha, \beta, \gamma}$ and $\text{Nb}_{\text{L}\alpha}$ and $\text{Nb}_{\text{L}\alpha} - \text{U}_{\text{M}\alpha, \beta, \gamma}$.

In order to use the $\text{Nb}_{\text{K}\alpha}$ peak it was necessary to strip the interfering $\text{U}_{\text{L}\beta 2}$ and $\text{U}_{\text{L}\beta 4}$ lines from the spectra with a numerical procedure. The $\text{U}_{\text{L}\alpha}/(\text{U}_{\text{L}\beta 2} + \text{U}_{\text{L}\beta 4})$ intensity ratio was measured in pure U. At 100 kV it was 3.85 ± 0.05 and at 200 kV it was 3.88 ± 0.05 . The $\text{U}_{\text{L}\beta 2} + \text{U}_{\text{L}\beta 4}$ intensity in the U-Nb alloys was calculated by dividing the $\text{U}_{\text{L}\alpha}$ intensity by the appropriate correction factor. The resulting value was subtracted from the $\text{Nb}_{\text{K}\alpha} + \text{U}_{\text{L}\beta 2} + \text{U}_{\text{L}\beta 4}$ peak to obtain the true $\text{Nb}_{\text{K}\alpha}$ intensity. With this empirical corrector, it was possible to strip the U lines from the $\text{Nb}_{\text{K}\alpha}$ peak in the spectra measured on the U-Nb alloys.

The peak intensities were determined by integration over the full peak widths. Table 2 summarizes the typical window widths used for each group of characteristic lines. At least six spectra were measured in each alloy. X-ray counts were accumulated for 60 s with a take-off angle of 45°. The $\text{U}_{\text{L}\alpha}$ integrated intensity was typically on the order of

10 000 counts. Table 3 summarizes the results of the k_{NbU} determinations. These data show clearly that k_{NbU} does not vary with composition. The error limits were calculated directly from x-ray counting statistics.^{2,3} Blank spaces in the data tabulation indicate that the $\text{Nb}_{\text{L}\alpha}$ peak intensity could not be determined accurately under those specific experimental conditions. The value of each k_{NbU} does not vary greatly with accelerating voltage. This result is to be expected for x-ray excitation in heavy elements like U and Nb. However, the average values of k_{NbU} determined at 200 kV are consistently larger than the values of k_{NbU} determined at 100 kV.

TABLE 2.--Typical window widths.

Window (KeV)	Inclusive Lines
2.08-2.86	$\text{Nb}_{\text{L}\alpha 1}, \text{Nb}_{\text{L}\beta 1}, \text{Nb}_{\text{L}\beta 2}, \text{Nb}_{\text{L}\gamma 1}, \text{Nb}_{\text{L}\gamma 3}$
3.00-3.72	$\text{U}_{\text{M}\alpha}, \text{U}_{\text{M}\beta}, \text{U}_{\text{M}\gamma}$
13.40-13.88	$\text{U}_{\text{L}\alpha 1}, \text{U}_{\text{L}\alpha 2}$
16.36-16.88	$\text{Nb}_{\text{K}\alpha 1}, \text{Nb}_{\text{K}\alpha 2}^*$

*The $\text{U}_{\text{L}\beta 2}$ and $\text{U}_{\text{L}\beta 4}$ lines must be stripped numerically from the $\text{Nb}_{\text{K}\alpha}$ lines.

TABLE 3.--Summary of experimental k_{NbU} results.

100 kV					
Characteristic Lines	Alloy				Average
	U-2.3 Nb	U-4.2 Nb	U-6.0 Nb	U-7.9 Nb	
Nb _{Kα} - U _{Lα}	0.56 ± 0.04	0.57 ± 0.02	0.53 ± 0.01	0.57 ± 0.01	0.56 ± 0.04
Nb _{Lα} - U _{Lα}	---	---	0.39 ± 0.02	0.39 ± 0.02	0.39 ± 0.03
Nb _{Kα} - U _{Mα+β+γ}	0.80 ± 0.06	0.82 ± 0.07	0.86 ± 0.04	0.83 ± 0.05	0.83 ± 0.07
Nb _{Lα} - U _{Mα+β+γ}	---	---	0.51 ± 0.04	0.47 ± 0.07	0.49 ± 0.07

200 kV					
Characteristic Lines	Alloy				Average
	U-2.3 Nb	U-4.2 Nb	U-6.0 Nb	U-7.9 Nb	
Nb _{Kα} - U _{Lα}	0.61 ± 0.02	0.58 ± 0.04	0.63 ± 0.03	0.64 ± 0.02	0.61 ± 0.04
Nb _{Lα} - U _{Lα}	---	---	0.39 ± 0.02	0.42 ± 0.03	0.41 ± 0.03
Nb _{Kα} - U _{Mα+β+γ}	0.84 ± 0.04	0.88 ± 0.05	0.82 ± 0.05	0.84 ± 0.04	0.85 ± 0.05
Nb _{Lα} - U _{Mα+β+γ}	---	---	0.53 ± 0.06	0.56 ± 0.05	0.55 ± 0.06

It is possible to calculate the theoretical value of k_{NbU} called k_{NbU}^* from first principles with the following equation:⁴

$$k_{\text{NbU}}^* = \frac{A_{\text{Nb}}(Q\omega a)_{\text{U}}}{A_{\text{U}}(Q\omega a)_{\text{Nb}}} \quad (2)$$

where A is the atomic number, Q is the ionization cross section, ω is the fluorescence yield, and a is the fraction of K or L line intensity which is measured as K_{α} or L_{α} . This value of k_{NbU}^* must be corrected for x-ray absorption in the solid-state detector by the Be window (BeF), the Au layer (AuF), and the Si dead layer (SiDLF). The measurable value of k_{NbU} then becomes

$$k_{NbU} = k_{NbU}^* \cdot \text{BeF} \cdot \text{AuF} \cdot \text{SiDLF} \quad (3)$$

where

$$\text{BeF} = \frac{\exp(-\mu/\rho|_{\text{Be}}^{\text{U}} \rho_{\text{Be}} t_{\text{window}})}{\exp(-\mu/\rho|_{\text{Be}}^{\text{Nb}} \rho_{\text{Be}} t_{\text{window}})} \quad (4a)$$

$$\text{AuF} = \frac{\exp(-\mu/\rho|_{\text{Au}}^{\text{U}} \rho_{\text{Au}} t_{\text{Au}})}{\exp(-\mu/\rho|_{\text{Au}}^{\text{Nb}} \rho_{\text{Au}} t_{\text{Au}})} \quad (4b)$$

$$\text{SiDLF} = \frac{\exp(-\mu/\rho|_{\text{Si}}^{\text{U}} \rho_{\text{Si}} t_{\text{Si}})}{\exp(-\mu/\rho|_{\text{Si}}^{\text{Nb}} \rho_{\text{Si}} t_{\text{Si}})} \quad (4c)$$

where μ/ρ = absorption coefficients for Nb and U x rays in Be, Au, and Si; ρ = bulk densities; and t = thickness of the Be window, Au layer, and Si dead layer.

The data needed to make the calculations for Eqs. (2)-(4) are well known for K lines. Some good data exist for L lines, but they are not nearly as complete or accurate as the K line data. Fundamental data for the M lines are virtually unknown. With Eqs. (2)-(4) k_{NbU} has been calculated at 100 and 200 kV for the K and L line combinations. Table 4 summarizes data sources or input data and the calculated results. The agreement between the experimentally determined and calculated values of k_{NbU} is excellent.

TABLE 4.--Input data for the calculation of k_{NbU} .

Variable	Source
Q	Goldstein et al. ⁴ ; Green and Coslett ⁵ ; Powell ⁶
ω	Wentzel ⁷
a	Slivinsky and Ebert ⁸ (K-lines); Heinrich ⁹ (K-lines); Scofield ¹⁰ (L-lines)
μ/ρ	Leroux ¹¹ (parameterized form to be computer compatible)
Thickness values	
Be window, 7.5 μm	Manufacturer's specifications (Kevex, Nuclear Semiconductor)
Au layer, 200 \AA	Zaluzec ¹²
Si dead layer, 0.3 μm	Zaluzec ¹²
<u>Calculated Results</u>	
Characteristic lines	100 kV 200 kV
Nb K_{α} - U L_{α}	0.61 kV 0.64 kV
Nb L_{α} - U L_{α}	0.35 kV 0.42 kV

Absorption Effects. The Cliff-Lorimer relation (Eq. 1) applies only when absorption and fluorescence effects are not significant. If either of these effects is significant, the thin-film criterion is not satisfied. With respect to absorption, the thin-film criterion is violated if⁴

$$\{1/2[\mu/\rho|_{\text{Spec}}^{\text{U}} - \mu/\rho|_{\text{Spec}}^{\text{Nb}}] (\csc \alpha) \rho t\} < 0.1 \quad (5)$$

where $\mu/\rho|_{\text{spec}}$ are the absorption coefficients of the U and Nb lines of interest in the specimen, α is the take-off angle, ρ is the specimen density, and t is the foil thickness at the point of the analysis. The thickness at which the thin-film criterion is violated

has been calculated for several U-Nb alloys. The results are listed in Table 5. These results indicate that at least with regards to absorption within the foil the best characteristic emission combinations are $Nb_{K\alpha}$ with $U_{L\alpha}$ and $Nb_{L\alpha}$ with $U_{M\alpha}$. Absorption effects generally become significant at lesser thicknesses than fluorescence effects. Hence, if absorption is not significant, fluorescence also should not be significant.

TABLE 5.-- Thin film criterion.
Absorption Coefficients¹¹ (μ/ρ in cm^2/g)

Absorber	Exciter			
	$Nb_{K\alpha}$	$Nb_{L\alpha}$	$U_{L\alpha}$	$U_{M\alpha}$
Nb	21.7	812.6	36.7	752
U	62.1	175.5	101.7	1776
U-10Nb	58.1	1673	95.2	1658

Thickness Limits

Line Combination	Composition			
	U-2Nb	U-5Nb	U-10Nb	U-20Nb
$Nb_{K\alpha} - U_{L\alpha}$	2.1 μm	2.3 μm	2.4 μm	2.6 μm
$Nb_{L\alpha} - U_{L\alpha}$	480 \AA	500 \AA	530 \AA	550 \AA
$Nb_{K\alpha} - U_{M\alpha} + \beta + \gamma$	460 \AA	480 \AA	500 \AA	530 \AA
$Nb_{L\alpha} - U_{M\alpha} + \beta + \gamma$	4.9 μm	5.2 μm	5.4 μm	5.9 μm

To verify the predicted absorption effects experimentally, a STEM trace was taken from the edge of a single-phase U-6w/oNb foil inward to the point where electron transparency was lost.* The thickness of the foil at each analysis point was determined by tilting the foil after the analysis and measuring the apparent displacement between the contamination spots on the top and bottom of the foil. Figure 3 shows the results of these experiments. Figure 3a shows the Nb/U intensity ratio for $Nb_{K\alpha}$ and $U_{L\alpha}$ lines as a function of thickness. The theoretical ratio corresponds to nominal alloy composition U-6Nb. The data demonstrate that no significant absorption occurs up to a foil thickness of about 5500 \AA . Figure 3b shows the data for the $Nb_{K\alpha}$ and $U_{M\alpha}$ peaks. In agreement with Table 5, absorption effects become significant if the foil thickness exceeds 500 \AA . The experimental data show the apparent increase in I_{Nb}/I_U as the $U_{M\alpha}$ is preferentially absorbed.

Tixier and Philibert¹⁶ and Goldstein et al.⁴ have proposed an absorption correction term of the following form:

*The limit of electron transparency here means the thickness at which the electron transmission has been reduced to the point where the photographic plate will no longer record the incident electron flux. This thickness is well beyond the normal thickness used for TEM/STEM work at 100 kV. The observed electron transmission goes to zero at a thickness of approximately 5500 \AA . These electron penetration observations are consistent with the electron range model of Kanaya and Okayama¹³ and extrapolated values from the experimental observations of Coslett and Thomas.^{14,15}

$$\frac{C_A}{C_B} = k_{AB} \frac{I_A}{I_B} \frac{\mu/\rho|_A^{\text{Spec}}}{\mu/\rho|_B^{\text{Spec}}} \frac{1 - \{\exp[-\mu/\rho|_B^{\text{Spec}}(\csc \alpha)(\text{pt})]\}}{1 - \{\exp[-\mu/\rho|_A^{\text{Spec}}(\csc \alpha)(\text{pt})]\}} \quad (6)$$

Equation (6) can be rearranged and used to correct the observed intensity ratio for absorption effects. Rearrangement and direct application to U-Nb yields:

$$\frac{I_{\text{Nb}}}{I_{\text{U}}} = \frac{C_{\text{Nb}}/C_{\text{U}}}{k_{\text{NbU}}} \frac{\mu/\rho|_{\text{Spec}}^{\text{U}}}{\mu/\rho|_{\text{Spec}}^{\text{Nb}}} \frac{1 - \{\exp[-\mu/\rho|_{\text{Spec}}^{\text{Nb}}(\csc \alpha)(\text{pt})]\}}{1 - \{\exp[-\mu/\rho|_{\text{Spec}}^{\text{U}}(\csc \alpha)(\text{pt})]\}} \quad (7)$$

With the measured thickness values, the absorption coefficients listed in Table 5, and Eq. (7), the raw $I_{\text{Nb}}(\text{NbK}\alpha)/I_{\text{U}}(\text{UM}\alpha)$ data in Fig. 3b can be corrected for absorption effects. Figure 3b also shows the results following the absorption correction.

X-ray spatial resolution. X-ray spatial resolution was investigated with the $\alpha + \gamma_2$ lamellar microstructure in a slow cooled U-6w/oNb sample. The analysis was made at 100 kV with a 180 Å probe in a region of the foil which was nominally 600 Å thick. A 60s count time was used for each analysis. The increment between analyses points was about 400 Å. Figure 4 shows the results of this trace. According to the data, the x-ray spatial resolution under these experimental conditions is less than 800 Å. An analysis point completely within the γ -phase indicates that the γ -phase contains about 12 w/oNb. An adjacent analysis point, 400 Å closer to the α/γ interface, shows an average composition in the range of 5-9 w/oNb. This composition is an average of the α and γ compositions since x rays are being generated in both the α and γ phases. After another 400 Å increment, now a total of 800 Å from the first analysis site, only the α -phase is being sampled and no Nb is detected. The first point uniquely measures the composition of the γ -phase, and a point 800 Å away uniquely measures only the α -phase. Hence, the spatial resolution must be better than 800 Å. The spatial resolution can be calculated with the elastic scattering model.⁴ The beam spreading is given by

$$b = 6.25 \times 10^5 \frac{Z}{E_0} \left(\frac{\rho}{A} \right)^{1/2} t^{3/2} \quad (8)$$

where b = beam spreading diameter (cm), Z = average atomic number, A = average atomic weight, ρ = average bulk density (g/cm^3), E_0 = accelerating potential (kV), and t = foil thickness (cm).

Equation (8) predicts the beam spreading under these experimental conditions to be about 250 Å. The spatial resolution is approximately equal to the sum of the beam spreading and the electron-probe diameter.² Hence, the total x-ray spatial resolution is approximately $250 + 180 = 430$ Å. This result is consistent with the experimentally observed x-ray spatial resolution. A more accurate value of beam spreading could be calculated with Monte Carlo techniques.^{17,18}

Application to the Decomposition of U-6 w/oNb (γ_1). The measured compositions of the coexisting phases in the two-phase microstructure were not the equilibrium phase compositions given by the U-Nb phase diagram (Fig. 1). X-ray diffraction showed the structure to contain an orthorhombic (α) and a bcc (γ) phase. At equilibrium, the α should be essentially Nb free and the γ should contain about 50 w/oNb. However, the STEM analysis showed the γ to contain only about 12 w/oNb (Fig. 5). The γ was therefore not the equilibrium γ_2 predicted by the phase diagram. Rather, it appears as if the parent γ_1 may have been retained because of the sluggish kinetics of the monotectoid decomposition reaction. The γ_1 apparently has the composition predicted by a metastable extension of the $(\alpha + \gamma_1)/\gamma_1$ solvus line below the monotectoid temperature. These results were consistent with X-ray diffractometry results from slow-cooled U-Nb.¹⁹

Summary

1. The experimentally determined k_{NbU} factors were:

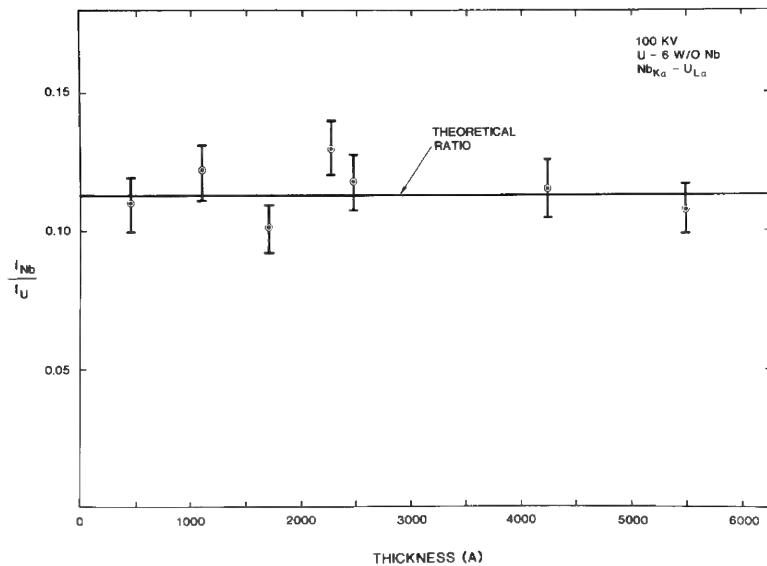


FIG. 3a.--STEM trace from foil thin edge inward to thicker regions of foil.

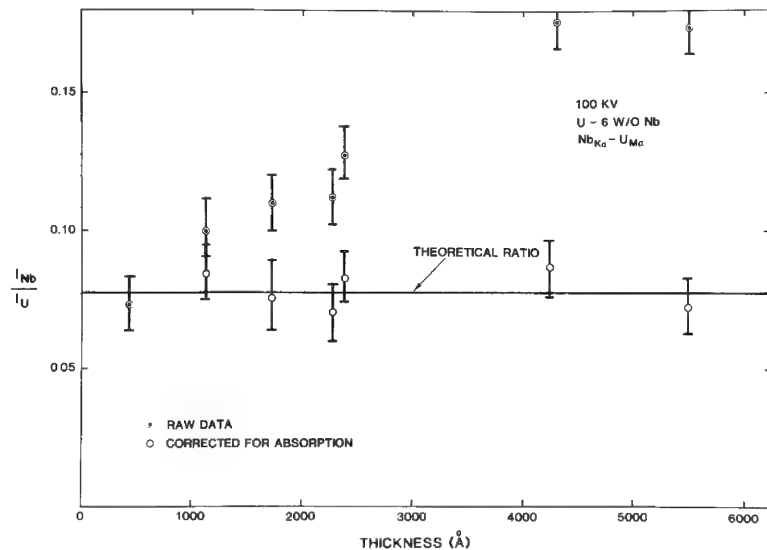


FIG. 3b.--STEM trace from foil thin edge outward to thicker regions of foil. Data corrected for absorption are also shown.

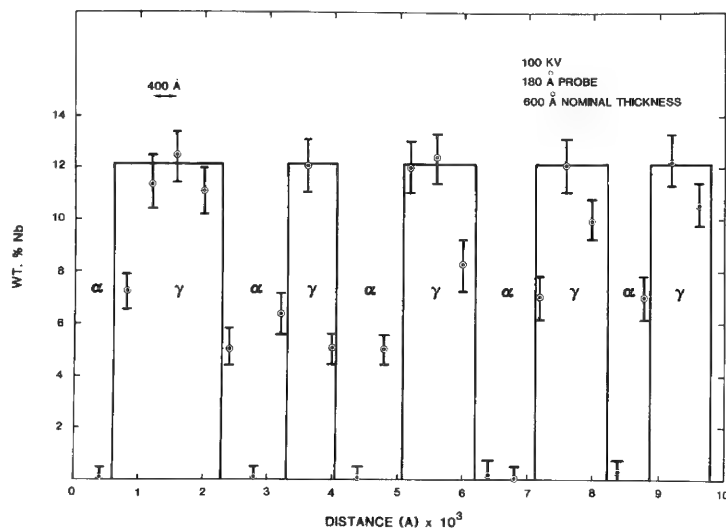


FIG. 4.--STEM trace across pearlite colony ($\alpha + \gamma$) in U-6 w/oNb alloy cooled from 800°C to room temperature at 0.04°C/s. Experimental parameters: Operating voltage 100 kV; spot size, 180 Å; step size, 400 Å; nominal foil thickness, 600 Å.

Peaks	100 kV	200 kV
Nb _{kα} - U _{Lα}	0.56 ± 0.04	0.61 ± 0.04
Nb _{Lα} - U _{Lα}	0.39 ± 0.03	0.41 ± 0.03
Nb _{kα} - U _{Mα+β+γ}	0.83 ± 0.07	0.85 ± 0.05
Nb _{Lα} - U _{Mα+β+γ}	0.49 ± 0.07	0.55 ± 0.06

2. X-ray absorption effects were not significant for the Nb_{kα}-U_{Lα} and Nb_{Lα}-U_{Mα} peak combinations.

3. The spatial resolution at 100 kV with ~ 180Å incident beam was determined by measurement of the concentration profiles across α/γ interfaces in U-Nb alloys. It was less than 800 Å in thin foils which were approximately 600 Å thick.

4. U-6 w/oNb γ₁ decomposed upon slow cooling (0.04°C/sec) to α(0 w/oNb) and γ(12 w/oNb), not the equilibrium phases predicted by the phase diagram.

References

1. R. P. Elliot, *Constitution of Binary Alloys* (First Supplement), New York: McGraw-Hill, 1965, 274.
2. A. D. Romig Jr. and J. I. Goldstein, "Detectability limit and spatial resolution in STEM x-ray analysis: Application to Fe-Ni alloys," *Microbeam Analysis--1979*, 124.
3. A. D. Romig Jr. and J. I. Goldstein, "Determination of the Fe-Ni and Fe-Ni-P phase diagrams at low temperatures (700 to 300°C)," *Met. Trans.* 11A: 1151, 1980.
4. J. I. Goldstein, J. L. Costley, G. W. Lorimer, and S. J. B. Reed, "Quantitative x-ray analysis in the electron microscope," *SEM/1977*, I, 315.
5. M. Green and V. E. Cosslett, "The efficiency of production of characteristic x-radiation in thick targets of pure elements," *Phys. Soc. (London) Proc.* 78: 1206, 1961.
6. C. J. Powell, "Evaluation of formulas for inner-shell ionization cross-sections," K. F. J. Heinrich et al., Eds., *Use of Monte Carlo Calculations in Electron Probe Microanalysis and Scanning Electron Microscopy*, NBS Special Publ. 460, 1976, 97.
7. G. Wentzel, "Über strahlungslose Quantensprünge" (On radiation-free quantum transitions), *Zeit. Phys.* 43: 524, 1927.
8. V. W. Slivinsky and P. J. Ebert, "K_β/K_α x-ray transition probability ratios for elements 18<Z<29," *Phys. Rev.* A5: 1581, 1972.
9. K. F. J. Heinrich, C. E. Fiori, and R. L. Mykelbust, "Progress in measurement of relative x-ray line intensities," *Proc. 11th MAS Conf.*, 1976, 29.
10. J. H. Scofield, "Radiation decay rates of vacancies in K and L shells," *Phys. Review* 179: 179, 1969.
11. J. Leroux, "Method for finding mass-absorption coefficients by empirical equations and graphs," in Mueller, Ed., *Advances in X-ray Analysis*, 5: 153, 1961.
12. N. Zaluzec, "Quantitative x-ray microanalysis: Instrumental considerations and applications to materials science," in J. J. Hren, J. I. Goldstein, and D. C. Joy, Eds., *Introduction to Analytical Electron Microscopy*, New York: Plenum Press, 121, 1979.
13. K. Kanaya and S. Okayama, "Penetration and energy-loss theory of electrons in solid targets," *J. Phys.* Df: 43, 1972.
14. V. E. Coslett and R. N. Thomas, "Multiple scattering of 5-30 keV electrons in evaporated metal films: I, Range-energy relations," *Brit. J. Appl. Phys.* 15: 882, 1969.
15. V. E. Coslett and R. N. Thomas, "Multiple scattering of 5-30 keV electrons in evaporated metal films: II. Range-energy relations," *Brit. J. Appl. Phys.* 15: 1283, 1969.
16. J. Philibert and R. Tixier, "Electron penetration and atomic number correction in electron probe microanalysis," *Brit. J. Appl. Phys.* D1: 685, 1968.
17. D. F. Kyser and R. H. Geiss, "Spatial resolution of x-ray microanalysis in STEM," *Proc. 12th MAS Conf.*, 1977, 110.
18. R. L. Mykelbust, D. E. Newbury, and H. Yakowitz, "NBS Monte Carlo electron trajectory calculation program," K. F. J. Heinrich et al., Eds., *Use of Monte Carlo Calculations in Electron Probe Microanalysis and Scanning Electron Microscopy*, NBS Special Publ. 460, 1976, 105.
19. C. D'Amato, F. S. Saraceno, and T. B. Wilson, "Phase transformation and equilibrium structures in uranium rich niobium alloys," *J. Nucl. Materials* 12: 291, 1964.

CATHODOLUMINESCENCE IMAGE ANALYSIS TECHNIQUE FOR OXIDE INCLUSION CLASSIFICATION OF NICKEL-BASE SUPERALLOYS

K. P. Gumz and J. M. Walsh

In order to produce durable powder-metallurgy rotating components for gas turbine engines, it is important to use material that has a low inclusion level. It has been shown that the minimum low-cycle fatigue life of the powder-metallurgy nickel-base superalloy materials used in this application is governed by the presence of small, nonmetallic oxide inclusions and therefore efforts are continually being made to reduce both the quantity and size of these inclusions. Their main sources are the ingot stock from which the powder is made and the powder-making process itself. This laboratory has been studying the factors that govern the cleanliness of the ingot stock and ways to improve the cleanliness of this material.¹ As the cleanliness goals for this class of materials are rather exacting (nonmetallic oxide inclusion levels of fractions of a part per million), it became apparent that the conventional methods for quantitative nonmetallic inclusion characterization were not adequate. Metallographic sectioning, for example, is not viable because it samples such a small volume of material and because the probability of finding an inclusion on any given sampled plane is extremely low. An inclusion assessment method has been developed that consists of concentrating the inclusions near the top of an analytical ingot by flotation, electrochemically extracting the inclusions, and quantitatively characterizing the inclusions by a cathodoluminescence image analysis technique on the electron microprobe.^{1,2}

The concentration of the inclusions is accomplished as follows. Sample slices are taken from the ingot stock of interest and melted by an electron beam under vacuum in a hemispherical water-cooled copper crucible, which results in the oxides floating to the top. An electrolytic extraction is then performed on the entire top surface of this hemispherical analytical ingot to a depth of about 2 mm and the extracted residue is collected on a membrane filter (typically 8 μ m Nuclepore or Unipore). If this material were pure oxide and of sufficient quantity, then a simple gravimetric determination would give the cleanliness level of the material. However, experience has shown that these extractions are rarely pure oxide; they may contain other species such as carbides, borides, undissolved base material, and occasionally artifacts of the extraction process. A technique based on the cathodoluminescence characteristics of these oxide inclusions was therefore developed that allows an oxide-specific measurement to be made even in the presence of extraneous species.

Cathodoluminescence detection is accomplished with a Hamamatsu R-268 photomultiplier installed in the light microscope of a JEOL JXA-50 microprobe. This detector was found to have optimum sensitivity for the oxide inclusions in the alloys of current interest, which are primarily hafnium oxide, aluminum oxide, and mixtures of hafnium and aluminum oxide. Figure 1 gives an example of how the cathodoluminescence signal is specific to only the oxides of interest and discriminates against other species in the extracted residue.

An areal fraction measurement of the nonmetallic oxide inclusions in the extracted residue should give an indication of the cleanliness of the material. The JXA-50A was fitted for the areal fraction measurements with a simple image-analysis system consisting of a digital scan generator and analog comparator (of LeMont Scientific design). The threshold of the analog comparator is adjusted for the cathodoluminescence signal from the oxides of interest and the areal fraction is established by the ratio of the number of picture elements above threshold to total number of picture elements. Because of non-uniformity in dispersion of the residue, it is usually necessary to perform the areal fraction determination over 100% of the extracted material. This requirement necessitated complete automation of the image analysis system. A hardwired asynchronous logic controller was designed and built to control the X and Y axes of the microprobe stage and interact with the rest of the image analysis system. This capability allows an automatic areal fraction analysis of a complete X-Y array of any number of fields (Fig. 2). The

The authors are with the Materials Engineering and Research Laboratory, Pratt & Whitney Aircraft, Middletown, CT 06457.

residue is processed through a special filtration system that confines all material to an area within the JXA-50A stage travel ($\approx 10 \times 22$ mm).

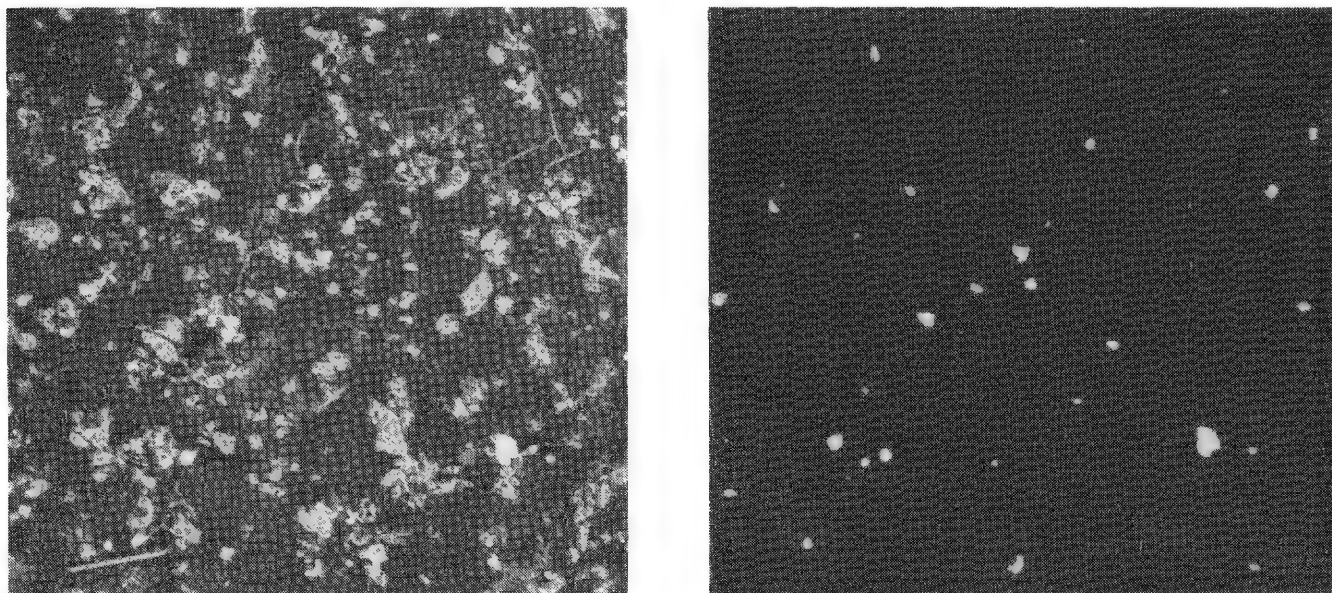


FIG. 1.--Backscattered electron image (left, 100 \times) showing total extracted material; and corresponding catholuminescence image (right, 100 \times) showing oxide inclusions.

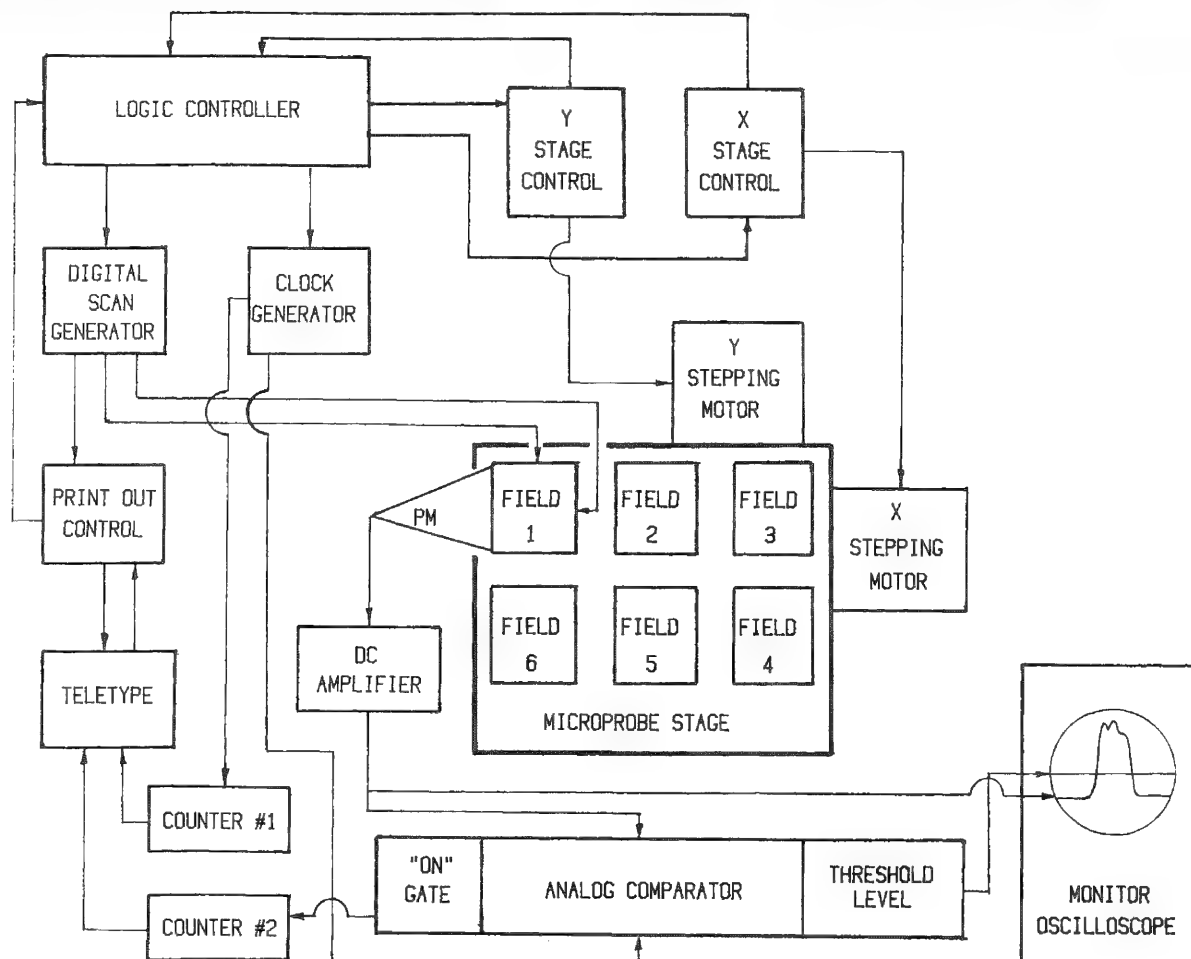


FIG. 2.--Schematic of automatic image-analysis system for cathodoluminescence measurement.

In addition to areal fraction cathodoluminescence, an areal fraction measurement is made by means of the backscattered electron signal, to gauge the purity of the extraction. These areal fractions are similar for very pure extractions but the backscattered electron areal fraction is much greater than the cathodoluminescence areal fraction for impure extractions, since it includes oxides plus extraneous material. The absolute determination of oxide inclusion level in the analytical ingot is taken from a calibration curve relating areal fraction cathodoluminescence to surface density (mg/cm^2) of oxide inclusions. The calibration curve is made from actual extracted oxides that have surface densities similar to the material being studied.

The power of this concept becomes especially obvious as the materials to be evaluated become cleaner. In very clean materials the oxides may make up only a small fraction of the extracted residue, yet cathodoluminescence detects the oxides exclusively. Furthermore, since the detection of cathodoluminescence is limited primarily by picture-element resolution, the measurements can be extended to a range of cleanliness that is well below anything that can be achieved gravimetrically. The method is not intended to be applied to a completely unknown system, but rather to provide reproducible quantitative measurements of cleanliness in metallic systems where the oxides present have been fairly well documented.

References

1. E. E. Brown et al., "The influence of VIM crucible composition, vacuum arc remelting, and electroslog remelting on the non-metallic inclusion content of MERL 76," in J. K. Tien et al., Eds., *Superalloys 1980, Proc. Fourth Intern. Symp. on Superalloys*, 1980.
2. D. E. Newbury and H. Yakowitz, "Contrast mechanisms of special interest in materials science," in J. I. Goldstein and H. Yakowitz, Eds., *Practical Scanning Electron Microscopy*, New York: Plenum Press, 1975, 204.

ANALYTICAL ELECTRON MICROSCOPY OF CATALYST MATERIALS

C. E. Lyman

Heterogeneous catalysts control the type and amount of product made in many commercial chemical reactions. Improvement in the properties of a particular catalyst requires detailed study of its microstructure in terms of particle size and shape, chemical composition, and crystallographic features. The analytical electron microscope (AEM) is uniquely suited to study these aspects of single catalyst particles. In this paper specimen preparation and chemical analysis by x-ray emission spectroscopy are considered for a Pd catalyst supported on Al_2O_3 .

Many techniques have been used to study the structure and composition of heterogeneous catalysts: x-ray diffraction, surface analysis, wet chemistry techniques, etc. However, none of these methods allows structural and chemical analysis of individual particles or of small amounts of impurity phases which may act as poisons and shorten catalyst life.

Analytical electron microscopy (AEM) in the scanning transmission electron microscope (STEM) allows microdiffraction, x-ray emission spectroscopy, and electron energy loss spectroscopy to be performed on individual particles. In order to analyze a single particle, it is important to image the particle in relatively high contrast. Several techniques for enhancing contrast of heavy metal particles in images of supported metal catalysts have been demonstrated.¹⁻³ Use of x-ray emission spectroscopy to analyze catalysts in an AEM is just beginning.⁴⁻⁶ This paper demonstrates some techniques of contrast enhancement and analysis for very small metal particles supported on a ceramic substrate.

Experimental Details

The specimen material was Pd supported on Al_2O_3 powder. Specimens were prepared by two methods. First, powders were dispersed on carbon films: the grid was dipped into the powder or the powder was spread out between two glass slides and a grid was laid upside down on the powder. In the second method, the powder was embedded in epoxy and microtomed with a diamond knife to a thickness of about 70 nm. The former method is quick but may select only particular particle sizes, which may not represent the powder as a whole. The latter method is time consuming and requires considerable skill. However, for some analysis techniques such as x-ray emission spectroscopy, a relatively flat specimen of uniform thickness is desirable. Both types of preparation can be carbon coated to reduce charging effects but such carbon layers might also interfere with the microanalysis; therefore, carbon coating was omitted in this work.

The specimens were examined at 100 kV in a Vacuum Generators HB5 STEM fitted with an Si(Li) x-ray spectrometer. Two methods were used to increase image contrast of the Pd particle relative to the Al_2O_3 support. High-angle Rutherford scattering from the Pd was collected with an annular dark-field detector. This method alone gave good contrast on the Pd particles. In addition, ratio images of the bright-field signal to the annular dark-field signal were also observed. For x-ray analysis, a virtual objective aperture was used between the gun and the condenser lens to reduce the number of uncollimated electrons hitting the entire specimen and generating spurious x rays. The selected area diffraction aperture was also used but the normal objective aperture adjacent to the specimen was removed from the beam. With this setup, the hole count intensity was < 0.1% of that for the major peaks from the specimen. All analyses were made with a graphite specimen cartridge. X-ray measurements were made at 10 million times magnification with a scanned raster. The counting time for all results given in this paper was 500 s.

The author is with the Central Research and Development Department of E. I. du Pont de Nemours and Co., Inc., at the Experimental Station, Wilmington, DE 19898. He thanks Prof. J. B. Vander Sande and Dr. A. J. Garratt-Reed of MIT and Dr. P. Bovey of VG Microscopes, Ltd., East Grinstead, England for their help in this work.

Results and Discussion

For a microtomed particle of Pd on Al_2O_3 , the Pd shows up white on a dark background in the annular dark-field image (Fig. 1). Bright-field images are also presented in Fig. 1 for comparison. The Pd particles shown are in the size range of 5-50 nm. Figure 2(a) shows a typical STEM bright-field image of a Pd/ Al_2O_3 particle resting on a thin carbon film. An x-ray spectrum from a 10nm-diameter Pd particle (arrow) on the Al_2O_3 is shown in Fig. 2(b). X rays from the copper support grid were produced by electrons and x-ray continuum scattered from or generated in the particle under examination. This was the most serious source of extraneous background. If the electron beam is placed only on the Al_2O_3 , no Pd peaks are observed. When the same type of particle is sectioned to a thickness of 70 nm with a microtome, the x-ray microanalysis is similar. Figure 3 shows a bright-field image and a ratio image (bright-field signal divided by annular dark-field signal) of Pd particles on an Al_2O_3 support. The x-ray spectrum from the particle marked by an arrow in Fig. 3(b) is shown in Fig. 4(a). The intensity of the Pd peak from this 8 nm diameter particle is about 25 counts/s. This signal is large enough to indicate that particles down to 2-3 nm should be detectable by this method. Figures 4(b) and (c) show x-ray spectra from the Al_2O_3 support and the embedding epoxy, respectively. In this instance the particles were not ground with a mortar and pestle where contamination might occur, so the sulfur and calcium peaks are suspected as impurities in the Al_2O_3 catalyst support.

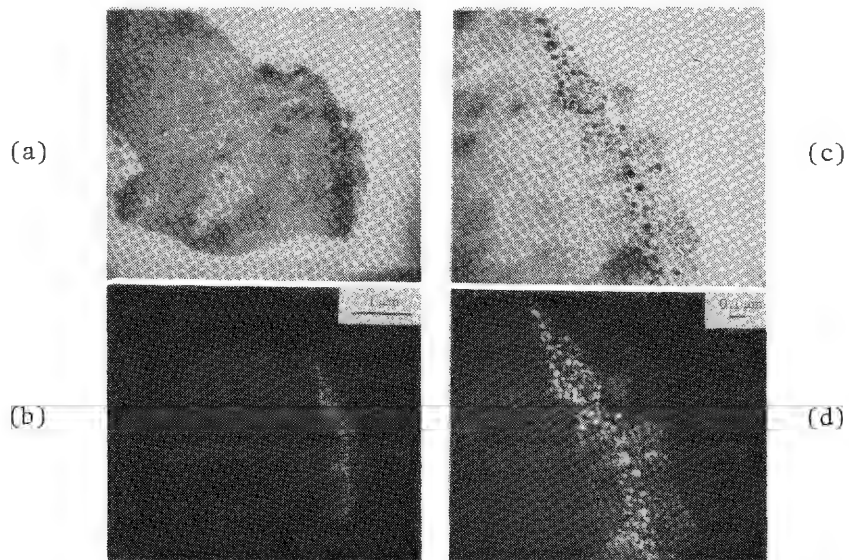


FIG. 1.--STEM images of Pd particles on Al_2O_3 embedded in epoxy and microtomed: (a) and (c) bright-field images; (b) and (d), annular dark-field images showing Pd particles in white.

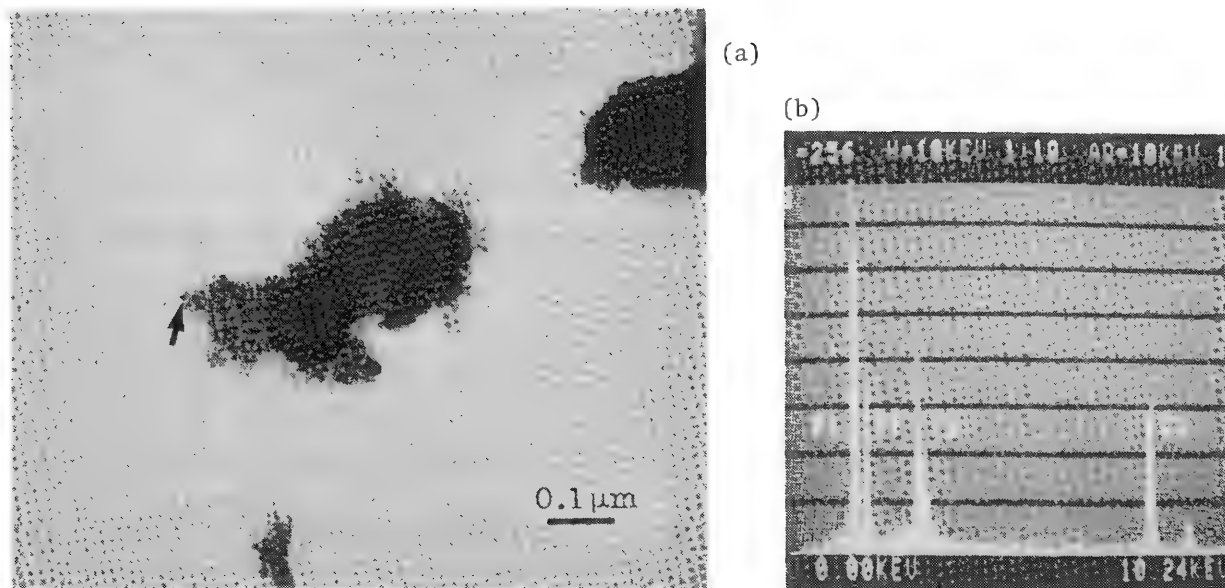


FIG. 2.--(a) STEM image of Pd on Al₂O₃ with specimen prepared by dispersion of powder on carbon support film; (b) x-ray emission spectrum from Pd particle indicated by an arrow in (a).

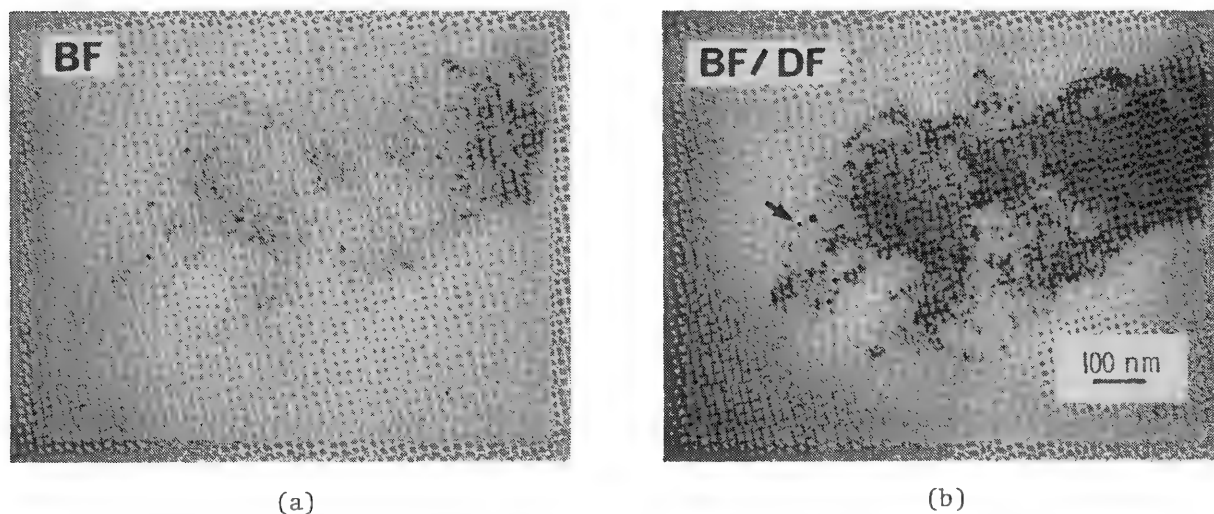


FIG. 3.--Microtomed section of embedded Pd/Al₂O₃ particle: (a) bright-field image, (b) ratio image formed by division of bright-field signal by annular dark-field signal. (Arrow shows particle analyzed in Fig. 4a).

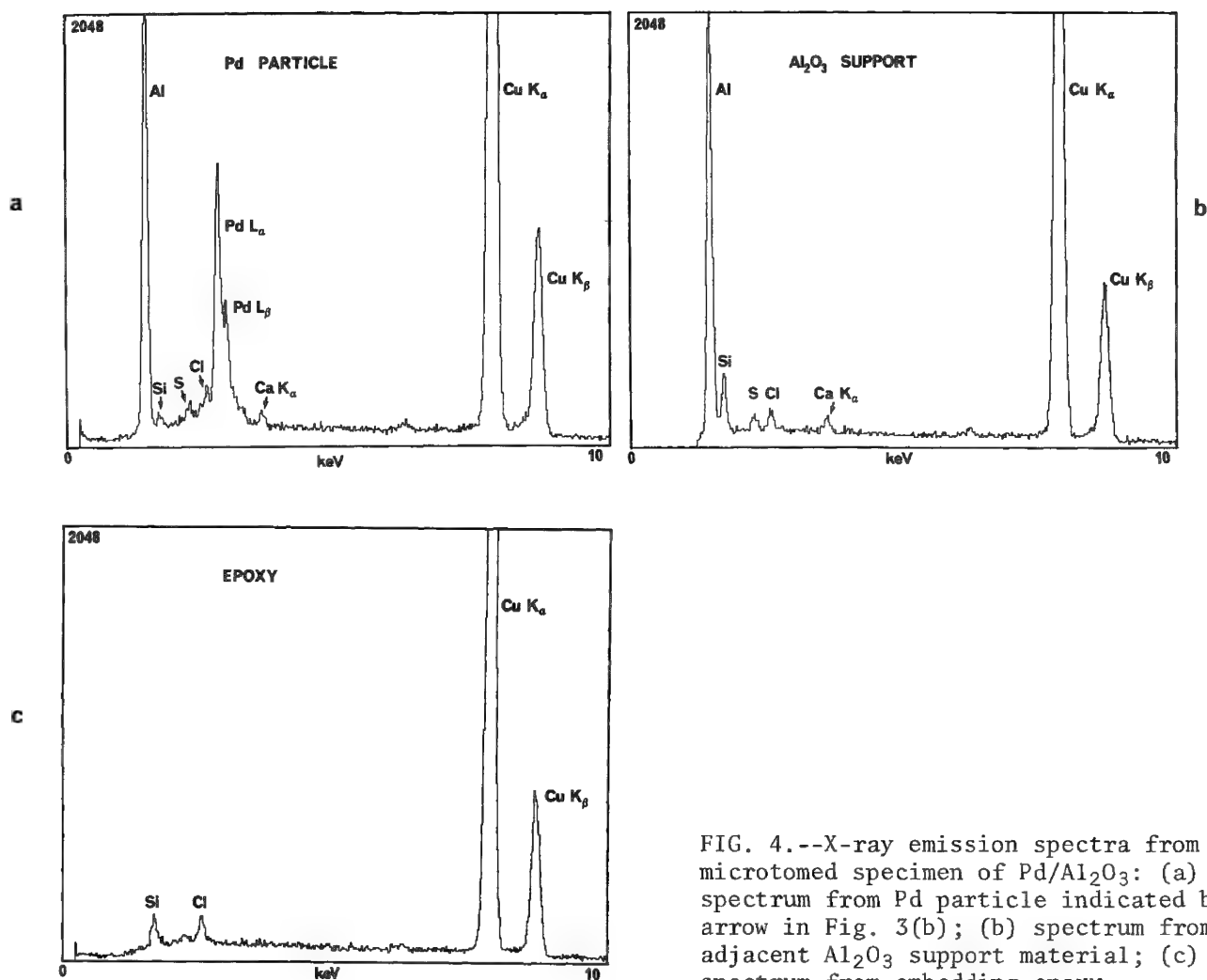


FIG. 4.--X-ray emission spectra from microtomed specimen of Pd/Al₂O₃: (a) spectrum from Pd particle indicated by arrow in Fig. 3(b); (b) spectrum from adjacent Al₂O₃ support material; (c) spectrum from embedding epoxy.

References

1. M. M. J. Treacy, A. Howie, and C. J. Wilson, *Phil Mag* A38, (1978), 569.
2. C. Stoeckert, B. Etherton, M. Beer and J. Gryder, *Proc. EMSA 38th Annual Meeting* (Reno), 1980, 202.
3. J. H. Butler, presentation at the symposium "STEM in Solid State Science," Castle Hot Springs, Ariz., 1981.
4. M. Raghavan, *Proc. EMSA 37th Annual Meeting* (San Antonio), 1979, 484.
5. R. L. Freed and M. J. Kelley, *Proc. EMSA 38th Annual Meeting* (Reno), 1980, 200.
6. F. Delannay, *Catal. Rev. Sci. Eng.* 22: 141, 1980.

RAPID TECHNIQUE TO DETERMINE EXTENT OF Pt-Si REACTION IN VERY THIN FILMS

B. Landau, G. Riga, S. Justi, and E. Goo

A scanning electron microscope with an energy-dispersive x-ray spectrometer can be used to determine the extent of the platinum-silicon reaction by calculation of the platinum-to-silicon x-ray count ratios. Thin films of platinum and platinum silicides of the order of 1000 Å have been investigated. The technique is simple and rapid, and the results compare well with those obtained by more complex techniques.

In the past few years there has been considerable interest in a group of platinum-silicon compounds known as platinum silicides, which are used on semiconductor devices for both Schottky diodes and ohmic contacts.^{1,2} One of the limiting factors in achieving increased device performance and high reliability is producing a stable contact. Instability as a result of uncontrollable interaction between aluminum and silicon leads to what is known as "spiking." As industry progresses towards smaller device configurations this problem becomes increasingly important. The barrier provided by the Pt-Si system against diffusion of Si into Al can only be effective if the Pt-Si reaction has gone to completion, i.e., if Pt and Si have formed the stable compound PtSi.^{3,4}

Analytical techniques used to characterize Pt-Si films are Auger electron spectroscopy (AES), x-ray diffraction (XRD), transmission electron microscopy (TEM), and Rutherford backscattering spectroscopy (RBS). All are time consuming, require expensive equipment, and usually cannot be carried out on the device itself. A fast indirect technique used in processing consists of measuring the voltage drop across a series of contacts on a test pattern. However, the results of this test depend not only on the Pt-Si reaction, but are also affected by previous processing steps.

In this paper a rapid and simple semiquantitative technique is described to determine the extent of the reaction between Pt and Si.

Sample Preparation

P-type silicon wafers of (111) orientation 75 mm in diameter with an average resistivity of 9.3 Ω-cm were dipped in a 10:1 HF solution for 10 s and rinsed in deionized water. The wafers were subsequently dried with nitrogen and loaded into an S-gun sputter deposition system, and about 400 Å of Pt was deposited on them. Each sample was alloyed in situ after the deposition was completed without a break in the vacuum. Alloying temperatures and times were chosen for best representation of the various states of the Pt-Si reaction (Table 1).

TABLE 1.--Sample identification and treatment.

Sample No.	Alloying temperature (°C)	Alloying time (min)
11	none	none
13	350	30
15	350	15

Results

AES, XRD, TEM, and RBS were chosen to characterize the films. The results were compared with those obtained by EDX.

Auger Electron Spectroscopy. Composition versus depth profiles were obtained by AES with an electron beam current of 1 µA at 5 kV and a Xenon ion sputtering gun. The peak-to-peak height vs depth (in minutes of sputtering time) of Sample 11 is shown in Fig. 1(a). The interface is well defined and free of oxygen. Figure 1(b) shows the depth profile of

The authors are with the Fairchild Research and Development Laboratory in Palo Alto, CA 94304. They gratefully acknowledge the aid of the Process Engineering Group of the Bipolar Memory Division in preparing samples and of M. Stratham of Lawrence Berkeley Laboratory in providing the RBS data.

Sample 13. The alloying is evidenced by a change in amplitude of both the Pt and Si peak-to-peak heights from the unalloyed state. The depth profile for Sample 15 (not shown) looks the same as for Sample 13. It appears that the reaction of Pt and Si to form PtSi has gone to completion at a temperature of 350°C and an alloying time of 30 min. Whether the reaction may have gone to completion after 15 min alloying time cannot be determined conclusively.

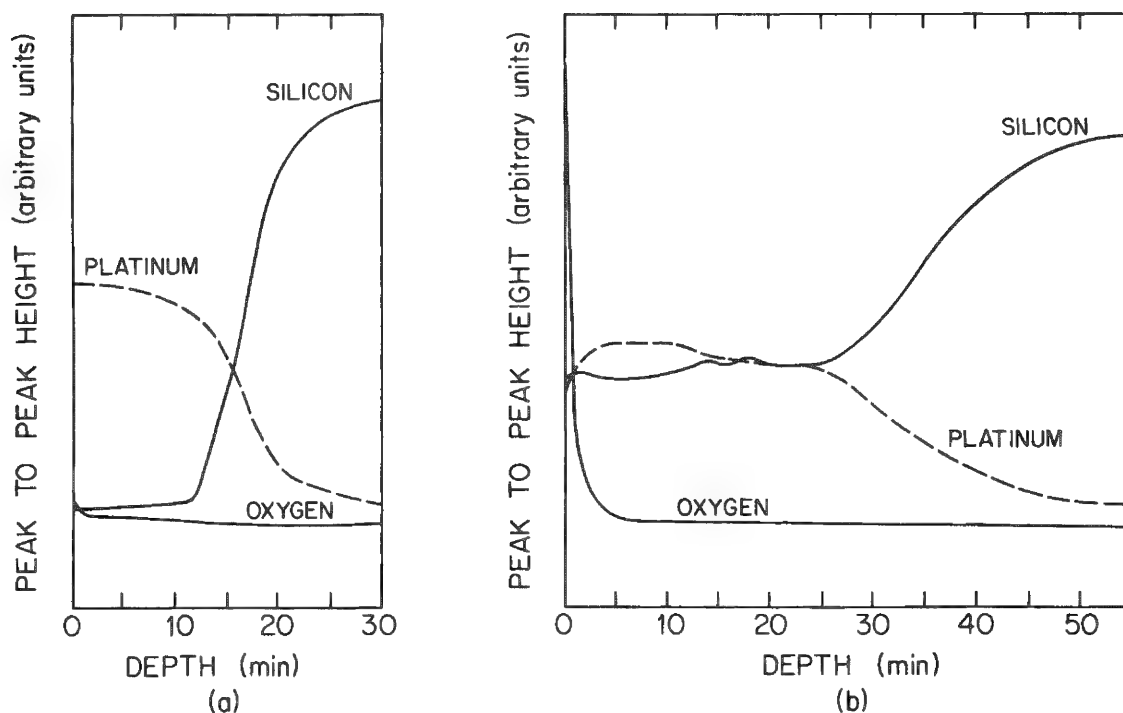


FIG. 1.--AES depth profile of (a) Sample 11, as deposited; (b) Sample 13, 30min anneal at 350°C.

X-ray Diffraction. X-ray diffraction spectra based on Cu K α radiation were obtained in order to identify the various phases of the Pt-Si system. Sample 11 (not shown) exhibits a strong (111) Pt peak and a weak (111) Si peak from the substrate. Diffractometer traces of Sample 13 and Sample 15 are shown in Fig. 2. The formation of the two silicides Pt₂Si and PtSi can be identified on Sample 15 (upper scan). The peak with the highest intensity is obtained from the Pt₂Si (110) reflection ($d = 2.784 \text{ \AA}$) or the PtSi (020) reflection ($d = 2.796 \text{ \AA}$), which overlap and could not be resolved. On Sample 13 (lower scan) no evidence of Pt₂Si could be found, but various reflections from PtSi can be identified.

Transmission Electron Microscopy. Darkfield micrographs and electron diffraction patterns obtained by TEM are shown in Fig. 3. The grain size of the as-deposited Pt film (Sample 11) is about 50 \AA . A preferred orientation relationship of Pt(111)//Si(111) is evidenced by the intensity of the electron diffraction rings, and supported by x-ray diffraction data. Electron diffraction of Sample 13 shows two continuous weak Pt₂Si rings and a spotty, highly textured PtSi pattern. The orientation relationship is PtSi <001>//Si <101> and PtSi (010)//Si (111) as reported by Sinha.⁵ The large grains in the dark field micrograph which have a diameter of about 1000 \AA are likely to be PtSi grains since the continuous Pt₂Si rings indicate a small grain size for Pt₂Si.

Rutherford Backscattering Spectroscopy. RBS was performed to determine the extent of interdiffusion between Pt and Si, and the thicknesses of the as-deposited platinum and the silicides. The spectra (Fig. 4) show that substantially more interdiffusion has occurred in Sample 13 than in Sample 15, as indicated by the shift of the Pt peak toward lower energies as the Pt moves away from the surface, and by the shift of the Si shoulder

toward higher energies, as the Si moves towards the surface. The thickness of the Pt on Sample 11 is 330 Å, obtained from the FWHM of the Pt energy peak and a stopping cross-section factor calculated with the surface energy approximation.⁶ The resulting thickness of the silicide in Sample 13 is calculated to be 690 Å from Bragg's law.⁷

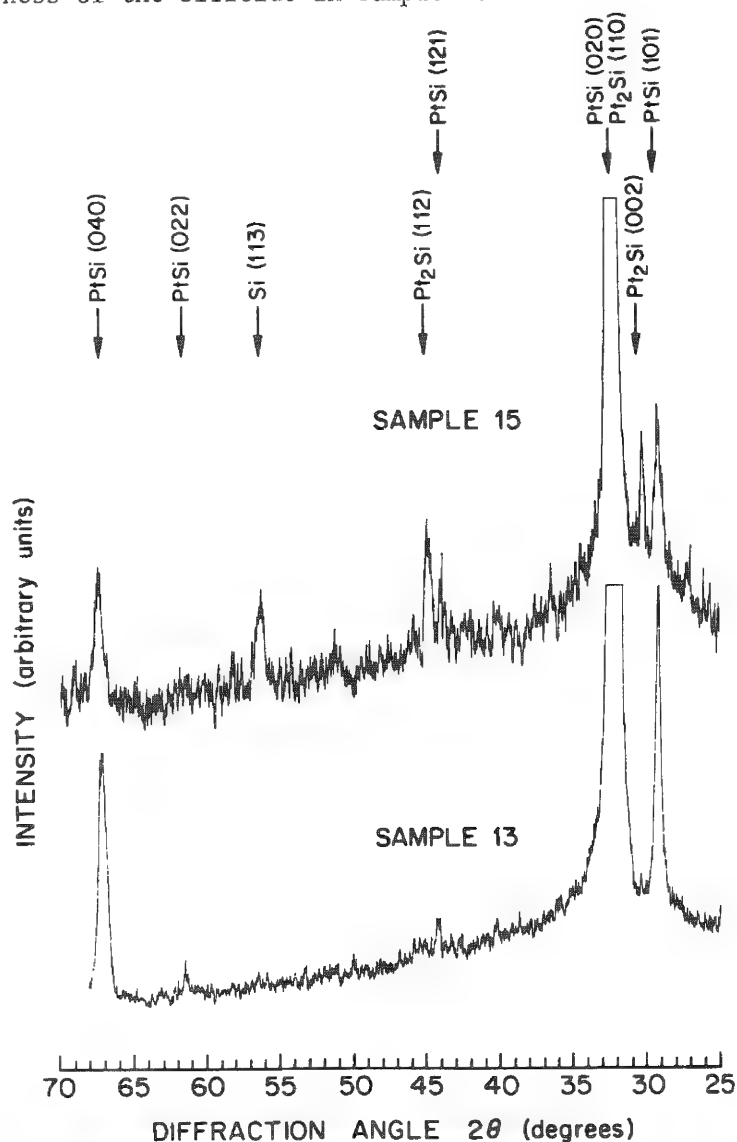


FIG. 2.--X-ray diffractometer traces.

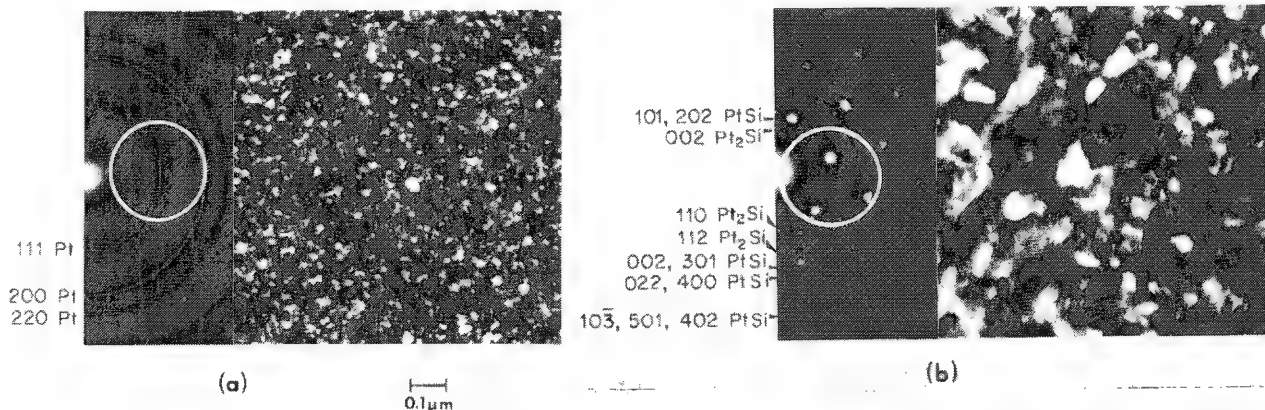


FIG. 3.--Darkfield transmission electron micrographs and electron diffraction patterns of (a) Sample 11, as deposited; (b) Sample 13, 30min anneal at 350°C.

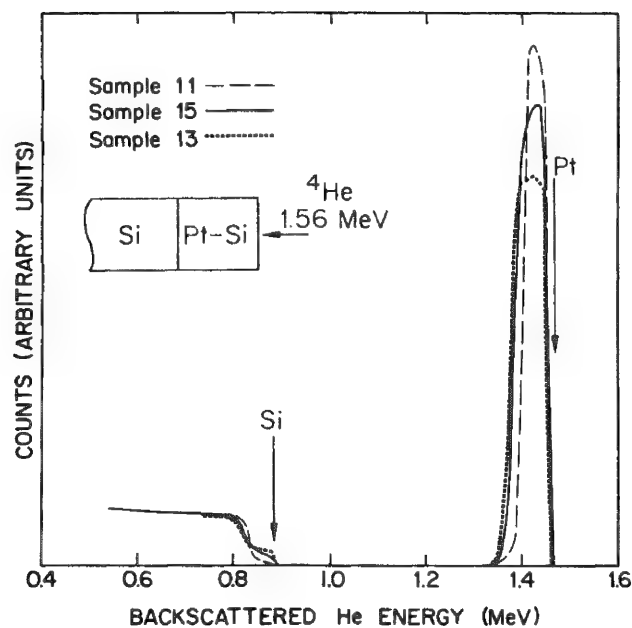


FIG. 4.--Energy spectra of 1.56 MeV ^4He ions backscattered from Samples 11, 13, and 15.

Energy-dispersive X-ray Spectroscopy. In addition to the analytical techniques mentioned above, energy-dispersive x-ray analysis (EDX) was performed on the Pt-Si samples. A low SEM electron-gun voltage of 5 kV was used to accommodate for low penetration of the thin films and sufficient generation of characteristic x rays. All samples were analyzed under identical conditions. For each analysis the number of counts for the Pt $\text{M}\alpha$ line and the Si $\text{K}\alpha$ line was recorded and the Pt $\text{M}\alpha$ /Si $\text{K}\alpha$ count ratio calculated. For statistical reasons as well as to assure repeatability, this procedure was done three times in three randomly chosen areas, yielding nine data points for each sample. The data are summarized in Table 2.

TABLE 2.--Platinum-to-silicon x-ray count ratios obtained by EDX.

Sample No.	No. of data	Pt/Si X-ray count ratio	
		Mean	Std. Dev.
11	9	3.385	0.1153
13	9	1.507	0.0275
15	9	1.797	0.0356

The results of these measurements clearly show that thin films 1000 Å thick or less can be characterized by an EDX system. The sensitivity of this technique is exemplified in the case of Samples 13 and 15, where the only difference in the preparation of the sample was the alloying time. Sample 13 indicates a lower Pt/Si count ratio than Sample 15, which means that less Si had diffused into the Pt film forming a silicide in Sample 15 than in Sample 13. Sample 13 is therefore likely to contain larger amounts of PtSi, as is indicated by a low Pt/Si count ratio. Sample 15 is likely to contain amounts of Pt Si with a Pt/Si count ratio somewhere between the as-deposited Pt film (Sample 11) and the fully reacted film (Sample 13). These findings are in good agreement with the results obtained from the other techniques. It is believed that this technique can be used to characterize other silicides.

Summary

It has been demonstrated that an energy-dispersive x-ray spectrometer attached to a scanning electron microscope can be used to determine the extent of the Pt-Si reaction of thin Pt films. By determining the Pt/Si X-ray count ratios, we obtain an indication of how much interdiffusion has taken place to form a silicide. The stable phase PtSi will have formed when the Pt/Si count ratio is at its lowest value. This technique is rapid, and the results compare well with those obtained through other techniques.

References

1. R. M. Anderson and T. M. Reith, *J. Electrochem. Soc.* 122: 1337, 1975.
2. J. M. Poate and T. C. Tisone, *Appl. Phys. Lett.* 24: 391, 1974.
3. J. B. Bindell, J. W. Colby, D. R. Wonsidler, J. M. Poate, B. K. Conley, and T. C. Tisone, *Thin Solid Films* 37: 411, 1976.
4. N. Severi, E. Gabilli, S. Guerri, and G. Celotti, *J. Appl. Phys.* 48: 1988, 1977.
5. A. K. Sinha, R. B. Marcus, T. T. Sheng, and S. E. Haszko, *J. Appl. Phys.* 43: 3637, 1972.
6. W. K. Chu, J. W. Mayer and M. A. Nicolet, *Backscattering Spectrometry*, New York: Academic Press, 1978, 63.
7. *Ibid.*, p. 43.

ELECTRON PROBE STUDY OF ELECTROCHEMICAL CORROSION OF Ti/Pd/Ag CONTACTS ON Si

T. D. Kirkendall and J. C. Hannsen

Silicon photovoltaic cells, typically numbering a few tens of thousands per spacecraft, are the prime power source for communications satellites. In the manufacture of these cells, the prevailing technology involves multicomponent metal structures consisting of vacuum-deposited layers of Ti, Pd, and Ag which are sintered to the n and p type silicon to form low-resistance ohmic contacts. Figure 1 is a schematic representation of the cell construction. Nominal thicknesses of the Ti, Pd, and Ag layers are 1500 Å, 200 Å, and 8 μm, respectively. The purpose of the Ti is to promote contact adhesion to the Si by reaction with the native SiO₂ film; the Ag provides a low-resistance current conductor. A thin Pd layer is interposed between the Ti/Ag couple to protect the Ti from moisture-induced electrochemical corrosion, which can lead to high contact resistance and poor metal adhesion.

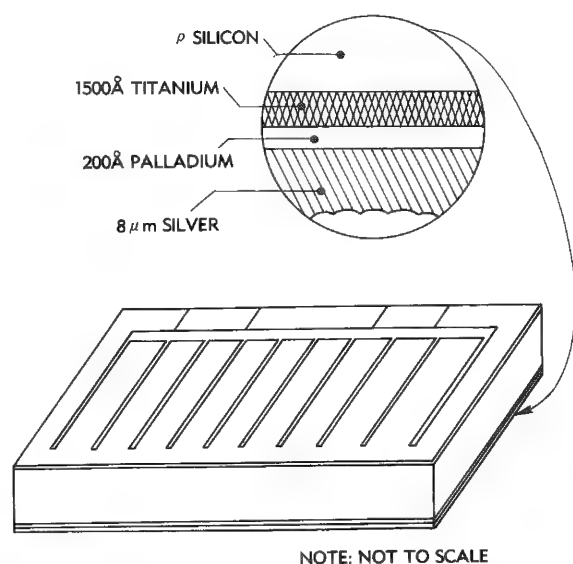


FIG. 1.--Schematic diagram of 2 × 4 cm Si solar cell showing metal contact structure consisting of Ti (~1500 Å), Pd (~200 Å) and Ag (~8 μm). Respective areal densities are Ti, 68 μg/cm²; Pd, 24 μg/cm²; Ag, 8.4 mg/cm². (Not to scale.)

Pd and Ti thicknesses was subjected to extensive periods of exposure to 65°C/95% relative humidity (T/RH), with frequent checks for signs of delaminations or bubbles forming in the p (back surface) contact. Electron-probe analysis of the underside of peeled contacts indicated that the delamination had occurred at the Pd/Ag interface and left all the Pd and Ti on the silicon. A large oxygen Kα signal was also detected in the Ti layer, which indicates electrochemical corrosion of the type associated with Ti/Ag contacts that have no protection against the effects of moisture.^{2,3}

Before the tri-metal Ti/Pd/Ag contact system was developed,¹ contacts were made of Ti/Ag, with a layer of Sn/Pb solder to facilitate bonding and to seal the outer surface of the Ag layer against moisture intrusion. Although effective, the solder coating exacts an undesirable (20%) weight penalty in spacecraft applications when compared with the more sophisticated Pd system. Also, because of the tin pest problem, solder-coated cells are unsuitable for use on deployed arrays where they would experience very low temperatures during eclipse seasons.

Problem Defined

A few solar cells for the INTELSAT V communications satellite program were found to have delaminated back contacts following exposure to a high-temperature, high-humidity environment during accelerated life tests. This problem resulted in a plan to study the dependence of contact integrity on the quantities of Ti and Pd incorporated in the cell.

Subsequently, the role of Pd in passivating the Ti/Ag couple was investigated by use of the electron probe to measure the amount of Pd and Ti in Ti/Pd/Ag contacts, as well as the degree to which the Ti layer may have oxidized. For this study, a group of solar cells of various

The authors are with COMSAT Laboratories, Communications Satellite Corp., Clarksburg, MD 20734. This paper is based in part upon work performed under the sponsorship of the International Telecommunications Satellite Organization (INTELSAT).

Thin-film Measurements

For the first step in the probe analysis, areas on cell contacts from which the Ag had peeled were measured for Pd and Ti thicknesses by means of evaporated Pd and Ti thin-film-on-Si substrate standards. Since several independent methods were to be used for quantizing the metal layers, agreement among the methods was tested by standard statistical processes to determine the correlation coefficients r . Thicknesses of the Pd films on the standards (ranging from 60 to 1000 Å) were determined to within $\pm 10\%$ by neutron activation analysis (NAA) and independently checked with Dektak profilometry ($r = 0.9999$) and atomic absorption spectrometry ($r = 0.9985$). The correlation coefficient for the Pd $L\alpha$ probe intensities and the equivalent NAA thickness values was 0.9959. Thicknesses of the Ti standards were determined by profilometry ($r = 0.9994$ with the Ti $K\alpha$ probe intensities) and by energy-dispersive x-ray fluorescence analysis ($r = 0.9934$). Portions of these same Ti thin film standards were fully oxidized to TiO_2 and used as standards to determine the oxygen content of the Ti/Pd/Si mixture on the backs of the cells.

Solar-cell Cross Sections

At this point the study was expanded to include not only the defective cells, but also cells that did not exhibit any signs of delamination. To facilitate the investigation, a method was devised to expose the Ti and Pd interface layers by means of standard metallographic polishing procedures. The resulting cross sections displayed geometrical magnifications of 10 to 60 \times because of the low angle of incidence used during the lapping process.

Although the metals were originally deposited in separate evaporations, the concept of discrete Ti and Pd layers is not strictly accurate. The roughness of the Si surface (~ 4 μm peak to peak) presents a serious obstacle to the production of integral films, especially in the case of Pd (200 Å nominal thickness). In addition, interdiffusion and mixing of the various "layers," including the formation of Pd and Ti silicides, should be expected to result from the sintering process.

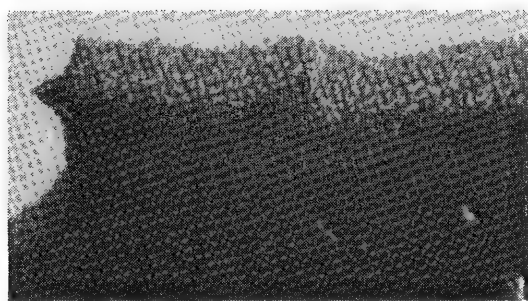
Following Pd and Ti thickness measurements under the peeled Ag, undelaminated portions of the same cell were also sectioned and measured for Ti and Pd thicknesses by recording of the Pd $L\alpha$ and Ti $K\alpha$ intensities in the exposed layers at their thickest points. In this way, the effects of polishing artifacts were minimized, which resulted in good correlation with thicknesses measured on unpolished surfaces. After it had been determined that the sample preparation did not significantly change the oxygen content of the contact layers, oxygen measurements were made in the same manner on polished cross sections. Thus, the exposed contact structure of any cell could be analyzed in the electron probe to evaluate the equivalent thicknesses of Ti and Pd as well as the degree of Ti oxidation (corrosion).

Influence of Pd and Ti Thickness on Corrosion

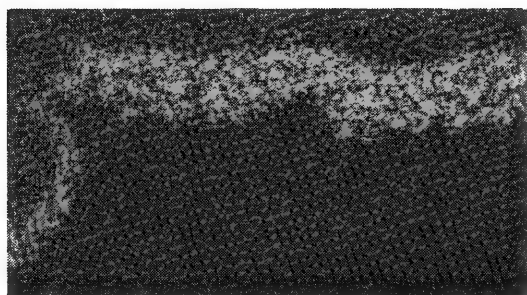
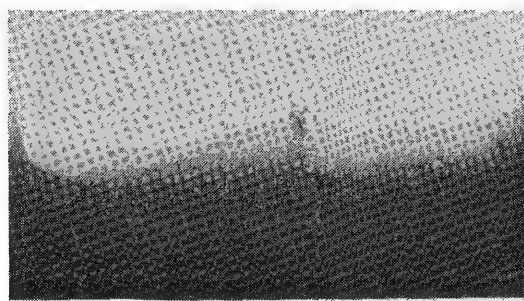
Figure 2 shows the cross-sectional analysis of the contact of a solar cell which had failed the T/RH test. The delamination of portions of the contact was attributed to oxidation of the Ti layer. The contact contained an equivalent thickness of Pd of 60 Å which, as clearly demonstrated by this study, is inadequate to passivate the Ti and prevent corrosion. Another feature of the contact structure that is apparent in the cross section is the aggregation of Pd-rich entities throughout the Ti layer. These islands are probably palladium silicide formed during the sintering step.⁴ Since only elemental Pd is effective in passivating the Ti, palladium silicide in the contact structure is undesirable to the extent that it depletes the amount of elemental Pd.

Figure 3, which shows the contrasting appearance of a cell contact made with 290 Å of equivalent Pd thickness, reveals two marked differences. In this contact, the semblance of an actual Pd layer has been retained at the Ag/Ti interface, which means that little diffusion or formation of palladium silicide has taken place. Furthermore, the amount of oxide in this Ti layer is only a few per cent of that measured in the inadequately protected cell shown in Fig. 2.

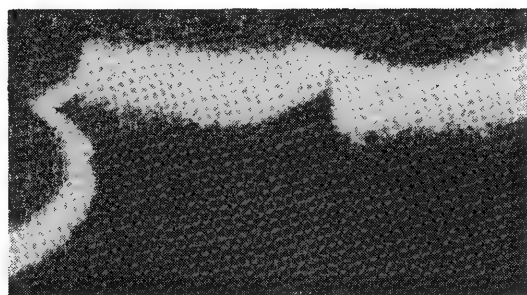
Electron-probe analysis of sectioned solar cells with various amounts of Pd and Ti and various histories of exposure to temperature and humidity showed a consistent relationship between corrosion of the Ti and low amounts of Pd. Following T/RH exposure, titanium oxi-



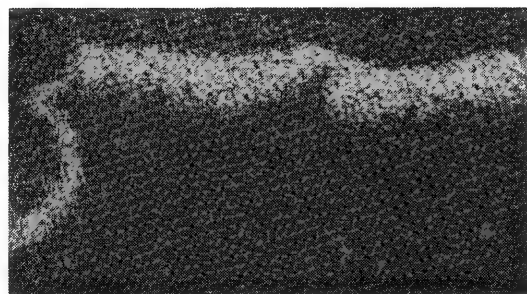
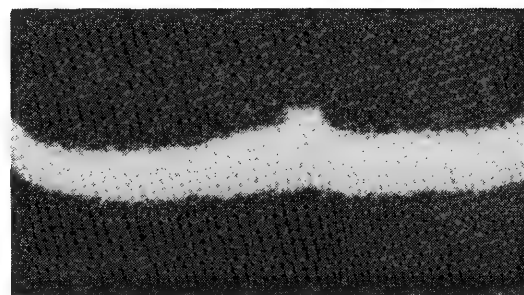
SE



Pd L α



Ti K α



O K α



FIG. 2.--Electron-probe analysis of taper-polished cross section of a cell contact made with 60 Å Pd. Exposure to T/RH has caused extensive oxidation of Ti. Note Pd-rich islands throughout Ti layer.

FIG. 3.--Electron-probe analysis of taper-polished cross section of a cell contact made with 290 Å Pd. The oxygen image shows only background counts; there is no corrosion. Note that Pd is retained in a layer as originally deposited between Ti and Ag.

dation levels up to 85% of that equivalent to TiO_2 were measured when the Pd thickness was less than 100 Å. Conversely, when the Pd thickness was at least 200 Å, the Ti oxidation never exceeded a few per cent. It has been calculated that 4% porosity of the Ag layer would be ample to store all the water necessary to oxidize 1000 Å of Ti totally to TiO_2 . This degree of porosity is not unreasonable in evaporated Ag layers; a mechanism for capillary condensation in Ag contacts has been previously described.⁵

Outcome of the Investigation

Considering the electrochemical nature of the Ti/Pd/Ag contact on Si, it is now evident that the presence of an adequate quantity of Pd protects the Ti from corrosion by raising the potential for hydrogen evolution compared to that of Ag.⁶ It is likely that the Pd actually promotes the formation of a thin, stable TiO_2 film which passivates the bulk of the Ti against corrosion by allowing the Ti to exist at a potential that is greater than the reversible hydrogen potential.⁷ An insufficient amount of elemental Pd may actually accelerate the corrosion of the Ti. It is also important to control sintering conditions to avoid the loss of elemental Pd to the formation of Pd silicides. In addition, a thicker Ti layer impedes the formation of Pd silicides by insuring greater physical separation of the Pd and Si.

Major benefits of this investigation are:

- a. Minimum Pd (200 Å) and Ti (1500 Å) thicknesses have been defined for corrosion-resistant, space-qualified solar cells.
- b. A technique based on energy-dispersive X-ray spectroscopy has been synthesized to test for the presence of these minima. The procedure is nondestructive when used for examination of Pd, but requires chemical stripping of the Ag when the Ti is measured.

References

1. H. Fischer and R. Gareth, "New aspects for the choice of contact materials for silicon solar cells," *Seventh Photovoltaic Specialists Conf.*, Pasadena, Calif., 1968.
2. C. J. Bishop, "The fundamental mechanism of humidity degradation in silver-titanium contacts," *Eighth Photovoltaic Specialists Conf.*, Seattle, Wash., 1970.
3. W. H. Becker and S. R. Pollack, "The formation and degradation of Ti-Ag and Ti-Pd-Ag solar cell contacts," *ibid.*
4. A. G. Revesz, COMSAT Laboratories, private communications.
5. W. F. Springate, "Investigation into the mechanism of degradation of solar cells with silver-titanium contacts," in *Ohmic Contacts to Semiconductors*, New York: Electrochemical Society, 1969.
6. M. Stern and H. Wissenberg, "The influence of noble metal alloy additions on the electrochemical and corrosion behavior of titanium," *J. Electrochem. Soc.* 106: 1959.
7. M. G. Fontana and N. D. Greene, *Corrosion Engineering*, New York: McGraw-Hill, 1967.

INVESTIGATION OF IN SITU RADIATION DAMAGE TO GLASS IN ELECTRON MICROSCOPE

J. F. DeNatale and D. G. Howitt

The radiation damage exhibited by a nuclear waste glass is shown to be a combination of chemical decomposition and the structural breakdown of the glass network which is accompanied by oxygen evolution.

The radiation damage that a nuclear waste glass is capable of bringing upon itself affects its chemical and physical properties to a still undetermined extent. The damage process itself depends on the composition of the glass and the temperature at which it is to be stored, parameters that have as yet not been defined. The analysis of the microstructures induced in glasses of this type by in situ irradiation in a high-voltage electron microscope represents the first stage in the determination of the likely effects and importance of radiation damage to their stability.

Samples of a simulated nuclear waste glass (Table 1) similar in composition to the borosilicate glasses proposed for the containment of commercial waste¹ were prepared as thin foils suitable for examination by transmission electron microscopy. The specimens were irradiated at beam current densities between 0.1 and 10 A/cm² for periods of up to 1 hr in the Berkeley high-voltage microscope by means of 650keV electrons.

The radiation damage to the nuclear waste glass is quite nonuniform in the sense that some regions of the specimens can be almost insensitive to the electron beam in regard to a detectable structural or chemical response, yet other regions can react in a quite spectacular fashion (Fig. 1). The radiation damage when it does occur is always characterized by the growth of bubbles from within the foil and is often preceded by the chemical decomposition of the glass into two or more amorphous phases. The decomposition processes are extremely rapid at moderate dose rates and take only a fraction of a second to achieve a metastable microstructure. The decomposing phases can be made to coarsen with continued irradiation; crystalline phases ultimately develop from them. The formation of the bubbled microstructure in a region of the foil that did not undergo phase separation is shown in Fig. 2. The development of this microstructure, in the regions of the specimen where it does occur, is quite reproducible and the total electron dose necessary to initiate this type of damage if found to be about 100 c/cm² (6×10^{20} electrons/cm²). The consistency of this total dose with variation to the electron dose rate is shown in Fig. 3; the behavior appears to be invariant to any prior chemical decomposition that occurs.

The microstructure characteristic of the phase decomposition is shown in Fig. 4 at the later stages of coarsening when the crystalline products are also forming in addition to the amorphous phases. The development of crystalline phases could be consistently attributed to the effects of enhanced diffusion since the displacement threshold for an atom is unlikely to be above about 5 ev and there would be much displacement activity after the high electron doses that are apparently necessary for devitrification. However,

TABLE 1.--Waste glass composition.

Host matrix component	Wt. percent	Waste composition	Wt. percent	Waste composition	Wt. percent
SiO ₂	59.7	Na ₂ O	16.25	BaO	1.81
B ₂ O ₃	14.2	Fe ₂ O ₃	31.47	La ₂ O ₃	1.71
Na ₂ O	11.2	U ₃ O ₈	13.51	Pr ₆ O ₁₁	1.71
ZnO	7.45	MoO ₅	5.98	PdO	1.71
CaO	3.0	ZrO ₂	5.72	Cr ₂ O ₃	1.33
TiO ₂	4.45	Nd ₂ O ₃	5.23	SrO	1.22
		CeO ₂	3.84	Sm ₂ O ₃	1.07
		RuO ₂	3.44	NiO	0.66
		Cs ₂ O	3.33		

The authors are in the Department of Mechanical Engineering of the University of California at Davis, CA 95616. The work was supported by U. S. Department of Energy contract DE-A503-765F-0034.



FIG. 1.--Localized distribution of bubble formation in thin glass foil irradiated uniformly.

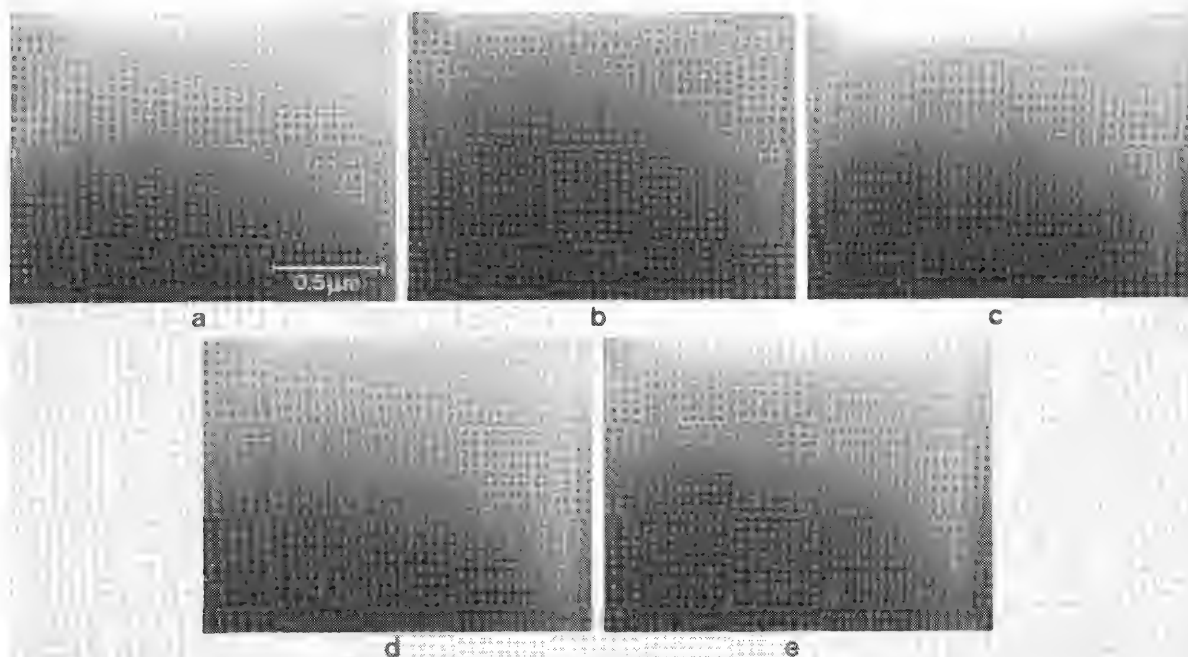


FIG. 2.--Development of radiation-induced damage in 10% wt glass.

the rapid formation of the amorphous phases suggests that ionization effects might well be responsible for the development of metastable phases and lead to glass immiscibility. The glass-preparation techniques did not involve the rapid quenching of the glasses and any subsequent decomposition at this rate could not be conceivably introduced by thermal effects.

In this type of radiation damage, both bubble formation and chemical decomposition can be induced at electron energies as low as 60 keV, which lends support to the assumption of a small displacement threshold for the creation of interstitial defects.

References

1. J. Mendel et al., *Annual Report on the Characteristics of High-level Waste Glass*, Battelle Pacific Northwest Laboratories, 1977.

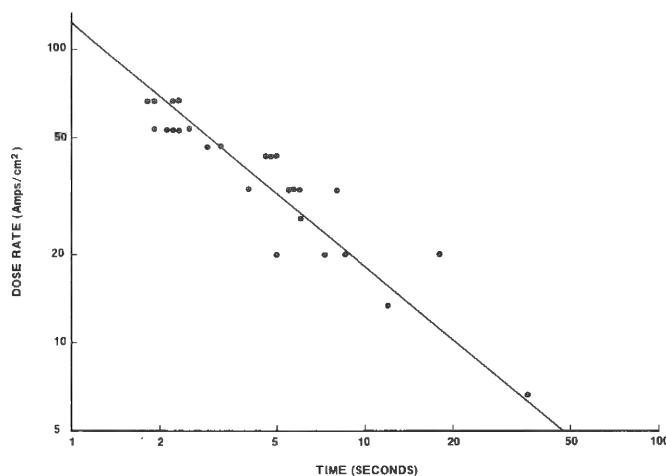


FIG. 3.--Dose-rate dependence of radiation damage for 33% wt. glass at 200°C.

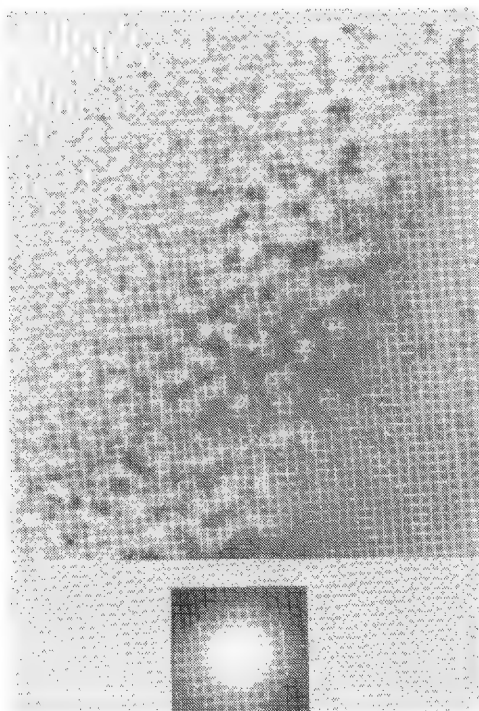


FIG. 4.--Radiation-induced phase separation in 33% wt. glass.

ELECTRON MICROSCOPY OF LEACHED GLASSES

D. K. McElfresh and D. G. Howitt

Electron microscopy experiments indicate that the dissolution of nuclear waste materials is significantly altered in the presence of radiolysis products that are absent from the leaching experiments performed with nonradioactive simulated wastes.

The ability of a nuclear waste containment material to resist the leaching of its components is thought to be the single most important factor in the determination of its suitability. Although leaching experiments are performed with various solutions to simulate the realistic environment of the nuclear waste form, very little attention has been paid to the role of radiation damage to these solutions brought about by the radiation emitted from the waste and its significance to the leaching problem. To determine the likely effects of this indirect action of the radiation to the radiolysis of a simulated nuclear waste glass, an in situ leaching experiment was conducted at room temperature in the environmental cell of an high-voltage electron microscope. Water saturated helium was the aqueous medium and the high-voltage electron beam (1 MeV) was the irradiation source. The region exposed to both the water vapor and the electron beam underwent a surface reaction in a matter of minutes (Fig. 1); the areas of the specimen exposed only to the water vapor were unaffected even after several hours of exposure. The glass that was examined was similar in composition to the borosilicate glasses proposed for the containment of commercial nuclear waste,¹ although it is quite likely that all the waste forms, both vitreous and crystalline, would be susceptible to an accelerated interaction in an experiment of this type.

The radiolysis products responsible for the accelerated interaction in the partial vacuum of the electron microscope might be significantly different from those expected in the presence of air, notably the absence of nitric acid. Therefore, additional leaching experiments were performed on the simulated waste glass with solutions of likely radiolysis products. The specimens of the glass were all leached in static solutions for 48 hr at room temperature prior to examination in the electron microscope. The transmission electron microscopy specimens were prepared by ion milling techniques and the transparent regions of the foils were about 50 μm beneath the original leached surfaces; the surfaces of the scanning electron microscopy specimens were the leached surfaces themselves. Of the solutions used nitric acid induced the most noticeable changes to the glass microstructure in transmission (Fig. 2); the specimens leached in distilled water were difficult to distinguish from those which had not been leached at all (Fig. 3). The scanning electron microscopy results also showed appreciable surface changes in the case of nitric acid both in structure and composition.

This leached glass showed a distinctly different surface from its unleached counterpart (Fig. 4) and was virtually depleted of uranium, zinc, and calcium and reduced in its concentration of iron and titanium, as shown in the x-ray spectra from the samples in Fig. 5. The spectra from the water-leached and untreated glass are shown for comparison.

The leaching process can be conveniently described as a surface interaction or dissolution mechanism coupled with the segregation of components between the glass interior and this surface.^{2,3} It would seem that not only the rate but the mechanism of the surface interaction changes significantly in the presence of a radiation fields and that this change can drastically alter the concomitant segregation and hence overall leach rates of these materials.

References

1. J. F. DeNatale and D. G. Howitt, *Microbeam Analysis*--1981, 273.
2. J. R. Wiley, *Nuclear Technology* 43: 268, 1979.
3. A. J. Machiels, "Scientific basis for nuclear waste management," *Proc. Mat. Res. Soc.*, Boston, 1980.

The authors are in the Department of Mechanical Engineering of the University of California at Davis, CA 95616. The work was supported by U. S. Department of Energy contract DE-A503-765F-00034.

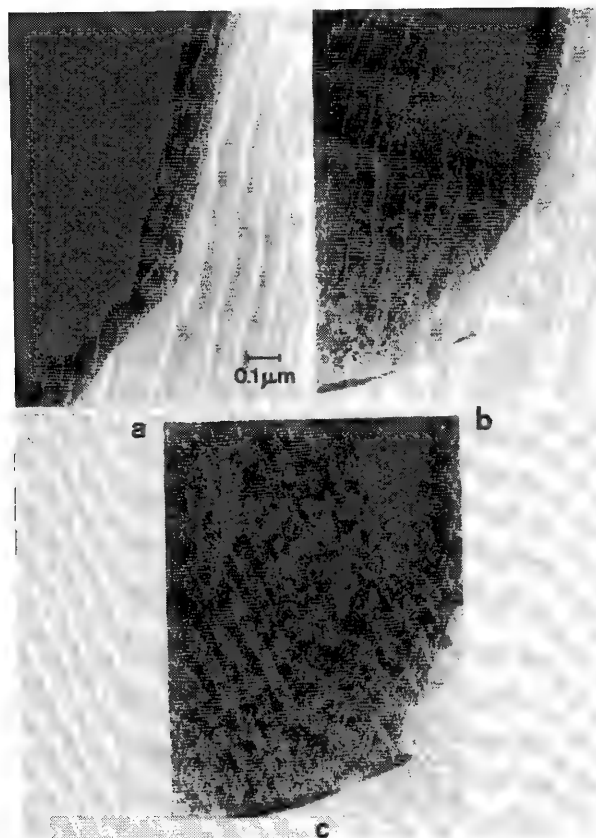


FIG. 1.--TEM micrographs of a simulated nuclear-waste glass exposed to both water vapor and a $0.5\text{A}/\text{cm}^2$ electron beam for (a) 0 s, (b) 560 s, and (c) 950 s.

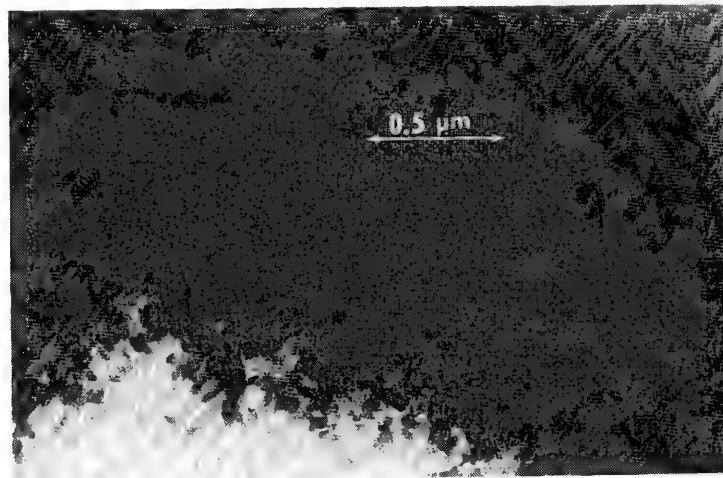


FIG. 2.--TEM micrograph of a simulated nuclear waste glass statically leached in 0.15 M nitric acid for 48 hours at room temperature.

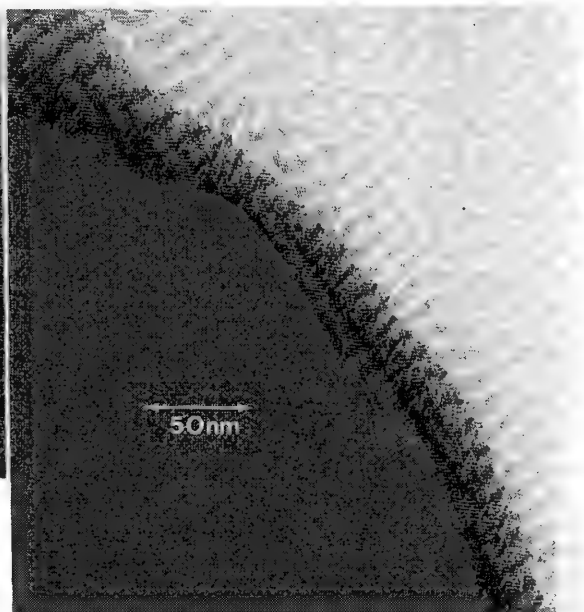


FIG. 3.--TEM micrograph of an untreated simulated nuclear waste glass.

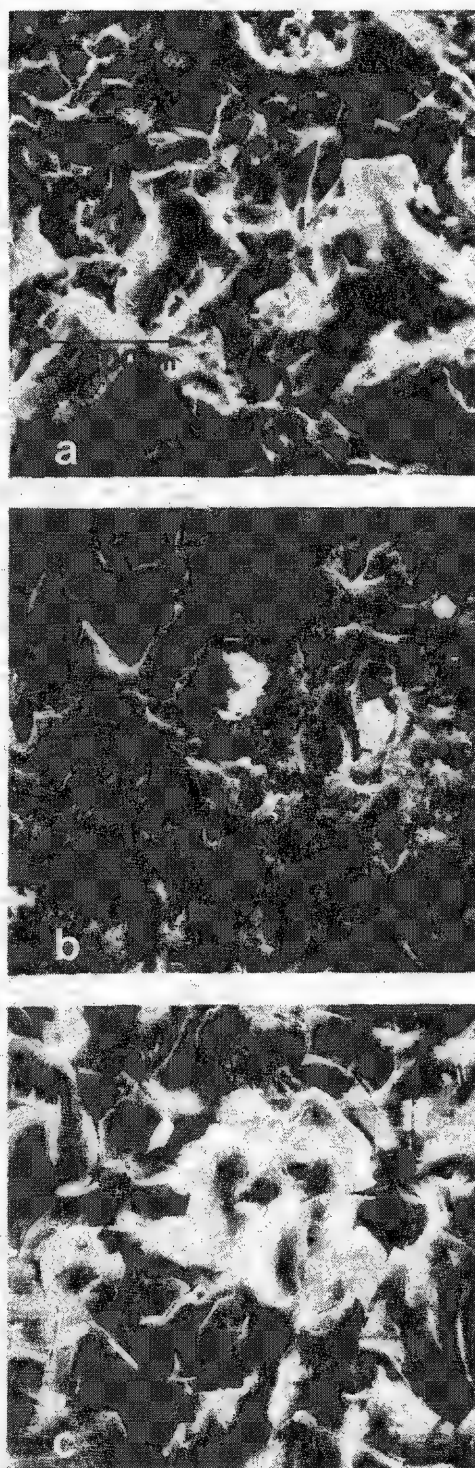


FIG. 4.--Scanning electron micrographs of the surface of simulated nuclear waste glasses that were (a) untreated (b) leached in flowing distilled water for 48 hours at 100°C and (c) statically leached at room temperature in 0.15 M nitric acid for 48 hours.

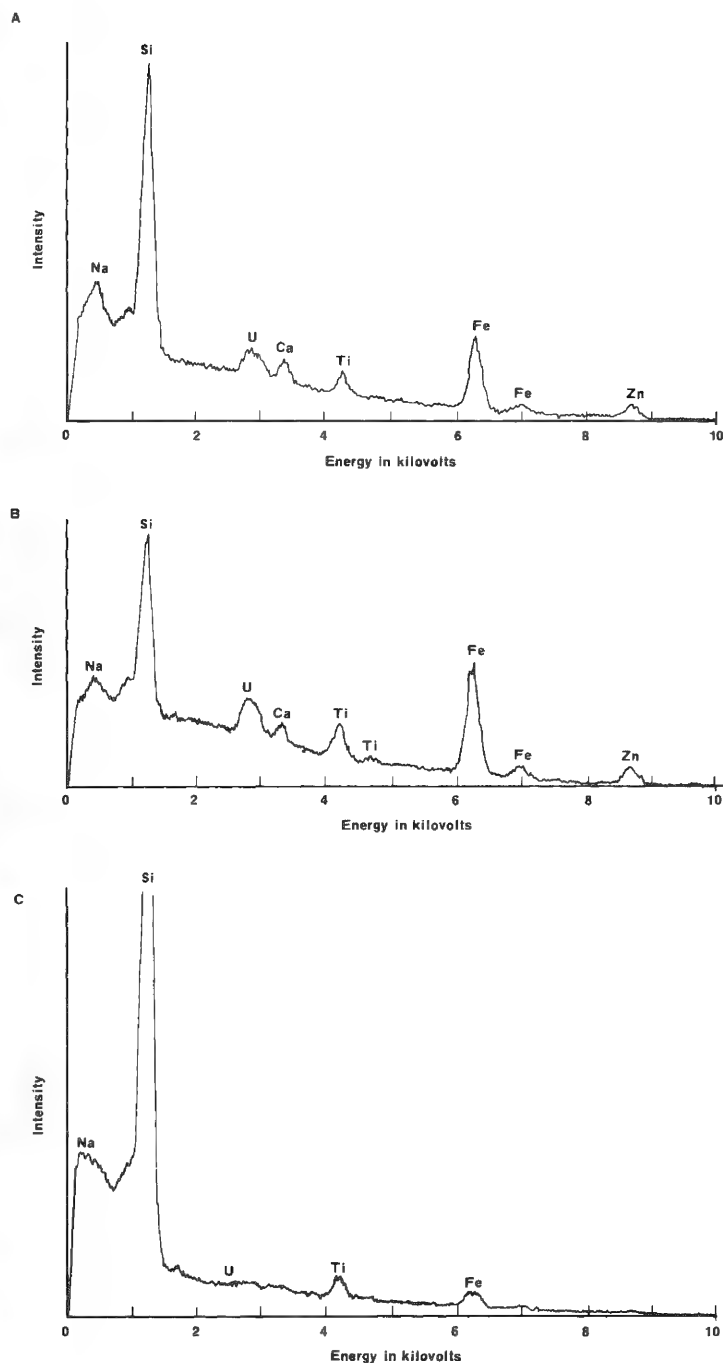


FIG. 5.--EDX spectra of the surfaces of the glasses shown in Fig. 5. (a) untreated (b) leached in flowing distilled water for 48 hours at 100°C and (c) statically leached at room temperature in 0.15 M nitric acid for 48 hours.

SOME ANALYTICAL USE OF STEM FOR STUDY OF OXIDATION ON METALS

Fumio Watari

With the combined use of diffraction including both selected area diffraction (SAED) and microdiffraction (MD), imaging modes, and energy loss spectroscopy (ELS), STEM has the capacity to analyze simultaneously the composition, structure, and morphology of a specimen. Such a concentration of analytical means is certainly of great value for materials science. However, the specimen conditions and the limitations for each technique often limit the effectiveness of the applications. It is therefore worthwhile to test the capabilities of a current STEM instrument used as an analytical electron microscope (AEM). The present paper shows some results related to the oxidation of metals, and in particular the surface oxide layer formed at an ambient temperature, which is relatively less ordered, is very thin and difficult to detect, and whose features are less known by other methods.

Qualitative Use

Using a pre-evacuation chamber (air-lock), we installed a simple in situ evaporation system in the HB5. This arrangement makes it possible to evaporate some metals in a vacuum of better than 1×10^{-7} Torr without exposure to air before observation. Although the vacuum used in this system is not really satisfactory, the specimens prepared in this way make observation of the effect of gas exposure on certain kinds of materials possible. Also, there is much less of the contamination which is usually a serious problem for metallic specimens. Whiskers of CuO with diameters about 200 Å were grown on a fine Cu grid by heating at 300°C in air and 99.9999% Al was evaporated and crystallized around the CuO whiskers. The CuO whiskers before evaporation are shown in Fig. 1A, together with ELS spectra with peaks from the O_K edge at 532 eV and the $Cu_{L, II, III}$ edge at about 930 eV.

After evaporation, the zero-loss BF image shows the thick Al crystallized on the CuO whiskers (Fig. 1B). In the image formed with the first plasmon-loss (15eV) electrons, the skeleton appearance of this composite material is clearly seen (Fig. 1C).

The ELS spectra B1 for Al as evaporated shows the slight O_K peak as well as the Al_K peak at 1560 eV. The vacuum in the range of 10^{-8} Torr is not satisfactory enough to prevent oxidation on the surface of Al. After exposure to air with an atmospheric pressure at 300°K, there is an increase of oxygen pick-up, as seen by the increase of the O/Al ratio from Fig. B1 to B2. The more detailed look of this specimen is shown in Fig. 2, which is imaged with electrons (including both zero-loss and energy-loss ones) by means of an optical recording system.¹ Spatially this specimen is classified into three parts a, b, c, corresponding to the image in Fig. 2. The darker areas of about 100 Å or less in size (type a) are distributed in the bright contrast area (type b) and in the center lies the CuO whisker. If we apply microanalysis with a probe size around 15 Å, and a resolution in ELS of 2 eV, both a and b regions show the plasmon peak at 15 eV characteristic of metallic Al. For the same detector gain, the absolute intensity in the zero-loss beam is considerably smaller in region a, although the ratio of plasmon to zero-loss peak is approximately the same. MD recorded with an optical system shows the strong excitation of Bragg reflection of Al (111) (see insertion). Generally in region b, there are spots weakly excited or far from the center one. The difference between the a and b regions is therefore a difference of diffraction conditions and not of composition, which also indicates that the grain size of Al is about 100 Å. The MD pattern from region C shows that of CuO associated with streaks. In ELS, 15 eV Al plasmon loss is not particularly observed; instead, a broader peak located at higher-energy region replaces it. The intensity is also decreased, which reflects the larger thickness and larger atomic scattering factor of Cu.

The author is with the Department of Physics at Arizona State University, Tempe, AZ 85281. This research was performed under U.S. Department of Energy Grant DE-AC02-76ER02995.

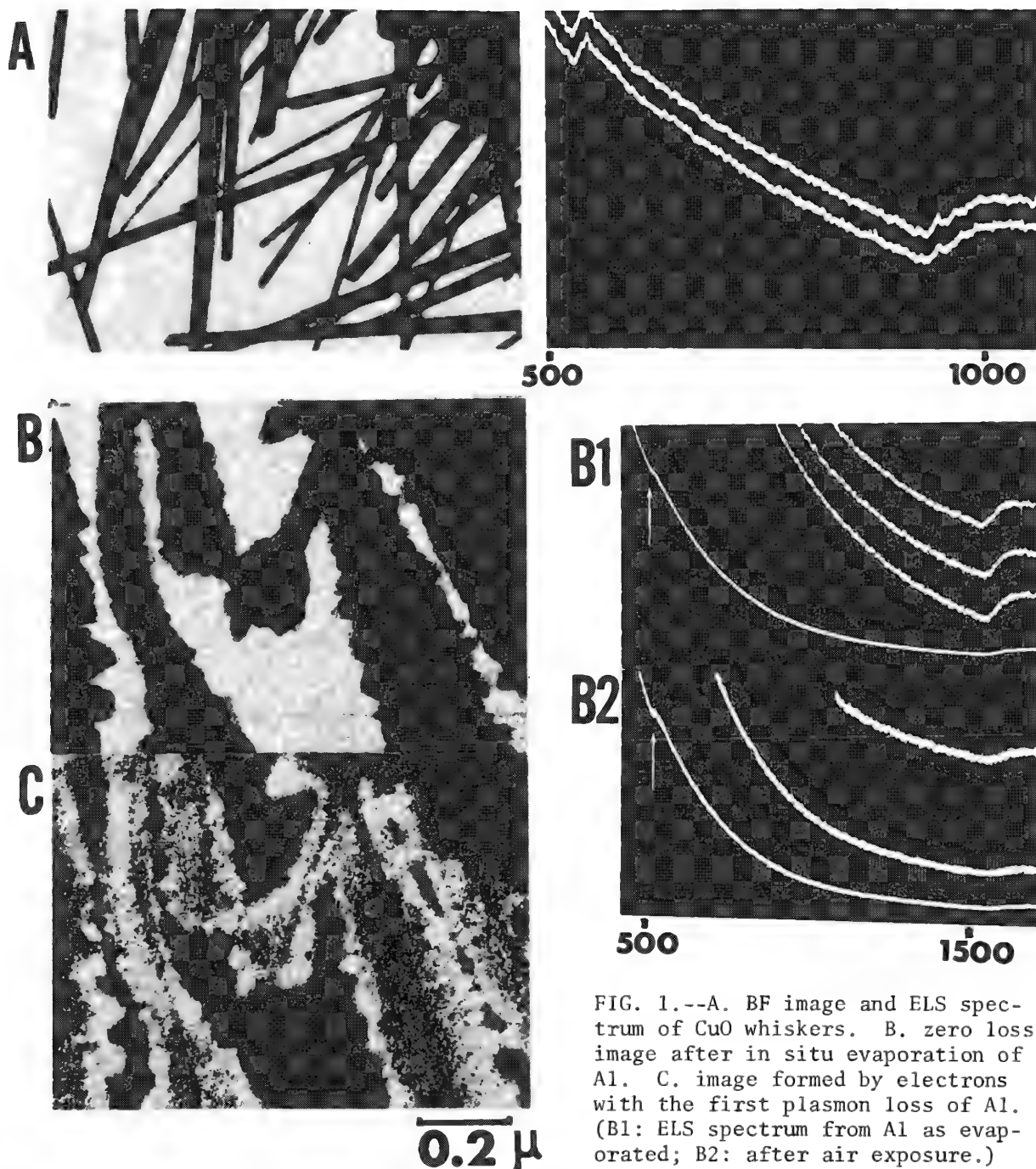


FIG. 1.--A. BF image and ELS spectrum of CuO whiskers. B. zero loss image after in situ evaporation of Al. C. image formed by electrons with the first plasmon loss of Al. (B1: ELS spectrum from Al as evaporated; B2: after air exposure.)

Next, 99.9% Fe was prepared by in-situ evaporation onto an amorphous carbon film. Figure 3 shows the change of SAED and ELS spectra with the time of exposure to air at 300°K. Because of the carbon substrate, the ELS spectra have a higher background but energy-loss electrons can be collected from a wider area. Figure 3a shows the ring pattern of the polycrystalline bcc Fe and there is a $Fe_{L II III}$ peak but no O_K peak in the ELS spectrum. After the 10min exposure to air, a slight shoulder occurs at the O_K peak position in ELS and a rather diffuse scattered ring corresponding to about 2.5 Å in real space appears on the SAED pattern inside the innermost ring of Fe (110), which may be easily overlooked in the usual situation. After 14 hr of exposure, both the O_K peak and 2.5 Å diffuse ring become prominent. It is clear that the 2.5 Å ring is related to oxide and that oxidation proceeds at an ambient temperature in Fe, which confirms a previous result.³

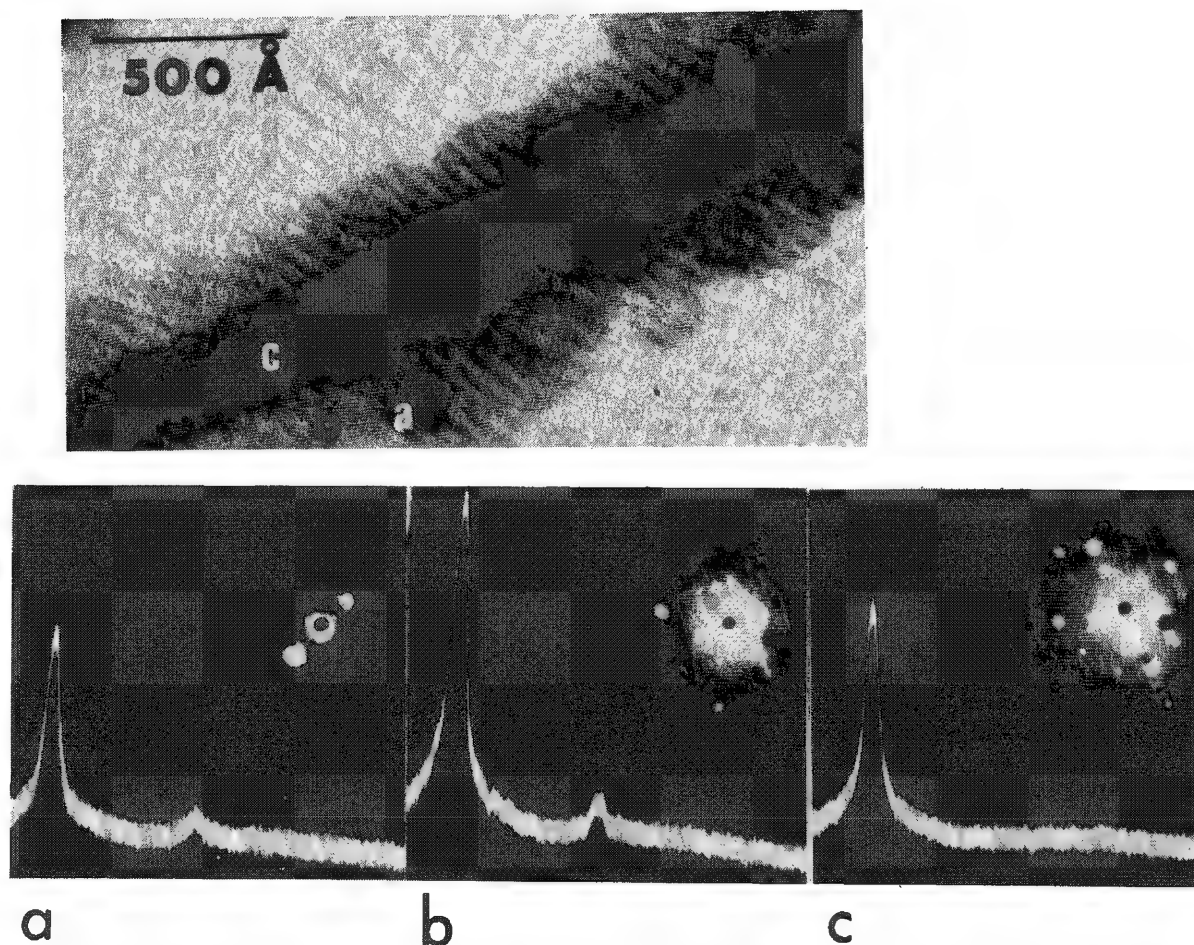


FIG. 2.--Microanalysis (ELS and MD) from region a, b, and c of Al image.

Quantitative Use⁴

The thin-film specimens of Cr, Fe, and Fe-Cr were prepared at 300°K by evaporation outside the microscope, then exposed to air. The total thickness changed systematically from 10 to 1500 Å and STEM observation was done without a supporting film. Such specimens with larger uniform areas, known values of thickness, and no substrate provide suitable conditions for quantitative analysis. Figure 4 shows the ELS spectra of oxidized specimens of 15Å-thick Cr, 160Å-thick Fe-25% Cr, and 200Å-thick Fe. By use of both calculated values for cross sections of particular energy loss edges and comparison with the oxides with their composition known as a standard, the composition and thickness of surface oxide layers were estimated. The ratios of cation/anion are 0.5 and 1, and the oxide thicknesses are about 10 Å and 100 Å for Cr and Fe, respectively. MD shows that the oxide film covers the metal specimen uniformly and its structure is close to being amorphous for some time after specimen preparation. The diffraction intensity profile was taken by a rocking beam method, and radial distribution function analysis was done. The cation-cation nearest neighbor distance is about 3.2 Å. In this way both structural and compositional analysis could be performed although there is a limit in their precision.

Conclusion

The present study shows the power of the combination of techniques to provide information that is not otherwise available. From the point of view of the application to the materials science, the restriction on the specimen thickness is serious. Quantitative use of peaks in the ELS spectra is limited to specimens with a certain range of thickness. Also, the spectroscopic study of chemical information depends on the EL spectrometer it-

self. Although quantification is limited at present the use of in situ specimen preparation seems promising with an ultrahigh vacuum system.

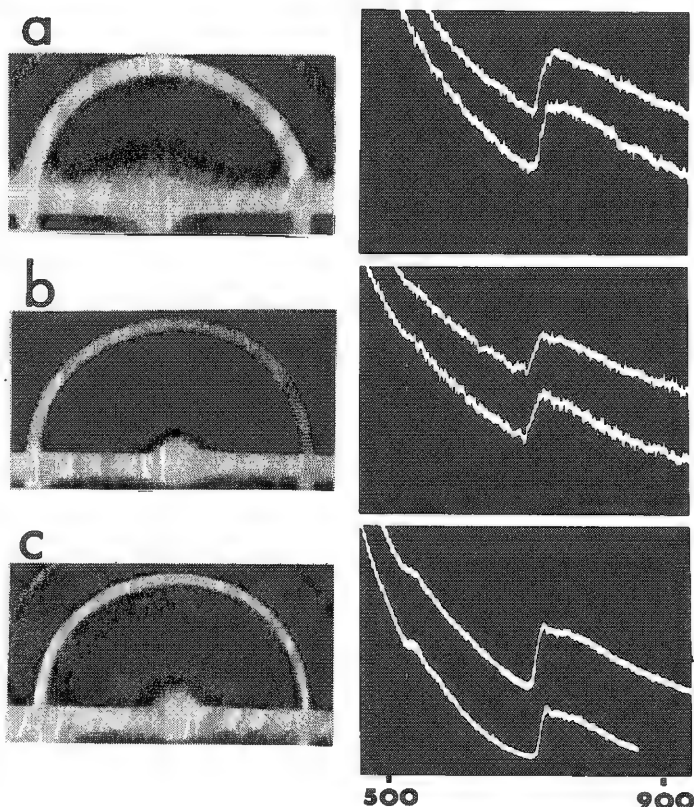


FIG. 3.--Change of SAED and ELS of in situ evaporated Fe on a carbon film (a) as evaporated, (b) after 10min air exposure, (c) after 14hr air exposure.

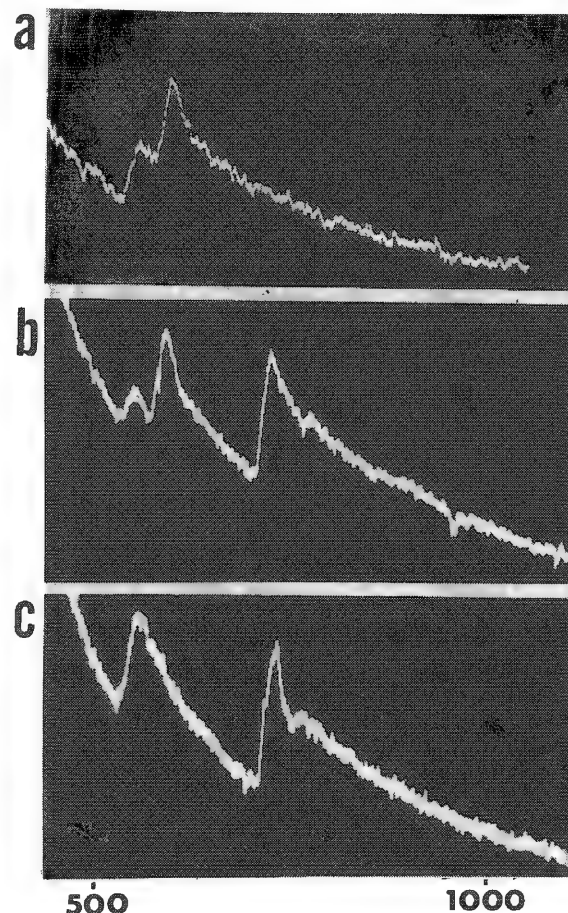


FIG. 4.--ELS spectra of oxidized (a) Cr (15 Å thick), (b) Fe-25% Cr (160 Å thick), (c) Fe (200 Å thick).

References

1. J. M. Cowley, "Optical processing of diffraction information in STEM," *SEM/1980*, I, 61.
2. Fumio Watari and J. M. Cowley, "Some applications of microdiffraction to the study of oxide formed on the surface of Cr," *Proc. STEM in Solid State Science* (Castle Hot Springs), 1981.
3. Fumio Watari and J. M. Cowley, in preparation.
4. Fumio Watari, "Detection of protective oxide layers on Cr formed by exposure to air," submitted to *Surface Science*.

ASEM ANALYSIS OF UNFIRED CERAMIC COMPACTS

W. E. Votava

Ceramic processing of many types of materials requires that organic additives be added. Knowledge of how well these additives are dispersed in the unfired compacts can provide information about the way that compact will perform during processing and also provide an insight into the properties of the final fired compact. The operating characteristics of an analytical scanning electron microscope (ASEM) that have been found most useful in the identification and characterization of organic additives in unfired ceramic compacts are described. Optimization of beam-sample-detector relationships has allowed positive identification of these additives and has provided a qualitative assessment of their distribution. Optimization of sample preparation procedures that can affect the production and detection of secondary, backscatter, and x-ray signals as they are used in the investigation of unfired ceramic compacts are discussed.¹

Experimental Procedure

Compositions of 97.5% A-12 alumina and 2.5% zinc stearate were wet mixed with acetone in a wrist-action shaker for 15 min. Compositions of 97% 400 mesh alumina and 3% polyvinyl alcohol (PVA) were also prepared by dissolving the PVA in warm distilled water to make a solution and then wet mixing with the powder in a wrist-action shaker for 15 min. A sample of the alumina-PVA system was doped with a small amount of a soluble cobalt salt, $\text{Co}(\text{ClO}_3)_2$, by addition of the cobalt salt to the PVA solution before the PVA solution was added to the alumina. Each of the above systems was allowed to dry until a hard compact was formed.

A final compact with a composition of 91% commercial barium titanate powder, 6% PVA, and 3% microcrystalline cellulose was also prepared. Suspensions of this mixture were mixed in a blender and cast into sheet by means of a doctor blade. The specimen used was isostatically pressed at $3.1 \times 10^8 \text{ N/m}^2$.

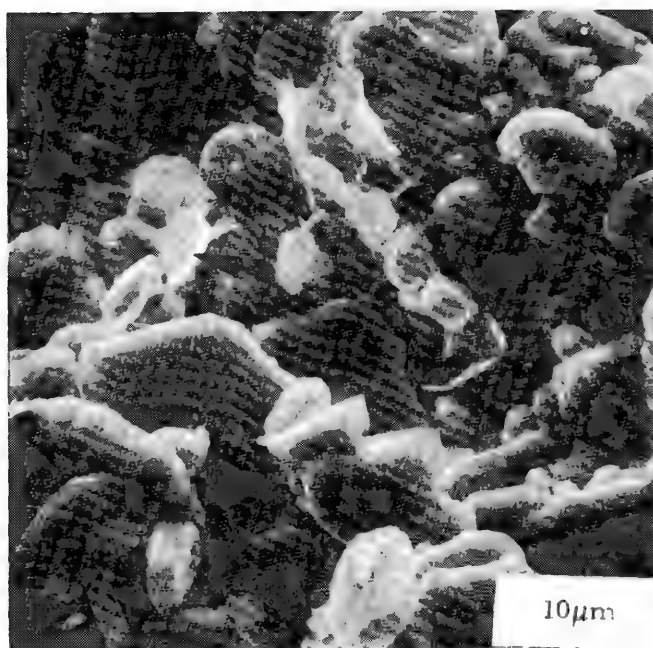
Each of the specimens was then fractured and glued to an aluminum stub by means of low-resistance contact cement (LRCC). Care was taken that the LRCC was brought up to the surface to be investigated. Further preparation included application of a coating of 250 Å of Au-Pd, sputtered onto the surface in an argon plasma at 150 µm of Hg. This process provides a very uniform coating for the very rough topography associated with unfired compacts.

An ETEC autoscan equipped with a solid-state backscatter detector and a Princeton Gamma Tech Alpha 1000 energy-dispersive spectrometer (EDS) was used in the investigation of the unfired compacts described above. Accelerating voltages of 20 and 10 kV were used for the investigation. Specimen currents ranged from 10^{-10} to 10^{-8} A, depending on which signal was being imaged. The working distance was varied between 8 and 25 mm to optimize the detection of each signal being imaged.

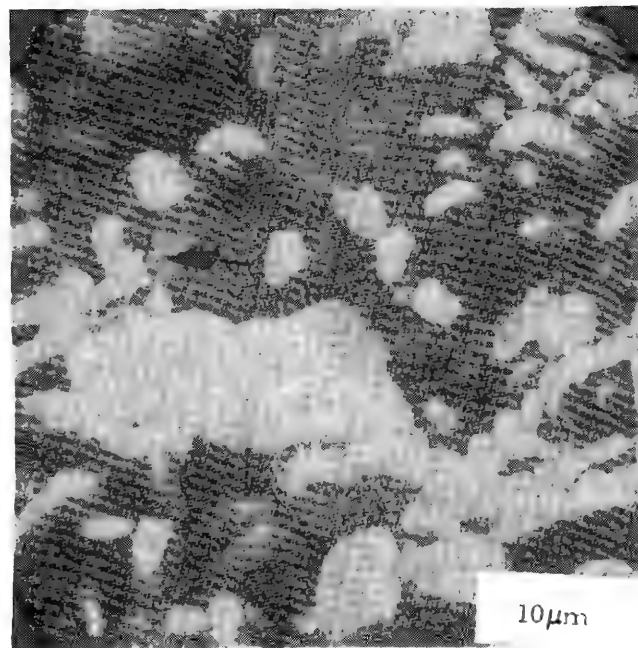
Results

Observation of each specimen sample was by the secondary-electron mode for the purpose of characterizing the differences between the organic additives on the basis of topographical differences between the major phase particles and the additive phase. Figures 1(a), 2(a), and 3(a) are secondary-electron micrographs of each system that illustrate the results as described above. In the case of the alumina-zinc stearate compacts, the zinc stearate phase is evident as very thin flakes of material. The low density and thinness of the flakes allows for increased production and escape of secondaries. The ability of the detector to collect a large number of these secondaries makes it quite evident that there is a separate phase present in the unfired compound. The alumina-PVA compacts and the barium titanate-PVA-microcrystalline cellulose compact also showed that the differences in the secondary-electron production from thin films extending between grains and sharp edges on organic particles presented contrast that helped to characterize these organic additives as being separate phases.

The author is with the New York State College of Ceramics at Alfred University, Alfred, NY 14802.

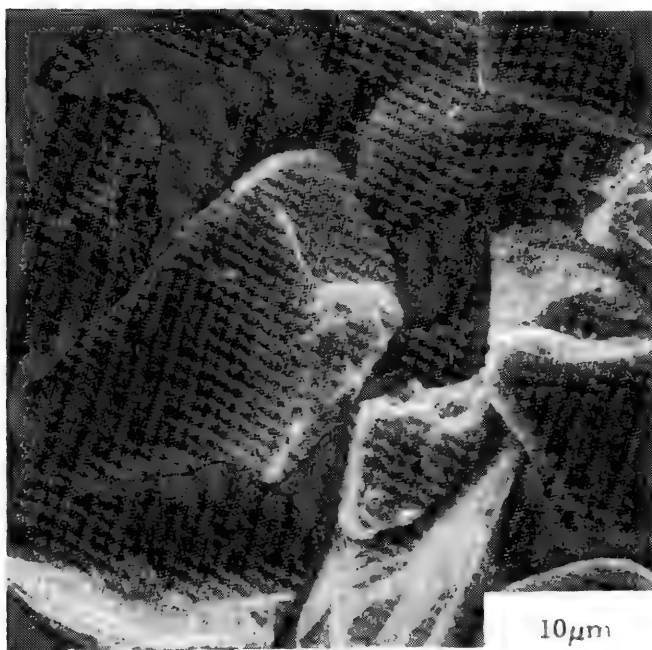


(a)

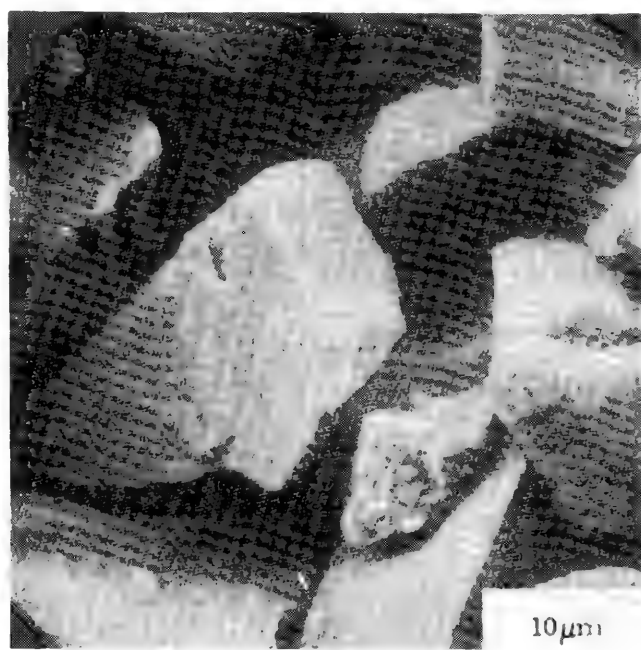


(b)

FIG. 1.--250 Å Au-Pd, 20 kV, 8mm working distance, 2.5% zinc stearate-97.5% A-12 alumina; (a) secondary-electron emission, (b) backscattered electron emission; arrows point to zinc stearate flakes.



(a)



(b)

FIG. 2.--250 Å Au-Pd, 20 kV, 8mm working distance, 400 mesh alumina and PVA with cobalt added; (a) secondary-electron emission, (b) backscattered electron emission; arrows point to PVA additive.

Each specimen was also observed by means of the solid-state backscatter detector to confirm the results found by observation of the secondary-electron signal. In each specimen the organic additive has a much lower average atomic number than either the alumina systems or the barium titanate system. Even though fracture surfaces of each sample were

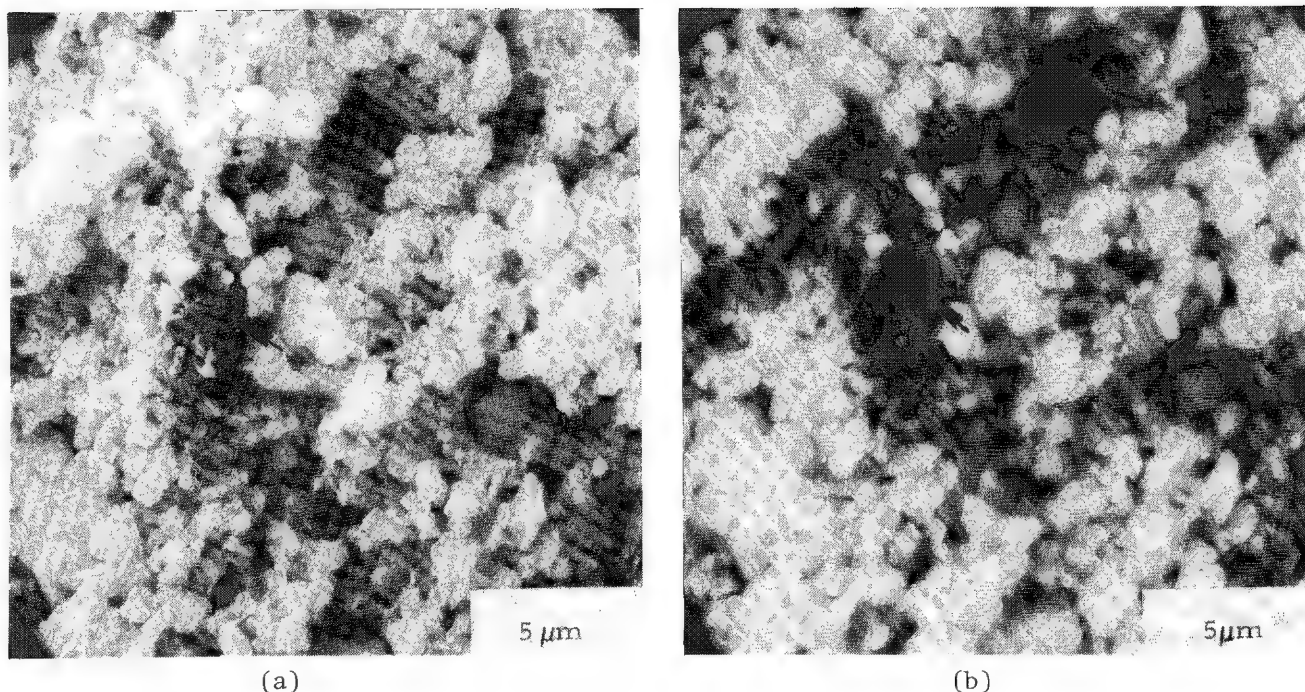


FIG. 3.--250 Å Au-Pd, 20 kV, 8mm working distance, barium titanate with 3% PVA and 6% microcrystalline cellulose; (a) secondary-electron emission, (b) backscattered electron emission; arrows point to microcrystalline cellulose.

used for the investigation, the contrast available clearly displays that both phases are present in the unfired compact. Even more significant was the comparison of the contrast differences between the same areas with the secondary-electron image and the backscattered electron image. In the alumina-zinc stearate system in Fig. 1(a) the flakes of zinc stearate show a lot of contrast owing to the increased secondary-electron production from the thin flakes. In Fig. 1(b) this contrast is absent because the low-atomic-number flakes produce very little contrast for the backscatter detector to collect. These contrast differences are also easily seen in Figs. 2 and 3.

The third and last piece of evidence that the organic additives can be identified as separate phases are the results of the EDS investigation. Figures 4 and 5 are EDS spectra showing the difference between the zinc and PVA (cobalt) phases and the alumina phases. The EDS spectra were obtained by focusing upon areas shown to be essentially single phases by secondary and backscattered electron analysis. The spectra in Fig. 4 show that there is a significant increase in the concentration of zinc from the area of the unfired compact which contained zinc stearate flakes. Figure 5 contains spectra that show that the PVA-cobalt phase can be clearly distinguished by the same procedure as for the alumina-zinc stearate system. To obtain all these results strict attention had to be paid to optimization of the specimen current, accelerating voltage, detector positioning, and sample position. For example, to obtain acceptable backscattered electron images the specimen current had to be raised to 10^{-8} A from the normal 10^{-10} A and a working distance of 8 mm had to be used. To obtain the EDS spectra the specimen current was left at the normal value of 10^{-10} A and a working distance of 25 mm was used so that the EDS detector could be brought as close to the sample as possible for the largest solid angle of collection.

The results reported above were all obtained with an accelerating voltage of 20 kV. Experiments at 10kV accelerating voltage failed to produce enough contrast in the backscattered image to obtain acceptable micrographs. Also, because of the high energy of the Zn and Co x rays, unacceptable spectra were produced, so the EDS analysis was also rejected as a valuable method of analysis at 10kV accelerating voltage. Since the backscattered electron image and the EDS analysis were both unacceptable, the secondary-electron image was not used either, even though it produced acceptable images.

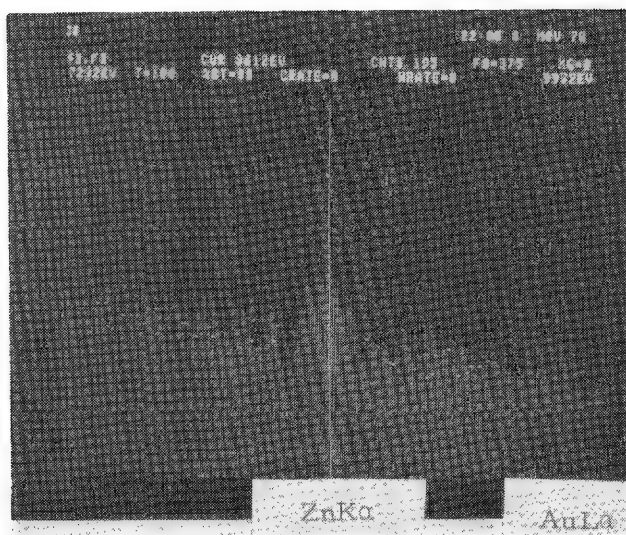


FIG. 4.--EDS comparison of alumina grain and zinc stearate flakes: lines are alumina grain, dots are zinc stearate flakes.

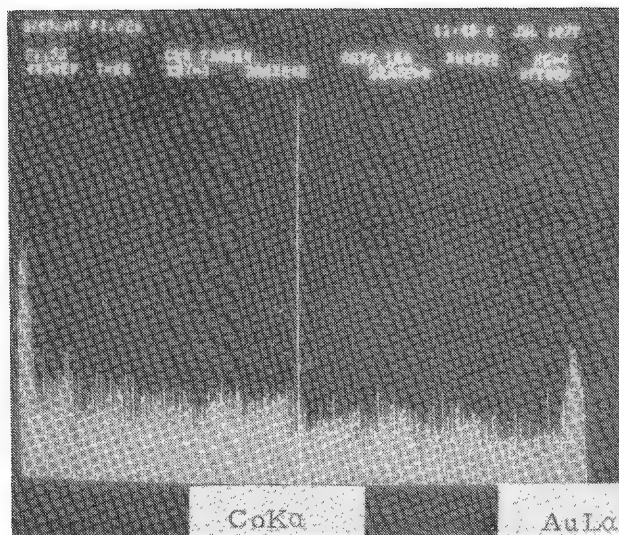


FIG. 5.--EDS comparison of alumina grain and PVA with cobalt: lines are alumina grain, dots are PVA with cobalt.

Conclusions

Unfired compacts have been investigated by means of a standard SEM with a standard solid-state backscatter detector and a standard EDS. Positive identification of minor organic additive phases can be made from combinations of the secondary-electron signal, the backscatter signal, and the x-ray signal. Characterization of how these minor organic additives are dispersed and fitted into the structures investigated can be performed. Instrumental parameters such as accelerating voltage, specimen current, sample position, and detector positioning are critical to the successful identification and characterization of minor organic additives in ceramic compacts. Finally, sample preparation to avoid charging of the unfired compacts is also very important. Procedures that provide a uniform coating and good conduction of the primary beam from the surface have been presented.

References

1. W. E. Votava, *Preparation and Analysis of Unfired Compacts Using the Scanning Electron Microscope*, Master's thesis, New York State College of Ceramics at Alfred University, 1980.

APPLIED SURFACE ANALYSIS

William Katz

Every analytical technique has associated with it an analytical volume, the volume of the matrix from which the species of interest is generated. This analytical volume may vary from bulk analysis, where the entire sample is consumed, to examining a single monolayer with no sample alteration. It is well known that the elemental (chemical) composition of a material may vary dramatically from interior to its surface. In many systems it is precisely the chemistry of the surface or near-surface region that controls the performance of the material. It is therefore vital for the materials scientist to be able to characterize the surface.

The types of surface analytical techniques currently available tend to use ion, electron, or x-ray excitation. Depending on the analytical species detected (primary backscattered ions, secondary ions, electrons, or photons), information regarding the elemental or chemical composition of the surface is obtained. We discuss four of the more common of the surface methods: Auger electron spectroscopy (AES), electron spectroscopy for chemical analysis (ESCA), ion scattering spectrometry (ISS), and secondary ion mass spectrometry (SIMS). The fundamentals of each technique are reviewed and their applications to materials characterization are illustrated. It is the goal of this discussion to contrast the strengths and weaknesses of each technique and demonstrate how two or more of these methods often complement one another to provide a more complete description of the surface region.

Ion Beam Techniques

A material under energetic ion bombardment can undergo a variety of processes, i.e., backscattering of the primary ion, sputtered ion emission, etc. The exact type of process that occurs is determined to a large extent by the kinetic energy of the primary ion used. Therefore, the discussion of ion beam methods will be divided into three energy regimes: (a) 300 keV-4 MeV, (b) 5-20 keV, and (c) 0.2-2 keV. In the high-energy regime, 300 keV-4 MeV, an alpha particle can penetrate deep into a sample (10 000 Å) and backscatter from a sample atom by a Rutherford collision. Such a process produces a non-destructive, quantitative in-depth analysis of the material. Although Rutherford backscattering spectrometry (RBS) has demonstrated its analytical usefulness, only recently has such instrumentation become available for "in-house" use. Therefore, the remainder of the discussion on ion beam methods will concentrate on lower energy beams.

The interaction between a 0.2-2keV ion and surface atom is an elastic binary collision that results in the backscattering of the primary ion (Fig. 1). Knowing the energy E_0 of the ion after backscattering from a surface atom into an angle θ , one can determine the mass of the surface atom by:

$$\frac{E}{E_0} = \frac{M_1^2}{(M_1 + M_2)^2} [\cos \theta + \sqrt{(M_2^2/M_1^2 - \sin^2 \theta)}]^2 \quad (1)$$

This technique is practically limited to only the outermost monolayer, since the probability of neutralization of the primary ion past the first few atomic layers is quite large. An ISS spectrum therefore provides both qualitative and quantitative information on the outer monolayer. Equation (1) shows that the ability to resolve a given mass increases as the difference in masses between the primary ion and target atom increases. Thus, in order to maximize mass resolution a variety of primary ions are used, typically $^4\text{He}^+$, $^{20}\text{Ne}^+$, and $^{40}\text{Ar}^+$.

ISS gives a spectrum of yield versus energy of the backscattered ion. From Eq. (1) one can readily calculate mass from the energy of the backscattered ion, which provides an elemental analysis of the outer monolayer. ISS is perhaps the most surface sensitive of the techniques, with detection limits of 10^{-2} (atomic fraction). The only real matrix

effect with the method is the noted change in intensity of the backscattered ion for a constant concentration due to the change in the neutralization probability in going from one material to another. Detailed discussions of ISS have been made by Taglauer and Heiland,^{1,2} Brongersma et al.,^{3,4} and Honig and Harrington.⁵

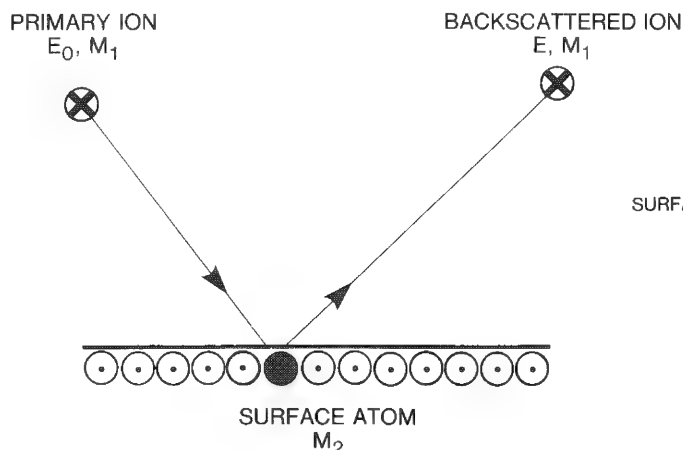


FIG. 1.--Low-energy (0.2-2.0keV) ion scattering (ISS).

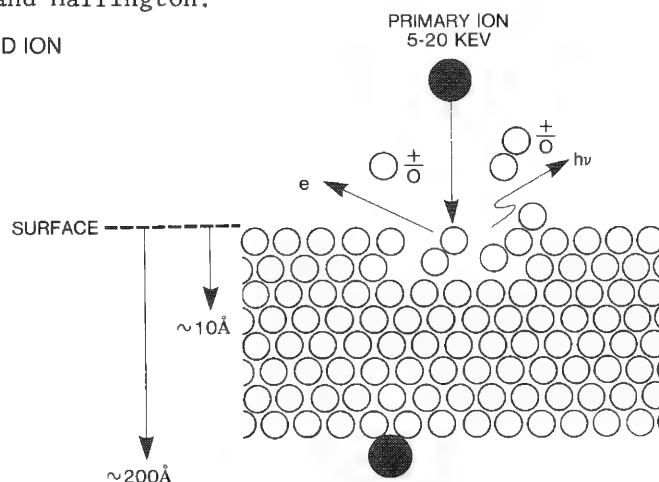


FIG. 2.--5-20keV ion bombardment (SIMS).

The final energy regime to be discussed is the 5-20keV range. In this energy range, ion bombardment of a material removes, or sputters, species characteristic of the sample. The species may be positive, negative, or neutral atoms; positive, negative, or neutral molecular clusters; photons; and electrons. A material under 5-20keV bombardment is shown schematically in Fig. 2. Secondary ion mass spectrometry (SIMS) involves the detection of these positive and negative atomic and molecular ions. Figure 2 shows that not only does the primary ion cause the ejection of secondary ions, but that it becomes implanted into the sample. The analytical significance of this will be discussed later.

Inherent to SIMS is the sputtering of surface layers from the analytical matrix. (This discussion will be restricted to SIMS used in the dynamic or sputtering mode, contrasted to static SIMS, which examines the outermost monolayer.) By monitoring of one or more of these secondary ions as material is removed, an in-depth analysis of the material is performed. The key to this profiling capability of SIMS is the shallow sampling depth. Two major factors affect this sampling depth. The first has to do with the actual interaction distance of the primary ion in the sample matrix. The parameters that affect this distance are the kinetic energy and mass of the primary ion and the mass of the target. The second factor that affects sampling depth is the escape depth of a secondary ion. The combination of these results in sampling depths of 5-50 Å. Detailed discussions of SIMS may be found in the literature.^{6,7}

The primary ion is of fundamental importance in SIMS. Depending on the choice of primary species and beam parameters such as energy and current density, different information may be extracted from a given sample. In most analytical situations the primary ion of choice is oxygen or cesium. It is well known that a reactive primary species enhances the secondary ion yield, by its effect on the surface or near-surface region of the sample under bombardment. As an electronegative element, oxygen has the effect of enhancing the production of ions from electropositive species. Conversely, cesium is seen to enhance negative ion emission. To realize the full analytical potential of SIMS, one needs both electronegative and electropositive primary ions. These factors result in a surface technique capable of elemental specificity from H to U with limits of detection of 10^{-4} - 10^{-8} (atomic fraction).

Despite the excellent sensitivity of SIMS, the technique has long been hampered by the extremely large variations in the secondary ion yields across the periodic table. Regardless of the primary ion used (O_2^+ , O^- , or Cs^+), both the positive and negative secondary ion yields from pure elements are known to vary by up to five orders of magnitude (Fig. 3).⁸ This single problem has probably done more to hinder SIMS than any other factor. The seemingly unpredictable ion yield variations have severely hampered

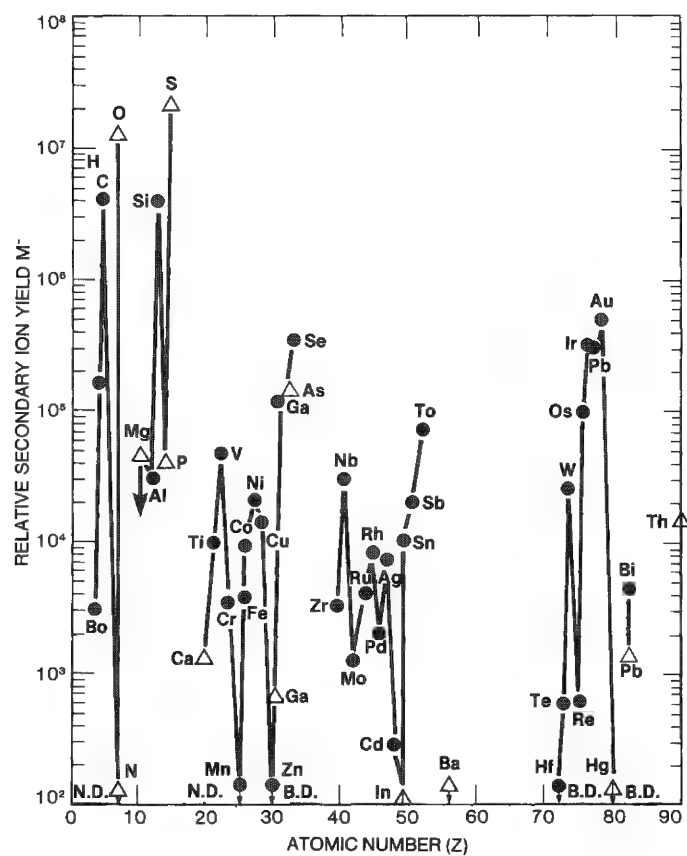
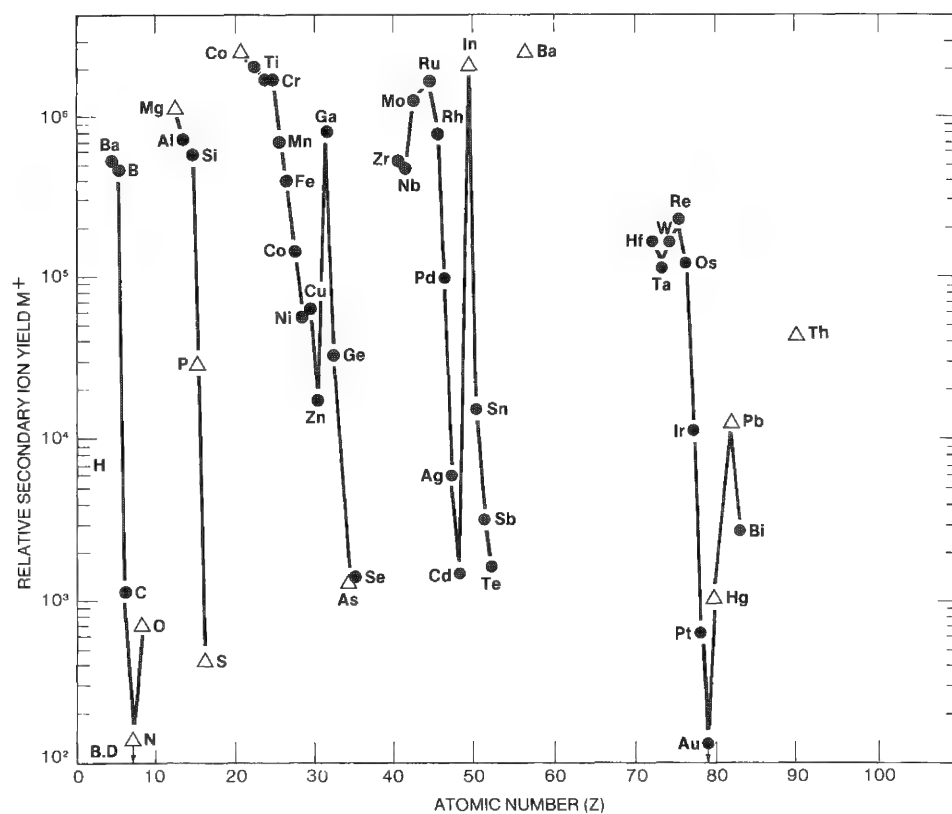


FIG. 3.--Variation of pure-element secondary-ion yields.

most attempts at quantitation.

Several mechanisms have been proposed in attempts to rationalize these ion yield variations. Models invoking bond-breaking⁹ and band-gap¹⁰ arguments have been proposed; each has its own merits and limitations. Without further adding to this controversy, we briefly discuss one recent model, the surface dipole model,¹¹ since it can be used to account for variations in *both* positive and negative secondary ion yields and lends itself to experimental verification.

From the work of Tsai and Morabito,¹² one may derive a relationship between the steady-state concentration of the implanted primary ion and the sputtering yield (atoms/incident primary atom). Following this concept, Deline¹³ found simple relationships between positive and negative ion yields and the linear sputtering rate:

$$\frac{n^{\pm}}{n^0} \propto \left(\frac{1}{S_{\ell}} \right)^{x^{\pm}} \propto [P]^{x^{\pm}} \quad (2)$$

where P is the surface or near-surface concentration of the implanted primary ion. Stated simply, the equilibrium concentration of the implanted primary ion in the surface or near-surface region (in the absence of preferential sputtering) appears to be the dominant factor in controlling ion yields. A viable model of ion emission must be therefore able to explain how a primary ion (oxygen) can act to enhance both positive and negative ion yields. The surface dipole model proposed by Williams¹⁴ views the bombarded surface as consisting of localized electron-retentive or electron-emissive sites. Regions with oxygen on the surface (electron-retentive sites) have a net dipole towards the bulk (high local work function) and thus high positive yields. During sputtering, oxygen is implanted (or recoiled) into the sample and forms sites with the dipole toward the surface (electron-emissive sites). Such sites have enhanced negative yields. This model is supported by experiments in which the transient behavior of ion-bombarded surfaces exposed to oxygen were studied.

Electron Spectroscopy

Both Auger electron spectroscopy (AES) and electron spectroscopy for chemical analysis (ESCA) involve the ejection of an electron whose energy is characteristic of the element(s) present and the chemical state of the element(s), respectively. The difference between the two techniques is the bombarding species, electrons in the case of AES and x rays for ESCA. When a sample is bombarded by a 1-10keV electron beam, several secondary processes occur. The two most important processes relevant to this discussion are the ejection of secondary electrons and ionization of surface atoms. A material under electron bombardment ejects a secondary electron and creates a core hole that leaves the atom in an excited state. The excited atom returns to a state nearer to the ground state by the decay of an upper-level electron. The recombination energy may be carried away by a photon (as in the x rays used in electron microprobe analysis) or by a third electron (Auger electron). This process is shown in Fig. 4. Since the energy of the Auger electron is determined by the energy levels of the atom, it is characteristic of the emitting atom according to:

$$E_{K,L1,L2,3} = E_K - E_{L1} - E_{L2,3} - \phi \quad (3)$$

The surface sensitivity of AES is determined by the escape depth of the Auger electron in a solid. For 50-2000eV electrons there is a high probability that the Auger electron will escape from the outer 3-20 Å of the sample surface maintaining its initial energy. Since the energy of the Auger electron is determined by the energy levels of the atom, it is characteristic of the emitting atom in the outer 3-20 Å. Auger electrons emitted deeper than approximately 20 Å undergo an inelastic collision and lose part of their initial energy. Such electrons are no longer characteristic of the emitting atom and contribute to the large continuum background signal. Since the relative intensities of the Auger signal is small compared to the continuum background, special detection modes such as differentiated spectra are often used. Energy analysis of the Auger electron permits both qualitative and quantitative elemental (and in some instances, chemical) analy-

sis to be performed on a volume of material defined by the primary electron beam diameter (500 Å-500 μm) and the Auger electron escape depth (3-20 Å). Elements detected by AES range from Li-U with typical detectabilities of 0.01% atomic.

If an Auger analysis is combined with neutral ion beam sputtering, the distribution of a particular element(s) can be obtained as a function of depth. Such an analysis readily lends itself to the examination of thin films, interfaces, etc. Another important feature of AES is the ability to raster the electron beam over a sample surface and so determine the spatial distribution of an element. The combination of scanning Auger spectroscopy (SAM) and ion beam sputtering provides a three-dimensional elemental analysis with high spatial and depth resolution. Review articles on Auger spectroscopy have been written by Morabito¹⁵ and Shirley.¹⁶

When characteristic x rays are used for ionization instead of electrons, photoelectrons are ejected with a well-defined energy described by

$$E_{\text{photoelectron}} = h\nu - E_K - \phi \quad (4)$$

The ejection of a photoelectron by x-ray bombardment is shown in Fig. 5. When an energy analysis of the ejected photoelectron is performed, the binding energy is determined. The binding energy is the amount of energy needed to raise an electron from a core level to the Fermi level. The binding energy of an electron is influenced by its chemical surrounding. Therefore, by measuring the binding energy of a photoelectron, one can determine the bonding characteristics of the emitting atom. Since the escape depth of a photoelectron is similar to that of an Auger electron, ESCA provides chemical information from the outer 3-20 Å. ESCA has elemental coverage from Li-U with typical limits of detectability of 0.01% atomic.

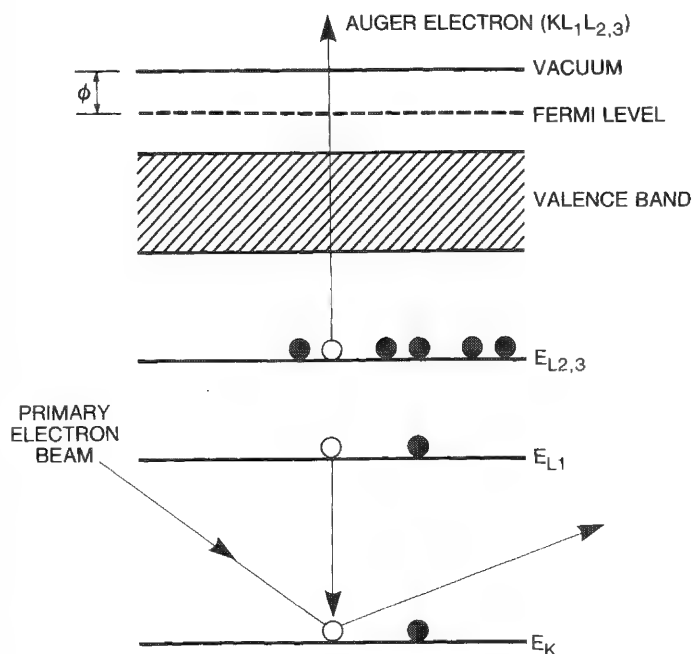


FIG. 4.--Auger electron emission.

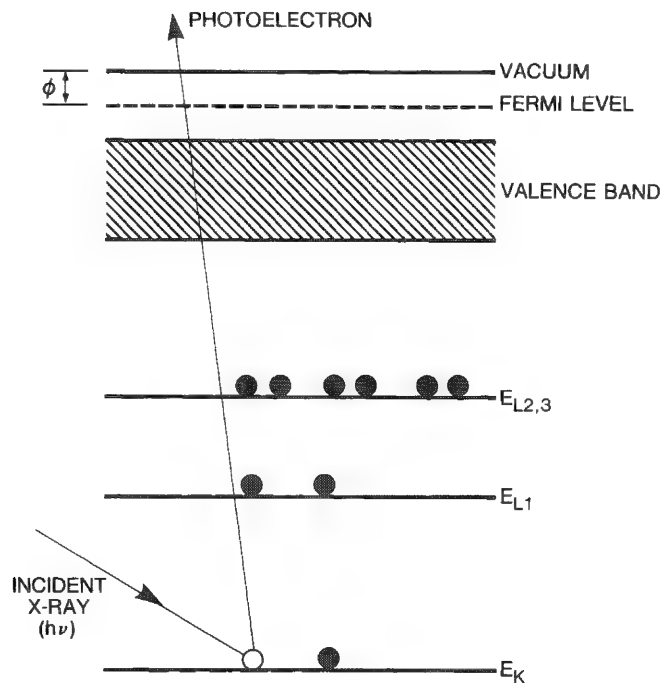


FIG. 5.--Photoelectron emission process.

As with AES, ESCA may be combined with ion sputtering to determine in-depth analysis. However, since with ESCA the analysis is usually for chemical information, one must be concerned that energetic ion bombardment may alter the original chemistry of the sample surface. The reader is referred to the literature¹⁶ for further details on ESCA.

Each of the techniques discussed has its own advantages and limitations. Some of the analytical characteristics of each method are compared in Fig. 6. The next section gives a variety of applications showing how each technique is of value and how the com-

bination of techniques complement one another.

TECHNIQUE	PROBING BEAM	SPECIES ANALYZED	ELEMENTAL COVERAGE	SENSITIVITY VARIATION	DETECTION LIMITS (ATOMIC FRACTION)	SAMPLE ALTERATION
ISS	He ⁺ , Ne ⁺ , Ar ⁺	BACKSCATTERED PRIMARY BEAM	Li-U	INCREASES WITH ATOMIC NUMBER	10 ⁻²	DESTRUCTIVE (LAYER(S) PROBED)
SIMS	O ₂ ⁺ , O ⁺ , Cs ⁺	SECONDARY IONS (POSITIVE OR NEGATIVE)	H-U	DEPENDS ON IONIZATION EFFICIENCY (10 ⁻⁴ -10 ⁻⁵)	10 ⁻⁴ -10 ⁻⁸	DESTRUCTIVE
AES	ELECTRONS (Ar ⁺ SPUTTERING)	AUGER ELECTRONS	Li-U	LESS THAN A FACTOR OF 10	10 ⁻³	DESTRUCTIVE WHEN DEPTH-PROFILING
ESCA	X-RAYS (Ar ⁺ SPUTTERING)	PHOTOELECTRONS	Li-U	LESS THAN A FACTOR OF 10	10 ⁻² -10 ⁻³	DESTRUCTIVE WHEN DEPTH-PROFILING

FIG. 6.--Summary of techniques.

Applications to Materials Characterization

The types of materials problems to which the various techniques described here are applicable stem from practically the entire scientific spectrum. Rather than describe the range of problems solvable by these surface methods, this section illustrates the practical uses of each technique.

Considerable analytical effort is currently being expended in the broad area of electronic materials characterization. The surface and subsurface regions (i.e., impurities, dopant profiles, interfacial regions, etc.) in semiconducting materials are of vital importance in determining the electrical properties of the device. Therefore, a detailed knowledge of these areas is crucial. The first example describes a new processing technique for the growth of thin SiO₂ films on Si.¹⁷ When single-crystal Si is irradiated by an intense UV laser (2660 Å), a layer of amorphous Si is produced. When this laser irradiation is done in air, an incorporation of oxygen in the Si is noted. Both SIMS and AES were used to characterize the oxide films formed. Figure 7 shows SIMS depth profiles of oxygen for a variety of incident laser energies.¹⁸ SIMS profiles were obtained using Cs⁺ bombardment and monitoring ¹⁶O⁻. The SIMS results indicate an increasingly thick oxide layer in going from 1.0 to 4.0 J-cm⁻² laser energy. It should be noted that the scales in the SIMS profiles are in concentration (atoms/cm³) versus depth (Å) rather than relative intensity (counts) versus time (s). The ability to use concentration versus depth scales was accomplished by comparison to an internal standard, an ion implant in this case, analyzed under similar conditions. Figure 8 shows¹⁸ the profile of a 150keV/10¹⁶-cm⁻² oxygen implant in silicon. The projected range R_p, the depth an ion will reach in a particular substrate, and the straggle ΔR_p, the standard deviation about the projected range, have been calculated from range statistics and tabulated for a variety of dopant-substrate combinations for a wide range of kinetic energies.¹⁹ From the implant concentration N (atoms/cm²) and the straggle ΔR_p (cm), the actual peak concentration N_p (atoms/cm³) may be calculated from

$$N_p = N / (\sqrt{2\pi} \Delta R_p)$$

Since the actual peak concentration and depth may be readily determined for any dopant-substrate combination, ion implants are excellent standards for SIMS (or any in-depth) analysis.

The same samples were analyzed by AES combined with ion sputtering.¹⁷ The Si LVV transition shows peaks at 92 eV and 59-76 eV characteristic of Si and SiO₂, respectively. By monitoring these two peaks, one is able to follow the transition from SiO₂ to Si. Figures 9(b), (c), and (d) show samples irradiated with increasing laser energy of 1.0, 1.8, and 4.0 J-cm⁻², respectively. As seen with SIMS, these data also indicate an increasing oxide layer with increasing laser energy. The results of the study indicate that oxygen is trapped in a molten silicon layer resulting from laser irradiation. With increasing laser energy the surface silicon is melted to greater depths with corresponding amounts of oxygen being trapped.

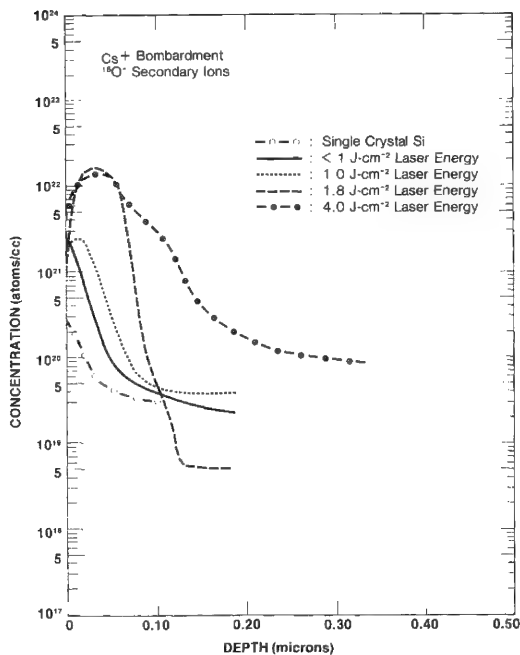


FIG. 7.--SIMS depth profiles of laser-induced oxidation.

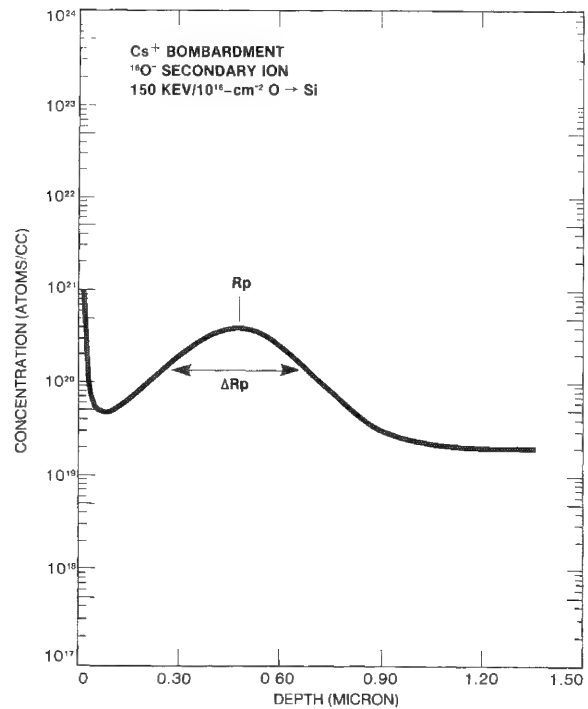
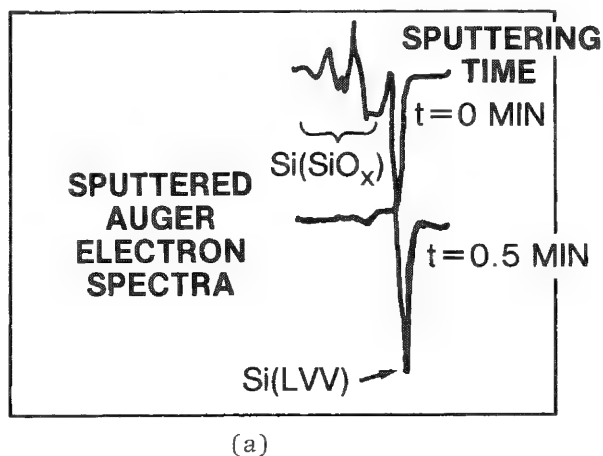
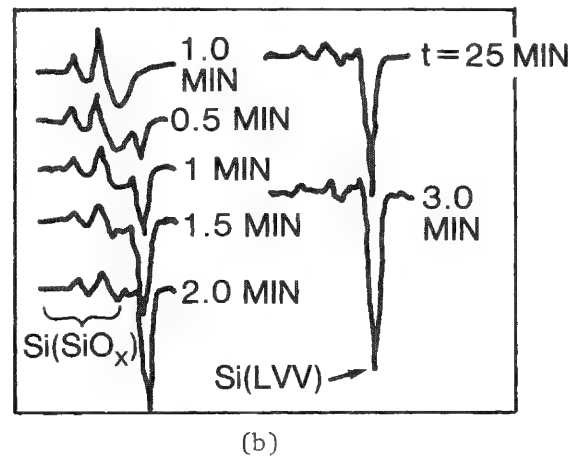


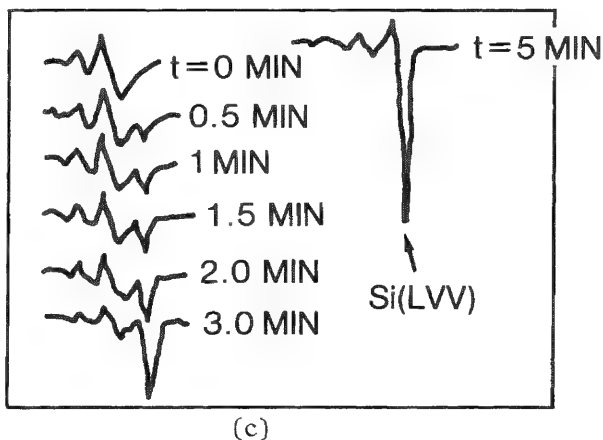
FIG. 8.--SIMS depth profile of 10^{16}-cm^{-2} oxygen implant into silicon.



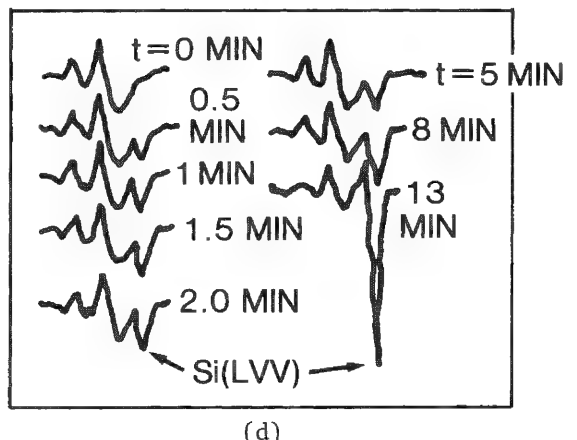
(a)



(b)



(c)



(d)

FIG. 9.--AES spectra of laser-induced oxidation: (a) crystalline Si before UV irradiation; (b) sample irradiated at $E = 1 \text{ J-cm}^{-2}$; (c) sample irradiated at $E = 1.8 \text{ J-cm}^{-2}$; (d) sample irradiated at $E = 4 \text{ J-cm}^{-2}$.

As discussed earlier, ISS is extremely surface sensitive in examination of the outer monolayer of a material. This property is particularly important in the examination of thin films. The chemical and/or physical properties of thin films are often influenced by surface contaminants. Figure 10 shows ISS spectra of an iron fluoride thin film formed by chemical vapor deposition (CVD) obtained with 1500eV He⁺ ions.²⁰ This particular film was found to have inferior optical properties. An in-depth analysis was obtained in this case by use of the He⁺ primary ions to sputter the sample slowly. From the energy and current density of the incident He⁺ ions, an approximate depth scale in monolayers was determined. For 1500eV He⁺ ions, an average sputtering rate of 0.2 atom/ion was determined. The data indicate a Cu impurity in the iron fluoride film. The Cu impurity was found to an approximate depth of 25 monolayers. The poor optical properties of the film were attributed to this surface contaminant. It is interesting to note the increase in both the Fe and F peaks in going from 4 to 19 monolayers into the material. The intensity of the scattered peak is related to the number of surface atoms involved in that particular scattering event. By comparison to the intensity of a scattered peak from a clean material, an approximate surface coverage may be determined. In this example the Fe and F peaks are seen to increase from the surface to the bulk by a factor of two, which indicates approximately 50% impurity coverage at the surface. Accordingly, the oxygen peak was attributed to a surface oxide rather than an FeO_x species, since the oxygen signal showed no corresponding increase as did Fe.

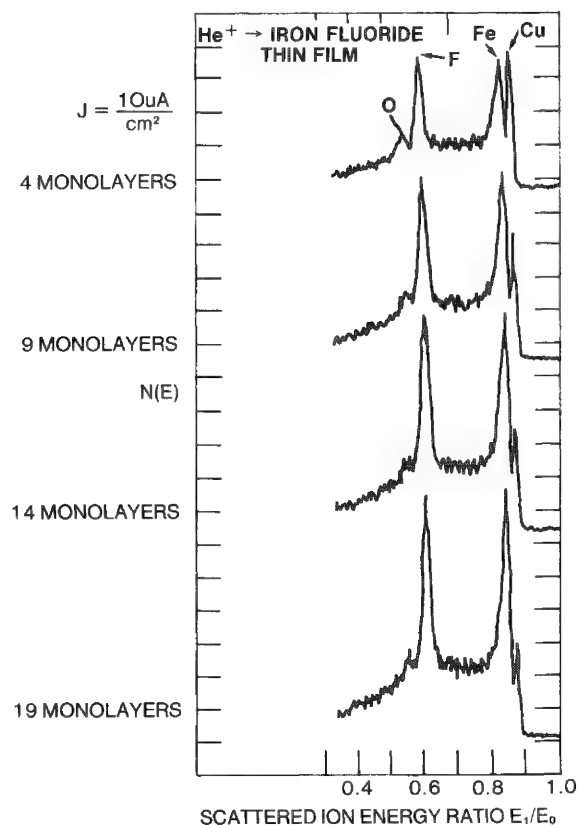


FIG. 10.--ISS study of iron fluoride thin-film indicating copper impurity.

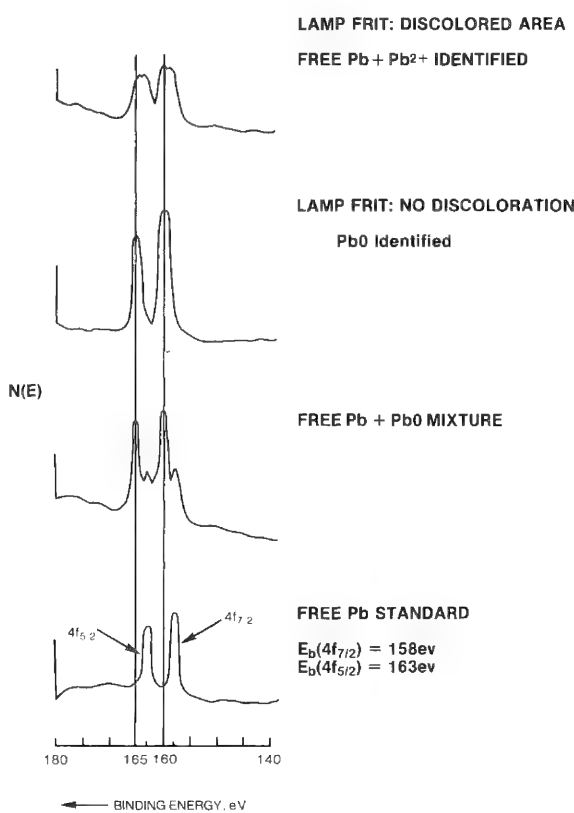


FIG. 11.--ESCA spectra of lead on lamp frit surfaces.

Often knowing the elemental analysis is not sufficient. In these situations, one must rely on techniques such as ESCA. An example of one such application is shown in Fig. 11.²¹ Lamp glass frit material contains PbO. After manufacture, the PbO frit material was seen to discolor as a function of time. The ESCA spectra in Fig. 11 show the Pb peaks from two lamp frit samples. The lamp frit sample showing a discolored area was seen to have broadened Pb peaks compared to the sample showing no discoloration. The bottom two spectra show characteristic peaks from a free Pb standard and a free Pb and PbO mixture. Comparison of the spectrum taken from the discolored area with standard spectra

indicates the presence of free Pb. The ESCA data indicates that the discoloration of the lamp frit material is due to reduction of the PbO to free Pb probably from the high-temperature firing of the glass during manufacture.

Summary

This paper has reviewed four of the more common surface analytical techniques AES, ESCA, ISS, and SIMS. The fundamentals governing each process were discussed and the advantages and limitations of each method were mentioned. Each method offers certain unique characteristics providing analytical information from the top 20 Å or less of material. Various examples illustrating each technique's analytical capability were given to show how these methods often provide complementary information.

References

1. E. Taglauer and W. Heiland, *Surf. Sci.* 47: 234, 1975.
2. W. Heiland and E. Taglauer, *Nucl. Instr. Meth.* 132: 535, 1976.
3. H. H. Brongersma and P. M. Mul, *Surf. Sci.* 35: 393, 1973.
4. H. H. Brongersma and T. M. Buck, *Nucl. Instr. Meth.* 132: 559, 1976.
5. R. E. Honig and W. L. Harrington, *Thin Solid Films* 19: 43, 1973.
6. C. A. Evans Jr., *J. Vac. Sci. Tech.* 12: 144, 1975.
7. J. M. Morabito and R. K. Lewis, *Anal. Chem.* 44: 869, 1973.
8. H. A. Storms, K. F. Brown, and J. D. Stein, *Anal. Chem.* 49: 2023, 1977.
9. G. Slodzian, *Surf. Sci.* 48: 161, 1975.
10. W. F. Van der Weg and D. J. Bierman, *Physica* 44: 206, 1969.
11. P. Williams, W. Katz, and C. A. Evans Jr., *Nucl. Instr. Meth.* 168: 373, 1980.
12. J. C. C. Tsai and J. M. Morabito, *Surf. Sci.* 44: 247, 1974.
13. V. R. Deline, W. Katz, C. A. Evans Jr., and P. Williams, *Appl. Phys. Lett.* 33: 832, 1978.
14. P. Williams and C. A. Evans Jr., *Surf. Sci.* 78: 324, 1978.
15. J. M. Morabito, *Thin Solid Films* 19: 21, 1973.
16. D. A. Shirley, *Electron Spectroscopy*, New York: American Elsevier, 1972.
17. Y. S. Liu, S. W. Chiang, and F. Bacon, in T. W. Sigmon et al., Eds., *Laser and Electron Beam Solid Interactions and Material Processing*, 1981 (to be published).
18. The author would like to thank Ms. C. Slater of Charles Evans and Associates for her assistance in obtaining the SIMS data.
19. J. Lindhard, M. Scharff, and H. S. Schiott, *Mat. Fys. Medd. Vid. Selsk.* 33: (No. 14), 1963.
20. R. F. Goff, *J. Vac. Sci. Tech.* 10: 355, 1973.
21. The author would like to acknowledge Dr. F. Bacon of the General Electric Corp. R & D Laboratory for obtaining the ESCA results.

AN ALTERNATIVE APPROACH TO THE SURFACE-EXCITATION MODEL IN SIMS

V. E. Krohn

Peter Williams has proposed a new theory of the secondary-ion emission process based on what he calls the *surface-excitation model*.¹ A particularly interesting feature of this model is that the effective temperature of the excited surface atoms may fall with time after the impact of the primary ion. This paper gives an argument for this part of the model that is considerably simpler and may be more robust. The comparison of this part of the model with the available experimental data is also discussed, but the comparison is sharply limited by the scantiness of the data.

The emission of secondary ions is a complicated process that has not been explained in any simple way; hence, it is not surprising that many investigators have tried to treat this process as if it were the better-understood emission phenomenon, surface ionization. Unfortunately, surface ionization is an equilibrium process, whereas secondary-ion emission is not.

Some of those who have advocated the use of the formalism of surface ionization to describe secondary-ion data have done so without a serious attempt to justify the procedure.^{2,3} Others have argued that there is local thermal equilibrium (LTE) and even a plasma at the sputtering site.^{4,5} On the other hand, many investigators have expressed serious reservations about describing secondary ionization by an equation that can only be justified in connection with surface ionization; as a result, the LTE concept has lost its popularity.⁶⁻¹² When all of the above is considered, we are left with limited empirical success as the main justification for the use of the Saha-Langmuir equation (or equations closely related to it) to describe secondary-ion data.

Indeed, the Saha-Langmuir equation has been surprisingly successful at relating secondary-ion yields to atomic concentrations. We can get some insight into the reason for this success by examining the Boltzmann factor, $\exp[(\phi - I)/kT]$, which tends to dominate the behavior of the Saha-Langmuir expression for the degree of ionization α . We see that this factor is small for ions whose production requires energies that are large compared with the available energy. Perhaps we should not be surprised to find that states that require energies large compared with kT are relatively unpopulated even when equilibrium has not been approached. This idea is even more appealing if one allows that, by substituting a parameter for the temperature, one is essentially replacing "available energy" by "energy available for ionization." The point here is that, in the absence of equilibrium, there may be only limited energy exchange between the various kinds of energy such as ionization energy, energy of atomic excitation, kinetic energy of electrons, kinetic energy of secondary ions, kinetic energy of sputtered atoms, etc.; and that the distributions of each of these kinds of energy may be fitted better if a different temperature parameter is used for each. Of course, the fact that the temperature parameters to fit each kind of energy tend to be different is evidence that sputtering does not involve even approximate thermal equilibrium.

The overwhelming evidence that secondary ions are not created in an equilibrium process is a good reason for seeking something better than the Saha-Langmuir equation to describe secondary-ion emission. However, the exponential in the surface-excitation model has the same source as the exponential in the Saha-Langmuir equation: it is a Boltzmann factor and it depends on the assumption that one may use equilibrium statistics which, according to the original exposition of the surface-excitation model, "cannot explicitly be defended."¹ Hence, it is clear that the surface-excitation model is equivalent to the Saha-Langmuir equation for the description of secondary-ion emission.

However, the idea that the temperature parameter in the Boltzmann factor might decrease with time following the impact of a primary ion is new and interesting. This idea does not depend on any of the other details of the surface-excitation model and it can be considered equally well in the application of the Saha-Langmuir equation to secondary-ion emission. If it is found to have some applicability, it should not be regarded as supporting the detailed description of the ionization process used in the original derivation of the surface-excitation model. In fact, one can arrive at the qualitative predic-

The author is at Argonne National Laboratory, Argonne, IL 60439. The work was performed under the auspices of the U.S. Department of Energy.

tion of the time-dependent temperature concept without assuming equilibrium. To do so one simply argues that the available energy (per atom) will be high during the early stages of a collision cascade and that the relative populations of sputtered species with high kinetic energy and of ions from high-ionization-potential atoms will be favored. Later, when the available energy is lower, the average kinetic energy will be lower and the probability of ionization of atoms with high ionization potential will be reduced. On the other hand, atoms of lower ionization potential may even require less energy for ion production than for the production of neutrals (if the effective work function exceeds their ionization potential, i.e., if $\phi > I$). That leads to the idea that the ionization probability of sputtered atoms of high ionization potential will increase more rapidly with kinetic energy than will be the case for those of lower ionization potential, and in fact that the latter may be expected to have ionization probabilities that decrease with increasing kinetic energy if the effective work function exceeds their ionization potential.

Lundquist found that for Cu and Ni, the ionization probabilities are proportional to E_m with $m = 0.65$ for Cu and 0.54 for Ni.¹³ This result supports the expectation of the time-dependent temperature concept since the quantity $I - \phi$ of Cu exceeds the same quantity for Ni. (These quantities are roughly 3.2 and 2.6 eV, respectively.) Of course, it is not clear that the observed trend is significant; and it could be in any case fortuitous.

A more definitive test would involve measurements of m for atoms of substantially different ionization potentials from the same substrate; or at least, for comparison with Lundquist's results, a measurement of m for a case where the time-dependent temperature concept predicts a negative value for m , e.g., Cs sputtered from a fractional monolayer of Cs on a high-work-function substrate (perhaps W). Meanwhile, in the absence of additional direct measurements of the energy dependence of ionization probabilities, one can obtain some information about these probabilities by fitting the energy distributions of secondary ions to a function proportional to E^{-n} and then comparing the measured value of n to the result ($n = 2$) predicted by collision cascade theory for sputtered material at energies well above the binding energy.¹⁴ Recent experimental results of Krauss and Gruen yield $n = 2.0$ for K^+ from an approximate monolayer of K on a Mo substrate.¹⁵ If one assumes that it is appropriate to use the work function of Mo here, then the time-dependent temperature concept would predict $m \approx 0$ and $n \approx 2.0$, in agreement with the experimental result. However, the situation is complicated by the fact that Krauss and Gruen have also observed the energy distributions of K^+ and Na^+ secondary ions from Be, Ti, Mo, and W substrates where the alkalis were contaminants of some sort.¹⁵ They found n values from 1.2 to 2.05, which suggests that these values are not determined only by the appropriate work function and the ionization potential of the atom involved but by complicated factors that are not understood. It would seem that additional experimental results should be considered before a final decision is reached concerning the validity and/or applicability of the time-dependent temperature concept.

References

1. Peter Williams, "The sputtering process and sputtered ion emission," *Surface Sci.* 90: 588, 1979.
2. A. R. Krauss and D. M. Gruen, private communication, unpublished; but see *Appl. Phys.* 14: 89, 1977 and *J. Nucl. Mat.* 85 and 86: 1179, 1979 for the techniques and some of the data.
2. H. J. Liebl and R. F. K. Herzog, "Sputtering ion source for solids," *J. Appl. Phys.* 34: 2893, 1963.
3. Jakob Schelten, "Massenspektrometrische Untersuchung der Sekundärionen-Emission von Legierungen," *Z. Naturforsch.* 23a: 109, 1968.
4. C. A. Andersen and J. R. Hinthorne, "Thermodynamic approach to the quantitative interpretation of sputtered ion mass spectra," *Anal. Chem.* 45: 1421, 1973.
5. Z. Jurela, "The application of nonequilibrium surface ionization to the emission of secondary ions," *Int. J. Mass. Spectrom. Ion Phys.* 12: 33, 1973.
6. V. E. Krohn, "Emission of negative ions from metal surfaces bombarded by positive cesium ions," *J. Appl. Phys.* 33: 3523, 1962.

7. A. Benninghoven, "Zum Mechanismus der Ionenbildung und Ionenemission bei der Festkörperzerstäubung," *Z. Physik* 220: 159, 1969.
8. G. Slodzian, "Some problems encountered in secondary ion emission applied to elementary analysis," *Surface Sci.* 48: 161, 1975.
9. V. E. Krohn, "Secondary ion emission," *Int. J. Mass Spectrom. Ion Phys.* 22: 43, 1976.
10. F. G. Rüdenauer, W. Steiger, and H. W. Werner, "On the use of the Saha-Eggert equation for quantitative SIMS analysis using argon primary ions," *Surface Sci.* 54: 553, 1976.
11. D. S. Simons, J. E. Baker, and C. A. Evans Jr., "Evaluation of the local thermal equilibrium model for quantitative secondary ion mass spectrometric analysis," *Anal. Chem.* 48: 1341, 1976.
12. K. J. Snowdon, "A fundamental analysis of the validity of thermodynamic models of ionized and excited particle production during sputtering," *Radiation Effects* 40: 9, 1979.
13. T. R. Lundquist, "Energy dependence of the ionization probability of sputtered Cu and Ni," *Surface Sci.* 90: 548, 1979.
14. M. W. Thompson, "The energy spectrum of ejected atoms during the high energy sputtering of gold," *Phil. Mag.* 18: 377, 1968.
15. A. R. Krauss and D. M. Gruen, private communication, unpublished; but see *Appl. Phys.* 14: 89, 1977 and *J. Nucl. Mat.* 85 and 86: 1179, 1979 for the techniques and some of the data.

ULTRASENSITIVE SIMS WITH NUCLEAR ACCELERATOR

J. C. Rucklidge, L. R. Kilius, and M. P. Gorton

Nuclear accelerators have been used in ultrasensitive mass spectrometry for several years. It is due to this application that spectacular results have been achieved in the measurement of isotope ratios such as $1:10^{14}$, which is approximately the concentration of ^{14}C in 10 000-year-old carbon. Both cyclotrons and tandem accelerators have been used for these measurements, and the details and applications have been reviewed recently by Litherland.¹ The tandem accelerator has been applied to the widest range of isotopes, and it is with large machines in nuclear physics laboratories, such as the 10MV MP Van de Graaff accelerator at the University of Rochester, that most of the pioneering experiments have been made. Smaller machines, such as the 3MV Tandetron (General Ionex Corp.) are about to be set up at the Universities of Oxford, Arizona, and Toronto, where they will be dedicated to various aspects of ultrasensitive mass spectrometry (Fig. 1).

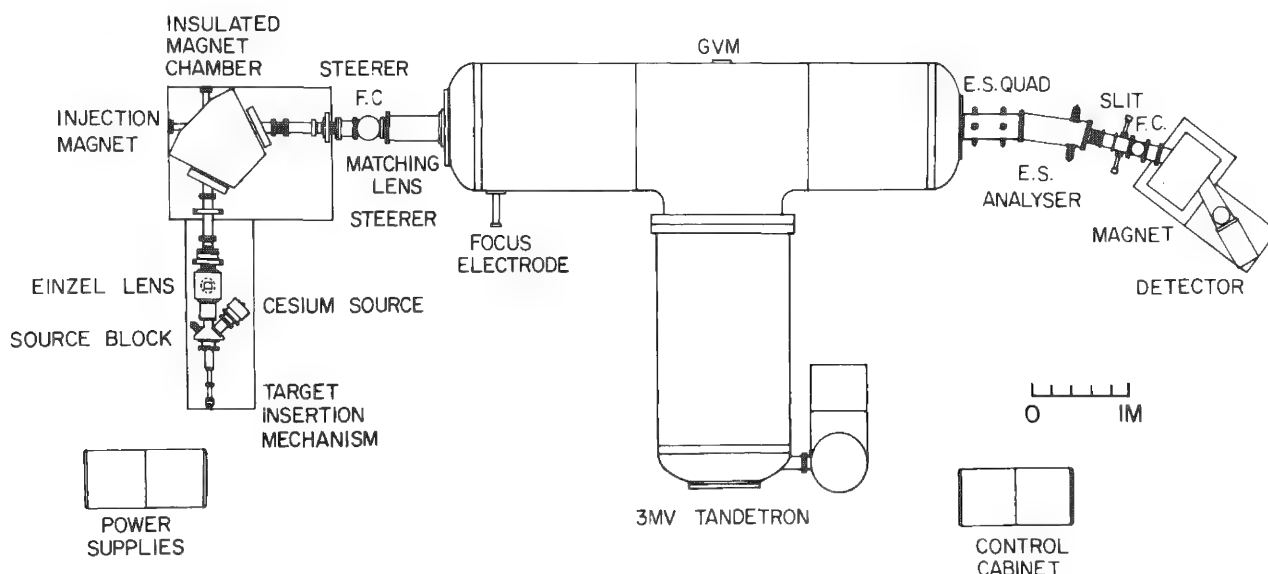


FIG. 1.--Plan of one version of one of the ultrasensitive mass spectrometers being built in various laboratories. FC, Faraday cups; ES, electrostatic elements at exit of 3MV tandem or molecular disintegrator; GVM, generating voltmeter for high-voltage measurements.

The basic reason for using a dc accelerator as part of an ultrasensitive mass spectrometer is that it can be made to function as a molecule disintegrator. In SIMS one major problem is that sensitivity is most often limited by the presence of molecules of the same nominal mass as the atomic ions in the beam. The removal of these molecules would effectively eliminate background from the measurements, except in cases where isobars coexist in the beam. In the application of the technique to SIMS, negative ions are required for injection into the accelerator. The yield of negative ions sputtered from a solid sample is optimized by use of a primary beam of an electropositive element such as cesium. A micro- or milliprobe front end can be of conventional ion-probe design. Negative ions are extracted from the surface and passed through an inflection magnet, and a narrow band of masses is injected into the accelerator. The terminal, in the center of the machine, is at +3 MV, so the singly charged negative ions are brought to this point with an energy of 3 MeV. At the terminal the ions pass through an argon gas canal in which collisions take place and several electrons are stripped from each ion, which is thus converted from

Authors Rucklidge and Gorton are with the Department of Geology, and Kilius with the Department of Physics, University of Toronto, Toronto, Canada M5S 1A1. NSERC and NSF funds are gratefully acknowledged, as is the assistance of H. E. Gove and D. Elmore of the University of Rochester, and the constant support and advice of A. E. Litherland.

a negative to a multiply positive charge state. The precise final charge state is determined by the experimental conditions which include Ar gas pressure and terminal voltage, and hence a particular charge state can be selected for any isotope. Positive charge states in excess of +2 are unknown for molecular ions because the component atoms fly apart in a "Coulomb explosion" when three or more electrons are removed from the molecule. In this way molecules are eliminated from the beam, leaving only atomic ions to pass through the second magnet and the electrostatic analyzer to the final detector. All that is accomplished without the use of high-resolution magnets and hence high transmission and consequently high sensitivity are preserved. In cases where there may be isobaric interference problems may arise, although they may be often solved by the different negative ion forming properties of the isobars. As an example $^{14}\text{C}^-$ is completely stable, with an electron binding energy of 1.25 eV; whereas for nitrogen the binding energy is negative and N^- is unstable, and hence never enters the accelerator. It is this comparative property that allowed the ^{14}C measurements to be made.

Much of the activity in this new field has been in the detection of radiogenic nuclei such as ^{14}C , ^{26}Al , and ^{36}Cl , but it can also be usefully applied to the measurement of stable isotopes which may also occur at ultralow levels in a variety of materials. Detection in the part per trillion (ppt) range is beyond the limits of most methods of geochemical analysis, and hence few data are available for this concentration range of elements in natural materials. We have made several experiments to investigate the heavy members of the platinum group elements (PGE) Pt, Ir, Os in several geological samples. These elements were selected for study because of the geochemical importance of understanding how they are apportioned among metallic, sulfide, and oxide mineral phases. In the former two, concentrations in the ppb to ppm range are encountered, but their concentrations in the associated silicate minerals are unknown, because they lie below the limits of the analytical technique usually used, neutron activation analysis (NAA). Sensitivity by NAA varies greatly among elements; Ir is quite easily measured with a limit of about 0.05 ppb, but Pt is much more difficult to measure with a sensitivity about 1000 times worse. NAA requires relatively large amounts (grams) of materials, and there are also the inconveniences and hazards associated with the handling of radioactive materials.

In our experiments we have taken approximately 10 mg of unprocessed material such as powdered rock and pressed it into an Al disk that is inserted into the ion source of the Rochester accelerator. Sputtering with a rather poorly defined beam of Cs^+ ions has enabled us to detect isotopes of Ir and Pt, both of which form negative ions readily, at count rates in the range of 1 cps per ppb. For reasonable counting periods this range gives a detection limit of about 1 in 10^{12} , or 1 ppt, and we have been able to demonstrate the presence of these elements in oxide minerals, where previously they were unknown.

A specific problem to which the new method could be applied appeared in the currently active subject of the trace element anomalies at the Cretaceous Tertiary boundary. Alvarez et al. and others have shown that an Ir anomaly exists at this stratigraphic horizon at various localities around the world, and they have ascribed it to the impact of an asteroid with the earth at that time.² They suggested that this event would have thrown up a cloud of dust that encircled the earth and blocked off the sunlight for several years. The major extinctions of some forms of life at that time were attributed to this event. An Ir anomaly would arise because some asteroids, like meteorites, are enriched in PGE relative to crustal rocks, and the dust that settled out of the cloud into the sediments contained a significant proportion of meteoritic debris.

This problem is related to the development of ultrasensitive mass spectrometry because of the low levels of PGE in the crust of the earth and the difficulties of detecting such low levels by NAA. Prior to the report of Alvarez et al., Pt at ppb levels had been detected at Rochester, and after the report a suite of samples from the Stevens Klint section of the Danish Fish Clay, one of the classic exposures of the marine Cretaceous Tertiary boundary, was examined for Ir and Pt.

The experiments on Pt and Ir were carried out in 1980 at Rochester and they have confirmed the Ir data of Alvarez et al. convincingly. Figure 2 shows the experimental set-up for these measurements, and a spectrum showing ^{193}Ir in a pyritiferous shale is seen in Fig. 3. The Ir, at about 2.9, ppb is cleanly separated from the molecular fragments with the same E/q and m/q , by an energy measurement in a silicon heavy ion detector. As Fig. 4 illustrates, Ir was shown to be concentrated within the region of the boundary with an

abundance approximately 100 times that in the adjacent Cretaceous chalk. The isotopes ^{194}Pt and ^{195}Pt are free from interfering isobars of other elements and, on a suite of specially prepared standards, they were analyzed to check the isotope ratio in normal samples and samples enriched with known amounts of ^{195}Pt . By this isotope-dilution technique the Pt concentration could be estimated, and sensitivities established. In the most Ir-enriched clay layer the Pt was also found to be enriched, but at levels much higher than would be expected if Ir and Pt were both meteoritic. A further observation was that Pt appeared to be inhomogeneously distributed in the clay, as judged from the erratic counting rate as the sample was exposed to the Cs beam. The clay contains significant pyrite (FeS_2) in which Pt might be expected to concentrate; the inference was that as the Cs beam eroded the sample, different mineral grains were consumed, each giving off different amounts of Pt, though no obvious similarity was noted for Ir.

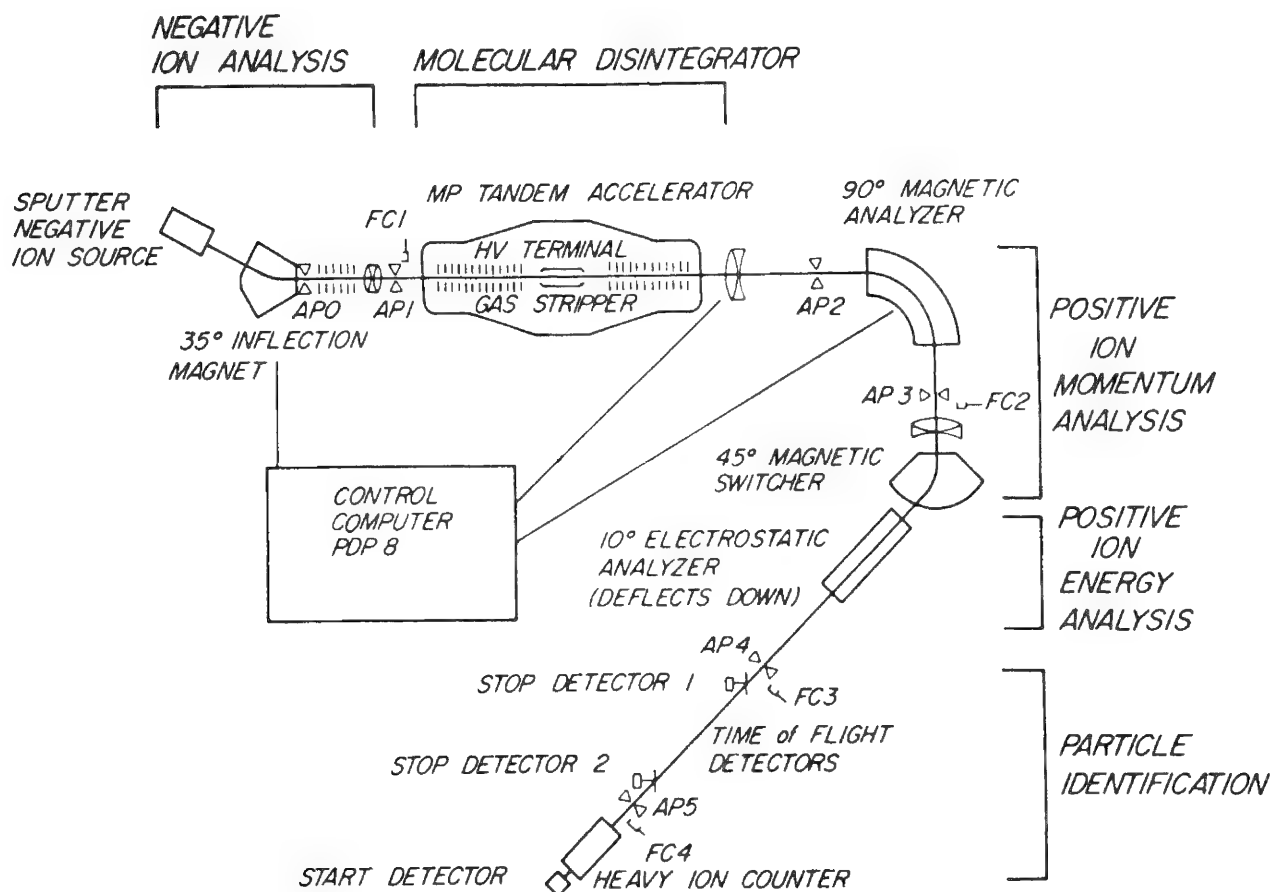


FIG. 2.--Ion-beam transport system of University of Rochester tandem accelerator. AP, ion-beam-defining apertures; FC, Faraday cups for ion-beam charge measurements.

Subsequent experiments indicated that Pt and Ir were both strongly enriched in the pyrite fractions of the clay. Pyrite forms by precipitation from sea water in a reducing environment and so the anomalies could be due to the chemical conditions prevailing on the sea floor, rather than directly from the influx of meteoritic debris. Similar measurements on material from a nonmarine exposure of the Cretaceous Tertiary boundary (Hell Creek, Mont.) has shown no matching anomaly, and so the ubiquity of this phenomenon around the world seems open to doubt. The situation at the boundary, though fascinating, may be more complex than imagined, and measurements with ultrasensitive mass spectrometry have complemented the NAA data and will doubtless provide key information in this and other problems.

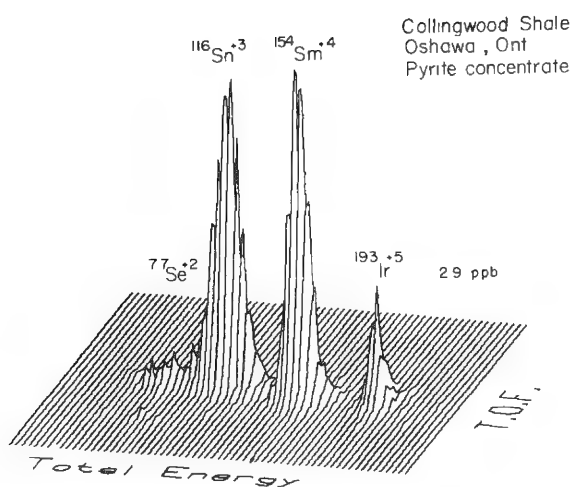


FIG. 3.--Three-dimensional linear plot of counts vs total ion energy and time of flight for sample of pyritiferous Collingwood shale from Oshawa, Ont. Observed Ir concentration is about 2.9 ppb.

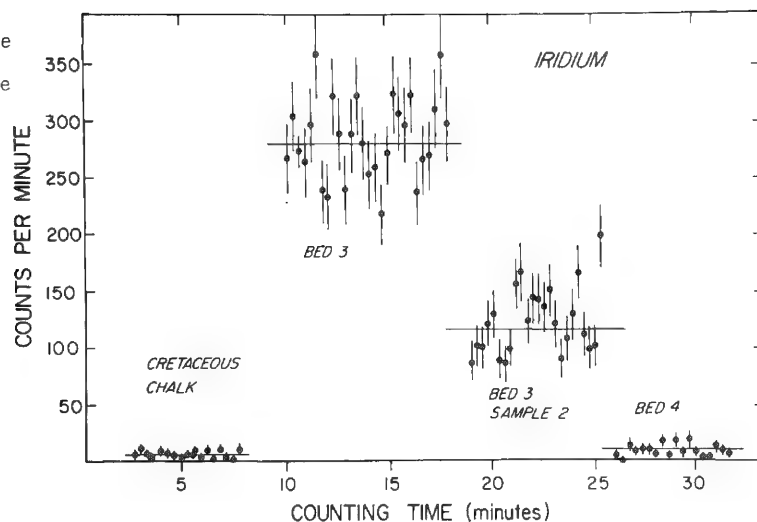


FIG. 4.--The ^{193}Ir counting rate against counting time for four samples taken from Danish Fish Clay. Samples were measured in ascending stratigraphical sequence left to right, with Bed 3 as the supposed boundary layer.

References

1. A. E. Litherland, "Ultrasensitive mass spectrometry with accelerators," *Ann. Rev. Nucl. Part. Sci.* 30: 437, 1980.
2. L. W. Alvarez et al., "An extra-terrestrial event at the Cretaceous Tertiary boundary," *Science* 208: 1095, 1980.

INVESTIGATION OF LITHIUM-GAS REACTIONS BY AES AND XPS

P. A. Lindfors and K. M. Black

A previous study¹ and industry references^{2,3} discuss the occurrence of LiOH, Li₂CO₃, Li₂O, and Li₃N. It is generally agreed in these references that the nitriding of Li is easily produced and proceeds rapidly in the presence of water. However, these results are based on indirect observations by wet chemical techniques. With the advent of AES and XPS the reactions of Li, with a variety of gases, can now be analyzed as they occur within the analytical chamber. The use of special handling and transfer techniques have minimized contamination of the highly reactive lithium surface.

Experimental Conditions

Lithium metal specimens from Foote Mineral Co. were stored under argon in a sealed metal container until the initiation of these experiments. The metal container and the inner plastic pouch were opened in an argon-filled glove box. The pieces of lithium were kept in a sealed glass container, under n-hexane, until just prior to analysis.

Individual pieces of lithium were removed from the n-hexane and cut to fit the XPS specimen holder, and the surface to be analyzed was then scraped in the argon atmosphere. The specimens were removed from the argon glove box to the analytical chamber via a sealed vessel (Fig. 1) that was part of the specimen transfer system (Perkin-Elmer PHI Model 04-100), which allows direct transfer into the interlock of the analytical chamber without exposure to the atmosphere.⁴ After the interlock was evacuated, the sealed vessel was opened in situ and the lithium specimen was inserted into the analytical chamber (Fig. 2).

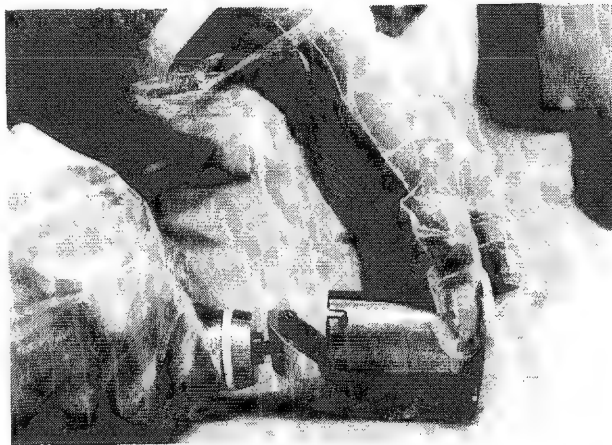


FIG. 1

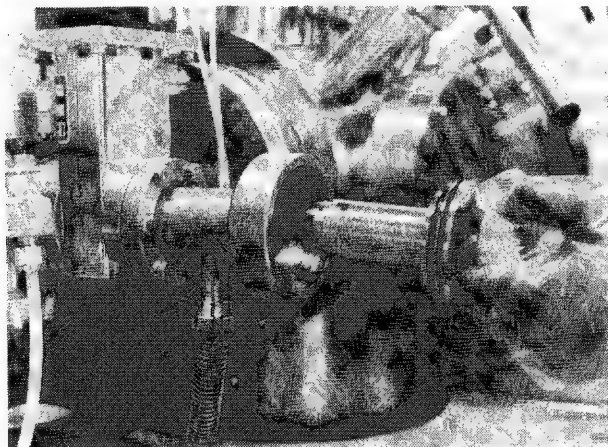


FIG. 2

Controlled introduction of N₂, CO₂, O₂, and H₂O was accomplished by use of research-grade gas bottles attached to the analytical chamber by ultrahigh-vacuum variable leak valves. Exposure of the lithium specimens to the gases was controlled by monitoring of the analytical chamber pressure (internal ionization gauge measurement) and time interval. All XPS spectra were charge-referenced to the C_{1s} peak at 284.6 eV. If insufficient amounts of adventitious carbon were present then the major O_{1s} peak energy was based on that seen for Li₂O (528.2 eV) and the charge referencing was based on this energy.

Results

Lithium. Lithium as received has a shiny, silvery surface. An XPS spectrum at the surface shows the presence of only O, Li, C, S, and Cl (Fig. 3). The binding energies

Dr. Lindfors is with the Physical Electronics Division of Perkin-Elmer Corp. in Eden Prairie, MN 55344; Ms. Black is with Cardiac Pacemakers, Inc., 4100 N. Hamline Ave., St. Paul, MN 55164.

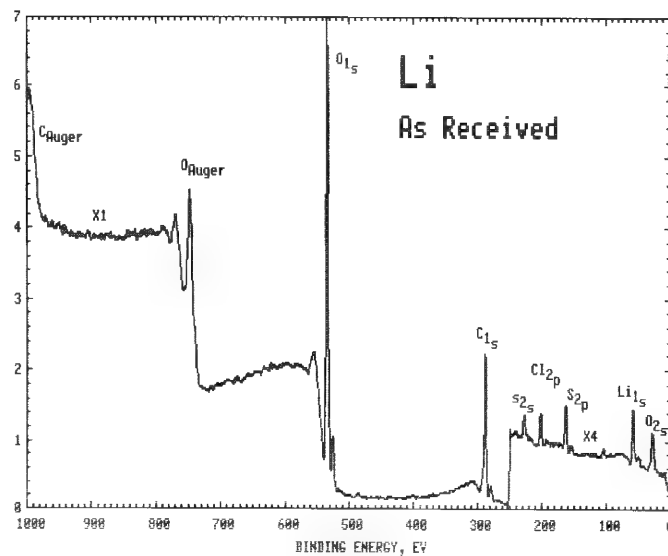


FIG. 3

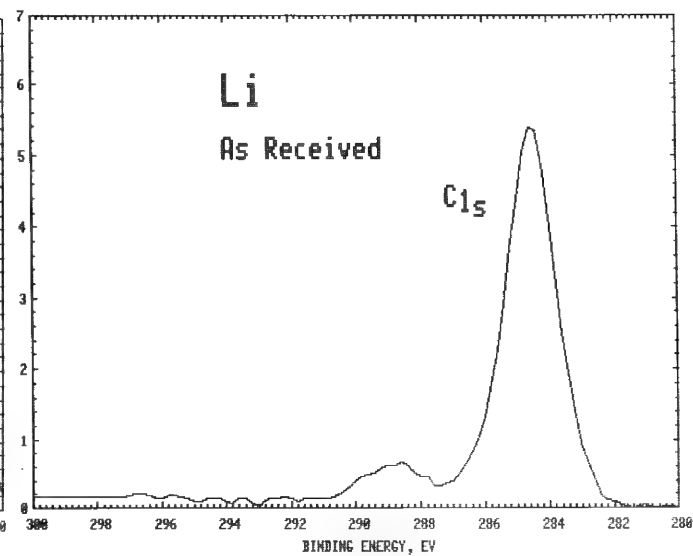


FIG. 4a

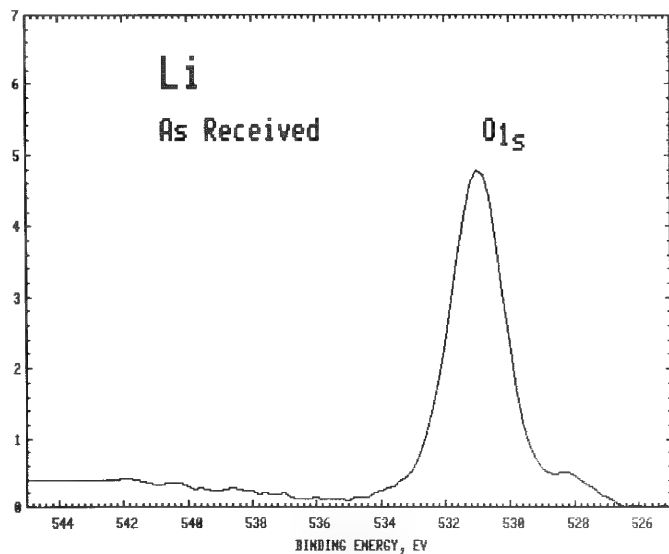


FIG. 4b

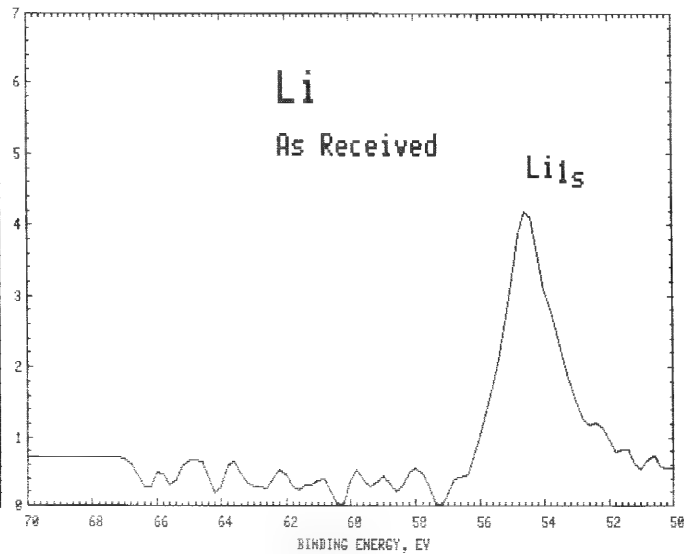


FIG. 4c

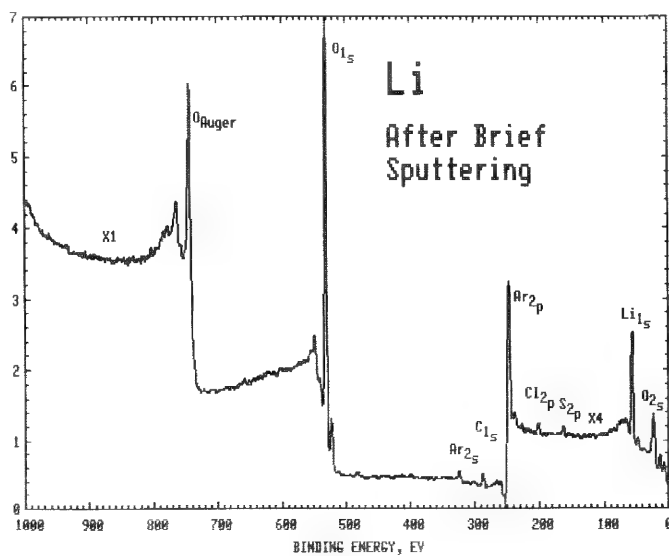


FIG. 5

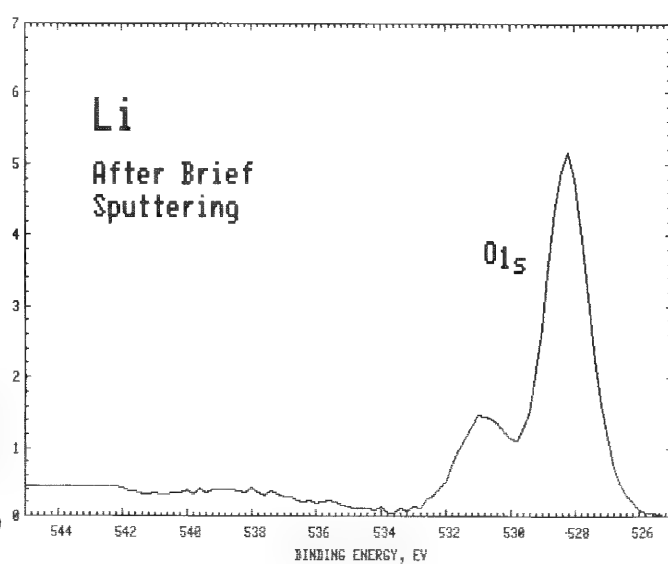


FIG. 6

of the O, Li, and C peaks indicate that the predominant surface constituent was LiOH (Fig. 4 and Table 1). The carbon was in the form of C-H bonding and had not reacted with the lithium to form Li_2CO_3 . Brief sputtering, with Ar^+ , removed the hydroxide from the surface. The specimen was dominated by Li_2O (Figs. 5 and 6) after sputtering. Following extensive sputtering the results indicate, by both AES (Fig. 7) and XPS (Fig. 8), that the dominant species were Li_2O and metallic lithium. The interpretation of Li_2O was confirmed by observation of the shape of the Auger O_{KLL} line in the XPS spectrum.⁵ The shape of the oxygen Auger peak (Fig. 9) is indicative of oxide, not hydroxide. Other specimens analyzed show Li_2CO_3 at the surface with oxide and hydroxide after sputtering.

TABLE 1

	Li_{1s}	C_{1s}	O_{1s}
Li	52.0	-	
LiOH	54.5	-	530.8
Li_2O	53.6	-	528.2
Li_2CO_3	54.6	289.5	531.4

Lithium/ $\text{O}_2/\text{H}_2\text{O}$. A lithium specimen which had been sputter cleaned with Ar^+ was exposed to approximately 200 Langmuirs of O_2 with the last 50 (L) simultaneous with 50 (L) of H_2O . An XPS survey spectrum showed that oxygen and lithium then dominated the surface (Fig. 10). A high-resolution XPS spectrum of the O_{1s} region (Fig. 11) indicated that both oxide and hydroxide bonding is present, with the oxide species dominant.

Lithium/ $\text{CO}_2/\text{H}_2\text{O}$. A lithium specimen which had been sputter cleaned with Ar^+ was exposed to approximately 60 (L) of CO_3 . Prior to the CO_3 exposure no carbon was found on the sputter cleaned surface. After the CO_3 exposure only low levels of both C-H and CO_3 bonding reaction had occurred between the lithium and dry CO_2 .

The same specimen was sputter cleaned again and the specimen exposed to a combination of approximately 150 (L) of CO_2 , simultaneous with approximately 30 (L) of H_2O vapor. The C_{1s} peak following exposure to combined $\text{CO}_2/\text{H}_2\text{O}$ indicated no substantial formation of carbonate species. Comparison of C_{1s} peaks (Fig. 12) following exposure to CO_2 with and without H_2O appears to indicate more carbonate formation with the presence of H_2O . The shape of the O_{KLL} peak (Fig. 13) no longer resembles that of an oxide (compare to Fig. 9) and the shape may be the result of an overlap of several states.

Lithium/ $\text{N}_2/\text{H}_2\text{O}$. After some sputtering, XPS data indicated the surface was predominantly Li_2O . This surface was exposed to N_2 and $\text{N}_2/\text{H}_2\text{O}$. The specimen was again sputter cleaned until metallic lithium was indicated in the XPS data. Again the surface was exposed to N_2 and $\text{N}_2/\text{H}_2\text{O}$. Following the N_2 and $\text{N}_2/\text{H}_2\text{O}$ exposure, no nitrogen was detected via either AES or XPS (Fig. 14). However, the lithium was porous enough to trap the argon and yield Ar peaks in the XPS survey spectrum. The O_{1s} peak, following exposure to $\text{N}_2/\text{H}_2\text{O}$, indicates more Li_2O than LiOH (Fig. 15).

Lithium/ $\text{O}_2/\text{N}_2/\text{CO}_2/\text{H}_2\text{O}$ at Atmospheric Pressure. A lithium specimen, scraped in humid laboratory air, showed results differing from those found for lithium exposed to N_2 , O_2 , CO_2 , and H_2O under high-vacuum conditions. XPS and AES survey spectra (Figs. 16 and 17, respectively) from the scraped in air specimen, show peaks for only Li, O, and C. No nitrogen was detected even when long analysis times were used to look for only the N peak.

High-resolution XPS data for the C_{1s} , O_{1s} and Li_{1s} peaks indicate that the surface was dominated by Li_2CO_3 . The identification of Li_2CO_3 was confirmed by quantitative arguments. The concentrations of Li, O, and C were estimated from areas under the high-resolution peaks for these elements. The quantitative calculations were as follows:

Li	28.1 At %
O	47.6 At %
C	24.3 At %

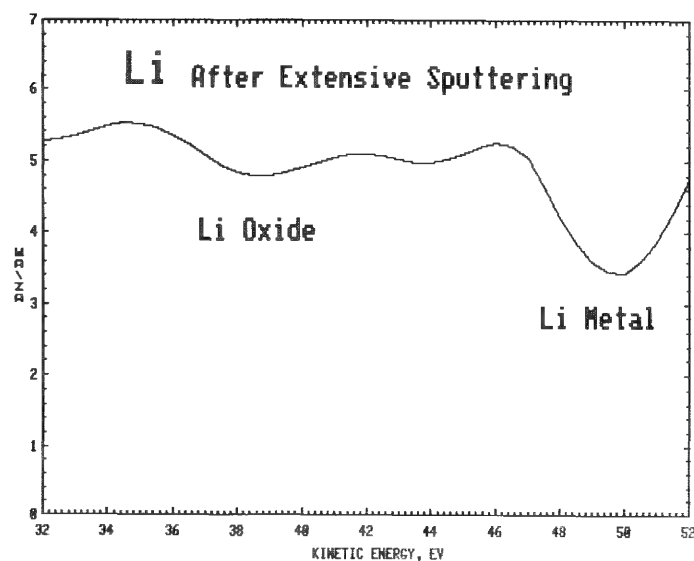


FIG. 7

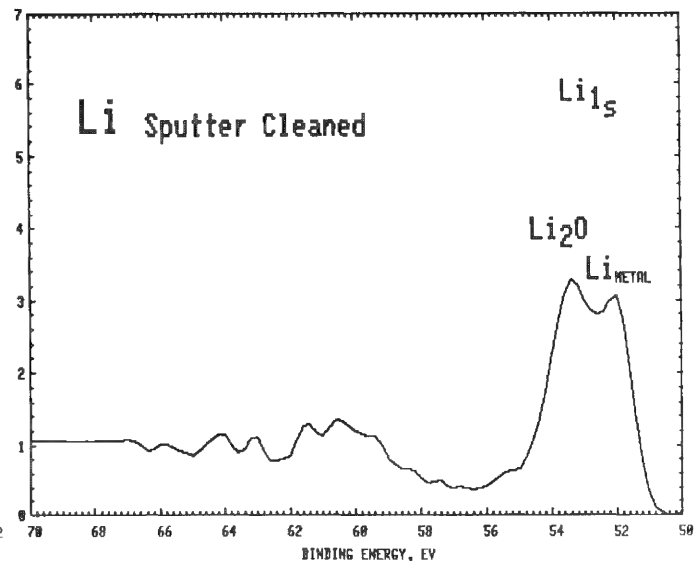


FIG. 8

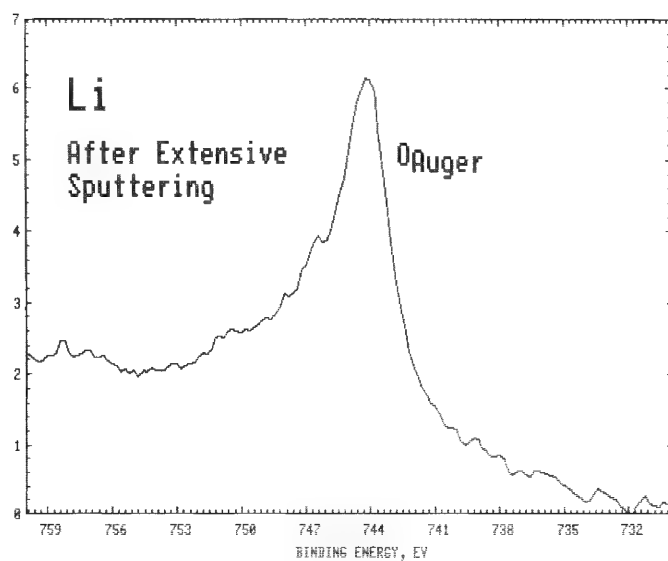


FIG. 9

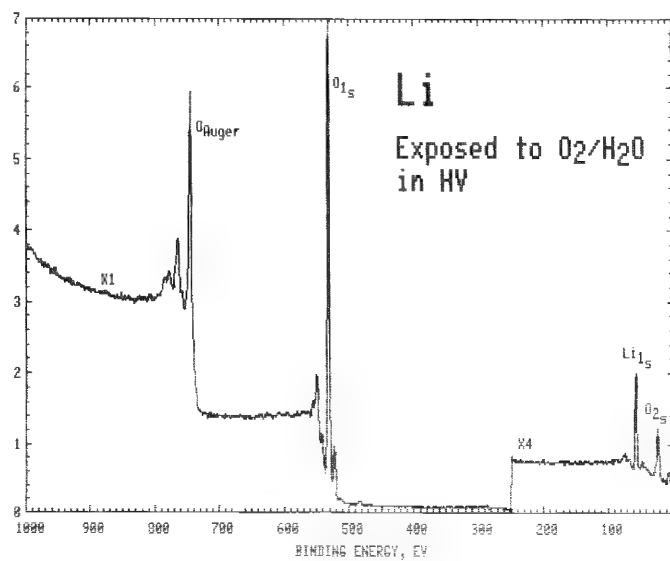


FIG. 10

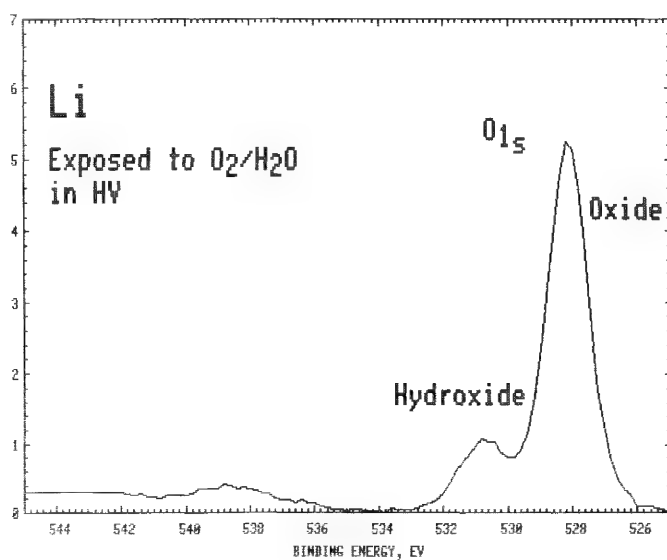


FIG. 11

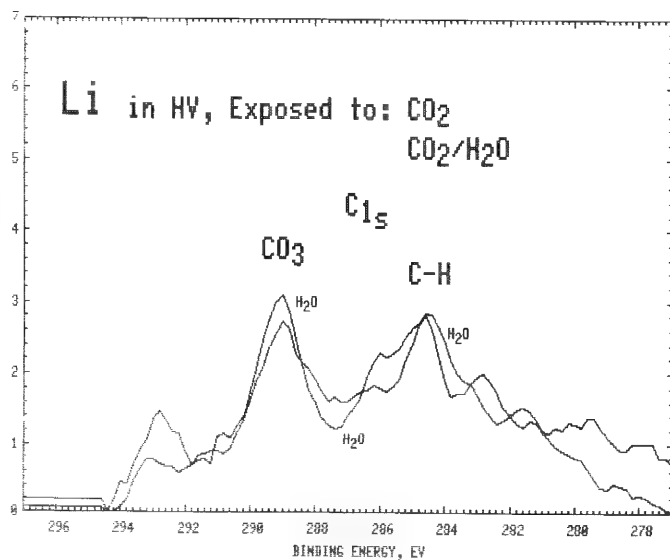


FIG. 12

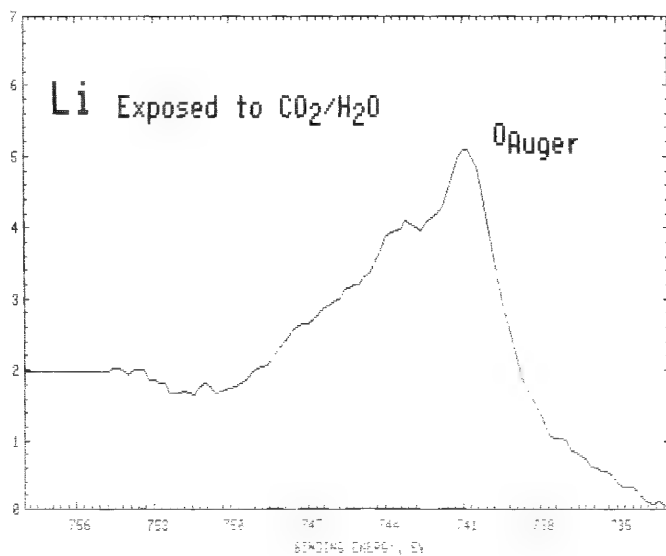


FIG. 13

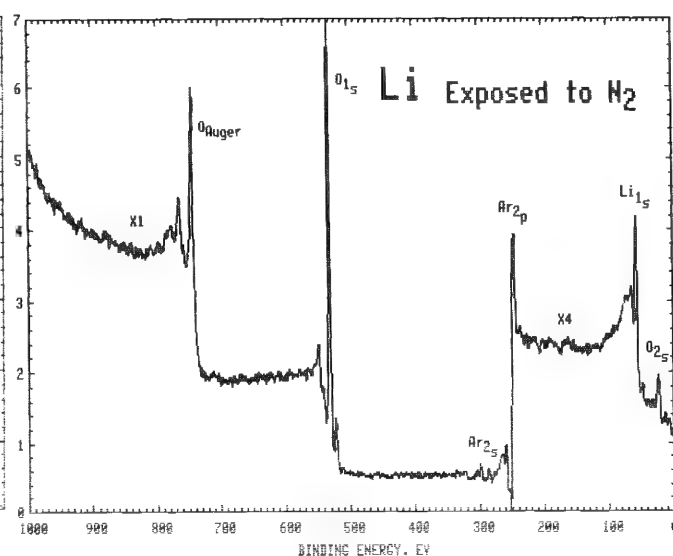


FIG. 14

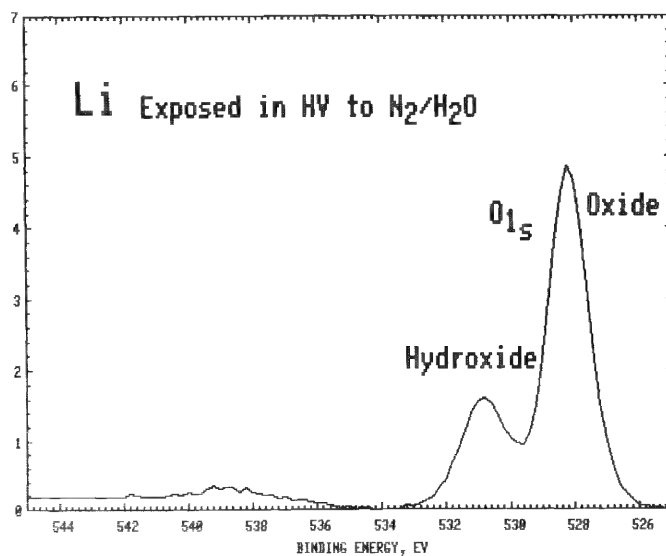


FIG. 15

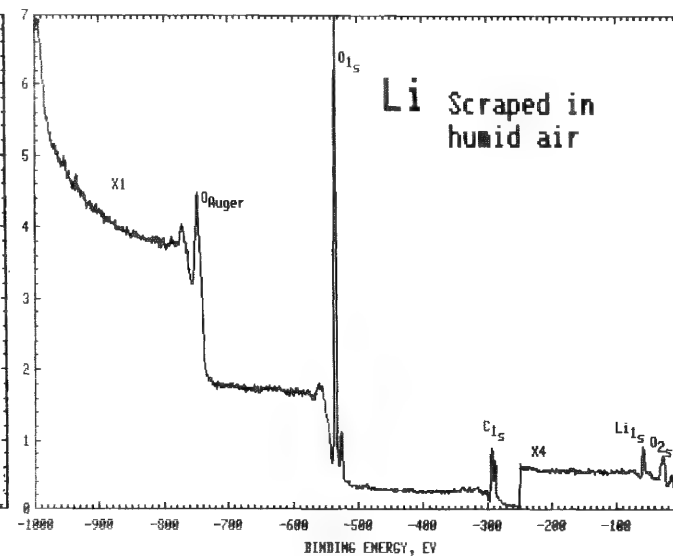


FIG. 16

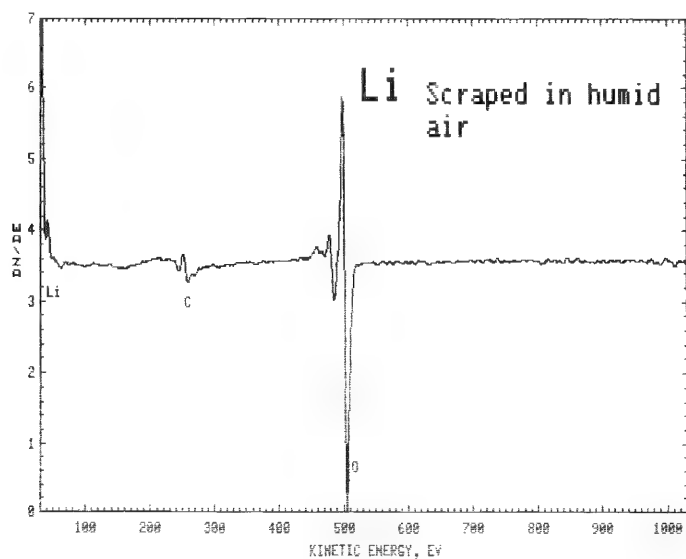


FIG. 17

The areas under the C_{1s} peaks for CO_3 and C-H bonding indicate:

CO_3	15.6 At %
C-H	8.7 At %

Assuming the carbon concentrations are correct, then 31.2% Li and 46.8% O could be bound up in Li_2CO_3 which is close to the totals for Li and O on the specimen.

Conclusions

The findings of this study are:

1. Lithium does not appear to react with nitrogen either under high vacuum or atmospheric pressure, even in the presence of water vapor. Other researchers, using surface analytical techniques, have found similar results.^{6,7}
2. Lithium reactions with N_2 , O_2 , CO_2 , and H_2O under high-vacuum pressure results in the formation of Li_2O and $LiOH$.
3. Lithium reactions with N_2 , O_2 , CO_2 , and H_2O under atmospheric pressure results in the formation of Li_2CO_3 .
4. The XPS binding energies for Li (metallic), Li_2O , $LiOH$, and Li_2CO_3 found here differs from those of other workers.^{8,9} Lithium metal, especially at approximately 52 ev binding energy, is 2 to 3 ev lower than reported elsewhere.

References

1. M. M. Markowitz, and D. A. Boryta, *J. Chem. Engg. Data* 7: 586-591, 1962.
2. F. A. Cotton and G. Wilkinson, Eds., *Advanced Inorganic Chemistry*, New York: Interscience, 1962, chap. 8.
3. Technical Data Bulletin 101, Foote Mineral Co.
4. K. M. Black, R. J. Bennett, and P. A. Lindfors. *Proc. Lithium Battery Symp.* (Electrochemical Society), 1980.
5. C. D. Wagner, D. A. Zatko, and R. H. Raymond, *Analytical Chem.* 52: 1445, 1980.
6. M. H. Froning et al., *Non-Aqueous Electrode Research*, Interium Tech. Report AFAPL-TR-79-2003, 1979.
7. R. G. Keil et al., *Non-Aqueous Electrode Research*, Tech. Report AFWAL-TR-80-2018, 1980.
8. C. D. Wagner et al., Eds., *Handbook of X-ray Photoelectron Spectroscopy*, Perkin-Elmer Corp. (Physical Electronics Div.), 1979.
9. J. D. Contour et al., *J. Micros. Spectros. Electron.* (France) 4(4), 1979.

Quantitative Analysis—Thin Films

CONSIDERATIONS OF X-RAY ABSORPTION FOR STEM X-RAY ANALYSIS OF Ni-Al FOILS

R. W. Glitz, M. R. Notis, D. B. Williams, and J. I. Goldstein

Several methods for quantitative x-ray analysis in absorbing thin film systems, have been proposed.^{1,2} A recent study of diffusion in the Ni-Al system utilizing STEM analysis has considered a number of variables such as foil orientation and thickness that affect the amount of x-ray absorption in thin foils.³ This paper discusses some of these variables and points out special considerations that must be taken into account during STEM analysis in highly absorbing systems.

STEM X-ray Analysis

For nonabsorbing systems the Cliff-Lorimer technique relates the concentration ratio of elements A and B (C_A , C_B) to the intensity ratios of these elements (I_A , I_B):

$$C_A/C_B = k_{AB}(I_A/I_B) \quad (1)$$

where k_{AB} is a constant for a given operating voltage independent of composition and thickness.⁴ If preferential absorption of one of the x-ray species occurs within the thin foil sample, the Cliff-Lorimer equation must be modified.

The effect of specimen absorption on x-ray intensity ratios as x rays are produced through a thin foil of thickness t has been given by Goldstein et al.⁵

$$\frac{C_A}{C_B} = k_{AB} \left[\frac{I_A}{I_B} \frac{\mu/\rho|_{\text{spec}}^A}{\mu/\rho|_{\text{spec}}^B} \right] \left[\frac{1 - e^{-\mu/\rho|_{\text{spec}}^B \csc \alpha (\rho t)}}{1 - e^{-\mu/\rho|_{\text{spec}}^A \csc \alpha (\rho t)}} \right] \quad (2)$$

where $\mu/\rho|_{\text{spec}}$ is the mass absorption coefficient of element A or B in the specimen, ρ is the density of the foil at the point of analysis, and $t \csc \alpha$ is the path length of the exiting x rays at a take-off angle α

Certain precautions must be taken when Eq. (2) is applied to practical systems. For example, the quantities μ/ρ and ρ are generally taken to be those at the point of analysis. Strictly speaking, these quantities must be representative of the material along the x-ray exit path. Care must be taken whenever possible to orient the foil in order to present an isocompositional path to the detected x rays. The path length of the detected x rays is equal to $t \csc \alpha$ if the thin foil is uniformly thick and planar in the region of the analysis. In wedge-shaped foils the path length is $t \csc \alpha$ only if the detector is oriented such that the analyzed x rays have a constant-thickness exit path. When this condition is not satisfied both the foil geometry and the x-ray detector orientation must be taken into consideration.

Experimental Procedures

A Philips EM 400T electron microscope equipped with an EDS detector oriented 90° to the specimen holder was used in this investigation. The thin foils were kept at 0° tilt to give a take-off angle α of 20°. The Ni and Al K α x-ray data were analyzed and the backgrounds stripped by use of an EDAX 9100 computer system. Suitable precautions were used to avoid spurious x-ray generation.⁶ Foil-thickness determinations were made at the points of analysis by the contamination spot separation technique.⁷ Specimens for the foil geometry experiment and k-factor determinations were made from a NiAl single crystal containing 32.47 wt% Al. Thin foils were produced from slices of this crystal by mechanical thinning followed by ion beam thinning.

The region of the ion beam thinned foil near the edge of a hole possesses a vaguely wedge-shaped cross section. Initially, an analysis was taken with the NiAl foil oriented

The authors are with the Department of Metallurgy and Materials Engineering, Lehigh University, Bethlehem, PA 18015. The support of the Materials Division of the National Science Foundation is gratefully acknowledged.

such that the detected x rays passed through the thinner portion of the wedge-shaped cross section. The foil was then physically rotated 180° and the analysis repeated. Contamination spots were then placed along a line parallel to the detector axis. These spots were used to determine foil thicknesses from which the foil cross section along the x-ray exit path was constructed.

Data for k factor determinations were collected with two different EDS x-ray detectors. The same thin foil was used for both determinations with a subsequent ion beam "cleaning" step employed between the two determinations. In order to minimize geometric effects the foil was oriented such that isothickness fringes in the analyzed region were parallel to the x-ray detector axis. X-ray data were collected with a 300Å spot size and 100s counting time. Analyses were taken in regions of the thin foil ranging in thickness from about 1000 to 4000 Å.

Results and Discussion

Geometric Effect. The geometry of the NiAl thin foil cross section used in this demonstration is illustrated in Fig. 1. Analysis #1 was taken at a foil thickness of about 2700 Å and x rays from point #1 passed through the thinner portion of the wedge en route to the detector. Analysis #2 was taken at a foil thickness of about 2600 Å and x rays from point #2 passed through the thicker portion of the wedge (Fig. 1). The ratio of Ni-K α to Al-K α peak intensities, foil thicknesses, and x-ray exit path lengths are listed in Table 1. One path length is calculated as $t \csc \alpha$; the other is the actual path length determined from the foil geometry.

TABLE 1.--Ni-Al STEM measurements in NiAl.

Analysis	$I_{\text{NiK}\alpha}/I_{\text{AlK}\alpha}$	Foil Thickness(A)	Path Length (Å)	
			Calculated	Actual
#1	2.64	2700	3976	2700
#2	5.18	2600	3760	6700

In spite of the fact that analysis #1 was taken in a slightly thicker portion of the foil, the measured Ni-K α /Al-K α intensity ratio from point #1 is 0.50 that of point #2, which indicates that the Al-K α x-rays from point #1 were absorbed less than those from point #2. Absorption calculations based on the calculated path length (Table 1) show that the intensity ratio at point #1 should be 1.04 times that at point #2. However, calculations based on the actual path lengths, which were in turn based on foil geometry/detector orientation considerations, show that the intensity ratio at point #1 should be 0.465 times that at point #2. From this measurement it is obvious that absorption calculations based on foil thickness without consideration of foil geometry can lead to erroneous answers in highly absorbing systems.

Determination of k Factor. Plots of measured Ni-K α /Al-K α intensity ratios from the NiAl specimen vs foil thickness for x-ray detectors A and B are given in Fig. 2. Presented along with the raw intensity data are intensity ratio data corrected for specimen absorption by use of Eq. (2) and appropriate mass absorption coefficients and densities.^{8,9} The data for detector B are displaced relative to those of detector A. This displacement is probably caused by differences in Be window thickness, which would change the detected AlK α peak intensity.¹⁰ Since both detectors yield the same slopes for the raw and corrected intensity ratio plots, the data are consistent for both detectors. The k_{NiAl} factor determined from extrapolation of the raw intensity ratio data to zero foil thickness are 1.01 and 1.39 for detectors A and B, respectively. The theoretical k_{NiAl} factor for 100 kV and for a detector with a 7.5 μm Be window is 1.29.⁵ The absorption-corrected intensity ratio plots (Fig. 2) have a negative slope, which indicates an overcorrection for the effect of absorption.

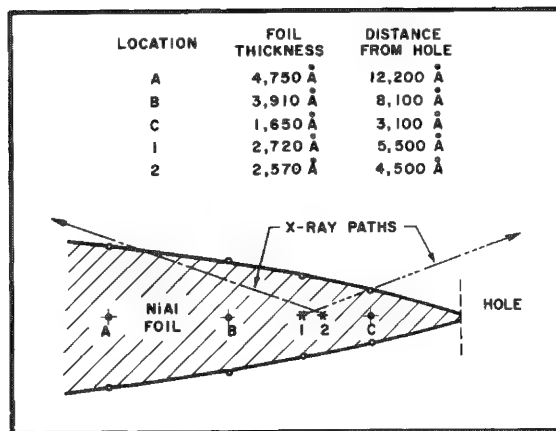


FIG. 1.--Geometry of NiAl thin foil cross section.

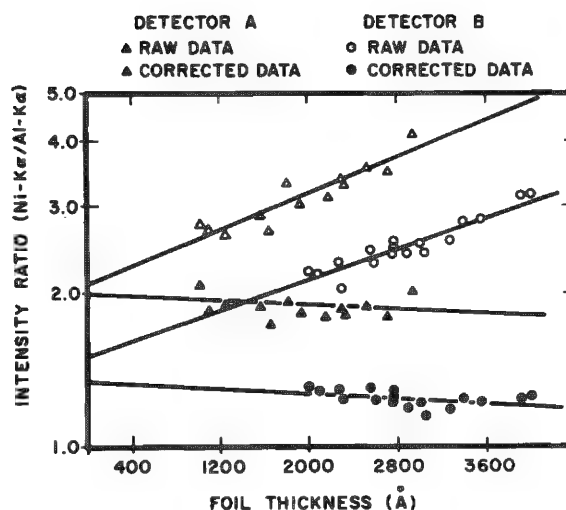


FIG. 2.--Data for k_{NiAl} determinations.

In the model for x-ray absorption it is assumed that the depth distribution of x-ray production, $\phi_A(\rho t) \approx \phi_B(\rho t) \approx 1.0$.⁵ However, using Monte Carlo simulations Kyser has shown that $\phi(\rho t)$ functions become thickness dependent with increasing density.¹¹ Although $\phi(\rho t)$ of Al is essentially constant, $\phi(\rho t)$ of Cu increases as much as 5% relative from 0 to a 4000Å-thick film. One can assume that $\phi(\rho t)$ of Ni is similar to $\phi(\rho t)$ of Cu. Therefore Eq. (2) would tend to overcorrect for absorption in the Ni-Al system, since it does not account for the increased generated intensity for Ni.

Another manifestation of the overcorrection for absorption is the nonconvergence of the raw and corrected intensity plots. The lack of convergence can be explained in part by a consistent overestimation of foil thickness. This overestimation is probably due to a systematic error present in the contamination spot measurement process which has been reported before.¹² The cause is most probably the presence of a surface layer of oxide and/or contamination, with a mass absorption coefficient much smaller than that of the specimen itself. The fact that data from detector A came closer to converging than data from detector B may be related to the length of time of ion beam thinning prior to STEM analysis. Prior to analysis with detector A the foil was cleaned in an ion thinner for about 30 min. Only 15 min of similar cleaning was employed in the case of detector B.

Assuming the presence of a 200Å surface layer (i.e., 400 Å total), which is similar to that previously observed, the absorption correction can be modified to bring the data for detector B into convergence.¹² However, for this modification to be valid the specimen thickness t should be reduced by about 400 Å to about $0.8t$. This geometric change would alter the slope of the experimental or raw data and under these circumstances convergence at zero thickness is not achieved. It appears that a combination of the variation in $\phi(\rho t)$ and the presence of surface layers should account for the experimental data in Fig. 2.

References

1. J. I. Goldstein, "Principles of thin film x-ray microanalysis," in J. J. Hren, J. I. Goldstein and D. C. Joy, Eds., *Introduction to Analytical Electron Microscopy*, New York: Plenum Press, 1979, 83.
2. P. L. Morris, "Quantitative thin foil x-ray microanalysis of materials," keynote Lecture--Metals Society Meeting: Microanalysis in the TEM, UMIST, Manchester, England, April 1979.
3. R. W. Glitz, *An Investigation into the Early Stages of Ni₃Al Layer Growth in NiAl/Ni Diffusion Couples*, M.S. Thesis, Lehigh University, 1980.
4. G. Cliff and G. W. Lorimer, "Quantitative analysis of thin metal foils using EMMA-4, the ratio technique," *Proc. Fifth Europ. Conf. on EM*, (London), 1972, 140.

5. J. I. Goldstein, J. L. Costley, G. W. Lorimer, and S. B. Reed, "Quantitative x-ray analysis in the electron microscope," *SEM/1977*, I, 315.
6. J. I. Goldstein and D. B. Williams, "X-ray analysis in the TEM/STEM," *SEM/1977*, I, 651.
7. G. W. Lorimer, G. Cliff, and J. N. Clark, in J. A. Venables, Ed., *Developments in Electron Microscopy and Analysis*, New York: Academic Press, 1976, 153.
8. K. F. J. Heinrich, in T. D. McKinley, K. F. J. Heinrich and D. B. Wittry, Eds., *The Electron Microprobe*, New York: Wiley, 1966, 351.
9. A. Taylor and N. J. Doyle, "Further Studies on the nickel-aluminum System: I. The β -NiAl and δ -Ni₂Al₃ phase fields," *J. Appl. Cryst.* 5: 201, 1972.
10. S. Mehta, J. I. Goldstein, D. B. Williams, and A. D. Romig Jr., "Determination of Cliff-Lorimer k calibration factors for thin foil x-ray microanalysis of Na, Mg, and Al in the STEM," *Microbeam Analysis--1979*, 119.
11. D. F. Kyser, "Monte Carlo simulation in analytical electron microscopy," in J. J. Hren, J. I. Goldstein, and D. C. Joy, Eds., *Introduction to Analytical Electron Microscopy*, New York: Plenum Press, 1979, 199.
12. G. Love, M. G. C. Cox and V. D. Scott, "Foil thickness measurement in transmission electron microscopy," in D. L. Missel, Ed., *Development in Electron Microscopy and Analysis*, Bristol and London: The Institute of Physics, 1977, 347.

QUANTITATIVE X-RAY MICROANALYSIS THIN-FILM METHOD WITH K-, L-, AND M-LINES

T. P. Schreiber and A. M. Wims

The early thin film work of Cliff and Lorimer,¹ which was based entirely on conversion of x-ray intensities to concentrations by experimentally determined sensitivity factors, was limited both in range of chemical elements and beam voltages. Later, standardless methods were developed by Goldstein et al.,² Zaluzec,³ and Colby,⁴ but were limited in accuracy and in range of applicable x-ray lines. The method of Colby⁴ supplied with the Kevex energy-dispersive x-ray spectrometer (EDS) system has been found to be inaccurate, especially for high atomic number K lines and for many L lines. This report describes the development of an improved method for the minicomputer-controlled x-ray spectrometer (Kevex 7000) on the JEM 200C scanning transmission electron microscope (STEM).

The Cliff and Lorimer¹ "k" factor can be expressed as a function of basic physical parameters of elements x and y as follows:

$$k_{xy} = \frac{A_x \epsilon_y Q_y \omega_y a_y}{A_y \epsilon_x Q_x \omega_x a_x} \quad (1)$$

where A is atomic weight, ϵ is the spectrometer efficiency, Q is the ionization cross section, ω is the fluorescence yield, and a is the relative intensity factor. Since Cliff and Lorimer¹ and Goldstein et al.² have used $k_{x, Si}$ as the scaling-factor, we shall do the same.

The factors in the k equation which require explanation are ω , a, and Q. The fluorescence yield ω , which is the fraction of ionizations that result in x-ray emission, can be calculated from an equation proposed by Burhop⁵ which has been fitted to the experimental data of Fink⁶ by Colby.⁷ The relative intensity factor a is the fraction of the total x-ray emission from a given atomic shell that is measured, and we have determined new values for the K-, L-, and M-shells.⁸ The ionization cross section Q is a measure of the probability that an incident electron will ionize a given atomic shell. The values of Q vary with electron beam energy and atomic number. Powell's extensive literature review and evaluation⁹ indicates that considerable confusion exists in calculating values of Q. Experimental data are limited and a wide variety of equations have been suggested to calculate values of Q for the K- and L-shells. K-shell cross-section formulas for use in x-ray analysis calculations have been developed by Goldstein² and Zaluzec.³ However, their data do not cover the atomic number range from 11 (Na) to 56 (Ba) that we need.

Based on the equations suggested in the literature,⁹ we arrived at the following general form for the ionization cross section equation:

$$Q_{x,l} = \pi e^4 z \frac{b \ln(cU_x)}{E_x^2 U_x^d} \quad (2)$$

where $Q_{x,l}$ is the ionization cross section for shell l of element x, πe^4 is an atomic constant = 6.4924×10^{-20} , z is the number of electrons in the l shell, E_x is the absorption edge energy (keV) for the l shell of element x, U_x is the overvoltage E_0/E_x (where E_0 is the beam voltage in kilovolts), and b, c, and d are functions of atomic number that can be varied to fit experimental data.

Equation (2) differs from others in the literature in that it incorporates the parameters b, c, and d as functions of atomic number. This feature allows a wider range of elements and overvoltages to be covered than is possible with other equations currently in use.

The authors are with the Analytical Chemistry Department, General Motors Research Laboratories, Warren, MI 48090.

Experimental

Measurements were made with Japan Electron Optics Laboratory (JEOL) Model JEM 200C, equipped with a Kevex x-ray spectrometer, Model 3203-200 VS with a 0.008mm Be window, 30mm active area with 148-eV resolution at 5.9 keV and 1000 Hz.

Standard Samples

Finely divided chemically pure powders of NaCl, Mg₂Si, CuS, ZnS, CdS, SnS, BaSO₄, AuCl₃, and PbCl₂ were dispersed in Freon 113, deposited on carbon-coated nylon grids, and mounted in the JEOL graphite specimen holders. Although specimen stability and x-ray absorption caused some problems, it was possible to get reliable results by analysis of protuberances and edges of large (1-2 μ m) particles which faced toward the x-ray spectrometer. Three semiconductor-grade compounds, plus specimens prepared from a lithium tetraborate fusion of Co₂O₃ and SiO₂, and a mixed oxide were used to evaluate the precision and accuracy of the final method.

Results and Discussion

The final step in developing a complete quantitative analysis method for thin samples was the systematic evaluation of the b, c, and d factors in the ionization cross section Eq. (2). To do so we used our experimental scaling factors and some selected values from the literature.^{2,10} Our values were chosen from measurements on a number of individual particles and at different locations on large particles. Values were selected for repeatability and minimum evidence of absorption. This method resulted in an accuracy and precision of about 7% of the amount present for most elements. The factors were evaluated for the K-, L-, and M-shell x-ray lines in the sequence, d, c, and then b.

d Factor. Reuter¹¹ has used $d_K = 0.7$ for microprobe analysis of bulk specimens at low overvoltages ($U \leq 4$) but our data showed that a value of $d_K = 0.8$ for barium improved the agreement between our 200kV ($U = 6.4$) and 100kV ($U = 2.94$) experimental data. At high overvoltages, the literature⁹ indicates that d_K approaches a value of one. Using for Ba $d_K = 0.8$ and for Si $d_K = 1$ as two points in a linear function, we obtained $d_K(Z) = 1.0667 - 0.00476Z$. Because the overvoltages for L- and M-shell x-ray lines are all greater than 17, we made $d_L = d_M = 1$.

c Factor. The factor c_K was evaluated with the above d_K equation and $b_K = 1$ in the scaling factor equation, with Si as the reference element. Values of c_K found in the literature (0.65-1.5) were tried and plots of k_{calc}/k_{exp} vs atomic number for Na, Mg, Cu, Zn, Cd, and Ba showed that a value of $c_K = 1$ gave a minimum difference between the 100 and 200 kV data. Because the sensitivity of k_{calc}/k_{exp} to variations in c decreases at higher overvoltages, values of $c_L = c_M = 1$ were also chosen.

b Factor. With values of c and d thus determined, the b parameter was evaluated. Equation (1) was again used to compute a k_{calc} with $b = 1$ and Si as the reference element and then the ratio k_{calc}/k_{exp} was calculated. Because $b = k_{calc}/k_{exp}$, a plot of k_{calc}/k_{exp} was used to obtain b as a function of Z. Figures 1 and 2 show the k_{calc}/k_{exp} data points for K- and L-shell plotted against log Z. The curves are least-square polynomial fits to selected data points indicated in the figures. Other points are included in the plots to show the variability of data from the literature. The equations for the b_K and b_L curves are shown below along with a straight line function for b_M determined from the Au and Pb points: $b_K (Z < 30) = 8.874 - 8.158 \ln Z + 2.9055(\ln Z)^2 - 0.35778(\ln Z)^3$, $b_K (Z > 30) = 0.661$, $b_L = 0.2704 + 0.007256(\ln Z)^3$, $b_M = 11.335 - 2.428 \ln Z$.

The values of b, c, and d determined above were incorporated into Eq. (2). We feel these ionization cross section equations are a marked improvement over those used by others.²⁻⁴ These ionization cross section equations are based upon the overvoltage ranges encountered in actual analysis and incorporate the d and b parameters as functions of atomic number to adjust to these conditions.

Calculated Scaling Factors $k_{x, Si}$. Figures 3 and 4 are plots of the K- and L-shell scaling factors calculated for each element using the new Q equations. These curves show that $k_{x, Si}$ is not a smooth function of Z and that reliable values cannot be obtained by

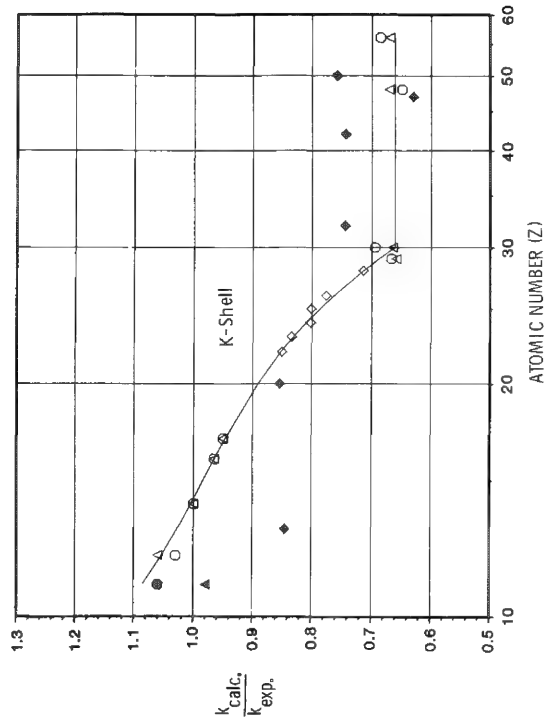


FIG. 1.--Plot of K-shell $k_{\text{calc}}/k_{\text{exp}}$ values: o our data at 100 kV, Δ our data at 200 kV, \diamond from data of Cliff and Lorimer¹⁰; b_K curves were obtained with polynomial fit of data excluding the solid points.

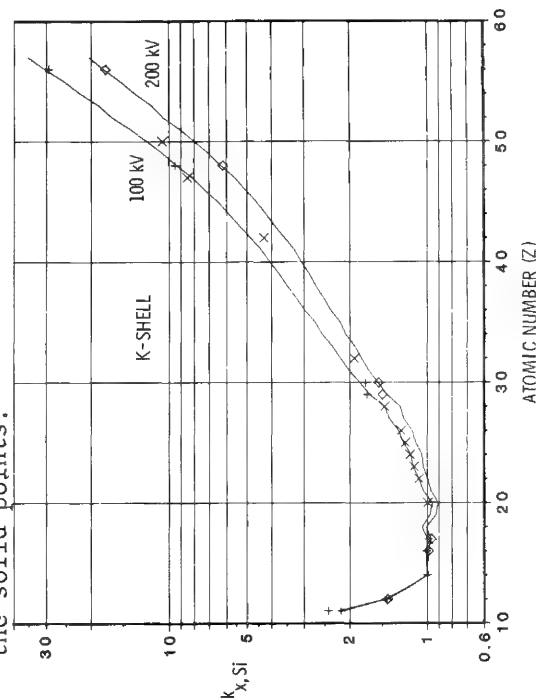


FIG. 3.--Plot of $k_{x,\text{Si}}$ scaling factor for $K\alpha_{1,2}$ lines obtained with our equation for Q_K : + our data at 100 kV, \times Cliff and Lorimer¹⁰ at 100 kV \diamond our data at 200 kV.

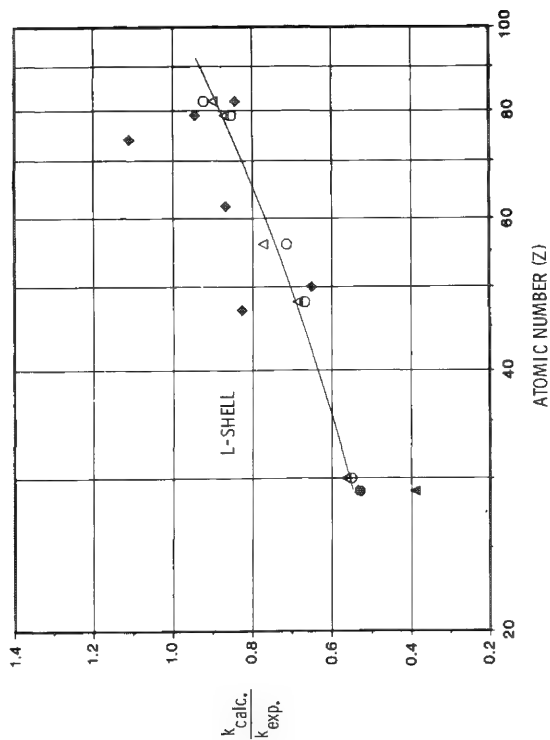


FIG. 2.--Plot of L-shell $k_{\text{calc}}/k_{\text{exp}}$ values: o our data at 100 kV, Δ our data at 200 kV, \diamond from data of Goldstein²; b_L curve was obtained by polynomial fit of data excluding the solid points.

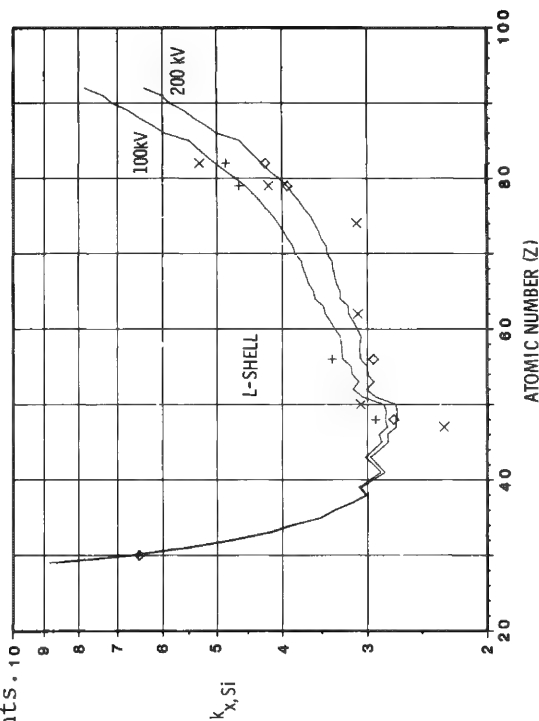


FIG. 4.--Plot of $k_{x,\text{Si}}$ scaling factor for $L\alpha_{1,2}$ lines obtained with our equation for Q_L : + our data at 100 kV, \times Goldstein² at 100 kV, \diamond our data at 200 kV.

interpolation between a few experimental values. These element-to-element variations arise from changes in atomic weights and the relative intensity factors which make calculations of $k_{x,Si}$ for individual elements a necessity.

Accuracy

Comparative results on a variety of materials showed an average relative error of $\pm 4.4\%$. Of particular interest were results with PbS and BaTiO₃ samples. Analyses on these samples are in good agreement with the relative chemical values despite the necessity for subtracting interfering lines with large intensities. The BaTiO₃ sample further illustrates the usefulness of going to high energy K lines. Without the ability for accurate analysis with the 32.2keV Ba K line this analysis would not have been possible.

References

1. G. Cliff and G. W. Lorimer, "Quantitative analysis of thin metal foils using EMMA--4, the ratio technique," *Proc. 5th European Congress on Electron Microscopy*, (Bristol), 1972, 140.
2. J. I. Goldstein, J. L. Costley, G. W. Lorimer, and S. J. B. Reed, "Quantitative x-ray analysis in the electron microscope," *SEM/1977*, I, 325.
3. N. J. Zaluzec, "Quantitative x-ray microanalysis: Instrumental considerations and applications to materials science," in J. J. Hren, J. I. Goldstein, and D. C. Joy, Eds., *Introduction to Analytical Electron Microscopy*, New York: Plenum Press, 1979, 121.
4. J. W. Colby, Kevex Quantex Program, Version 3.1 W, October 1979.
5. E. H. S. Burhop, "Fluorescence yields," *J. Physics of Radium* 16: 625, 1955.
6. F. W. Fink, R. C. Jopson, H. Mark, and C. D. Swift, "Atomic fluorescence yields," *Rev. Mod. Phys.* 38: 513, 1966.
7. J. W. Colby, "Quantitative microprobe analysis of thin insulating films," J. Newkirk, G. Mallett, and H. Pfeiffer, Eds., *Advances in X-ray Analysis*, New York: Plenum Press, 11: 287, 1968.
8. T. P. Schreiber and A. M. Wims, "Relative intensity factors for K-, L-, and M-shell x-ray lines," *Microbeam Analysis--1981*, 000.
9. C. J. Powell, "Cross sections for ionization of inner-shell electrons by electrons," *Rev. Mod. Phys.* 48: 33, 1976.
10. G. Cliff and G. W. Lorimer, "The quantitative analysis of thin specimens," *J. Microscopy* 103: 20, 1975.
11. W. Reuter, "The ionization function and its application to electron probe analysis of thin films," G. Shinoda, K. Kohra, and T. Ichinokawa, Eds., *Proc. 6th Intern. Symp. X-ray Optics and Microanal.*, University of Tokyo Press, 1971, 121.

RELATIVE INTENSITY FACTORS FOR K-, L-, AND M-SHELL X-RAY LINES

T. P. Schreiber and A. M. Wims

This report describes our calculation and comparison with experiment of the relative intensity factors for the K-, L-, and M-atomic shells. Our main contribution is for the L-shell relative intensity factor (a_L) where data in the microanalysis literature is essentially nonexistent. In addition, we have evaluated the factor for the K-shell (a_K) by comparing existing theoretical and experimental data, and determined an effective though limited M-shell relative intensity factor (a_M).

The a_K , a_L , and a_M values developed in this study are required for energy-dispersive x-ray analysis with Kevex Quantex software where the following definitions apply: $a_K = I(K\alpha_{1,2})/I(\text{total K-spectrum})$; $a_L = I(L\alpha_{1,2})/I(\text{total L-spectrum})$; $a_M = I(M\alpha_{1,2})/I(\text{total M-spectrum})$.

Experimental

Relative-intensity data for the calculation of a_L values were obtained with two instruments: a Japan Electron Optics Laboratory Model JEM 200C scanning transmission electron microscope (STEM) equipped with a Kevex energy-dispersive spectrometer (EDS); and an Applied Research Laboratories, Model EMX, electron probe microanalyzer (EPA) equipped with crystal spectrometers.

Results and Discussion

a_L : The determination of a_L values is our most important contribution and will be described first. The emission of L-shell x rays is complicated by the subshell structure where Coster-Kronig¹ transitions, which occur among the subshells, change the vacancy location within the shell. Since the distribution of the vacancies is reflected in the relative line intensities, the Coster-Kronig transitions are important in determining a_L .

Burhop and Asaad² have shown that the Coster-Kronig transitions alter the initial vacancy distribution N_i to an effective distribution V_i (where "i" refers to the subshell), as follows: $V_1 = N_1$; $V_2 = N_2 + f_{12}N_1$; $V_3 = N_3 + f_{23}N_2 + (f_{13} + f_{12}f_{23})N_1$; where f_{12} , f_{13} , f_{23} are the probabilities of the Coster-Kronig transitions $L_1 \rightarrow L_2$, $L_1 \rightarrow L_3$, and $L_2 \rightarrow L_3$, respectively.

The primary vacancy distribution N_i is a function of the mode of excitation, but for electron impact on thin specimens where the electron beam voltage is greater than three times the ionization voltage of the particular atomic level, the value of N_i is nearly equal to the statistical weight of the level. Since the electron distribution for the L-shells is $L_1 = 2$, $L_2 = 2$, and $L_3 = 4$, the values of N_i are $N_1 = 0.25$, $N_2 = 0.25$, and $N_3 = 0.5$.

To calculate relative intensities and a_L values, we developed the following equation to utilize the data from the literature:

$$a_L = \frac{I(L\alpha_{1,2})}{I(\text{total L-spectrum})} = \frac{\omega_3 V_3}{\omega_1 V_1 + \omega_2 V_2 + \omega_3 V_3} \frac{\Gamma_R(L_3^M 4,5)}{\Gamma_R(L_3)}$$

where ω_i is the fluorescence yield for the subscripted level, V_i is as defined above, and Γ_R is the x-ray emission rate for the bracketed transition to the bracketed final level.

Values of a_L were either calculated from this equation or obtained experimentally with the EPA or the STEM. The values of ω_i and V_i used in the calculations were obtained from the theoretical ω and f values of McGuire,³ Chen,⁴ and Craseman⁵ which are in Bambynek's⁶ Table IV.XV. The values of Γ_R were obtained from Scofield's⁷ calculations.

Figure 1 shows a plot of our calculated and experimental a_L values along with a plot (dashed line) of Colby's⁸ equation, which is used in many computer programs for quantita-

The authors are with the Analytical Chemistry Department, General Motors Research Laboratories, Warren, MI 48090.

tive microanalysis. The agreement among our calculated and experimental results is good even though there is some scatter. Our data give a relationship (solid line) for a_L which differs markedly from that of Colby. The two segments of the solid line in Fig. 1 represent separate fits to the data over the ranges indicated. The coefficients for the two segments were generated (Table 1) for a line drawn through the data which was weighted towards the experimental data. The discontinuity at $Z = 50$, we believe, is real because the change is predicted by the theoretical data for the Coster-Kronig $f_{1,3}$ factor which drops abruptly by 50% from $Z = 50$ to $Z = 51$. The electron probe data and the calculated data for a_L also indicate a change near $Z = 50$.

TABLE 1.--Functions for calculating a_K , a_L , and a_M values.

Atomic Number	Equations
11 to 19	$a_K = 1.052 - 4.39 \times 10^{-4}Z^2$
20 to 29	$a_K = 0.896 - 6.575 \times 10^{-4}Z$
30 to 60	$a_K = 1.0366 - 6.82 \times 10^{-3}Z + 4.815 \times 10^{-5}Z^2$
27 to 50	$a_L = 1.617 - 0.0398Z + 3.766 \times 10^{-4}Z^2$
51 to 92	$a_L = 0.609 - 1.619 \times 10^{-3}Z - 0.03248 \sin [0.161(Z - 51)]$
60 to 92	$a_M \approx 0.65$

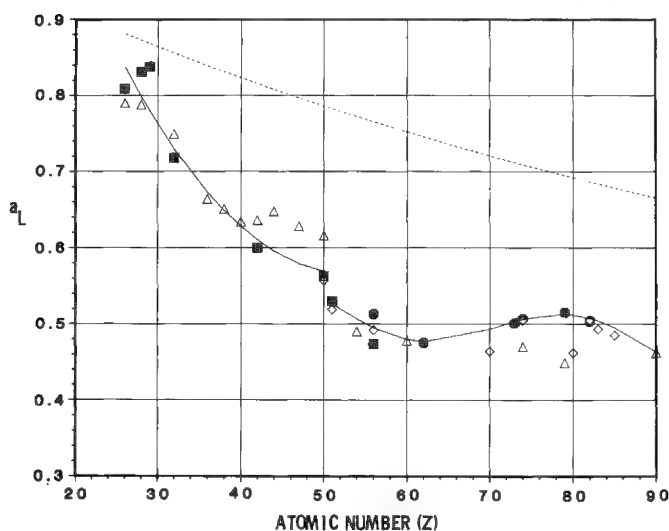


FIG. 1.--Plot of theoretical and experimental a_L values: Δ calculated from Refs. 3 and 7, \diamond calculated from Refs. 4, 5, and 7, \bullet EDS, \blacksquare EPA. Solid curves represent equations for a_L shown in Table 1; dotted curve calculated from Colby's⁸ BETA function.

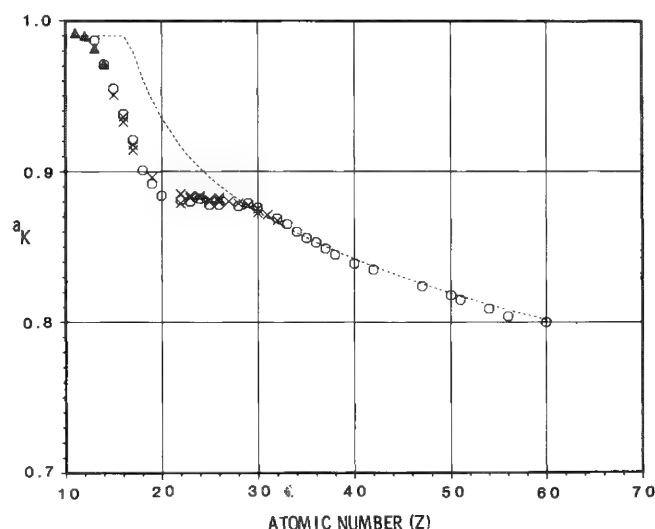


FIG. 2.--Plot of theoretical and experimental a_K values: \circ theoretical values calculated from Scofield's¹¹ data, \times experimental values calculated from data of Heinrich,⁹ \blacktriangle experimental values from data of Salem.¹⁰ Equations for fit to data are in Table 1; dashed curve calculated from Colby's⁸ BETA function.

a_K : Figure 2 shows a plot of the experimental data of Heinrich⁹ and Salem,¹⁰ and the theoretical data of Scofield¹¹ along with a curve for a_K calculated with Colby's⁸ BETA function. It is clear that the points define a curve with a plateau in the important region from atomic number 20 to 30. Table 1 contains coefficients for three curve segments fitted to the Heinrich-Scofield data.

a_M : Although the subshell structure for the M-shell is much more complicated than that for the L-shell, the relative intensity distribution is greatly simplified by the very strong Coster-Kronig transitions which concentrate the energy in the $M\alpha$ and $M\beta$ lines. In addition, the range of elements of analytical interest is limited to those above $Z =$

60. Because of a lack of theoretical and experimental relative intensities, we experimentally determined an a_M value with the EDS and found that $a_M \approx 0.65$ for data collected on the Kevex system.

References

1. D. Coster and R. de L. Kronig, "A new type of Auger effect and its influence on the x-ray spectrum," *Physica* 2: 13, 1935.
2. E. H. S. Burhop and W. N. Asaad, "The Auger effect," in D. R. Bates and I. Esterman, Eds., *Adv. Atomic Mol. Phys.*, New York: Academic Press, 8: 62, 1972.
3. E. J. McGuire, "Atomic L-shell Coster-Kronig, Auger, and radiative rates and fluorescence yields for Na-Th," *Phys. Rev.* A3: 587, 1971.
4. M. H. Chen, B. Craseman, and V. O. Kostroun, "Theoretical L_2 - and L_3 -subshell fluorescence yields and L_2 - L_3 Coster-Kronig transition probabilities," *Phys. Rev.* A4: 1, 1971.
5. B. Craseman, M. H. Chen, and V. O. Kostroun, "Auger and Coster-Kronig transition probabilities to the atomic 2s state and theoretical L_1 fluorescence yields," *Phys. Rev.* A4: 2161, 1971.
6. W. Bambynek et al., "X-ray fluorescence yields, Auger and Coster-Kronig transition probabilities," *Rev. of Mod. Phys.* 44: 716, 1972.
7. J. H. Scofield, "Hartree-Fock values of L x-ray emission rates," *Phys. Rev.* A10: 1507, 1974.
8. J. W. Colby, Kevex Quantex Program, Version 3.1W, Oct., 1979.
9. K. F. J. Heinrich, C. E. Fiori, and R. L. Myklebust, "Relative transition probabilities for x-ray lines from the K level," *J. Appl. Phys.* 50: 5589, 1979.
10. S. I. Salem, T. H. Falconer, and R. W. Windrell, " $K\beta/K\alpha$ radiative-transition probability ratios for elements of low atomic numbers in amorphous and crystal forms," *Phys. Rev.* A6: 2147, 1972.
11. J. H. Scofield, "Exchange corrections of K x-ray emissions rates," *Phys. Rev.* A9: 1041, 1974.

APPLICATION OF THE TOP-HAT DIGITAL FILTER TO A NONLINEAR SPECTRAL UNRAVELING PROCEDURE IN ENERGY-DISPERSIVE X-RAY MICROANALYSIS

C. E. Fiori, C. R. Swyt, and K. E. Gorlen

To measure the intensity of a characteristic x-ray peak in a spectrum one must separate the peak from the average effects of other peaks, the continuum, and any other source of background radiation. All the mathematical procedures for isolating one peak from the interfering effects of other peaks can be classified into one of two categories: linear or nonlinear procedures. Procedures that separate characteristic x-ray peaks from the background can also be classified into one of two categories: background modeling and background filtering.

Both background modeling and background filtering methods have been previously combined with linear unraveling procedures and cast into quantitative X-ray microanalysis data reduction programs.¹⁻⁴ Background modeling has also been combined with a nonlinear procedure.^{5,6} The purpose of this paper is to report on a background filtering method combined with a nonlinear peak unraveling procedure for x-ray microanalysis applications.

We first describe the two components of the proposed method and review the advantages and disadvantages of each: the top-hat digital filter to suppress the background radiation and the sequential simplex to unravel spectral overlaps.

Top-hat Digital Filter

Background modeling consists of calculating or measuring a continuum energy distribution and combining it with a mathematical description of the detector response function. The resulting function is then used to calculate an average background spectrum that can be subtracted from the observed spectral distribution. Background filtering ignores the physics of x-ray production, emission, and detection; the background is viewed as an undesirable signal to be removed by modification of the frequency distribution of the spectrum. Examples are digital filtering and Fourier analysis.

A method that does not require an explicit model of the background radiation is clearly advantageous in applications such as x-ray fluorescence analysis, energy-dispersive microanalysis of irregular specimens, and analysis in the electron microscope operating in the energy range above 50 keV. In the latter case one can in principle calculate background from a continuum model. However, in practice it is extremely difficult and often impossible to make such a prediction since a significant proportion of the background does not originate from the impact point of the primary electron beam but from grid bars or the specimen holder. Furthermore, Compton recoil electrons generated in the active volume of the silicon detector from high-energy x rays (above 80 keV) further distort the expected shape of the background.⁷

The top-hat digital filter was first applied to energy dispersive x-ray spectra by Schamber.⁴ The algorithm is both simple and elegant. Briefly stated, counts in a group of adjacent channels of a spectrum are *averaged* and the *average* assigned to a channel equivalent to the center *channel* of the filter; the procedure is repeated as the filter is stepped through the spectrum and a new, filtered spectrum is created. The original spectrum is retained unaltered. One may describe the *averaging* by the following equation, using the notation of Statham⁸:

$$y'_i = \frac{1}{2M+1} \sum_{j=i-M}^{i+M} y_j - \frac{1}{2N} \left(\sum_{j=i-M-N}^{i-M-1} y_j + \sum_{j=i+M+1}^{i+M+N} y_j \right) \quad (1)$$

where y'_i is the contents of the i th channel of the filtered spectrum and y_j is the contents of the j th channel of the original spectrum.

Authors Fiori and Swyt are with the Biomedical Engineering and Instrumentation Branch, Division of Research Services, and author Gorlen is with the Computer Systems Laboratory of the National Institutes of Health, Bethesda, MD 20205.

The filter is divided into three sections: a positive, central section consisting of $2M+1$ channels and two side sections each containing N channels. The grand *average* of the side sections is subtracted from the grand *average* of the central section.

The effect of this particular averaging procedure is as follows: If the original spectrum is straight, across the width of the filter, then the *average* is zero. If the original spectrum is curved concave upward, across the width of the filter, the *average* is negative; if curved convex upward, the *average* is positive. The greater the curvature, the larger the *average*.

In order for the filter to respond with the greatest measure to the curvature found in spectral peaks, and with the least measure to the curvature found in the spectral background, the width of the filter must be carefully chosen. For a detailed treatment of the subject see Schamber⁴ and Statham.⁸ In general, the width of the filter for any given spectrometer system is chosen to be twice the full width at half the maximum amplitude (FWHM) of the Mn K α peak, with the number of channels in the central section equal to or slightly more than the combined number of channels in the side sections.

Nonlinear Spectral Unraveling: The Sequential Simplex

In our context, linearity (or nonlinearity) is a property of the fitting parameters. If all the parameters that are being adjusted to provide a best fit in a given procedure are used in a simple multiplicative or additive fashion, then the procedure is linear. A procedure that utilizes a Gaussian peak profile and adjusts either width and/or profile center during the fitting is therefore nonlinear because the width and position parameters are exponentiated. In general, the differences between linear and nonlinear are as follows. Linear methods provide a set of equations that when solved gives a single, unique answer (i.e., a set of peak amplitudes). In the nonlinear methods techniques such as iteration or search procedures are often required to provide a solution. The nonlinear methods require starting estimates for the fitting parameters which, if sufficiently incorrect, can allow the procedure to converge to any one of several statistically acceptable, though incorrect, fits. The linear methods provide a built-in estimate of the fitting error, the so-called error matrix which, if there is no source of systematic error, provides a good measure of the random error of the fitting process. The nonlinear methods do not provide as convenient nor as accurate an estimation of random error.

The assumption that is made for the use of a linear procedure for x-ray spectral unraveling is that the width and energy of every peak in the overlapped group is accurately known. That is often not the case, particularly in an instrument such as the analytical electron microscope, where the energy-dispersive detector can respond to the environment and produce unexpected peak shifts and broadening. For example, short-term (10 min to 1 h) peak broadening of up to 10 eV can occur when analysis in the scanning mode follows operation in the conventional transmission mode.⁷ Peak shifts and/or broadening can occur due to interaction between the microscope scan coils and a top-looking energy-dispersive detector. The degree of the interaction is a function of the scan speed and magnification. Further systematic errors arise from the effects of electrical ground loops and normal drift with time of the characteristics of critical circuit components.

It is for the reason of uncontrolled systematic error in peak position and width in spectra from the analytical electron microscope that we have chosen a nonlinear spectral unraveling procedure for this application. The particular nonlinear algorithm we use is the accelerating sequential simplex.^{9,10} A simplex procedure is an organized technique to search for the set of independent variables in a mathematical expression which cause the expression to be a *best* fit in the statistical sense to a set of data points. The algorithm is too complicated to be fully described in this paper. The interested reader is referred to Refs. 9, 10, and 11. In our application of the simplex procedure¹¹ we have introduced several simplifications that reduce the number of fitting parameters to be determined. Since the energies of x-ray lines are well known, they are entered as known quantities and the energy of the principal peak only is required as a parameter to correct for energy shifts. The energies of all other peaks in the overlapped bundle are determined from the energy of the principal peak. In addition, the width of only the

principal peak is determined as a fitting parameter; the widths of the other peaks can be calculated given that width.

Description of Algorithm

The proposed procedure works as follows: the digital filter (Eq. 1) is passed through the part of a spectrum containing the peaks to be unraveled. The average effect of the background is strongly suppressed. The filtered spectrum resembles the smoothed and scaled second derivative of the original spectrum. An initial Gaussian profile is estimated for each peak in the overlapped bundle. These profiles are added and the same digital filter is passed through the *constructed* spectrum. The filtered original spectrum is then compared, channel by channel, to the filtered *constructed* spectrum. A measure of the goodness of fit is recorded and a new set of profile parameter estimates are calculated by the simplex procedure. The resulting profiles are then added, filtered, and tested again against the filtered original spectrum. If the new estimates have produced a better *fit* the simplex procedure continues to move the fitting parameters in this general *direction*. The process repeats until convergence is obtained. In the computer program an option is included that constrains the width and energy parameters to certain specified regions. It may be known that the width parameter will not increase more than 5 eV under any condition of operation or, similarly, that the position of a peak will not vary more than ± 5 eV. It would seem reasonable, then, to forbid the assignment of values that lie beyond these bounds. We shall see in the next section that such constraints are essential to permit unraveling severely overlapped peaks in the presence of counting noise.

Results

To test the proposed procedure a computer program was written that could *generate* an x-ray spectrum for any given element or combination of elements. All the germane physics of characteristic and continuous x-ray generation, emission, and detection are incorporated and the statistical effect due to counting can also be included. The last feature can be applied any number of times to produce a set of spectra differing only in their random error due to counting. For the tests reported in this paper a spectrum was generated that consisted of two peaks of 1000 counts amplitude each at the energies of S K α (2.307 keV) and Pb M α (2.346 keV) on a background of 500 counts in the channel corresponding to the energy of the S K α peak. The shape of the background was that from a thin film of PbS excited by 20keV electrons. The detector was assumed to have a resolution of 150 eV FWHM at Mn K α . For a given set of starting estimates and constraints the unraveling was performed on each of 500 such spectra to which the noise option had been applied. These spectra displayed extreme overlap and poor statistics and provided a severe test of the method. Since we know the constituent parts of the spectrum, before the application of statistical noise, we can obtain a good measure of random and systematic errors intrinsic to the algorithm. These errors provide a limit that can only increase when real spectra are processed. Table 1 summarizes the pertinent statistics of several of these 500 run sets where various combinations of starting parameters and constraints were employed.

In the first column are given the starting estimates for peak amplitudes. Peak position and width were started at the *true* values with the exception of the last two entries in the table. Constraints are given in eV centered about the starting estimate for the relevant parameter. A dash indicates that a parameter is not constrained. In the next four columns are given the means and standard deviations (in parentheses) for the set, of the effective FWHM (Mn), the energy of the first peak, and the two peak amplitudes unraveled. The effective FWHM (Mn) is calculated from the fitted width of the highest peak.

One can see from the table that by constraining the region over which the position parameter can vary, the spread of unraveled amplitudes about the true value can be reduced significantly. Constraining the width parameter produces some additional improvement. These results suggest that for a particular detector and a given set of experimental conditions, one might determine the maximum deviations of energy and width for known lines and use them as constraints in unraveling spectra from unknown specimens.

TABLE 1.--Summary of results from 18 500-run sets. Entries are explained in the text.

STARTING Amplitudes (counts)	UNRAVELED VALUES				
	Constraints ± w(ev), ± E(ev)	FWHM(Mn) (ev)	ENERGY SK α (ev)	AMPLITUDE PEAK 1 (counts)	AMPLITUDE PEAK 2 (counts)
1000, 1000	-- --	150.9 (1.8)	2306(0.8)	956 (369)	1020 (360)
1000, 1000	2 --	150.4 (1.3)	2307(0.6)	978 (314)	1004 (309)
1000, 1000	-- 2	149.7 (1.2)	2307 (0.6)	998 (95)	998 (94)
1000, 1000	2 2	149.7 (1.1)	2307 (0.2)	997 (96)	1000 (96)
1000, 1000	-- 1	149.7 (1.2)	2307 (0.1)	989 (58)	1009 (60)
1000, 1000	0.5 --	150.1 (0.5)	2308 (0.5)	1014 (257)	972 (256)
1000, 1000	-- 0.5	149.7 (1.3)	2307 (0.05)	994 (39)	1002 (39)
1000, 1000	0.5 0.5	149.9 (0.4)	2307 (0.04)	993 (38)	1004 (39)
1200, 700	-- --	150.8 (1.8)	2307 (0.8)	977 (369)	997 (363)
1200, 700	-- 2	149.8 (1.2)	2307 (0.2)	1000 (94)	993 (95)
1200, 700	2 2	150.5 (1.3)	2308 (0.2)	1042 (86)	955 (86)
1200, 700	-- 1	149.6 (1.2)	2307 (0.1)	996 (56)	1002 (56)
1200, 700	-- 0.5	149.7 (1.2)	2307 (0.04)	997 (38)	1000 (39)
1200, 700	0.5 0.5	149.8 (0.4)	2307 (0.04)	997 (39)	1002 (37)
5000, 300	-- 1	150.4 (2.4)	2308 (0.07)	1048 (91)	947 (95)
5000, 5000	-- 1	149.8 (1.4)	2308 (0.07)	1016 (53)	980 (52)
1200, 700*	-- 2	149.7 (1.2)	2308 (0.2)	1052 (97)	945 (97)
1200, 700**	-- --	151.1 (2.1)	2308 (0.8)	1045 (397)	926 (407)

*Starting energy of peak 1 = 2308.5eV and detector resolution = 155eV.

**Starting energy of peak 1 = 2312eV and detector resolution = 155 eV.

Once the unraveling is completed one might use the peak parameters determined to generate Gaussians that could be subtracted from the original spectrum. The resulting background spectrum can be used in several ways. For example, by examining the residuals in this background, one can determine if any peaks were unaccounted for. Furthermore, since the peaks are no longer present one can accurately determine the background under any given peak. This information can be used in *peak-to-local background* quantitative procedures. The algorithm as implemented is effective in removing spectral overlap in situations where the background cannot be modeled and/or the position and width of spectral peaks vary with experimental conditions.

References

1. R. L. Myklebust, C. E. Fiori, and K. F. J. Heinrich, "FRAME C: A compact procedure for quantitative energy-dispersive electron probe x-ray microanalysis." *Proc. 12th MAS Conf.*, 1977, 18.
2. P. J. Statham, "A comparative study of techniques for quantitative analysis of the x-ray spectra obtained with a Si(Li) detector," *X-ray Spect.* 5: 16-28, 1976.
3. D. G. W. Smith, C. M. Gold, and D. A. Tomlinson, "The atomic number dependence of the x-ray continuum intensity and the practical calculation of background in energy dispersive electron microprobe analysis," *X-ray Spect.* 4: 149-156, 1975.
4. R. H. Schamber, "A modification of the linear least-squares fitting method which provides continuum suppression," in T. Dzubay, Ed., *X-ray Fluorescence Analysis of Environmental Samples*, Ann Arbor Science Publications, Mich., 1977, 241-257.
5. H. Nullens, P. Van Espen, and F. Adams, "Linear and non-linear peak fitting in energy-dispersive x-ray fluorescence," *X-ray Spect.* 8: 104-109, 1979.
6. C. E. Fiori and R. L. Myklebust, "A Simplex method for fitting Gaussian profiles to x-ray spectra obtained with an energy dispersive detector," *Proc. ANS Topical Conf.* at Mayaguez, Puerto Rico, DOE Publication CONF 780421, 1978, 139-148.
7. C. E. Fiori and D. E. Newbury, "Artifacts in energy dispersive x-ray spectrometry in the scanning electron microscope II," *SEM/1980 II*, 251-258.

8. P. J. Statham, "Deconvolution and background subtraction by least-squares fitting with prefiltering of spectra," *Anal. Chem.* 49: 2149-2154, 1977.
9. J. A. Nelder and R. Mead, "A Simplex method for function minimization," *Comput. J.* 7: 308, 1965.
10. S. N. Deming and S. L. Morgan, "Simplex optimization of variables in analytical chemistry," *Anal. Chem.* 45: 379A, 1973.
11. C. E. Fiori, R. L. Myklebust, and K. E. Gorlen, "Sequential Simplex: A procedure for resolving spectral interference in energy dispersive x-ray spectrometry," in K. F. J. Heinrich, D. E. Newbury, R. L. Myklebust, and C. E. Fiori, Eds., *Energy Dispersive X-ray Spectrometry*, National Bureau of Standards Special Publication SP 604, 1981 233.

ON THE GEOMETRY OF THE ABSORPTION CORRECTION FOR ANALYTICAL ELECTRON MICROSCOPY

N. J. Zaluzec

The absorption correction in AEM-based x-ray microanalysis is by no means a new topic and has been considered by several authors.¹⁻⁴ In general, these derivations arrive at an equation of the form

$$\frac{C_i}{C_j} = \frac{\epsilon_j \kappa_j}{\epsilon_i \kappa_i} \cdot \frac{\delta_j}{\delta_i} \cdot \frac{I_i}{I_j} \quad (1)$$

where

$$\kappa_i = Q_i \omega_i f_i / A_i \quad (2)$$

and

$$\frac{\delta_j}{\delta_i} = \frac{(\mu/\rho)_{ij}^i}{(\mu/\rho)_{ij}^j} \cdot \frac{1 - \exp(-\chi_j \cdot \rho \cdot t)}{1 - \exp(-\chi_i \cdot \rho \cdot t)} \quad (3)$$

where C_i is the composition of element i , and I_i the measured characteristic intensity for that species. The terms ϵ_i , Q_i , ω_i , f_i and A_i are, respectively, the detector efficiency, ionization cross section, x-ray fluorescence yield, relative line intensity, and atomic weight; $(\mu/\rho)_{ij}^i$ is the corresponding mass absorption coefficient for the measured line of element i in the ij compound; ρ its density and t the specimen thickness measured along the incident beam direction; and χ_i is the product of $(\mu/\rho)_{ij}^i$ and a geometric correction term that relates the x-ray absorption pathlength to the depth of x-ray production within the specimen. In conventional bulk specimen microanalysis this geometric term is normally the cosec θ , where θ is the x-ray take-off angle. In an analytical electron microscope the geometry can be considerably different from that encountered in an SEM or an electron microprobe (EMP) and thus only in very specialized cases is the geometric correction factor equal to cosec θ . This paper reports on a generalization of an earlier formulation of the absorption geometry³ which can be employed for any x-ray detector/microscope combination; all other simplified models^{1,2,5} can be easily shown to be special cases of this formulation.

Owing to constraints on detector size and position imposed by the objective lens of an AEM the x-ray geometry, as mentioned previously, is generally not as simple as encountered in an SEM or EMP. In the majority of AEMs the x-ray detector axis lies in nearly the same plane as the specimen and as a consequence one must usually tilt the specimen stage by as much as 20-30° before characteristic x rays from the specimen may be reliably measured. In some of the newer AEMs the detector axis is noncoplanar with the specimen stage and thus reduces the overall tilt required; however, one still tilts the specimen to optimize experimental conditions. Thus, the general geometry found in an analytical electron microscope is as shown in Fig. 1, which illustrates a plane section through the specimen (which we may regard as a parallel slab of uniform thickness) containing the incident beam direction and the detector axis. The two angles θ_E and β specify the geometric relationship between absorption pathlength and depth of production. The detector elevation angle θ_E is defined relative to an imaginary plane perpendicular to the incident beam direction at the eucentric height of the specimen stage; β is the angle between the incident probe and the sample surface measured in the plane of the figure. From this diagram it is a straightforward procedure to show that the relationship between depth of production (t) and absorption pathlength d is

$$d = \frac{\sin \beta}{\cos(\beta - \theta_E)} \cdot t \quad (4)$$

from which one can immediately see that for the special case of normal incidence ($\beta = \pi/2$), Eq. (4) reduces to the conventional absorption geometry used previously,¹⁻² $d = \text{cosec } \theta \cdot t$.

The author is at the Materials Science Division of Argonne National Laboratory, Argonne, IL 60439, where this work was done with the support of the U. S. Department of Energy.

The angle of electron incidence β is a function of detector-specimen geometry as well as specimen tilt. In a previous derivation of Eq. (4) we showed one could easily obtain β by standard stereographic projection techniques.³ In this study this relationship has been formulated analytically which makes the correction a straightforward procedure, particularly when computer programs are used to perform iterative calculations.

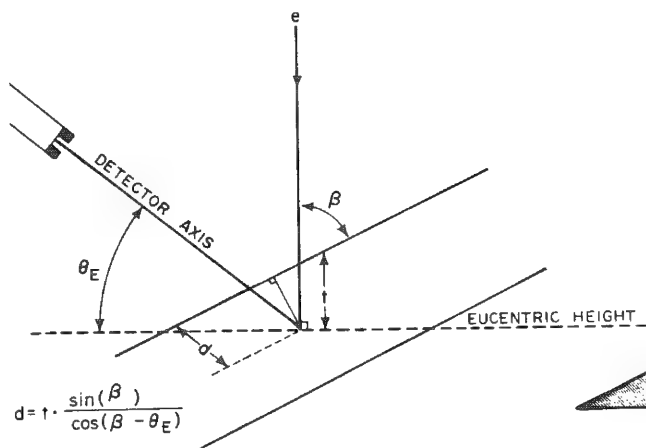


FIG. 1.--Pathlength/depth of production relationships used in x-ray absorption correction for parallel-slab specimen in AEM.

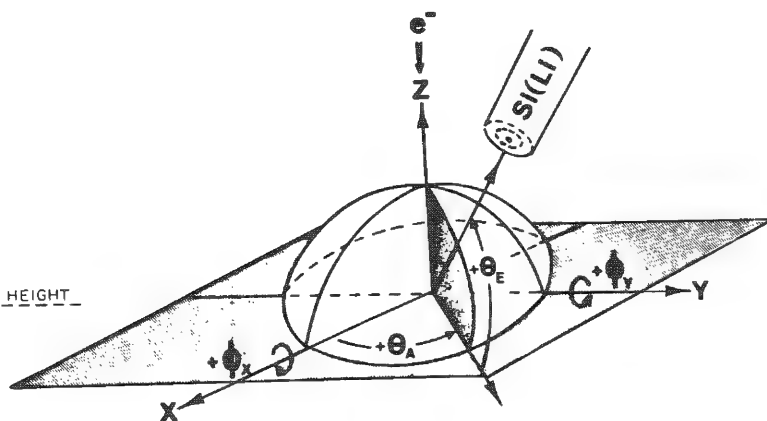


FIG. 2.--Definition of coordinate system used in absorption correction. Note positive directions of θ_A , θ_E , ϕ_x , and ϕ_y as indicated.

We proceed by first defining a Cartesian coordinate system within the microscope; the vectors defined by the two perpendicular specimen translate directions (x, y) and the electron-optical axis (z) form a convenient set. Relative to this coordinate system, one can next uniquely specify the position of the x-ray detector by two angles. The azimuthal angle θ_A is the rotation in the x - y plane about the z -axis of the detector plane (i.e., the plane defined by the z -axis and the centerline of the detector axis); and the elevation angle θ_E , as discussed previously, is the angle between the x - y plane and the detector axis (measured in the detector plane). In addition, we define the specimen tilt angles for the x and y axes respectively as ϕ_x and ϕ_y . These angles as well as the conventions chosen for the positive direction of tilt are shown schematically in Fig. 2. By performing appropriate coordinate transformations and noting that the desired angle of incidence β must be resolved in the detector plane (Fig. 1); one obtains the general result

$$\beta = \arccos \left(\frac{\sin \phi_y \cdot \cos \theta_A \cdot \cos \theta_E + \sin \phi_x \cdot \cos \phi_y \cdot \cos \theta_E \cdot \cos \theta_A}{\sqrt{a^2 + b^2 + c^2}} \right) \quad (5)$$

where

$$a = \cos \phi_x \cdot \cos \phi_y \cdot \cos \theta_A \cdot \cos \theta_E$$

$$b = \cos \phi_x \cdot \cos \phi_y \cdot \cos \theta_E \cdot \sin \theta_A$$

$$c = \sin \phi_y \cdot \cos \theta_A \cdot \cos \theta_E + \sin \phi_x \cdot \cos \phi_y \cdot \cos \theta_E \cdot \sin \theta_A$$

All terms have been defined previously. As a special note, since not all calculators or computer systems have an arc cos (x) algorithm, the relation

$$\arccos(x) = \frac{\pi}{2} - \arctan \left(\frac{x}{1 + x^2} \right) \quad (6)$$

is useful in computing β . We further note that the thin-film criterion as first proposed by Tixier and Philibert¹ now becomes:

$$x_i \cdot \rho \cdot t = \left(\frac{\mu}{\rho} \right)_{ij}^i \cdot \frac{\sin \beta}{\cos(\beta - \theta)} \cdot \rho \cdot t \leq 0.1 \quad (7)$$

In deriving the preceeding equations we assumed for simplicity that the specimen was a parallel slab of uniform thickness. In reality most specimens used in materials science investigations are tapered or wedge shaped. If the change in thickness with lateral distance across the specimen is well behaved, so that we can model specimen profile by a simple triangular wedge, then one can incorporate this into the equations just presented. Two cases will be considered next: the symmetric wedge and the half wedge (Figs. 3 and 4).

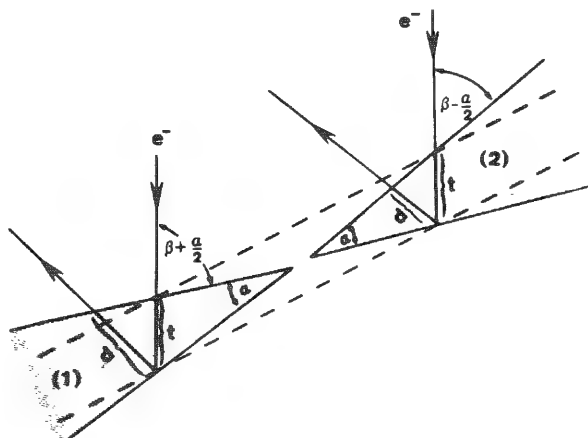


FIG. 3.--Cross section through symmetric-wedge specimen used in absorption correction, variants 1 and 2 as indicated. Dotted lines indicate equivalent parallel slab model of thickness t for comparison.

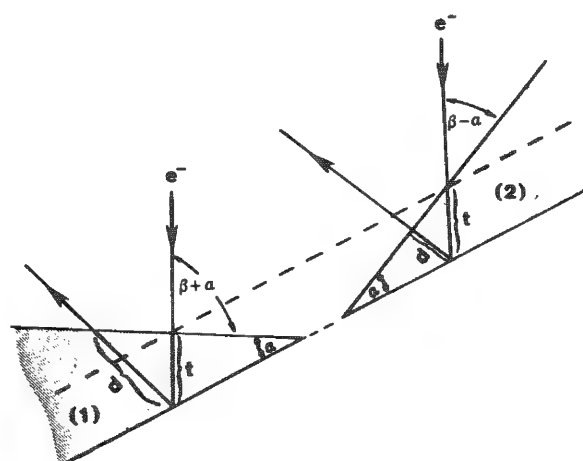


FIG. 4.--Cross section through half-wedge specimen, variants 1 and 2 as indicated. Dotted lines indicate equivalent parallel-slab model of thickness t for comparison.

The symmetric-wedge model serves as an approximation to the profile of a TEM specimen produced, for example, by electrochemical thinning of a disk from both sides simultaneously. In this model we define the wedge angle α as shown in Fig. 3 and note that two possible variants exist, depending on whether the wedge angle produces an effective increase or decrease in β corresponding to variants 1 and 2 of Fig. 3. The net effect of the wedge shape of the specimen, relative to the parallel slab model of Fig. 1, is either to add or to remove material from the absorption pathlength. It is a simple geometric construction to show that the modification to Eq. (4) needed to compensate for this effect is to replace β by $\beta^* = \beta \pm \alpha/2$. The term in $+\alpha/2$ corresponds to variant 1, where the wedge acts to increase the absorption pathlength, and $-\alpha/2$ corresponds to variant 2, where the wedge acts to decrease the absorption pathlength.

The second model, the half wedge, represents the specimen cross section that would be produced if the specimen were prepared by thinning only from one side. As in the case of the symmetric wedge we can again define 2 variants as shown in Fig. 4, positions 1 and 2; and obtain the result that β in Eq. (4) now needs to be replaced by $\beta^* = \beta \pm \alpha$. As previously, the $+\alpha$ term applies to variant 1, where the wedge acts to increase the pathlength; and the $-\alpha$ term, to variant 2, where the pathlength decreases. A third and trivial variation to this model may also be included at this point namely the inverted half wedge. In this configuration (the inversion of Fig. 4), one finds the "flat" surface facing the x-ray detector and it is simple to show that Eq. (4) requires no modification.

Two final comments remain, on beam broadening and homogeneity. First, for the simple parallel-slab model, one can show that beam broadening has no effect on changing the absorption pathlength; for a wedge-shaped specimen there is a change in the net absorption pathlength from one side of the probe center to the other, but for small values of α or t the effects to a first approximation cancel. Second, Eqs. (1) through (3) assume that over the excited volume and along the exiting absorption pathlength the specimen is homogeneous. If it is not, one must reformulate the equations 1-3 to take into account changes in $(\mu/\rho)_i$ through the respective phases. As this task is not trivial (because of the amount of information required about each volume element along the pathlength), it is fundamentally simpler to spend more time preparing suitably thin specimens that do not require an absorption correction.

References

1. R. Tixier and J. Philibert, in G. Möllenstedt, K. H. Gaukler, Eds., *Proc. 5th Int. Cong. X-ray Optics and Microanalysis*, Berlin: Springer, 1969, 180.
2. J. I. Goldstein, J. L. Costley, G. W. Lorimer, and S. J. B. Reed, *SEM/1977* I, 315.
3. N. J. Zaluzec, Ph.D. Thesis, University of Illinois, 1978, also published as ORNL TM-6705, copies available from NTIS, U. S. Department of Commerce, Springfield, VA 22161; also published in part in J. Hren, D. Joy, and J. Goldstein, Eds., *Introduction to Analytical Electron Microscopy*, New York: Plenum Press, 1979, chap. 4.
4. J. Bentley and E. A. Kenik, *Scripta Met.* 11: 261, 1977.
5. S. H. Moll, N. Baumgarten and W. Donnelly, in *Proc. of 8th Int. Conf. on X-ray Optics and Microanalysis*, 1977, 87.

PROPAGATION OF ERRORS IN QUANTITATIVE AEM MICROANALYSIS BY XEDS AND EELS

N. J. Zaluzec

Quantitative microanalysis in an analytical electron microscope (AEM) through the use of x-ray energy-dispersive spectroscopy (XEDS) or electron energy loss spectroscopy (EELS) is becoming increasingly important in material science. As a result it becomes correspondingly relevant to know the accuracy of the quantitative results obtained, which is ultimately governed by the errors associated with the experimental measurement. There are essentially three sources of error in obtaining a given quantitative result: (1) errors in the measurement of the intensity of the x-ray or electron energy loss event, (2) errors in the models used to convert the intensity measurement into a quantitative result, and (3) errors due to uncertainties of the various input parameters required by the respective models. In this text we shall address only the question of propagation of errors through the basic equations used during AEM-based thin-film analysis. A detailed discussion on the validity of the various models and the influence of errors due to input parameters used for these calculations is beyond the scope of this paper, and will be considered at a later date.

For the purposes of this work we shall consider quantitative microanalysis obtained through the use of equation of the form:

$$R_{ij} = \frac{C_i}{C_j} = \frac{\sigma_j}{\sigma_i} \cdot \frac{I_i}{I_j} \quad (1)$$

which is applicable to both XEDS and EELS analysis. In Eq. (1) C_i is the composition of element i in the specimen, I_i is the corresponding characteristic intensity measured during the analysis, R_{ij} is the composition ratio of the elements i and j , and σ_i is the "constant" of proportionality relating the composition of the i^{th} element in the specimen to the intensity of its given characteristic line or edge. For the case of "standardless" x-ray microanalysis, σ_i is in the thin film approximation given by¹

$$\sigma_i = \epsilon_i \frac{Q_i \omega_i f_i}{A_i} \quad (2)$$

and, when an absorption correction needs to be considered, by

$$\sigma_i = \epsilon_i \frac{Q_i \omega_i f_i}{A_i} \cdot \delta_i \quad (3)$$

$$\left\{ 1 - \exp \left[-(\mu/\rho)_{ij}^i \cdot \rho \cdot \frac{\sin \beta}{\cos(\beta - \theta_E)} \cdot t \right] \right\}$$

where

$$\delta_i = \frac{1}{(\mu/\rho)_{ij}^i}$$

In these equations Q_i , ω_i , and f_i are respectively the ionization-cross section, x-ray fluorescence yield, and relative line intensity of the measured x-ray line of element i ; A_i is that element's atomic weight and ϵ_i the respective detector efficiency for the x-ray in question; $(\mu/\rho)_{ij}^i$ is the appropriate mass absorption coefficient for x-rays of element i in the compound ij ; ρt is the respective mass thickness of the analyzed volume, and the term $\sin(\beta)/\cos(\beta - \theta_E)$ is a geometrical correction factor appropriate to AEM-based analysis and is discussed elsewhere in these proceedings.² Thin-film x-ray microanalysis can, in addition, be formulated in an alternate way such that the experimentalist employs thin standards^{3,4}; in that case σ_i is given by

The author is at the Materials Science Division of Argonne National Laboratory, Argonne, IL 60439, where this work was done with the support of the U. S. Department of Energy.

$$\sigma_i = \eta_i \rho_i t_i \quad (4)$$

where η_i , ρ_i , and t_i are now respectively the *absolute* electron flux, density, and specimen thickness. For the case of EELS microanalysis based on Eq. (1),

$$\sigma_i = \sigma_i(E_0, \Delta E, \alpha, \beta) \quad (5)$$

namely the partial ionization cross section for the appropriate shell of element i for incident electrons of energy E_0 , measured over the energy loss window ΔE , for electrons having been scattered through the angle α , at an incident beam divergence of β .^{5,7}

Since only the second of these three applications of Eq. (1) yields an absolute quantification, one additional expression is subsequently used to convert the R_{ij} values into individual concentrations: the assumption that

$$\sum_{n=1}^N C_n = 1 \quad (6)$$

Equation (6) is of major importance to the determination of the absolute accuracy of the respective composition values. Implicit in the use of this equation is the assumption that the experimentalist has, in fact, measured the intensity of at least one characteristic line or edge for every element in the specimen. If one or more elements is inadvertently omitted because its characteristic line was not within the detection range of the measured XEDS or EELS spectrum, then the composition values obtained by use of Eqs. (1) and (6) will contain a possibly large systematic error. Since this type of error can only be accounted for and corrected by the experimentalist, it will not be considered further in the remaining discussion; however, its effects should not be ignored by the investigator.

By conventional error propagation⁸ one can show that the relative error in the measured composition ratio R_{ij} is given by

$$\frac{\Delta R_{ij}}{R_{ij}} = \frac{\Delta \sigma_i}{\sigma_i} - \frac{\Delta \sigma_j}{\sigma_j} + \frac{\Delta I_i}{I_i} - \frac{\Delta I_j}{I_j} \quad (7)$$

from which one can see that the relative error in a given ratio R_{ij} depends not only on the error in the intensity measurement but also that associated with the value of σ_i . The use of Eq. (7) to determine the relative error in a specific composition ratio presumes that one knows the absolute magnitude and sign of all errors associated with each pair of elements i, j . Since in general we do not know all that, we are forced to assume that all errors add in quadrature to yield

$$\frac{\Delta R_{ij}}{R_{ij}} = \left[\left(\frac{\Delta \sigma_i}{\sigma_i} \right)^2 + \left(\frac{\Delta \sigma_j}{\sigma_j} \right)^2 + \left(\frac{\Delta I_i}{I_i} \right)^2 + \left(\frac{\Delta I_j}{I_j} \right)^2 \right]^{1/2} \quad (8)$$

The error in an intensity measurement may be obtained by reference to standard statistical arguments regarding counting experiments that follow Poisson statistics. Thus, the error in a given intensity measurement is given by $\Delta I_i / I_i = N_i^{-1/2}$, where N_i is the total number of counts over the region of interest. However, in both XEDS and EELS one must subtract a finite background intensity in order to obtain the actual intensity of the characteristic signal, and one can easily show that the corresponding error in I_i for this situation is given by:

$$\frac{\Delta I_i}{I_i} = \left[\frac{N_T + N_B}{(N_T - N_B)^2} \right]^{1/2} \quad (9)$$

Here N_T is the total number of counts of the measured data (signal and background) and N_B is the corresponding background intensity. In general, systematic errors in determining N_T are negligible, and similarly for N_B in XEDS analysis; however, for application to EELS care should be exercised in the evaluation of N_B , which one obtains by extrapolating a curve fitted to the background region prior to an edge and extrapolating the re-

sulting fit over an energy window ΔE beyond the edge onset.⁵ For thin specimens, where single scattering processes dominate, the systematic error in N_B by this approach should be small. However, in thicker specimens, where the effects of multiple inelastic scattering are appreciable, the extrapolated background may result in a large systematic error, since the functional dependence of the background intensity profile may no longer follow the parametrization of AE^{-R} as used frequently in quantitative analysis⁴ and thus result in a systematic error in N_B .

For the case of quantitative microanalysis that uses Eqs. (1) and (6) both, as would be typical of microanalysis by "standardless" XEDS or EELS approaches, we proceed by noting that from Eq. (6) the composition of the m^{th} element is given by

$$C_m = \frac{1}{\sum_{n=1}^N (C_n/C_m)} = \frac{1}{\sum_{n=1}^N R_{nm}} = \left(\sum_{n=1}^N R_{nm} \right)^{-1} \quad (10)$$

and the relative error in C_m is

$$\frac{\Delta C_m}{C_m} = \frac{1}{C_m} \left[\sum_{i=1}^N \left(\frac{\partial C_m}{\partial I_i} \right)^2 (\Delta I_i)^2 + \left(\frac{\partial C_m}{\partial \sigma_i} \right)^2 (\Delta \sigma_i)^2 \right]^{1/2} \quad (11)$$

where $\partial/\partial I_i$ is the usual notation for partial differentiation. Next, noting the following three relationships

$$\frac{\partial C_m}{\partial I_i} = -C_m^2 \cdot \frac{R_{im}}{I_i} \quad (12)$$

$$\frac{\partial C_m}{\partial \sigma_i} = C_m^2 \cdot \frac{R_{im}}{\sigma_i} \quad (13)$$

$$\frac{\partial}{\partial R_{im}} \left(\sum_{n=1}^N R_{nm} \right) = \delta_{in} \quad (14)$$

where δ_{in} is the conventional delta function, which is unity only when $i = n$. All these relations can be derived through chain rule differentiation of Eqs. 1 and 10. Substitution into Eq. (11) yields the result

$$\frac{\Delta C_m}{C_m} = C_m \cdot \left\{ \sum_{i=1}^N R_{im}^2 \cdot \left[\left(\frac{\Delta I_i}{I_i} \right)^2 + \left(\frac{\Delta \sigma_i}{\sigma_i} \right)^2 \right] \right\}^{1/2} \quad (15)$$

A direct consequence of this equation is that even under conditions where random errors are minimal ($\Delta I_i/I_i \rightarrow 0$), the relative error in a given composition measurement is still of the order of

$$\frac{\Delta C_m}{C_m} = C_m \cdot \left[\sum_{i=1}^N R_{im}^2 \left(\frac{\Delta \sigma_i}{\sigma_i} \right)^2 \right]^{1/2} \quad (16)$$

being controlled by the accuracy to which we know or can compute the various values of σ_i required for the analysis. Having determined a general expression for $\Delta C/C$ we shall next briefly address the question of estimation of the relative error in $\Delta \sigma/\sigma$ for the three applications of Eq. (1) outlined previously.

For the case of x-ray microanalysis by thin standards it is a straightforward exercise to show that

$$\frac{\Delta \sigma_i}{\sigma_i} = \left[\left(\frac{\Delta \rho}{\rho} \right)^2 + \left(\frac{\Delta \eta}{\eta} \right)^2 + \left(\frac{\Delta t}{t} \right)^2 \right]^{1/2} \quad (17)$$

and thus a 5% error in the measurement of *absolute* value of ρ , η , and t translates into about an 8% error in σ_i . The result is that the accuracy of quantitative analysis by this approach is governed by the degree to which we know or can measure ρ , η , and t , providing the composition of the standard is known to sufficient accuracy.⁹

To use Eq. (16) for standardless x-ray microanalysis we must evaluate the expression

$$\frac{\Delta\sigma}{\sigma} = \left[\left(\frac{\Delta Q}{Q} \right)^2 + \left(\frac{\Delta\omega}{\omega} \right)^2 + \left(\frac{\Delta f}{f} \right)^2 + \left(\frac{\Delta\epsilon}{\epsilon} \right)^2 + \left(\frac{\Delta\delta}{\delta} \right)^2 \right]^{1/2}$$

the details of which depend on the specific models used to calculate Q , ω , f , ϵ , and δ and will be considered in depth in a later paper. For the moment, an optimistic estimate of $\Delta\sigma/\sigma$ is of the order of 5% for $K\alpha$ line analysis and 10% for $L\alpha$ lines and is based on a comparison of experimental measurements of specimens of known composition.¹

Lastly, as in standardless x-ray analysis, the evaluation of $\Delta\sigma/\sigma$ for EELS studies depends on the specific model used to calculate the partial ionization cross section $\sigma(E_0, \Delta E, \alpha, \beta)$. A recent study by Joy et al. has placed an estimate on $\Delta\sigma/\sigma$ for K shell microanalysis at $\pm 20\%$ and in the absence of detailed studies provides the analyst with a starting point for error analysis in this situation.

In summary, a general expression has been derived that relates the relative error in a composition measurement to relative errors in the respective input parameters needed for quantitative XEDS and EELS microanalysis. Further work is in progress to determine the detailed dependence of errors in the input parameters used within the respective models for calculating σ_i for both XEDS and EELS.

References

1. N. J. Zaluzec, in J. Hren, D. Joy, and J. Goldstein, Eds., *Introduction to Analytical Electron Microscopy*, New York: Plenum Press, 1979, chap. 4.
2. N. J. Zaluzec, "On the geometry of the absorption correction in analytical electron microscopy," *Microbeam Analysis--1981*, 167.
3. N. J. Zaluzec, Ph.D. Thesis, University of Illinois, 1978; also published as ORNL TM#6705, copies available from NTIS, U. S. Dept. of Commerce, Springfield, VA 22161.
4. H. L. Fraser, *Micron* 11: 267-273, 1980.
5. R. R. Egerton, *SEM/1978* I, 133.
6. R. F. Egerton, to be published in Proc. of 39th EMSA Meeting, Atlanta, August 1981.
7. D. C. Joy, D. M. Maher, R. F. Egerton, *SEM/1979* II, 817.
8. H. H. Kui, *J. Res. NBS* 70C: 263, 1966.
9. H. L. Fraser and M. H. Loretto, *Analytical Electron Microscopy--1981* (in press).

SIMPLE CALCULATIONS OF X-RAY SPATIAL DISTRIBUTIONS APPLIED TO HIGH RESOLUTION MICROANALYSIS

R. T. Kerr, J. M. Titchmarsh, and E. D. Boyes

The effect of electron-beam spreading on the spatial resolution of x-ray microanalysis in thin foils in the TEM has attracted much attention in recent years. Accurate theoretical calculations of beam spreading have been attempted by Monte Carlo methods,¹⁻³ as well as simpler estimates made by rough approximations to the complex scattering processes, of which the most widely used method is that of Goldstein et al.⁴ Broad agreement between results derived by the two methods for homogeneous specimens is limited to a small range of foil thicknesses. Moreover, recent results by Hall and Vander Sande⁵ suggest that the x-ray spatial resolution is appreciably better than that predicted by the model of Goldstein et al. for the case of impurity (Fe) segregation in an MgO matrix. These experimental results have since been reproduced by Monte Carlo calculations⁶ that take into account the geometric factors involved.

These results clearly show the limitations of the simple model, but the Monte Carlo calculations are still relatively time consuming on a small laboratory computer. The precise form of the cross sections used and the assumed amorphous nature of the specimen also limit the absolute accuracy of the Monte Carlo calculations.

The purpose of this paper is to describe modifications to the simple model of Goldstein et al. to enhance the accuracy and to produce values for x-ray spatial distributions that are much closer to those derived from full Monte Carlo calculations. It is still assumed that all the electrons undergo a Rutherford scattering process somewhere within the foil, which is less satisfactory for foils much thinner than the mean free path.

Modifications to the Model of Goldstein et al.

Goldstein et al. assumed that all electrons in the beam were scattered at the center of the foil through an angle ϕ , whose distribution was derived from the Rutherford expression for Coulomb scattering. An expression was obtained to describe the extent of the beam spreading at the exit surface of the foil. This electron spreading has been generally equated to the spatial resolution attainable in x-ray microanalysis by many workers.

The model is extended in two ways. First, the probability for x-ray production (assumed to be constant along any trajectory) is calculated as a function of radial distance from the point of entry of the beam into the foil. This calculation takes into account the distribution of trajectories as a function of scattering angle. The distribution of x-ray production can be integrated to produce a value for the diameter within which 90% of the x rays are produced, which allows a direct comparison to be made with the electron spreading derived from the Goldstein et al. parameter. Second, the scattering of electrons is allowed to occur uniformly throughout the foil. The distributions, both of electrons on the exit surface and the production of x-rays within the foil, as a function of radius, are derived.

The effects arising from these modifications are described in the next section. Further improvements to the model, including a more accurate distribution of electron scattering and allowance for the initial spatial distribution in the electron beam, will be reported later.

Results

The values for the spatial resolution of x-ray production, defined as the diameter within which 90% of the x rays are produced, are given in Table 1 for aluminum and copper excited by 100kV electrons. Included for comparison are the values for spreading derived from the Goldstein et al.⁴ model and the Monte Carlo calculations of Newbury et al.¹

Authors Kerr and Boyes are at the Department of Metallurgy and Science of Materials at Oxford University, England OX1 3PH; author Titchmarsh is at the Metallurgy Division of the Atomic Energy Research Establishment at Harwell, England.

TABLE 1.--Comparison of estimates of x-ray spatial resolution (diam.--in nm--containing 90% of the distribution). A = value of Goldstein et al. parameter for electron spreading⁴; B = this work--x-ray distribution from simple Goldstein et al. model; C = Monte Carlo values for x-ray distribution¹; D = this work--x-ray distribution for distributed electron scattering.

		Foil thickness (nm)				
		10	50	100	300	500
Aluminum, 100 kV	A	0.26	2.9	8.1	42.2	90.9
	B	0.14	1.6	4.3	22.6	49.2
	C	0.41	3.0	7.6	30.0	66.4
	D	0.19	2.4	6.4	32.6	70.0
Copper, 100 kV	A	0.68	7.6	21.4	111.7	-
	B	0.36	4.1	11.8	64.0	-
	C	0.78	5.8	17.5	97.0	244.0
	D	0.51	6.4	17.6	90.4	197.6

It is apparent that the two modifications described in the previous section make it possible for values of x-ray spreading to be calculated that are much closer to those of the Monte Carlo method for all but the thinnest foils (10 nm). The divergence in the case of copper, $t = 500$ nm, is probably a consequence of the increased chance of multiple scattering as the atomic number and foil thickness increase. An empirical relationship of broadening d , with energy E and thickness t , $d \propto t^{1.5}/E$, can be derived from the results.

It is instructive to compare the radial distribution of electrons at the exit surface of the foil with that of x-ray production for the cases where (i) all electrons are scattered at the center of the foil (Figs. 1a and 1b) and (ii) the number of electrons scattered in each element of thickness is constant (Figs. 1c and 1d), for copper ($t = 100$ nm, $E = 100$ keV). From Fig. 1(a) and 1(b) it can be seen that the x-ray distribution is narrower than the corresponding electron distribution. There is zero electron intensity out to some specific radius, defined by the foil thickness and the lower limit of scattering angle assumed in the Rutherford scattering expression, because all electrons are scattered at the center of the foil through at least this minimum angle. However, the x-ray production is a maximum over this same range because x rays are produced continuously by all electrons. The incorporation of uniform scattering through the thickness drastically changes the form of the electron distribution on the exit surface (Fig. 1c) and also the corresponding x-ray distribution (Fig. 1d) which is significantly narrower than in Fig. 1b. The "knee" on the curve in Fig. 1c is a direct consequence of there being a minimum angle of scatter defined by the Rutherford formula.

It is relatively simple to extend the model to consider the experimental conditions used by Hall and Vander Sande,⁵ because the intergration over electron trajectories to determine the distribution of x rays is essentially the same as that used by Newbury et al.¹ and others in Monte Carlo calculations. Boundaries representing the limits of the slab of segregated impurity can be incorporated into the programme. The present results show that for a slab of iron 10 nm thick segregated in MgO, the full width for half maximum for x-ray production is about 9 nm for $t = 200$ nm and about 12 nm for $t = 300$ nm. These values are very similar to those measured by Hall and Vander Sande and those derived by Monte Carlo methods by Newbury and Myklebust.⁶ It is of interest to note that the modifications to the Goldstein model used here do not simplify the x-ray production probability to the uniform value within the cone of scattered electrons used by Newbury and Myklebust⁶ when they showed that the Goldstein model could not explain the Hall and Vander Sande results.

To summarize, we have developed a simple model, based on single, high-angle scattering, from which can be derived distributions of x-ray production. Over a wide range of conditions the results are significantly closer to those derived by Monte Carlo calculations than are the estimates made by the simple theory of Goldstein et al. A detailed description incorporating further modifications and results will be published soon.

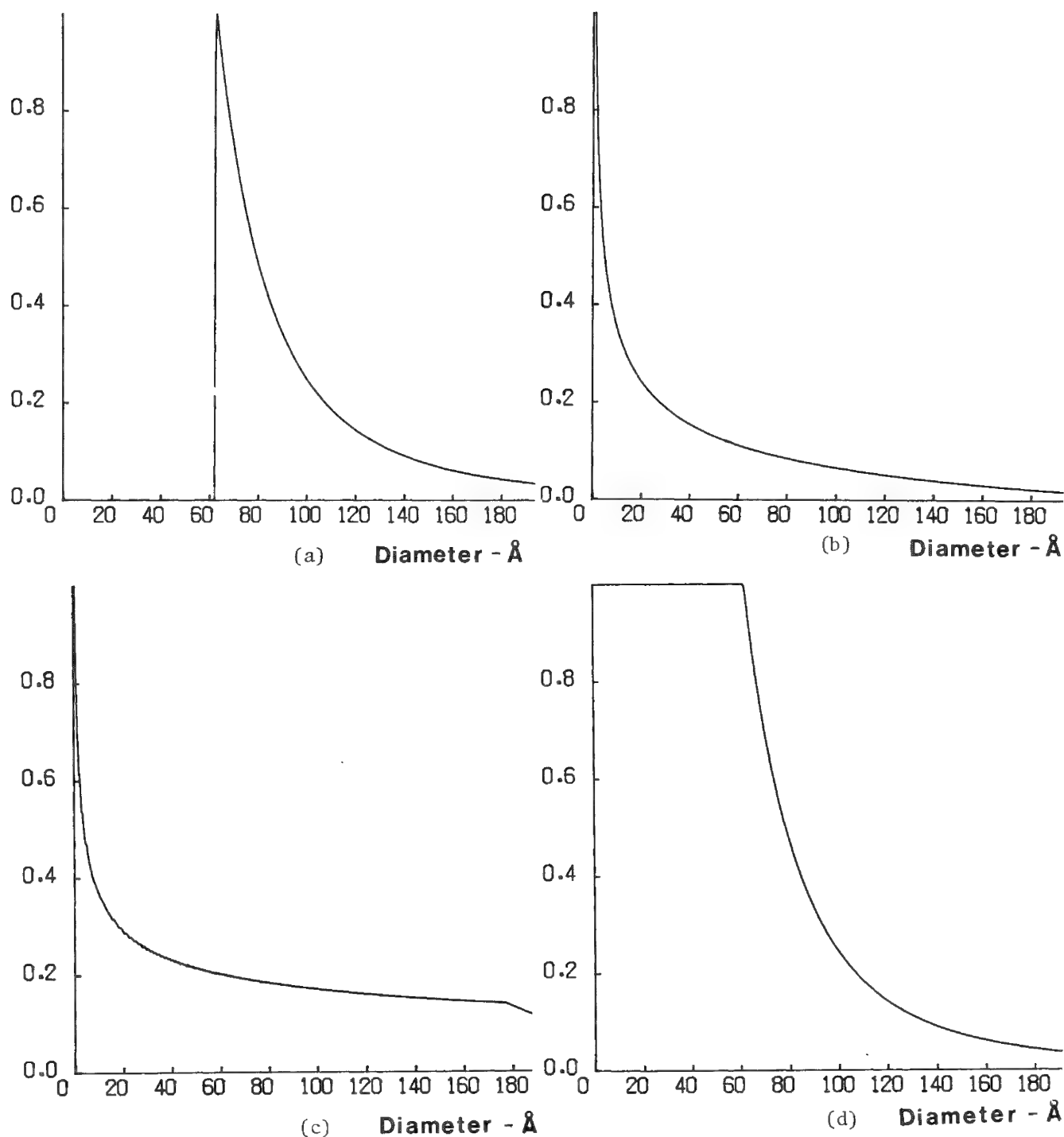


FIG. 1.--Radial distributions of electrons and x rays in copper foil 100nm thick, 100kV incident electrons: (a) electron distribution on exit surface when all electrons are scattered at center of foil; (b) distribution of x rays corresponding to (a); (c) as (a) but distributed electron scattering; (d) distribution of x rays corresponding to (c).

References

1. D. E. Newbury and R. L. Myklebust, *Ultramicroscopy* 3: 391, 1979.
2. R. H. Geiss and D. F. Kyser, *ibid.*, p. 397.
3. R. G. Faulkner, T. C. Hopkins, and K. Norrgard, *X-ray Spectrometry* 6: 73, 1977.
4. J. I. Goldstein, J. L. Costley, G. W. Lorimer, and S. J. B. Reed, *SEM/1977 I*, 315.
5. E. L. Hall and J. B. Vander Sande, *Proc. 37th Ann. EMSA Meeting*, 1979, 474.
6. D. E. Newbury and R. L. Myklebust, *Microbeam Analysis--1980*, 173.

DIRECT-IMAGING LASER MASS ANALYZER

B. K. Furman and C. A. Evans Jr.

The laser microprobe mass analyzer (LAMMA) provides elemental detection with high sensitivity for localized analysis.¹ This technique is based on the mass analysis of ions produced by the interaction of a UV pulsed laser beam with the surface of a sample. Previous studies with a highly focused beam and a time-of-flight spectrometer have shown the technique to be a valuable tool in microanalysis that produces complete mass spectra from a single point or pixel.

The CAMECA IMS-3f Ion Microscope is a unique mass spectrometer in that ions extracted from the surface of a sample maintain their spatial relationship throughout energy and mass filtering and so collect the ion image.² This mode not only provides superior transmission to the conventional ion microprobe, it also allows one to image simultaneously the distribution of an element over an entire 400 μm field of the surface of a sample with 1 μm lateral resolution.

The combination of a Nd:YAG laser and a CAMECA IMS-3f Ion Microanalyzer to provide a direct imaging laser mass analyzer (DILMA) has successfully produced the first ion images to result from photon irradiation of various materials. This paper presents data collected from conducting and nonconducting inorganic materials. In addition, spectra from an organic thin film are presented. Emphasis is on combining laser excitation with the imaging capabilities of the IMS-3f Ion Microanalyzer.

Experimental

Figure 1 shows a diagram of the instrumentation used in this experiment. The Nd:YAG laser was operated in the frequency-doubled mode to provide laser radiation at 530 nm. The laser beam was focused by a lens with a focal length of about 1 m to a spot about 1 mm in diameter. The beam was introduced into the CAMECA IMS-3f through a glass window and irradiated the sample surface at 45° incidence. This configuration allowed the laser beam to strike the sample surface in the same area as the conventional ion beam. Secondary ions produced by the laser were then extracted by an immersion lens in an identical manner as those produced by ion bombardment.

Both positive and negative secondary ions could be extracted. For imaging the laser was repeatedly pulsed at 10 pps. Spectra were obtained by repeatedly pulsing while scanning the magnet and moving the sample as described by Hersch et al., who called this technique repetitive laser desorption (RLD).³ In all cases the laser was operated in the desorption mode at lower power ($< 10^7$ W/cm²).

Results

Silicon coated with a thin layer of arginine and NaCl was examined by both ion and laser bombardment. The resulting Na⁺ images of an edge are shown in Fig. 2. The mass spectrum obtained in the RLD mode by means of laser desorption only is shown in Fig. 3. Molecular ion peaks of (M + H)⁺, (M + Na)⁺ and (M + K)⁺ are in excellent agreement with results previously reported with laser desorption.^{3,4} In contrast, spectra obtained by ion bombardment in a dynamic mode show no indication of arginine molecular ions and are saturated with silicon molecular ion peaks.

The authors, who are with Charles Evans & Associates, 1670 S. Amphlett Blvd., San Mateo, CA 94402, are grateful to A. F. Findeis for the initial suggestions that led to this research, to the San Francisco Laser Center (University of California at Berkeley and Stanford University) supported by the NSF Grant CHE-79-16250, and to R. J. Blattner for his continued harassment. The partial financial support of this research by CAMECA Instruments was greatly appreciated.

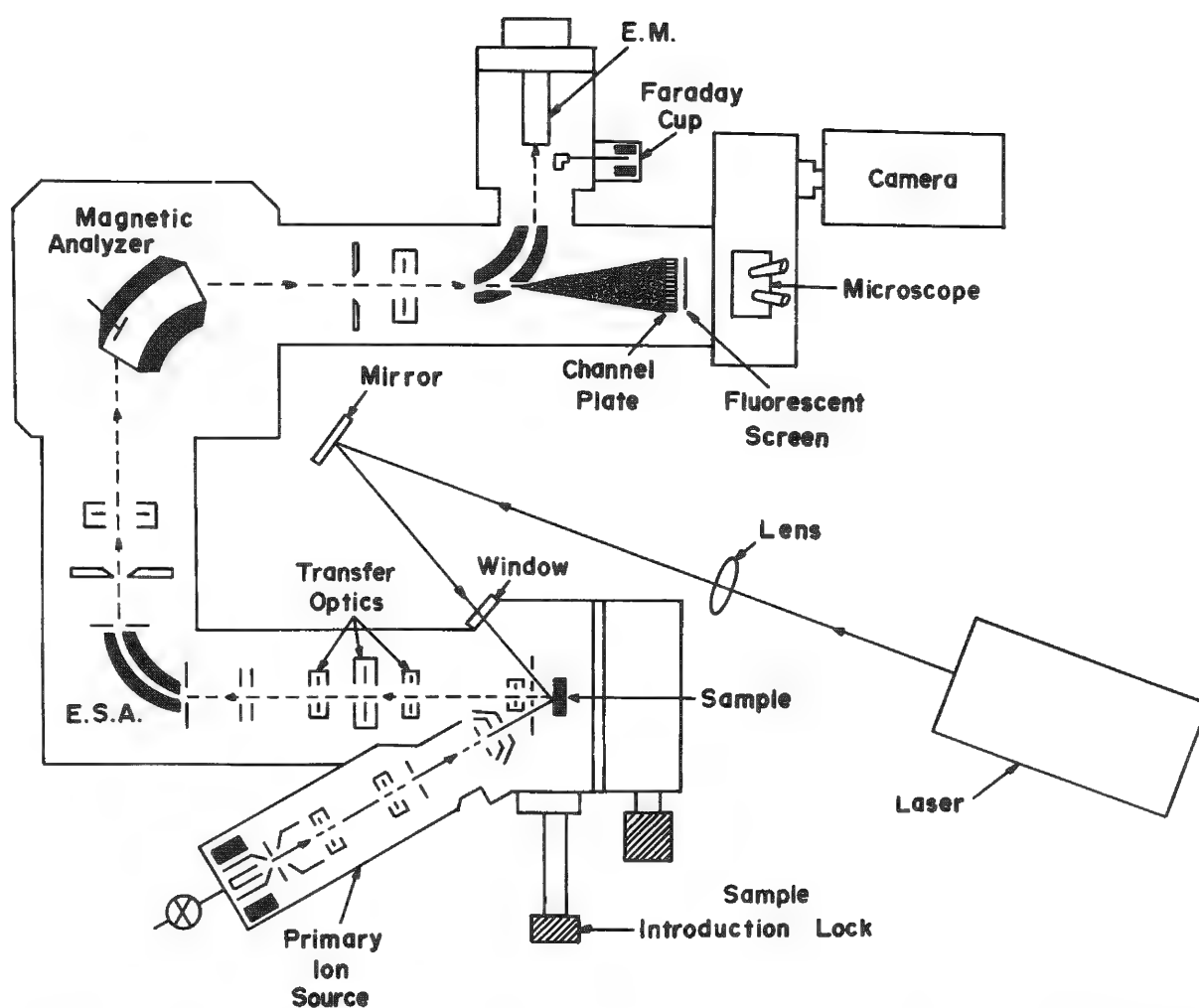


FIG. 1.--Schematic drawing of CAMECA IMS-3f Ion Microanalyzer with laser.

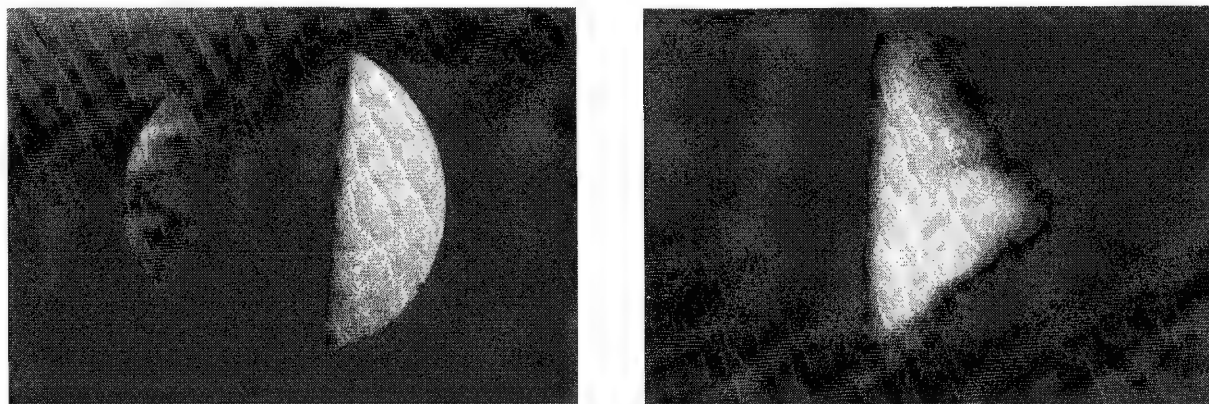


FIG. 2.--Ion image of Na⁺ distribution at edge of Si wafer obtained by (a) Cs⁺ primary ion bombardment, (b) laser radiation only. Imaged field 150 μ m.

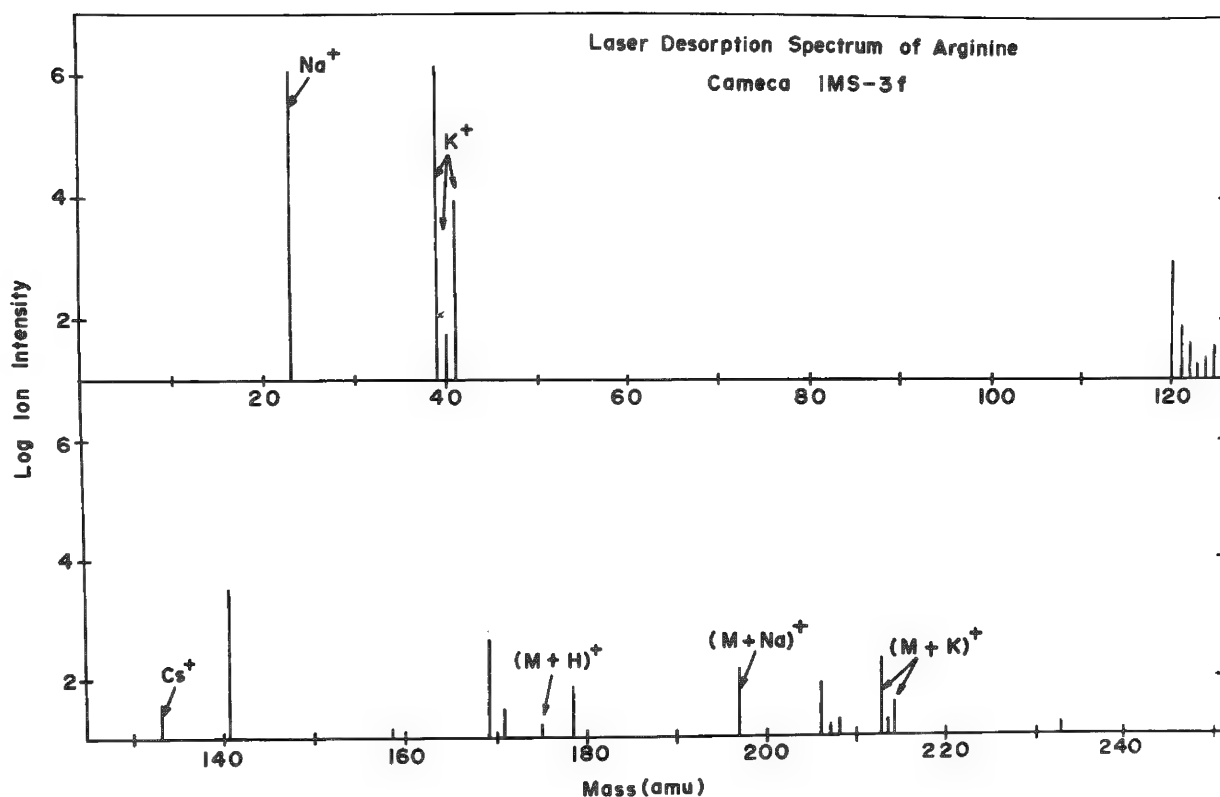


FIG. 3.--Mass spectrum of arginine thin film obtained by use of RLD mode of DILMA.

Figure 4 represents an image obtained by laser desorption of an NBS 661 glass sample. This image is characteristic of the contaminating Na, K, Rb, and Cs distribution on the surface of the sample. These elements are all of low ionization potential and are characteristic of a desorption process. The bright areas that represent high concentration are caused by small pits on the surface that provide an area for surface contamination to collect and be slowly removed by repetitive laser pulses.

Conclusions

The advantages of DILMA over conventional LAMMA systems or the ion microscope itself are numerous. The ability directly to image ions produced by laser desorption with $1\mu\text{m}$ resolution is by far the most important. Other areas of interest include: combined studies of ion and laser ionization, in-situ laser annealing of semiconductors while dopant distributions are monitored, analysis of insulating materials, and the development of laser depth profiling techniques.

References

1. F. Hillenkamp et al., *Appl. Phys.* 8: 341, 1975.
2. M. Lepareur, *Rev. Tech. Thomson-CSF* 12: 225, 1980.
3. F. Heresch, E. R., Schmid and J. F. K. Huber, *Anal. Chem.* 52: 1803, 1980.
4. M. A. Posthumus, P. G. Kistemaker,

and H. L. C. Meuzelaar, *Anal. Chem.* 50: 985, 1978.



FIG. 4.--Ion image of Rb distribution in NBS 661 glass obtained by laser desorption.

PROSPECTS FOR ROOM-TEMPERATURE SOLID-STATE X-RAY DETECTORS IN ELECTRON PROBE MICROANALYSIS

D. B. Wittry

In recent years, there has been considerable interest in room-temperature solid-state x-ray detectors that can be used as proportional counters. The principal efforts in this field have been based on two approaches: the use of semiconductor materials of wider energy band-gap than silicon (e.g., CdTe, HgI₂),¹ the use of silicon pin,²⁻⁴ and MIS diodes.⁵

The most promising results for room-temperature solid-state detectors with high energy band-gap have been reported for HgI₂ detectors.⁶ However, these detectors have their problems: the materials are not reproducible and HgI₂ has a vapor pressure so high that the detectors must be encapsulated if they are to be used in a vacuum.

In this paper, the prospects of an optimized silicon detector and preamplifier for use with a curved-crystal x-ray spectrometer are considered. In this application, the detector geometry must be matched to the exit slit of the spectrometer to yield the smallest possible detector capacitance, and the time constants of the amplifier must be optimized to minimize the noise. The fact that an optimum time constant exists for a given detector capacitance and leakage current can be seen from the following equation for the pulse height broadening due to noise:⁷

$$\Delta E_n = \Delta E_p + \frac{2.355\epsilon}{q} \frac{e}{\sqrt{2}} \left[\frac{qI_d}{2} \tau + kT R_s (C_d^2 + 2C_d C_0) \frac{1}{\tau} + A_f (C_d^2 + C_d C_0) \right]^{1/2} \quad (1)$$

where

- ΔE_n = full width at half maximum of the electronic noise line in eV
- ΔE_p = FWHM of the electronic noise of the preamplifier without the detector ($I_d = 0$, $C_d = 0$) in eV
- ϵ = mean energy required to create one electron-hole pair in the detector in eV
- q = electron charge in C
- e = 2.718 . . .
- I_d = leakage current of the detector in A
- τ = time constant of the equal integrating and differentiating network in s
- k = Boltzmann's constant
- T = absolute temperature in degrees K
- R_s = equivalent series resistance of the FET in Ω
- C_d = capacitance of the detector in F
- C_0 = capacitance of the gate-source of the FET and all stray capacitances expressed in F
- A_f = constant, typically 10^{-14} V^2

Typical values of the contribution of the three terms in brackets in Eq. (1) are plotted in Fig. 1 for conventional pin photodiodes and a typical charge-sensitive preamplifier. It is technologically feasible to develop a detector with 1/10 the capacitance of solid-state detectors commonly used in EDS. For example, an EDS detector⁸ with an area of 30 mm² and a thickness of 3 mm would have a capacitance of 1.08 pF if operated fully depleted. For a detector with geometry optimized to match the exit slit of a typical crystal spectrometer (0.01 × 2.5 cm) the capacitance would be 0.085 pF. However, the noise due to carrier generation and recombination increases with detector thickness; thus, for room temperature operation the detector should have the smallest thickness consistent with adequate detection efficiency.

Concerning the detector efficiency, it is important to note that in electron probe microanalysis with crystal spectrometers (WDS) wavelengths less than 1 Å are rarely used. The mass absorption coefficient for 1 Å x rays in silicon is approximately 18 cm²/g and the density of silicon is 2.42 g/cm³. Therefore a detector 1 mm thick would have an ef-

The author is with the Departments of Materials Science and of Electrical Engineering, University of Southern California, Los Angeles, CA 90007. The support of the Air Force Office of Scientific Research is gratefully acknowledged.

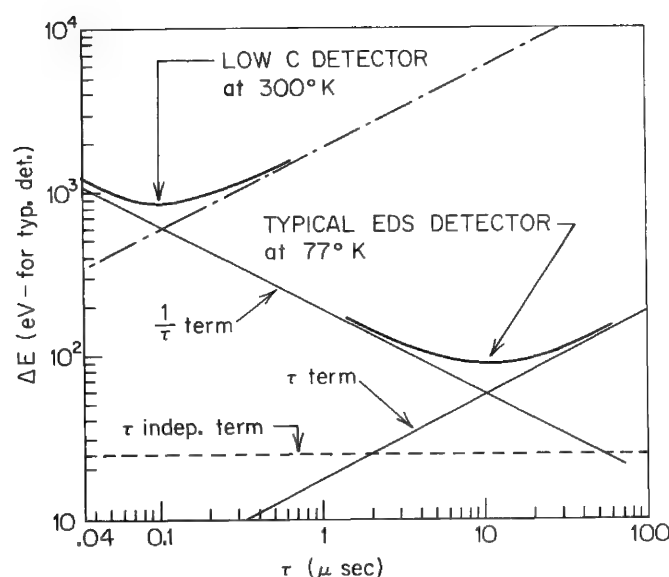


FIG. 1.--Limitations in resolution of EDS systems due to detector-preamplifier combination for typical EDS detector at 77°K compared with low-capacitance detector and preamp used at room temperature with short time constants; low-capacitance detector provides greater pulse heights so that $\Delta E/E$ at room temperature is not significantly different from values obtained at low temperature.

(b) a pin configuration with the i region compensated with a nonmobile impurity or (c) a MIS configuration.⁵ In any case, it is desirable to use material with high carrier lifetimes and a low dislocation density to avoid microplasma breakdown at the high fields necessary to get high collection efficiency and short collection time. Similar considerations indicate that potentially useful pn junction structures should be fabricated by ion implantation rather than by conventional diffusion processes.

For a fully depleted p^+nn^+ structure, the reverse saturation current density is given by

$$J = J_e + J_h + J_g \quad (2)$$

where J_e is the current density due to electron emission into the p^+ material at the ohmic contact, J_h is the current density due to hole emission into the n^+ material at the ohmic contact, and J_g is the saturation current due to thermal generation of carriers in the depleted region, given by⁵

$$J_g = qn_i w / \tau_i \quad (3)$$

where n_i is the intrinsic carrier concentration, w is the width of the depletion region, and τ_i is an effective lifetime parameter. With Richardson's equation used as a model for J_e and J_h it is found that the contribution of J_e and J_h can be small (about 1 pA) compared to the thermal generation term (about 6 nA). Thus it appears feasible to construct an optimized Si detector for proportional counting at room temperature with crystal spectrometers.

However, the feasibility of utilizing room-temperature silicon detectors in x-ray crystal spectrometers depends to a large degree on the developments in FET technology, just as the development of the liquid nitrogen-cooled Si(Li) detector systems has been limited by the availability of low-noise JFETs.⁹ The requirement of very low capacitance

efficiency of nearly 99%. The maximum transit time of carriers would be 2×10^{-8} s for an electric field of 10^4 V/cm. The 1mm-thick detector would have a capacitance of about 0.25 pF, which could be reduced to 0.125 pF if the active area is only 0.005 cm wide.

With a detector having only 1/10 of the capacitance of typical EDS detectors, the voltage produced during arrival of an x-ray pulse would be 10 times higher (if we neglect the input capacitance of the preamp). The increase in signal by a factor of ten makes it possible to have an increase in noise by a factor of ten without degrading the signal-to-background ratio.

As indicated in Eq. (1), the increase in noise due to higher leakage of the detector when used at room temperature necessitates the use of shorter time constants. A decrease in time constant from 10 to 0.1 μ s would permit an increase in detector leakage by a factor of 10^4 if the second term in brackets remains the same (Fig. 1). Actually the leakage current can be less than that shown in Fig. 1, which indicates an optimum value of τ between 0.1 and 1 μ s.

Several possibilities exist for obtaining low leakage current in room-temperature detectors. In addition to the use of guard rings, several different configurations can be used, for example: (a) a p^+nn^+ detector with high-resistivity ($> 3000 \Omega\text{-cm}$) n region,

of the detector and FET gate may require the use of a hybrid package or an integrated circuit in which the detector and preamp are fabricated on the same chip. With modern techniques of microfabrication, JFETS can be made with 1/10 the input capacitance of existing JFETS without sacrifice in the transconductance.

The use of solid-state room-temperature x-ray detectors with curved crystal x-ray spectrometers will be important in future instrumentation because of the following advantages over gas proportional counters:

- (1) "windowless" operation
- (2) reduced background due to higher order diffracted radiation, scattered radiation, and fluorescence radiation from the crystal by use of pulse-height selection with higher energy resolution
- (3) lower voltage operation
- (4) smaller size
- (5) smaller dead time and less pulse height shrinkage with counting rate
- (6) lower cost

References

1. R. C. Whited and M. M. Schieber, "Cadmium telluride and mercuric iodide gamma radiation detectors," *Nuclear Inst. and Meth.* 162: 113-123, 1979.
2. R. Nowotny and W. L. Reiter, "The use of silicon pin-photodiodes as a low-energy photonspectrometer," *Nuclear Inst. and Meth.* 147: 477-480, 1977.
3. R. Nowotny and W. L. Reiter, "A comparison of commercial pin-photodiodes for x-ray spectrometry," *Nuclear Inst. and Meth.* 153: 597-598, 1978.
4. S. Desi, "High resolution x-ray spectroscopy using silicon photodiodes," *Nuclear Inst. and Meth.* 164: 201-203, 1979.
5. A. A. Konova, "MIS-diode as a low-energy x- and γ -ray spectrometer," *Nuclear Inst. and Meth.* 160: 115-119, 1979.
6. M. Singh et al., "X-ray fluorescence analysis at room temperature with an energy dispersive mercuric iodide spectrometer, in J. R. Rhodes, Ed., *Advances in X-Ray Analysis*, New York: Plenum, 1980, vol. 23, p. 249.
7. A. J. Dabrowski and G. C. Huth, "Toward the energy resolution limit of mercuric iodide in room-temperature low energy x-ray spectrometry," *IEEE Trans.* NS-25: 205, 1978.
8. "What you should know about x-ray energy detectors," Kevex Corporation, Burlingame, CA 94010, 1977.
9. F. S. Goulding, "Some aspects of detectors and electronics for x-ray fluorescence analysis," *Nuclear Inst. and Meth.* 142: 213-223, 1977.

Recent Developments in Secondary Ion Mass Spectrometry: A Bibliography of SIMS, 1976-1980

Shaiw-Yih Yin

Introduction--by D.B. Wittry

The literature concerning secondary ion mass spectrometry seems to be growing at an exponential rate. After the publication of the last bibliography covering the years 1958-1975, it appeared that the next five years would provide approximately the same number of literature citations. Instead, it appears that this period has provided approximately twice the number of publications anticipated. However, during the past three years the number of publications per year seems to be approaching a constant value so that publications in this field may increase more linearly with time in the future.

The apparent exponential increase in publications concerning SIMS in the part of the past five years is undoubtedly due in part to a genuine increase in the number of SIMS instruments in use and a corresponding increase in the number of researchers involved in the use of SIMS. However there is also a tendency for each of the researchers using SIMS to publish several papers of a general or review nature emphasizing the advantages of this technique based on their own experience.

This bibliography, like the one previously published by S.Y. Yin¹ is an objective report of the literature published and does not attempt to make any distinction between major publications, i.e. extended journal articles and minor publications such as brief communications and conference proceedings. It will be apparent to the reader that there is considerable duplication of some of the work in the literature.

In this bibliography, there are also included a number of references to work that is not primarily concerned with SIMS as an analytical technique but have an important influence on the interpretation of SIMS results. Examples of these cases include references to sputtering phenomena, to topographical effects resulting from sputtering, and to instrumentation for mass spectrometry. Inclusion of these references is considered important because of the many complications that can occur in practical utilization of the SIMS technique and because of the impact of new developments in instrumentation for mass spectrometry on future developments in SIMS instrumentation.

Taking account of all these factors, it appears that the number of publications per year cited in this bibliography is not a valid criterion for assessing the interest in the SIMS technique. While the total number of publications appears to be growing at an exponential rate, the interest in the SIMS technique is probably growing at a rate that is approximately linear or perhaps quadratic with time.

In any case, it is clear that the SIMS technique has become a well-accepted technique for the micro-analysis of solids (in spite of the fact that problems still remain in quantitation of this method) and that it will become increasingly important in the future.

Reference

1. Yin, S.Y., "Eighteen Years of Secondary Ion Mass Spectrometry: A Bibliography of SIMS, 1958-1975", Microbeam Analysis, D.B. Wittry, Ed., (San Francisco, CA: San Francisco Press Inc. 1980) p. 289.

INDEX

Applications

Biology: (1976): 90; (1977): 11, 48, 49, 75, 78; (1978): 24, 56, 116, 161; (1979): 34, 69
(1980): 25, 33, 142, 148, 153, 239, 244, 252.

Geology: (1976): 138; (1977): 131, 162; (1978): 23, 27, 52, 127, 157, 183, 245; (1979): 126, 203, 224, 246; (1980): 114, 243.

Metallurgy: (1976): 1, 2, 3, 8, 12, 17, 19, 24, 26, 27, 35, 36, 49, 59, 62, 68, 76, 77, 79, 85, 91, 95, 101, 109, 113, 117, 118, 127, 128; (1977): 1, 4, 8, 12, 24, 31, 46, 52, 65, 73, 82, 83, 86, 89, 93, 101, 103, 107, 109, 110, 111, 112, 121, 122, 127, 139, 140, 141, 142, 147, 160, 161; (1978): 5, 7, 8, 10, 17, 20, 29, 30, 32, 34, 35, 37, 41, 62, 79, 80, 81, 99, 106, 108, 115, 134, 136, 141, 163, 171, 173, 179, 181, 187, 190, 191, 194, 208, 210, 239,

S.Y. Yin and D.B. Wittry are in the Materials Science Department at the University of Southern California, Los Angeles, CA 90007. The support of the National Science Foundation and the Air Force Office of Scientific Research in the preparation of this bibliography is gratefully acknowledged.

241; (1979): 5, 18, 21, 25, 27, 31, 39, 42, 43, 53, 54, 55, 57, 59, 67, 83, 86, 91, 96, 99, 113, 132, 155, 164, 166, 167, 179, 184, 189, 191, 205, 216, 221, 227, 230, 240, 241, 260, 262, 263; (1980): 12, 16, 45, 56, 69, 70, 93, 94, 103, 110, 134, 138, 144, 158, 159, 166, 170, 174, 175, 176, 198, 200, 206, 215, 232, 245, 280, 287.

Solid State Electronics: (1976): 11, 29, 32, 33, 40, 41, 53, 55, 60, 61, 63, 67, 72, 78, 83, 92, 93, 94, 96, 97, 99, 105, 123, 127, 133, 137; (1977): 2, 3, 25, 26, 27, 29, 30, 32, 34, 39, 54, 55, 56, 57, 61, 62, 63, 64, 77, 85, 97, 102, 108, 114, 116, 124, 138, 150, 152, 158; (1978): 1, 3, 9, 13, 25, 43, 67, 68, 71, 74, 91, 92, 104, 118, 119, 120, 121, 126, 131, 134, 142, 143, 144, 154, 158, 165, 167, 170, 191, 199, 200, 203, 205, 207, 211, 213, 214, 220, 223, 237; (1979): 28, 32, 35, 40, 58, 62, 63, 65, 66, 68, 72, 73, 75, 78, 84, 93, 94, 95, 101, 102, 103, 104, 109, 119, 120, 121, 122, 123, 131, 136, 137, 148, 149, 150, 151, 152, 153, 158, 161, 165, 168, 177, 178, 183, 190, 202, 207, 209, 215, 226, 232, 233, 239, 245, 247, 248, 258; (1980): 4, 5, 9, 11, 22, 35, 36, 38, 39, 40, 41, 49, 50, 52, 59, 62, 64, 66, 67, 71, 75, 79, 81, 82, 86, 87, 89, 90, 91, 95, 96, 99, 100, 102, 104, 106, 111, 116, 117, 118, 119, 120, 121, 122, 123, 128, 130, 131, 136, 139, 140, 141, 145, 147, 150, 156, 157, 160, 161, 162, 163, 165, 167, 168, 169, 181, 183, 185, 190, 194, 195, 246, 247, 251, 255, 260, 261, 267, 274, 275, 276, 284.

Miscellaneous: (1976): 9, 17, 31, 39, 43, 44, 45, 46, 48, 53, 59, 71, 74, 75, 81, 82, 84, 88, 100, 120, 124; (1977): 16, 22, 23, 38, 40, 44, 47, 53, 59, 66, 71, 76, 84, 95, 96, 98, 100, 105, 106, 120, 136, 146, 153, 154, 159; (1978): 11, 12, 14, 15, 18, 21, 33, 38, 48, 49, 73, 86, 87, 88, 89, 98, 110, 114, 135, 140, 145, 146, 147, 149, 156, 171, 192, 195, 201, 206, 208, 236, 244; (1979): 6, 20, 29, 41, 47, 48, 56, 60, 74, 79, 80, 97, 100, 108, 110, 128, 129, 130, 139, 140, 159, 163, 174, 180, 186, 228, 238, 244, 251; (1980): 13, 14, 18, 21, 24, 26, 47, 51, 53, 73, 74, 77, 92, 113, 137, 172, 191, 197, 199, 207, 208, 209, 214, 216, 231, 232, 234, 236, 238, 242, 249, 254, 271, 277.

Quantitative Analysis

Mechanisms, Models and Their Experimental Evaluation: (1976): 4, 18, 27, 30, 38, 75, 86, 102, 103, 110; (1977): 6, 17, 88, 96, 98, 99, 119; (1978): 16, 72, 107, 130, 151, 153, 160, 169, 186, 193, 196, 209, 217, 240; (1979): 23, 45, 77, 88, 111, 143, 144, 146, 169, 173, 175, 192, 219, 223, 235, 236, 242, 256; (1980): 5, 19, 109, 112, 180, 182, 188, 237, 241, 258, 272, 278, 282.

Empirical Methods of Quantitative Analysis: (1976): 58, 114, 117; (1977): 11, 50, 67, 75, 99, 113; (1978): 51, 65, 66, 178; (1979): 77, 116, 166, 177, 200, 225; (1980): 57, 90, 91, 92, 145, 146, 188, 243.

Specimen Charging Problems and Solutions: (1976): 125; (1977): 66, 150; (1979): 49, 109, 253; (1980): 187, 213, 288.

General Discussion of Quantitative Analysis and Its Problems: (1976): 28, 69, 81, 87, 112, 119; (1977): 19, 106, 120, 123, 129, 132, 157; (1978): 16, 31, 39, 54, 97, 124, 150, 155, 177, 178, 197, 229; (1979): 4, 44, 46, 170, 213, 249; (1980): 61, 97, 181, 184, 189, 253, 277.

Instrumentation

General Description of SIMS Instruments: (1976): 89; (1977): 21, 33, 35, 41, 117, 118, 130, 143, 156; (1978): 38, 47, 63, 85, 90, 94, 96, 104, 117, 125, 133, 176, 230, 233; (1979): 81, 87, 90, 125, 199, 234; (1980): 48, 68, 78, 83, 135, 143, 151, 177, 199, 218, 280.

Ion Optics of SIMS Instruments: (1977): 80, 128, 155; (1978): 122, 168, 185, 206; (1979): 142, 188, 197, 204, 229; (1980): 80, 171.

Mass Spectrometers for SIMS Instruments: (1976): 104, 135; (1977): 9, 28, 72; (1978): 85, 132, 182; (1979): 33, 106, 201, 210, 211, 212, 234; (1980): 6, 27, 28, 44, 46, 55, 80, 107, 108, 173, 262, 283.

Ion Sources for SIMS Instruments: (1976): 73; (1977): 79, 115, 133, 151; (1978): 76, 95, 102, 172, 184, 198, 224; (1979): 124, 144, 208, 214, 254; (1980): 2, 76, 129, 248.

Detectors for SIMS Instruments: (1977): 45, 67, 69; (1978): 28, 50, 103, 174, 179; (1979): 8, 145, 194, 259.

Computers Used for Data Analysis or Instrument Control: (1977): 28, 45, 87, 117; (1978): 53, 59, 60, 63; (1979): 64, 193, 203, 225; (1980): 34, 57, 72, 126, 152, 196.

Miscellaneous: (1976): 42, 52, 57, 70, 104, 106, 129; (1977): 46, 70, 104, 121, 150; (1978): 36, 61, 75, 175; (1979): 1, 185; (1980): 126, 277.

Sputtering Phenomena Important in SIMS:

Chemical and Matrix Effects on Ion Yields: (1976): 25, 122; (1977): 37, 50, 82, 83, 100, 139;
(1978): 6, 19, 44, 45, 65, 234, 238; (1979): 37; (1980): 17, 89, 91, 188, 201, 202,
224, 286, 288.

Effects of Reactive Gases on Sputtering Rates or on Ion Yields: (1976): 14, 42, 64, 118, 134;
(1977): 7, 14, 15, 37, 126, 137, 139; (1978): 6, 46, 84, 111, 223, 225, 226; (1979): 82,
181, 182, 196, 198, 251, 264; (1980): 42, 32, 134, 165, 179, 212, 214, 286.

Energy and Angular Distributions of Sputtered Ions: (1976): 5, 21, 107; (1977): 5, 10, 37, 42, 90;
(1978): 55, 109, 112, 128, 188, 189, 200, 215, 232, 245; (1979): 15, 37, 76, 92, 96, 145,
195, 196, 198, 218, 235, 261; (1980): 15, 88, 101, 132, 193, 236.

Computer Calculations of the Sputtering Process: (1977): 124, 125; (1978): 69, 70, 77, 78, 212,
235; (1979): 70, 71, 117, 118, 206; (1980): 61, 105.

Yields of Various Ion Species: (1976): 14, 24, 62, 66, 80, 109, 113; (1977): 69, 137; (1978): 54,
149, 150, 163, 173, 201; (1979): 13, 16, 98, 112, 139, 162, 176, 187, 216, 240, 243, 255,
258; (1980): 17, 48, 49, 90, 134, 164, 170, 201, 273.

Sputtering Mechanisms and Sputtering Effects: (1976): 4, 7, 13, 16, 20, 30, 38, 56, 65, 108, 126,
130, 131, 132; (1977): 7, 36, 58, 62, 68, 81; (1978): 19, 22, 26, 59, 78, 87, 93, 97,
105, 113, 164, 166, 202, 222, 228; (1979): 3, 17, 22, 24, 36, 50, 61, 89, 97, 105, 107,
127, 134, 135, 138, 141, 156, 157, 160, 207, 226, 230, 231, 244, 250, 252; (1980): 1, 3,
10, 15, 19, 30, 31, 37, 58, 60, 65, 98, 103, 115, 124, 127, 154, 155, 166, 174, 175, 192,
210, 211, 215, 217, 228, 229, 249, 250, 256, 257, 263, 269, 270, 273, 279.

Surface Topography of Sputtered Targets: (1976): 23, 34, 50, 51, 115, 118; (1977): 18, 20, 144,
145; (1978): 100, 221; (1979): 2, 7, 9, 10, 11, 12, 26, 30, 38, 51, 52, 114, 115, 133,
147, 154, 172, 237; (1980): 7, 8, 20, 29, 43, 54, 125, 149, 186, 220, 235, 259, 268.

SIMS Compared with or Used with Other Surface Analytical Techniques: (1976): 3, 6, 22, 40, 45, 47, 54,
57, 68, 77, 85, 98, 111, 121, 136; (1977): 13, 26, 32, 35, 44, 51, 74, 76, 84, 88, 89,
91, 92, 94, 104, 110, 114, 126, 130, 134, 135, 149; (1978): 2, 4, 5, 7, 20, 21, 35, 37,
40, 41, 48, 57, 62, 64, 74, 79, 80, 81, 82, 83, 86, 94, 99, 101, 108, 112, 129, 130, 135,
137, 140, 141, 146, 147, 148, 159, 165, 167, 171, 180, 181, 191, 192, 218, 227, 236, 243;
(1979): 21, 42, 48, 53, 54, 55, 67, 69, 84, 90, 93, 97, 99, 122, 123, 137, 158, 160, 164,
174, 179, 189, 205, 209, 213, 217, 222, 227, 260, 263; (1980): 13, 14, 23, 42, 51, 67,
68, 73, 83, 84, 85, 86, 87, 93, 102, 110, 113, 117, 118, 119, 121, 122, 123, 137, 139,
144, 158, 159, 212, 222, 223, 231, 232, 251, 279.

Review and General Papers: (1976): 10, 15, 37, 55, 89, 116; (1977): 43, 47, 60, 101, 148; (1978): 42,
57, 58, 123, 138, 139, 152, 162, 204, 216, 219, 231, 242; (1979): 14, 19, 41, 140, 143,
171, 220, 243, 247, 257; (1980): 32, 63, 178, 203, 204, 205, 209, 221, 226, 231, 242,
264, 265, 266.

1. Abd Rabbo, M.F., Richardson, J.A., and Wood, G.C., "A Study of the Effects of Inhibitive and Aggressive Ions on Oxide-Coated Aluminum Using Secondary Ion Mass Spectrometry", *Corros. Sci.*, **16**, 677 (1976).
2. Abd Rabbo, M. F., Richardson, J.A., and Wood, G.C., "A Study of Barrier Film Growth on Aluminum in Solutions of Film-Promoting and Aggressive Ions Using Secondary Ion Mass Spectrometry", *Corros. Sci.*, **16**, 689 (1976).
3. Andrews, J.M. and Morabito, J.M., "Detection of Al and Mg Contamination in Sputtered Pt Films by Auger Electron Spectroscopy and Secondary Ion Mass Spectrometry", *Thin Solid Films*, **37**, 357 (1976).
4. Antal, J., "On the Quantum Theory of the Emission of Secondary Ions", *Phys. Lett. A*, **55**, 493 (1976).
5. Arikawa, T., Narushima, K., and Inoue, M., "Energy Spectrum of Sputtered K⁺ Ions from KCl Crystals Bombarded with Energetic Rare Gas Ions", *Japan J. Appl. Phys.*, **15**, 1565 (1976).
6. Baun, W.L., "Experimental Methods to Determine Locus of Failure and Bond Failure Mechanism in Adhesive Joints and Coating-Substrate Combinations", *Adhesion Measurement of Thin Films, Thick Films and Bulk Coatings*, Philadelphia, PA USA, Nov. 1976. (Philadelphia, PA. USA: ASTM 1978) p. 41.
7. Bayly, A.R., Martin, P.J., and MacDonald, R.J., "Inelastic Collisions at Ion Bombarded Surface, I. Studies in Secondary Ion and Photon Excitation", *Nucl. Instrum. & Methods*, **132**, 459 (1976).
8. Benjamin, J.D., and Dearnaley, G., "Further Investigation of the Effects of Ion Implantation on the Thermal Oxidation of Titanium", *Inst. Phys. Conf. Ser.*, No. 28, 141 (1976).
9. Benninghoven, A., Jaspers, D., and Sichtermann, W., "Secondary-Ion Emission of Amino Acids", *Appl. Phys.*, **11**, 35 (1976).
10. Benninghoven, A., "Surface Analysis by Means of Ion Beams", *Crit. Rev. Solid State Sci.*, **6**, 291 (1976).
11. Berenz, J.J., Scilla, G.J., Wrick, V.L., Eastman, L.F., and Morrison, G.H., "Evaluation of 'Barrier' Metals for Sintered Platinum-GaAs Contacts", *J. Vac. Sci. & Technol.*, **13**, 1152 (1976).
12. Berner, A.I., Bokstein, B.S., Gubchenko, L.I., Sursaeva, V.G., and Shvindlerman, L.S., "Distribution of Aluminium for Very Dilute Solutions in Zinc Single Crystals", *Sov. Phys. Solid State*, **18**, 359 (1976).
13. Bernhardt, F., Oechsner, H., and Stumpe, E., "Energy Distributions of Neutral Atoms and Molecules Sputtered from Polycrystalline Silver", *Nucl. Instrum. & Methods*, **132**, 329 (1976).
14. Bernheim, M., and Slodzian, G., "Lattice Influence on Ion Emission Under Oxygen Bombardment", *Int. J. Mass Spectrom. & Ion Phys.*, **20**, 295 (1976).
15. Blaise, G., "Fundamental Aspects of Ion Microanalysis", *Material Characterization Using Ion Beams. Lectures presented at the NATO Advanced Study Institute on Material Characterization Using Ion Beams, Aleria, Corsica, 29 Aug. - 12 Sept. 1976.* (New York, USA: Plenum, 1978) p. 143.
16. Blaise, G., "Similarities in Photon and Ion Emissions Induced by Sputtering", *Surf. Sci.*, **60**, 65 (1976).
17. Blanchard, B., "Boron-Implanted Profiles in Diamond", *Appl. Phys. Lett.*, **28**, 7 (1976).
18. Brown, J.D., and Von Rosensteil, A.P., "Revised Calculation of Oxygen Concentration in the LTE Model", *Proc. 11th Nat. Conf. of the Microbeam Analysis Soc.*, Miami, Aug. 1976. Paper No. 40.
19. Brown, J.D., Gras, D.J., Von Rosensteil, A.P. and Kolster, B.H., "Sensitivity Effects in the Analysis of Ni-Cr-Fe Alloys by IMMA", *Proc. 11th Nat. Conf. of the Microbeam Analysis Society*, Miami, Aug. 1976. Paper No. 44.
20. Buger, P.A., Blum, F., and Schilling, J.H., "Comparison of Sputtering Processes Obtained during Analysis in a Glow Discharge Lamp and in an Ion Microprobe", *Electron Microscopy Soc. So. Africa 15th Ann. Conf.*, Johannesburg, So. Africa, Dec. 1976. (Johannesburg, So. Africa: Electron Microscopy Soc. South Africa, 1976) p. 97.
21. Bukhanov, V.M., Motavakh, Kh. A., and Yurasove, V.E., "Angular Dependence of the Emission of Secondary Ions Along Close-Packed Directions", *Sov. Phys. Solid State*, **18**, 1025 (1976).
22. Canali, C., and Prudenziati, M., "Microanalysis Techniques of Thin Film Surface Layers", *Alta Freq.*, **45**, 266 (1976).
23. Carter, G., "The Influence of Surface Diffusion on Topography Development of an Amorphous Solid during Sputtering", *J. Mat. Sci.*, **11**, 1091 (1976).
24. Cherepin, V.T., and Vasil'ev, M.A., "Secondary Ion-Ion Emission of Metals and Alloys", *Met. Sci. & Heat Treat*, **18**, 560 (1976).
25. Cherepin, V.T., Kosyachkov, A.A., and Vasilyov, M.A., "Effect of Initial Ion Bombardment and Oxidation on Emission of Secondary Ions", *Surf. Sci.*, **58**, 609 (1976).
26. Christie, W.H., Smith, D.H., and Inouye, H., "Ion Microprobe Study of the Tensile Failure of a Pt-Rh-W Alloy", *J. Radioanal. Chem.*, **32**, 85 (1976).
27. Cini, M., "A New Theory of SIMS at Metal Surfaces", *Surf. Sci.*, **54**, 71 (1976).
28. Coburn, J.W., "Sputtering in the Surface Analysis of Solids: A Discussion of Some Problems", *J. Vac. Sci. & Technol.*, **13**, 1037 (1976).
29. Colby, J.W., and Katz, L.E., "Boron Segregation at Si-SiO₂ Interface as a Function of Temperature and Orientation", *J. Electrochem. Soc.*, **123**, 409 (1976).
30. Coles, J.N., "Surface Ionization-'Plasma' in Disguise", *Surf. Sci.*, **55**, 721 (1976).
31. Colligon, J.S., and Fuller, D., "Secondary Ion Emission Studies of the Range Profiles of Implanted Ions", *Rad. Eff.*, **28**, 183 (1976).
32. Comas, J., and Plew, L., "Beryllium and Sulfur Ion-Implanted Profiles in GaAs", *J. Electron Mat.*, **5**, 209 (1976).
33. Croset, M., and Dieumegard, D., "Quantitative Secondary Ion Mass Spectrometry Analysis of Oxygen Isotopes and Other Light Elements in Silicon Oxide Films", *Corros. Sci.*, **16**, 703 (1976).

- Soc. 1976) p. 476.
100. Reed, S.J.B., Long, J.V.P., Coles, J.N., and Astill, D.M., "Ion Microprobe Trace Element Analysis with High Mass Resolution", *Int. J. Mass Spectrom. & Ion Phys.*, 22, 333 (1976).
 101. Rodriguez-Murcia, H., and Beske, H.E., "Investigations on the Cu-Ni and Cu-Al Systems with Secondary Ion Mass Spectrometry (SIMS)", Report JUL-1292, Kernforschungsanlage, Julich, Germany (April, 1976), 92 pp.
 102. Rudenauer, F.G., and Steiger, W., "Quantitative Evaluation of SIMS-Spectra Using Saha-Eggert Type Equations", *Vacuum*, 26, 537 (1976).
 103. Rudenauer, F.G., Steiger, W., and Werner, H.W., "On the Use of the SAHA-EGGERT Equation for Quantitative SIMS Analysis Using Argon Primary Ions", *Surf. Sci.*, 54, 553 (1976).
 104. Satake, T., Narusawa, T., Tsukakoshi, O., and Komiya, S., "A Simple Ion Energy Analyser Equipped with a Quadrupole Mass Spectrometer", *Japan J. Appl. Phys.*, 15, 1359 (1976).
 105. Schilling, J.H., and Buger, P.A., "Surface Contaminations on InSb Investigated with an Ion Microprobe Mass Analyser", *Electron Microscopy Soc. So. Africa 15th Ann. Conf.*, Johannesburg, South Africa, Dec. 1976. (Johannesburg, So. Africa: Electron Microscopy Soc. South Africa, 1976) p. 95.
 106. Schoberi, E., and Prager, L., "Rasterkonvertierungsgerat mit Analogspeicher", *Nucl. Instrum. & Methods*, 135, 379 (1976).
 107. Schootbrugge, G.A.v.d., de Wit, A.G.J., and Fluit, J.M., "Secondary Ion Emission from Polycrystalline Molybdenum, Energy and Angular Distribution", *Nucl. Instrum. & Methods*, 132, 321 (1976).
 108. Schulz, F., and Wittmaack, K., "Model Calculation of Ion Collection in the Presence of Sputtering", *Rad. Eff.*, 29, 31 (1976).
 109. Shepard, A., Hewitt, R.W., Slusser, G.J., Baitinger, W.E., Cooks, R.G., Winograd, N., Delgass, W.N., Varon, A., and Devant, G., "Detection of High Mass Cluster Ions Sputtered from Bi Surfaces", *Chem. Phys. Lett.*, 44, 371 (1976).
 110. Simons, D.S., Baker, J.E., and Evans, C.A., Jr., "Evaluation of the Local Thermal Equilibrium Model for Quantitative Secondary Ion Mass Spectrometric Analysis", *Anal. Chem.*, 48, 1342 (1976).
 111. Smith, D.P., "Surface Analysis by ISS and SIMS", *Proc. 14th Ann. Reliability Physics. Las Vegas, Nev., USA, April, 1976.* (New York, USA: IEEE 1976) p. 295.
 112. Someno, M., Saito, H., and Kobayashi, M., "Some Fundamental Factors in Quantitative Analysis by Ion Microanalyzer", *Mass Spectrosc.*, 24, 173 (1976).
 113. Steele, I.M., Solberg, T.N., Smith, J.V., Hutcheon, I.D., and Clayton, R.N., "Secondary Ion Yields of Metals and Oxides of Ti Through Zn", *Proc. 11th Nat. Conf. Microbeam Analysis Society, Miami Beach, Florida, Aug. 1976.* Paper No. 41.
 114. Tamura, H., Ishitani, T., Kanomata, I., Suzuki, K., and Shibata, A., "Correction of Secondary Ion Intensity by the Total Ion Monitoring Method", *J. Vac. Soc. Japan*, 19, 280 (1976).
 115. Tanovic, L., and Perovic, B., "The Surface Microtopography Induced by Ion Bombardment on Cu Single Crystals", *Nucl. Instrum. & Methods*, 132, 393 (1976).
 116. Townsend, P.D., Kelly, J.C., and Hartley, N.E.W., "Ion Implantation Sputtering and Their Applications", (London, England: Academic Press, 1976).
 117. Tsunoyama, K., Ohashi, Y., and Suzuki, T., "Quantitative Analysis of Low Alloy Steels with the Ion Microprobe Mass Analyzer", *Anal. Chem.*, 48, 832 (1976).
 118. Tsunoyama, K., Suzuki, T., and Ohashi, Y., "Sputtering of Iron with Ion Beams of O_2^+ , N_2^+ and Ar^+ ", *Japan J. Appl. Phys.*, 15, 349 (1976).
 119. Tsunoyama, K., Suzuki, T., and Ohashi, Y., "Some Aspects of the Quantitative Interpretation of Sputtered Ion Mass Spectra", *Japan J. Appl. Phys.*, 15, 513 (1976).
 120. Vancea, I., "The Analysis of Solid Surfaces by Secondary Ion Mass Spectrometry", *Stud. & Cercet. Fiz.*, 28, 921 (1976).
 121. Vasile, M.J., and Malm, D.J., "Simultaneous Ion Scattering and Secondary Ion Mass Spectrometry", *Int. J. Mass Spectrom. & Ion Phys.*, 21, 145 (1976).
 122. Vasil'ev, M.A., Chenakin, S.P., and Cherepin, V.T., "Peculiarities of Secondary Ion-Ion Emission from the Interface Between Unlike Metals", *Bull. Acad. Sci. USSR, Phys. Ser.*, 40, 106 (1976).
 123. Wang, K.L. and Storms, H.A., "A Study of Germanium/SiO₂ MIS Structures by the use of Secondary Ion Mass Spectrometry", *J. Appl. Phys.*, 47, 2539 (1976).
 124. Werner, H.W., "Analysis of Implanted Layers by Means of Secondary Ion Mass Spectrometry (SIMS)", *Acta Electronica*, 19, 53 (1976).
 125. Werner, H.W., and Morgan, A.E., "Charging of Insulators by Ion Bombardment and Its Minimization for Secondary Ion Mass Spectrometry (SIMS) Measurements", *J. Appl. Phys.*, 47, 1232 (1976).
 126. Werner, H.W., and Warmoltz, N., "The Influence of Selective Sputtering on Surface Composition", *Surf. Sci.*, 57, 706 (1976).
 127. Whatley, T.A., and Firalick, R.D., "Thin Film Studies with the QMAS: Metallurgical and Electronic Applications", *Proc. 11th Nat. Conf. Microbeam Analysis Society, Miami Beach, Florida, Aug. 1976.* Paper No. 48.
 128. Williams, P., Evans, C.A., Jr., Grossbeck, M.L., and Birnbaum, H.K., "Ion Microprobe Analysis for Niobium Hydride in Hydrogen-Embrittled Niobium", *Anal. Chem.*, 48, 964 (1976).
 129. Williams, P., and Evans, C.A., Jr., "A Simple Electronic Aperture for Rastered-Beam Depth Profiles", *Int. J. Mass Spectrom. & Ion Phys.*, 22, 327 (1976).
 130. Williams, M.M.R., "The Energy Spectrum of Sputtered Atoms", *Philos. Mag.*, 34, 669 (1976).
 131. Winters, H.F., "Physical Sputtering: A Discussion of Experimental and Theory", *Radiation Effects on Solid Surfaces*, M. Kaminsky, Ed., (Washington, D.C.: American Chemical Society, 1976) p. 1.
 132. Witcomb, M.J., "The Angular Dependence of the Sputter Yield Maxima", *Rad. Eff.*, 27, 223 (1976).
 133. Wittmaack, K., "High-Sensitivity Depth Profiling of Arsenic and Phosphorus in Silicon by Means of SIMS", *Appl. Phys. Lett.*, 29, 552 (1976).

134. Wittmaack, K., "Current Density Effects in Secondary Ion Emission Studies", Nucl. Instrum. & Methods, 132, 381 (1976).
135. Wittmaack, K., "Successful Operation of a Scanning Ion Microscope with Quadrupole Mass Filter", Rev. Sci. Instrum., 47, 157 (1976).
136. Wittry, D.B., "Present and Future Possibilities for Local Chemical Analysis of Solids Based on Physical Techniques", Proc. 11th Nat. Conf. Microbeam Analysis Society, Miami Beach, Florida, Aug. 1976. Paper No. 20.
137. Yamaguchi, M., and Hirayama, T., "Surface Contamination of Silicon Produced by Ion Implantation", Japan J. Appl. Phys., 15, 365 (1976).
138. Zinner, E., Walker, R.M., Chavmont, J., and Dran, J. C., "Ion Probe Analysis of Artificially Implanted Ions in Terrestrial Samples and Surface Enhanced Ions in Lunar Sample 76215,77", Proc. of the 7th Lunar Science Conf., Houston, Texas, March 1976, Compiled by The Lunar Science Institute, (New York: Pergamon Press Inc., 1976) p. 953.

1977

1. Abd Rabbo, M.F., Richardson, J.A., and Wood, G.C., "Detection of Hydrogen Profiles Through Anodic Films on Aluminium by Secondary Ion Mass Spectrometry", Electrochim. Acta, 22, 1375 (1977).
2. Aleksenko, A.E., Vavilov, V.S., Deryagin, B.V., Gukasyan, M.A., Karatygina, T.A., Konorova, E.A., Sergienko, V.F., Spitsyn, B.V., and Tkachenko, S.D., "Charge Transfer and the Nature of the Acceptor in Semiconducting Epitaxial Diamond Layers", Sov. Phys. Dokl., 22, 166 (1977).
3. Andrews, J.E., Duhamel, A.P., and Littlejohn, M.A., "Qualitative Analysis of Thin Gallium Nitride Films with Secondary Ion Mass Spectrometry", Anal. Chem., 49, 1536 (1977).
4. Arita, M., and Someno, M., "Preferential Sputtering on Binary Alloys by SIMS", Proc. of the 7th Int. Vac. Congr. and 3rd Int. Conf. on Solid Surfaces, Sept. 1977, R. Dobrozemsky, F. Rudenauer, F.P. Viehbock and A. Breth Ed., (Vienna, Austria: 7th Int. Vac. Congr.) p. 2511.
5. Avakov, A.S., Veksler, V.I., and Tsipinyuk, B.A., "Angular Dependences of the Energy Spectra of Sputtered Ions", Sov. Phys. Solid State, 19, 1825 (1977).
6. Ayukhanov, A. Kh., and Turmashev, E., "Negative Ionization in Sputtering", Sov. Phys. Tech. Phys., 22, 708 (1977).
7. Ayukhanov, A. Kh., and Turmashev, E., "Negative-Ion Emission in Electron-Stimulated Desorption", Sov. Phys. Tech. Phys., 22, 1289 (1977).
8. Barber, M., Vickerman, J.C., and Wolstenholme, J., "The Application of SIMS to the Study of CO Adsorption on Polycrystalline Metal Surfaces", Surf. Sci., 68, 130 (1977).
9. Bayly, A.R., and MacDonald, R.J., "A Mass and Energy Spectrometer for Secondary Ion Analysis", J. Phys. E, 10, 79 (1977).
10. Bayly, A.R., and MacDonald, R.J., "The Energy Spectra of Secondary Ions Emitted During Ion Bombardment", Rad. Eff., 34, 169 (1977).
11. Bellhorn, M.B., and File, D.M., "Empirical Standards for Quantitative Analysis of Biological Tissues by Secondary Ion Mass Spectrometry", Proc. 8th Int. Conf. on X-Ray Optics and Microanalysis, Boston, Mass., Aug. 1977. Paper No. 137.
12. Benninghoven, A., Muller, K.H., Plog, C., Schemmer, M., and Steffens, P., "SIMS, EID and Flash-Filament Investigation of O₂, H₂, (O₂ + H₂) and H₂O Interaction with Vanadium", Surf. Sci., 63, 403 (1977).
13. Benninghoven, A., Bispinck, H., Ganschow, O., and Wiedmann, L., "Quasisimultaneous SIMS-AES-XPS Investigation of the Oxidation of Ti in the Monolayer Range", Appl. Phys. Lett., 31, 341 (1977).
14. Bernheim, M., and Slodzian, G., "Caesium Flooding on Metal Surfaces and Sputtered Negative Ion Yields", J. Phys. Lett., 38, L325 (1977).
15. Bernheim, M., and Slodzian, G., "Secondary Negative Ions Yield in Presence of Caesium", J. Microsc. & Spectrosc. Electron., 2, 291 (1977).
16. Bisdon, E.B., Houstra, S., Jongerius, A., Brown, J.D., Von Rosensteil, A.P., and Gas, D.J., "Light and Heavy Element Detection in Thin Sections of Soils by IMMA", Neth. J. of Agric. Sci., 25, 1 (1977).
17. Brown, J.D., and Short, J.M., "Quantitative Ion Microprobe Mass Analysis Using Negative Secondary Ions", Proc. 8th Int. Conf. on X-Ray Optics and Microanalysis, Boston, Mass., Aug. 1977. Paper No. 138.
18. Carter, G., Nobes, M.J., Paton, F., Williams, J.S., and Whitton, J.L., "Ion Bombardment Induced Ripple Topography on Amorphous Solids", Rad. Eff., 33, 65 (1977).
19. Castaing, R., and Blaise, G., "Analysis of Solid Surfaces by Thermal Ionization of Sputtered Particles", Proc. 8th Int. Conf. on X-Ray Optics and Microanalysis, Boston, Mass., Aug. 1977. Paper No. 2.
20. Chadderton, L.T., "On a Relationship Between the Geometry of Cones on Sputtered and the Angular Dependence of Sputtered Yields", Rad. Eff., 33, 129 (1977).
21. Chakraborty, P., and Dey, S.D., "Apparatus for the Study of Secondary Ions from Solid Surfaces Under Ion Bombardment", Indian J. Phys. Part B, 51B, 473 (1977).
22. Chamberlain, M.B., and Lederich, R.J., "The Surface Film Composition of Plasma-Anodized Titanium", Thin Solid Films, 41, 167 (1977).
23. Cherepin, V.T., Vasil'ev, M.A., Kosyachkov, A.A., Morozov, V.V., Shlyuko, V. Ya., and Kresanov, V.S., "Secondary Ion-Ion Emission from Alloys of the LaB₆-SmB₆ and LaB₆-YbB₆ Systems", Sov. Powder Metall. & Met. Ceram., 16, 738 (1977).
24. Christie, W.H., and Kollie, T., "An Ion Microprobe Investigation of the High Temperature Decalibration of Al₂O₃-Insulated Pt-Rh Thermocouples", 25th Ann. Conf. Mass Spectrometry and Allied Topics, Washington, D.C., May 31-June 3, 1977. American Society for Mass Spectrometry, c/o Harrison Limited Distribution, 1977, p. 435.

25. Chu, A., and Gibbons, J.F., "A Theoretical Approach to the Calculation of Impurity Profiles for Annealed, Ion Implanted B in Si", Ion Implantation in Semiconductors, F. Chernow, J.A. Borders, and D.K. Brice, Ed., (New York: Plenum Press, 1977) p. 711.
26. Clark, G.J., White, C.W., Allred, D.D., Appleton, B.R., Magee, C.W., and Carlson, D.E., "The Use of Nuclear Reactions and SIMS for Quantitative Depth Profiling of Hydrogen in Amorphous Silicon", Appl. Phys. Lett., 31, 582 (1977).
27. Comas, J., Plew, L., Chatterjee, P.K., McLevige, W.V., Vaidyanathan, K.V., and Streetman, B.G., "Impurity Distribution of Ion-Implanted Be in GaAs by SIMS, Photoluminescence, and Electrical Profiling", Ion Implantation in Semiconductors, F. Chernow, J.A. Borders, and D.K. Brice, Ed., (New York: Plenum Press, 1977) p. 141.
28. Conrad, R.L., Whatley, T.A., and Fralick, R.D., "Rapid Data Acquisition Using an Automated SIMS Quadrupole Mass Analyzer for Solids: Application to High Resolution Depth Profiling", Proc. 8th Int. Conf. on X-Ray Optics and Microanalysis, Boston, Mass., Aug. 1977. Paper No. 134.
29. Croset, M., and Dieumegard, D., "Analysis of As and Ga in Thin Films of Si_3N_4 Deposited by Reactive Cathode Sputtering on Si or GaAs", J. Microsc. & Spectrosc. Electron., 2, 329 (1977).
30. Dawson, P.H., "Oxygen Adsorption on Molybdenum Studied by Low-Energy Secondary-Ion Mass Spectrometry and Electron-Induced Desorption", Phys. Rev. B, 15, 5522 (1977).
31. Dawson, P.H., "SIMS Studies of the Adsorption of O_2 , CO and CO_2 on Titanium Using Low Primary Energies", Surf. Sci., 65, 41 (1977).
32. Dawson, P.H., "SIMS and EID Observations of Propane Adsorbed on Aluminum", J. Vac. Sci. & Technol., 14, 786 (1977).
33. Dawson, P.H., and Redhead, P.A., "High Performance SIMS System", Rev. Sci. Instrum., 48, 159 (1977).
34. Dietrich, H.B., and Comas, J., "Anomalous Redistribution of Ion-Implanted Dopants", Ion Implantation in Semiconductors, F. Chernow, J.A. Borders, and D.K. Brice Ed., (New York: Plenum Press, 1977) p. 735.
35. Doi, H., "Development of Secondary Ion Mass Spectrometer. I. Development of the AES-IMA Device and its Application to Solid Surfaces", Mass Spectrosc., 25, 325 (1977).
36. Dolotov, S.K., Evstigneev, S.A., and Luk'yanov, S.Yu., "Removal of Foreign Atoms from a Metal Surface Bombarded with Fast Atomic Particles", Nucl. Fusion, Suppl. Vol. 3, 327 (1977).
37. Doucas, G., "Energy Distribution of Negative Ions Sputtered From Caesiated Surfaces", Int. J. Mass Spectrom. & Ion Phys., 25, 71 (1977).
38. Dowsett, M.G., King, R.M., and Parker, E.H.C., "Evaluation of Impurity and Contamination Levels on Mica Surfaces Using SSIMS", J. Vac. Sci. & Technol., 14, 711 (1977).
39. Dowsett, M.G., King, R.M., and Parker, E.H.C., "SIMS Evaluation of Contamination on Ion-cleaned (100) InP Substrates", Appl. Phys. Lett., 31, 529 (1977).
40. Drzal, L.T., "The Surface Composition and Energetics of Type A Graphite Fibers (for Fiber Reinforced Polymers)", Carbon, 15, 129 (1977).
41. Dusterhoft, H., Manns, R., and Rogaschewskii, S., "An Apparatus for Measurements of Positive Secondary Ion Emission from Solid Surfaces", Exp. Tech. Phys., 25, 117 (1977).
42. Dusterhoft, H., and Ihlenfeld, A., "The Energy Distribution of Positive Secondary Ions Emitted from Metal and Semiconductor Targets Bombarded with 12 KeV Ar^+ Ions", Phys. Status Solidi A, 39, K147 (1977).
43. Evans, C.A., Jr., "Secondary Ion Mass Spectrometry: A Review of Recent Advances", Proc. 8th Int. Conf. on X-Ray Optics and Microanalysis, Boston, Mass., Aug. 1977. Paper No. 128.
44. Fasiska, E.J., and Janocko, P.B., "The Routine Application of the SIMS/SEM/EDX Combination to Practical Surface Problems", Proc. 8th Int. Conf. on X-Ray Optics and Microanalysis, Boston, Mass., Aug. 1977. Paper No. 76.
45. Fassett, J.D., Roth, J.R., and Morrison, G.H., "Quantitation of Secondary Ion Mass Spectrometric Images by Microphotodensitometry and Digital Image Processing", Anal. Chem., 49, 2322 (1977).
46. Fischer, A.K., Steidl, D.V., and Johnson, C.E., "Adaptation of an Ion Microprobe for Ion Bombardment of Liquid Metals", Rev. Sci. Instrum., 48, 219 (1977).
47. Fralick, R.D., and Conrad, R.L., "Quantitative Multielement Analysis with SIMS", Res./Dev., 28, 32 (1977).
48. Frostell, G., Larsson, S.J., Lodding, A., Odelius, H., and Petersson, L.G., "SIMS Study of Element Concentration Profiles in Enamel and Dentin", Scand. J. Dent. Res., 85, 18 (1977).
49. Galle, P., and Berry, J.P., "Microanalysis in Biology: A Review of Some Specific Problems", Proc. 8th Int. Conf. on X-Ray Optics and Microanalysis, Boston, Mass., Aug. 1977. Paper No. 167.
50. Ganjei, J.D., Leta, D.P., Roth, J.R., and Morrison, G.H., "Matrix Species Ratio Method for Quantitative Ion Probe Analysis", Proc. 8th Int. Conf. on X-Ray Optics and Microanalysis, Boston, Mass., Aug. 1977. Paper No. 139.
51. Gavrilovic, J., and Majewski, E., "Use of Ion and Electron Microprobes for Characterization of Particulate Matter", Am. Lab., 9, 19 (1977).
52. Gerlach, R.L., and Davis, L.E., "Semiquantitative Analysis of Alloys with SIMS", J. Vac. Sci. & Technol., 14, 339 (1977).
53. Gettings, M., and Kinloch, A.J., "Surface Analysis of Polysiloxane/Metal Oxide Interfaces", J. Mat. Sci., 12, 2511 (1977).
54. Hartemann, P., and Morizot, M., "Ion Implantation in Piezoelectric Substrates", Ion Implantation in Semiconductors, F. Chernow, J.A. Borders, and D.K. Brice, Eds., (New York: Plenum Press, 1977) p. 257.
55. Hashimoto, N., and Tsuyama, H., "Depth Profile of Phosphorus and Arsenic in Polycrystalline Si/ SiO_2 /Si Structure", Mass Spectrosc., 25, 363 (1977).
56. Hirao, T., Inoue, K., Takayanagi, S., and Yaegashi, Y., "Depth Distribution of Knock-on Nitrogen in Si by Phosphorus Implantation Through Si_3N_4 Films", Appl. Phys. Lett., 31, 505 (1977).

57. Hirao, T., Inoue, K., and Takayanagi, S., "Annealing Behaviors of Phosphorus Implanted in Silicon", Ion Implantation in Semiconductors, F. Chernow, J.A. Borders, and D. K. Brice, Ed., (New York: Plenum Press, 1977). p. 1.
58. Hofmann, S., "Depth Resolution in Sputter Profiling", *Appl. Phys.*, **13**, 205 (1977).
59. Kaarmann, H., Hoinkes, H., and Wilsch, H., "Quantitative Determination of Water Coverage on KCl (001) by Secondary Ion Mass Spectroscopy", *J. Chem. Phys.*, **66**, 4572 (1977).
60. Kane, P.F., and Larrabee, G.B., "Surface Characterization", *Anal. Chem.*, **49**, 221R (1977).
61. Kang, S.T., Shimizu, R., and Koshikawa, T., "Measurement of Depth Profiles of Boron Atoms Implanted in Polycrystalline Silicon by IMA", *Technol. Rep. Osaka Univ.*, **27**, 1364 (1977).
62. Kempf, J., and Kaus, G., "3 to 15 keV Ar⁺ Induced Auger Electron Emission from Si and Ar", *Appl. Phys.*, **13**, 261 (1977).
63. Kim, H.B., Barrett, D.L., Sweeney, G.G., and Heng, T.M.S., "Effects of Heat Treatment on Semi-Insulating GaAs Characterized by Secondary Ion Mass Spectrometry", *Inst. Phys. Conf. Ser.*, No. 33b, 136 (1977).
64. Kim, H.B., Lovas, A.F., Sweeney, G.G., and Heng, T.M.S., "Effects of Heat Treatment on Metal-InP Schottky Barriers Characterized by Secondary Ion Mass Spectrometry", *Inst. Phys. Conf. Ser.*, No. 33b, 145 (1977).
65. Kitada, A., and Tamura, H., "Application of Characteristic Secondary Ion Mass Spectra to a Depth Analysis of Iron Aluminum Oxide", *Mass Spectrometry*, **25**, 85 (1977).
66. Kobayashi, H., Suzuki, K., Yanagisawa, Y., and Yukawa, K., "Utilization of Neutral Particle Beam in Ion Microanalyzer", *Mass Spectrosc.*, **25**, 315 (1977).
67. Kobayashi, H., Suzuki, K., Yukawa, K., Tamura, H., and Ishitani, T., "Correction of Secondary Ion Intensity by a New Total Ion Monitoring Method", *Rev. Sci. Instrum.*, **48**, 1298 (1977).
68. Kovarskii, A.P., "Influence of the Degree of Magnetization of a Specimen on Secondary Ion Emission", *Pis'ma V Zh. Tekh. Fiz.*, **3**, 897 (1977).
69. Krauss, A.R., and Gruen, D.M., "Relative Ion Sputtering Yield Measurements by Integration of Secondary Ion Energy Distribution Using a Retarding-Dispersive Ion Energy Analyzer", *Appl. Phys.*, **14**, 89 (1977).
70. Krohn, V.E., and Ringo, G.R., "Some Proposed Improvements in the Scanning Ion Microprobe", *J. Microsc.*, **110**, pt.1, 59 (1977).
71. Kusao, K., Yoshioka, Y., and Konishi, F., "Use of SIMS to Determine Pure and Oxidized Elements in a Solid Surface", *Mass Spectrosc.*, **25**, 305 (1977).
72. Kusao, K., Yoshioka, Y., and Konishi, F., "Development and Applications of Quadrupole Type Secondary Ion Mass Spectrometer (QSIMS)", *Nat. Tech. Rep.*, **23**, 14 (1977).
73. Larikov, L.N., Ryzhkov, V.I., Nikitin, B.G., Sosnitskii, V.N., Chenakin, S.P., and Shmatko, O.A., "Reasons for the Redistribution of Atom Components in Lead-Indium Films", *Natallofizika*, Kiev, No. 69, 99 (1977).
74. Larrabee, G.B., "The Characterization of Solid Surfaces", Scanning Electron Microscopy, Vol. 1, Om Johari Ed., (Chicago, IL: ITT Research Institute, 1977) p. 639.
75. Larsson, S.J., Lodding, A., Odelius, H., and Petersson, L.G., "Calibration Methods for the Ion Probe Determination of Fluorine in Mineralized Tissue", *Calcif. Tiss. Res.*, **24**, 179 (1977).
76. Lawson, K.E., and Rusnak, R.M., "SAM/SIMS Investigation of Pt. Films on Yttria-Stabilized Zirconia", *Proc. 8th Int. Conf. on X-Ray Optics and Microanalysis*, Aug. 1977, Boston Mass., Paper No. 75.
77. Lee, D.H., Malbon, R.M., and Whelan, J.M., "Characteristics of Implanted N-Type Profiles in GaAs Annealed in a Controlled Atmosphere", Ion Implantation in Semiconductors, F. Chernow, J.A. Borders, and D.K. Brice, Ed., (New York: Plenum Press, 1977) p. 115.
78. Leferve, R., "Secondary Ion Microanalysis of Some Phosphate and Carbonate of Calcium Biomineralisations", *Proc. 8th Int. Conf. on X-Ray Optics and Microanalysis*, Boston, Mass., Aug. 1977. Paper No. 143.
79. Lewis, R.K., Williams, P., Evans, C.A., Jr., and Hanley, P.R., "Use of a Cesium Primary Ion Source on Ion Microprobe Mass Spectrometer", *Proc. 8th Int. Conf. on X-Ray Optics and Microanalysis*, Boston, Mass., Aug. 1977. Paper No. 130.
80. Liebl, H., "Ion Optics for Surface Analysis", *Int. Conf. Low Energy Ion Beams*, Salford, England, Sept. 1977. (Bristol, England: *Inst. Phys.*, 1978) p. 266.
81. Limoge, Y., Seguin, R., and Seran, J.L., "Irradiation Effects in SIMS Analysis, Their Consequences on Depth Resolution", *Proc. 8th Int. Conf. X-Ray Optics and Microanalysis*, Boston, Mass., Aug. 1977. Paper No. 136.
82. Limoge, Y., Maurice, F., and Seran, J.L., "Contribution to the Study of Ion Emission in the Ni-Cu, Ni-Fe, Al-Cu and Al-Fe Alloys: Influence of the Chemical Affinity of Components for Oxygen", *Proc. 8th Int. Conf. on X-Ray Optics and Microanalysis*, Boston, Mass., Aug. 1977. Paper No. 141.
83. Limoge, Y., Maurice, F., and Seran, J.L., "Chemical Emission in Cu-Ni, Ni-Fe, Fe-Al, Cu-Al Alloys", *J. Microsc. & Spectrosc. Electron.*, **2**, 323 (1977).
84. Linton, R.W., Williams, P., Evans, C.A., Jr., and Natusch, D.F.S., "Determination of the Surface Predominance of Toxic Elements in Airborne Particles by Ion Microprobe Mass Spectrometry and Auger Electron Spectrometry", *Anal. Chem.*, **49**, 1514 (1977).
85. Litovchenko, V.G., Marchenko, R.I., Romanova, G. Ph., and Vasilevskaya, V.N., "Some Properties of the Structure of the Si-SiO₂ Interface", *Thin Solid Films*, **44**, 295 (1977).
86. Lodding, A., Odelius, H., and Ekblom, L., "Quantitative SIMS of Tungsten Base Composite Alloy", *Proc. of the 7th Int. Vac. Cong. and 3rd Int. Conf. on Solid Surfaces*, Sept. 1977, R. Dobrozemsky, F. Rudenauer, F.P. Viehbock and A. Breth Ed., (Vienna, Austria: 7th Int. Vac. Congr.) p. 2531.
87. Long, J.V.P., Astill, D.M., Coles, J.N., Reed, S.J.B., and Charley, N.R., "A Computer-Based Recording System for High Mass-Resolution Ion-Probe Analysis", *Presented at the Proc. 8th Int. Conf. on X-Ray Optics and Microanalysis*, Boston, Mass., Aug. 1977. Paper No. 132.

88. MacDonald, R.J., and Martin, P.J., "Quantitative Surface Analysis Using Ion-Induced Secondary Ion and Photon Emission", *Surf. Sci.*, **66**, 423 (1977).
89. MacDonald, R.J., and Martin, P.J., "A Study of the Interaction of Oxygen with Chromium Using Ion Bombardment Induced, Photon and Secondary Ion Emission", *Surf. Sci.*, **67**, 237 (1977).
90. Manns, R., and Hildebrandt, D., "Experimental Determination of the Average Kinetic Energy of Sputtered Atoms", *Exp. Tech. Phys.*, **25**, 469 (1977).
91. Marcus, H.L., "Surface Techniques for the Study of Materials: AES, ESCA, SIMS", *J. Met.*, **29**, 20 (1977).
92. Martin, P.J., and MacDonald, R.J., "The Influence of Single Crystal Structure on Photon and Secondary Ion Emission from Ar^+ Ion Bombarded Aluminum", *Rad. Eff.*, **32**, 177 (1977).
93. Marwick, A.D., and Piller, R.C., "The Effect of Point Defect Fluxes on Radiation-Enhanced Diffusion in Nickel", *Rad. Eff.*, **33**, 245 (1977).
94. Mateescu, G.D., "Concerted ESCA-ISS-SIMS Investigations in Surface Analysis", *Proc. 8th Int. Conf. on X-Ray Optics and Microanalysis*, Boston, Mass., Aug. 1977. Paper No. 63.
95. McDevitt, N.T., Baun, W.L., Solomon, J.S., and Fugate, G.W., "Surface Studies of Anodic Aluminium Oxide Layers Formed in Phosphoric Acid Solutions", *Electrochem. Soc.*, Philadelphia, Pa., USA, May 1977. (Princeton, NJ, USA: *Electrochem. Soc.* 1977) p. 144.
96. Morgan, A.E., and Werner, H.W., "Test of a Quantitative Approach to Secondary Ion Mass Spectrometry on Glass and Silicate Standards", *Anal. Chem.*, **49**, 927 (1977).
97. Morgan, A.E., Werner, H.W., and Gourgout, J.M., "In-Depth Concentration Profiling of Garnet Epilayers Using Secondary Ion Mass Spectrometry", *Appl. Phys.*, **12**, 283 (1977).
98. Morgan, A.E., and Werner, H.W., "Quantitative Analysis of Glasses and Silicates Using Secondary Ion Mass Spectrometry", *J. Microsc. & Spectrosc. Electron.*, **2**, 88 (1977).
99. Morgan, A.E., and Werner, H.W., "Semiquantitative Analysis by Secondary Ion Mass Spectrometry", *J. Microsc. & Spectrosc. Electron.*, **2**, 285 (1977).
100. Morgan, A.E., and Werner, H.W., "Quantitative SIMS Studies with a Uranium Matrix", *Surf. Sci.*, **65**, 687 (1977).
101. Morrison, G.H., "Ion Microscopy and Surface Analysis", *Characterization of Metal and Polymer Surfaces*, L.H. Lee Ed., Vol. 1, (New York: Academic Press, 1977) p. 351.
102. Nakamura, K., Hirose, H., Shibata, A., and Tamura, H., "Detection of SiO_2^- Ions from SiO_2 -Si Interface by Means of SIMS", *Japan J. Appl. Phys.*, **16**, 1307 (1977).
103. Namdar-irani, R., "Identification of Iron Oxides by Secondary Ion Emission Using Ion Probe Microanalysis", *J. Microsc. & Spectrosc. Electron.*, **2**, 293 (1977).
104. Nauman, D.A., "Extension of SEM Capabilities with SIMS", *Proc. 8th Int. Conf. on X-Ray Optics and Microanalysis*, Boston, Mass., Aug. 1977. Paper No. 77.
105. Newbury, D.E., "Ion Imaging in Secondary Ion Mass Spectrometry", *Multidisciplinary Microscopy*, R. L. Whitman Ed., (Bellingham, Wash.: Society of Photo-Optical Instrumentation Engineers and the Society of Photographic Scientists and Engineers, 1977) p. 85.
106. Newbury, D.E., "Quantitative Analysis of Glasses by Secondary Ion Mass Spectrometry", *Proc. 8th Int. Conf. on X-Ray Optics and Microanalysis*, Boston, Mass., Aug. 1977. Paper No. 140.
107. Okazima, Y., and Aizawa, Y., "Quantitative Analysis of High Temperature Alloys with an Ion Microanalyzer", *Mass Spectrosc.*, **25**, 91 (1977).
108. Oshima, M., "Quantitative Analysis of Compound Semiconductors with an Ion Microanalyzer", *Mass Spectrosc.*, **25**, 99 (1977).
109. Pavlyak, F., Bori, L., Giber, J., and Ruhl, R., "Detection of Hydrogen in Metals by the SIMS-Method with Quadrupole Mass Filter", *Japan. J. Appl. Phys.*, **16**, 335 (1977).
110. Pivin, J.C., Roques-Carnes, C., and Lacombe, P., "Comparative Study by Secondary Ion Emission and Electron Microprobe of the Composition and Structure of Oxide Layers Formed on Ni-Cr, Fe-Ni-Cr Alloys", *J. Microsc. & Spectrosc. Electron.*, **2**, 90 (1977).
111. Pivin, J.C., and Roques-Carnes, C., "Chemical Emission of the FeNi, FeCr, NiCr Alloys", *J. Microsc. & Spectrosc. Electron.*, **2**, 301 (1977).
112. Pivin, J.C., Roques-Carnes, C., and Lacombe, P., "Application of Secondary Ionic Emission to the Study of the Oxide Films Formed on Ni-Cr 80/20 Alloy by Oxidation in pure Oxygen between 800 and 1200°C", *Mem. Sci. Rev. Metall.*, **74**, 161 (1977).
113. Plog, C., Wiedmann, L., and Benninghoven, A., "Empirical Formula for the Calculation of Secondary Ion Yields from Oxidized Metal Surfaces and Metal Oxides", *Surf. Sci.*, **67**, 565 (1977).
114. Ploog, K., and Fischer, A., "In situ Characterization of MBE Grown GaAs and $\text{Al}_x\text{Ga}_{1-x}\text{As}$ Films Using RHEED, SIMS, and AES Techniques", *Appl. Phys.*, **13**, 111 (1977).
115. Popov, V.F., Tserpitskii, B.D., and Raitsyn, A.B., "Investigation of Duoplasmatron as a Source of Argon Ions in an Ion Microanalyzer", *Instrum. & Exp. Tech.*, **20**, 814 (1977).
116. Rao, E.V.K., Dubamel, N., Favennec, P.N., and L'haridon, H., "Vacancy-Impurity Complexes in Implanted and High Temperature Annealed n-GaAs", *Ion Implantation in Semiconductors*, F. Chernow, J.A. Borders, and D.K. Brice, Ed., (New York: Plenum Press, 1977) p. 77.
117. Roth, J.R., and Morrison, G.H., "A Computerized CAMECA Ion Probe System", *Proc. 8th Int. Conf. on X-Ray Optics and Microanalysis*, Boston, Mass., Aug. 1977. Paper No. 48.
118. Rouberol, J.M., Lepareur, M., Antier, B., and Gourgout, J.M., "A New Secondary Ion Emission Microanalyzer", *Proc. 8th Int. Conf. on X-Ray Optics and Microanalysis*, Boston, Mass., Aug. 1977. Paper No. 133.
119. Rudenauer, F.G., "A Comparison of Quantitative Models for SIMS Analysis", *Mikrochimica Acta (Wien)*, Suppl. **7**, 85 (1977).
120. Rudenauer, F.G., and Steiger, W., "Quantitative SIMS-Analysis on Nonplanar Surfaces", *Proc. of the 7th Int. Vac. Congr. and 3rd Int. Conf. on Solid Surfaces*, Sept. 1977, R. Dobrozemsky, F. Rudenauer, F.P. Viehbock and A. Breth Ed., (Vienna, Austria: 7th Int. Vac. Congr.) p. 2535.

121. Sato, K., Suzuki, K., Matsumoto, R., and Nagashima, S., "Specimen Fracturing Device for Ion Microprobe Mass Analyzer and its Application to the Analysis of Grain Boundary Segregation", *Trans. Japan Inst. Met.*, **18**, 61 (1977).
122. Schroeder, J.M., "Secondary-Ion Emission from Iron Alloys under Various Bombarding Conditions", *J. Vac. Sci. & Technol.*, **14**, 343 (1977).
123. Scilla, G.J., and Morrison, G.H., "Sampling Error in Ion Microprobe Analysis", *Anal. Chem.*, **49**, 1529 (1977).
124. Shimizu, R., Kang, S.T., Koshikawa, T., Ogata, H., Kanayama, K., Ogata, Y., Akasaka, Y., and Horie, K., "Monte Carlo Simulation of Depth and Lateral Profiles of Boron Atoms Implanted in Polycrystalline Silicon", *J. Appl. Phys.*, **48**, 1745 (1977).
125. Shimizu, R., "Some Recent Development in Microbeam Analysis in Japan. I. Application of Monte Carlo Calculation to Fundamentals of Microbeam Analysis", *Technol. Rep. Osaka Univ.*, **27**, no. 1337-1363, 69 (1977).
126. Shimizu, R., Okutani, T., Ishitani, T., and Tamura, H., "Simultaneous Measurements of Photon and Ion Emissions from Ion Bombarded Al in Oxygen Atmosphere", *Surf. Sci.*, **69**, 349 (1977).
127. Shiraiwa, T., Fujino, N., Murayama, J., and Usuki, N., "IMMA Surface Analysis of Alloy Steel Using N_2^+ Primary Ion", *Proc. 8th Int. Conf. on X-Ray Optics and Microanalysis*, Boston, Mass., Aug. 1977. Paper No. 142.
128. Slodizian, G., and Figieras, A., "A Transfer Optics for Microanalysis by Secondary Ion Emission", *Proc. 8th Int. Conf. on X-Ray Optics and Microanalysis*, Boston, Mass., Aug. 1977. Paper No. 127.
129. Smith, D.H., and Christie, W.H., "A Study of the Quantification of SIMS Data", *25th Ann. Conf. Mass Spectrom. and Allied Topics*, Washington, D.C., May 31-June 3, p. 309 (1977).
130. Sparrow, G.R., "Combined SIMS/SEM for Three Dimensional Surface Analysis", *Proc. 8th Int. Conf. on X-Ray Optics and Microanalysis*, Boston, Mass., Aug. 1977. Paper No. 78.
131. Steele, I.M., Hutcheon, I.D., Solberg, T.N., Clayton, R.N., and Smith, J.V., "Ion Microprobe Analysis of Plagioclase Feldspars ($Ca_{x-1}Na_{1-x}Al_{1-x}Si_{3-x}O_8$) for Major and Minor Elements", *Proc. 8th Int. Conf. on X-Ray Optics and Microanalysis*, Boston, Mass., Aug. 1977. Paper No. 180.
132. Steele, I.M., Hutcheon, I.D., Solberg, T.N., Smith, J.V., and Clayton, R.N., "Effect of Energy Selection on Quantitative Analysis in Secondary Ion Microanalysis", *Int. J. Mass Spectrom. & Ion Phys.*, **23**, 293 (1977).
133. Storms, H.A., Brown, K.F., and Stein, J.D., "Evaluation of a Cesium Positive Ion Source for Secondary Ion Mass Spectrometry", *Anal. Chem.*, **49**, 2023 (1977).
134. Taya, S., Tsuyama, H., Itoh, M., and Kanomata, I., "A Comparative Study of Solid Surface Analysis Between Low Energy Ion Scattering Spectroscopy (ISS) and Secondary Ion Mass Spectroscopy (SIMS)", *Mass Spectrosc.*, **25**, 251 (1977).
135. Treitz, N., "Analysis of Solid Surface Monolayers by Mass and Energy Spectrometry Methods", *J. Phys. E*, **10**, 573 (1977).
136. Tsukizoe, T., Nakai, T., and Okame, N., "Ion-Beam Plating Using Mass-Analyzed Ions", *J. Appl. Phys.*, **48**, 4770 (1977).
137. Tsunoyama, K., Ohashi, Y., and Suzuki, T., "On the Emission of Secondary Ions during Oxygen Ion Bombardment", *Mass Spectrosc.*, **25**, 297 (1977).
138. Tsuyama, H., and Hashimoto, N., "Quantitative Analysis of Phosphorus and Arsenic in Silicon by Means of Ion Microanalyzer", *Mass Spectrosc.*, **25**, 351 (1977).
139. Vallerand, P., et Baril, M., "Etude de L'emission Ionique Secondaire Negative du Cuivre et de Quelques-Uns de ses Alliages par Impact D'ions Cs^+ ", *Int. J. Mass Spectrom. & Ion Phys.*, **24**, 241 (1977).
140. van Deventer, E.H., Renner, T.A., Pelto, R.H., and Maroni, V.A., "Effects of Surface Impurity Layers on the Hydrogen Permeability of Vanadium", *J. Nucl. Mat.*, **64**, 241 (1977).
141. Vasil'ev, M.O. Koval, Yu. N., Kosyachkov, O.O., and Cherepin, V.T., "Qualitative Analysis of Fe-Ni Alloys by Secondary Ion-Ion Emission", *Dopov. Akad. Nauk. UKRSR, Ser. A*, No. 4, 354 (1977).
142. Vasil'ev, M.A., Chenakin, S.P., Popov, V.I., and Trofimenko, V.I., "Laws of the Formation of the Composition of thin Films Based on Multicomponent Copper Alloys (Secondary Ion Emission Measurement)", *Fiz. Met. & Metalloved.*, **44**, 99 (1977).
143. Vasil'ev, M.A., Krasnyuk, A.D., and Cherepin, V.T., "MI-1305 Mass Spectrometer with an Ion Probe and an Energy Analyzer for Studying Solids", *Instrum. & Exp. Tech.*, **20**, 806 (1977).
144. Vasiliu, F., "Sputtering Erosion, Apparent Growth and Equilibrium of Triangular Microprofiles Submitted to Ion Bombardment at Oblique Incidence", *Rev. Roum. Phys.*, **22**, 523 (1977).
145. Vasiliu, F., and Frunza, S., "Angular Ranges for Sputtering Erosion, Apparent Growth and Equilibrium of a Symmetric Triangular Microprofile", *Rev. Roum. Phys.*, **22**, 601 (1977).
146. von Rosensteil, A.P., Brown, J.D., Gras, D.J., Bisdom, E.B.A., Henstra, S., and Jongerius, A., "Electron and Ion Microprobe Analysis of Clayified Roots in Thin Sections of Soil", *Proc. 8th Int. Conf. on X-Ray Optics and Microanalysis*, Boston, Mass., Aug. 1977. Paper No. 203.
147. von Rosensteil, A.P., Brown, J.D., and Gras, D.J., "Quantitative Carbon Analysis in Steels with the Ion Microprobe", *Proc. 8th Int. Conf. on X-Ray Optics and Microanalysis*, Boston, Mass., Aug. 1977. Paper No. 204.
148. Werner, H.W., "Applications of Secondary Ion Mass Spectrometry (SIMS)", *Mikrochimica Acta*, (Wien), Suppl. 7, 63 (1977).
149. Werner, H.W., "Comparison of Thin Film Analytical Methods", *Proc. of the 7th Int. Vac. Congr. and 3rd Int. Conf. on Solid Surfaces*, Sept. 1977, R. Dobrozemsky, F. Rudenauer, F.P. Viehbock and A. Breth Ed., (Vienna, Austria: 7th Int. Vac. Congr.) p. 2135.
150. Whatley, T.A., Conrad, R.L., and Fraick, R.D., "Improved SIMS Depth Profiles by Control of Sample Surface Potential", *Proc. 8th Int. Conf. on X-Ray Optics and Microanalysis*, Boston, Mass., Aug. 1977. Paper No. 135.

151. Williams, P., Lewis, R.K., Evans, C.A., Jr., and Hanley, P.R., "Evaluation of a Cesium Primary Ion Source on an Ion Microprobe Mass Spectrometer", *Anal. Chem.*, **49**, 1399 (1977).
152. Williams, P., and Evans, C.A., Jr., "Depth Profile Detection Limit of 3×10^{15} Atom cm^{-3} for As in Si Using Cs^+ Bombardment Negative Secondary Ion Mass Spectrometry", *Appl. Phys. Lett.*, **30**, 559 (1977).
153. Wittmaack, K., "Raster Scanning Depth Profiling of Layer Structures", *Appl. Phys.*, **12**, 149 (1977).
154. Wittmaack, K., "The Use of Secondary Ion Mass Spectrometry for Studies of Oxygen Adsorption and Oxidation", *Surf. Sci.*, **68**, 118 (1977).
155. Wittmaack, K., "Low Energy Ion Beam Transport through Apertures", *Nucl. Instrum. & Methods*, **143**, 1 (1977).
156. Wittmaack, K., "DIDA-A Multipurpose Scanning Ion Microprobe", *Proc. 8th Int. Conf. on X-Ray Optics and Microanalysis*, Boston, Mass., Aug. 1977. Paper No. 131.
157. Wittry, D.B., "Critical Problems in Quantitative Secondary Ion Mass Spectroscopy", *Proc. 8th Int. Conf. on X-Ray Optics and Microanalysis*, Boston, Mass., Aug. 1977. Paper No. 129.
158. Yaegashi, Y., and Inaguma, K., "Analysis of Semiconductors by Means of Ion Microanalyzer", *Natl. Tech. Rep.*, **23**, 116 (1977).
159. Yaegashi, Y., and Nakajima, S., "In-Depth Profiling by Means of Secondary Ion Mass Spectrometry", *Mass Spectrosc.*, **25**, 279 (1977).
160. Yu, M.L., "Study of Chemisorbed Oxygen on Tungsten Using Secondary Ion Mass Spectrometry", *Appl. Phys. Lett.*, **30**, 654 (1977).
161. Yu, M.L., "Isotope Effect in the Study of H-W (100) and O-W (100) Chemisorption Systems Using SIMS", *Nucl. Instrum. & Methods*, **149**, 559 (1977).
162. Zinner, E., Walker, R.M., Chavmont, J., and Dran, U.C., "Ion Probe Surface Concentration Measurements of Mg and Fe and Microcenters in Crystals for Lunar Rock and Soil Sample", *Proc. 8th Lunar Sci. Conf.*, Houston, Texas, March 1977, Compiled by the Lunar Science Institute, (New York: Pergamon Press Inc., 1977) p. 3859.

1978

1. Alexandre, F., "Study of the Surface Segregation of Alkali Metal Impurities Implanted in Gallium Arsenide", *J. Phys.*, **39**, 701 (1978).
2. Anderson, D.P., "Separation of Particles", *Ind. Res./Dev.*, **20**, 75 (1978).
3. Barsony, I., Marton, D., and Giber, J., "Secondary Ion Mass Spectrometry Depth Profiling and Simultaneous Electrical Investigation of MOS Structure", *Thin Solid Films*, **51**, 275 (1978).
4. Benndorf, C., Goetz, R., Gressman, K.H., Kessler, J., and Thieme, F., "SIMS, AES, Work Function and Flash Desorption Measurements of the CO Adsorption on NiCu Alloy Surfaces", *Surf. Sci.*, **76**, 509 (1978).
5. Benninghoven, A., Muller, K.H., Schemmer, M., and Beckmann, P., "SIMS and Flash Desorption Studies of Nickel Oxygen Interaction", *Appl. Phys.*, **16**, 367 (1978).
6. Benninghoven, A., and Wiedmann, L., "Quantitative Determination of Secondary Ion Yield of Oxygen-Covered Metals", *Forschungsber. Landes Nordrhein-Westfalen*, no. 2784, 1 (1978).
7. Benninghoven, A., Ganschow, O., and Wiedmann, L., "Quasisimultaneous SIMS, AES and XPS Investigations of the Oxidation of Mo, Ti, and Co in the Monolayer Range", *J. Vac. Sci. & Technol.*, **15**, 506 (1978).
8. Benninghoven, A., Muller, K.H., and Schemmer, M., "Hydrogen Detection by SIMS: Hydrogen on Polycrystalline Vanadium", *Surf. Sci.*, **78**, 565 (1978).
9. Benninghoven, A., Sichtermann, W., and Storp, S., "Comparative Study of Si(111), Silicon Oxide, SiC and Si_3N_4 Surfaces by Secondary Ion Mass Spectroscopy (SIMS)", *Thin Solid Films*, **28**, 59 (1978).
10. Benninghoven, A., Mueller, K.H., and Schemmer, M., "Detection of Hydrogen on Metal Surfaces: The Interaction of H_2 with Polycrystalline Vanadium", *Advances in Mass Spectrometry*, Vol. 7A, N.R. Daly, Ed., (London: The Institute of Petroleum, 1978) p. 784.
11. Benninghoven, A., Jaspers, D., and Sichtermann, W., "Secondary Ion Emission of Organic Compounds: Amino Acids", *Advances in Mass Spectrometry*, Vol. 7B, N.R. Daly, Ed., (London: The Institute of Petroleum, 1978) p. 1433.
12. Benninghoven, A., "Organic SIMS", *Proc. 13th Nat. Conf. of the Microbeam Analysis Soc.*, Ann Arbor, Michigan, June, 1978, Paper No. 27.
13. Berna, A., Nemeth-Sallay, M., Szep, I.C., Didenko, P.I., Litovchenko, V.G., Marchenko, P.I., and Romanova, G.F., "Room Temperature Transformations Induced in SiO_2 Layers by Chemical Compounds", *Thin Solid Films*, **55**, 355 (1978).
14. Beske, H.E., and Holzbrecher, H., "Detection of Deposition and Diffusion of Cleavage Products by Secondary-Ion Mass Spectrometry", *Mikrochimica Acta (Wien)*, **1**, 201 (1978).
15. Blaise, G., "Sputtering of a Solid and Ion Microanalysis", *Vide*, **33**, No. 190, 1 (1978).
16. Blaise, G., and Castaing, R., "Method of Solid Microanalysis of Solid Based on Thermal Ionisation of Sputtered Products", *J. Microsc. & Spectrosc. Electron.*, **3**, 439 (1978).
17. Blaise, G., Lyon, O., and Roques-Carmes, C., "Sputtering and Secondary Ion Emission of a Two Phase System Composed of Small Oxide Precipitates Dispersed in a Copper Matrix", *Surf. Sci.*, **71**, 630 (1978).
18. Blanc, C., "Spectroscopic Methods for Surface Analysis in the Area of Lubrication", *Report LYCEN/7868*, Univ. Lyon, France, (1978) 83 pp.
19. Blattner, R.J., and Evans, C.A., Jr., "Improvements in the Sensitivity of Secondary Ion Mass Spectrometry - Cs^+ Ion Bombardment and Negative Ion Spectrometry", *Thin Solid Films*, **53**, 39 (1978).
20. Boes, N., and Zuchner, H., "Secondary Ion Mass Spectrometry and Auger Electron Spectroscopy Investigations of Vb Metal Foils Prepared for Hydrogen Permeation Measurements", *Surf. Technol.*, **7**, 401 (1978).

21. Bolliger, J., "A Review on Depth Profiling of Hydrogen and Helium Isotopes within the Near-Surface Region of Solids by Use of Ion Beams", *J. Nucl. Mat.*, **78**, 161 (1978).
22. Borisov, A.M., Mashkova, E.S., and Molchanov, V.A., "Chain Effect for Fast Recoils", *Phys. Lett. A*, **66**, 129 (1978).
23. Bradley, J.G., Huneke, J.C., and Wassenborg, G.J., "Ion Microprobe Evidence for the Presence of Excess ^{26}Mg in an Allende Anorthite Crystal", *J. Geophys. Res.*, **83**, 244 (1978).
24. Burns-Bellhorn, M.S., "A Review of Secondary Ion Mass Spectrometry In Biological Research", *Proc. 13th Nat. Conf. of the Microbeam Analysis Soc.*, Ann Arbor, Michigan, June, 1978. Paper No. 28.
25. Carlson, D.E., and Magee, C.W., "A SIMS Analysis of Deuterium Diffusion in Hydrogenated Amorphous Silicon", *Appl. Phys. Lett.*, **33**, 81 (1978).
26. Carter, G., Armour, D.G., and Snowdon, K.J., "Cascade and Quasi Thermal Processes in Excited Atom Sputtering", *Rad. Eff.*, **35**, 175 (1978).
27. Castaing, R., Bizouard, H., Clocchiatti, R., and Havette, A., "Some Applications of the Electron Microprobe and of the Ion Microanalyser in Mineralogy", *Bull. Soc. Fr. Mineral & Crystallogr.*, **101**, 245 (1978).
28. Chaintreau, M., and Slodzian, G., "Secondary Ion Image Observation Utilising Channel Plate", *J. Microsc. & Spectrosc. Electron.*, **3**, 457 (1978).
29. Cherepin, V.T., Kosyachkov, A.A., and Vasilev, M.A., "Secondary Ion Emission of Transition Metal Carbides", *Phys. Status Solidi A*, **50**, K113 (1978).
30. Cherepin, V.T., "Secondary Ion Mass Spectrometry of Metals and Alloys", *Advances in Mass Spectrometry*, Vol. 7A, N.R. Daly, Ed., (London: The Institute of Petroleum, 1978) p. 776.
31. Christie, W.H., Smith, D.H., Eby, R.E., and Carter, J.A., "Quantification of SIMS Data Results, Problems, and Promises", *Am. Lab.*, **10**, 19 (1978).
32. Christie, W.H., Kollie, T.G., Eby, R.E., and Anderson, R.L., "Ion Microprobe Investigation of Large Decalibrations in Inconel-Sheathed, Magnesite-Insulated, Platinum-Rhodium/Platinum, Thermocouple Assemblies During Use at 1200°C", *J. Less Common Metals*, **59**, 17 (1978).
33. Clark, G.J., White, C.W., Allred, D.D., Appleton, B.P., Koch, F.B., and Magee, C.W., "The Application of Nuclear Reactions for Quantitative Hydrogen Analysis in a Variety of Different Materials Problems", *Nucl. Instrum. & Methods*, **149**, 9 (1978).
34. Clausing, R.E., Emerson, L.C., and Heatherly, L., "Sputtering and Chemical Attack of 304 Stainless Steel, Aluminum and Gold by Hydrogen Ions of 100 eV Energy", *J. Nucl. Mat.*, **76 & 77**, 199 (1978).
35. Conner, G.R., "Combination Analysis of Metal Oxides Using ESCA, AES and SIMS", *J. Vac. Sci. & Technol.*, **15**, 343 (1978).
36. Conner, G.R., and McGinnis, P.F., "New Modular Surface Analysis System", *J. Vac. Sci. & Technol.*, **15**, 785 (1978).
37. Conner, G.R., "Combination Analysis of Oxide Films on Metals and Metal Alloys Using Electron Spectroscopy for Chemical Analysis, Auger Electron Spectroscopy and Secondary Ion Mass Spectrometry", *Thin Solid Films*, **53**, 38 (1978).
38. Conty, C., "Application Using Second Generation High Resolution Ion Microanalyzer", *Proc. 13th Nat. Conf. of the Microbeam Analysis Soc.*, Ann Arbor, Michigan, June 1978, Paper No. 14.
39. Cuomo, J.J., Gambino, R.J., Harper, J.M.E., Kuptis, J.D., and Webber, J.C., "Significance of Negative Ion Formation in Sputtering and SIMS Analysis", *J. Vac. Sci. & Technol.*, **15**, 281 (1978).
40. Czanderna, A.W., Miller, A.C., and Helbig, H.F., "Surface Analysis from Scattered and Sputtered Ions", *Scanning Electron Microscopy*, Vol. 1, Om Johari, Ed., (AMF O'Hare, IL: Scanning Electron Microscopy Inc., 1978) p. 259.
41. Dawson, P.H., "The Adsorption of CO on Molybdenum Studied by Low Energy SIMS and EID", *Surf. Sci.*, **71**, 247 (1978).
42. Dawson, P.H., "Secondary Ion Mass Spectrometry of Surfaces at Low Energies", *Advances in Mass Spectrometry*, Vol. 7A, N.R. Daly, Ed., (London: The Institute of Petroleum, 1978) p. 789.
43. Deal, B.E., Hurrie, A., and Schulz, M.J., "Chlorine Concentration Profiles in O_2/HCl and $\text{H}_2\text{O}/\text{HCl}$ Thermal Silicon Oxides Using SIMS Measurements", *J. Electrochem. Soc.*, **125**, 2024 (1978).
44. Deline, V.R., Evans, C.A., Jr., and Williams, P., "A Unified Explanation for Secondary Ion Yields", *Appl. Phys. Lett.*, **33**, 578 (1978).
45. Deline, V.R., Katz, W., Evans, C.A., Jr., and Williams, P., "Mechanism of the SIMS Matrix Effect", *Appl. Phys. Lett.*, **33**, 832 (1978).
46. Deline, V.R., Williams, P., and Evans, C.A., Jr., "Advances in Quantitative Studies Using Cs^+ Secondary Ion Mass Spectrometry", *Proc. 13th Nat. Conf. of the Microbeam Analysis Soc.*, Ann Arbor, Michigan, June 1978, Paper No. 5.
47. Dennebouy, R., and Slodzian, G., "An Experimental Procedure for Adjusting the Energy Band Center of Secondary Ions Collated by the Ion Microanalyser", *J. Microsc. & Spectrosc. Electron.*, **3**, 451 (1978).
48. DiBenedetto, A.T., and Scola, D.A., "Characterization of S-Glass/Polymer Interfaces Using Ion Scattering Spectroscopy and Scattered Ion Mass Spectroscopy", *J. Colloid & Interface Sci.*, **64**, 480 (1978).
49. Diebold, A., Grillo, A.C., and Noblet, M.M., "Tridimensional Characterization of Solid Surfaces by SIMS Analysis", *J. Vac. Sci. & Technol.*, **15**, 790 (1978).
50. Dietz, L.A., and Hanrahan, L.R., "Electron Multiplier-Scintillator Detector for Pulse Counting Positive or Negative Ions", *Rev. Sci. Instrum.*, **49**, 1250 (1978).
51. Dobrott, R.D., and Larrabee, G.B., "SIMS Analysis: The Determination of Detection Limits. Sample Volume Relationship Using Microdot Standards", *Proc. 13th Nat. Conf. of the Microbeam Analysis Soc.*, Ann Arbor, Michigan, June 1978. Paper No. 4.
52. Dowsett, M.G., King, R.M., and Parker, E.H.C., "Static Secondary Ion Mass Spectroscopy (SSIMS) Analysis of the Mica Surface", *Surf. Sci.*, **71**, 541 (1978).
53. Drummer, D.M., Fassett, J.D., and Morrison, G.H., "Computerized Image Processing for Evaluation of Sampling Errors in Ion Microprobe Analysis", *Anal. Chim. Acta*, **100**, 15 (1978).

54. Dusterhoft, H., "Dependence of Secondary Ion Emission on the Mass of the Bombarding Ions (Z_1 -Dependence)", *Phys. Status Solidi A*, 50, 503 (1978).
55. Elbern, A. Hintz, E., and Schweer, B., "Measurement of the Velocity Distribution of Metal Atoms Sputtered by Light and Heavy Particles", *J. Nucl. Mat.*, 76 & 77, 143 (1978).
56. Elbers, P., Gras, D., von Rosenstiel, A., and Brown, J., "Ion Microprobe Analysis of Li in Snail Eggs in Early Cleavage Stages", *Proc. 13th Nat. Conf. of the Microbeam Analysis Soc.*, Ann Arbor, Michigan, June 1978, Paper No. 29.
57. Evans, C.A., Jr., "Ion Probe Mass Spectrometry: Overview", *Thin Solid Films*, 19, 11 (1978).
58. Evans, C.A., Jr., and Blattner, R.J., "Modern Experimental Methods for Surface and Thin-Film Chemical Analysis", *Annual Review of Materials Science*, Vol. 8, R.A. Huggins, R.H. Bube, and R.W. Roberts, Eds., (Palo Alto, CA. USA: Annual Reviews Inc., 1978) p. 181.
59. Fasset, J.D., and Morrison, G.H., "Digital Image Processing in Ion Microscope Analysis: Study of Crystal Structure Effects in Secondary Ion Mass Spectrometry", *Anal. Chem.*, 50, 1861 (1978).
60. Fasset, J.D., and Morrison, G.H., "Multifeature Mass Analysis Utilizing Digital Image Processing of Secondary Ion Mass Spectrometric Images", *Proc. 13th Nat. Conf. of the Microbeam Analysis Soc.*, Ann Arbor, Michigan, June 1978, Paper No. 12.
61. Fleisch, T., Shepard, A.T., Ridley, T.Y., Vaughn, W.E., Winograd, N., Baitinger, W.E., Ott, G.L., and Delgass, W.N., "System for Transferring Samples Between Chambers in UHV", *J. Vac. Sci. & Tech.*, 15, 1756 (1978).
62. Fleisch, T., Winograd, N., and Delgass, W.N., "Chemisorption of Oxygen on Ni (100) by SIMS and XPS", *Surf. Sci.*, 78, 141 (1978).
63. Franzen, J., "Instrumental Development and Data Processing", *Advances in Mass Spectrometry*, Vol. 7B, N.R. Daly, Ed., (London: The Institute of Petroleum, 1978) p. 817.
64. Frisch, M.A., Reuter, W., and Wittmaack, K., "A System for Combined SIMS-AES-XPS Analysis of Solids", *Proc. 13th Nat. Conf. of the Microbeam Analysis Soc.*, Ann Arbor, Michigan, June, 1978. Paper No. 8.
65. Ganjei, J.D., Leta, O.P., and Morrison, G.H., "Quantitative Ion Probe Measurement Using Matrix Ion Species Ratios", *Anal. Chem.*, 50, 285 (1978).
66. Ganjei, J.D., and Morrison, G.H., "Quantitative Ion Probe Analysis of Glasses by Empirical Calibration Methods", *Anal. Chem.*, 50, 2034 (1978).
67. Gat, A., Gibbons, J.F., Magee, T.J., Peng, J., Deline, V.R., Williams, P., and Evans, C.A., Jr., "Physical and Electrical Properties of Laser-Annealed Ion-Implanted Silicon", *Appl. Phys. Lett.*, 32, 276 (1978).
68. Gibbons, J.F., Gat, A., Gerzberg, L., Lieloila, A., Regolini, J.L., Sigmon, T.W., Pease, R.F.W., Magee, T.J., Peng, J., Hong, J., Deline, V., Katz, W., Williams, P., and Evans, C.A., Jr., "Annealing of Ion-Implanted Si Using Scanned Laser and Electron Beams", *AIP Conf. Proc.*, No. 50, 365 (1978).
69. Giber, J., Kazsoki, J., and Koblinger, L., "Computer Modelling of Sputtering Processes", *Acta Phys. Acad. Sci. Hung.*, 44, 227, (1978).
70. Giber, J., Kazsoki, J., and Koblinger, L., "Collision Cascades and the Disturbed Zone During Sputtering Processes (Model Computation)", *Acta Phys. Acad. Sci. Hung.*, 45, 275 (1978).
71. Gimelfarb, F.A., Lototskii, A.G., Onlov, P.B., and Fistul', V.I., "Reactive Secondary-Ion Emission in Film-Composition Monitoring", *Ind. Lab.*, 44, 1360 (1978).
72. Good-Zamin, C.J., Shehata, M.T., Squires, D.B., and Kelly, R., "On the Problem of Whether Excited States Amongst Sputtered Particles are of Thermal Origin", *Rad. Eff.*, 35, 139 (1978).
73. Gossink, R.G., "SIMS Analysis of Field-Assisted Glass-to-Metal Seal", *J. Am. Ceram. Soc.*, 61, 539 (1978).
74. Grunthaner, F.J., and Maserjian, J., "Chemical Structure of the Transitional Region of the SiO₂-Si Interface", *J. Vac. Sci. & Technol.*, 15, 1518 (1978).
75. Guo, F., and Wittry, D.B., "Use of Specimen Current Integration in SIMS", *Proc. 13th Nat. Conf. of the Microbeam Analysis Soc.*, Ann Arbor, Michigan, June 1978, Paper No. 13.
76. Gurevich, G.M., Danilyuk, Yu. L., and Kovarskii, A.P., "Plasma Source for Bombardment of Solids by Positive and Negative Ions", *Instrum. & Exp. Tech.*, 21, 1041 (1978).
77. Haggmark, L.G., and Wilson, W.D., "Monte Carlo Studies of Sputtering", *J. Nucl. Mat.*, 76 & 77, 149 (1978).
78. Harrison, D.E., Jr., Kelly, P.W., Garrison, B.J., and Winograd, N., "Low Energy Ion Impact Phenomena on Single Crystal Surfaces", *Surf. Sci.*, 76, 311 (1978).
79. Herion, J., and Seggern, J., "Diffusion of Cs into High Temperature Alloys (An Investigation by Scanning Auger Electron Microscopy and Secondary Ion Mass Spectrometry)", Report JUL-1483, Kernforschungsanlage, Julich, Germany (Jan. 1978). 38 pp.
80. Hewitt, R.W., Shepard, A.T., Baitinger, W.E., Winograd, N., Ott, G.L., and Delgass, W.N., "Characterization of Metal Surfaces by Secondary Ion Mass Spectrometry and X-Ray Photoelectron Spectroscopy", *Anal. Chem.*, 50, 1286 (1978).
81. Hewitt, R.W., and Winograd, N., "Investigation of the Oxidation of Polycrystalline Lead by XPS and SIMS", *Surf. Sci.*, 78, 1 (1978).
82. Hibino, M., and Sakaki, Y., "Present Status of SIMS and AES in Japan", *Am. Lab.*, 10, 36 (1978).
83. Higgsberger, M.J., "Static and Dynamic Surface Analysis with a Secondary Ion Mass Spectrometer, a Mossbauer Spectrometer, and a Pure Germanium Gamma Spectrometer", *Acta Phys. Austriaca.*, 49, 181 (1978).
84. Hofer, W.O., and Martin, P.J., "On the Influence of Reactive Gases on Sputtering and Secondary Ion Emission. Oxidation of Titanium and Vanadium During Energetic Particle Irradiation", *Appl. Phys.*, 16, 271 (1978).
85. Hofer, W.O., and Thum, F., "A Simple Axially-Symmetric Quadrupole SIMS Spectrometer", *Nucl. Instrum. & Methods*, 149, 535 (1978).

86. Holloway, P.H., and McGuire, G.E., "Chemical Characterization of Coatings by Analytical Techniques Sensitive to the Surface and Near-Surface", *Thin Solid Films*, 53, 3 (1978).
87. Honda, F., Lancaster, G.M., Fukuda, Y., and Rabalais, J.W., "SIMS Study of the Mechanism of Cluster Formation During Ion Bombardment of Alkali Halides", *J. Chem. Phys.*, 69, 4931 (1978).
88. Honda, F., Lancaster, G.M., and Rabalais, J.W., "High Mass Secondary Ion Clusters of Caesium Iodide Detected by SIMS", *Surf. Sci.*, 76, L613 (1978).
89. Hong, J., Newbury, D., and Davis, R., "Ion Microprobe Analysis of ³⁰Si Diffusion in α -SiC", *Proc. 13th Nat. Conf. of the Microbeam Analysis, Soc.*, Ann Arbor, Michigan, June, 1978. Paper No. 30.
90. Hu, Z.H., "LT-1 Ion Microprobe Mass Analyser", *Wuli*, 7, 233 (1978).
91. Huber, A.M., Morillot, G., Linh, N.T., Debrun, J.L., and Valladon, M., "Quantitative Analysis of Oxygen in Thin Epitaxial Layers of GaAs by SIMS", *Nucl. Instrum. & Methods*, 149, 543 (1978).
92. Hubler, G.K., Comas, J., and Plew, L., "Profiles of Ion-Implanted Be in GaAs by Means of (P α) Nuclear Reaction and SIMS Methods", *Nucl. Instrum. & Methods*, 149, 635 (1978).
93. Hucks, P., Stocklin, G., Vietzke, E., and Vogelbruch, K., "Energy and Angular Distribution of Gold and Copper Atoms Sputtered with Either 15 or 30 KeV H⁺, He⁺ and Ar⁺ Ions", *J. Nucl. Mat.*, 76 & 77, 136 (1978).
94. Ishitani, T., and Itoh, M., "Surface Analyzer Combining Secondary Ion Mass Spectrometry and Ion Scattering Spectrometry", *Hitachi Rev.*, 27, 160 (1978).
95. Ishitani, T., Tamura, H., and Kanomata, I., "Construction of Sputter Ion Sources and Application to IMA Analysis", *J. Vac. Soc. Japan*, 21, 307 (1978).
96. Jackson, C.K., "Modifications to the CAMECA Ion Analyser", *J. Microsc. & Spectrosc. Electron.*, 3, 491 (1978).
97. Jager, I., "The Influence of Surface Diffusion on the Results of Surface Analysis-A Model Calculation", *Surf. Sci.*, 78, 93 (1978).
98. Jamba, D.M., "Secondary Particle Collection in Ion Implantation Dose Measurement", *Rev. Sci. Instrum.*, 49, 634 (1978).
99. Kalz, A., Storbeck, F., and Blasek, G., "Adsorption of H₂O on α -Fe (111) under the Influence of 2.5 KeV Electrons", *Phys. Status Solidi A*, 50, K247 (1978).
100. Kaminsky, M., and Das, S.K., "Radiation Blistering-Recent Developments", *The Physics of Ionized Gases. Invited Lectures and Progress Reports of SPIG-78*, Dubrovnik, Yugoslavia, 28 Aug. - 2 Sept. 1978. (Beograd, Yugoslavia: Inst. Phys. 1978) p. 401.
101. Karasek, F.W., "Developments in ISS/SIMS", *Res./Dev.*, 29, 26 (1978).
102. Kaufman, H.R., "Technology of Ion Beam Sources Used in Sputtering", *J. Vac. Sci. & Technol.*, 15, 272 (1978).
103. Kaus, G., Kempf, J., Schmid, G., and Schroeck, A., "SIMS Detector", *IBM Tech. Disclosure Bull.*, 21, 669 (1978).
104. Kirkpatrick, C.G., Norton, J.F., Parks, H.G., and Possin, G.E., "New Concepts for Electron-Ion Beam and Electron-Electron Beam Memories", *J. Vac. Sci. & Technol.*, 15, 841 (1978).
105. Kishinevskii, M.E., "Secondary Negative-Ion Emission", *Sov. Phys. Tech. Phys.*, 23, 456 (1978).
106. Kjellsson, L., Svensson, L.E., Sundberg, R., and Dunlop, G.L., "High Temperature Stress Relief Cavitation of an Al-Bearing α -Brass", *J. Mat. Sci.*, 13, 2441 (1978).
107. Komiya, S., "An Introduction of a Theoretical Model for Mechanism of Secondary Ion Emission in SIMS. For Auto-Ionization Process Model", *Mass Spectrosc.*, 26, 113 (1978).
108. Komiya, S., Umez, N., and Narusawa, T., "Formation of Thick Titanium Carbide Films by the Hollow Cathode Discharge Reactive Deposition Process", *Thin Solid Films*, 54, 51 (1978).
109. Komori, K., and Okano, J., "Dependence of the Energy Distribution on the Emission Angle for the Secondary Ions from Polycrystalline Aluminum", *Int. J. Mass Spectrom. & Ion Phys.*, 27, 379 (1978).
110. Konorova, E.A., Sergienko, V.F., Tkachenko, S.D., Dravin, V.A., and Spitsyn, A.V., "Investigation of the Distribution of Ion-Implanted Lithium Atoms in Diamond", *Sov. Phys. Lebedev Inst. Rep.*, No. 4, 9 (1978).
111. Kozlov, V.F., Pistryak, V.M., and Zats, A.V., "On the Nature of Oxygen-Stimulated Emission of Secondary Negative Ions of Some Metals", *Ukr. Fiz. Zh.*, 23, 1994 (1978).
112. Krauss, A.R., and Gruen, D.M., "Energy Analyzed Secondary Ion Mass Spectroscopy and Simultaneous Auger and XPS Measurements of Ion Bombarded Surfaces", *Nucl. Instrum. & Methods*, 149, 547 (1978).
113. Krueger, F.R., and Wien, K., "High Energy Sputtering from Cleaned Metal Foils", *Z. Naturforsch. A*, 33, 638 (1978).
114. Lancaster, G.M., Honda, F., Fukuda, Y., and Rabalais, J.W., "AIB Induced Chemical Reactions at Surfaces Detected by SIMS", *Chem. Phys. Lett.*, 59, 356 (1978).
115. Larere, A., and Roques-Carnes, C., "Intergranular Precipitation Studies by Ion Imaging Microanalyser on Nickel 99.5% After Annealing Treatment at 625 Degrees C", *J. Microsc. & Spectrosc. Electron.*, 3, 485 (1978).
116. Larsson, S.J., Lodding, A., Odelius, H., and Film, G.J., "Application of SIMS: Study of Fluorine in Dental Enamel", *Advances in Mass Spectrometry*, Vol. 7A, N.R. Daly, Ed., (London: The Institute of Petroleum, 1978) p. 797.
117. Lays, J., and Ruscica, R., "New Dimension in Problem Solving (Scanning Electron Microscopy)", *Ind. Rev./Dev.*, 20, 114 (1973).
118. Liao, Z.L., Lau, S.S., Nicolet, M.A., Mayer, J.W., Blattner, R.J., Williams, P., and Evans, C.A., Jr., "Kinetic Aspects of Solid-Phase Epitaxial Growth of Amorphous Si", *Nucl. Instrum. & Methods*, 149, 623 (1978).
119. Lidow, A., Gibbons, J.F., Deline, V.R., and Evans, C.A., Jr., "Ion-Implanted Selenium Profiles in GaAs as Measured by Secondary Ion Mass Spectrometry", *Appl. Phys. Lett.*, 32, 15 (1978).
120. Lidow, A., Gibbons, J.F., Deline, V.R., and Evans, C.A., Jr., "Fast Diffusion of Elevated-Temperature Ion-Implanted Se in GaAs As Measured by Secondary Ion Mass Spectrometry", *Appl. Phys. Lett.*, 32, 149 (1978).

121. Lidow, A., Gibbons, J.F., Deline, V.R., and Evans, C.A., Jr., "Solid Solubility of Selenium in GaAs as Measured by Secondary Ion Mass Spectrometry", *Appl. Phys. Lett.*, **32**, 572 (1978).
122. Liebl, H., "Ion Optics for Surface Analysis", *Inst. Phys. Conf. Ser. No. 38*, 266 (1978).
123. Liebl, H., "Mass Spectrometry of Solids--With Special Emphasis on Probe Sampling", *Mikrochimica Acta* (Wien), **1**, 241 (1978).
124. Liebl, H., "Limits of Lateral Resolution in Ion Probe Microanalysis", *Advances in Mass Spectrometry*, Vol. 7A, N.R. Daly, Ed., (London: The Institute of Petroleum, 1978) p. 751.
125. Liebl, H., "Progress in Secondary Ion Mass Spectrometry Instrumentation", *Advances in Mass Spectrometry*, Vol. 7A, N.R. Daly, Ed., (London: The Institute of Petroleum, 1978) p. 807.
126. Liu, S.G., Wu, C.P., and Magee, C.W., "Annealing of Ion-Implanted GaAs with Nd:Glass Laser", *AIP Conf. Proc.*, No. 50, p. 603 (1978).
127. Lodding, A., Larsson, S.J., and Odelius, H., "Secondary Ion Mass Spectra of Apatites", *Z. Naturforsch. A*, **33**, 697 (1978).
128. Lundquist, T.R., "Energy Distributions of Sputtered Copper Neutrals and Ions", *J. Vac. Sci. & Technol.*, **15**, 684 (1978).
129. MacDonald, R.J., Heiland, W., and Taglauer, E., "A Comparison of Surface Analysis using Ion Scattering, Ion-Produced Photons, and Secondary Ion Emission", *Appl. Phys. Lett.*, **33**, 576 (1978).
130. MacDonald, R.J., and Garrett, R.F., "A Method of Quantitative Analysis Based on Ion Bombardment Induced Secondary Ion and Photon Emission", *Surf. Sci.*, **78**, 371 (1978).
131. Magee, C.W., and Harrington, W.L., "Depth Profiling of Sodium in SiO₂ Films by Secondary Ion Mass Spectrometry", *Appl. Phys. Lett.*, **33**, 193 (1978).
132. Magee, C.W., and Wu, C.P., "Hydrogen Ion Implantation Profiles as Determined by SIMS", *Nucl. Instrum. & Methods*, **149**, 529 (1978).
133. Magee, C.W., Harrington, W.L., and Honig, R.E., "Secondary Ion Quadrupole Mass Spectrometer for Depth Profiling Design and Performance Evaluation", *Rev. Sci. Instrum.*, **49**, 477 (1978).
134. Majni, G., and Ottaviani, G., "Substrate Effects in Si-Al Solid Phase Epitaxial Growth", *Thin Solid Films*, **55**, 235 (1978).
135. Malm, D.L., Vasile, M.J., Padden, F.J., Dove, D.B., and Pantano, C.G., Jr., "Depth Profiles of Sodium and Calcium in Glasses: A Comparison of Secondary Ion Mass Analysis and Auger Spectrometry", *J. Vac. Sci. & Technol.*, **15**, 35 (1978).
136. Marwick, A.D., and Piller, R.C., "The Effect of Irradiation and Sputtering on the Near Surface Composition of Dilute Alloys", Rep. AERE-R9175, UKAEA, Harwell, Oxon., England (July, 1978), 8 pp.
137. Mateescu, G.D., "A Kaleidoscopic View of Recent Advances in ESCA-ISS-SIMS", *Proc. 13th Nat. Conf. of the Microbeam Analysis Soc.*, Ann Arbor Michigan, June, 1978. Paper No. 77.
138. Maul, J., and Fluckiger, U., "Secondary Ion Mass Spectrometry (SIMS), A New Method for the Analysis of Solids", *Kerntechnik*, **20**, 467 (1978).
139. Maul, J.L., "Secondary-Ion Mass Spectrometry", *Electron Anz.*, **10**, 39 (1978).
140. Mayer, J.W., and Poate, J.M., "Depth Profiling Techniques (Thin Film Interdiffusion and Interfacial Reactions)", *Thin Films Interdiffusion and Reactions*, J.M. Poate, K.N. Tu, and J.W. Mayer, Eds., (Chichester, England: Wiley, 1978) p. 119.
141. McCune, R.C., "Characterization of Anodic Barrier Films on Tantalum and 1100 Aluminum by ISS/SIMS", *J. Vac. Sci. & Technol.*, **15**, 31 (1978).
142. McLevige, W.V., Vaidyanathan, K.V., Streetman, B.G., Ilegems, M., Comas, J., and Plew, L., "Annealing Studies of Be-Doped GaAs Grown by Molecular Beam Epitaxy", *Appl. Phys. Lett.*, **33**, 127 (1978).
143. McLevige, W.V., Vaidyanathan, K.V., Streetman, B.G., Comas, J., and Plew, L., "Annealing Studies of Be-Implanted GaAs_{0.6}P_{0.4}", *J. Electron. Mat.*, **7**, 547 (1978).
144. McLevige, W.V., Vaidyanathan, K.V., Streetman, B.G., Comas, J., and Plew, L., "Diffusion Studies of Be-Implanted GaAs by SIMS and Electrical Profiling", *Solid State Commun.*, **25**, 1003 (1978).
145. Meyer, M., Dubois, C., and Barbezat, S., "Comparison of ¹⁸O Concentration Profiles Determined by Secondary Emission of Negative or Positive Ions", *J. Microsc. & Spectrosc. Electron.*, **3**, 477 (1978).
146. Mohri, M., Nakamura, K., Watanabe, K., Yamashina, T., Doi, H., and Hayakawa, K., "Surface Characterization of SiC as a First Wall Material of Fusion Devices by Means of a Combined System of AES-IMA", *J. Vac. Soc. Japan*, **21**, 372 (1978).
147. Mohri, M., Kakibayashi, H., Watanabe, K., and Yamashina, T., "Application of SIMS-FDS-AES Combined System to Surface Studies-Adsorption and Decomposition of Formic Acid over Clean Surface of Nickel", *Appl. Surf. Sci.*, **1**, 170 (1978).
148. Mohri, M., Watanabe, K., and Yamashina, T., "Sputtering Process of a Silicon Carbide Surface with Energetic Ions by Means of an AES-SIMS-Combined System", *J. Nucl. Mat.*, **75**, 7 (1978).
149. Morgan, A.E., and Werner, H.W., "Molecular versus Atomic Secondary Ion Emission from Solids", *J. Chem. Phys.*, **68**, 3900 (1978).
150. Morgan, A.E., and Werner, H.W., "Molecular versus Atomic Secondary Ion Emission and its Implications for Quantitative Analysis", *J. Microsc. & Spectrosc. Electron.*, **3**, 495 (1978).
151. Morgan, A.E., and Werner, H.W., "Semiquantitative Analysis by Secondary Ion Mass Spectrometry Using One Fitting Parameter", *Mikrochimica Acta* (Wien) **II**, 31 (1978).
152. Morgan, A.E., and Werner, H.W., "Modern Methods for Solid Surface and Thin Films Analysis", *Phys. Scr.*, **18**, 451 (1978).
153. Morgan, A.E., and Werner, H.W., "A One Fitting Parameter Method For Quantitative SIMS", *Proc. 13th Nat. Conf. of the Microbeam Analysis Soc.*, Ann Arbor, Michigan, June, 1978. Paper No. 2.
154. Narayan, J., Larson, B.C., and Christie, W.H., "Effect of Thermal Annealing in Boron Implanted, Laser Annealed Silicon", *AIP Conf. Proc.*, **50**, 440 (1978).
155. Newbury, D.E., "On the Accuracy of Quantitative Analysis in Secondary Ion Mass Spectrometry Round Robin Results", *Proc. 13th Nat. Conf. of the Microbeam Analysis Soc.*, Ann Arbor, Michigan, June 1978. Paper No. 6.

156. Newbury, D.E., "Secondary Ion Mass Spectrometry for Particle Analysis", Proc. 13th Nat. Conf. of the Microbeam Analysis Soc., Ann Arbor, Michigan, June 1978. Paper No. 65.
157. Nishimura, H., and Okano, J., "Isotopic Abundance of Nickel in Iron Meteorites Measured with a Sputtering Ion Mass Spectrometer", Advances in Mass Spectrometry, Vol. 7A, N.R. Daly, Ed., (London: The Institute of Petroleum, 1978) p. 569.
158. Oshima, M., Seki, M., and Kawashima, I., "Quantitative Analysis of Na in Si with SIMS", Japan J. Appl. Phys., 17, 1697 (1978).
159. Palmberg, P.W., and Riggs, W.M., "Unique Instrument for Multiple Technique Surface Characterization by ESCA, Scanning Auger, UPS and SIMS", J. Vac. Sci. & Technol., 15, 786 (1978).
160. Pazderskii, V.A., and Tsipinyuk, B.A., "Ionization of an Atom near a Metal Surface", Sov. Phys. Solid State, 20, 1893 (1978).
161. Petersson, L.G., Lodding, A., and Koch, G., "Elemental Microanalysis of Enamel and Dentin by Secondary Ion Mass Spectrometry (SIMS)", Swed. Dent. J. 2, 41 (1978).
162. Phillips, B.F., "Secondary Ion Mass Spectrometry", ASTM Stand. News, 6, 23 (1978).
163. Pivin, J.C., Roques-Carmes, C., and Slodzian, G., "Variation des Rendements D'emission Ionique Secondaire des Alliages Ni-Cr, Fe-Cr, Fe-Ni en Fonction de la Teneur en Solute", Int. J. Mass Spectrom. & Ion Phys., 26, 219 (1978).
164. Pletnev, V.V., "Angular Distribution of Atoms Sputtered from the Surface of an Amorphous Target", Sov. Phys. Solid State, 20, 1950 (1978).
165. Ploong, K., and Fischer, A., "Surface Segregation of Sn During MBE of n-Type GaAs Established by SIMS and AES", J. Vac. Sci. & Technol., 15, 255 (1978).
166. Pollitt, K.R., Robb, J.C., and Thomas, D.W., "Mechanism of Sputtering of Solid Surfaces by Ion-Impact", Nature, 272, No. 5652, 436 (1978).
167. Ponpon, J.P., Grob, J.J., Grob, A., Stuck, R., and Siffert, P., "Interface Studies of Metal-Semiconductor Contacts by Means of SIMS, Nuclear Reaction and RBS", Nucl. Instrum. & Methods, 149, 647 (1978).
168. Potosky, J.C., and Wittry, D.B., "The Secondary Ion Optics of a Quadrupole Ion Microprobe", Proc. 13th Nat. Conf. of the Microbeam Analysis Soc., Ann Arbor, Michigan, June 1978. Paper No. 9.
169. Prival, H.G., "A Model of the Ion Sputtering Process", Surf. Sci., 76, 443 (1978).
170. Rao, E.V.K., Duhamel, N., Favannec, P.N., and L'Haridon, H., "Investigation of Compensation in Implanted n-GaAs", J. Appl. Phys., 49, 3898 (1978).
171. Rieder, K.H., "A Combined SIMS-AES/LEED Study of the Room-Temperature Oxidation of Ni (110) and Ni (111) Surfaces", Appl. Surf. Sci., 2, 74 (1978).
172. Ringo, G.R., and Krohn, V.E., "Possible Applications of a High Brightness Gallium Source to Ion Microprobes", Nucl. Instrum. & Methods, 149, 735 (1978).
173. Rodriguez Murcia, H., and Beske, H.E., "Cluster Emission from Cu-Ni and Cu-Al Alloys", Advances in Mass Spectrometry, Vol. 7A, N.R. Daly, Ed., (London: The Institute of Petroleum, 1978) p. 593.
174. Rudat, M.A., and Morrison, G. H., "Detector Discrimination in SIMS: Ion-to-Electron Converter Yield Factors for Positive Ions", Int. J. Mass Spectrom. & Ion Phys., 27, 249 (1978).
175. Rudat, M.A., and Morrison, G.H., "Instrumental Discrimination Effects in SIMS", Proc. 13th Nat. Conf. of the Microbeam Analysis Soc., Ann Arbor, Michigan, June, 1978. Paper No. 10.
176. Schilling, J.H., and Buger, P.A., "Problems in Elemental Imaging with an Ion Microprobe Mass Analyser", Appl. Phys., 15, 115 (1978).
177. Schilling, J.H., and Buger, P.A., "Problems in Elemental Concentration Depth Profiling with an Ion Microprobe", Int. J. Mass Spectrom. & Ion Phys., 26, 163 (1978).
178. Schilling, J.H., and Buger, P.A., "On Quantifying Images of Element Distributions Obtained with an Ion Microprobe", Int. J. Mass Spectrom. & Ion Phys., 27, 283 (1978).
179. Schilling, J.H., Buger, P.A., and Fidos, H., "Elemental Imaging Facilities of the Ion Microprobe Applied to Nodular Cast Iron", Proc. 13th Nat. Conf. of the Microbeam Analysis Soc., Ann Arbor, Michigan, June, 1978. Paper No. 31.
180. Schilling, J.H., Comins, N.R., and Hengstberger, M.M.E., "Combined Element Depth Profiling with the IMMA and the SEM Based on Wedge Shaped Craters", Electron Microscopy Soc. S. Africa 17th Ann. Conf., Pretoria, South Africa, Dec. 1978. (Joannesburg, South Africa: Electron Microscopy Soc. South Africa, 1978) p. 23.
181. Schubert, R., "Analysis of SnNi Electroplate by Secondary Ion Mass Spectrometry, Ion Scattering Spectrometry, and Rutherford Backscattering", J. Electrochem. Soc., 125, 1215 (1978).
182. Sheretov, E.P., Samodurov, V.F., Kolotilin, B.I., Tuzhilkin, N.K., and Veselkin, N.V., "Three-Dimensional Quadrupole Mass Spectrometer with Elliptical Electrodes", Instrum. & Exp. Tech., 21, 1584 (1978).
183. Shimizu, N., Semet, M.P., and Allegre, C.J., "Geochemical Applications of Quantitative Ion-Microprobe Analysis", Geochimica et Cosmochimica Acta, 42, 1321 (1978).
184. Sidenius, G., "Ion Sources for Low Energy Accelerators", Nucl. Instrum. & Methods, 151, 349 (1978).
185. Slodzian, G., "A Transfer Optic for Microanalysis by Secondary Ion Emission", J. Microsc. & Spectrosc. Electron., 3, 447 (1978).
186. Smith, D.H., and Christie, W.H., "A Comparison of a Theoretical Model and Sensitivity Factor Calculations for Quantification of SIMS Data", Int. J. Mass Spectrom. & Ion Phys., 26, 61 (1978).
187. Smith, J.N., Jr., "Secondary Ion Emission from Stainless Steel and Inconel due to Hydrogen Ion Bombardment", J. Nucl. Mat., 78, 117 (1978).
188. Snowdon, K.J., and MacDonald, R.J., "Secondary Ion Energy Spectra of Polycrystalline Transition Metals and Aluminum", Int. J. Mass Spectrom. & Ion Phys., 28, 233 (1978).
189. Snowdon, K.J., "A Comparison of Experimental Secondary Ion Energy Spectra of Polycrystalline Metals with Theory", Rad. Eff., 38, 141 (1978).
190. Someno, M., Kobayashi, M., Tsunekawa, S., and Saits, H., "Quantitative Analysis of Deuterium in Ti,

- Ti Alloys, Zr, V, Nb and Ta by Ion Microanalyser", *Trans. Japan Inst. Met.*, **19**, 233 (1978).
191. Sparrow, G.R., "Extending SEM Capabilities Using a SIMS Attachment to Chemical Characterization of Semiconductors and Metals", *Scanning Electron Microscopy*, Vol. 1, Om Johari, Ed., (AMF O'Hare IL: Scanning Electron Microscopy Inc., 1978) p. 711.
 192. Sparrow, G.R., "Surface Characterization of Metals, Polymers, and Composites by Combined Techniques: ISS, SIMS, SEM and EDX", *Proc. 13th Nat. Conf. of the Microbeam Analysis Soc.*, Ann Arbor, Michigan, June, 1978. Paper No. 78.
 193. Sroubek, Z., Zavadil, J., Kubec, F., and Zdansky, K., "Model of Ionization of Atoms Sputtered from Solids", *Surf. Sci.*, **77**, 603 (1978).
 194. Staudenmaier, G., Staib, P., Venus, G., and TFR-Group, "Impurity Fluxes in the Scrape off Layer of TFR 400 and TFR 600", *J. Nucl. Mat.*, **76**, 445 (1978).
 195. Stefani, R., "Mass Spectrometry: A Versatile Aid to Inorganic Analysis", *Advances in Mass Spectrometry*, Vol. 7A, N.R. Daly, Ed., (London: The Institute of Petroleum, 1978) p. 729.
 196. Steiger, W., and Rudenauer, F.G., "Quantitative Evaluation of SIMS Spectra Including Spectrum Interpretation and Saha-Eggert Correction", *Advances in Mass Spectrometry*, Vol. 7A, N.R. Daly, Ed., (London: The Institute of Petroleum, 1978) p. 770.
 197. Storbeck, F., "The Influence of Primary Ion Beam Profile on Monolayer Analysis as Studied by SIMS", *Krist. & Tech.*, **13**, 331 (1978).
 198. Storms, H.A., "Selection of Primary Ion Source for SIMS", *Proc. 13th Nat. Conf. of the Microbeam Analysis Soc.*, Ann Arbor, Michigan, June, 1978. Paper No. 7.
 199. Taya, S., Suzuki, M., Tsuyama, H., and Kanomata, I., "Analyses of Silicon Wafers by High-Resolution Secondary Ion Mass Spectrometer", *Int. J. Mass Spectrom. & Ion Phys.*, **27**, 63 (1978).
 200. Taya, S., "Energy and Mass Analyses of Secondary Positive Ions from Silicon Wafer Surfaces", *Mass Spectrosc.*, **26**, 89 (1978).
 201. Taylor, J.A., and Rabalais, J.W., "Molecular Rearrangement and Cluster Formation in the Secondary Ion Mass Spectra (SIMS) of Fluoride Salts", *Surf. Sci.*, **74**, 229 (1978).
 202. Thompson, M.W., "Mechanisms of Sputtering", *The Physics of Ionized Gases. Invited Lectures and Progress Reports of SPIG-78*, Dubrovnik, Yugoslavia, 28 Aug. - 2 Sept. 1978, (Beograd, Yugoslavia: Inst. Phys. 1978) p. 289.
 203. Toulouse, B., Favenec, P.N., Guivarih, A., and Pelous, G., "Physicochemical and Resistivity Studies of Boron-Implanted GaAs", *Gallium Arsenide and Related Compounds 1978* St. Louis, MO, USA, Sept. 1978. (London, England: Inst. Phys., 1979) p. 501.
 204. Tousset, J., "Physical Methods of Surface Characterization", *Vide*, **33**, 201 (1978).
 205. Trihe, J., Borel, J., and Duchemin, J.P., "Characterization of the Silicon-Sapphire Interface", *J. Cryst. Growth*, **45**, 439 (1978).
 206. Truchet, M., and Trottier, S., "Contribution of Electrostatic Filter and Transfer Optic Equipped with Multichannel Plate to the Study of Experimental Epilepsy in Secondary Ions Microanalysis", *J. Microsc. & Spectrosc. Electron.*, **3**, 463 (1978).
 207. Tsai, M.Y., Streetman, B.H., Williams, P., and Evans, C.A., Jr., "Anomalous Migration of Fluorine and Electrical Activation of Boron in BF_2 -Implanted Silicon", *Appl. Phys. Lett.*, **32**, 144 (1978).
 208. Uwamino, Y., Ishizuka, T., Nakajima, K., and Sunahara, H., "Determination of Rare-Earth Oxides Using Ion Microanalyzer", *Rep. Gov. Ind. Res. Inst. Nagoya*, **27**, 75 (1978).
 209. Vasil'ev, M.A., "Theoretical Models for the Mechanism of Secondary Ion-Ion Emission", *Metallofizika*, Kiev, **72**, 3 (1978).
 210. Vasil'ev, M.A., Kosyachkov, A.A., Trofimova, L.N., Cherepin, V.T., and Chuistov, K.V., "Investigation of the Decomposition of Supersaturated Solid Solutions Aluminium-Lithium by the Method of Secondary Ion-Ion Emission", *Fiz. Met. & Metalloved.*, **45**, 1117 (1978).
 211. Vyas, P.D., and Sharma, B.L., "Behavior of Gold in the Vicinity of the Au-Ge/n-GaAs Interface During Annealing", *Thin Solid Films*, **51**, L21 (1978).
 212. Walker, R.S., and Thompson, D.A., "Computer Simulation of Ion Bombardment Collision Cascades", *Rad. Eff.*, **37**, 113 (1978).
 213. Wang, J.C., Wood, R.F., White, C.W., Appleton, B.R., Pronko, P.P., Wilson, S.R., and Christie, W.H., "Dopant Profile Changes Induced by Laser Irradiation of Silicon: Comparison of Theory and Experiment", *AIP Conf. Proc.*, **50**, 123 (1978).
 214. Watanabe, K., Hashiba, M., and Yamashina, T., "Quantitative In-Depth Profile of Passivated Oxide Layers of GaAs by AES-SIMS—a Comparison of Thermal, Anodic, and Plasma Oxidations", *Japan. J. Appl. Phys.*, Suppl. 17-1, 335 (1978).
 215. Weller, R.A., and Tombrells, T.A., "Energy Spectrum of Sputtered Uranium—A New Technique", *Rad. Eff.*, **37**, 83 (1978).
 216. Werner, H.W., and Morgan, A.E., "Secondary Ion Mass Spectrometry", *Ned. Tijdschr. Natuurkd. A*, **44**, 122 (1978).
 217. Werner, H.W., and Morgan, A.E., "Some Considerations Regarding the Applicability of the Saha-Eggert Equation to Quantitative SIMS Analysis", *Advances in Mass Spectrometry*, Vol. 7A, N.R. Daly, Ed., (London: The Institute of Petroleum, 1978) p. 764.
 218. Werner, H.W., "Round Table on Comparison of Secondary Ion Mass Spectrometry with Other Analytical Methods", *Advances in Mass Spectrometry*, Vol. 7A, N.R. Daly, Ed., (London: The Institute of Petroleum, 1978) p. 804.
 219. Werner, H.W., "Introduction to Secondary Ion Mass Spectrometry (SIMS)", *Electron and Ion Spectroscopy of Solids*, L. Fiermans, J. Vennik, and W. Dekeyser, Eds., (New York, NY: Plenum Press, 1978) p. 324.
 220. White, C.W., Christie, W.H., Appleton, B.R., Wilson, S.R., Pronko, P.P., and Magee, C.W., "Redistribution of Dopants in Ion-Implanted Silicon by Pulsed-Laser Annealing", *Appl. Phys. Lett.*, **33**, 662 (1978).

221. Whitton, J.L., Tanovic, L., and Williams, J.S., "The Production of Regular Pyramids on Argon Ion Bombarded Surfaces of Copper Crystals", *Appl. Surf. Sci.*, **1**, 408 (1978).
222. Whitton, J.L., "Sputtering as a Means of Depth Profiling", *The Physics of Ionized Gases. Invited Lectures and Progress Reports of SPIG-78*, Dubrovnik, Yugoslavia, 28 Aug. - 2 Sept. 1978 (Beograd, Yugoslavia: Inst. Phys. 1978) p. 335.
223. Williams, P., and Evans, C.A., Jr., "Depth Profile Detection Limit of 3×10^{15} Atom cm^{-3} for As in Si Using Cs^+ Bombardment Negative Secondary Ion Mass Spectrometry", *Appl. Phys. Lett.*, **30**, 559 (1978).
224. Williams, P., Lewis, R.K., Evans, C.A., Jr., and Hanley, P.R., "Improvements in the Chemistry of Secondary Ion Mass Spectrometry-negative Ion Techniques", *Nucl. Instrum. & Methods*, **149**, 567 (1978).
225. Williams, P., and Evans, C.A., Jr., "Anomalous Enhancement of Negative Sputtered Ion Emission by Oxygen", *Surf. Sci.*, **78**, 324 (1978).
226. Williams, P., "Mechanism of Oxygen Enhancement of Sputtered Ion Yields", *Proc. 13th Nat. Conf. of the Microbeam Analysers Soc.*, Ann Arbor, Michigan, June, 1978. Paper No. 1.
227. Wilsch, H., "Surface Analysis: Aspects of Atomic Beam Scattering, Secondary Ion Mass Spectroscopy and Vibrational Spectroscopies", *Festkorperprobleme XVIII (Advances in Solid State Phys.)* J. Treusch Ed., (Wiesbaden, Germany: Friedr. Vieweg & Sohn, 1978) p. 109.
228. Winograd, N., Harrison, D.E., Jr., and Garrison, B.J., "Structure Sensitive Factors in Molecular Cluster Formation by Ion Bombardment of Single Crystal Surfaces", *Surf. Sci.*, **78**, 467 (1978).
229. Wittmaack, K., and Schulz, F., "Depth Resolution in Sputter Profiling: Evidence Against the Sequential Layer Sputtering Model", *Thin Solid Films*, **52**, 259 (1978).
230. Wittmaack, K., "Characteristics of the DIDA Scanning Ion Microprobe", *Advances in Mass Spectrometry*, Vol. 7A, N.R. Daly, Ed., (London: The Institute of Petroleum, 1978) p. 758.
231. Wittmaack, K., "Principles and Practice of SIMS Microanalysis", *Proc. 13th Nat. Conf. of the Microbeam Analysis Soc.*, Ann Arbor, Michigan, USA, June, 1978. Paper No. 11.
232. Wittry, D.B., and Whatley, T.A., "Energy Distribution of Positive Ions of Group III and Group V Elements Sputtered from Semiconductors", *Proc. 13th Nat. Conf. of the Microbeam Analysis Soc.*, Ann Arbor, Michigan, June, 1978. Paper No. 3.
233. Wittry, D.B., "Optimization of Recording Secondary Ion Mass Spectra", *Proc. 13th Nat. Conf. of the Microbeam Analysis Soc.*, Ann Arbor, Michigan, June, 1978. Paper No. 11.
234. Wright, R.B., Liu, M.B., and Gruen, D.M., "Chemical Effects on Secondary Photon and Ion Emission of Ion Bombarded Beryllium, Carbon and Boron Carbide Surfaces", *J. Nucl. Mat.*, **76 & 77**, 205 (1978).
235. Yamamura, Y., and Kitazoe, Y., "Computer Simulation of Cascade Development in Amorphous Targets", *Rad. Eff.*, **39**, 251 (1978).
236. Yamashina, T., Mohri, M., Watanabe, K., Doi, H., and Hayakawa, K., "Application of AES-SIMS (IMA)-FDS Combined Systems to Physical and Chemical Sputtering Processes of Graphite and Silicon Carbide Surfaces with Energetic Ions", *J. Nucl. Mat.*, **76 & 77**, 202 (1978).
237. Young, R.T., White, C.W., Clark, G.J., Narayan, J., Christie, W.H., Nurakami, M., King, P.W., and Kramer, S.D., "Laser Annealing of Boron-Implanted Silicon", *Appl. Phys. Lett.*, **32**, 139 (1978).
238. Yu, M.L., "Effect of Primary Ion Energy and Surface Chemistry on the Secondary Ion Yields in Low-Energy SIMS Experiments", *J. Vac. Sci. & Technol.*, **15**, 668 (1978).
239. Yu, M.L., "Isotope Effect in the Study of H-W(100) and O-W(100) Chemisorption Systems Using SIMS", *Nucl. Instrum. & Methods*, **149**, 559 (1978).
240. Yu, M.L., "Work-Function Dependence of Negative-Ion Production during Sputtering", *Phys. Rev. Lett.*, **40**, 574 (1978).
241. Yu, M.L., "The SIMS Spectrum of the O-W(100) Chemisorption System", *Surf. Sci.*, **71**, 121 (1978).
242. Zhao, L.Z., "Rapidly Developing Methods of Surface Analysis", *Wuli*, **7**, 18 (1978).
243. Ziegler, F., Wu, C.P., Williams, P., White, C.W., Terreault, B., Scharzer, B.M.U., Schulte, R.L., Schneid, E.J., Magee, C.W., Liglon, E., L'Ecuyer, J., Lanford, W.A., Kuehne, F.J., Kamykowski, E.A., Hofer, W.O., Guivarch, A., Brassard, C.H.C., Blewer, R.S., Behrisch, R., Appleton, B.R., and Allred, D.D., "Profiling Hydrogen in Materials Using Ion Beams", *Nucl. Instrum. & Methods*, **149**, 19 (1978).
244. Ziegler, E., Siegel, W., Kuhnel, G., and Buhrig, E., "Incorporation of Gallium in ZnSiP_2 ", *Phys. Status Solidi A*, **48**, K63 (1978).
245. Zinner, E., "The Effect of Preferential Sputtering on Ion Microprobe Depth Profiles in Minerals", *Proc. 13th Nat. Conf. of the Microbeam Analysers Soc.*, Ann Arbor, Michigan, June, 1978. Paper No. 32.

1979

1. Abbrecht, P.H., Badman, W.S., Cassman, M., and Stryer, L., "Biomedical Instrumentation Development: Recommendations of a Workshop on the Status and Future of Biophysical and Biochemical Instrumentation", *Am. Lab.*, **11**, 53 (1979).
2. Afrikanov, I.N., Gusev, V.M., Guseva, M.I., Mansurova, A.N., Martynenko, Yu. V., Morozov, V.N., and Chelnokov, O.I., "Helium Blistering under High Irradiation Doses", *Sov. At. Energy*, **46**, 190 (1979).
3. Alimov, V. Kh., Gorodetskii, A.E., and Zakharov, A.P., "Helium Accumulation and Distribution in Molybdenum Bombarded by He^+ Ions at 1-9 KeV", *Sov. Phys. Tech. Phys.*, **24**, 705 (1979).
4. Andersen H.H., "The Depth Resolution of Sputter Profiling", *Appl. Phys.*, **18**, 131 (1979).
5. Arifuku, F., Yoneyama, H., and Tamura, H., "Distribution Profiles of Antimony as a Function of Depth in Corrosion Films on a Pb-Sb Alloy", *J. Appl. Electrochem.*, **9**, 629 (1979).
6. Arita, M., Hosoya, M., Kobayashi, M., and Someno, M., "Depth Profile Measurement by Secondary Ion Mass Spectrometry for Determining the Tracer Diffusivity of Oxygen in Rutile", *J. Am. Ceram. Soc.*, **62**, 443 (1979).
7. Armstrong, T.R., "The onset of Radiation-Blistering in Low-Temperature D^+ -Irradiated Copper", *J. Nucl. Mat.*, **84**, 118 (1979).
8. Asano, M., Kimura, H., and Kubo, K., "Determinations of Gains of Electron Multiplier by Pulse Count-

- ing Method", *Mass Spectrosc.*, 27, 157 (1979).
9. Auciello, O., and Kelly, R., "Bombardment-Induced Surface Topography: Latest Experimental Results", *J. Electrochem. Soc.*, 126, 343C (1979).
10. Auciello, O., Kelly, R., and Iricibar, R., "On the Problem of the Stability of Pyramidal Structures on Bombarded Copper Surfaces", *Rad. Eff. Lett.*, 43, 37 (1979).
11. Auciello, O., "Further Experimental Evidence on the Importance of Tertiary Effects in the Evolution of Pyramids on Bombarded Copper", *Rad. Eff. Lett.*, 43, 117 (1979).
12. Auciello, O., and Kelly, R., "On the Relative Stability of Different Topographical Features Developed on Bombarded Copper Surfaces", *Rad. Eff. Lett.*, 43, 187 (1979).
13. Avakov, A.S., Veksler, V.I., and Tsipinyuk, B.A., "Anomalies in the Secondary Ion Emission of Vanadium", *Sov. Phys. Tech. Phys.*, 24, 746 (1979).
14. Bajpai, R.P., and Garg, R.K., "Instruments for Analysis and Imaging of Atomically Clean Surfaces", *CSIO Commun.*, 6, no. 4, 83 (1979).
15. Balashova, L.L., Borisov, A.M., Dodonov, A.I., Mashkova, E.S., and Molchanova, V.A., "Effect of Surface Subchannels on the Energy Distribution of Fast Ionized Recoil Atoms", *Sov. Tech. Phys. Lett.*, 5, 159 (1979).
16. Bay, H.L., and Bohdansky, J., "Sputtering Yields for Light Ions as a Function of Angle of Incidence", *Appl. Phys.*, 19, 421 (1979).
17. Belyi, I.M., Komarov, F.F., Openchuk, E.G., and Shiryaev, S. Yu., "Structural and Phase Changes in Aluminum Films during Bombardment with Nitrogen and Oxygen Ions", *Sov. Phys. Crystallogr.*, 24, 233 (1979).
18. Benninghoven, A., Beckmann, P., Muller, K.H., and Schemmer, M., "Investigation of Multi-component Surface Reactions by SIMS: Interaction Between Hydrogen and Oxygen on Polycrystalline Nickel", *Surf. Sci.*, 89, 701 (1979).
19. Benninghoven, A., Evans, C.A., Jr., Powell, R.A., Shimizu, R., and Storms, H.A., Eds., *Secondary Ion Mass Spectrometry SIMS II*, (New York: Springer-Verlag, 1979).
20. Beynon, J.H., Morgan, R.P., and Brenton, A.G., "New Methods of Identifying Organic Compounds (Mass Spectrometry)", *Philos. Trans. R. Soc. London A*, 293, 157 (1979).
21. Bispinck, H., Ganschow, O., Wiedmann, L., and Benninghoven, A., "Combined SIMS, AES, and XPS Investigation of Tantalum Oxide Layers", *Appl. Phys.*, 18, 113 (1979).
22. Bitenskii, I.S., Murakhmetov, M.N., and Parilis, E.S., "Sputtering of Nonmetals by Intermediate-Energy Multiply Charged Ions through a Coulomb 'Explosion'", *Sov. Phys. Tech. Phys.*, 24, 618 (1979).
23. Blaise, G., and Nourtier, A., "Experimental and Theoretical Approaches to the Ionization Process in Secondary-Ion Emission", *Surf. Sci.*, 90, 495 (1979).
24. Blank, P., and Wittmaack, K., "Energy and Fluence Dependence of the Sputtering Yield of Silicon Bombarded with Argon and Xenon", *J. Appl. Phys.*, 50, 1519 (1979).
25. Blasek, G., and Weihert, M., "A Study of the Initial Oxidation of Chromium-Nickel Steel by SIMS", *Surf. Sci.*, 82, 215 (1979).
26. Bodhansky, J., Roth, J., and Brossa, F., "Formation of Various Coatings and their Behavior under Particle Bombardment", *J. Nucl. Mat.*, 85-86, 1145 (1979).
27. Bordoli, R.S., Vickerman, J.C., and Wolstenholme, J., "Surface Coverage Measurements by SIMS for CO Adsorption on a Number of Metals and for CO and H₂S CO-Adsorption on Ni(110) and (111)", *Surf. Sci.*, 85, 244 (1979).
28. Bourgoïn, J.C., Krynicki, J., and Blanchard, B., "Boron Concentration and Impurity-to-Band Activation Energy in Diamond", *Phys. Status Solidi A*, 52, 293 (1979).
29. Brandeis, C., Greschner, J., Kempf, J., and Schmid, G.E., "Determination of Doping Profiles by Means of SIMS Analysis", *IBM Tech. Disclosure Bull.*, 21, 3241 (1979).
30. Braun, M., Emmoth, B., and Whitton, J.L., "Helium Induced Surface Exfoliation of Aluminium and the Correlation between Flake Thickness and Ion Energy in the Range 10-80 KeV", *J. Nucl. Mat.*, 85-86, 1091 (1979).
31. Bresse, J.F., and Rossi, A., "Microanalysis of Thin Layers of Metallic Compounds Deposited on a Substrate", *J. Microsc. & Spectrosc. Electron.*, 4, 311 (1979).
32. Bubulac, L.O., Tennant, W.E., Shin, S.H., Wang, C.C., Lanir, M., Gertner, E.R., and Marshall, E.D., "Ion Implantation Study of HgCdTe", *Japan. J. Appl. Phys.*, 19, Suppl. 19-1, 495 (1979).
33. Buchmann, P., and Baumgartner, W., "Adaptor-Unit for Secondary-Ion Analysis by Quadrupole Mass-Filter", *Helv. Phys. Acta*, 52, 63 (1979).
34. Burns, M.S., "Secondary Ion Mass Spectrometry: Applications to Biological Problems", *Proc. 14th Ann. Conf. of the Microbeam Analysis Soc.*, San Antonio, Texas, Aug. 1979. *Microbeam Analysis*, D.E. Newbury, Ed., (San Francisco, CA: San Francisco Press Inc., 1979) p. 61.
35. Carlson, D.E., Magee, C.W., and Triano, A.R., "The Effect of Hydrogen Content on the Photovoltaic Properties of Amorphous Silicon", *J. Electrochem. Soc.*, 126, 688 (1979).
36. Carter, G., Armour, D.G., Ingram, D.C., Webb, R., and Newcombe, R., "Diffusion Approximations to Cascade Mixing", *Rad. Eff. Lett.*, 43, 233 (1979).
37. Carter, G., Fischer, G., Webb, R., Dzioba, S., Kelly, R., and Auciello, O., "On the Surface-Normal Energy Distribution of Sputtered Recoils", *Rad. Eff.*, 45, 45 (1979).
38. Chadderton, L.T., "The Stability of Cones and Pyramids on Sputtered Surfaces of Copper", *Rad. Eff. Lett.*, 43, 91 (1979).
39. Champigny, M., Maurice, F., Meny L., and Seguin, R., "Analysis of Boron in a Non-Oxidizable Austenitic Steel by Secondary Ion Emission and X-Ray Microanalysis", *J. Microsc. & Spectrosc. Electron.*, 4, 163 (1979).
40. Chen, D.R., and Eisen, F.H., "Ion Implanted High Frequency High Speed GaAs Integrated Circuits Technology", *J. Vac. Sci. Technol.*, 16, 2054 (1979).
41. Chirulescu, T., "Applications of Secondary Ion Mass Spectrometry to the Investigation of Solid Surfaces", *Stud. & Cercet. Fiz.*, 31, 1115 (1979).

42. Christou, A., "Interdiffusion in Au-Refractory Thin Film Systems Studied by a Combination of Scattering Techniques", Scanning Electron Microscopy, Vol. 1, Om Johari, Ed., (AMF O'hare, IL: Scanning Electron Microscopy, Inc., 1979) p. 191.
43. Christie, W.H., Eby, R.E., Anderson, R.L., and Kollie, T.G., "Ion Microprobe Investigation of De-calibrated Chromel versus Alumel Thermocouples: A Quantitative SIMS Analysis using Indexed Sensitivity Factors and Oxygen Flooding", Appl. Surf. Sci., 3, 329 (1979).
44. Coburn, J.W., "The Influence of Ion Sputtering on the Elemental Analysis of Solid Surfaces", Thin Solid Films, 64, 371 (1979).
45. Coles, J.N., "A Study of the Feasibility of a Surface Plasma Influencing Secondary Ion and Photon Emission under Medium-Energy Ion Bombardment", Surf. Sci., 79, 549 (1979).
46. Colligon, J.S., and Kiriakidis, G., "Effect of Impurities on SIMS", Vacuum, 29, 357 (1979).
47. Colton, R.J., and Murday, J.S., "Static SIMS of Amino Acid Overlayers", J. Vac. Sci. Technol., 16, 519 (1979).
48. Colton, R.J., Murday, J.S., Wyatt, J.R., and Decorpo, J.J., "Combined XPS and SIMS Study of Amino Acid Overlayers", Surf. Sci., 84, 235 (1979).
49. Crawford, C.K., "Charge Neutralization Using Very Low Energy Ions", Scanning Electron Microscopy, Vol. 2, Om Johari, Ed., (AMF O'Hare, IL: Scanning Electron Microscopy Inc., 1979) p. 31.
50. Danilin, B.S., Kireey, V. Yu., and Sychin, V.K., "Energy Efficiency of Process of Ion Sputtering of Materials and Systems for Carrying it out", Fiz. & Khim. Obrab. Mater., no. 2, 52 (1979).
51. Das, S.K., Kaminsky, M., and Fenske, G., "On the Correlation of Blister Diameter and Blister Skin Thickness in Helium Ion-Irradiated Nb", J. Appl. Phys., 50, 3304 (1979).
52. Das, S., Kaminsky, M., Gusev, V.M., Guseva, M.I., Krasulin, Yu. L., and Martynenko, Yu. V., "Blistering in Niobium under Implantation of Helium Ions at Energy Expected in a Thermonuclear Reactor", Sov. At. Energy, 46, 185 (1979).
53. Dawson, P.H., "An AES and SIMS Study of the CO-Adsorption of CO₂ and O₂ on Molybdenum", J. Vac. Sci. Technol., 16, 1 (1979).
54. Dawson, P.H., and Tam, W.C., "A Comparison of Low Energy SIMS and AES in a Study of the Interaction of Oxygen with Polycrystalline Nickel", Surf. Sci., 81, 164 (1979).
55. Dawson, P.H., and Tam, W.C., "The Interaction of Oxygen with Polycrystalline Niobium Studied Using AES and Low-Energy SIMS", Surf. Sci., 81, 464 (1979).
56. Degreve, F., Figaret, R., and Laty, P., "Depth Profiling by Ion Microprobe with High Mass Resolution", Int. J. Mass Spectrom. Ion Phys., 29, 351 (1979).
57. De Wit, A.G.J., Bronckers, R.P.N., Hupkens, Th.M., and Fluit, J.M., "Investigation of Oxygen Adsorption on Cu (110) by Low-Energy Ion Bombardment", Surf. Sci., 90, 676 (1979).
58. Dowsett, M.G., and Parker, E.H.C., "Study of Low Coverage Adsorption on Cleaved (110) InP Surfaces Using SIMS", J. Vac. Sci. Technol., 16, 1207 (1979).
59. Drechsler, M., Hoinkes, H., Kaarmann, H., Wilsch, H., Ertl, G., and Weiss, M., "Interaction of NH₃ with Fe(110): Identification of Surface Species by Means of Secondary Ion Mass Spectroscopy (SIMS)", Appl. Surf. Sci., 3, 217 (1979).
60. Drzal, L.T., Mescher, J.A., and Hall, D.L., "The Surface Composition and Energetics of Type HM Graphite Fibers", Carbon, 17, 375 (1979).
61. Dzhemaliev, N. Kh., Kurbanov, R.I., "Investigation of Sputtering of Copper in the Form of Clusters", Bull. Acad. Sci. USSR. Phys. Ser., 43, 132 (1979).
62. Evans, C.A., Jr., Deline, V.R., Sigmon, T.W., and Lindow, A., "Redistribution of Cr During Annealing of ⁸⁰Se-Implanted GaAs", Appl. Phys. Lett., 35, 291 (1979).
63. Evans, C.A., Jr., Deline, V.R., Sigmon, T.W., and Lindow, A., "Gettering of Cr by Residual Damage and Encapsulant Stress in Ion Implanted Semi-Insulating GaAs", J. Electrochem. Soc., 126, 360C (1979).
64. Fassett, J.D., Drummer, D.M., and Morrison, G.H., "A Computerized System for the Digital Image Processing of Ion Microscope Images", Anal. Chim. Acta, 112, 165 (1979).
65. Favennec, P.N., and L'Haridon, H., "Implantation of Shallow Impurities in Cr-Doped Semi-Insulating GaAs", Appl. Phys. Lett., 35, 699 (1979).
66. Fisher, D.G., and Olsen, G.H., "Properties of High Sensitivity GaP/In_xGa_{1-x}P/GaAs: (Cs-0) Transmission Photocathodes", J. Appl. Phys., 50, 2930 (1979).
67. Fleish, T., Ott, G.L., Delgass, W.N., and Winograd, N., "Chemisorption of CO on Ni (100) by SIMS and XPS", Surf. Sci., 81, 1 (1979).
68. Frenzel, H., and Balk, P., "Structure and Composition of the Si/SiO₂ Interfacial Region on TCE/O₂ and CCl₄/O₂ Oxidized Silicon", J. Vac. Sci. & Technol., 16, 1454 (1979).
69. Galle, P., Berry, J.P., and Lefevre, R., "Microanalysis in Biology and Medicine. A Review of Results Obtained with Three Microanalytical Methods", Scanning Electron Microscopy, Om Johari and R.P. Becker, Eds., (AMF O'Hare, IL: Scanning Electron Microscopy Inc., 1979) p. 703.
70. Garrison, B.J., Winograd, N., and Harrison, D.E., Jr., "Classical Trajectory Calculations of Energy Distribution of Ejected Atoms from Ion Bombarded Single Crystal", Surf. Sci., 87, 101 (1979).
71. Garrison, B.J., "Theory of Ion Scattering from Single Crystal", Surf. Sci., 87, 683 (1979).
72. Gat, A., Magee, T.J., Peng, J., Deline, V.R., and Evans, C.A., Jr., "CW Laser Annealing of Boron and Arsenic-Implanted Silicon; Electrical Properties, Crystalline Structure and Limitations", Solid State Technol., 22, 59 (1979).
73. Gaworzewski, P., Kalman, L., Rausch, H., and Trapp, M., "Doping Profile Techniques for Epitaxial Layers", J. Rad. Chem., 52, 93 (1979).
74. Georges, J.M., Montes, H., and Martin, J.M., "Applications of Surface Analysis to Problems of Lubrication", Vide Les Couches Minces, 34, 163 (1979).
75. Georgiev, V.K., and Petrov, I.N., "Effect of High-Temperature Treatments in Oxidative and Inert Media on the Distribution Profiles of Uniformly Boron-Doped Silicon", Bulg. J. Phys., 6, 49 (1979).
76. Ghose, D., "On the Angular Dependence of Sputtering Yield", Japan. J. Appl. Phys., 18, 1847 (1979).

77. Giber, J., Riedel, M., and Solyom, A., "New Results and Possibilities in Quantitative Secondary Ion Mass Spectrometry Investigations", *Magy. Fiz. Foly.*, 27, 579 (1979).
78. Golecki, I., Nicolet, M.A., Tandon, J.L., Asbeck, P.M., Sadana, D.K., and Washburn, J., "Transient Annealing of GaAs by Electron and Laser Beams", *J. Electrochem. Soc.*, 126, 361C (1979).
79. Gossink, R.G., and Lommen, T.P.A., "Secondary Ion Mass Spectrometry (SIMS) Analysis of Electron-Bombarded Soda-Lime-Silica Glass", *Appl. Phys. Lett.*, 34, 444 (1979).
80. Gossink, R.G., De Grefte, H.A.M., and Werner, H.W., "SIMS Analysis of Aqueous Corrosion Profiles in Soda-Lime-Silica Glass", *J. Am. Ceram. Soc.*, 62, 4 (1979).
81. Gourgout, J.M., Lepareur, M., and Conty, C., "Use of the IMS 3F High Mass Resolving Power", *Proc. 14th Ann. Conf. of the Microbeam Analysis Soc.*, San Antonio, Texas, Aug. 1979, *Microbeam Analysis*, D.E. Newbury, Ed., (San Francisco, CA: San Francisco Press Inc., 1979) p. 343.
82. Guo, F., and Wittry, D.B., "Secondary-Ion Mass Spectrometry Using Selected Primary Ions and Variation of the Partial Pressure of Selected Gases in the Specimen Region", *Proc. 14th Ann. Conf. of the Microbeam Analysis Soc.*, San Antonio, Texas, Aug. 1979, *Microbeam Analysis*, D.E. Newbury, Ed., (San Francisco, CA: San Francisco Press Inc., 1979) p. 333.
83. Habraken, L., Shungu, T.D., and Leroy, V., "Influence of Surface Segregation on Metallurgical Properties", *Vide Les Couches Minces*, 34, 385 (1979).
84. Hage-Ali, M., Stuck, R., Saxena, A.N., and Siffert, P., "Studies of CdTe Surfaces with Secondary Ion Mass Spectrometry, Rutherford Backscattering and Ellipsometry", *Appl. Phys.*, 19, 25 (1979).
85. Hart, R.G., and Copper, C.B., "Investigation of the Binary Model of Scattering of 1 KeV to 25 eV Ar⁺ Ions from a Cu Surface", *Surf. Sci.*, 82, L283 (1979).
86. Hehenkamp, Th., Ludecke, D., and Manz, M., "Some Applications of the Analysis of Thin Films in Metallurgy and Metal Physics", *Mikrochimica Acta* (Wien), Suppl. 8, 361 (1979).
87. Hennequin, J.F., and Couchouron, M., "An Apparatus for Surface Ionisation of Ion Sputtered Products", *Rev. Phys. Appl.*, 14, 993 (1979).
88. Hennequin, J.F., and Couchouron, M., "Application of Surface Ionisation to the Analysis of the Products of Sputtering", *J. Microsc. & Spectrosc. Electron.*, 4, 513 (1979).
89. Hertel, B., "Electron Microscopy Study of Defects in Copper after 5 KeV Argon Irradiation", *Philos. Mag. A*, 40, 331 (1979).
90. Hewitt, R.W., Shepard, A.T., Baitinger, W.E., Winograd, N., and Delgass, W.N., "Instrument Combining X-Ray Photoelectron Spectroscopy and Secondary Ion Mass Spectrometry for Surface Studies", *Rev. Sci. Instrum.*, 50, 1386 (1979).
91. Hieber, H., "The Early Stage in the Recovery and Diffusion of Gold Sandwiches", *Thin Solid Films*, 57, 108 (1979).
92. Hildebrandt, D., and Manns, R., "Angular Distribution of the Kinetic Energy Re-Emitted during Ion Bombardment", *Rad. Eff.*, 41, 193 (1979).
93. Hinkel, H., Kaus, G., and Kempf, J., "Analysis of Doped Silicon by Combined SIMS-RBS", *IBM Tech. Disclosure Bull.*, 22, 621 (1979).
94. Hirao, T., Inoue, K., Takayanagi, S., and Yaegashi, Y., "The Concentration Profiles of Projectiles and Recoiled Nitrogen in Si after Ion Implantation through Si₃N₄ Films", *J. Appl. Phys.*, 50, 193 (1979).
95. Hirao, T., Inoue, K., Yaegashi, Y., and Takayanagi, S., "The Concentration Profiles of Phosphorus, Arsenic and Recoiled Oxygen Atoms in Si by Ion Implantation into SiO₂-Si", *Japan. J. Appl. Phys.*, 18, 647 (1979).
96. Holland, S.P., Garrison, B.J., and Winograd, N., "Surface Structure from Angle-Resolved Secondary-Ion Mass Spectrometry: Oxygen on Cu(001)", *Phys. Rev. Lett.*, 43, 220 (1979).
97. Holloway, P.H., and Nelson, G.C., "Preferential Sputtering of Ta₂O₅ by Argon Ions", *J. Vac. Sci. & Technol.*, 16, 793 (1979).
98. Honda, F., Fukuda, Y., and Rabalais, J.W., "Clustering Distances Critical to Metal Dimer Formation in the Secondary Ion Mass Spectra (SIMS) of Cesium Chloride", *J. Chem. Phys.*, 70, 4834 (1979).
99. Hopster, H., and Brundle, C.R., "Use of SIMS for Studies of Adsorption on Well-Defined Metal Surfaces. I. Combined XPS/LEED/SIMS Studies of O₂, CO, H₂O, and H₂ on Ni(100)", *J. Vac. Sci. & Technol.*, 16, 548 (1979).
100. Hosaka, S., Sakudo, N., and Hashimoto, S., "Monitoring Secondary Ions During Ion Etching", *J. Vac. Sci. & Technol.*, 16, 913 (1979).
101. Huber, A.M., Morillot, G., Linh, N.T., Favennec, P.N., Deveaud, B., and Toulouse, B., "Chromium Profiles in Semi-insulating GaAs after Annealing with a Si₃N₄ Encapsulant", *Appl. Phys. Lett.*, 34, 858 (1979).
102. Huber, A.M., Linh, N.T., Valladon, M., Debrun, J.L., Martin, G.M., Mitonneau, A., and Mircea, A., "Direct Evidence for the Nonassignment to Oxygen of the Main Electron Trap in GaAs", *J. Appl. Phys.*, 50, 4022 (1979).
103. Huber, A., Morillot, G., and Merenda, P., "Application of Ionic Analysis to Semiconductor Materials", *J. Microsc. & Spectrosc. Electron.*, 4, 493 (1979).
104. Inoue, K., Hirao, T., Takayanagi, S., and Yaegashi, Y., "Asymmetrical Profiles of Ion Implanted Phosphorus in Silicon", *Japan. J. Appl. Phys.*, 18, 367 (1979).
105. Ishitani, T., and Tamura, H., "Simple Model for Surface Composition Changes of Alloys and Compounds by Ion Bombardment", *Rad. Eff. Lett.*, 43, 149 (1979).
106. Ivansva, L.P., and Shpak, E.V., "Nonzero-Emittance Beams in a System with Quadrupole Lenses and Sector Magnets", *Sov. Phys. Tech. Phys.*, 24, 492 (1979).
107. Johar, S.S., and Thompson, D.A., "Spike Effects in Heavy-Ion Sputtering of Ag, Au and Pt Thin Films", *Surf. Sci.*, 90, 319 (1979).
108. Johnson, P.B., and Mazey, D.J., "Helium Gas-Bubble Superlattice in Copper and Nickel", *Nature*, 281, 359 (1979).
109. Joite, S., Hoinkes, H., Kaarmann, H., and Wilsch, H., "SIMS on ZnO Surfaces: The Influence of

- Space Charge Accumulation Layers on Secondary Ion Yields and Measurement of True Hydrogen Concentration", *Surf. Sci.*, **84**, 462 (1979).
110. Joshi, A., Hartsough, L.D., and Denison, D.R., "Segregation Effects in Thin Films", *Thin Solid Films*, **64**, 409 (1979).
 111. Joyes, P., "A Model for the Secondary Emission of Slow Ions", *C.R. Hebd. Seances Acad. Sci. Ser. B*, **288**, 155 (1979).
 112. Joyes, P., Leleyter, M., and Hoareau, A., "Electronic Properties of Cr_pC_n and Fe_pC_n Clusters Investigated by Mass Spectrometry", *J. Phys. Lett.*, **40**, L131 (1979).
 113. Kakibayashi, H., Mohri, M., Watanabe, K., and Yamashina, T., "Surface Segregation and Growth Process of Altered Layer on Cu-Ni Clean Surfaces", *J. Vac. Soc. Japan*, **22**, 220 (1979).
 114. Kalin, B.A., Skorov, D.M., and Yakushin, V.L., "Effects of Ion-Bombardment Dose and Previous Surface Treatment on the Erosion of Molybdenum", *Sov. At. Energy*, **47**, 562 (1979).
 115. Kaminsky, M., and Das, S.K., "Surface Damage of TiB_2 and C Coatings under Energetic D^+ and $^4\text{He}^+$ Irradiations", *J. Nucl. Mat.*, **85-86**, 1095 (1979).
 116. Kamykowski, E.A., Kuehne, F.J., Schneid, E.J., and Schulte, R.L., "Application of Bulk Hydrogen Standards to the Calibration of Ion Beam Surface Analysis", *Nucl. Instrum. Methods*, **165**, 573 (1979).
 117. Kang, S.T., Shimizu, R., and Okutani, T., "Sputtering of Si with KeV Ar^+ Ions. I. Measurement and Monte Carlo Calculations of Sputtering Yield", *Japan. J. Appl. Phys.*, **18**, 1717 (1979).
 118. Kang, S.T., Shimizu, R., and Okutani, T., "Sputtering of Si with KeV Ar^+ Ions. II. Computer Simulation of Sputter Broadening due to Ion Bombardment in Depth Profiling", *Japan. J. Appl. Phys.*, **18**, 1987 (1979).
 119. Katzeff, J.S., "Ion-Implanted Laser Annealed Silicon Solar Cells", *Proc. Soc. Photo-Opt. Instrum. Eng.*, **198**, 42 (1979).
 120. Kaus, G., Kempf, J., Schmid, G., Schmid, G.E., and Seybold, D., "Measuring Potential Steps in Semiconductors by Means of Secondary Ions", *IBM Tech. Disclosure Bull.*, **22**, 1520 (1979).
 121. Kazmerski, L.L., and Ireland, P.J., "A Study of Interface Problems in Polycrystalline GaAs Schottky Barrier and MIS Solar Cells", *Surf. & Interface Anal.*, **1**, 144 (1979).
 122. Kazmerski, L.L., "Grain Boundary and Interdiffusion Studies in Compound Semiconductor Thin Films and Devices Utilizing Auger Electron Spectroscopy and Secondary Ion Mass Spectroscopy", *Thin Solid Films*, **57**, 99 (1979).
 123. Kazmerski, L.L., "Applications of Auger Electron Spectroscopy and Secondary Ion Mass Spectroscopy in Solar Energy Research", *Trans. Am. Nucl. Soc.*, **33**, 245 (1979).
 124. Keller, R., "A Reliable Noble Gas Duoplasmatron for the 10mA Range", *Rad. Eff.*, **44**, 201 (1979).
 125. Kiko, J., Muller, H.W., Buchler, K., Kalbitzer, S., Kirsten, T., and Warhaut, M., "The Gas Ion Probe: A Novel Instrument for Analyzing Concentration Profiles of Gases in Solids", *Int. J. Mass Spectrom. & Ion Phys.*, **29**, 87 (1979).
 126. Kilius, L.R., Beukens, R.P., Chang, K.H., Lee, H.W., Litherland, A.E., and Elmore, D., "Separation of ^{26}Al and ^{26}Mg Isobars by Negative Ion Mass Spectrometry", *Nature*, **282**, 488 (1979).
 127. Kiriakidis, G., Colligon, J.S., and Chenakin, S.P., "Secondary Ion Mass Spectrometric Study of Self-Sputtered Copper", *Rad. Eff.*, **41**, 119 (1979).
 128. Kloppel, K.D., and Seidel, W., "Investigation of Monolayers by Secondary Ion Mass Spectroscopy (SIMS)", *Int. J. Mass Spectrom. Ion Phys.*, **31**, 151 (1979).
 129. Kolonits, V.P., Koltai, M., and Marton, D., "Cross-Sectional Compositions of Sputtered Tantalum Nitride Thin Films by Secondary Ion Mass Spectrometry", *Thin Solid Films*, **57**, 221 (1979).
 130. Komiya, S., Umez, N., and Hayashi, C., "Titanium Nitride Film as a Protective Coating for a Vacuum Deposition Chamber", *Thin Solid Films*, **63**, 341 (1979).
 131. Konig, U., Heime, K., and Kubalek, E., "The Influence of the Growth Process on Doping Profile and Mobility Profile During LPE of the Pseudobinary Sn-GaAs System", *J. Electrochem. Soc.*, **126**, 296 (1979).
 132. Krauss, A.R., and Gruen, D.M., "Secondary-Ion Emission from Oxygen and Hydrogen-Covered Beryllium Surfaces. I. Coverage Dependence", *Surf. Sci.*, **90**, 564 (1979).
 133. Krotov, V.I., and Lebedev, S. Ya., "Effect of Helium-Ion Energy and Irradiation Temperature on the Blistering of Nickel", *Sov. At. Energy*, **46**, 139 (1979).
 134. Krueger, F.R., "Fast Ion Induced Desorption and Collective Electronic Perturbation at the Surface", *Surf. Sci.*, **86**, 246 (1979).
 135. Kuvakin, M.V., Lusnikov, A.V., and Motavakh, Kh. A., "Influence of the Curvature of a Surface Barrier on the Sputtering Characteristics", *Sov. Phys. Solid State*, **21**, 1657 (1979).
 136. LaForce, R.W., and Short, J.M., "Quantitative Ion Microprobe Analysis of Chlorine in Selenium", *Proc. 14th Ann. Conf. of the Microbeam Analysis Soc.*, San Antonio, Texas, Aug. 1979. *Microbeam Analysis*, D.E. Newbury, Ed., (San Francisco, CA: San Francisco Press Inc., 1979) p. 350.
 137. LaForce, R.W., and Johnson, J.K., "Quantitative Analysis of Se Alloy Thin Films by Ion-Microprobe Mass Analysis and Transmission Electron Microscopy", *Proc. 14th Ann. Conf. of the Microbeam Analysis Soc.*, San Antonio, Texas, Aug. 1979. *Microbeam Analysis*, D.E. Newbury, Ed., (San Francisco, CA: San Francisco Press Inc., 1979) p. 354.
 138. Lam, N.Q., Leaf, G.K., and Wiedersich, H., "Effects of Radiation-Induced Segregation and Preferential Sputtering on the Sputtering Rate of Alloys", *J. Nucl. Mat.*, **85-86** pt. B, 1085 (1979).
 139. Lancaster, G.M., Honda, F., Fukuda, Y., and Rabalais, J.W., "Macromolecular Ionic Clusters of Water Detected by SIMS", *Int. J. Mass Spectrom. Ion Phys.*, **29**, 199 (1979).
 140. Larson, D.T., "Surface Analytic Techniques in Corrosion Science", *Corros. Sci.*, **19**, 657 (1979).
 141. Lee, H.Y., "Temperature Dependence in Sputtering", *Rad. Eff. Lett.*, **43**, 161 (1979).
 142. Liebl, H., "A New Emission Lens", *Optik*, **53**, 69 (1979).
 143. Lin, Z.R., "Mass Spectrometry Microanalysis with an Ion Probe. I. Basic Physics", *Wuli*, **8**, 434 (1979).
 144. Lukner, Ch., "Mechanisms for the Production of Negative Ions in Sputtering Sources", *Nucl. Instrum.*

- & Methods, 167, 249 (1979).
145. Lundquist, T.R., "Comment on Relative Ion Sputtering Yield Measurements by Inegration of Secondary Ion Energy Distribution Using a Retarding-Dispersive Ion Energy Analyzer", Appl. Phys., 18, 221 (1979).
 146. Lundquist, T.R., "Energy Dependence of the Ionization Probability of Sputtered Cu and Ni", Surf. Sci., 90, 548 (1979).
 147. Luthra, J.M., "Correlation Between Exfoliation Depth, the Maximum in the Damage-Energy Distribution and Ranges of He^+ Ions in Nickel", Indian J. Pure & Appl. Phys., 17, 336 (1979).
 148. Magee, T.J., Peng, J., Hong, J.D., Evans, C.A., Jr., Deline, V.R., and Malbon, R.M., "Outdiffusion of Cr in VPE GaAs Layers and Back-Surface Gettering", J. Electrochem. Soc., 126, 360C (1979).
 149. Magee, C.W., "Depth Profiling of n-Type Dopants in Si and GaAs Using Cs^+ Bombardment Negative Secondary Ion Mass Spectrometry in Ultrahigh Vacuum", J. Electrochem. Soc., 126, 660 (1979).
 150. Magee, T.J., Peng, J., Hong, J.D., Deline, V.R., and Evans, C.A., Jr., "Alloying of Au layers and Redistribution of Cr in GaAs", Appl. Phys. Lett., 35, 615 (1979).
 151. Magee, T.J., Peng, J., Hong, J.D., Katz, W., and Evans, C.A., Jr., "Back Surface Gettering of Au in GaAs", Phys. Status Solid A, 55, 161 (1979).
 152. Magee, T.J., Peng, J., Hong, J.D., Evans, C.A., Jr., and Deline, V.R., "Gettering of Cr in GaAs by Back Surface Mechanical Damage", Phys. Status Solidi A, 55, 169 (1979).
 153. Manifacier, J.C., Szepessy, L., Bresse, J.F., Perotin, M., and Stuck, R., " $\text{In}_2\text{O}_3:(\text{Sn})$ and $\text{Sn}_2\text{O}_3:(\text{F})$ Films-Application to Solar Energy Conversion. I. Preparation and Characterization", Mat. Res. Bull., 14, 109 (1979).
 154. Marinov, M., "Influence of Ion Bombardment on the Surface Structure of Silicon Single Crystals", Thin Solid Films, 61, 363 (1979).
 155. Marton, D., Josepovits, V.K., and Csanady, A., "Investigation of the Initial Stages of Oxidation of Differently Prepared Aluminium by SIMS", Surf. & Interface Anal., 1, 132 (1979).
 156. Martynenko, Yu. V., "The Theory of Blister Formation", Rad. Eff., 45, 93 (1979).
 157. McDonnell, W.R., "A General Mechanism for Helium Blistering Involving Displaced Atom Transport", J. Nucl. Mat., 85-86, 1117 (1979).
 158. Mezey, G., Kotai, E., Nagy, T., Lohner, L., Manuba, A., Gyulai, J., Deline, V.R., Evans, C.A., Jr., and Blattner, R.J., "A Comparison of Techniques for Depth Profiling Oxygen in Silicon", Nucl. Instrum. Methods, 167, 279 (1979).
 159. Mizuike, A., and Iino, A., "Coating of Borosilicate Glass Containers for Preventing Contamination in Trace Element Analysis", Anal. Chim. Acta, 111, 251 (1979).
 160. Mohri, M., Watanabe, K., Yamashina, T., Doi, H., and Hayakawa, K., "AES-SIMS(IMA) Study of Physical and Chemical Sputtering Processes of Low-Z Materials by Energetic Ions", J. Nucl. Mat., 85, 1185 (1979).
 161. Monemar, B., and Lagerstedt, O., "Properties of VPE-Grown GaN Doped with Al and Some Iron-Group Metals", J. Appl. Phys., 50, 6480 (1979).
 162. Morozov, S.N., Gurich, D.D., and Arifov, T.U., "Ion and Electron Emission of LiF, NaCl, and Si Single Crystals Acted upon by Multiply Charged Ions of Various Elements", Bull. Acad. Sci. USSR, Phys. Ser., 43, 137 (1979).
 163. Muller, G., Trapp, M., Schimko, R., and Richter, C.E., "Measurement of Range Distributions of Zinc and Nitrogen Ions in Multiple-layer Substrates with the Secondary Ion Microprobe", Phys. Status Solidi A, 51, 87 (1979).
 164. Muller, K.H., Beckmann, P., Schemmer, M., and Benninghoven, A., "SIMS and Flash Filament Study of the Interaction of Polycrystalline Nickel with Oxygen", Surf. Sci., 80, 325 (1979).
 165. Myers, D.R., Wilson, R.G., and Comas, J., "Considerations of Ion Channeling for Semiconductor Microstructure Fabrication", J. Vac. Sci. & Technol., 16, 1893 (1979).
 166. Nakao, F., Birakawa, M., and Yamamoto, T., "Quantitative Depth Profiling Analyses of the Surface Layer in Be-Cu Dynodes", J. Vac. Sci. Technol., 16, 1017 (1979).
 167. Naya, A., Kuriki, S., Natsumoto, G., and Hirano, M., "A Study of Gold Migration in Au- Y_2O_3 -Y Junctions by Secondary Ion Mass Spectrometry", Thin Solid Films, 59, 143 (1979).
 168. Nestyurina, E.E., Lototskii, A.G., and Ufimtsev, V.B., "Concentration Profile of Chromium in Epitaxial Layers of Gallium Phosphide", Ind. Lab., 45, 548 (1979).
 169. Newbury, D.E., and Heinrich, K.F.J., "Quantitative Procedures in Ion-Probe Microanalysis", Mikrochimica Acta (Wien), Suppl. 8, 3 (1979).
 170. Newbury, D.E., "The Influence of Instrumental Sensitivity Variations on Quantitative Analysis by Secondary Ion Mass Spectrometry", Proc. 14th Ann. Conf. of the Microbeam Analysis Soc., San Antonio, Texas, Aug. 1979. Microbeam Analysis, D.E. Newbury, Ed., (San Francisco, CA: San Francisco Press Inc., 1979) p. 335.
 171. Newbury, D.E., "Microanalysis in the Scanning Electron Microscope: Progress and Prospects", Scanning Electron Microscopy, Vol. 2, Om Johari, Ed., (AMF O'Hare, IL: Scanning Electron Microscopy Inc., 1979) p.1.
 172. Newton, C.S., and Hay, H.J., "Helium Irradiation of Alkali Halides", Rad. Eff. Lett., 43, 211 (1979).
 173. Norskov, J.K., and Lundqvist, B.I., "Secondary Ion Emission Probability in Sputtering", Phys. Rev. B, 19, 5661 (1979).
 174. Oechsner, H., Rube, W., and Stumpe, E., "Comparative SNMS and SIMS Studies of Oxidized Ce and Gd", Surf. Sci., 85, 289 (1979).
 175. Okutani, T., and Shimizu, R., "Fundamental Studies of the LTE Model Using Secondary Ion and Ion-Induced Photon Emission", Surf. Sci., 88, L51 (1979).
 176. Oliva-Florio, A.R., Alonso, E.V., Baragiola, R.A., Ferron, J., and Jakas, M.M., "Energy Dependence of the Molecular Effect in Sputtering", Rad. Eff. Lett., 50, 3 (1979).
 177. Oshima, M., Kawashima, I., and Yoshii, S., "Quantitative Analysis of Semiconductor Materials with

- Secondary Ion Mass Spectrometer", Japan. J. Appl. Phys., 19, Suppl. 19-1, 501 (1979).
178. Oshima, M., "A Study of Dry Etching-Related Contaminations on Si and SiO₂", Surf. Sci., 86, 858 (1979).
 179. Pavlyak, F., Perczel, I.V., and Giber, J., "A SIMS and AES Examination of a Cu/Co/Si Alloy", Surf. & Interface Anal., 1, 139 (1979).
 180. Perderau, M., "Application of SIMS to the Study of Several Surface Reactions. The Chemist's Point of View", J. Microsc. & Spectrosc. Electron., 4, 505 (1979).
 181. Pivin, J.C., Roques-Carnes, C., and Slodzian, G., "Couche Formees sur Le Fer, Le Nickel et Le Chrome Sons Bombardment Ioni que en Presence D'oxygene", Int. J. Mass Spectrom. Ion Phys., 31, 293 (1979).
 182. Pivin, J.C., Roques-Carnes, C., and Slodzian, G., "Couches Formees sur Les Alliages Fe-Ni, Fe-Cr, Ni-Cr Sons Bombardment Ionique en Presence D'oxygene", Int. J. Mass Spectrom. Ion Phys., 31, 311 (1979).
 183. Ploog, K., "Surface Studies During Molecular Beam Epitaxy of Gallium Arsenide", J. Vac. Sci. Technol., 16, 838 (1979).
 184. Pontau, A.E., Haggmark, L.G., Wilson, K.L., Bastasz, R., Malinowski, M.E., Dawson, D.B., and Bauer, W., "Deuterium Profiles in Titanium and Alloys", J. Nucl. Mat., 85, 1013 (1979).
 185. Purser, K.H., Litherland, A.E., and Rucklidge, J.C., "Secondary Ion Mass Spectrometry at Close to Single-Atom Concentration Using DC Accelerators", Surf. Interface Anal., 1, 12 (1979).
 186. Rauschenbach, B., and Blasek, G., "Determination of Very Low Diffusion Coefficients in Glass with Means of Secondary-Ion Mass Spectrometry", Phys. Status Solidi A, 53, K11 (1979).
 187. Ray, J.A., Barnett, C.F., and Van Zyl, B., "Absolute Measurement of Low-Energy H⁰ Fluxes by a Secondary Emission Detector", J. Appl. Phys., 50, 6516 (1979).
 188. Read, F.H., "Electrostatic Lenses", Rad. Eff., 44, 129 (1979).
 189. Riviere, J.C., "Metallurgical Applications of XPS, AES and SIMS", Mem. Sci. Rev. Metall., 76, 759 (1979).
 190. Robertson, J.M., Damen, J.P.M., and Algra, H.A., "Liquid Phase Epitaxial Growth and Properties of Spinel Thin Films", IEEE Trans. Magn., MAG-15, 1870 (1979).
 191. Roques-Carnes, C., and Monlouis, M.C., "SIMS Quantitative Analysis of Beryllium Distribution in the Vicinity of an Oxidation Boundary", J. Microsc. & Spectrosc. Electron., 4, 165 (1979).
 192. Rudat, M.A., and Morrison, G.H., "Evaluation of Several Semi-Theoretical Methods for Quantitative Secondary Ion Mass Spectrometric Analysis after Discrimination--Correction of Data", Anal. Chem., 51, 1179 (1979).
 193. Rudat, M.A., and Morrison, G.H., "A Computerized System for Determining Secondary Ion Energy Spectra", Anal. Chim. Acta, 112, 1 (1979).
 194. Rudat, M.A., and Morrison, G.H., "Detector Discrimination in SIMS. II. Ion-to-Electron Converter Yield Factors for Negative Ions", Int. J. Mass Spectrom. & Ion Phys., 29, 1 (1979).
 195. Rudat, M.A., and Morrison, G.H., "A Study of the Energy Spectra of Secondary Ions from Metal Matrices", Int. J. Mass Spectrom. Ion Phys., 30, 197 (1979).
 196. Rudat, M.A., and Morrison, G.H., "The Effects of Oxygen and Nitrogen Adsorption on Secondary Ion Energy Spectra", Int. J. Mass Spectrom. Ion Phys., 30, 233 (1979).
 197. Rudat, M.A., and Morrison, G.H., "Discrimination Effects in SIMS, Part III. Ion Optical and Energy Discrimination", Int. J. Mass Spectrom. Ion Phys., 32, 53 (1979).
 198. Rudat, M.A., and Morrison, G.H., "Energy Spectra of Ions Sputtered from Elements by O₂⁺ A Comprehensive Study", Surf. Sci., 82, 549 (1979).
 199. Rudenauer, F.G., Steiger, W., and Kraus, U., "Microanalysis with a Quadrupole Ion Microprobe", Mikrochimica Acta (Wien), Suppl. 8, 51 (1979).
 200. Rudenauer, F.G., Steiger, W., and Werner, H.W., "Quantitative Evaluation of Secondary-Ion Micrographs", Mikrochimica Acta (Wien), Suppl. 8, 59 (1979).
 201. Sachenko, V.D., Gall, R.N., and Fridlyanskii, G.V., "Simultaneous Angle and Energy Focusing of Approximately Equal Masses in a Tandem Mass Spectrometer with an Intermediate Image", Sov. Phys. Tech. Phys., 24, 829 (1979).
 202. Scherrer, H., Pineau, G., and Scherrer, S., "Diffusion of ¹¹⁷Sn in Tin Telluride", Phys. Lett. A, 75A, 118 (1979).
 203. Schilling, J.H., "Element Distributions in Geological Materials by Image Processing of Scanning Ion Microprobe Data", Proc. 14th Ann. Conf. of the Microbeam Analysis Soc., San Antonio, Texas, Aug. 1979. Microbeam Analysis, D.E. Newbury, Ed., (San Francisco, CA: San Francisco Press Inc., 1979) p. 345.
 204. Shimizu, J., "Beam Trajectories Through an Einzel Lens by Numerical Computation", Rep. Inst. Phys. & Chem. Rev., 55, 17 (1979).
 205. Schlecker, H., Blank, P., and Feller, H.G., "Examination of the Anodic Behavior of Ni-Pd-Alloys. II. Examination of the Formation and Composition of Passive Films on Ni-Pd-Surfaces by Electrochemical Methods, SEM, SIMS and XPS", Z. Metallkd., 70, 638 (1979).
 206. Schwarz, S.A., and Helms, C.R., "A Statistical Model of Sputtering", J. Appl. Phys., 50, 5492 (1979).
 207. Schwarz, S.A., and Helms, C.R., "Model of Ion Knock-On Mixing with Application to Si-SiO₂ Interface Studies", J. Vac. Sci. Technol., 16, 781 (1979).
 208. Seliger, R.L., and Ward, J.W., "A High-Intensity Scanning Ion Probe with Submicrometer Spot Size", Appl. Phys. Lett., 34, 310 (1979).
 209. Shappirio, J.R., and Cook, C.F., Jr., "Modern Analytical Techniques for Failure Analysis", Solid State Technol., 22, No. 9, 89 (1979).
 210. Sheretov, E.P., "Theory of the Three-Dimensional Quadrupole Mass Spectrometer. I", Sov. Phys. Tech. Phys., 24, 18 (1979).
 211. Sheretov, E.P., "Theory of the Three-Dimensional Quadrupole Mass Spectrometer. II", Sov. Phys. Tech. Phys., 24, 21 (1979).

212. Sheretov, E.P., Safonov, M.P., and Samodurov, V.F., "Structure of the Ion Beam in a Three-Dimensional Quadrupole Mass Spectrometer", *Sov. Phys. Tech. Phys.*, 24, 250 (1979).
213. Shimizu, R., "Comment on 'Evaluation of Concentration-Depth Profiles by Sputtering in SIMS and AES' by S. Hoffman", *Appl. Phys.*, 18, 425 (1979).
214. Sidenius, G., "The Fundamental Features and Characteristics of Discharge and Plasma Ion Sources", *Rad. Eff.*, 44, 145 (1979).
215. Sixt, G., Ziegler, K.H., and Fahrner, W.R., "Properties of Anodic Oxide Films on n-Type GaAs, GaAs_{0.6}P_{0.4} and GaP", *Thin Solid Films*, 56, 107 (1979).
216. Smith, J.N., Jr., "Angular Effects in the Sputtering of Cr⁺ from Stainless Steel by 10 KeV H₃⁺", *J. Nucl. Mat.*, 80, 356 (1979).
217. Smith, J.N., Jr., "Surface Cleanup and Sputtered Ion Production: Observations with AES and SIMS", *J. Nucl. Mat.*, 82, 179 (1979).
218. Snowdon, K.J., and MacDonald, R.J., "Secondary Ion Energy per Unit Mass Spectra From Polycrystalline Copper", *Int. J. Mass Spectrom. Ion Phys.*, 29, 101 (1979).
219. Snowdon, K.J., "A Fundamental Analysis of the Validity of Thermodynamic Models of Ionized and Excited Particle Production During Sputtering", *Rad. Eff.*, 40, 9 (1979).
220. Someno, M., and Wittry, D.B., Eds., Secondary Ion Mass Spectrometry: Fundamentals and Applications, A report of the 2nd Japan-U.S. Seminar on SIMS, (Tokyo, Japan: Riaru-Kogeisha, Ltd., 1979). 326 pp.
221. Sotkowski, P., Larsson, S., and Easterling, K.E., "Secondary Ion Analysis of Segregation in Welded Steels", *Met. Sci.*, 13, 597 (1979).
222. Sparrow, G.R., "Reconstructing the Outer Few Angstroms of a Surface by SIMS and ISS Techniques", *Proc. 14th Ann. Conf. of the Microbeam Analysis Soc.*, San Antonio, Texas, Aug. 1979. Microbeam Analysis, D.E. Newbury, Ed., (San Francisco, CA: San Francisco Press Inc., 1979) p. 325.
223. Sroubek, Z., "Ionization of Atomic Particles Sputtered from TiO₂(100) Surfaces", *Solid State Commun.*, 32, 809(1979).
224. Steele, I., and Hutcheon, I., "Ion Probe Analysis of Natural Olivine: Secondary-Ion Intensity Variation and Systematics for a Simple Binary Silicate", *Proc. 14th Ann. Conf. of the Microbeam Analysis Soc.*, San Antonio, Texas, Aug. 1979. Microbeam Analysis, D.E. Newbury, Ed., (San Francisco, CA: San Francisco Press Inc., 1979) p. 338.
225. Steiger, W., and Rudenauer, F.G., "Determination of Elemental Concentration Maps from Digital Secondary Ion Images", *Anal. Chem.*, 51, 2107 (1979).
226. Szymonski, M., and Bhattacharya, R.S., "The Sputtering of Gallium Arsenide at Elevated Temperatures", *Appl. Phys.*, 20, 207 (1979).
227. Taglauer, E., Heiland, W., and MacDonald, R.J., "The Study of Sputtering Effects in Oxides and Metal-Adsorbed-Gas Systems Using Combined Analytical Techniques", *Surf. Sci.*, 90, 661 (1979).
228. Temnenko, V.P., Karaulov, A.K., and Chenakin, S.P., "Investigation of Friction by the Method of Secondary Ion-Ion Emission", *Sov. Mat. Sci.*, 15, 68 (1979).
229. Terzic, I., and Circi, D., "The Double Cylindrical Electrostatic Sector as an Ion Energy Analyzer", *Nucl. Instrum. & Methods*, 166, 419 (1979).
230. Tompkins, H.G., "Preferential Sputtering in Gold-Nickel and Gold-Copper Alloys", *J. Vac. Sci. Technol.*, 16, 778 (1979).
231. Tortorelli, P.F., and Altstetter, C.J., "Sputtering of Two-Phase Polycrystalline Metals", *J. Vac. Sci. Technol.*, 16, 804 (1979).
232. Tsai, M.Y., Day, D.S., Streetman, B.G., Williams, P., and Evans, C.A., Jr., "Recrystallization of Implanted Amorphous Silicon Layers. II. Migration of Fluorine in BF₂⁺-Implanted Silicon", *J. Appl. Phys.*, 50, 188 (1979).
233. Tsai, M.Y., Streetman, B.F., Deline, V.R., and Evans, C.A., Jr., "Gallium Distribution and Electrical Activation in Ga⁺-Implanted Si", *J. Electrochem. Mat.*, 8, 111 (1979).
234. Tserpitskii, B.D., and Popov, V.F., "Enhancement of the Sensitivity of An Ion Analyzer Based on an MI-1305 Mass Spectrometer", *Instrum. & Exp. Tech.*, 22, 1386 (1979).
235. Tsipinyuk, B.A., and Veksler, V.I., "Energy Spectra of Secondary Ions and Secondary Ion Emission (SIE) Mechanisms", *Vacuum*, 29, 155 (1979).
236. Tsong, I.S.T., and Yusuf, N.A., "Does Local Thermodynamic Equilibrium Exist in the Excitation Process of Sputtered Atoms?", *Surf. Sci.*, 90, 417 (1979).
237. Tyler, S.K., and Goodhew, P.J., "Irregular Helium Bubbles in Niobium Alloys", *J. Microsc.*, 116, 55 (1979).
238. Ullmann, R., "Secondary Ion Mass Spectrometric Investigations on Thin Films of Organic Ammonia Salts on Noble Metals", *Mikrochimica Acta* (Wien) 1, 221 (1979).
239. Vaidyanathan, K.V., Anderson, C.L., Barrett, B., Dunlap, H.L., Hess, L.D., Golecki, I., and Nicolet, M.A., "Pulsed Electron Beam Annealing of Ion-Implanted GaAs", *J. Electrochem. Soc.*, 126, 361C (1979).
240. Vasil'ev, M.A., "Secondary Ion Emission of Borides and Carbides of Transition Metals", *Fiz. Met. Metalloved*, 47, 1010 (1979).
241. Vasil'ev, M.A., Kosyachkov, A.A., Panarin, V.E., Shurin, A.K., and Cherepin, V.T., "Investigation into Fe-TiB₂ Alloys Using Secondary Ion-Ion Emission Method", *Izv. Akad. Nauk. SSSR Met.*, No. 4, 202 (1979).
242. Vasil'ev, M.A., Goncharenko, A.B., Chenakin, S.P., and Cherepin, V.T., "Mechanism of Effect of Inert Gas Primary Ion Nature on Sputtered Atom Ionization Probability", *Metallofizika Kiev*, 1, 101 (1979).
243. Vasil'ev, M.A., Kosyachkov, A.A., Nemoshkalenko, I.N., and Cherepin, V.T., "Secondary Complex Ion Emission (Review)", *Metallofizika Kiev*, 1, 103 (1979).
244. Vasil'ev, F., "Electron-Microscopical Analysis of Surface Effects and Volume Defects Induced by Ion Bombardment", *Stud. & Cercet. Fiz.*, 31, 853 (1979).
245. Watanabe, K., Hashiba, M., Hirohata, Y., Nishino, M., and Yamashina, T., "Oxide Layers on GaAs Pre-

- pared by Thermal, Anodic and Plasma Oxidation: In-depth Profiles and Annealing Effects", *Thin Solid Films*, 56, 63 (1979).
246. Weinke, H.H., Kiesl, W., and Gijbek, R., "Investigation of Meteoritical Iron with an Ion Microprobe", *Mikrochimica Acta* (Wien), Suppl. 8, 87 (1979).
 247. Werner, H.W., "Microanalysis of Materials Used in the Electronics Industry", *Mikrochimica Acta* (Wien), Suppl. 8, 25 (1979).
 248. White, C.W., "Characterization of Ion-Implanted, Laser-Annealed Silicon for Solar Cell Applications", *Trans. Am. Nucl. Soc.*, 33, 246 (1979).
 249. Williams, P., "Current Problems in Low Energy Ion Beam Materials Analysis with SIMS", *IEEE Trans. Nucl. Sci.*, ns-26, 1807 (1979).
 250. Williams, P., "The Sputtering Process and Sputtered Ion Emission", *Surf. Sci.*, 90, 588 (1979).
 251. Winograd, N., Garrison, B.J., Fleisch, T., Delgass, W.N., and Harrison, D.E., Jr., "Particle Ejection from Ion-Bombarded Clean and Reacted Single Crystal Surfaces", *J. Vac. Sci. & Technol.*, 16, 629 (1979).
 252. Winograd, N., Foley, K.E., Garrison, B.J., Harrison, D.E., Jr., "Evidence for a Recombination Mechanism of Cluster Emission from Ion Bombarded Metal Surfaces", *Phys. Lett. A*, 73, 253 (1979).
 253. Wittmaack, K., "Primary-Ion Charge Compensation in SIMS Analysis of Insulators", *J. Appl. Phys.*, 50, 493 (1979).
 254. Wittmaack, K., "Production of Molecular Noble Gas Ions in a Hot Cathode Ion Source", *J. Vac. Sci. Technol.*, 16, 1027 (1979).
 255. Wittmaack, K., "On the Mechanism of Cluster Emission in Sputtering", *Phys. Lett. A*, 69, 322 (1979).
 256. Wittmaack, K., "Ionization Mechanism of H^+ Sputtered from Hydrogenated Silicon", *Phys. Rev. Lett.*, 43, 872 (1979).
 257. Wittmaack, K., "Secondary Ion Mass Spectrometry as a Means of Surface Analysis", *Surf. Sci.*, 89, 668 (1979).
 258. Wittmaack, K., "Secondary Ion Emission from Silicon Bombarded with Atomic and Molecular Noble-Gas Ions", *Surf. Sci.*, 90, 557 (1979).
 259. Wittry, D.B., and Guo, F., "Adaption of the Deitz Detector to an ARL Ion Microprobe Mass Analyzer", *Proc. 14th Ann. Conf. of the Microbeam Analysis Soc.*, San Antonio, Texas, Aug. 1979. *Microbeam Analysis*, D.E. Newbury, Ed., (San Francisco, CA: San Francisco Press Inc., 1979) p. 341.
 260. Yabumoto, M., Kakibayashi, H., Mohri, M., Watanabe, K., and Yamashina, T., "An Auger Electron Spectroscopy-Secondary Ion Mass Spectrometry Study of Layers of Cu-Ni and Ag-Au Alloys Modified by Ion Bombardment", *Thin Solid Films*, 63, 263 (1979).
 261. Yamada, R., Sone, K., and Saidoh, M., "Surface Microstructural Effects on Angular Distribution of Molybdenum Particles Sputtered with Low Energy Ne^+ Ion", *J. Nucl. Mat.*, 84, 101 (1979).
 262. Yamaguchi, N., Suzuki, K., Sato, K., and Tamura, H., "Determination of Carbon in Steel by Secondary Negative Ion Mass Spectrometry", *Anal. Chem.*, 51, 695 (1979).
 263. Yanabe, T., and Imoto, S., "Surface Analysis of SUS 316 by SIMS, SEM and ESCA", *J. Nucl. Mat.*, 80, 361 (1979).
 264. Yu, M.L., "A Comment on the Effects of Cs on Photon and Secondary Ion Emission During Sputtering", *Surf. Sci.*, 90, 442 (1979).

1980

1. Ahmad, S., Farmery, B.W., and Thompson, M.W., "The Effect of Ion Mass and Target Temperature on the Energy Distribution of Sputtered Atoms", *Nucl. Instrum. & Methods*, 170, 327 (1980).
2. Aitken, K.L., and Mair, G.L., "Emission Characteristics of a Liquid Caesium Ion Source", *J. Phys. D*, 13, 2165 (1980).
3. Alonso, E.V., Baragiola, R.A., Ferron, J., Jakas, M.M., and Oliva-Florio, A., " Z_1 Dependence of Ion-Induced Electron Emission from Aluminium", *Phys. Rev. B*, 22, 80 (1980).
4. Andrews, J.M., Katz, L.E., and Colby, J.W., "Detection of Sputter Contamination and Sputter-Etch Residue by Ion Microprobe Analysis", *Thin Solid Films*, 67, 325 (1980).
5. Aoki, A., "A Modified Semi-Quantitative Method for Dopant in ZnS thin Film with an Ion Microanalyzer", *Japan. J. Appl. Phys.*, 19, 1901 (1980).
6. Ast, T., and Beynon, J.H., "Advantages of Reversed Geometry Mass Spectrometers for Studying Charge Permutation Mass Spectra", *Int. J. Mass Spectrom. & Ion Phys.*, 32, 385 (1980).
7. Ato, Y., "Blistering and Flaking of SiC due to Light Ion Bombardment", *J. At. Energy Soc. Japan*, 22, 47 (1980).
8. Auciello, O., Kelly, R., and Iricibar, R., "New Insight into the Development of Pyramidal Structures on Bombarded Copper Surfaces", *Rad. Eff.*, 46, 105 (1980).
9. Badawi, M.H., Sealy, B.J., and Clegg, J.B., "Redistribution of Chromium in Semi-Insulating GaAs:Cr During Laser Annealing", *Electron. Lett.*, 16, 554 (1980).
10. Balashova, L.L., Borisov, A.M., Mashkova, E.S., and Molchanov, V.A., "Energy Features of the Blocking Effect for Fast Ionized Recoils", *Phys. Rev. A*, 21, 1185 (1980).
11. Barsony, I., and Giber, J., "SIMS Depth Profiling for the Characterization of Si-SiO₂ Structures", *Appl. Surf. Sci.*, 4, 1 (1980).
12. Bauch, R., Cambini, M., Weisgerber, P., DeAsmundis, C., and Plog, C., "Investigations on Oxide Formed in High-Temperature Water on Austenitic Steel", *J. Nucl. Mat.*, 92, 334 (1980).
13. Baum, W.L., "Applications of Surface Analysis Techniques to Studies of Adhesion", *Appl. Surf. Sci.*, 4, 291 (1980).
14. Baum, W.L., "Characterization of Tungsten Impregnated Dispenser Cathodes Using ISS and SIMS", *Appl. Surf. Sci.*, 4, 374 (1980).
15. Bay, H.L., Bohdansky, J., Hofer, W.O., and Roth, J., "Angular Distribution and Differential Sputtering Yields for Low-Energy Light-Ion Irradiation of Polycrystalline Nickel and Tungsten", *Appl. Phys.*,

- 21, 327 (1980).
16. Benoit, D., Namdar-irani, R., and Tixier, R., "Oxidation of Fatigue Surfaces at Low Crack Growth Rates", *Mat. Sci. & Eng.*, **45**, 1 (1980).
17. Bernheim, M., Rebiere, J., and Slodzian, G., "Negative Ion Emission on Caesiated Surfaces", *J. Microsc. & Spectrosc. Electron.*, **5**, 261 (1980).
18. Bertrand, P.A., Bauer, R., and Fleischauer, P.D., "Determination of Lead in Lubricating Oils by Isotopic Dilution Secondary Ion Mass Spectrometry", *Anal. Chem.*, **52**, 1279 (1980).
19. Bohdansky, J., Roth, J., and Bay, H.L., "An Analytical Formula and Important Parameters for Low-Energy Ion Sputtering", *J. Appl. Phys.*, **51**, 2861 (1980).
20. Bones, M.J., Webb, R.P., Carter, G., and Whitton, J.L., "The Development of Surface Morphology During Sputtering with Spatially Non-Uniform Ion Beam", *Rad. Eff. Lett.*, **50**, 133 (1980).
21. Borchardt, G., Scherrer, H., Weber, S., and Scherrer, S., "Local In-Depth Analysis of Ceramic Materials by Neutral Beam Secondary Ion Mass Spectrometry", *Int. J. Mass Spectrom. & Ion Phys.*, **34**, 361 (1980).
22. Brebec, G., Seguin, R., Sella, C., Bevenot, J., and Martin, J.C., "Diffusion of Silicon in Amorphous Silica", *Acta Metall.*, **28**, 327 (1980).
23. Brundie, C.R., "Chemical Characterization of Surfaces and Interfaces of Industrial Materials by X-Ray Photoelectron Spectroscopy, Auger Electron Spectroscopy and Secondary Ion Mass Spectrometry", *Thin Solid Films*, **72**, 3 (1980).
24. Buhl, R., and Preisinger, A., "Studies of Dynamic Effects at Non-Metal Surfaces with Incident Low Energy Electrons", *Vacuum*, **30**, 209 (1980).
25. Burns, M.S., and File, D.M., "Localization Quantitation of Sodium, Potassium, and Calcium in Galactose-Induced Cataracts in Rats by Secondary-Ion Mass Spectrometry (SIMS)", *Microbeam Analysis*, D.B. Wittry, Ed., (San Francisco, CA: San Francisco Press, Inc., 1980) p. 283.
26. Cahn, R.W., Evetts, J.E., Patterson, J., Somekh, R.E., and Kenway Jackson C., "Direct Measurement by Secondary Ion Mass Spectrometry of Self-Diffusion of Boron in $\text{Fe}_{40}\text{Ni}_{40}\text{B}_{20}$ Glass", *J. Mat. Sci.*, **15**, 702 (1980).
27. Campana, J.E., "Elementary Theory of the Quadrupole Mass Filter", *Int. J. Mass Spectrom. & Ion Phys.*, **33**, 101 (1980).
28. Campana, J.E., and Jurs, P.C., "Computer Simulation of the Quadrupole Mass Filter", *Int. J. Mass Spectrom. & Ion Phys.*, **33**, 119 (1980).
29. Carter, G., Nobes, M.J., Lewis, G.W., and Whitton, J.L., "The Kinetics and Energetics of Sputtering Induced Topography on Solids", *Rad. Eff. Lett.*, **50**, 97 (1980).
30. Carter, G., "A Semi Quantitative Approach to Ion Impact Induced Shock Processes in Solids", *Rad. Eff. Lett.*, **50**, 105 (1980).
31. Carter, G., and Armour, D.G., "The Relationship Between Vacuum and Atomic Collisions in Solids", *Vacuum*, **30**, 1 (1980).
32. Castaing, R., "Probing and Imaging Techniques for Surface Studies", *Mat. Sci. & Eng.*, **42**, 13 (1980).
33. Chassard-Bouchaud, C., and Galle, P., "Detection and Localization of Trace Elements in the Human Eye by Secondary Ion Mass Spectrometry", *Electron Microscopy*, Vol. 3, P. Brederoo and V.E. Cosslett, Eds., (Leiden, The Netherlands: 7th European Congr. on Electron Microscopy Foundation, 1980) p. 222.
34. Cherepin, V.T., Kosyachkov, A.A., and Gudzenko, G.I., "Computer Peak Identification in SIMS", *Int. J. Mass Spectrom. & Ion Phys.*, **35**, 225 (1980).
35. Chevrier, J., Armand, M., Huber, A.M., and Linh, N.T., "Vapor Growth of InP for MESFET'S", *J. Electron. Mat.*, **9**, 745 (1980).
36. Chikawam, J., and Sato, F., "Impurity Incorporation at Melt-Crystal Interfaces in Pulsed Laser Annealing of Silicon", *Japan. J. Appl. Phys.*, **19**, L159 (1980).
37. Chou, N.J., and Shafer, M.W., "On the Phenomenological Model of Preferred Sputtering for SIMS and Auger Profiling: A Critical Analysis", *Surf. Sci.*, **92**, 601 (1980).
38. Christie, W.H., and White, C.W., "SIMS Depth-Profiling Studies: The Effect of Laser Annealing on the Distribution of Ion-Implanted Boron in Silicon", *Surf. Sci.*, **100**, 43 (1980).
39. Chu, W.K., Kastl, R.H., and Murley, P.C., "Low-Energy Antimony Implantation in Silicon. I. Profile Measurements and Calculation", *Rad. Eff.*, **47**, 1 (1980).
40. Comas, J., and Wilson, R.G., "Channeling and Random Equivalent Depth Distributions of 150 KeV Li, Be, and B Implanted in Si", *J. Appl. Phys.*, **51**, 3697 (1980).
41. Covington, D.W., Comas, J., and Yu, P.W., "Iron Doping in Gallium Arsenide by Molecular Beam Epitaxy", *Appl. Phys. Lett.*, **37**, 1094 (1980).
42. Czanderna, A.W., "Solid Surfaces, Surface Processes, and Solid/Gas Interaction", *J. Vac. Sci. & Tech.*, **17**, 72 (1980).
43. Daly, J.G., and Sinha, M.K., "Blistering of Molybdenum-Base Alloy TZM under Helium Ion Bombardment", *J. Appl. Phys.*, **51**, 3198 (1980).
44. Dawson, P.H., "Ion Optical Design Data for the Quadrupole Mass Filter", *Int. J. Mass Spectrom. & Ion Phys.*, **36**, 353 (1980).
45. Dawson, P.H., and Tam, W.C., "The Use of Low Energy SIMS to Study the Chemisorption of CO on Ni(100) and Polycrystalline Nickel", *Surf. Sci.*, **91**, 153 (1980).
46. Dawson, P.H., "Ion Optical Properties of Quadrupole Mass Filters", *Advances in Electronics and Electron Physics*, L. Marton and C. Marton Eds., (New York, Academic Press Inc., 1980) p. 153.
47. Day, R.J., Unger, S.E., and Cooks, R.G., "Phenanthroline Cationization by Various Metals in Secondary Ion Mass Spectrometry", *Anal. Chem.*, **52**, 353 (1980).
48. Day, R.J., Unger, S.E., and Cooks, R.G., "Molecular Secondary Ion Mass Spectrometry", *Anal. Chem.*, **52**, 557A (1980).
49. Deline, V.R., Blattner, R.J., and Evans, C.A., Jr., "Trace-Level Microanalysis of Carbon and Oxygen in Electronic Materials by Cs Bombardment SIMS", *Microbeam Analysis*, D.B. Wittry, Ed., (San Francisco, CA: San Francisco Press, Inc., 1980) p. 239.

50. Desalvo, A., Galloni, R., Rosa, R., and Zignani, F., "Experimental and Computer Analysis of P^+ -Ion Penetration Tails in a SiO_2 -Si Two-Layer System", *J. Appl. Phys.*, **51**, 1994 (1980).
51. Dibeneditts, A.T., and Scola, D.A., "Characterization of S-Glass/Polysulfone Adhesive Failure Using Ion Scattering Spectroscopy and Secondary Ion Mass Spectrometry", *J. Colloid & Interface Sci.*, **74**, 150 (1980).
52. Didenko, P.I., Litovchenko, V.G., Marchenko, R.I., and Romanova, G.F., "Investigating the Structural Changes in Laminar Ion-Implanted Si- SiO_2 Systems by the MSSI Method", *Poluprovodn. Tehk. & Mikroelektron.*, no. 31, 38 (1980).
53. Domanski, M., and Wojtowicz-Natanson, B., "A Possible Application of the SIMS Method to Determine the Provenance of Archaeological Objects", *Nucl. Instrum. & Methods*, **168** 435 (1980).
54. Donnelly, S.E., Debras, G., Gilles, J.M., and Lucas, A.A., "The Deformation of Thin Aluminium Films under Helium Ion Bombardment", *Rad. Eff. Lett.*, **50**, 57 (1980).
55. Doran, M.C., Fulford, J.E., Hughes, R.J., Morita, Y., and March, R.E., "Effects of Charge-Exchange Reactions on the Motion of Ions in Three-Dimensional Quadrupole Electric Fields. III. A Two-Ion Model", *Int. J. Mass Spectrom. & Ion Phys.*, **33**, 139 (1980).
56. Dörner, P., Gust, W., Hintz, M.B., Predel, B., Lodding, A., and Odelius, H., "SIMS Investigations on the Diffusion of Cu in Ag Single Crystals", *Acta Metall.*, **28**, 291 (1980).
57. Drummer, D.M., and Morrison, G.H., "Digital Image Processing for Image Quantification in Ion Microscope Analysis", *Anal. Chem.*, **52**, 2147 (1980).
58. Duck, P., Treu, W., Fröhlich, H., Galster, W., and Voit, H., "Desorption of Organic Compounds from Solid Surfaces by Bombardment with Heavy Ions from a Tandem Accelerator", *Surf. Sci.*, **95**, 603 (1980).
59. Dvoryankina, G.G., Dvoryankin, V.F., and Cherevatsky, N., Ya., "Investigation of Influence of Heating and Ion Bombardment upon Chemical Composition and Structure of (100) Surfaces of GaAs and InP", *Electron Microscopy*, Vol. 1, P. Brederoo and G. Boom, Eds., (Leiden, The Netherlands, 7th European Congr. on Electron Microscopy Foundation, 1980) p. 360.
60. Dzioba, S., Auciello, O., and Kelly, R., "On the Kinetic Energies of Sputtered Excited Particles, I. Atoms Sputtered from Li, LiF, and NaCl", *Rad. Eff.*, **45**, 235 (1980).
61. Erlewein, J., and Hofmann, S., "A Model Calculation of the Influence of Surface Transport of the Depth Resolution in Sputter Profiling", *Thin Solid Films*, **69**, L39 (1980).
62. Eu, V., Feng, M., Henderson, W.B., Kim, H.B., and Whelan, J.M., "Cr Profiles in Semi-Insulating GaAs After Annealing with and without SiO_2 Encapsulants in a H_2 - As_4 Atmosphere", *Appl. Phys. Lett.*, **37**, 473 (1980).
63. Ferralli, M.W., and Madura, A.R., "Product Improvement with Surface Analysis by Ion Beam Techniques", *Ind. Res./Dev.*, **22**, 138 (1980).
64. Fogarassy, E., Stuck, R., Muller, J.C., Grob, A., Grob, J.J., and Siffert, P., "Effects of Laser Irradiation on Phosphorus Diffused Layers in Silicon", *J. Electron. Mat.*, **9**, 197 (1980).
65. Foley, K.E., and Garrison, B.J., "Mechanisms of Particle Ejection from Cu(001) Induced by the Relative Orientation of the Bombarding Primary Ion", *J. Chem. Phys.*, **72**, 1018 (1980).
66. Foti, G., Bean, J.C., Poate, J.M., and Magee, C.M., "Effect of Structure and Impurities on the Epitaxial Regrowth of Amorphous Silicon", *Appl. Phys. Lett.*, **36**, 840 (1980).
67. Foxon, C.T., Joyce, B.A., and Norris, M.T., "Composition Effects in the Growth of $Ga(In)As_{y1-y}$ Alloys by MBE", *J. Cryst. Growth*, **49**, 132 (1980).
68. Frisch, M.A., Reuter, W., and Wittmaack, K., "System for Combined SIMS-AES-XPS Studies of Solids", *Rev. Sci. Instrum.*, **51**, 695 (1980).
69. Fujino, N., Murayama, J., and Usuki, N., "Surface Analysis of Oxidized Stainless Steels", *Electron Microscopy*, Vol. 3, P. Brederoo and V.E. Cosslett, Eds., (Leiden, The Netherlands: 7th European Congr. on Electron Microscopy Foundation, 1980) p. 220.
70. Fukuda, Y., Honda, F., and Rabalais, J.W., "Quantitative Surface Analysis of Copper-Nickel Alloys by Secondary Ion Mass Spectrometry", *Anal. Chem.*, **52**, 2213 (1980).
71. Fuoss, D., and Topich, J.A., "Heavy-Doping Effects and Impurity Segregation During High-Pressure Oxidation of Silicon", *Appl. Phys. Lett.*, **36**, 275 (1980).
72. Furman, B.K., and Morrison, G.H., "Direct Digitization System for Quantification in Ion Microscopy", *Anal. Chem.*, **52**, 2305 (1980).
73. Furman, B.K., Morrison, G.H., Saunders, V.I., and Tan, Y.T., "Secondary Ion Mass Spectrometry and Ion Scattering Spectrometry Determination of Iodide Distribution in Ag (Br, I)", *J. Appl. Phys.*, **51**, 5342 (1980).
74. Gardella, J.A., and Hercules, D.M., "Static Secondary Ion Mass Spectrometry of Polymer Systems", *Anal. Chem.*, **52**, 226 (1980).
75. Gat, A., Gerzberg, L., Gibbons, J.F., Lietoila, A., Johnson, N.M., Magee, T.J., Peng, J., Deline, V., Williams, P., and Evans, C.A., Jr., "Annealing of Ion-Implanted Si Using a Scanned CW Laser System", *Rad. Eff.*, **48**, 195 (1980).
76. Ghaisas, S.V., Chaudhari, S.M., Bhiday, M.R., and Bhoraskar, V.N., "A Modified Electron Bombardment Type Ion Source for the Study of Solids", *Pramana*, **14**, 289 (1980).
77. Gossink, R.G., Application of Secondary Ion Mass Spectrometry (SIMS) to Glass Surface Problems", *Glass, Technol.*, **21**, 125 (1980).
78. Gourgout, J.M., "Development of an Advanced Ion Microprobe Analyzer", *Microbeam Analysis*, D.B. Wittry, Ed., (San Francisco, CA: San Francisco Press, Inc., 1980) p. 68.
79. Gourrier, S., Mircea, A., and Bacal, M., "Oxidation of GaAs in an Oxygen Multipole Plasma", *Thin Solid Films*, **65**, 315 (1980).
80. Gove, H.E., "Ultrasensitive Mass Spectrometry with Tandem Electrostatic Accelerators", *Nukleonika*, **25**, 31 (1980).
81. Grimmeiss, H.G., Janzen, E., Skarstam, B., and Lodding, A., "Chemical Identification of Deep Energy Levels in Si:Se", *J. Appl. Phys.*, **51**, 6238 (1980).

82. Grinolds, H.R., and Robinson, G.Y., "Pd/Ge Contacts to n-Type GaAs", *Solid State Electron.*, **23**, 973 (1980).
83. Haeussler, E.N., "SIMS Analysis in a conventional Scanning Electron Microscope", *Scanning*, **3**, 127 (1980).
84. Haeussler, E.N., "ISS and SIMS: Two Complementary Techniques for Surface Analysis", *Electron Microscopy*, Vol. 1, P. Brederoo and G. Boom Eds., (Leiden, The Netherlands: 7th European Congr. on Electron Microscopy Foundation, 1980) p. 516.
85. Haeussler, E.N., "Surface Analysis in the SEM by Means of a SIMS Accessory", *Electron Microscopy*, Vol. 1, P. Brederoo and G. Boom, Eds., (Leiden, The Netherlands, 7th European Congr. on Electron Microscopy Foundation, 1980) p. 518.
86. Hage-Ali, M., Stuck, R., Toulemonde, M., and Siffert, P., "Characterization of EFG Silicon Ribbons by Ion Beam Techniques", *Sol. Cells*, **1**, 153 (1980).
87. Hanoka, J.I., and Bathey, B., "A Combined Quantitative EBIC and Ion Microprobe Analysis of SiC Particles in EFG Ribbon", 14th IEEE Photovoltaic Specialists Conf. 1980. San Diego, CA, USA, Jan. 1980. (New York, NY: IEEE, 1980) p. 478.
88. Hart, R.G., and Cooper, C.B., "Energies of Cu^+ Ions Sputtered from Cu by very Low Energy (50 eV $< E < 1$ KeV) Inert Gas Ions", *Surf. Sci.*, **94**, 105 (1980).
89. Havette, A., "Matrix Effects in Secondary Ion Emission: Quantitative Analysis of Silicates", *C.R. Hebd. Seances Acad. Sci. Ser. B*, **290**, 51 (1980).
90. Havette, A., and Slodzian, G., "Linear Variation of the Secondary Ion Yield. Quantitative Analysis of Numerical Silicates", *J. Microsc. & Spectrosc. Electron.*, **5**, 231 (1980).
91. Havette, A., and Slodzian, G., "Matrix Effects in Secondary Ion Emission: Quantitative Analysis of Silicates", *J. Phys. Lett.*, **41**, L247 (1980).
92. Henstra, S., Bisdom, E.B.A., Jongerius, A., Morgan, A.E., Werner, H.W., and de Grefte, H.A.M., "Quantitative Analysis on Thin Sections of Solids by Secondary Ion Mass Spectrometry", *Electron Microscopy*, Vol. 3, P. Brederoo and V.E. Cosslett, Eds., (Leiden, The Netherlands: 7th European Congr. on Electron Microscopy Foundation, 1980) p. 224.
93. Hewitt, R.W., and Winograd, N., "Oxidation of Polycrystalline Indium Studied by X-Ray Photoelectron Spectroscopy and Static Secondary Ion Mass Spectroscopy", *J. Appl. Phys.*, **51**, 2620 (1980).
94. Hieber, K., and Lautenbacher, E., "Stabilization of Sputtered β -Tantalum by a Tantalum Silicide Interlayer", *Thin Solid Films*, **66**, 191 (1980).
95. Hirao, T., Fuse, G., Inoue, K., Takayanagi, S., Yaegashi, Y., Ichikawa, S., and Izumi, T., "Electrical Properties of Si Implanted with As through SiO_2 Films", *J. Appl. Phys.*, **51**, 262 (1980).
96. Hirao, T., Inoue, K., Fuse, G., Takayanagi, S., and Yaegashi, Y., "The Concentration Profiles of the Recoil Implanted Oxygen in Si after Ion Implantations into SiO_2 -Si Substrates", *Rad. Eff.*, **47**, 95 (1980).
97. Hoffman, D.W., Tsong, I.S.T., and Power, G.L., "Analytic Correction of Edge Effects in Ion-Beam Sputtered Depth Profiles", *J. Vac. Sci. & Technol.*, **17**, 613 (1980).
98. Hofer, W.O., "Emission of Atoms and Electrons from High-Density Collision Cascades in Metals", *Nucl. Instrum. & Methods*, **170**, 275 (1980).
99. Hofker, W.K., and Politék, J., "Ion Implantation in Semiconductors", *Philips Tech. Rev.*, **39**, 1 (1980).
100. Hoh, K., Koyama, H., Uda, K., and Miura, Y., "Incorporation of Oxygen into Silicon During Pulsed-Laser Irradiation", *Japan. J. Appl. Phys.*, **19**, L375 (1980).
101. Holland, S.P., Garrison, B.J., and Winograd, N., "Azimuthal Anisotropies of Dimer Ions Ejected from Ion Bombarded Ni(001)", *Phys. Rev. Lett.*, **44**, 756 (1980).
102. Holloway, P.H., and McGuire, G.E., "Characterization of Electronic Devices and Materials by Surface-Sensitive Analytical Techniques", *Appl. Surf. Sci.*, **4**, 410 (1980).
103. Honda, F., Fukuda, Y., and Rabalais, J.W., "Sputtering Induced Recombination of Nitrogen Isotopes on Tungsten", *Chem. Phys.*, **47**, 59 (1980).
104. Hopkins, C.G., Deline, V.R., Blattner, R.J., Evans, C.A., Jr., and Magee, T.J., "Incorporation of Boron during the Growth of GaAs Single Crystals", *Appl. Phys. Lett.*, **36**, 989 (1980).
105. Hou, M., Reid, I., and Tompson, M.W., "Computer Studies of Surface Recoil Ejection Mechanisms from Gold Single Crystals", *Nucl. Instrum. & Methods*, **170**, 337 (1980).
106. Hung, L.S., Lau, S.S., von Allmen, M., Mayer, J.W., Ullrich, B.M., Baker, J.E., Williams, P., and Tseng, W.F., "Epitaxial Growth of Si Deposited on (100) Si", *Appl. Phys. Lett.*, **37**, 909 (1980).
107. Inglebert, R.L., and Hennequin, J.F., "Transmission of Quadrupole Mass Spectrometer", *J. Microsc. & Spectrosc. Electron.*, **5**, 215 (1980).
108. Inglebert, R.L., and Hennequin, J.F., "Transmission of a Quadrupole Mass Filter. II. Calculation of the Overall Transmission of a Quadrupole Spectrometer", *Rev. Phys. Appl.*, **15**, 1489 (1980).
109. Janev, R.K., and Vojvodic, S.B., "Interaction of Atomic Particles with Solid Surfaces. IV. One-Electron Resonant Processes in the Presence of a Surface Sub-Monolayer", *J. Phys. B*, **13**, 2481 (1980).
110. Janssen, E., "Chemical Characterization of Industrial Steel and Aluminium Sheet Surfaces by Secondary Ion Mass Spectrometry, Glow Discharge Optical Spectroscopy and other Surface-Sensitive Techniques", *Mat. Sci. & Eng.*, **42**, 309 (1980).
111. Jowett, C.E., "Surface Analytical Techniques Applied to Electronic Components (Si LSI Chip Inspection)", *Microelectron. J.*, **11**, 35 (1980).
112. Joyes, P., and Ortolí, S., "On New Applications of the Parity Rule in SIMS", *J. Phys. Lett.*, **41**, L193 (1980).
113. Joyner, D.J., and Hercules, D.M., "Chemical Bonding and Electronic Structure of B_2O_3 , H_3BO_3 , and BN: an ESCA, Auger, SIMS, and SXS Study", *J. Chem. Phys.*, **72**, 1095 (1980).
114. Juli, A.J.T., Wilson, G.C., Long, J.V.P., Reed, S.J.B., and Pillinger, C.T., "Sputtering Rates of Minerals and Implications for Abundances of Solar Elements in Lunar Samples", *Nucl. Instrum. &*

- Methods, 168, 357 (1980).
115. Kaletta, D., "Light Element Implantations in Metals", *Rad. Eff.*, 47, 237 (1980).
 116. Kasahara, J., and Watanabe, N., "Redistribution of Cr in Capless-Annealed GaAs under Arsenic Pressure", *Japan. J. Appl. Phys.*, 19, L151 (1980).
 117. Kazmerski, L.L., Ireland, P.J., and Ciszek, T.F., "Evidence for the Segregation of Impurities to Grain Boundaries in Multigrained Silicon Using Auger Electron Spectroscopy and Secondary Ion Mass Spectroscopy", *Appl. Phys. Lett.*, 36, 323 (1980).
 118. Kazmerski, L.L., Ireland, P.J., and Ciszek, T.F., "Electrical and Compositional Properties of Grain Boundaries in Multigrained Silicon Using Surface Analysis Techniques", *J. Vac. Sci. & Technol.*, 17, 34 (1980).
 119. Kazmerski, L.L., Ireland, P.J., Chu, S.S., and Lee, Y.T., "Comparative Study of Wet and Dry Oxides on Polycrystalline GaAs by AES, SIMS and XPS", *J. Vac. Sci. & Technol.*, 17, 521 (1980).
 120. Kazmerski, L.L., and Ireland, P.J., "Evidence for Grain Boundary Passivation by Oxidation in Polycrystalline GaAs Solar Cells", *J. Vac. Sci. & Technol.*, 17, 525 (1980).
 121. Kazmerski, L.L., Ireland, P.J., Sheldon, P., Chu, T.L., Chu, S.S., and Lin, C.L., "Comparison of Low-Temperature Oxides on Polycrystalline InP by AES, SIMS AND XPS", *J. Vac. Sci. & Technol.*, 17, 1061 (1980).
 122. Kazmerski, L.L., and Ireland, P.J., "Correlation of Grain Boundary Electrical Properties with Grain Boundary Impurities in Multigrained Silicon Using Surface Analytical Techniques", *Sol. Cells*, 1, 178 (1980).
 123. Kazmerski, L.L., "Photovoltaics: The Applications of Auger Electron Spectroscopy and Complementary Surface Analysis Techniques", *Scanning Electron Microscopy*, Vol. 1, Om Johari, Ed., (AMF O'Hare, IL: Scanning Electron Microscopy, Inc., 1980) p. 455.
 124. Kelly, R., "On the Problem of Whether Mass or Chemical Bonding is More Important to Bombardment-Induced Compositional Changes in Alloys and Oxides", *Surf. Sci.*, 100, 85 (1980).
 125. Kelly, R., and Auciello, O., "On the Origin of Pyramids and Cones on Ion-Bombarded Copper Surfaces", *Surf. Sci.*, 100, 135 (1980).
 126. Kenway Jackson, C., "Automatic Sequential Mass Analysis. A Method of Depth Profiling for Multi-Constituents in a Single Erosion", *J. Microsc. & Spectrosc. Electron.*, 5, 247 (1980).
 127. Kitazoe, Y., and Yamamura, Y., "Hydrodynamical Approach to Non-Linear Effects in Sputtering Fields", *Rad. Eff. Lett.*, 50, 39 (1980).
 128. Klein, P.B., Nordquist, P.E.R., and Siebenmann, P.G., "Thermal Conversion of GaAs", *J. Appl. Phys.*, 51, 4861 (1980).
 129. Kloppe, K.D., and Seidel, W., "A Plasma Ion Source with Plane Beam Profile for UHV-SIMS Measurements", *Nucl. Instrum. & Methods*, 177, 309 (1980).
 130. Koyama, H., "Cathodoluminescence Study of SiO₂", *J. Appl. Phys.*, 51, 2228 (1980).
 131. Koyama, H., "Redistribution of Implanted Oxygen and Carbon in Silicon", *J. Appl. Phys.*, 51, 3202 (1980).
 132. Kozlov, V.F., and Zats, A.V., "Studies in Efficiency of Oxygen-Stimulated Yields of Secondary Negative Ions in Cathode Sputtering Sources", *Ukr. Fiz. Zh.*, 25, 1359 (1980).
 133. Krauss, A.R., and Wright, R.B., "Energy and Mass Distributions of Sputtered Particles", *J. Nucl. Mat.*, 89, 229 (1980).
 134. Krauss, A.R., and Gruen, D.M., "Secondary-Ion Emission from Clean and Oxygen-Covered Beryllium Surfaces. II. Energy Dependence", *Surf. Sci.*, 92, 14 (1980).
 135. Krejčík, P., Kelly, J.C., and Dalglish, R.L., "A New Electrostatic Ion Microprobe System", *Nucl. Instrum. & Methods*, 168, 247 (1980).
 136. Kumagai, O., Kasahara, J., and Kaneko, K., "DLTS Study of Cr Trap Density in Thermally Converted Semi-Insulating GaAs", *Japan. J. Appl. Phys.*, 19, L409 (1980).
 137. Lamartine, B.C., Haas, T.W., and Solomon, J.S., "Characterization of TiH_x and TiD_{0.9} Surfaces: AES, ELS, SIMS and XPS Studies", *Appl. Surf. Sci.*, 4, 537 (1980).
 138. Lanford, W.A., Alwitt, R.S., and Dyer, C.K., "Hydrogen Profiles of Anodic Aluminium Oxide Films", *J. Electrochem. Soc.*, 127, 405 (1980).
 139. Larson, B.C., and Barhorst, J.F., "X-Ray Study of Lattice Strain in Boron Implanted Laser Annealed Silicon", *J. Appl. Phys.*, 51, 3181 (1980).
 140. Lecrosnier, D., Pelons, G., and Richou, F., "Long Range Enhancement of Boron Diffusivity by Phosphorus Diffusion", *Rad. Eff.*, 48, 101 (1980).
 141. Lee, K.S., Ess, J.M., Littlejohn, M.A., Benson, R.B., Jr., and Comas, J., "A Comparison between Atomic Concentration Profiles and Defect Density Profiles in GaAs Annealed After Implantation with Beryllium", *J. Electron. Mat.*, 9, 185 (1980).
 142. Lefevre, R., Cournot-Witmer, G., and Galle, P., "Electron Microprobe Analysis and Analytical Ion Microscopy of Normal and Pathological Bone (Dialysis Osteomalacia)", *Electron Microscopy*, Vol. 3, P. Brederoo and V.E. Cosslett, Eds., (Leiden, The Netherlands: 7th European Congr. on Electron Microscopy Foundation, 1980) p. 106.
 143. Lepareur, M., "The Cameca Second-Generation Ion Microanalyser, Model 3F", *Rev. Tech. Thomson-CSF*, 12, 225 (1980).
 144. Leroy, V., "Metallurgical Applications of Surface Analytical Techniques", *Mat. Sci. & Eng.*, 42, 289 (1980).
 145. Leta, D.P., and Morrison, G.H., "Ion Implantation for in-situ Quantitative Ion Microprobe Analysis", *Anal. Chem.*, 52, 277 (1980).
 146. Leta, D.P., and Morrison, G.H., "Ion Implanted Standards for Secondary Ion Mass Spectrometric Determination of the 1a-7a Group Elements in Semiconducting Matrices", *Anal. Chem.*, 52, 514 (1980).
 147. Leta, D.P., Morrison, G.H., Harris, G.L., and Lee, C.A., "SIMS Determinations of Ion-Implanted Depth Distributions", *Int. J. Mass Spectrom. & Ion Phys.*, 34, 147 (1980).

148. Levi-Setti, R., and Fox, T.R., "High Resolution Scanning Ion Probes: Applications to Physics and Biology", Nucl. Instrum. & Methods, 168, 139 (1980).
149. Lewis, G.W., Nobes, M.J., Carter, G., and Whitton, J.L., "The Mechanisms of Etch Pit and Ripple Structure Formation on Ion Bombarded Si other Amorphous Solids", Nucl. Instrum. & Methods, 170, 363 (1980).
150. Lidow, A., Gibbons, J.F., Deline, V.R., and Evans, C.A., Jr., "Ion-Implanted Se in GaAs", J. Appl. Phys., 51, 4130 (1980).
151. Liebl, H., "SIMS Instrumentation and Imaging Techniques", Scanning, 3, 79 (1980).
152. Ligon, W.V., Jr., "Mass-Spectrometric Determinations of Unit Mass for Ions of Known Mass Difference Utilizing Peak-Matching Techniques", Int. J. Mass Spectrom. & Ion Phys., 34, 193 (1980).
153. Linton, R.W., Walker, S.R., DeVries, C.R., Ingram, P., and Shelburne, J.D., "Ion Microanalysis of Cells", Scanning Electron Microscopy, Vol. 2, Om Johari, Ed., (AMF O'Hare, IL: Scanning Electron Microscopy, Inc., 1980) p. 583.
154. Littmark, U., and Hofer, W.O., "Recoil Mixing in Solids by Energetic Ion Beams", Nucl. Instrum. & Methods, 168, 329 (1980).
155. Littmark, U., and Hofer, W.O., "Recoil Mixing in High-Fluence Ion Implantation", Nucl. Instrum. & Methods, 170, 177 (1980).
156. Liu, S.G., Douglas, E.C., Magee, C.W., Kolondra, F., and Jain, S., "High-Energy Implantation of Silicon in GaAs", Appl. Phys. Lett., 37, 79 (1980).
157. Liu, S.G., Douglas, E.C., Wu, C.P., Magee, C.W., Narayan, S.Y., Jolly, S.T., Kolondra, F., and Jain, S., "Ion Implantation of Sulfur and Silicon in GaAs", RCA Rev., 41, 227 (1980).
158. Lloyd, G.O., Kent, B., Saunders, S.R.J., and Lea, C., "The Action of Borates as Inhibitors for the High Temperature Oxidation of Alloys", Philos. Trans. R. Soc. London A, 295, 334 (1980).
159. MacDonald, R.J., Taglauer, E., and Heiland, W., "The Effect of CO Adsorption on Ion and Photon Yields from Ion Bombarded Metal Surfaces", Appl. Surf. Sci., 5, 197 (1980).
160. Magee, T.J., Hung, J., Deline, V.R., and Evans, C.A., Jr., "Low-Temperature Gettering of Cr in GaAs", Appl. Phys. Lett., 37, 53 (1980).
161. Magee, T.J., Lee, K.S., Ormond, R., Blattner, R.J., and Evans, C.A., Jr., "Annealing of Damage and Redistribution of Cr in Boron-Implanted Si₃N₄-Capped GaAs", Appl. Phys. Lett., 37, 447 (1980).
162. Magee, T.J., Lee, K.S., Ormond, R., Evans, C.A., Jr., Blattner, R.J., and Hopkins, C., "Low Temperature Redistribution of Cr in Boron-Implanted GaAs in the Absence of Encapsulant Stress", Appl. Phys. Lett., 37, 635 (1980).
163. Magee, C.W., Cohen, S.A., Voss, D.E., and Brice, D.K., "Depth Distributions of Low Energy Deuterium Implanted into Silicon as Determined by SIMS", Nucl. Instrum. & Methods, 168, 383 (1980).
164. Martin, T.P., "The Structure of Ionic Clusters: Thermodynamic Functions, Energy Surfaces and SIMS", J. Chem. Phys., 72, 3506 (1980).
165. Marton, D., "A SIMS Study of the Adsorption of Oxygen on Ion-Bombarded Silicon (111) Surfaces", Appl. Surf. Sci., 5, 65 (1980).
166. Marwick, A.D., and Piller, R.C., "Modification of Implant Profiles in Nickel by Radiation-Enhanced Diffusion and Segregation", Rad. Eff., 47, 195 (1980).
167. Masuyama, A., Nicolet, M.A., Golecki, I., Tandon, J.L., Sadana, D.K., and Washburn, J., "Steady-State Thermally Annealed GaAs with Room-Temperature-Implanted Si", Appl. Phys. Lett., 36, 749 (1980).
168. Mathiot, D., and Edelin, G., "Diffusion of Indium in GaSb", Philos. Mag. A, 41, 447 (1980).
169. Matsumoto, S., Gibbons, J.F., Deline, V., and Evans, C.A., Jr., "High-Temperature Scanning CW Laser-Induced Diffusion of Arsenic and Phosphorus in Silicon", Appl. Phys. Lett., 37, 821 (1980).
170. McCaughan, D.V., Sloane, R.H., and Geddes, J., "Secondary Ions from Hydrogen Ion Bombardment of Metal Surfaces", J. Appl. Phys., 51, 4426 (1980).
171. McCorkle, R.A., and Wynne, J.J., "Atomic Resolution Scanning Ion Microscope", IBM Tech. Disclosure Bull., 22, 5476 (1980).
172. McIntyre, N.S., Strathdee, G.G., and Phillips, B.F., "Secondary-Ion Mass-Spectrometric Studies of the Aqueous Leaching of a Borosilicate Waste Glass", Surf. Sci., 100, 71 (1980).
173. McLafferty, F.W., Todd, P.J., McGilvery, D.C., and Baldwin, M.A., "High-Resolution Tandem Mass Spectrometer (MS/MS) of Increased Sensitivity and Mass Range", J. Am. Chem. Soc., 102, 3360 (1980).
174. Meyer, M., Houch, E.L., and Barbezat, S., "Implantation of ¹⁸⁰⁺ Ions in Channelling Directions of Aluminium, Copper and Nickel Single Crystals. I. Experimental Conditions and Range Profile Determination", J. Phys., 41, 403 (1980).
175. Meyer, M., "Implantation of ¹⁸⁰⁺ Ions in Channelling Directions of Aluminium, Copper and Nickel Single Crystals. II. Stopping Power Determination by Maximum Range Measurements", J. Phys., 41, 409 (1980).
176. Meyer, M., Barbezat, S., Houch, C. El., and Talon, R., "Diffusion Study of Oxygen Implanted in Nickel Oxide", J. Phys. Colloq., 41, C-6, p. C6/327 (1980).
177. Migeon, H.N., and Gourgout, J.M., "High Performance Secondary Ion Mass Spectrometry (SIMS)", Electron Microscopy, Vol. 1, P. Brederoo and G. Boom Eds., (Leiden, The Netherlands: 7th European Congr. on Electron Microscopy Foundation, 1980) p. 514.
178. Millett, E.J., "Progress in the Analysis of Crystalline Solids", J. Cryst. Growth, 48, 666 (1980).
179. Modler, G., and Beske, H.E., "Investigations of Secondary Ion Formation on Oxygen Covered Surfaces of Binary Alloys", Report Jul-1651, Kernforschungsanlage, Julich, Germany (March 1980), 97pp.
180. Morgan, A.E., "Further Developments in Semiquantitative SIMS", J. Microsc. & Spectrosc. Electron., 5, 221 (1980).
181. Morkoc, H., Hopkins, C., Evans, C.A., Jr., and Cho, A.Y., "Chromium and Tellurium Redistribution in GaAs and Al_{0.3}Ga_{0.7}As Grown by Molecular Beam Epitaxy", J. Appl. Phys., 51, 5986 (1980).
182. Muda, Y., and Hanawa, T., "Theory of Ion Neutralization near the Surface", Surf. Sci., 97, 283 (1980).
183. Muller, J.C., Grob, J.J., Grob, A., Stuck, R., and Siffert, P., "Laser Annealing of Silicon Layers

- Amorphized by Molecular Ions", *Rad. Eff.*, **48**, 115 (1980).
184. Myers, S.M., "Ion-Beam-Induced Migration and Its Effect on Concentration Profiles", *Nucl. Instrum. & Methods*, **168**, 265 (1980).
 185. Nakhodkin, N.G., Bardamid, A.F., Shaldervan, A.I., and Chenakin, S.P., "Depth Profiling of Oxygen in Amorphous Germanium Films by Secondary Ion Mass Spectrometry", *Thin Solid Films*, **65**, 209 (1980).
 186. Naundorf, V., and Macht, M.P., "Surface Roughening of Copper by Low Energy Ion Bombardment", *Nucl. Instrum. & Methods*, **168**, 405 (1980).
 187. Nelson, A., and Green, A.K., "Method to Control Specimen Charging for SIMS and AES of Insulators", *J. Vac. Sci. & Technol.*, **17**, 855 (1980).
 188. Newbury, D.E., "Methods for Quantitative Analysis in Secondary Ion Mass Spectrometry", *Scanning*, **3**, 110 (1980).
 189. Newbury, D.E., "The Impact of Instrumental Sensitivity Variations on Analysis with the Local Thermal Equilibrium Model in Secondary Ion Mass Spectrometry", *Electron Microscopy*, Vol. 3, P. Brederoo and V.E. Cosslett Eds., (Leiden, The Netherlands: 7th European Congr. on Electron Microscopy Foundation, 1980) p. 212.
 190. Nissim, Y.I., Gibbons, J.F., Evans, C.A., Jr., Deline, V.R., and Norberg, J.C., "Thermal Diffusion of Tin in GaAs from a Spin-on SnO₂/SiO₂ Source", *Appl. Phys. Lett.*, **37**, 89 (1980).
 191. Oi, T., "Retarded Deposition of Li₃N Thin Films on WO₃ Substrates", *Appl. Phys. Lett.*, **37**, 244 (1980).
 192. Okajima, Y., "Estimation of Sputtering Rate by Bombardment with Argon Gas Ions", *J. Appl. Phys.*, **51**, 715 (1980).
 193. Okutani, T., Shikata, M., Ichimura, S., and Shimizu, R., "Angular Distribution of Si Atoms Sputtered by KeV Ar⁺ Ions", *J. Appl. Phys.*, **51**, 2884 (1980).
 194. Ota, Y., "Silicon Molecular Beam Epitaxy with Simultaneous Ion Implant Doping", *J. Appl. Phys.*, **51**, 1102 (1980).
 195. Pankove, J.I., Wu, C.P., Magee, C.W., and McGinn, J.T., "Laser Annealing of Hydrogenated Amorphous Silicon", *J. Electron. Mat.*, **9**, 905 (1980).
 196. Patkin, A.J., Furman, B.K., and Morrison, G.H., "Three-Dimensional SIMS Analysis by Image Depth Profiling", *Microbeam Analysis*, D.B. Wittry, Ed., (San Francisco, CA: San Francisco Press, Inc., 1980) p. 181.
 197. Pena, J.L., Farias, M.H., and Sanchez Sinencio, F., "Implantation of 100 KeV H⁺ in MoO₃ and TiO₂ as Determined by SIMS", *Surf. Sci.*, **100**, L440 (1980).
 198. Perinet, F., Barbezat, S., and Monty, C., "New Investigation of Oxygen Self-Diffusion in Cu₂O", *J. Phys. Colloq.*, **41**, C-6, p. C6/315, 1980.
 199. Phillips, B.F., and Gerlach, R.L., "The SIMS II: A New Approach to SIMS Analysis", *Microbeam Analysis*, D.B. Wittry, Ed., (San Francisco, CA: San Francisco Press, Inc., 1980) p. 85.
 200. Pivin, J.C., Delaunay, D., Roques-Carmes, C., Huntz, A.M., and Lacombe, P., "Oxidation Mechanism of Fe-Ni-20-25Cr-5Al Alloys - Influence of Small Amounts of Yttrium on Oxidation Kinetics and Oxide Adherence", *Corros. Sci.*, **20**, 351 (1980).
 201. Pivin, J.C., Roques-Carmes, C., and Slodzian, G., "Variation of Secondary Ion Emission Yield with Atomic Concentrations of Fe, Ni and Cr Ternary Alloys and Oxides: Application to the Analysis of Thin Oxide Films", *J. Appl. Phys.*, **51**, 4158 (1980).
 202. Pokhodnya, I.K., Ustinov, V.G., and Shvachko, V.I., "Influence of Phase Transformations in Iron-Nitrogen Alloys on Secondary Ion-Ion Emission", *Fiz. Met. & Metalloved.*, **49**, 418 (1980).
 203. Polaschegg, H.D., "Surface Analysis of Thin Films. I. A Survey", *Finomtech. Mikrotech.*, **19**, 23 (1980).
 204. Polaschegg, H.D., "Surface Analysis of Thin Films - A Survey. II", *Finomtech. Mikrotech.*, **19**, 42 (1980).
 205. Powell, C.J., "Recent Progress in Quantification of Surface Analysis Techniques", *Appl. Surf. Sci.*, **4**, 492 (1980).
 206. Pregesbauer, F., Rudenauer, F.G., and Steiger, W., "Neutron Dose Determination in Stainless Steel by Mass Spectrometric Measurement of Stable-Isotope Abundance Ratios", *SASP Symposium on Atomic and Surface Physics 80*, Salzburg, Austria, Feb. 1980 (Innsbruck, Austria: Institut fur Atomphysik der Universitat Innsbruck 1980), p. 140.
 207. Rauschenbach, B., and Blasek, G., "Investigations of Near Region of Surface of Soda-Lime-Silica Glass and Lithium-Silica Glass with Secondary Ion Mass Spectrometry", *Appl. Phys.*, **22**, 233 (1980).
 208. Reed, D.J., and Wuensch, B.J., "Ion-Probe Measurement of Oxygen Self-Diffusion in Single-Crystal Al₂O₃", *J. Am. Ceram. Soc.*, **63**, 88 (1980).
 209. Reed, S.J.B., "Trace Element Analysis with the Ion Probe", *Scanning*, **3**, 119 (1980).
 210. Reid, I., Thompson, M.W., and Farmery, B.W., "Focused Ejection from Ion-Bombarded Gold Crystals", *Philos. Mag. A*, **42**, 151 (1980).
 211. Reid, I., Thompson, M.W., and Farmery, B.W., "Atomic Collision Processes in Sputtering", *Rad. Eff.*, **46**, 163 (1980).
 212. Reuter, W., and Wittmaack, K., "An AES-SIMS Study of Silicon Oxidation Induced by Ion or Electron Bombardment", *Appl. Surf. Sci.*, **5**, 221 (1980).
 213. Reuter, W., Yu, M.L., Frisch, M.A., and Small, M.B., "Charging Effects in the Secondary Ion Mass Spectrometric Analysis of Targets Containing Low-Conductivity Regions", *J. Appl. Phys.*, **51**, 850 (1980).
 214. Rieder, K.H., "On the Interaction of Oxygen with Nb (110) and Nb (750)", *Appl. Surf. Sci.*, **4**, 183 (1980).
 215. Riviere, J.C., "Effect of Ion Bombardment Conditions on the Chemical Profile through the Surface of Tinplate", *Mat. Sci. & Eng.*, **42**, 49 (1980).
 216. Roques-Carmes, C., Ducrocq, C., and da Cunha Belo, M., "Secondary Ion Emission Study of Chlorine Distribution in Oxide Films Formed on Stainless Steels in MgCl₂ Solution", *J. Microsc. & Spectrosc. Electron.*, **5**, 251 (1980).

217. Roth, J., Bohdansky, J., and Martinelli, A.P., "Low Energy Light Ion Sputtering of Metals and Carbides", *Rad. Eff.*, 48, 213 (1980).
218. Russell, D.H., Smith, D.H., Warmack, R.J., and Bertram, L.K., "The Design and Performance Evaluation of a New High-Performance Mass-Analyzed Ion Kinetic Energy (MIKE) Spectrometer", *Int. J. Mass Spectrom. & Ion Phys.*, 35, 381 (1980).
219. Sadana, D.K., Strathman, M., Washburn, J., Magee, C.W., Maenpaa, M., and Booker, G.R., "Effect on Electrical Properties of Segregation of Implanted P^+ at Defect Sites in Si", *Appl. Phys. Lett.*, 37, 615 (1980).
220. Saint-Jacques, R.G., Veilleux, G., and Terreault, B., "Correlation of Swelling with Local Gas Concentration in Helium Irradiated Niobium", *Nucl. Instrum. & Methods*, 170, 461 (1980).
221. Satkiewicz, F.G., "Secondary Ion Mass Spectrometry for the Study of Solids", *Johns Hopkins APL Tech. Dig.*, 1, 45 (1980).
222. Scharager, C., Stuck, R., Siffert, P., Cailleret, J., Heitz, Ch., Lagarde, G., and Tenorio, D., "Trace Analysis in Cadmium Telluride by heavy Ion Induced X-Ray Emission and SIMS", *Nucl. Instrum. & Methods*, 168, 367 (1980).
223. Scherrer, H., Weber, S., and Scherrer, S., "Diffusion of ^{125}Te in Tin Telluride", *Phys. Lett. A*, 77, 189 (1980).
224. Scilla, G.J., LaForce, R.W., and Fowler, A.B., "Correction for SIMS Matrix Effects in the Analysis of High As(75%)Se Alloys", *Microbeam Analysis*, D.B. Wittry, Ed., (San Francisco, CA: San Francisco Press, Inc., 1980) p. 59.
225. Seguin, R., and Brebec, G., "Study of the Silicon Diffusion in Amorphous Silica by Secondary Ion Mass Spectrometry", *J. Microsc. & Spectrosc. Electron.*, 5, 243 (1980).
226. Sickafus, E.N., "Surface Analysis - A Mixed Bag of Tricks", *Ind. Res./Dev.*, 22, 126 (1980).
227. Sigmon, T.W., Deline, V.R., Evans, C.A., Jr., and Katz, W.M., "Anomalous Boron Profiles Produced by BF_2 Implantation Into Silicon", *J. Electrochem. Soc.*, 127, 981 (1980).
228. Sigmund, P., "Sputtering of Single and Multiple Component Materials", *J. Vac. Sci. & Tech.*, 17, 396 (1980).
229. Sigmund, P., and Gras-Marti, A., "Distortion of Depth Profiles During Sputtering. I. General Description of Collisional Mixing", *Nucl. Instrum. & Methods*, 168, 389 (1980).
230. Simondet, F., Venger, C., Martin, G.M., and Chaumont, J., "Distribution and Heat-Treatment Migration Studies of Cr Implanted GaAs by SIMS", *Appl. Phys.*, 23, 21 (1980).
231. Simons, D.S., "Ion Microprobe, Ion Microscope and Laser Microprobe Mass Analysis of Particulates", *Microbeam Analysis*, D.B. Wittry, Ed., (San Francisco, CA: San Francisco Press, Inc., 1980) p. 178.
232. Slusser, G.J., and Winograd, N., "SIMS/XPS Study of CO Chemisorption on Polycrystalline Pd, Ag and a PdAg Alloy", *Surf. Sci.*, 95, 53 (1980).
233. Small, M.B., Ghez, R., Potemski, R.M., and Reuter, W., "The Dissolution Kinetics of GaAs in Under-saturated Isothermal Solutions in the Ga-Al-As System", *J. Electrochem. Soc.*, 127, 1177 (1980).
234. Smith, D.H., Christie, W.H., and Eby, R.E., "The Resin Bead as a Thermal Ion Source: A SIMS Study", *Int. J. Mass Spectrom. & Ion Phys.*, 36, 301 (1980).
235. Smith, R., and Walls, J.M., "The Development of a General Three-Dimensional Surface under Ion Bombardment", *Philos. Mag. A*, 42, 235 (1980).
236. Snowden, K.J., "A New Technique to Study the Stages of Oxidation of Metals Using Oxidation Induced Changes in the Shape of Secondary Ion Energy Spectra", *Corros. Sci.*, 20, 53 (1980).
237. Sockel, H.G., Hallwig, D., and Schachtner, R., "Investigations of Slow Exchange Processes at Metal and Oxide Surfaces and Interfaces Using Secondary Ion Mass Spectrometry", *Mat. Sci. & Eng.*, 42, 59 (1980).
238. Spitzer-Aronson, M., "Layers and Profiles of SiOH, CaOH and KOH Polyatomic Ion Groups Found in the Glass, as an Effect of a Special Corrosion", *J. Non-Cryst. Solids*, 38, 613 (1980).
239. Spurr, A.R., "Applications of SIMS in Biology and Medicine", *Scanning*, 3, 97 (1980).
240. Sroubek, Z., "Analysis of Semiconductor Surfaces and Interfaces", *Czech. J. Phys. Sect. B*, 30, 375 (1980).
241. Sroubek, Z., Zdansky, K., and Zavadil, J., "Ionization of Atomic Particles Sputtered from Solids", *Phys. Rev. Lett.*, 45, 580 (1980).
242. Sroubek, Z., Zavadil, J., Zdansky, K., and Kubec, F., "Mass Spectrometry of Secondary Ions - A Promising Method for Investigating the Physico-Chemical Properties of Solid Substance Surfaces", *Slaboproudý Obz.*, 41, 319 (1980).
243. Steel, I., Hervig, R., and Hutcheon, I., "Quantitative Ion Microprobe Analysis of Mg, Fe Silicates", *Microbeam Analysis*, D.B. Wittry, Ed., (San Francisco, CA: San Francisco Press, Inc., 1980) p. 151.
244. Stika, K.M., Bielat, K.L., and Morrison, G.H., "Diffusible Ion Localization by Ion Microscopy: A Comparison of Chemically Prepared and Fast-Frozen, Freeze-Dried, Unfixed Liver Sections", *J. Microsc.*, 118, 409 (1980).
245. Stoddart, C.T.H., and Hunt, C.P., "Alloy Surface Composition Resulting from Fabrication, as Determined by s.i.m.s. (Secondary Ion Mass Spectrometry)", *Philos. Trans. R. Soc. London A*, 295, 134 (1980).
246. Sugano, T., "Oxide Film Growth on GaAs and Silicon Substrates by Anodization in Oxygen Plasma and its Application to Devices and Integrated Circuit Fabrication", *Thin Solid Films*, 72, 9 (1980).
247. Suzuki, T., Mimura, A., Kamei, T., and Ogawa, T., "Deformation in Dielectric-Isolated Substrates and Its Control by a Multilayer Polysilicon Support Structure", *J. Electrochem. Soc.*, 127, 1537 (1980).
248. Swingler, D.L., "A Cold-Cathode Ion Source for Mass Spectrometry", *Int. J. Mass Spectrom. & Ion Phys.*, 33, 57 (1980).
249. Taglauer, E., Heiland, W., and Onsgaard, J., "Ion Beam Induced Desorption of Surface Layers", *Nucl. Instrum. & Methods*, 168, 571 (1980).
250. Thompson, D.A., and Johar, S.S., "Sputtering of Silver by Heavy Atomic and Molecular Ion Bombard-

- ment", Nucl. Instrum. & Methods, 170, 281 (1980).
251. Toulemonde, M., Hage-Ali, M., Stuck, R., Siffert, P., Wald, F.V., and Bell, R.O., "Determination of Carbon in EFG Silicon Ribbons by Nuclear Techniques and SIMS", Nucl. Instrum. & Methods, 168, 415 (1980).
 252. Truchet, M., "Some New Data on the High Mass Resolution in the Histological Section Analysis by Ionic Analyser", J. Microsc. & Spectrosc. Electron., 5, 273 (1980).
 253. Tsong, I.S.T., Power, G.L., Hoffman, D.W., and Magee, C.W., "Edge-Effects Correction in Depth Profiles Obtained by Ion-Beam Sputtering", Nucl. Instrum. & Methods, 168, 399 (1980).
 254. Unger, S.E., Ryan, T.M., and Cooks, R.G., "Detection Limits for Organic Salts in Secondary Ion Mass Spectrometry", Anal. Chim. Acta, 118, 169 (1980).
 255. van Gorp, G.J., Slotboom, J.W., Smolders, F.J.B., Stacy, W.T., and Tamminga, Y., "Enhanced Diffusion of Implanted Arsenic and Boron in Silicon by Low-Temperature Heat-Treatment", J. Electrochem. Soc., 127, 1813 (1980).
 256. Van Veen, A., and Fluit, J.M., "Low Yield Sputtering of Monocrystalline Metals", Nucl. Instrum., & Methods, 170, 341 (1980).
 257. van Wyk, G.N., and Smith, H.J., "The Influence of Ion Bombardment Induced Preferential Orientation on the Sputter-Behavior of Cu", S. Afr. J. Phys., 3, 24 (1980).
 258. Vasil'ev, M.A., Goncharenko, A.B., Chenakin, S.P., and Cherepin, V.T., "Secondary Ion Emission Kinetics Characteristics", Metallofizika, Kiev, 2, 117 (1980).
 259. Vasiliiu, F., "Oblique Incidence Sputtering of Triangular Microprofiles", Rad. Eff., 45, 213 (1980).
 260. Vasudev, P.K., Wilson, R.G., and Evans, C.A., Jr., "Chromium Redistribution During Thermal Annealing of Semi-Insulating GaAs as a Function of Encapsulant and Implant Fluence", Appl. Phys. Lett., 36, 837 (1980).
 261. Vasudev, P.K., Wilson, R.G., and Evans, C.A., Jr., "Damage Gettering of Cr During the Annealing of Cr and S Implants in Semi-Insulating GaAs", Appl. Phys. Lett., 37, 308 (1980).
 262. Vrscaj, V., Kramer, V., Medved, M., Kralj, B., Marsel, J., Beynon, J.H., and Ast, T., "Modification of a Mattauch-Herzog Mass Spectrometer for Ion Kinetic Energy Measurements", Int. J. Mass Spectrom. & Ion Phys., 33, 409 (1980).
 263. Watson, C.C., and Haff, P.K., "Sputter-Induced Isotopic Fractionation at Solid Surfaces", J. Appl. Phys., 51, 691 (1980).
 264. Werner, H.W., "Modern Methods for Thin Film and Surface Analyses", Mat. Sci. & Eng., 42, 1 (1980).
 265. Werner, H.W., "New Developments in Secondary Ion Mass Spectrometry", Applied Surface Analysis, ASTM Spec. Tech. Publ. 699, T.L. Bair and L.E. Davis, Eds., (Philadelphia, PA: American Soc. for Testing and Materials, 1980) p. 81.
 266. Werner, H.W., "Modern Methods for Thin Film and Surface Analysis", Electron Microscopy, Vol. 3, P. Brederoo and V.E. Cosslett, Eds., (Leiden, The Netherlands: 7th European Congr. on Electron Microscopy Foundations, 1980) p. 200.
 267. White, C.W., Christie, W.H., Pronko, P.P., Appleton, B.R., Wilson, S.R., Young, R.T., Wang, J.C., Wood, R.F., Narayan, J., and Magee, C.W., "Dopant Profile Changes Induced by Pulsed Laser Annealing", Rad. Eff., 47, 37 (1980).
 268. Whitton, J.L., Holck, O., Carter, G., and Nobes, M.J., "The Crystallographic Dependence of Surface Topographical Features Formed by Energetic Ion Bombardment of Copper", Nucl. Instrum. & Methods, 170, 371 (1980).
 269. Williams, M.M.R., "The Intensity of Sputtered Atoms from a Half-Space and Its Dependence on the Angle of Incidence", Rad. Eff. Lett., 57, 5 (1980).
 270. Williams, P., "Anomalous Sputter Yields Due to Cascade Mixing", Appl. Phys. Lett., 36, 758 (1980).
 271. Williams, P., and Baker, J.E., "Quantitative Analysis of Interfacial Impurities Using Secondary Ion Mass Spectrometry", Appl. Phys. Lett., 36, 842 (1980).
 272. Williams, P., Katz, W., and Evans, C.A., Jr., "Towards a Universal Model for Sputtered Ion Emission", Nucl. Instrum. & Methods, 168, 373 (1980).
 273. Williams, P., Tsong, I.S.T., and Tsuji, S., "A Comparison of Absolute Yields of Excited Neutrals and Positive Ions from Ion-Bombarded Surfaces", Nucl. Instrum. & Methods, 170, 591 (1980).
 274. Wilson, R.G., Vasudev, P.K., Jamba, D.M., Evans, C.A., Jr., and Deline, V.R., "Chromium Concentrations, Depth Distributions, and Diffusion Coefficient in Bulk and Epitaxial GaAs and in Si", Appl. Phys. Lett., 36, 215 (1980).
 275. Wilson, R.G., and Deline, V.R., "Ion Channeling in GaAs:Si, S, Se and Te", Appl. Phys. Lett., 37, 793 (1980).
 276. Wilson, R.G., and Comas, J., "Correlation of Atomic Distribution and Implantation Induced Damage Profiles in Be-Ion Implanted Si", Rad. Eff., 47, 137 (1980).
 277. Wittmaack, K., and Clegg, J.B., "Dynamic Range of 10^6 In-Depth Profiling Using Secondary-Ion Mass Spectrometry", Appl. Phys. Lett., 37, 285 (1980).
 278. Wittmaack, K., "Aspects of Quantitative Secondary Ion Mass Spectrometry", Nucl. Instrum. & Methods, 168, 343 (1980).
 279. Wittmaack, K., "Comparison of Ion-Excited Auger Electron Emission and Secondary Ion Emission from Silicon Bombarded with Noble Gas Ions", Nucl. Instrum. & Methods, 170, 565 (1980).
 280. Wittmaack, K., "Time-of-Flight Effects in Quadrupole-Based Scanning Ion Microprobes", Scanning, 3, 133 (1980).
 281. Wittry, D.B., "Spectroscopy in Microscopy and Microanalysis, The Search for an Ultimate Analytical Technique", Electron Microscopy, Vol. 3, P. Brederoo and V.E. Cosslett, Eds., (Leiden, The Netherlands: 7th European Congr. on Electron Microscopy Foundation, 1980) p. 14.
 282. Wright, R.B., and Gruen, D.M., "Discussion of the Origin of Secondary Photon and Secondary Ion Emission During Energetic Particle Irradiation of Solids. I. The Collision Cascade", J. Chem. Phys., 72, 147 (1980).
 283. Ximen, J.Y., "The Ion Optical Properties and Second Order Aberration of the Crossed Toroidal

- Electric and Inhomogeneous Magnetic Fields as a Mass Spectrometer", *Acta Phys. Sin.*, 29, 330 (1980).
284. Yamasaki, K., and Sugano, T., "Mechanism of Oxide Film Growth on GaAs by Plasma Anodization", *J. Vac. Sci. & Technol.*, 17, 959 (1980).
285. Yin, S.Y., "Eighteen Years of Secondary Ion Mass Spectrometry: A Bibliography of SIMS, 1958-1975", *Microbeam Analysis*, D.B. Wittry, Ed., (San Francisco, CA: San Francisco Press, Inc. 1980) p. 289.
286. Yu, M.L., and Reuter, W., "Matrix Effect in SIMS Analysis Using an O_2^+ Primary Beam", *J. Vac. Sci. & Tech.*, 17, 36 (1980).
287. Zelenskii, Y.F., Morozov, A.N., and Rekova, L.P., "The Effect of Helium Ion Irradiation on Nickel-Oxygen Interaction", *Ukr. Fiz. Zh.*, 25, 1502 (1980).
288. Zinner, E., "Depth Profiling by Secondary Ion Mass Spectrometry", *Scanning*, 3, 57 (1980).

Author Index

- | | | | |
|-----------------------|-------------------------|----------------------|---------------------|
| Abraham, 226 | Garratt-Reed, 241 | Lindfors, 303 | Riga, 265 |
| Abrecht, 160 | Gause, 237 | Lusk, 49 | Romig, 249 |
| Adar, 67 | Gay, 229 | Lyman, 261 | Rosencwaig, 105 |
| Albee, 143 | Geiss, 119 | McCarthy, 30, 57 | Rosensteil, 229 |
| Alben, 222 | Glitz, 309 | McConville, 206 | Rucklidge, 299 |
| Annamalai, 171 | Goetze, 45 | McElfresh, 276 | Russ, 186 |
| Beall, 24, 109 | Goldstein, 309 | McGuire, 35 | Schreiber, 313, 317 |
| Bence, 151 | Goo, 265 | Marchiando, 123 | Sedwick, 119 |
| Berry, 171 | Gorlen, 320 | Méranger, 53 | Shpirt, 222 |
| Black, 303 | Gorton, 229 | Miller, E. L., 113 | Silva, 113 |
| Blaha, 61 | Gumz, 258 | Miller, N. C., 178 | Smith, 35 |
| Bonventre, 213 | Hamilton, 45 | Milliken, 174 | Solberg, 155, 160, |
| Boyes, 333 | Hanchett, 119 | Mitchell, G. D., 148 | 163 |
| Brown, 174 | Hannsen, 269 | Mitchell, M., 167 | Speer, 155 |
| Chambers, 43 | Hare, 186 | Morris, 9 | Stott, 53 |
| Chatfield, 53 | Hausdorff, 91 | Myers, 210 | Swyt, 320 |
| Chodos, 143 | Hembree, 123 | Myklebust, 61, 175 | Titchmarch, 333 |
| Coleman, 203 | Hewitt, 160 | Nabelek, 151 | Van, 210 |
| Couch, 49 | Hopkins, 131 | Navapbour, 45 | Vander Sande, 241 |
| Craig, 163 | Howitt, 276 | Newbury, 1, 175 | Van Duin, 229 |
| Davidson, 17, 237 | Imeson, 241 | Nichols, 215 | Votava, 283 |
| De Groot, 195 | Ingram, F. D., 215, 219 | Notis, 309 | Wade, 203 |
| Demoncy, 96 | Ingram, M. J., 215, 219 | Othmer, 131 | Waitzkin, 226 |
| DeNatala, 273 | Jensen, 123 | Packwood, 174 | Walsh, 258 |
| Depp, 119 | Justi, 265 | Park, 65 | Warner, 210 |
| Doyle, 79 | Katz, 287 | Parker, 190, 199 | Watari, 279 |
| Echols, 109 | Kerr, 333 | Peercy, 79 | Wells, 127 |
| Etz, 61, 73 | Kilius, 299 | Perrins, 222 | Williams, 309 |
| Evans, C. A. Jr., 336 | Kirkendall, 269 | Piety, 113 | Wilson, 109 |
| Evans, K. C., 113 | Konopka, 183 | Quick, 143 | Wims, 313, 317 |
| Fiori, 320 | Krohn, 296 | Rabito, 213 | Wing, 79 |
| Friel, 148 | Landau, 265 | Ramsey, 91 | Wittry, 339, 342 |
| Fritz, 30, 57 | Langmuir, 151 | Reed, 87 | Yin, 342 |
| Furman, 336 | Lechene, 49 | Rez, 183 | Young, 203 |
| Gantz, 49 | Lee, 30, 57 | Ridley, 139 | Zaluzec, 325, 329 |